Development of Detectors and Simulation Methods for Measurement of Hadrons from Neutrino Interactions

Toby Nonnenmacher
of Imperial College London, Department of Physics

A dissertation submitted to the Imperial College London
for the degree of Doctor of Philosophy

Abstract

As neutrino physics enters the precision era, the need for more data and better interpretation of those data grows ever more crucial. Building new detectors with improved sensitivity that can make novel kinematic measurements underpins the drive for more data and allowing data to be used to best effect in particle physics analyses requires constant improvement on the understanding of neutrino physics models and their implementation in simulation.

This thesis describes both work on a new neutrino detector with sensitivity to low momentum hadrons from neutrino interactions, and development of the NEUT interaction generator for providing better handling of the final state interactions of such hadrons.

Described herein, a prototype high pressure time projection chamber with optical and charge readout was built, commissioned, and operated at a beam test at the T10 beamline at the European Organization for Nuclear Research (CERN). A characterisation of the beam is presented based on simulation and analysis of two time of flight systems, as well as a description of techniques used for analysing the time projection chamber optical readout. This thesis also includes development of variable parameters governing nucleon final state interactions in the NEUT generator used by the Tokai to Kamiokande (T2K) experiment. A method of reweighting was produced to allow the use of these parameters in analyses, and extensive validations of this method are presented.

Declaration

This dissertation is the result of my own work. Where figures and results are taken from other sources this is indicated by an appropriate reference. Some figures referenced as from other sources were created by me, but appear in other public documents.

The analysis described in Chapters 5 and 6 was the joint work in equal measure of myself and Seb Jones. These chapters follow the structure of [1], a paper on which Seb Jones and I are primary authors out of 35 authors in total. Specifically, I produced all the simulations for comparison to data, while Seb determined the systematic uncertainties on the time of flight systems. The data were collected at the CERN beam test at which Seb and I both took shifts operating the detectors, and many of the plots shown are the result of our collaborative work. In addition to the analysis of beam test data, my work on the prototype high pressure time projection chamber was broad. I worked extensively on hardware, building and commissioning the HPTPC with other students from Imperial College London and Royal Hollow, University of London. I also was the sole student working on simulation of the prototype, which informed the experimental setup chosen for the CERN beamtest. I have additionally worked on the handling and analysis of camera images from the HPTPC prototype readout, including producing a clustering algorithm, together with Will Parker, Abbey Waldron, and Patrick Dunne.

The simulation work described in Chapter 7, was entirely my own work, and I was solely responsible for producing all figures shown in this chapter. I reported on this work continuously to the T2K Neutrino Interactions Working Group. I took shifts both at the T2K near detector, and at SK during the period of open tank work.

As well as the work described in this thesis I also worked for 9 months on a project working on a Gabor Lens as a prototype for use in future laser accelerated beams in proton cancer therapy, in a working group of three physicists. We operated the lens in a beam test at the Surrey Ion Beam Centre; I wrote up analysis of the data from that beam test in a paper on which I am first author out of five authors, which is currently in preparation. This work is not presented in this thesis, because it is not thematically linked to my other work.

Toby Nonnenmacher

Copyright Declaration

"The copyright of this thesis rests with the author. Unless otherwise indicated, its contents are licensed under a Creative Commons Attribution-Non Commercial 4.0 International Licence (CC BY-NC).

Under this licence, you may copy and redistribute the material in any medium or format. You may also create and distribute modified versions of the work. This is on the condition that: you credit the author and do not use it, or any derivative works, for a commercial purpose.

When reusing or sharing this work, ensure you make the licence terms clear to others by naming the licence and linking to the licence text. Where a work has been adapted, you should indicate that the work has been changed and describe those changes.

Please seek permission from the copyright holder for uses of this work that are not included in this licence or permitted under UK Copyright Law."

Toby Nonnenmacher

Acknowledgements

I owe a great deal of thanks to a number of people, without whom this thesis could not have been written:

I would first like to thank Morgan Wascko, my supervisor, for his support throughout my PhD and the comments on this thesis, and to Patrick Dunne, my assistant supervisor, for all the help he has given me over the last 4 years.

I would particularly like to thank Seb Jones for his equal share in the HPTPC analysis and paper writing. I would also like to give a very special word of thanks to Dom Brailsford and Clarence Wret for their many hundreds of hours of hands-on help without which this PhD would never have been completed.

Thanks are due to Will Parker and Ed Atkin for keeping me sane and entertained from the office to Egham, Tokai to Geneva. I'd like to thank the denizens of Blackett 530: Abbey Waldron, Wilf Shorrock, Artur Sztuc, and Charlie Naseby, as well as Callum Wilkinson for the good times and rounds of tea, and our adventures various in the office and abroad.

For their help and supervision, I would like to thank Mark Scott, Jocelyn Munroe, Yoshi Uchida, and Phill Litchfield. For all the work we did together at Royal Holloway and at CERN, I would like to thank Asher Kaboth, Alexander Desiting, Adriana Dias, Jen Haigh, Sammy Valder, and Harison Ritchie-Yates. I would also like to thank the NIWG conveners for their support, in particular to Luke Pickering and Yoshinari Hayato for their extensive help and experience, and to Stephen Dolan as well as Luke for taking on the task of making my work available to the collaboration now that I have finished. Cheers to Felix Kress, Rob Taylor, Nellie Marangou, and the rest of my coursemates for the fun times we enjoyed at Imperial, and to all my friends in T2K UK for all the joy and karaoke abroad.

Finally thanks to all my friends and family outside physics who have supported me over the last four years, including my parents, Dorothy and Peter, my sister, Hannah,

to Kyle, Helen, JR, and above all to Isi, not least for putting up with me while I was writing up during lockdown; apologies to her and our downstairs neighbours for all the pacing.

Contents

1. Introduction **1**

2. Neutrino Physics **3**

2.1. Discovery of the three known neutrinos 3

2.2. Neutrino oscillation 4

2.2.1. Matter effects 6

2.3. Experimental overview of oscillation physics 7

2.3.1. Solar neutrino experiments 8

2.3.2. Atmospheric neutrinos 10

2.3.3. Accelerator-based neutrino oscillation experiments 12

3. Experimental Layout and Detectors **15**

3.1. The Tokai to Kamiokande Experiment 15

3.1.1. Beamline 16

3.1.2. ND280 19

3.1.3. INGRID 21

3.1.4. Super Kamiokande 23

3.1.5. Neutrino interaction simulation 25

3.2. The High Pressure Time Projection Chamber 26

3.2.1. HPTPC: motivation in neutrino physics 26

3.3. The HPTPC prototpye 28

3.3.1. The HPTPC prototype: the vessel 29

3.3.2. Gas system 31

3.3.3. Time Projection Chamber and readout 31

3.3.4. High-voltage distribution system 33

3.3.5. Charge signal measurement 34

3.3.6. Optical signal measurement 34

3.4. Time of Flight systems 37

3.4.1. Upstream Time of Flight 38

3.4.2. Downstream Time of Flight 42

4. Theory **45**
4.1. Neutrino interactions 45
4.1.1. Interaction with a free nucleon 45
4.1.2. Interaction with a nucleus 47
4.2. Particle mean free path 47
4.3. The nucleon cascade in NEUT 49
4.4. Reweighting 50

5. Beam Test **53**
5.1. Beam test motivation 53
5.2. Initial beam test simulations 55
5.3. Composition of the beam test 60
5.3.1. Survey and coordinate system 62

6. Test Beam Flux Measurements **65**
6.1. Time of Flight analysis 65
6.2. Beam flux measurement 75
6.2.1. Flux measurements with S3 75
6.2.2. Flux measurements with S4 77
6.2.3. Monte Carlo studies 80
6.3. CCD analysis 84
6.3.1. Calibration sources 84
6.3.2. Clustering algorithm 85

7. Nucleon FSI in NEUT **89**
7.1. The nucleon cascade in NEUT 89
7.1.1. Introduction of nucleon dials to NEUT 89
7.2. Reweighting the nucleon dials 97
7.2.1. Previous reweighting attempts 97
7.2.2. The novel reweighting process 97
7.2.3. Validations of the reweighting 98
7.2.4. Limitations of reweighting 106
7.2.5. Comparisons of speed of reweighting and regeneration 109

8. Conclusions and Outlook **111**

A. Validation plots **113**
A.1. Total Dial: varied up to 1.44 114
A.2. Total Dial: varied down to 0.64 133
A.3. Elastic Dial: varied up to 1.44 152
A.4. Elastic Dial: varied down to 0.64 171
A.5. Single Pion Dial: varied up to 1.44 190
A.6. Single Pion Dial: varied down to 0.64 209
A.7. Double Pion Dial: varied up to 1.44 228
A.8. Double Pion Dial: varied down to 0.64 247

Bibliography **267**

List of figures **275**

List of tables **285**

Acronyms **287**

"Everything starts somewhere, although many physicists disagree."

— Terry Pratchett

Chapter 1.

Introduction

In the ninety years since its theoretical proposal, the neutrino has been a source of great interest to the physics community. Now, the physics of neutrino oscillation enters the precision era, and the next generation of higher statistics experiments are in development. The ability to answer questions such as "how do neutrinos and antineutrinos differ?" and "what is the correct ordering of the neutrino mass states?" hinges both on the ability to build new detectors with never before seen sensitivity to new regions of physics, and on the ability to use the data gathered by these detectors to inform modelling and simulation.

This work concerns related examples in both of these areas; I was central to the building, simulating, and commissioning of a new detector prototype capable of making measurements of secondary recoil protons in the largely uncharted low momentum region. This prototype was operated at a beam test, and I analysed the resultant low momentum beam data. The possible impact of a detector with sensitivity to low momentum hadrons is pivotal in improving modelling of neutrino interactions. These models underpin simulations used by neutrino oscillation experiments in evaluating systematic uncertainty in analysis of their data. I implemented and validated the capacity to include low momentum hadron data in one such neutrino event generator and worked on making these changes available to all data analyses on the T2K experiment. These areas of work are described in the following chapters.

In this thesis, a brief overview of the history of neutrino physics is presented in Chapter 2. The relevant detectors and their experimental layouts are described in Chapter 3. Chapter 4 explores the theory underlying neutrino physics and Monte Carlo methods, and the 2018 detector prototype beam test is described in Chapter 5. The analysis of the beamtest data is provided in Chapter 6. Simulation work on final state

interactions of nucleons is reported in Chapter 7. Finally, conclusions are presented in Chapter 8.

Chapter 2.

Neutrino Physics

2.1. Discovery of the three known neutrinos

The neutrino was discovered in 1953 in Reines and Cowan's experiments observing inverse beta decays near a nuclear reactor [2]. The experiment was composed of two water tanks in between liquid scintillator tanks filled with photomultiplier tubes (PMTs). Electron anti-neutrinos emitted by the reactor with a neutrino flux of 5×10^{13} s^{-1}cm^{-2} interacted in the water with protons to produce a detectable two photon (γ) signal from the annihilation of electrons with positrons. The water was doped with cadmium chloride to aid detection of free neutrons through the process of $n + {}^{108}\mathrm{Cd} \rightarrow {}^{109\mathrm{m}}\mathrm{Cd} \rightarrow {}^{109\mathrm{m}}\mathrm{Cd} + \gamma$ several microseconds after the 2γ annihilation signal. This result was compared with similar measurements taken while the reactor was off, to demonstrate an increase in the rate of events due to neutrinos.

Two decades prior to that initial experimental discovery, neutrinos had been proposed as a "desperate remedy" to the problem of apparent energy nonconservation in radioactive decay by Pauli [3]. In 1933, Fermi named this particle the neutrino in his theory of β decay in which the products of the process $n \rightarrow p + e^-$ additionally include an invisible four-momentum carrier (the electron anti-neutrino) [4].

Further to the experiments of Reines and Cowan, Davis performed experiments in 1964 exposing tanks of ${}^{37}\mathrm{Cl}$ to reactor electron anti-neutrinos in the Homestake Gold Mine in South Dakota [5]. The reaction process of $\nu_e + {}^{37}\mathrm{Cl} \rightarrow e^- + {}^{37}\mathrm{Ar}$ produced atoms of ${}^{37}\mathrm{Ar}$ which could be removed by bubbling Helium through the tank, and used to count the number of neutrino interactions. Thus the experiment placed limits on the flux of solar neutrinos.

In 1962, Lederman, Schwartz, Steinberger, and others observed a second type of neutrino, using a beam of protons striking a target to create a pion beam [6]. These pions decayed through $\pi^+ \rightarrow \mu^+ + \nu_\mu$, after which further interactions of the ν_μ were sought in a 10 tonne aluminium spark chamber; similar experiments were performed at the European Organization for Nuclear Research (CERN) for confirmation in 1964 [7].

Following the discovery of the τ lepton at the e^+e^- accelerator at the Stanford Linear Accelerator (SLAC) in 1975 [8], the search for the tau neutrino began — only for the particle to be discovered at DONUT in 2000 [9]. This discovery was heralded by Z decay measurements at SLAC and the Large Electron-Positron collider (LEP), which determined the number of different types of neutrino (with a mass less than that of the Z boson) to be $N_\nu = 2.9840 \pm 0.0082$ [10].

The discovery of the τ neutrino at DONUT completed the discovery of the three known neutrinos. These different types of neutrinos are referred to as having a "flavour", one each corresponding to the charged leptons — electron, muon, and tauon. However due to the scarcity of neutrino interactions, much remained unknown about the properties of these relatively newly discovered particles.

2.2. Neutrino oscillation

The neutrino is considered massless in the Standard Model of Particle Physics, but there is now overwhelming evidence that the neutrinos have a small non-zero mass [11] [12] [13] [14]. This evidence comprises observation of flavour change in neutrinos produced in nuclear reactions in the Sun, cosmic ray interactions, and man-made reactors and accelerator neutrino beams. Neutrinos from these sources have been observed to change flavour as a function of production flavour, energy, and distance travelled between production and observation. This process, neutrino oscillation, has been firmly established, but individual parameters underlying the process have been constrained to different degrees. An overview of these parameters and the theory underlying neutrino oscillations is provided in this section. A review of some of the major experiments that contributed to the experimental discovery of neutrino oscillation is given in section 2.3.

Oscillation occurs because the three neutrino flavour eigenstates, ν_e, ν_μ, and ν_τ are not identical to the mass eigenstates which propagate between interaction vertices, ν_1, ν_2,

and ν_3. The relationship between these states is described by the Pontecorvo-Maki-Nakagawa-Sakata (PMNS) matrix, expressed as:

$$\begin{pmatrix} \nu_e \\ \nu_\mu \\ \nu_\tau \end{pmatrix} = \underbrace{\begin{bmatrix} U_{e1} & U_{e2} & U_{e3} \\ U_{\mu 1} & U_{\mu 2} & U_{\mu 3} \\ U_{\tau 1} & U_{\tau 2} & U_{\tau 3} \end{bmatrix}}_{\mathbf{M_{PMNS}}} \begin{pmatrix} \nu_1 \\ \nu_2 \\ \nu_3 \end{pmatrix} \tag{2.1}$$

This unitary matrix can be parameterised in terms of three real angles θ_{12}, θ_{13}, and θ_{23}, and one complex phase, δ_{cp} as:

$$\mathbf{M_{PMNS}} = \begin{bmatrix} 1 & 0 & 0 \\ 0 & C_{23} & S_{23} \\ 0 & -S_{23} & C_{23} \end{bmatrix} \begin{bmatrix} C_{13} & 0 & S_{13}e^{-i\delta_{cp}} \\ 0 & 1 & 0 \\ -S_{13}e^{+i\delta_{cp}} & 0 & C_{13} \end{bmatrix} \begin{bmatrix} C_{12} & S_{12} & 0 \\ -S_{12} & C_{12} & 0 \\ 0 & 0 & 1 \end{bmatrix} \tag{2.2}$$

where $C_{ij} = cos\theta_{ij}$ and $S_{ij} = sin\theta_{ij}$. The angles in this equation are the neutrino mixing angles, where θ_{12} is referred to as "solar", θ_{23} as "atmospheric", and θ_{13} as "reactor", respectively, based on the sources which provide sensitivity to measuring that angle. The probability of observing an initial muon neutrino of energy E_ν travelling through a vacuum as an electron neutrino a distance L later is:

$$\begin{aligned} P_{\substack{(-) \\ \nu_\mu \to \nu_e}}^{(-)}(L,E) = &-4\sum_{i<j}^{3} Re\left[U_{\mu i}U_{ei}^{*}U_{\mu j}^{*}U_{ej}\right] sin^2(\Delta m_{ij}^2 \frac{L}{4E_\nu}) \\ &\mp 2\sum_{i<j}^{3} Im\left[U_{\mu i}U_{ei}^{*}U_{\mu j}^{*}U_{ej}\right] sin(\Delta m_{ij}^2 \frac{L}{2E_\nu}) \end{aligned} \tag{2.3}$$

where $\Delta m_{ij}^2 = m_i^2 - m_j^2$ is the difference in mass squared of the neutrino mass states. The probability for the anti-neutrino case differs only by a sign in the second term of the equation. The derivation of these oscillation probabilities is provided in [15]. The probability for a neutrino produced in one flavour state to subsequently be observed in another is therefore sinusoidally dependent on $\frac{L}{E_\nu}$, giving rise to use of the term

"oscillation". In the theoretical case of two mass states (with a third state being degenerate), equation 2.3 may be reduced to:

$$P_{\nu_\alpha \leftrightarrow \nu_\beta, \alpha \neq \beta} = sin^2(2\theta) sin^2(\frac{\Delta m^2 L}{4E}) \tag{2.4}$$

This equation well approximates oscillation of $\nu_\mu \leftrightarrow \nu_\tau$, in which the electron neutrino's role is very small, and $\nu_e \leftrightarrow \nu_{\mu/\tau}$ where $\nu_{\mu/\tau}$ refers to a superposition of the muon and tau neutrinos. The approximation holds in these cases because θ_{13} is small, and because two of the mass states are close in size relative to the third.

Currently, one of the oscillation parameters of paramount interest is the complex phase, δ_{cp}, which encapsulates the difference in oscillation behaviour between neutrinos and anti-neutrinos. If the PMNS matrix were purely real, the second term in equation 2.3 would be 0, and neutrinos and antineutrinos would oscillate identically. However, for some values of δ_{cp}, the neutrino sector would be able to produce a large amount of Charge Parity (CP) violation which could result in an explanation for matter-anti-matter asymmetry in the universe. Models capable of demonstrating the observed deficit of anti-matter in the universe based on neutrinos as a source of CP violation exist [16]. The search for CP violation in the neutrino sector primarily makes use of long-baseline (typically L $\sim$100-1000 km) oscillation experiments using man-made beams of muon neutrinos.

2.2.1. Matter effects

The expression given in equation 2.3 assumed propagation of neutrinos through a vacuum. Wolfenstein [17] proposed in 1978, that neutrinos propagating in matter would scatter coherently on particles in the medium, and were therefore subject to an effective potential, modifying the evolution of flavour states. Mikheev and Smirnov generalised this in 1985 and showed that neutrinos propagating through a medium with varying density experience a resonant flavour transition [18]. This Mikheyev-Smirnov-Wolfenstein (MSW) effect, results in a maximal mixing angle of $\pi/4$ in accordance with the $sin^2(\theta)$ term in equation 2.4, whereby the probability of transition is at a maximum.

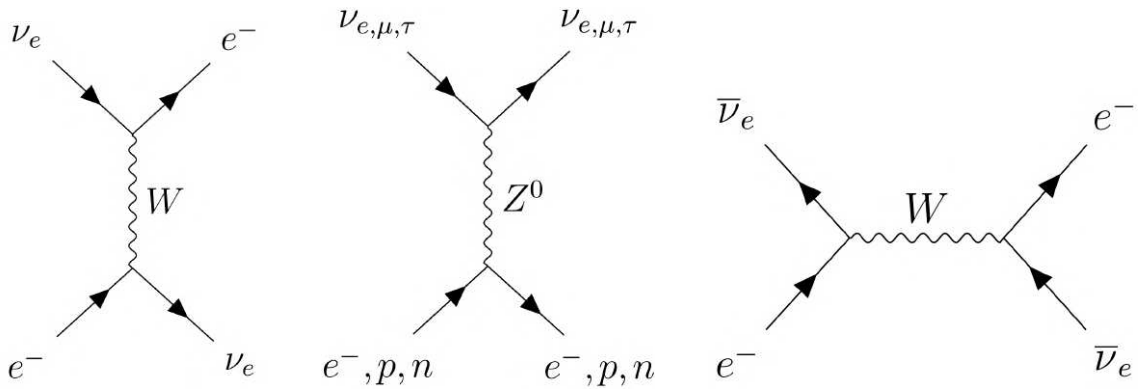

Figure 2.1.: Interacton diagrams for different neutrino flavours with electrons in matter. The difference in diagrams corresponding to different matter effects for electron type neutrinos and antineutrinos is highlighted.

The MSW effect differentiates electron neutrinos from muon and tau neutrinos, as they have an additional weak interaction with electrons in matter, as portrayed in figure 2.1.

Electron neutrinos experience a modified Hamiltonian potential $\Delta V = \pm 2\sqrt{2} G_F E_\nu N_e$, where G_F is the Fermi constant, E_ν the neutrino energy, and N_e the electron number density of the matter, where the anti-neutrino and neutrino pick up the negative and positive terms respectively. The effect results in the oscillation probability having stronger dependence on the term including the sine of Δm^2, and as such the sign of Δm^2 may be resolved when there are significant matter interactions [19].

2.3. Experimental overview of oscillation physics

In 2015, the Nobel Prize in Physics was awarded to Takaaki Kajita of Super Kamiokande (SK) and Art McDonald of Sudbury Neutrino Observatory (SNO) for their experiments which made measurements of oscillation of solar and atmospheric neutrinos. In this section, an overview of neutrino oscillation experiments is provided. Which oscillation parameters an experiment has sensitivity to depends largely on baseline distance and neutrino energy. An overview of neutrino experiments, characterised by baseline distance and neutrino energy is given in figure 2.2.

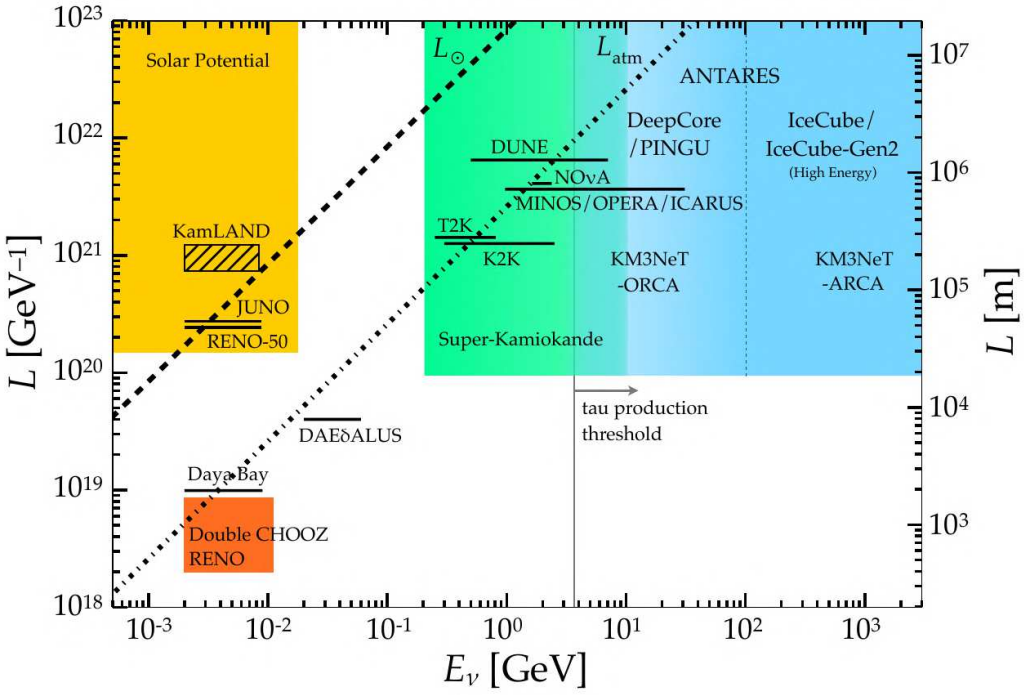

Figure 2.2.: Overview of neutrino experiments, distinguished by characteristic baseline and neutrino energy. Plot taken from [20].

2.3.1. Solar neutrino experiments

"The solar neutrino problem" was born when measurements by Davis and Bachall in 1964-1968 [21] showed a discrepancy between the flux of solar neutrinos calculated from the Sun's luminosity, and that measured directly. A solution to this problem was proposed in 1969 by Pontecorvo and Gribov. Their solution involved an oscillation between electron and muon neutrinos analogous to oscillation of the neutral kaon. In 1989, the Kamiokande experiment [22] confirmed Bachall and Davis' measurements of solar neutrinos with the characteristic energy of the ^{8}B interaction in the sun. Kamiokande measured approximately half the expected number of solar neutrinos, a deficit confirmed by data with larger event samples from Homestake [23]. The solar flux from ^{8}B is shown in figure 2.3. Additional confirmation was provided by the Soviet-American Gallium Experiment (SAGE) [24] and the Gallium Experiment (GALLEX) [25], both of which also measured neutrinos using the process $^{71}\mathrm{Ga} + \nu_e \rightarrow {}^{71}\mathrm{Ge} + e^-$.

Finally, SNO made measurements of neutrinos from ^{8}B in charged current (mediated by a charged W boson), neutral current (mediated by a neutral Z boson), and elastic scattering channels. The measured neutrino profile contained both an electron neutrino

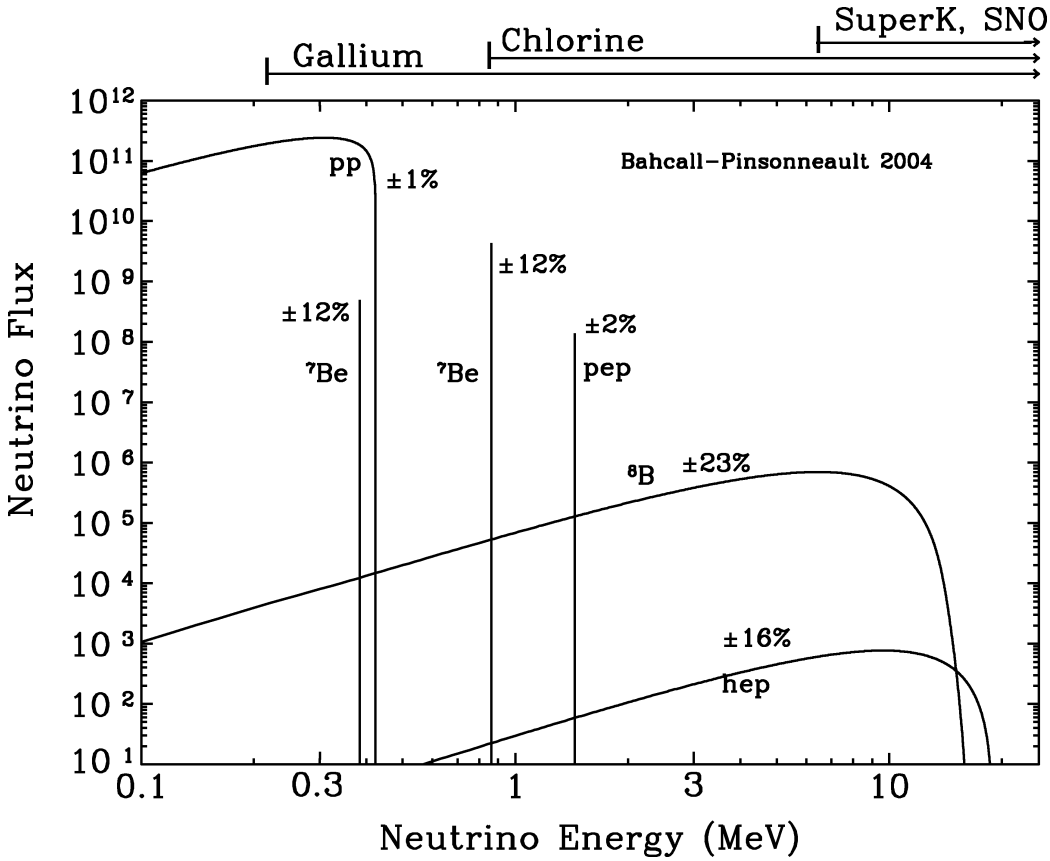

Figure 2.3.: Flux from different solar fusion processes. The thresholds of different experiments are shown. Figure taken from [26].

deficit and a non-ν_e component consistent with the oscillation hypothesis at 5.3σ compared with the no-oscillation hypothesis. The result of the measurements at SNO confirmed the impact of the MSW effect on the solar mixing angle.

Due to their characteristic baseline and energy, solar neutrinos provide sensitivity to the oscillation parameters corresponding to the first and second mass states. The solar neutrino oscillation parameters Δm^2_{21} and $sin^2(2\theta_{12})$ are well-constrained at $7.53 \pm 0.18 \times 10^{-5}$ eV^2 and 0.846 ± 0.021, respectively [27]. However, a tension of 2σ exists between the Δm^2_{21} measurements of SK/SNO and the long baseline reactor experiment, Kamioka Liquid Scintillator Antineutrino Detector (KamLAND) [28], which measured the same process with a different neutrino source. Given the number of neutrino experiments discussed in this chapter, a 2σ outlier is not anomalous.

2.3.2. Atmospheric neutrinos

Atmospheric neutrinos are emitted from the interaction of cosmic rays with nuclei in the earth's atmosphere. These interactions produce mesons which decay into neutrinos including by the following primary decay:

$\pi^{\pm} \rightarrow \mu^{\pm} + \nu_{\mu}(\bar{\nu_{\mu}})$

$\mu^{\pm} \rightarrow e^{\pm} + \bar{\nu_{\mu}}(\nu_{\mu}) + \nu_e(\bar{\nu_e})$

resulting in a total output of three neutrinos. In the case that all products decay, a ratio of half the number of electron type neutrinos as muon type neutrinos would be expected.

Reines et al and Achar et al saw initial hints of disappearance of atmospheric muon neutrinos in 1965 in deep underground laboratories [29] [30]. In 1986, the Irvine-Michigan-Brookhaven (IMB) experiment saw further deficits of ν_{μ} compared with no oscillation, while two years later, the Kamiokande II experiment verified this deficit, observing $59 \pm 7\%$ the number of muon-like events predicted under the no-oscillation hypothesis [31].

In 1998, SK published results [32] showing $(\mu/e)_{Data}/(\mu/e)_{MC} = 0.65 \pm 0.05 \pm 0.08$, where MC refers to simulation not assuming oscillations. Through additional fitting of oscillation parameters, the data were found to be consistent with $\nu_{\mu} \leftrightarrow \nu_{\tau}$ oscillation, rather than $\nu_{\mu} \leftrightarrow \nu_e$. The flavour ratio for atmospheric neutrinos observed by a number of experiments is shown in figure 2.4.

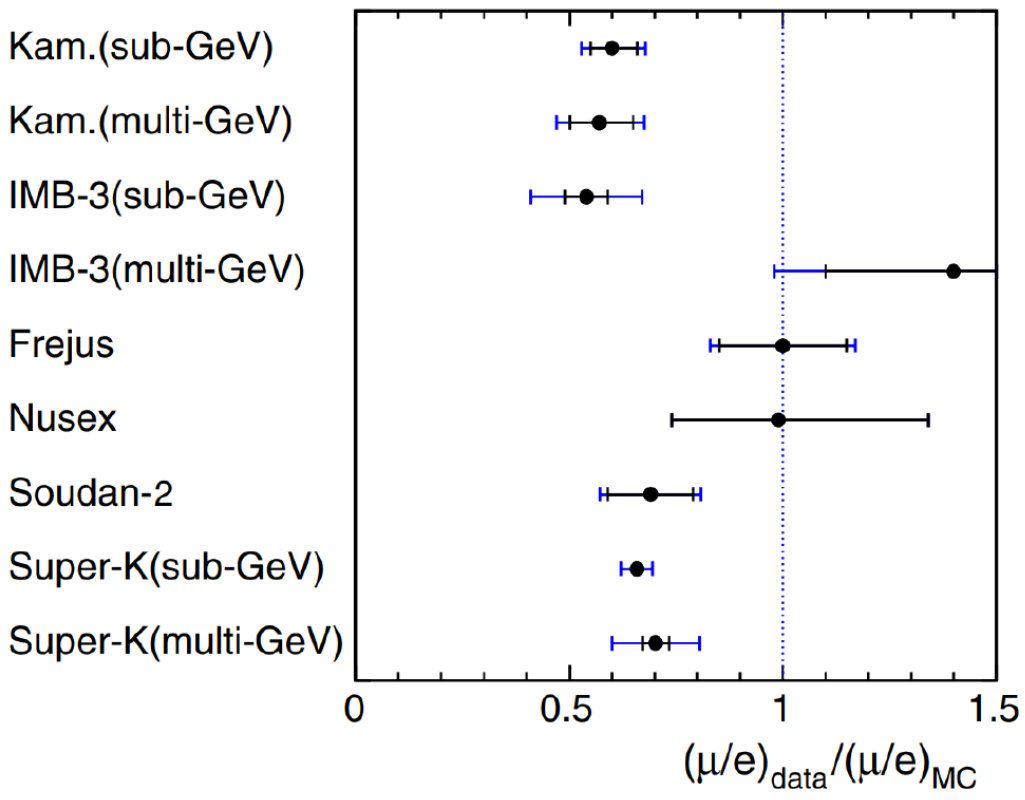

Figure 2.4.: Historic flavour ratios of atmospheric neutrino experiments. Figure taken from [33].

Subsequent atmospheric neutrino observation experiments have primarily made precision measurements of muon neutrino disappearance. By restricting observations to a range of specific baseline lengths, L, using the observed azimuthal angle, the extent of the matter effects experienced by the neutrinos are studied. This in turn allows for resolution on the ordering of the neutrino mass states. Atmospheric neutrino programmes of research at SNO [34], SK [35], as well as work at the Astronomy with a Neutrino Telescope and Abyss environmental RESearch project (ANTARES) [36] and IceCube [37] are largely focussed on this area.

2.3.3. Accelerator-based neutrino oscillation experiments

Man-made neutrino beams are also used to investigate flavour oscillations produced by PMNS mass-flavour mixing. Experiments using neutrino beams of typically a few GeV are used to investigate oscillation over long baseline distances of hundreds of kilometres. These experiments are similar to atmospheric experiments in baseline divided by neutrino energy, and production mechanism of neutrinos. Neutrinos are produced by impinging accelerated protons on a target, producing mesons (primarily pions and kaons) which decay into muon (and other) flavour neutrinos. Accelerator beams are typically more than 90% muon flavoured.

The ability to tune both the baseline and the neutrino energy has allowed accelerator experiments to produce high statistics results in the region of the of the first oscillation maximum found by the atmospheric neutrino experiments. On the other hand, the reduction of neutrino flux over distance to the far detector due to beam dispersion has thus far enforced a baseline of less than 1000 km, limiting the impact of the matter effect and sensitivity of experiments to the mass ordering.

In most accelerator experiments, one or more "near detectors" make measurements of the neutrino beam near to the production site. These near detectors enable characterisation of the neutrino beam prior to significant oscillation. Subsequently, after oscillation has occurred, measurements of the properties of neutrino oscillation may be made at a large distance from the production site. Two of the earliest accelerator long-baseline neutrino oscillation experiments were KEK to Kamioka (K2K) and the Main Injector Neutrino Oscillation Search (MINOS), which began taking data in 1999 and 2005 respectively. Over the course of its lifetime, K2K measured disappearance of muon neutrinos with a statistical confidence of 4.3σ [38]. MINOS and K2K made measurements of one mass squared splitting oscillation parameter, $|\Delta m^2_{23}|$, and of the

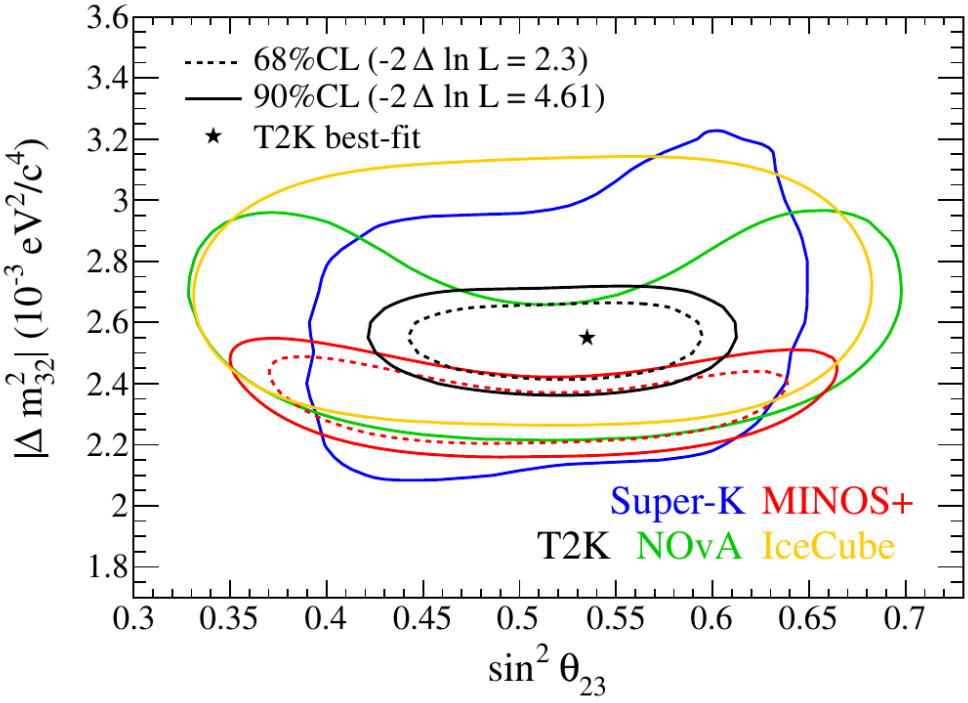

Figure 2.5.: The state of measurements of $|\Delta m^2_{23}|$ and $sin^2(2\theta_{23})$ by five neutrino experiments in 2017. Plot taken from [42].

mixing angle $sin^2(2\theta_{23})$ [39]. Initially world-leading, these results have since been surpassed by the accelerator-based experiments Tokai to Kamioka (T2K) [40] and NuMI Off-Axis ν_e Appearance (NOvA) [41]. The confidence intervals for measurements of these two parameters as they stood in 2017 by a number of neutrino experiments are shown in Figure 2.5.

In addition to $\nu_\mu \rightarrow \nu_e$, T2K and NOvA found evidence of $\bar{\nu_\mu} \rightarrow \bar{\nu_e}$, which had not been found with statistical significance at the previous generation of experiments. The Japanese experiment T2K, like its precursor, K2K, before, uses a 50,000 t water Cherenkov far detector, with plastic scintillator based near detectors, a baseline of L $\sim$ 250-300 km, and a neutrino energy of E $\sim$ 0.5-2 GeV. In contrast, NOvA, just as MINOS before it, uses a $\sim$ 700 km baseline and an energy of E $\sim$ 2-5 GeV, along with functionally identical near and far-detectors.

Chapter 3.

Experimental Layout and Detectors

3.1. The Tokai to Kamiokande Experiment

T2K is a long baseline neutrino experiment built to detect the appearance of ν_e in a ν_μ beam [43] [44]. The experiment was proposed and designed in the early to mid 2000s. The muon neutrino beam is produced at the Japan Proton Accelerator Research Complex (J-PARC) in Tokai, Japan. The near detector comprises multiple detectors 280 m downstream of the proton target. The far detector is a 50 kt water Cherenkov detector, SK, 295 km away in Kamioka, Japan. The primary aim of the experiment was to measure θ_{13}, as well as making precision measurements of $sin^2(2\theta_{23})$ and $|\Delta m^2_{23}|$. Given the larger than expected value of θ_{13}, T2K is also able to constrain the δ_{cp} parameter. In addition to oscillation physics, T2K has a strong programme measuring neutrino-nucleus cross sections at the near detector, on a range of targets. Furthermore, T2K conducts sterile neutrino searches and measures neutrino time of flight.

T2K employs an off-axis method by directing the neutrino beam such that it is at an angle of 2.5 deg with respect to the line from the production target to the far detector. This off-axis method reduces the energy spread of the beam, giving a narrow-band

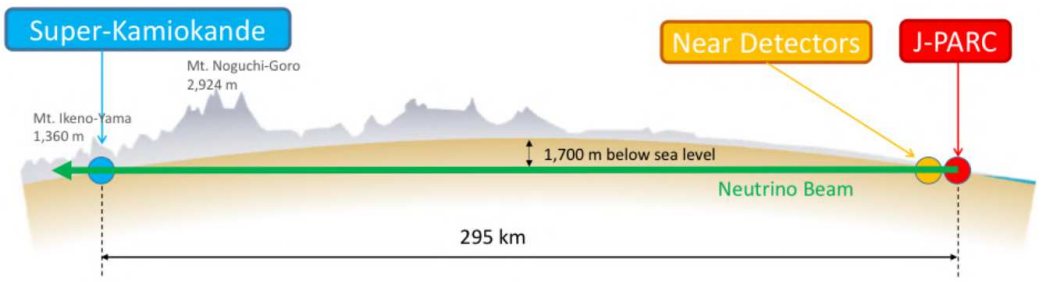

Figure 3.1.: Schematic view of the T2K experiment.

neutrino beam with a peak energy of ~ 0.6 GeV. This energy lies at the oscillation maximum for muon neutrino disappearance, maximising sensitivity to θ_{13} and θ_{23}, and reduces backgrounds to measurements of electron neutrino appearance. A schematic depiction of the T2K experiment is presented in figure 3.1.

3.1.1. Beamline

T2K's beam begins with H^- particles. These are accelerated to 400 MeV by a linear accelerator (LINAC) before reaching the rapid-cycling synchrotron (RCS). The beam is converted to H^+ particles by charge stripping foils at the RCS and accelerated further to 3 GeV. A fraction of these particles are delivered to the main ring (MR) synchrotron and accelerated to 30 GeV before being extracted into the primary neutrino beamline. Spills consist of 8 bunches and are 5 μs long, with an intensity for recent runs of approximately 2.6×10^{14} protons per spill. A number of beam monitors guarantee the stability of the beam, measuring beam intensity, profile, position, and beam loss. The beamline is shown in figure 3.2.

The secondary beamline consists of the target station, decay volume, and beam dump. The primary proton beam enters the target station and passes through a baffle, in order to reduce the horn's exposure to the radiation damage due to beam loss protons. Subsequently the beam passes through the optical transition radiation (OTR) monitor, where the beam profile is measured by collecting transition radiation produced by the beam as it passes through a thin layer of titanium-alloy foil. Finally the proton beam impinges the target — a graphite rod of density 1.8 g/cm^3 which is 91.4 cm long and 2.6 cm in diameter. The target is positioned within the first of three magnetic horns. This first horn sign-selects pions produced in the target, which are then focused by the second and third horns. Each horn comprises two coaxial aluminium alloy conductors which encompass a closed cylindrical volume. The horns generate a maximum magnetic field of 2.1 T when pulsed in time with the beam spill. The horns were designed to maximise the neutrino flux at the far detector.

The focused pion beam enters the decay volume, a 96 m long steel tunnel shielded with 6 m of concrete. The distance from the centre of the target to the beam dump is 109 m, over which almost all charged pions will have decayed to muon and neutrino pairs. The beam dump itself is composed of a 3.17 m thick graphite core and 15 iron plates of total thickness 2.4 m. Only muons with energy above 5 GeV can penetrate

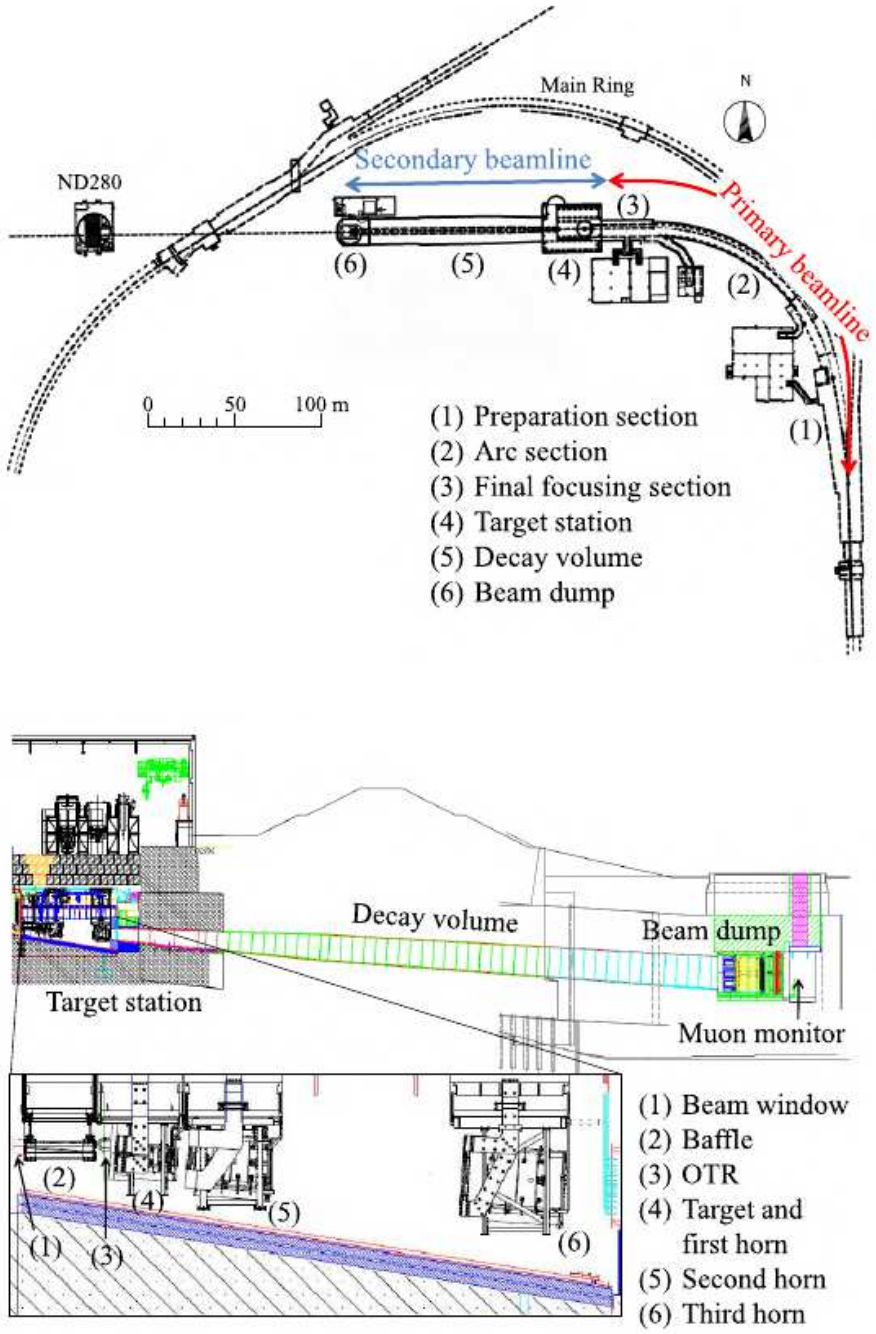

Figure 3.2.: Schematic view of T2K beamline. Top: top-view of the primary and secondary beamlines. Bottom: side view of the secondary beamline.

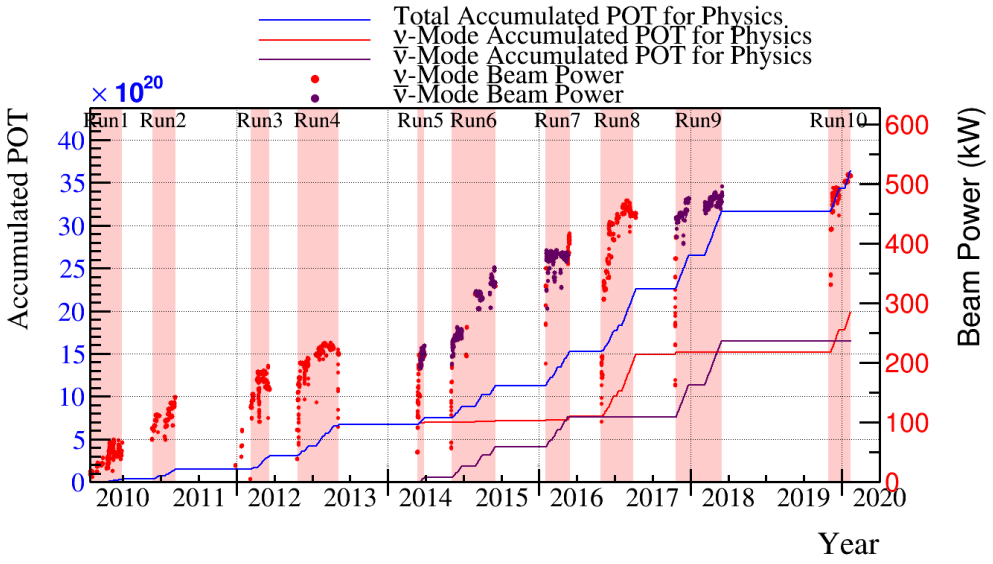

Figure 3.3.: Protons on target and beam power for T2K runs 1-10.

the beam dump. The primary and secondary beamlines are shown in figure 3.2, top, while the decay volume, horns, and OTR are shown in figure 3.2, bottom.

The steps involved in beam production must be carefully simulated in order to correctly predict the T2K flux. Modelling of the proton interactions with the target is performed using simulation package FLUktuierende KAskade (FLUKA) 2008 [45]. Thereafter, the propagation of the mesons produced through the secondary beamline is simulated using GEometry ANd Tracking - 3 (GEANT3) [46]. The interactions of particles leaving the secondary beamline with the surrounding material are modelled using GCALOR [47]. To provide the most accurate flux prediction possible, the hadron interaction models are tuned to data from the NA61/SPS Heavy Ion and Neutrino Experiment (NA61/SHINE) [48]. NA61/SHINE measures the hadron production of a 30 GeV proton beam, previously on a thin graphite target, and now on a replica of the T2K target, to which future analyses will be tuned.

The accumulated protons on target (POT) and delivered beam power have been steadily increasing throughout runs 1-10 (from 2010 to 2020). Run 10 concluded with >500 kW beam power, and an accumulated total POT of $>35 \times 10^{20}$. The accumulation of data over time is shown in figure 3.3.

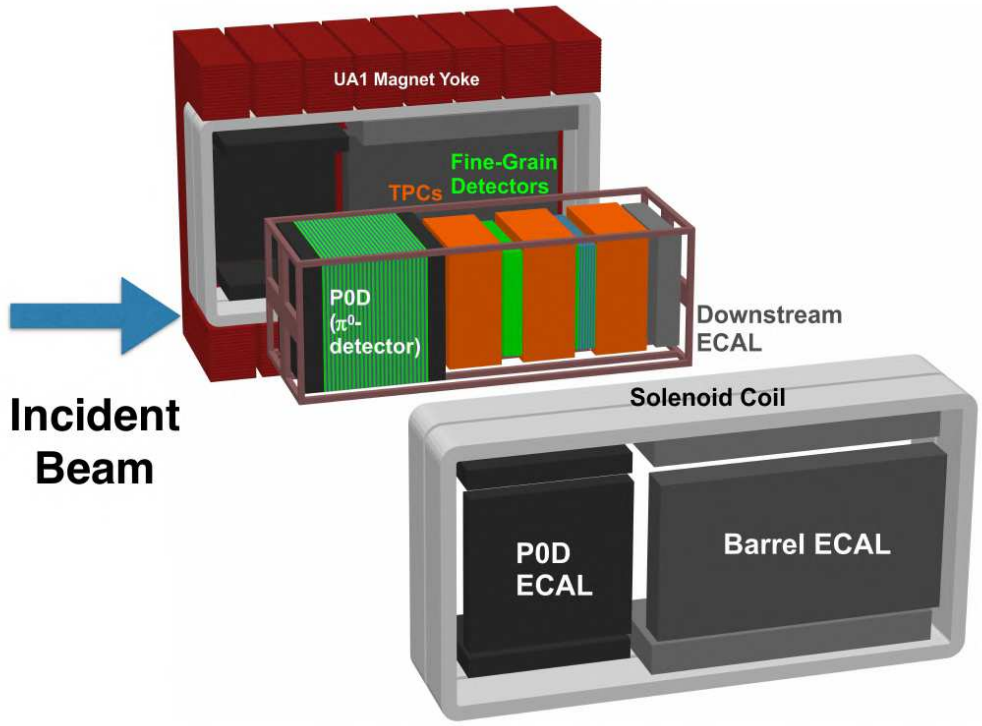

Figure 3.4.: Diagram of the subdetectors that comprise ND280.

3.1.2. ND280

The off-axis near detector for T2K is ND280, so named because it lies 280 m downstream of the graphite target. It is a magnetised, off-axis general purpose detector, designed to reconstruct and track particles emanating from primary neutrino interactions in several high density target subdetectors. By analysing these reconstructed events, T2K is able to characterise the neutrino flux passing through the detector and the interaction cross-section of those neutrinos.

A diagram of ND280 is shown in figure 3.4. The inner region comprises "the Tracker" and contains three time projection chambers (TPCs) filled with gaseous argon, interspersed with two fine grained detectors (FGDs) which are finely segmented tracking detectors composed of plastic scintillator. The Tracker is bordered at the downsteam end by a sampling electromagnetic calorimeter (DsECal). The TPCs are required for high precision reconstruction and tracking of the kinematics of charged particles. This is crucial for particle identification. The primary target for neutrino interactions is formed by the FGDs, the first of which is comprised entirely of layers of plastic bars. This provides good reconstruction of the positions of interaction vertices and tracking of the nearby charged particles. To achieve three dimensional reconstruction, alternate

planes of scintillator are at right angles to one another. The further downstream FGD includes some layers filled with water as a second target for beam neutrino interactions. The two FGDs are used in combination to make comparative measurements between neutrino interactions on carbon and oxygen. Understanding interactions with water is crucial as it is the material of the far detector.

The Barrel electromagnetic calorimeter (ECal) surrounds the Tracker and consists of six modules. Both the Barrel and Downstream ECals are formed of layers of plastic scintillator bars interwoven with lead absorber sheets. The layers of lead are used to increase the number of radiation lengths across the subdetector module to cater to sampling a range of particle energies. Discriminating between electrons and muons as they leave the Tracker is made possible by the ECals, with electrons undergoing full electromagnetic showers, while muons leave simple track-like signatures.

Further upstream lies the dedicated π^0 detector, the P0D. The P0D is used to study neutral pion production caused by neutrinos, as neutral pions decaying to photons provide a background at the far detector. The P0D uses water bags between scintillator layers and the water bags may be filled with water or air to provide comparison.

The surrounding magnet yoke is interleaved with a side muon range detector (SMRD) made of strips of plastic scintillator. These allow for high angle tracing of muons, and provide a cosmic trigger.

As a general purpose detector, ND280 is used to measure many neutrino interaction channels. This includes but is not limited to published measurements of charged-current cross sections of muon and electron neutrinos on carbon, and charged-current measurements on carbon and water with varying numbers of pions. However, for the work described in the following chapters, the most relevant aspect of ND280 is its ability to reconstruct nucleons from neutrino interactions. Protons may be differentiated from other particle types in the TPCs and FGDs. An example is shown in figure 3.5.

Improving knowledge of secondary protons from neutrino interactions is a theme of the work described in the thesis. Reconstructing protons from ND280 data requires various selections to be made, and the ultimate selection efficiency is not uniform as a function of energy. An example of the reconstruction of protons, published in [49] is shown in figure 3.6. Here, after a number of selection steps, the predicted efficiencies by the neutrino interaction generators NEUT and GENIE are shown, which are described in greater detail in subsection 3.1.5. The reconstruction efficiency is

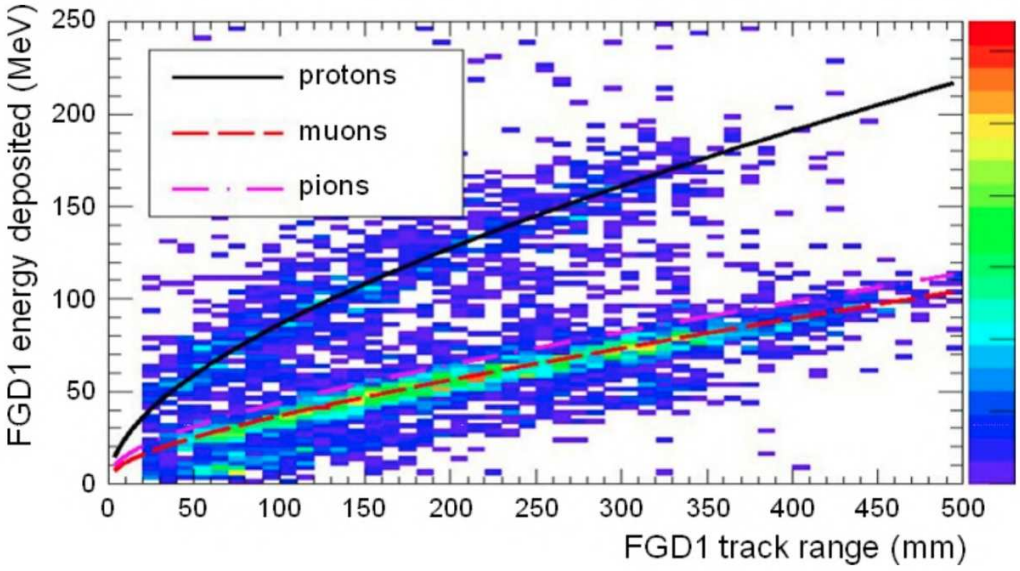

Figure 3.5.: Deposited energy against range for particles stopping in the first FGD. The curves show the simulated expectations for different particle types - above an energy momentum threshold, protons may be distinguished from pions and muons. Figure taken from [50].

shown as a function of momentum and angle of the final state protons. The selection steps for this particular analysis aimed to identify muon neutrino interactions with a hydrocarbon target producing one muon, no pions and any number of protons in the final state. Pre-selection involved identifying a vertex in the most upstream FGD associated with the highest momentum track in the central TPC and determining it to be muon-like using the TPC particle identification. Additional tracks sharing a common vertex were required to be proton-like according to the TPC or FGD particle identification. Inclusion of any events including low momentum charged or neutral pions was avoided by rejecting events with Michel electrons — electrons produced from decay of a muon that has itself been produced by pion decay. The resultant plot shows that protons in the low momentum region around 400 MeV/c can be reconstructed.

3.1.3. INGRID

The off-axis method employed by T2K requires precise determination of the neutrino beam direction, with a 1 mrad beam direction uncertainty corresponding to a 2-3% uncertainty on the neutrino energy scale due to the off-axis technique [40]. Measurements of the beam direction are made on a spill-by-spill basis.

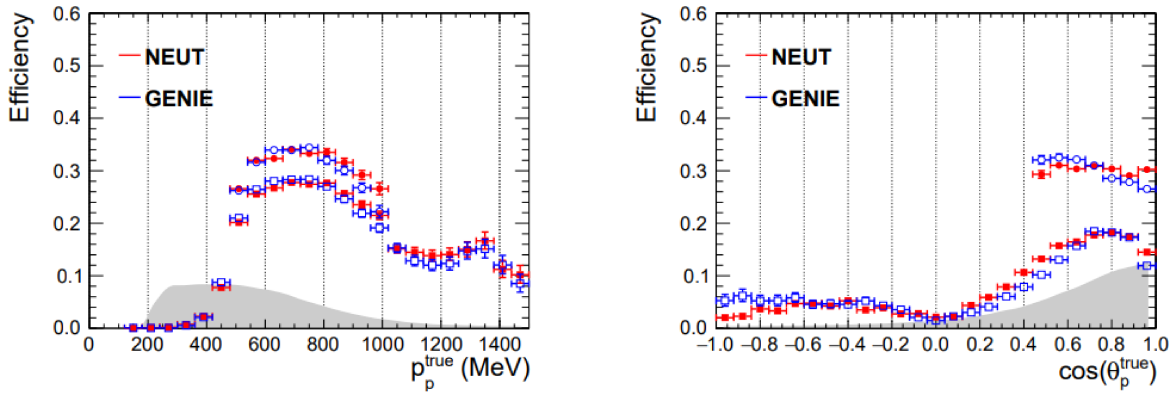

Figure 3.6.: Reconstruction efficiencies, following selection steps, as a function of true proton kinematics, as predicted by NEUT 5.3.2 and GENIE 2.8.0. Left: momentum distribution. Right: angular distribution. The square points show the efficiency prediction before any phase-space constraints whilst the circular points have had additional proton and muon kinematic constraints applied. The grey areas shows the shape of the pionless charged current cross section predicted by NEUT 5.3.2.2. Figure taken from [49].

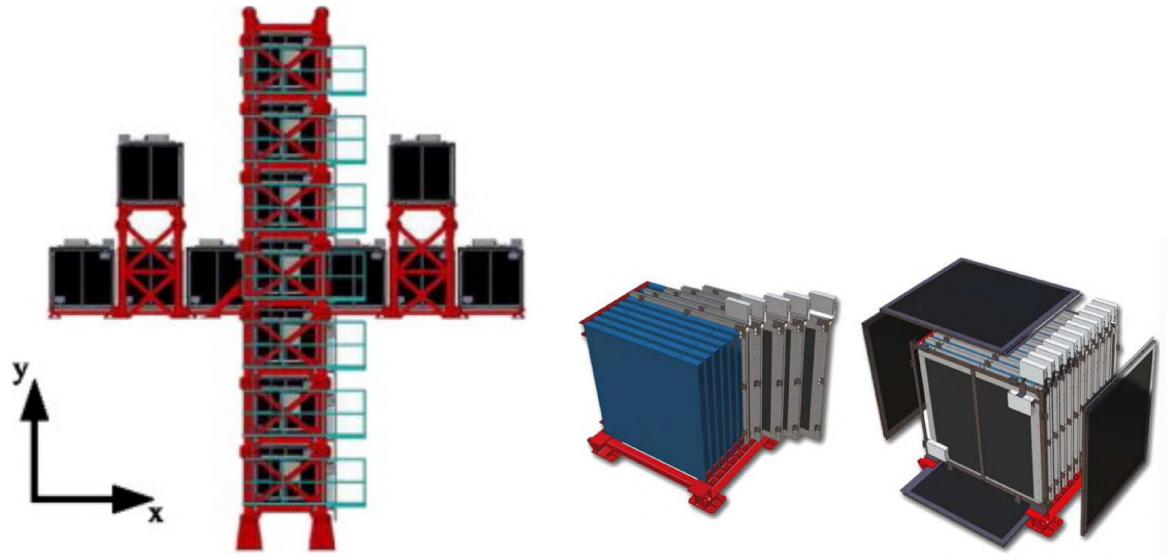

Figure 3.7.: The INGRID detector used for neutrino beam monitoring. Left: the downstream beam view of the full detector. Right: an individual INGRID module.

The Interactive Neutrino GRID (INGRID) detector is the on-axis component of the near detector. Like ND280, it lies 280 m from the production target. INGRID measures the neutrino profile in order to make accurate predictions of the off-axis angle and flux at ND280 and SK. Additionally, INGRID may be used to make inclusive neutrino cross-section measurements [51]. INGRID's geometry is cross-shaped, extending 10 m in the horizontal and vertical direction. It is composed of 14 identical modules in the main cross shape, in order to make measurements of the axial symmetry of the beam. The INGRID detector is shown in figure 3.7, left, while an individual module is shown in figure 3.7, right. Each INGRID module is made up of 9 iron plates and 11 tracking scintillator plates, with a fiducial mass of 7.1 tonnes per module, which is surrounded by veto planes in order to reject cosmic backgrounds [52]. An additional proton module is placed in the centre of the cross in order to measure neutrino interactions on plastic scintillator. This module consists of 34 tracking plates, also surrounded by veto planes. In addition, an INGRID water module measuring neutrino interactions on water is included in some T2K runs.

INGRID makes measurements of the beam directionality with a precision of 0.2 mrad, resolving the centre of the neutrino beam to 5 cm.

3.1.4. Super Kamiokande

SK is located near the West coast of Japan, 295 km from the production target. The detector lies 1 km underground, in the Mozumi mine, providing shielding against cosmic rays. The 41.4 m tall cylindrical tank has a diameter of 39.3 m and is filled with 50 kt of ultra-pure water. SK is a water Cherenkov detector, instrumented with PMTs capturing Cherenkov radiation emitted by the charged products of neutrino interactions travelling faster than the speed of light in water. SK is divided into the Outer Detector (OD) and Inner Detector (ID). The ID has a diameter of 33.8 m and height of 36.2 m, and is covered in 11,146 inward facing, 50 cm diameter PMTs. These PMTs provide approximately 40% coverage. The OD, meanwhile, is covered in 1,884 outward facing PMTs, of 20 cm diameter, which provide a veto and shielding for the inner detector. The OD and ID are separated by a 55 cm thick stainless steel structure, which holds the PMTs and other electronics. A diagram of the structure of SK within the Mozumi mine is shown in figure 3.8, left, while an example of a neutrino event in SK is shown in figure 3.8, right.

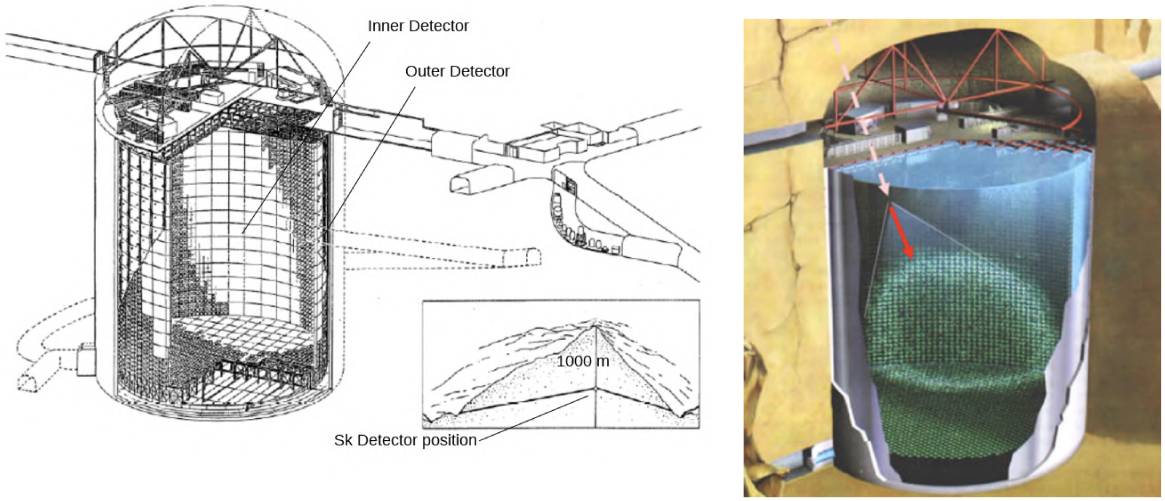

Figure 3.8.: The SK detector. Left: schematic of the detector within the Mozumi mine. Right: schematic of a neutrino event within SK. The neutrino enters the inner detector, interacts with the water, and the resulting ring of photons is detected by the surrounding PMTs. Diagram taken from [53].

Particle identification in SK is performed by distinguishing Cherenkov rings corresponding to muons and electrons. The distinction is achieved by observing the "fuzziness" of the rings and, as such, the extent to which the charged particle produced in a neutrino interaction has scattered. Muons (and pions) are typically more highly penetrating than electrons, which scatter often and at typical T2K energies produce electromagnetic showers. Rings from these electrons are therefore fuzzier, while muon or pion rings are more sharply focussed. An example of each ring is shown in figure 3.9.

A plan to dope the pure water in SK with gadolinium is currently underway, following the opening of the detector for repair work and fixing of leaks. As of July 2020, gadolinium doping of SK has begun. Ultimately Gd will be dissolved in the form of $Gd_2(SO_3)$ to form a 0.2% solution [54]. Gadolinium doped water will improve the efficiency of SK at performing neutron-tagging, as gadolinium has a thermal neutron capture cross-section of 49000 barn, compared with 0.3 barn for free protons [55]. This concentration will provide a detection efficiency of photons from Gd of 90% [56], resulting in an overall improvement in neutron tagging efficiency to 80% from less than 20% currently.

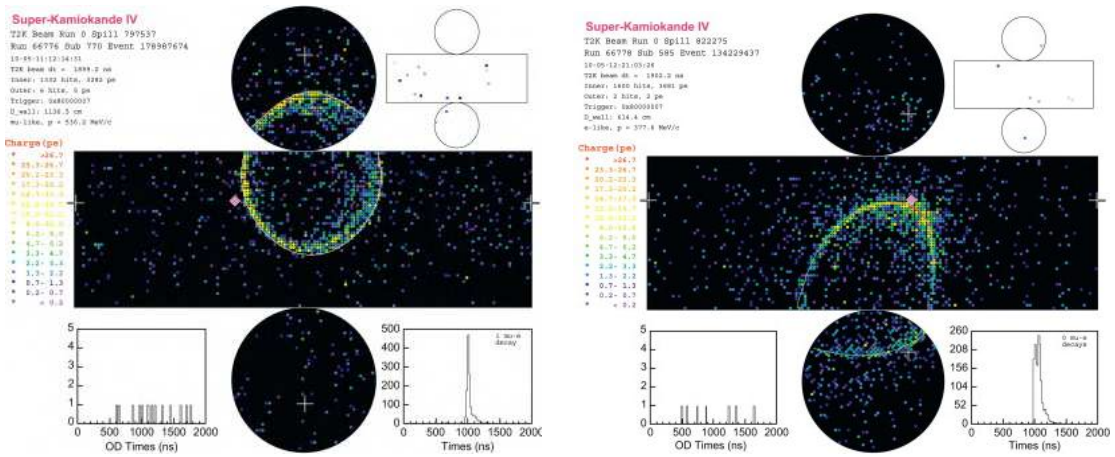

Figure 3.9.: Reconstructed images from SK. Left: a muon-like ring. Right: an electron-like ring. The muon-like ring is more sharply focussed. The overall shape of the plot is the cylindrical shape of the detector, represented in two dimensions. Figure taken from [40].

3.1.5. Neutrino interaction simulation

Event generators which use Monte Carlo (MC) techniques are required in order to produce fully simulated neutrino interaction events based on theoretical models. The use of these allows neutrino scattering data to be interpreted in the context of full interaction models. Any interpretations made are restricted by the degree to which predictions of data can be made based on the model.

INGRID, ND280, and SK are modelled using the neutrino interaction MC NEUT [57]. NEUT is an event generator written for the SK experiment, with large contributions from K2K and T2K collaborators. The program library was initially created to study atmospheric neutrino interactions and detection efficiencies of nucleon decay with the Kamiokande water Cherenkov detector, but subsequently was updated and used in the SK, K2K, and SciBar Booster Neutrino Experiment (SciBooNE) experiments before becoming the primary neutrino interaction generator for T2K. The interaction generation handles a number of charged and neutral current neutrino interactions with various detector nucleus targets including the constituents of water (hydrogen and oxygen), as well as scintillator or iron.

3.2. The High Pressure Time Projection Chamber

Time Projection Chambers have long been constituents of major particle physics experiments. Initially invented by David Nygren in the late 1970s [58], TPCs use a sensitive volume of liquid or gas under the influence of magnetic and electric fields to reconstruct particle trajectories and interactions. The T2K experiment makes use of three argon TPCs at the near detector, as described in Section 3.1.2.

High Pressure gaseous Time Projection Chambers (HPTPCs) are an area of detector research and development that are of great international interest. An HPTPC is a part of the technical design [59] of Deep Underground Neutrino Experiment (DUNE). HPTPCs are of particular interest given their use in constraining uncertainties on neutrino interaction physics.

3.2.1. HPTPC: motivation in neutrino physics

In order to convert measured interaction rates to PMNS parameter values, neutrino experiments must accurately know the interaction probability of the detector medium with neutrinos and antineutrinos. It is therefore crucial to reduce the systematic uncertainty on cross section measurements which are inputs to the analysis. Detector interactions are not simple: in the detector, the target nucleon resides in a complicated nucleus, and the nuclear model has significant effects on the measured final-state particle kinematic distributions. Therefore, observing and making measurements of cross-sections depends on theoretical models.

The T2K experiment records neutrino interaction systematic uncertainties at the 5-7% level [60]. In order to achieve their physics goals, DUNE and Hyper-K will require systematic errors at the 1-2% level. Reducing nuclear-model uncertainties will be pivotal in achieving this reduction in overall systematic uncertainty. Precise measurements of final state particles are the key to this, and these kinematic distributions are governed by Final State Interactions (FSI) of the secondary particles travelling through and leaving the target nucleus.

The key to reducing these uncertainties is twofold: making precise measurements of the multiplicity and momentum distribution of final-state particles [61] and successfully implementing the data informed results in simulation.

In terms of simulation, the most commonly used MC neutrino generators, NEUT, GENIE, and NuWro, simulate FSI with semi-classical (NEUT and NuWro) and effec-

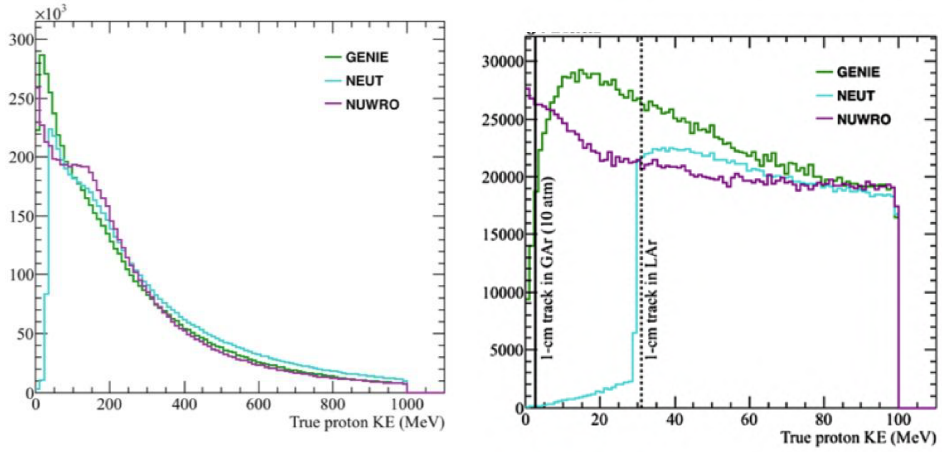

Figure 3.10.: Predicted proton energy spectra from GENIE, NEUT, and NuWro [62]. Left: the full energy spectrum up to 1 GeV. Right: the specific low momentum region of interest. The figure uses the Long Baseline Neutrino Facility (LBNF) simulation for DUNE's beam energy and flux. The dashed vertical line indicates the expected proton automated-reconstruction/ID threshold in liquid argon, and the solid vertical line shows the same for gaseous argon at 10 atm. These plots are taken from [63].

tive cascade (GENIE) models, tuned to external measurements of hadron-nucleus scattering. Currently, data in the low momentum region is very sparse; few proton-nucleus scattering measurements exist on relevant nuclei. As a direct result of this, the semi-empirical cascade models are required to extrapolate in momentum and atomic mass of the nucleus. Therefore, by design, NEUT, GENIE, and NuWro show order of magnitude scale differences in this low momentum region, both in kinematics and multiplicity of final state nucleons. This difference is shown in figure 3.10. Both event selection and neutrino energy reconstruction in neutrino oscillation analyses are affected by proton final state modelling in these MC outputs, and as such, nucleon FSI effects are a dominant contribution in total neutrino interaction systematic uncertainty [42].

An HPTPC is an ideal candidate for a neutrino detector, given its capacity to precisely characterize FSI effects. The advantages of gas TPCs include very high track reconstruction efficiency, a low momentum threshold and 4π angular coverage of final state particles. All of these are crucial in distinguishing between interaction models. Currently, the proton multiplicity and momentum distributions for ν charged current interactions on argon calculated by the NEUT, GENIE, NuWro are discrepant in the fraction of events with few ejected protons, and at low proton momentum, below

250 MeV/c. In water Cherenkov detectors, this is below the proton detection threshold of 1100 MeV/c and even liquid argon TPCs with a threshold of around 400 MeV/c [64] would be unable to make relevant measurements in this region. In contrast, a gas-filled HPTPC has a low enough momentum threshold to resolve discrepancies in FSI models, and therefore has unique capability to address the driving systematic uncertainty in ν cross-sections. The momentum thresholds required for a proton to create a 1 cm track in liquid argon and gaseous argon at 10 atm, respectively, are shown clearly in figure 3.10. Raising the gas TPC to high pressure increases the target mass providing sufficient events for future physics studies when combined with neutrino beams from megawatt facilities.

3.3. The HPTPC prototpye

A prototype HPTPC was proposed in 2015 while testing the protoype in a low momentum beam was proposed in 2017 [65]. The detector was built at Royal Holloway, University of London in 2018. The prototype HPTPC detector is housed in a stainless steel (type 304L) vessel of volume 1472 l, which is rated to 5 bar gauge pressure (barG) equivalent to 6 bar absolute pressure (barA). A sketch of the detector layout is given in figure 3.11. The TPC has diameter 44.7 cm and a drift length of up to 111 cm and is supported on a system of rail supports inside the vessel. The cylindrical vessel includes feed-throughs for high voltage and instrumentation at one face, and optical windows together with hardware required for mounting cameras at the other. The TPC drift region is enclosed by the cathode mesh at negative voltage on one side and the first anode mesh on the other. In order to amplify primary ionisations, two more anode meshes follow at increasingly positive voltages.

The working principle of the detector is included in figure 3.11. A particle, such as a neutrino, entering the drift volume scatters at time, t_0, on an atom of the target gas causing the ejection of a proton from the nucleus. This final state particle ionises the gas along its path. The resulting ionisation electrons drift in the electric field, E, toward the anode meshes (t_1 in the figure) and are subsequently amplified in the high electric field close to the wires of a mesh and between the different meshes (t_2 in the figure). In this avalanche, electrons and photons are produced. The prototype makes use of a dual readout system: traditional charge readout of the anodes, in combination with relatively newly developed optical readout. The photons produced in the avalanche may be imaged by the cameras, which provide a two dimensional

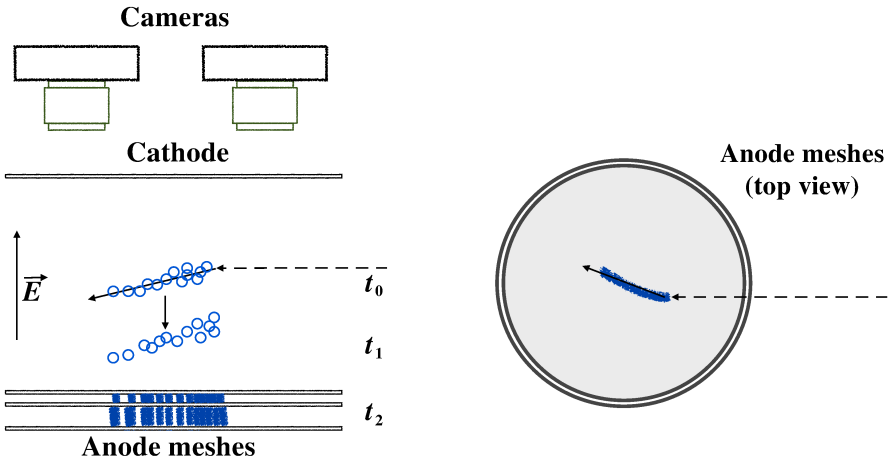

Figure 3.11.: Schematic diagram of the HPTPC. Left: the plane of the HPTPC parallel to the drift field E. Right: the plane perpendicular to E. A particle scattering on a gas atom at time t_0 ejects a charged particle from the nucleus, in turn ionising other gas atoms (shown as circles, left) along its trajectory. These ionisation electrons are moved by E toward the anode meshes at t_1, and are amplified at t_2. Photons produced during the amplification (shown as thick lines, left) are then imaged by cameras, providing a 2D projection of the interaction as seen, right. Additionally, the voltage changes on the meshes during this avalanche are observed. Figure taken from [66].

picture of the interaction. The charge signals induced by the avalanches at any of the anode meshes are read out, providing additional time information of higher precision: the time taken for the particle to traverse the TPC, which in turn is proportional to the track length projected onto the drift direction, for a given particle. The prototype and its dual methods of readout are described in greater detail in the following subsections.

3.3.1. The HPTPC prototype: the vessel

The stainless steel pressure vessel has inner and outer diameter 140 cm and 142 cm respectively. The vessel design is shown in figure 3.12. The length of the straight cylindrical middle of the vessel, which contains the TPC, is 73.6 cm, with each domed end section having a length of 32.5 cm, giving the vessel a total length of 138.6 cm. The total weight of the empty vessel is 2370 kg.

One domed end of the cylinder is detachable, providing access to the vessel's interior and enabling the installation and maintenance of the TPC. This door is connected to the body of the vessel via two large DN 1500 flanges. Gas tightness between the

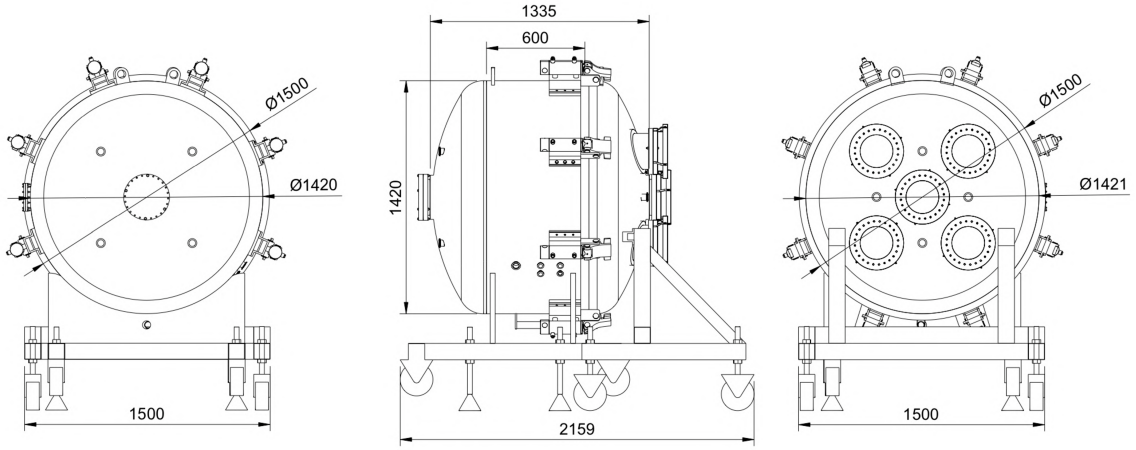

Figure 3.12.: CAD model of the HPTPC pressure vessel. Left: the feed-through side. Middle: the main body. Right: the door side which houses the cameras. Figure taken from [67].

door and body flanges is provided by a double O-ring seal of viton and a rectangular silicone layer. The door and body flanges are clamped together with 8 hydraulic pistons and 8 screwable clamps, with a force up to 50 Nm. The helium leak tightness specification is 2.5×10^{-9} litre mbar/s.

The flanging of the vessel is shown in figure 3.12. The door includes nine flanges in total: five DN200 and four KF40 flanges, while the body features 5 flanges: one DN200 and four KF40 flanges on the face opposite the door. The main body contains four KF25 flanges and one KF40 flange on the left side and and four KF40 flanges on the right. The KF flanges are used for high voltage (HV), gas, and vacuum system feed-throughs. The 5 DN200 flanges on the door are each equipped with a custom optical window flange and a 60 mm thick quartz optical window on a dedicated camera mount. Two independent pressure relief systems are hosted on the body flanges: one, a 6 barA burst disk on an independent body flange, and the other a 5 barA burst disk backed by a 5 barA pressure relief valve. All unused feed-throughs are closed with blanks.

Three steel rails on which the TPC is installed are mounted along the walls on the interior of vessel, separated by 120°, on which the TPC is mounted. The vessel is rated to a 6 barA pressure verified by subjecting the vessel to an internal water pressure of 7.2 barG for 10 minutes with no leaks or material deformation. Subsequently, the vessel was tested with a water pressure of 5 barA (the working pressure of the TPC) for 90 minutes to verify the tightness of the pressurized vessel. All optical windows were installed during this test, verifying that the custom DN200 optical flanges function at pressure.

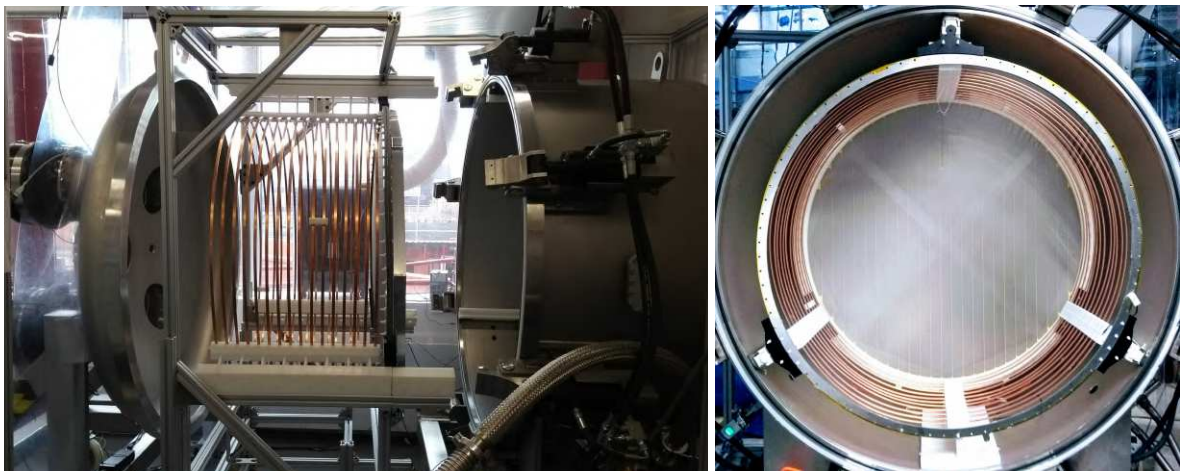

Figure 3.13.: Left: the field cage before insertion into the pressure vessel. Right: the field cage after insertion. The right hand picture is photographed through the high-transparency cathode mesh in the direction of the amplification region, showing the full TPC. Figure taken from [67].

3.3.2. Gas system

The ability to change gases with ease, in order to take data on different target nuclei, is a major advantage of a gaseous TPC. The gas filling strategy for the HPTPC prototype involves evacuating and purging the vessel prior to the target gas fill. The vessel is pumped down to a pressure of approximately 1×10^{-6} barA using an Agilent Triscroll 800 dry vacuum pump. The same pump is used in order to evacuate the fill line from the gas system to the vessel, thus reducing contamination in case a gas fill requires later adjustment to a higher pressure. Gases can be mixed from four different inputs, using 8 Aura gas pressure regulators with manometers and threaded connections (4 in the primary 200-10 bar stage and 4 in the secondary 10-0 bar stage). Gas mixtures are produced by filling with different gases in turn, with relative proportions being adjusted by partial pressure. Purging of the lines from the gas bottle to the gas system is performed whenever a new bottle is connected using gas from the bottle .

3.3.3. Time Projection Chamber and readout

The main components of the TPC are the electrodes that generate the drift and amplification regions and the field cage. Figure 3.13 shows the cathode, field cage ring structure, and amplification region before the assembly is inserted into the pressure vessel (left), and in-situ before the pressure vessel is closed (right).

Field cage

The field cage comprises 12 copper rings with an inner diameter of 111 cm, and length of 1.0 cm in the drift direction and 0.6 cm radially. Neighbouring rings are separated by 2.5 cm Each ring is supplied with HV in series through the cathode with 3 $M\Omega$ resistors between subsequent rings. The final ring on the field cage, close to the amplification region is connected to ground via an adjustable resistor. The total length of the field cage is 42.4 cm, resulting in a 44.7 cm drift distance between the cathode and the amplification region.

The field cage assembly is supported from the three internal rails on the pressure vessel by machined Delrin parts. The chain of resistors is contained in these supports, and the height of the bottom rail supports are adjustable.

Cathode electrode

The cathode electrode is a 25 lpi (lines per inch) steel mesh made from wires of diameter 27 µm. The wire density is so low that the mesh has a $\sim$97% transparency. This makes camera imaging of the amplification region through the cathode mesh possible. The 122 cm by 122 cm mesh is stretched to a tension of 6.4 N/cm on a Grünig G-STRETCH 210 mesh stretching machine. Following the stretching process, the mesh is epoxied to a stainless steel ring, of outer diameter 118 cm, inner diameter 112 cm, and thickness 0.3 cm, using DP460. This tension is calculated from the average of measurements at 9 locations along the mesh, after stretching and relaxation procedures have been performed. The standard deviation of repeated tension measurements across the 9 spatial locations is measured to be 0.4-0.8 N/cm [68].

The full cathode assembly is supported by the three internal rails of the vessel affixed with machined Delrin pieces. The Delrin supports of the cathode and the mating support parts of the field cage ring closest to the cathode constrain the spacing between the cathode and initial field cage ring.

Gas amplification stage

The amplification stage comprises three anodes, separated by resistive spacers. As for the cathode, the three anodes are constructed from steel meshes, with a diameter of 121 cm. The first two anodes are made from 100 lpi meshes with a wire diameter of 27 µm. The optical transparency of the anode 1 and 2 meshes is $\sim$89%. Anode 3 is

made from a 250 lpi mesh with diameter 40 µm. Meshes with smaller wire diameters were selected for the first two meshes in order to achieve the highest gas amplification in the first stages and minimize light loss while taking optical data through the cathode, anode 1 and anode 2 meshes. The distance between mesh anodes 1, 2, and 3 is 0.5 mm and 1 mm respectively. The spacing is maintained by resistive spacers, laser cut from polyester shim. The spacer is a 122 cm outer diameter, 112 cm inner diameter ring, with 24 0.1 cm wide beams crossing it, cut from polyester shim. The spacer beams are visible as vertical lines in the anode plane in figure 3.13, right.

Similarly to the cathode, after stretching, the anode meshes are epoxied to stainless steel rings (outer diameter 118 cm, inner-diameter 112 cm, thickness 0.1 cm). The full procedure for stretching the anode meshes takes approximately a week of successive stretching and relaxation. Thereafter, the average tension on the anode 1 and 2 meshes is 6.8 N/cm. The measured tension is uniform over the plane of the anode mesh to better than 5%. The average tension force on the anode 3 mesh is larger at 38 N/cm.

The flatness of the amplification region is constrained by the support frame, consisting of two ring-shaped Nylon frames bolted together, which sandwich the anodes and resistive separators. The frame has a 118 cm outer diameter, a 112 cm inner diameter, and a thickness in the drift direction of 1.6 cm. The two halves of the frame are bolted together at 88 support points, and on the side facing away from the camera readout, an aluminium stiffener is bolted to the framed assembly, constrained at 16 points.

The amplification region assembly is supported from the three internal rails on the pressure vessel by machined Delrin parts. These supports constrain the amplification region distance to the closest field cage ring.

3.3.4. High-voltage distribution system

Either a CAEN NDT1470 or N1470 multi-channel Power Supply (PS) provide the anode meshes with positive HV and are controlled through a serial link over USB. The cathode power supply is a Spellman SL 30 PS with a maximum voltage output of 30 kV providing a maximal electric field in excess of 600 V/cm. This is controlled by a 0-10 V analogue signal from a LabJack U3-HV USB Data Acquisition (DAQ) device.

Outside the pressure vessel, shielded cables connect the anode feed-throughs to custom boxes in which charge signals are decoupled from the HV line. The HV lines from the PS also connect to these bias boxes, as does the respective signal line, which is

routed from the box to the preamplifier. A circuit diagram of the HV circuit is shown in figure 3.14.

Inside the pressure vessel all electrodes are connected to high voltage feed-throughs via kapton coated cables threaded through ceramic beads which are surrounded by a fibreglass sheath. For the anodes, the feed-throughs are rated to 10 kV, while for the cathode, the feed-through is rated to 20 kV.

The RC constant of the R_{in} resistor and the corresponding mesh capacitance of ~ 5 nF limit the speed of applying charge to the meshes and therefore help to quench discharges. The cathode feed-through is connected to its power supply through a custom Delrin assembly which manages the ground isolation, and is mated to a shielded high voltage cable. The grounds of the anode and cathode power supplies are connected in a grounding circuit coupled to the pressure vessel. The voltages and currents supplied by each power supply channel are recorded in the slow control system, for use in analysis.

3.3.5. Charge signal measurement

The charge readout signals are decoupled from the bias-lines of the three anode meshes using a 10 nF decoupling capacitor, which is located in the custom bias box. The decoupled signals are then fed into charge sensitive pre-amplifiers CREMAT CR-113 hosted in CR-150-R5 evaluation boards. The specified gains of the pre-amplifiers are 1.3 mV/pC. The output signals are then digitised by a CAEN N6730 8-channel digitizer, with 2 V dynamic range and 500 MHz sampling frequency. The data acquisition of the digitiser can be triggered externally or run in a self triggered mode where a single channel crossing a pre-configured threshold is the trigger. All eight channels are always read out simultaneously. The digitizer baseline and threshold are independently configurable in the DAQ.

3.3.6. Optical signal measurement

The optical readout system comprises four FLI Proline PL09000 Charge-Coupled Device (CCD)s featuring a front-illuminated Kodak KAF-09000 chip with 3056×3056 active pixels (9.3 Mp), and an individual pixel size of 12×12 µm. The chip has a Quantum Efficiency (QE) of $50 - 70\%$ for photons in the wavelength range 475 nm to

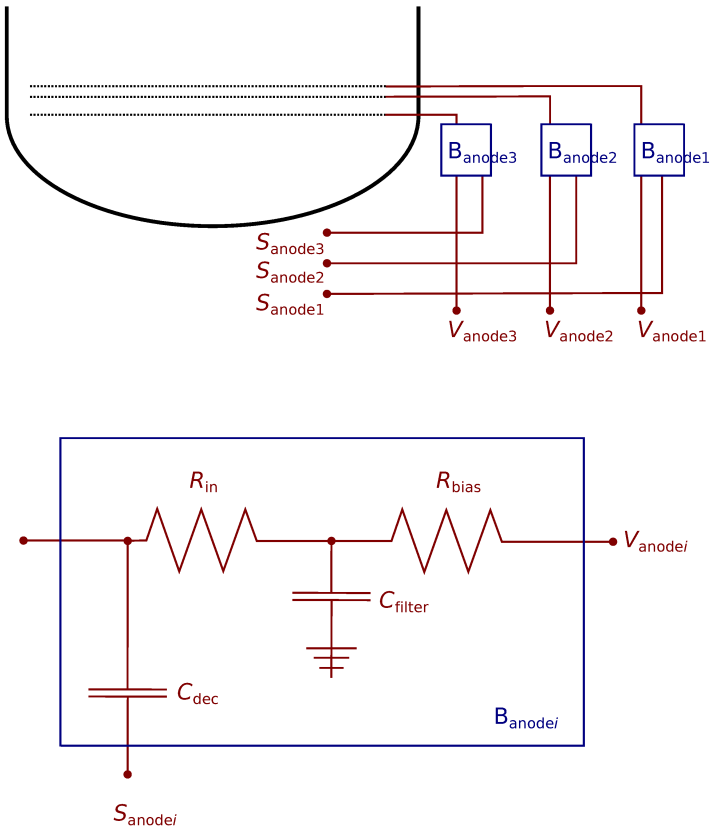

Figure 3.14.: Circuit diagram of the high voltage system. Meshes are provided ($V_{\text{anode}i}$) while the signal is decoupled from the meshes ($S_{\text{anode}i}$). Bias boxes are used with $B_{\text{anode}i}$, which feature a protection and filtering circuit consisting of a bias resistor ($R_{\text{bias}} = 200\ \text{M}\Omega$), filter capacitor ($C_{\text{filter}} = 10$ nF) and input resistor at the detector input (R_{in}). Figure taken from [67].

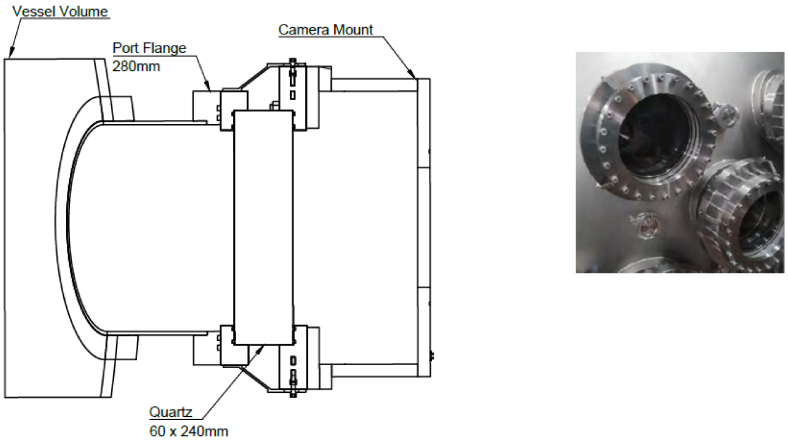

Figure 3.15.: Left: drawing of the optical flange with the camera mount.The thickness of the quartz is required to ensure that the assembly can withstand the pressure difference between vessel and ambient pressure. Right: the full assembly including a flange is shown. Figure taken from [67].

750 nm. This wavelength range covers the full visible spectrum, and extends towards the near infra red.

Each camera has a field of view centred on a quadrant of the amplification plane (with some small overlap between cameras) and is coupled to a Nikon f/1.2 50 mm focal length lens with a 54.8° angle of view. The cameras are mounted to optical flanges as shown in figure 3.15. Due to the high pressure requirement, quartz windows of thickness 6 cm are used. The object distance, calculated as the sum of the drift distance, the length between the cathode and vessel door, and the path through the camera assembly, is 85 cm. At this distance the system images a 71×71 cm field of view with a vixel size of 230 µm.

The noise per vixel depends on the quadrature sum of the shot noise, $\sqrt{N_{\text{signal}}}$, the read noise N_{read}, and the dark rate of the camera times the exposure time:

$$N_{\text{noise}} = \sqrt{N_{\text{signal}} + N_{\text{read}}^2 + n_{\text{pixels}} \cdot R(T) \cdot t_{\text{exposure}}}. \tag{3.1}$$

The number of electrons collected in a pixel varies from photon to photon following a Poisson distribution. Therefore the shot noise can be parametrised by $N_{shot} = \sqrt{S}$, where S is the per-pixel signal. Readout noise stems from the on-chip electronics. These convert the electrons released in the silicon into a voltage and ultimately into Analogue-to-Digital Units (ADUs). Readout noise is measured as follows: using the pixel-wise standard deviation (σ) of the difference of two frames taken while the CCD is illuminated in the exact same uniform way, e.g. for two separate bias frames taken while the CCD is kept in the dark, $N_{readout}$ is defined as $\sigma(bias_i - bias_j)/\sqrt{2}$. The dark current is caused by thermally generated charges in the absence of any sources and varies logarithmically with temperature of the CCD. It is given by: $N_{dark} = \sqrt{DarkRate \cdot t_{exposure} \cdot N_{pixel}}$, where $DarkRate$ is the dark current per pixel and N_{pixel} is the number of pixels in a frame.

In order to minimise noise, the CCDs are cooled to between -25°C and -30°C. The cameras are equipped with an internal thermoelectric cooler with which they may be cooled to 50°C below the ambient camera temperature. Furthermore, a water cooling system is attached to each camera allowing for an additional 15°C of cooling. At -25°C operating temperature, the dark rate is $0.006 - 0.025 e^{-}$/pixel/s.

The CCD cameras digitize the quantity of electrons that are collected in each pixel per exposure. The typical conversion gains of the cameras are $1.52 - 1.55$ e^{-}/ADC. In exposures of 1 s, the read noise is close to 440 times the dark current per pixel. To reduce the effect of read noise, pixel grouping is performed prior to digitization. The size of groupings is typically in 8×8 as this is the largest grouping consistent with the requirement of 2 mm effective pad size. The noise per pixel in the group is therefore effectively reduced by $1/\sqrt{n_{\text{pixels}}}$.

3.4. Time of Flight systems

During August and September of 2018, the HPTPC prototype described in section 3.3 underwent a beam test at the CERN East Area T10 beamline. Two time of flight systems were used throughout, to make invaluable measurements of the energy and multiplicity of particles upstream and downstream of the vessel. These systems are described below.

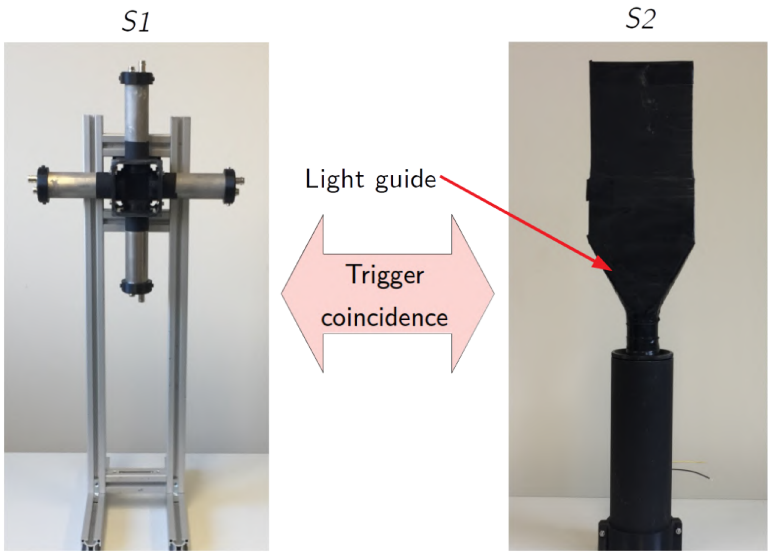

Figure 3.16.: The S1 and S2 beam counters. Events were determined by coincidence of signals in the beam counters and recorded by the DAQ systems. Figure taken from [67].

3.4.1. Upstream Time of Flight

The upstream ToF system was built by University College London, and comprised 3 constituents described in the following subsections:

- *S1*, a small-area beam trigger;
- *S2*, a coincidence measurement with *S1*;
- *S3*, a wall of plastic scintillator bars placed directly upstream of the TPC vessel;

These constituents are described in this section.

S1 and S2 - the upstream counters

The upstream beam counters *S1* and *S2* are shown in figure 3.16. The *S1* counter, which was placed at the beam entrance, is a $40 \times 40 \times 5$ mm^3 plastic scintillator cross attached to 1" Hamamatsu R4998 phototubes at each end providing light readout. Using the DAQ system of the upstream ToF, the time resolution of the counter was measured as approximately 30 ps. This is estimated with the distribution of the average PMT hit times; $t_{ave} = \frac{1}{4}((t_{PMT0} + t_{PMT1}) - (t_{PMT2} + t_{PMT3}))$ was used as it has the same spread as the simple average but is conveniently centred at zero. An example of the t_{ave} distribution for a single run of *S1* data is shown in figure 3.17. The FWHM of the distribution is 62 ps.

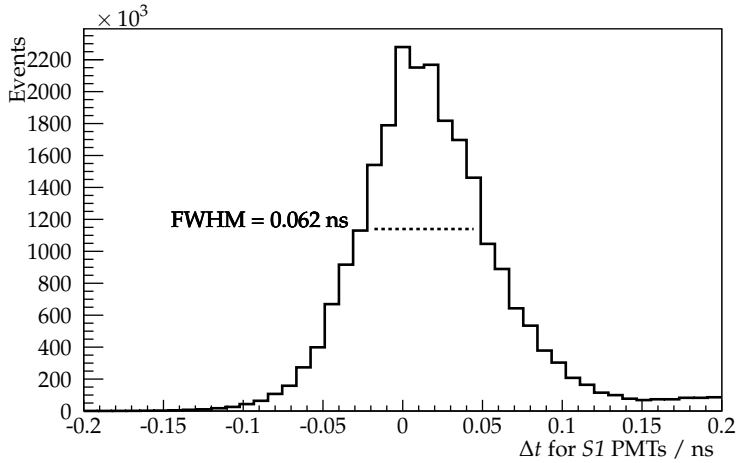

Figure 3.17.: Timing spread of *S1* hits. The time is calculated from the mean of the hit times in each of the four PMTs.

The *S2* counter is a scintillator tile of size $120 \times 120 \times 5$ mm^3, coupled to a 2" PMT R1309 connected to the scintillator via a long light-guide. The purpose of *S2*, placed downstream of *S1* was to record coincidences with *S1*.

The analogue signals from one of the *S1* PMTs and *S2* PMT were fed into NIM discriminator units with a threshold of 30 mV. Subsequently, the discriminated signals were fed into a NIM coincidence unit, and the two signals were recorded by the DAQ system of the downstream ToF wall (*S4*). These data were then used to provide an analysis of the time-of-flight to (*S4*). In order to change the properties of the incoming beam (motivated in section 5.1), a variable number of moderator blocks were placed in between *S1* and *S2*. These are shown in figure 3.18. The transverse position of *S2* was adjusted to account for the beam divergence in the moderator blocks.

S3 - the upstream wall

The third component of the upstream time of flight was a large wall of plastic scintillator placed directly upstream of the HPTPC vessel. A schematic drawing of the *S3* ToF wall is shown in figure 3.19. The detector is composed of 22 staggered scintillator bars: 20 bars with dimensions $168 \times 6.0 \times 1.0$ cm^3 and 2 bars of $1 \times 6.0 \times 1.0$ cm^3 placed on top and bottom [69]. The overlap between bars was set to 5 mm, thus the active area of the detector was 2.02 cm^2.

The bars are made from the plastic scintillator, EJ-200 [70] which provides a brightness of 10,000 photons/MeV deposited. It also has a suitable optical attenuation length

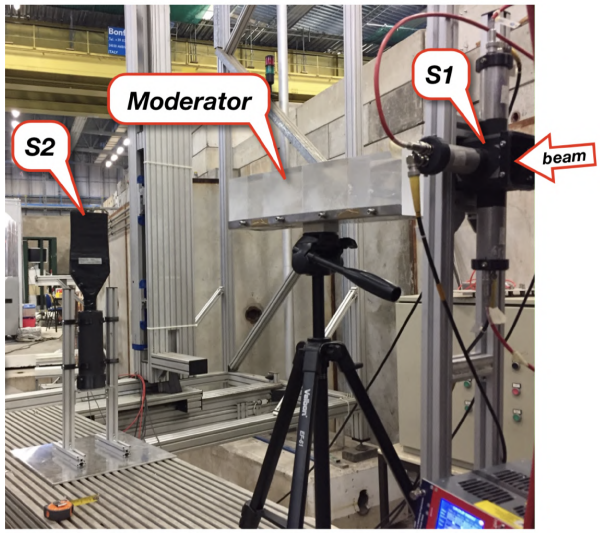

Figure 3.18.: Photo illustrating the *S1* and *S2* counters and the stand with four acrylic moderator blocks between them.

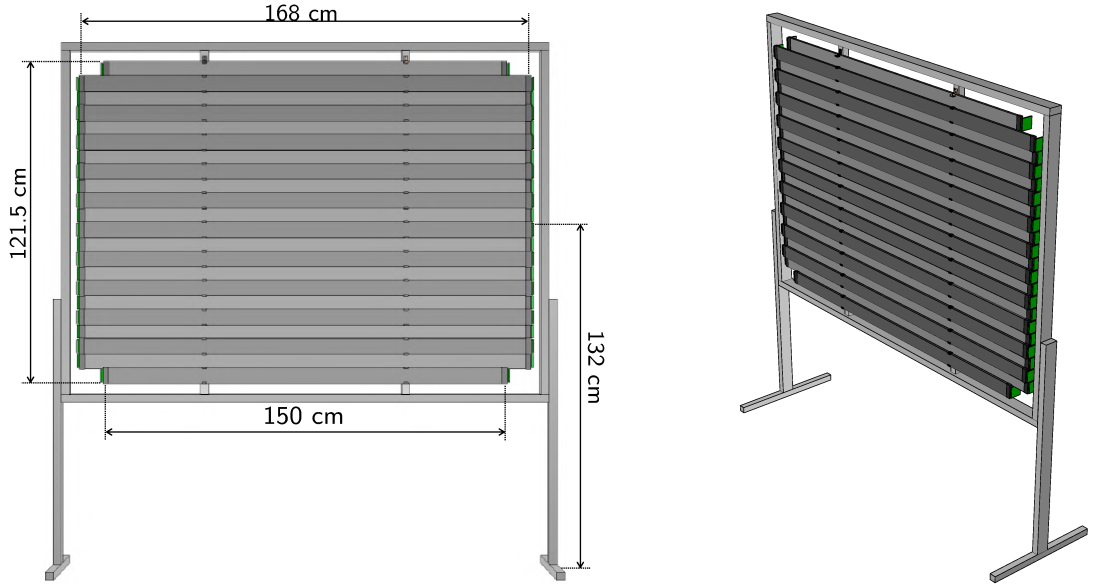

Figure 3.19.: Sketch of the *S3* wall [69]. Left: front view. Right: rotated view.

of 4 m and fast timing, with a rise time of 0.9 ns and decay time constant of 2.1 ns. The scintillation emission spectrum of EJ-200 peaks in the violet region of the visible spectrum (435 nm) [70], which corresponds well to the photon detection efficiency wavelength range of photosensors used for the readout. The bars were wrapped with an aluminium foil to maximize the light collected. The foil used had a reflectivity of approximately 60%.

Arrays of eight 6×6 mm^2 area silicon photomultipliers (SiPMs) S13360-6050PE from Hamamatsu Photonics [71] were coupled to each end of the bar to collect scintillation photons. The anode signals of the SiPMs were read out, summed and shaped by a dedicated circuit as described in [72].

A 64-ch SAMPIC module was used for the data acquisition. A SAMPIC chip is a Waveform and Time to Digital Converter (WTDC) 16-channel ASIC which provides a raw time with an ultrafast analog memory allowing fine timing extraction as well as other parameters of the pulse [73]. Each channel contains a discriminator that can trigger itself independently or participate in a more complex combined trigger. Three module ASICs ($16 \times 3 = 48$ channels) were connected to the 44 channels of *S3* and were operated in self-triggering mode.

The trigger conditions are as follows: at least three out of the four *S1* PMTs must have a signal above a 30 mV threshold. Additionally, there must be at least one signal in *S3* above 30 mV. These *S1* and *S3* signals must be coincident within a gate of 70 ns.

A 4th ASIC was used to acquire data from *S1*, the coincidence signal $S1 \cap S2$, and the start-of-spill signal from PS. A second level trigger was implemented in firmware and run on the level of the ASICs: the data were only sent to the hard disk of the DAQ notebook in the case of coincidence between *S1* channels and channels of three ASICs used for *S3*.

A mean time of light signals detected at two ends of a single bar provides a time reference with a resolution of about 100 ps, while the difference between the time of the light signals gives the position of the interaction along the bar, with a resolution of 1.6 cm.

Examples of reconstructed XY distributions are shown in figure 3.20. The axes of the distributions shown in figure 3.20 are local coordinates for *S3* where $y = 0$ cm is the bottom of the active area and $y = 120$ cm is the top of the active area. In the x direction, 0 cm is the left-hand side of *S3* as viewed from *S1*, while $x = 170$ cm is the right-hand edge of *S3*. Figure 3.20, left, shows the spatial distribution of hits in *S3* thought to be

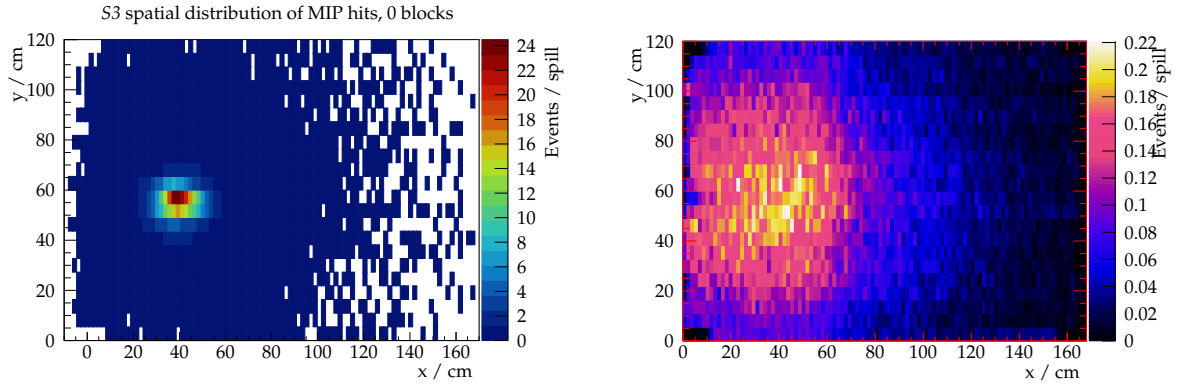

Figure 3.20.: Reconstructed spatial distribution of hits observed in *S3*. In this case a timing cut and an amplitude cut have been applied to select only those hits thought to come from protons. Left: data taken without moderator blocks in the beamline. Right: data taken with 4 moderator blocks in the beamline.

produced by MIPs when no moderator was present in the beamline. This distribution shows that most of the hits are concentrated in one small spot of the detector (the beam centre).

Figure 3.20, right, shows the spatial distribution of hits identified in *S3* as protons when 4 moderator blocks were in the beamline. In contrast to figure 3.20, left, the pattern of hits is far more diffuse. This clearly shows the scattering effect of the moderator blocks.

3.4.2. Downstream Time of Flight

The downstream ToF constituent, *S4*, was another scintillator wall directly downstream of the TPC vessel, and built by the universities of Geneva and Zurich as a part of R&D for the timing detector of the Search for Hidden Particles (SHiP) experiment [74]. It consists of 10 bars of Nuvia NuDET plastic scintillator which has a wavelength of maximum emission of 425 nm and a decay time constant of 2.5 ns [75]. Each of these bars measure $10 \times 1 \times 140$ cm^3. Attached to either end of each of these scintillator bars is a 5" Hamamatsu R6594 photomultiplier tube [71]. The bars are arranged in two rows of five, such that there is complete coverage for any beam particles incident upon the detector. The total active area of the *S4* wall is 1.4×0.78 m^2. A diagram of *S4* along with its dimensions is presented in figure 3.22.

The time resolution of the bars and PMTs is measured to be 1 ns using a ^{90}Sr source placed at measured distances along the bar. Figure 3.21 shows an example of the

distribution from which this value was derived: the measured time difference for signals coming from the PMTs at either end of a bar caused by the ^{90}Sr at a given position. The corresponding spatial resolution of the bars and PMTs was measured to be 8.3 cm.

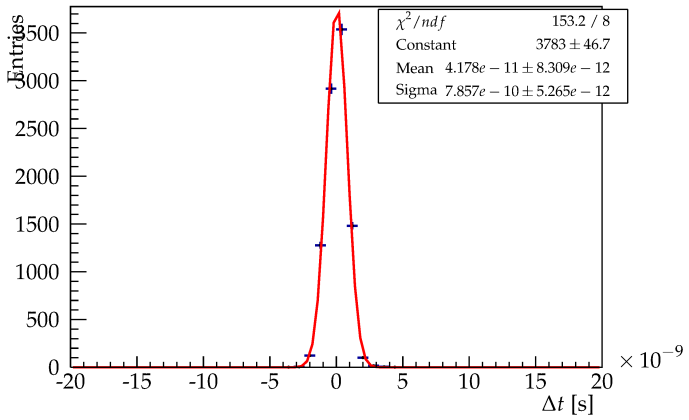

Figure 3.21.: Difference in signal arrival time PMTs at each end of a bar as measured using a ^{90}Sr source placed 64 cm from one end of the bar.

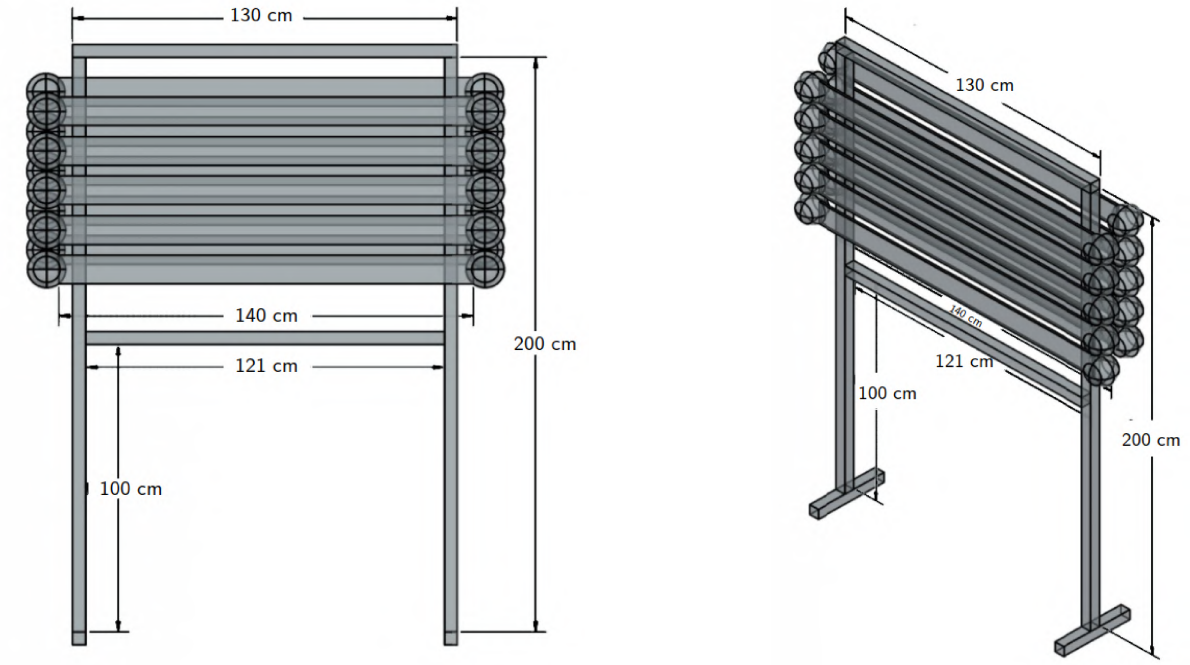

Figure 3.22.: Schematic of the *S4* wall. Left: front facing view. Right: rotated view. The staggering of the scintillator bars and PMTs is seen clearly in the rotated view.

The anode signals of all 20 of the PMTs are discriminated using LeCroy 620AL NIM discriminators, at a threshold of 20 mV. The discriminated signals are then fed into

a time-to-digital converter. A signal in *S4* is deemed to have occurred if a signal is seen in both PMTs, above the discriminator threshold, on the same bar within 20 ns of each other. This timing window is determined through testing performed with a ^{90}Sr source at known positions on the bar.

The $S1 - S2$ coincidence signal is digitized by the same time-to-digital converter. This signal is used to calculate the particle time of flight from *S2* to *S4*.

Chapter 4.

Theory

4.1. Neutrino interactions

Neutrinos are detected by measurement of final-state particles produced through interactions with matter mediated by the weak force. However, only a fraction of the neutrinos of each flavour passing through the detector will interact. Inferring the true number of neutrinos depends on knowledge of neutrino interaction properties, as well as the efficiency of the detector.

A number of factors constrain at which energies oscillation physics can be studied. Neutrinos of a given flavour are typically observed through charged current interactions, producing a charged lepton of corresponding flavour. Producing massive leptons is only possible above the energy threshold for that lepton, providing a lower bound on the possible neutrino energy regime. The inclusive charged current neutrino-matter cross section rises nearly proportionally with neutrino energy. However in order to reach the highest probability of flavour change at the far detector in accordance with equation 2.3, $\Delta m^2_{ij} \frac{L}{2E_\nu} \approx \pi$. Therefore a higher choice of energy necessarily corresponds to a longer experimental baseline, causing a decrease in neutrino flux due to beam dispersion.

4.1.1. Interaction with a free nucleon

Three primary methods of interaction between neutrinos and free nucleons exist: quasi-elastic scattering, single pion production, and deep inelastic scattering. Feynman diagrams of these 3 processes are shown in figure 4.1.

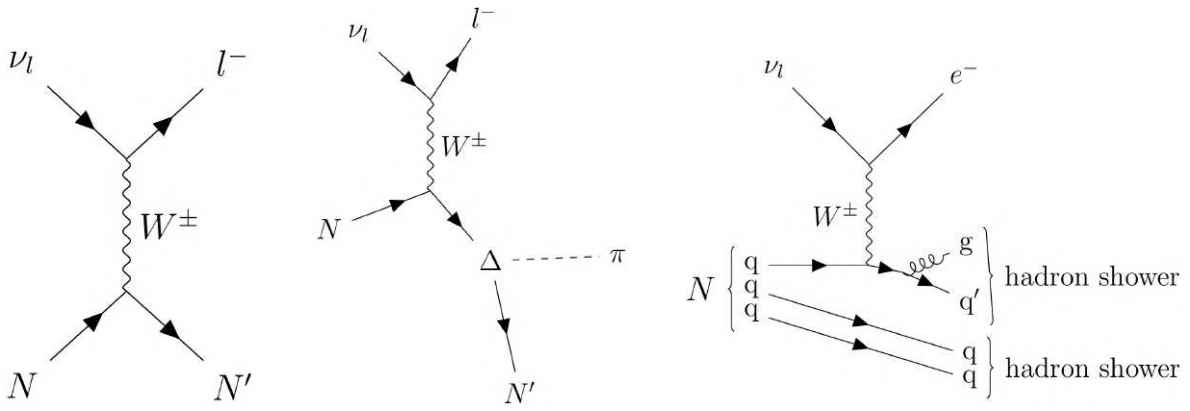

Figure 4.1.: Feynman diagrams for three charged-current scattering channels. Left: quasi elastic scattering. Middle: resonant pion production. Right: deep inelastic scattering.

Charged current quasi-elastic (CCQE) scattering has historically been considered the "golden" interaction channel because of the ability to calculate initial neutrino energy from the final state charged lepton kinematics alone. CCQE interactions have typically been modelled using the Llewellyn Smith formalism [76]. As oscillation probability is determined by the neutrino energy, reconstructing neutrino energy without bias is crucial for oscillation experiments. However, as the neutrino source includes a range of neutrino energies, it is not possible to use CCQE interactions alone.

Single pion production (SPP) occurs in large part due to neutrino-induced baryon resonance excitation and subsequent decay. Pion production in non-resonant channels is also possible. Models for SPP are more complex than for CCQE, and typically the Rein Sehgal model has been used [77]. More recent models including the GiBUU model [78] and the Hernández Nieves Valverde model [79] have shown strong predictive power [80], and may also be capable of describing pion production in other processes such as electron scattering. In addition to lepton kinematics, measurement of final state hadrons' kinematics is also required to reconstruct the neutrino energy for SPP, and this reconstruction is therefore more difficult than in the case of CCQE.

Deep inelastic scattering (DIS) occurs at energies greater than around 2.5 GeV and forms the majority process of the total cross-section for energies of greater than around 5-6 GeV. Reconstructing neutrino energies for DIS interactions is dependent on accurate treatment of the final-state hadronic system.

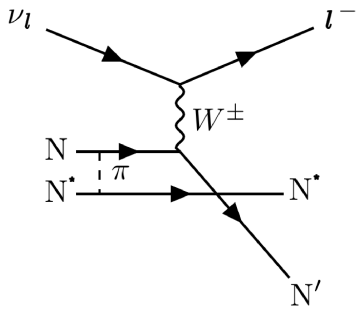

Figure 4.2.: Schematic diagram of a two particle two hole interaction. The neutrino scatters not just off one bound nucleon, but off two in combination.

4.1.2. Interaction with a nucleus

In all current neutrino experiments, neutrinos primarily interact not with a free nucleon, but with a nucleon in the context of its nucleus. To extend free-nucleon models to nuclear targets, one solution would be to use the momentum distribution of a nuclear model and account for the effect of nucleon binding energies. However, this overly simple solution has shown discrepancy in measurements of the CCQE channel made by NOMAD [81] and MiniBooNE [82]. Latest models in contrast include a number of updated components to model multi-nucleon effects. These typically use additional multi-nucleon interaction channels, referred to as "two particle, two hole" (2p2h) channels. A typical 2p2h diagram is shown in figure 4.2. A further effect of the nucleus is that hadrons produced in the interaction may undergo further reinteractions with the nucleus, referred to as final state interactions (FSI).

4.2. Particle mean free path

A particle traversing any material has a particular probability of interacting with the nuclei (or electrons) present. In a thin slice of matter, this probability is in proportion to the slice's thickness and the number of possible target particles per volume of material. The probability also depends on the type of interaction that occurs. The probability can be described by a cross-section, σ, which is a convenient quantity to describe particles in matter and is defined as:

$$dW = dxN\sigma, \tag{4.1}$$

where dW is the probability of an interaction of a certain type occuring, dx is the thickness of the thin slice of material, and N is the number of scattering centres per unit volume. The cross section has the dimensions of area, and is typically described in barns which are equivalent to $10^{-24}\ cm^2$.

For a beam of particles entering a real material, the fraction of beam particles affected is increased due to collisions with nuclei or electrons in the material. Defining $P(x)$ as the probability that a particle has interacted after travelling a distance x through the material, it is clear that $P(0) = 0$ is a boundary condition. From equation 4.1, $P(x)$ and $P(x + \Delta x)$ must be related by

$$P(x + \Delta x) = P(x) + (1 - P(x))\Delta x N\sigma, \tag{4.2}$$

leading to

$$\frac{P(x + \Delta x) - P(x)}{\Delta x} = (1 - P(x))N\sigma, \tag{4.3}$$

where Δx represents a small distance in direction x. As $\lim_{\Delta x \to 0}$, $P(x)$ satisfies the differential equation:

$$\frac{dP(x)}{dx} = (1 - P(x))N\sigma, \tag{4.4}$$

leading to

$$\frac{d(1 - P(x))}{dx} = -(1 - P(x))N\sigma. \tag{4.5}$$

This differential equation is solved, with the boundary condition $1 - P(O) = 1$, as

$$1 - P(x) = e^{-xN\sigma}. \tag{4.6}$$

The probability density function of a particle interacting after travelling a distance, x, in the medium is given by

$$W(x) = (1 - P(x))N\sigma = e^{-xN\sigma}N\sigma. \tag{4.7}$$

Therefore, the mean free path of a particle prior to collision is given by

$$\lambda = \int_0^\infty W(x)xdx = \int_0^\infty e^{-xN\sigma}xN\sigma dx = \frac{1}{N\sigma}. \tag{4.8}$$

For collisions on the nuclei of an atom specifically, N is the number of atoms per unit volume, and is defined as

$$N = \frac{\rho N_A}{A_r}, \tag{4.9}$$

where A_r is the relative atomic weight of the element, ρ is the density of the material, and N_A is Avogadro's constant. The cross section is the sum of all partial cross sections corresponding to all possible types of interaction.

4.3. The nucleon cascade in NEUT

Nucleons and pions produced in neutrino interactions in NEUT simulations are modelled as a cascade through the target nucleus wherein the nucleon may undergo FSI. In this case the nucleon or pion path is split into a finite number of steps, and at each point the probability of any interaction occurring is calculated as in equation 4.6. A random number is thrown based on this probability, that determines whether the particle survives or interacts. As the particle continues on its path, its position in the target nucleus is tracked, and the probability of interaction is scaled by the nuclear density at that point. There also exists a maximum radius beyond which a particle is considered to have escaped the target nucleus.

For the case of nucleons, if a final state interaction does occur, it may be categorised in the NEUT cascade as one of three following: quasi-elastic (including charge-exchange) if kinematic changes occur but no pions are produced, single pion production, or

double pion production. Which of these interactions is selected depends on the kinematics of the incident nucleon and another weighted random number. Below the single pion production limit, the only possible interaction type is quasi-elastic, while below the double pion production limit, quasi-elastic and single pion events are both possible. Above the pion production limit, all three interaction types can occur, and their relative probabilities are drawn from experimental data collected by Bertini between 1968 and 1971 [83] [84] [85]. The drawn probability depends solely upon the nucleon energy, and whether the nucleon-nucleon interaction is same species (proton on proton or neutron on neutron) or different species (proton on neutron or neutron on proton). This process continues at every step along the cascade until the incident nucleon and every other particle produced during the cascade have escaped the nucleus (or in the case of charge exchange, the resultant nucleon and all other particles produced in the cascade have escaped the nucleus). Daughter nucleons or pions undergo their own cascades, and may in turn produce daughter particles which undergo further cascades and so forth.

In contrast to nucleons, interaction probabilities in the NEUT pion cascade are taken from different sources for different pion energies. Low energy pion interactions are based on tables computed from the Salcedo Oset model [86], while higher energy pion's probabilities are calculated from $\pi^{\pm}$ scattering off free proton and deuteron cross section data compiled by the Particle Data Group [87].

4.4. Reweighting

Simulation of particle interactions is a process with a large time cost, wherein interaction events are generated according to a cross-section model. Monte Carlo methods are used to correctly distribute event properties. Event generators typically use rejection sampling whereby calculated interaction properties are accepted or rejected with probability proportional to predicted cross sections. For use in a particle physics analysis, generators may be required to tune simulation predictions. This tuning uses free parameters in the model, which may be varied to improve agreement between prediction and observed data. The process requires frequent variations of a large number of parameters, and therefore a full regeneration of the simulation for each variation is prohibitively inefficient.

Reweighting is an approximation process designed to circumvent the issue of computational inefficiency. In reweighting, every generated event is assigned a weight

that is proportional to the probability for that event. A scaling factor is calculated that can be combined with the original weight to determine the new weight that the same event would have with one or more varied model parameter values. As a result, only a fraction of the original simulation must be rerun, and the reweighting process may be faster than re-generation by many orders of magnitude, making large studies of agreement between models and data possible.

Typically, using reweighting to observe the response of a given parameter variation requires only re-evaluating the cross section for the event kinematics. Thus the scale factor, S, and the weight, W, for the event are defined as

$$S(\mathbf{x}', \mathbf{k}) = \frac{\sigma(\mathbf{x}', \mathbf{k})}{\sigma(\mathbf{x}, \mathbf{k})}, \tag{4.10}$$

leading to

$$W(\mathbf{x}', \mathbf{k}) = S(\mathbf{x}', \mathbf{k}) \times W(\mathbf{x}, \mathbf{k}), \tag{4.11}$$

where $\mathbf{x}$ and $\mathbf{x}'$ are the original and varied parameters, respectively, and $\mathbf{k}$ is the vector of event kinematics or other properties required to calculate the event cross section, σ. The reweighting process has some limitations. Only those events that feature in the original simulated set with a non-zero weight can appear in the set with varied parameters. The process is thus vulnerable if simulation statistics are low or parameter variations very high. Therefore, careful validation of reweighting is required prior to use in analyses.

Chapter 5.

Beam Test[1]

Following its construction, the HPTPC prototype was exposed to a charged particle beam in the T10 beamline at CERN in August and September 2018 [88]. For the purposes of the beam test, the T10 beam was run at a very low momentum, adjusted from 6.5 GeV/c down to 0.8 GeV/c. The beam test is described in detail in this section, including discussion of the physics goals of the experiment in section 5.1, the preliminary simulations that informed the decisions on how the beam test should be conducted in section 5.2, and the individual elements of the beam test set up itself in section 5.3. Thereafter, an analysis of the beam test results is provided in section 6.1.

5.1. Beam test motivation

The impact of final state interactions on the cross section modelling that is crucial for long baseline neutrino analyses is described in chapter 4. The key proton kinetic energy range to be explored in order to distinguish between nuclear models is the region below 100 MeV. The proton multiplicity and kinetic energy distributions for ν_μ charged-current (CC) interactions on argon calculated by GENIE, NEUT, and NuWro are highly discrepant, particularly in the fraction of events with few ejected protons, and at low proton kinetic energy. This is predominantly below the proton detection threshold in liquid Argon TPCs (40 MeV) and in water Cherenkov detectors (500 MeV). The lower threshold in high pressure gas provides a unique opportunity to distinguish between neutrino interaction models for the same nuclear target.

[1] The structure of the description in the following two chapters follows that of the paper [1] of which I am one of two primary authors

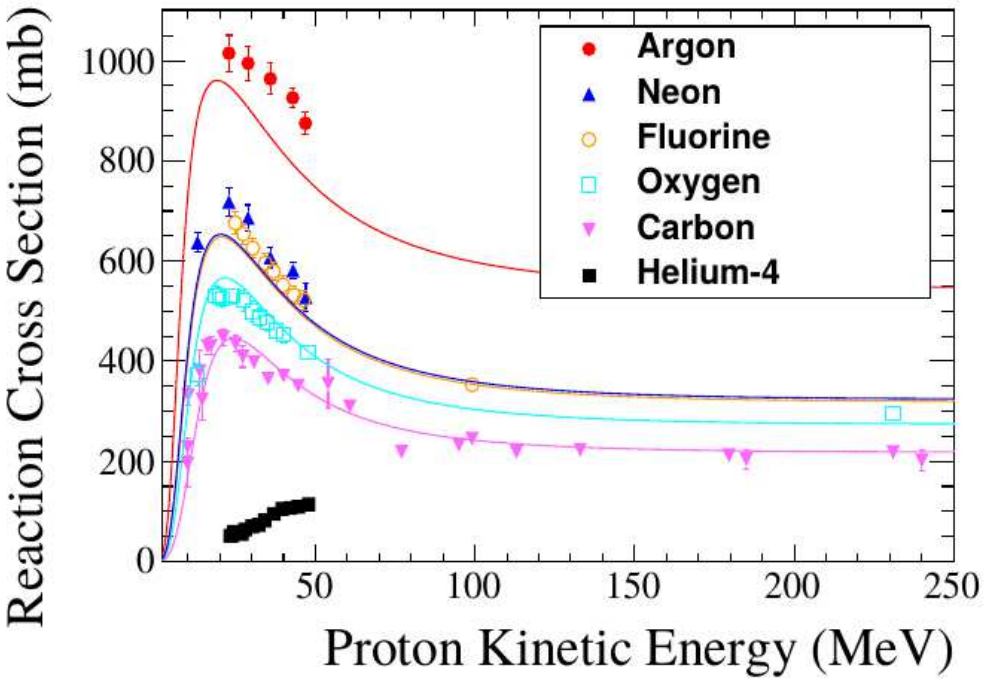

Figure 5.1.: Figure showing general state of measurements in the low momentum proton region. A number of data points have been collected for Carbon, but measurements in the region are sparse for other elements. The applied curves show the semi-empirical Wellisch and Axen model [89] applied to the data points [90].

The research and development goal of the beam test was to provide proof of concept of the HPTPC prototype with dual charge and optical readout, observing hadrons with energies comparable to those from neutrino interactions. Additionally, the physics objective of the HPTPC beam test was to make measurements of these protons on argon at kinetic energies below 200 MeV. This would provide data in the relatively bare low momentum region to inform cross-section modelling. The sparsity of data in this region is shown in figure 5.1

To enhance the low energy proton flux at the T10 beamline, a novel technique was designed: acrylic moderator blocks would be placed directly in the beamline, in order to spread and slow the beam particles via multiple Coulomb scattering. Subsequently, the TPC would be placed in an off-axis position, to achieve a beam composition with lower-energy protons than would otherwise have been possible in the T10 beamline. These techniques were designed to increase the ratio of protons to minimum ionizing particles (MIP) in the HPTPC, and to decrease the proton momentum and multiplicity

Table 5.1.: Total number of spills recorded for each moderator block configuration included in this paper.

Number of moderator blocks	Recorded spills
0	257
1	254
2	267
3	220
4	3884

in the active region of the TPC. Initial studies performed to decide on the details of the application of this technique are described in the following section.

Additionally, two time of flight systems described in section 3.4 were used. Their main use was as follows: to assess how successfully the combination of off-axis positioning and a moderated beam at the PS produced momenta more closely in line with neutrino cross-section studies, and to characterize the incident flux on the TPC active region, as well as the flux exiting the TPC, for the analysis of TPC data. The number of spills recorded for each number of moderator blocks is shown in table 5.1. More data were taken for 4 blocks as that was the primary configuration used for the beam test.

5.2. Initial beam test simulations

The method of using moderator blocks and placing the TPC in an off-axis position was informed by simulations performed in GEANT4. The basis for deciding on these methods, as well as determining the inputs to these simulations was data taken by other members of the collaboration at an earlier commissioning beam test at the T9 and T10 beamlines in 2016 [65]. A measurement of the time of flight of particles during those studies is given in figure 5.2. A time of flight system with much less precise timing resolution than those described in section 3.4 was used but, nonetheless, distinct proton and pion peaks can be seen.

Additionally, measurements of the multiplicity of protons and other minimum ionizing particles (MIPs) (labeled here as pions) at different energies were made. The distribution for T10 is shown in figure 5.3. The proton and pion fluxes are shown as a function of beam energy. At the energy relevant to the 2018 beam test, 0.8 GeV, the ratio of protons to pions is approximately 0.2. The width of the beam was determined

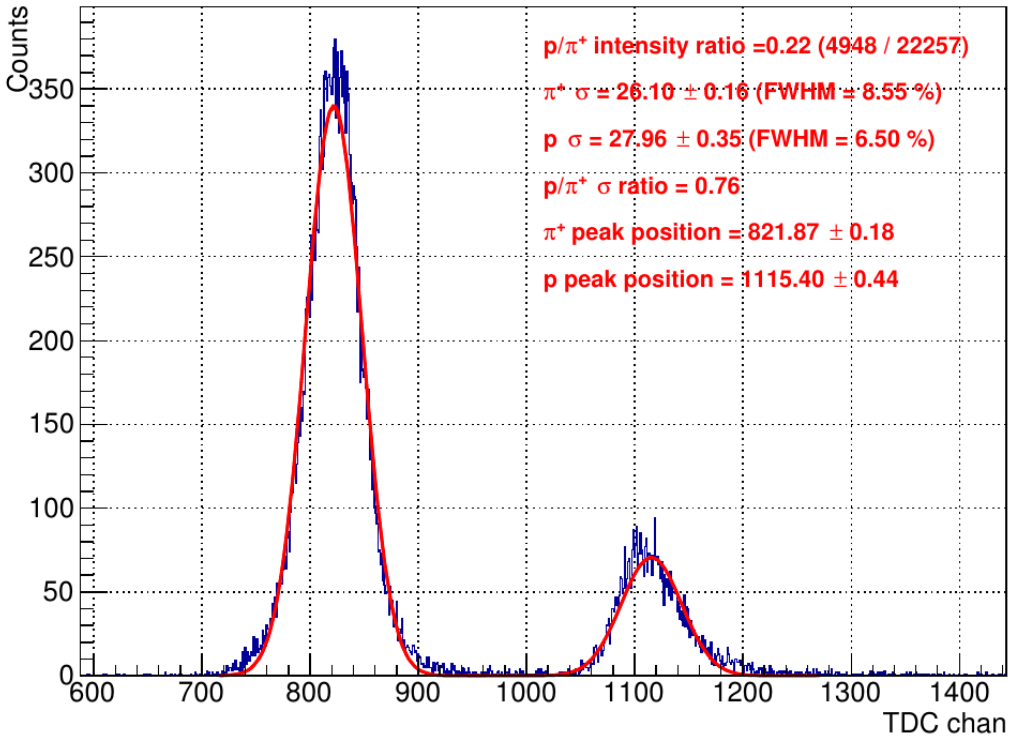

Figure 5.2.: Figure showing ToF spectrum measured at the T10 beamline, at an energy of 0.9 GeV. A Gaussian is fitted to each peak in red. Figure taken from [65].

by collimators, and no measurement was made of the initial dispersion of the beam.

In order to inform the operation of the beam test, MC simulations were run prior to it. The initial beam conditions simulated were chosen based on documentation of the 2016 beam test. A beam of protons of 0.8 GeV protons and pions in the ratio 1:5 were simulated. The initial width of the beam had to be estimated, and a Gaussian form was chosen, with a standard deviation of 0.2 m and 0.1 m in the vertical direction and other directions, respectively. Subsequently, a collimation of 0.14 mm was applied to the beam in both directions at the beam entrance. The initial direction of all beam particles was estimated to be entirely in the beam direction coordinate with negligible dispersion.

The primary purpose of the simulation was to determine the efficacy of using moderator blocks and the off-axis method. As such, an acrylic moderator block of length 35cm was simulated at the start of the beam line, and the results of the simulation are shown as a function of the angle of the beam axis.

The simulated composition of the beam of particles actually reaching the TPC active area is shown in figure 5.4 as a function of off-axis angle of the centre of the TPC, along

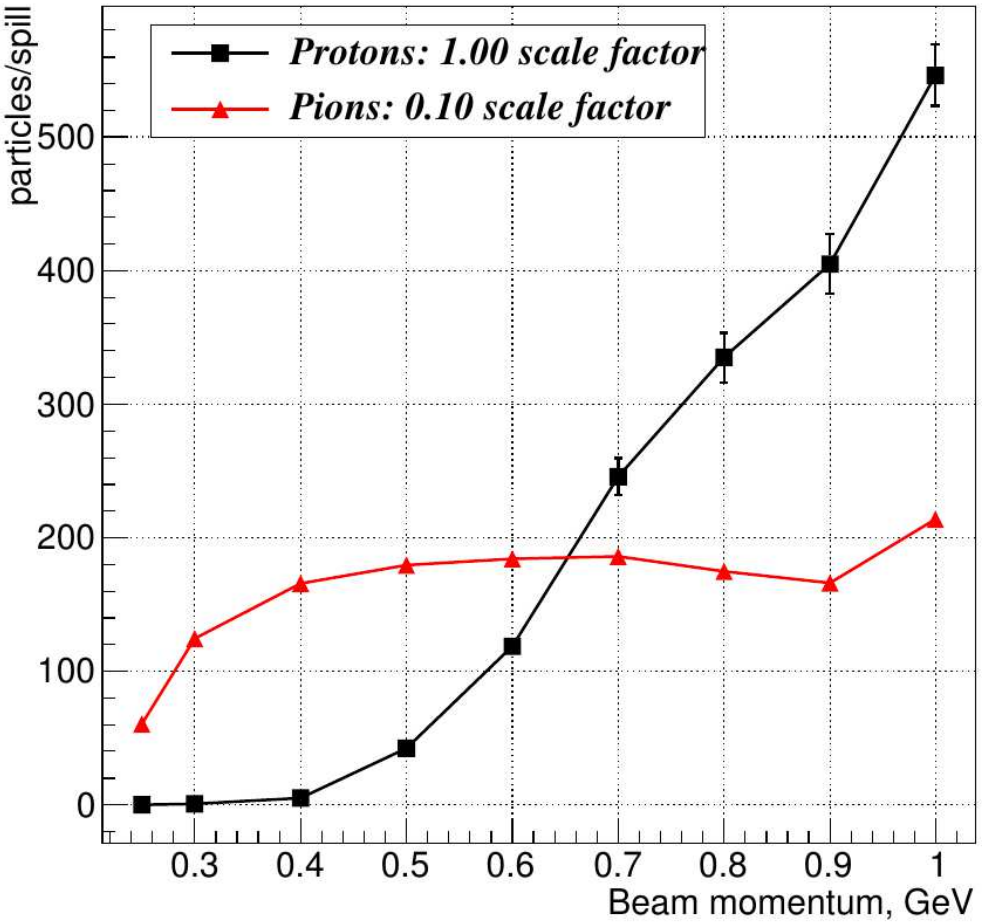

Figure 5.3.: Particle rates at the T10 beamline measured in 2016. The proton and pion rates are shown at multiple different beam energies. For clarity, the pion rate has been scaled by a factor of 0.1. Figure taken from [65].

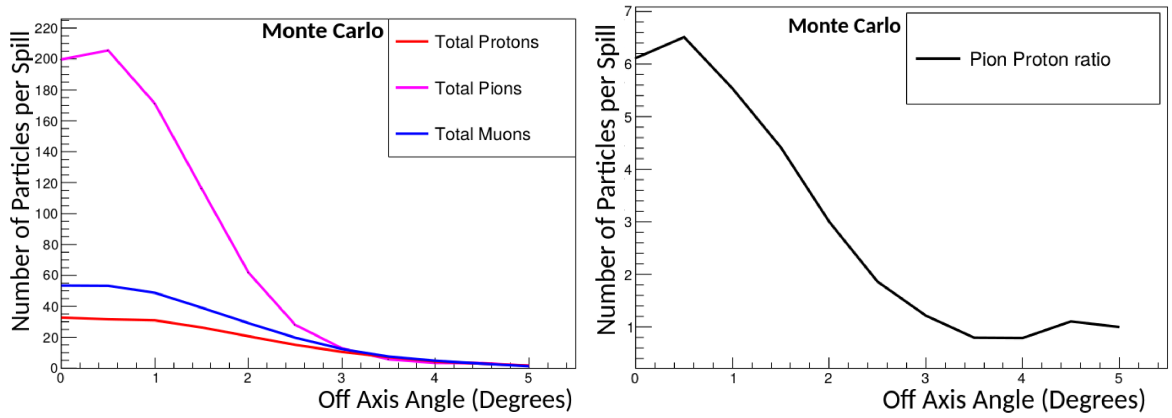

Figure 5.4.: Composition of simulated particles arriving at the active region of the TPC as a function of off-axis angle. Left: Number of particles of each type per spill. Right: Ratio of pions to protons.

with the ratio of pions to protons. The range of off-axis angles shown is the range over which the TPC could physically be placed. The number of particles per spill decreases as the TPC is placed further off axis, but protons diminish at a slower rate than pions. Therefore, the further off axis the TPC is placed, the larger the ratio of protons to pions, up to a maximum of about 4°, beyond which such a large proportion of the protons have been attenuated in the walls of the steel vessel, that the ratio begins to rise again.

Figure 5.5 shows the number of protons in different energy bands reaching the TPC, as a function of the angle between the centre of the TPC and the beam. Placing the TPC at around 2-3.5° off-axis produces the greatest number of 0-200 MeV protons as a proportion of all particles reaching the TPC. The continuous range of energies is shown for two specific TPC positions in figure 5.6: on axis and 4° off axis. Going from the beam axis to 4° off axis shows a large increase in the proportion of low energy particles, including protons in the low energy region of interest. However, the total number of particles reaching the TPC is strongly reduced.

From these studies, it is clear that the position of the TPC is a tradeoff between, on the one hand, accessing the low energy region with a greater ratio of protons to background pions, and on the other hand reducing the total flux of particles entering the detector. While some reduction in flux is welcome, to avoid oversaturation of the detector, too much would decrease the number of event samples in the data below an acceptable level. Based on the results of this study, the position at the beam test of

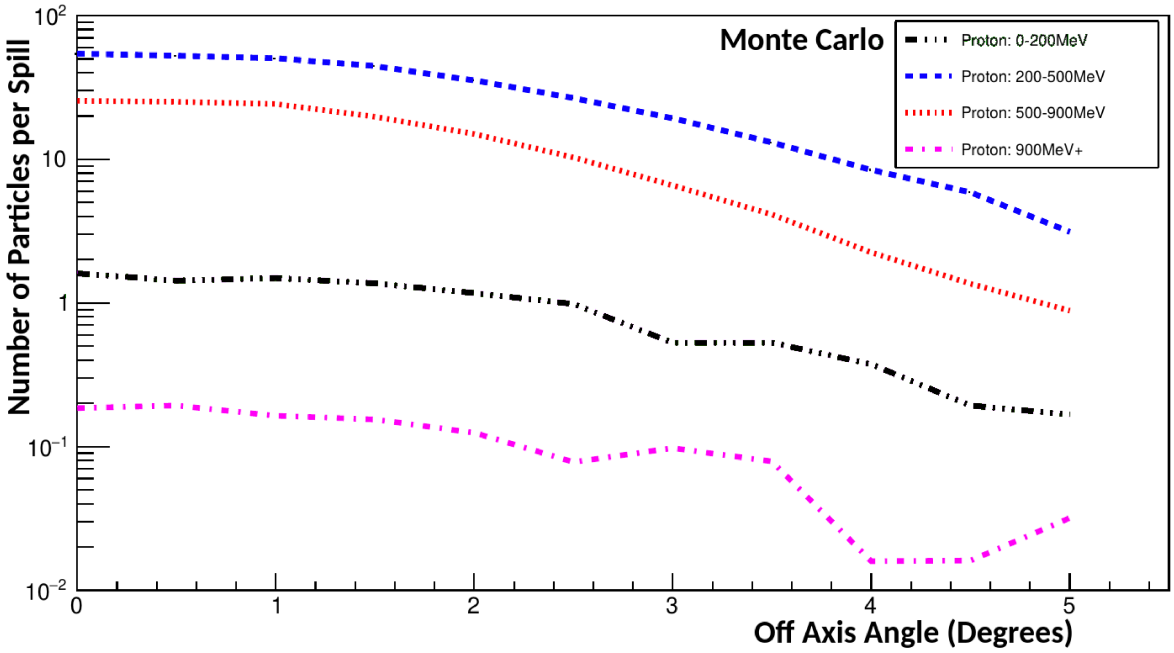

Figure 5.5.: Energy of simulated protons reaching the active TPC region as a function of off axis angle, on a log scale.

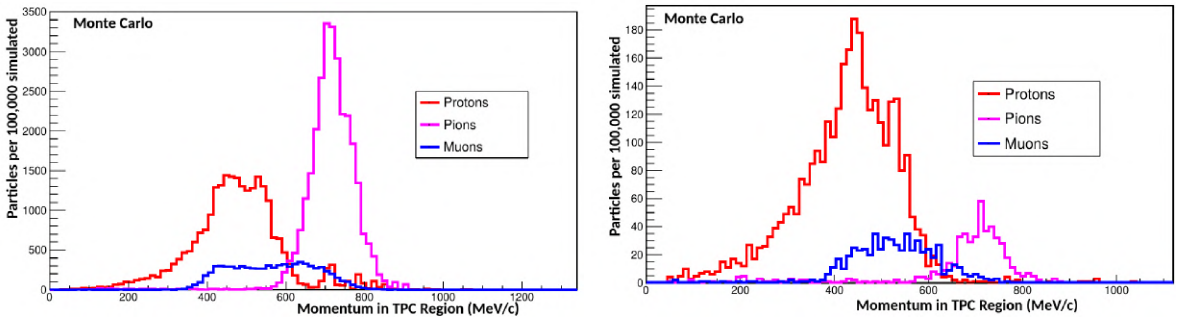

Figure 5.6.: Momentum profile of different simulated particle species reaching the TPC active region in a spill. Left: Directly on the beam axis. Right: 4° off the beam axis.

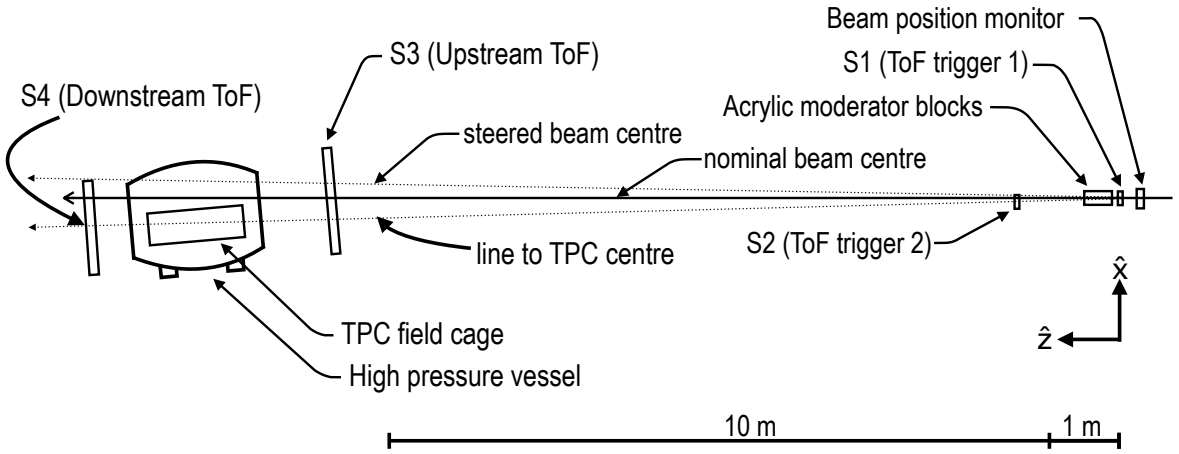

Figure 5.7.: Plan view diagram of the HPTPC beam test configuration at the CERN T10 area.

the centre of the TPC was chosen to be at an off-axis angle of 2.5°, with the full TPC spanning the off-axis range 2-3°.

5.3. Composition of the beam test

The beam test took place in the T10 beam line, in the East Area at the Proton Synchrotron (PS) at CERN from 15 August to 18 September 2018. The T10 beamline, a secondary beam derived from the PS beam, consists primarily of protons, electrons and charged pions [91]. The main components of the experimental setup are shown schematically in figure 5.7.

Upstream of all the ToF constituents and the TPC, a beam position monitor (BPM) was situated at the beam entrance into the test area. The TPC was placed 13 m downstream of the BPM and 0.67 m away from the beam centre, such that the TPC active region spanned off-axis angles 1.4–3.8°. The TPC position was determined to be between 2° and 3° off the beam axis. However, space constraints required the TPC not be placed that far off the nominal beam centre. Therefore, the beam was steered away from its nominal position by an angle of about 1°, with the TPC placed 1.5° from the nominal beam centre. There were four ToF constituents:

- *S1*, a small-area beam trigger, as described in 3.4.1;
- *S2*, a coincidence measurement with *S1*, as described in 3.4.1;

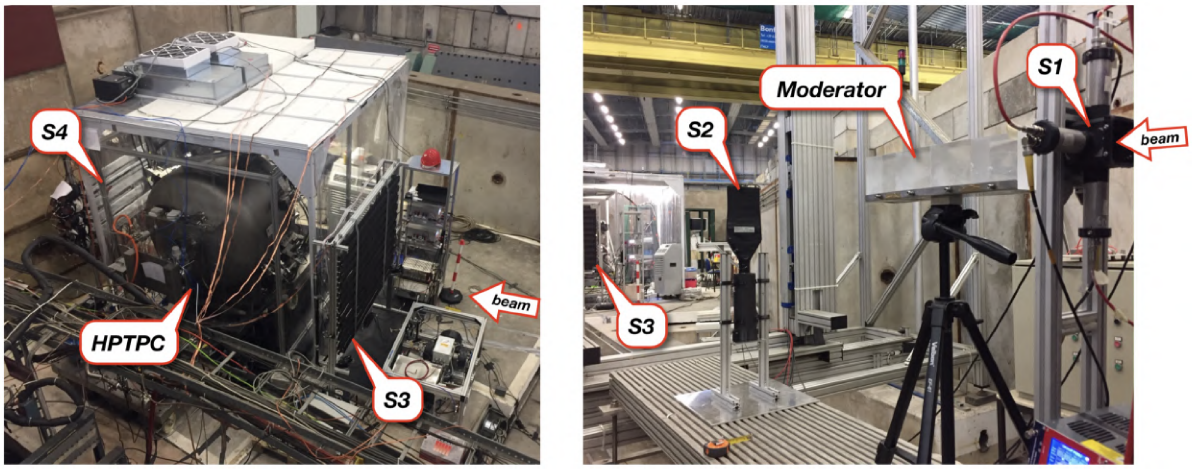

Figure 5.8.: The full HPTPC beam test set up. Left: the downstream section of the set up including the *S3*, *S4* detectors and HPTPC. Right: the *S1* and *S2* counters and the stand with four acrylic moderator blocks further upstream.

- *S3*, a wall of plastic scintillator bars placed directly upstream of the TPC vessel, as described in 3.4.1;
- *S4*, a wall of plastic scintillator bars placed directly downstream of the TPC vessel, as described in 3.4.2.

Directly between *S1* and *S2*, a variable number of blocks of acrylic were placed, and are shown in figure 5.8. Both the TPC and ToF systems were placed at an off-axis angle with respect to the direction of the beam (see section 5.3.1 for further details). To study the impact of moderator thickness, a variable number of blocks of acrylic, each of dimension $10 \times 10 \times 10$ cm^3, were placed in the beamline and are shown in figure 5.8. The moderator blocks have the effect of both reducing the energy of incoming particles as well as scattering protons in the beam through higher angles than beam MIPs. This tends to increase the proton-to-MIP ratio at low off-axis angles from the beam, while decreasing the total number of protons and MIPs traversing the TPC. Data were collected with the T10 beam momentum setting at 0.8 GeV/c, and with each configuration of 0 to 4 moderator blocks.

The data acquisition (DAQ) systems of the upstream (*S3*) and downstream (*S4*) ToF systems were fully independent. Synchronization between ToF DAQ systems was performed offline. The synchronization used the reference signal from the PS at the beginning of every spill. T10 received between 1 and 3 spills from the PS each supercycle, which has an average duration of 33 s. The spill duration is approximately 400 ms, with a minimum separation in time between two spills of approximately 1

Table 5.2.: Angular positions of detector elements within the T10 beamline as measured with respect to *S1*.

Object	Minimum θ	Maximum θ	Minimum ϕ	Maximum ϕ
S2	$-3.96^\circ \pm 0.03^\circ$	$-0.36^\circ \pm 0.03^\circ$	$-2.01^\circ \pm 0.03^\circ$	$2.94^\circ \pm 0.03^\circ$
S3	$-5.923^\circ \pm 0.004^\circ$	$3.040^\circ \pm 0.004^\circ$	$-3.215^\circ \pm 0.004^\circ$	$3.344^\circ \pm 0.004^\circ$
S4	$-6.083^\circ \pm 0.003^\circ$	$-0.401\circ \pm 0.003^\circ$	$-1.426\circ \pm 0.003^\circ$	$1.771^\circ \pm 0.003^\circ$
TPC upstream face	$-3.590^\circ \pm 0.010^\circ$	$-1.439^\circ \pm 0.010^\circ$	$-2.662^\circ \pm 0.010^\circ$	$2.575^\circ \pm 0.010^\circ$
TPC downstream face	$-3.778^\circ \pm 0.009^\circ$	$-1.806^\circ \pm 0.009^\circ$	$-2.440^\circ \pm 0.009^\circ$	$2.361^\circ \pm 0.009^\circ$

second. Therefore the start-of-spill signal frequency is 1 Hz or smaller. The trigger condition of the upstream ToF (*S3*) was based on the coincidence between *S1* and *S3* constituents. *S2* signals were also recorded by the upstream ToF DAQ, however these did not feature in the trigger. The DAQ of the downstream ToF (*S4*) was run in self-triggering mode with a gate open during the spill. Additionally, coincidence signals between *S2* and *S4* counters were recorded by the downstream ToF DAQ and were used in the particle identification (PID), described in section 6.1.

5.3.1. Survey and coordinate system

The T10 beamline area was surveyed, and the distances to various components measured to a precision of 0.5 mm by the CERN Survey, Mechatronics and Measurements (SMM) group. Multiple points on each of *S1*, *S2*, *S3*, *S4* and the TPC frame have had their positions measured relative to an origin located at the nominal T10 beam focussing point.

The axes of a right-handed coordinate system are defined as follows: $\hat{x}$ describes the non-beam horizontal direction, $\hat{y}$ the vertical direction, and $\hat{z}$ the beam direction, as shown in figure 5.7. Results are shown in terms of two off-axis angles: θ, which is measured in the $\hat{x} - \hat{z}$ plane with positive angles measured in the $+\hat{x}$ direction, and ϕ, which is measured in the $\hat{y} - \hat{z}$ plane with positive angles measured in the $+\hat{y}$ direction. The origin is defined to be at *S1*.

Figure 5.9 shows the angular positioning of objects within the beamline according to this coordinate system. Table 5.2 shows the calculated angular positions of the various beamline components measured from *S1*.

Table 5.3 shows the distances between centres of the objects in the T10 beamline. These distances were calculated using the survey data gathered.

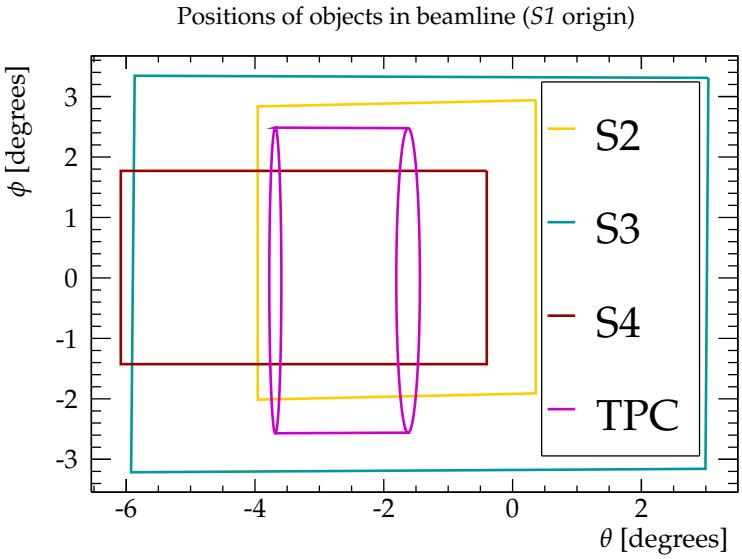

Figure 5.9.: Angular position of the detectors the T10 beamline. The origin in this view is at the centre of *S1*; the true centre of the steered beam is at $+1^{\circ}$ in θ and 0° in ϕ.

Table 5.3.: Relative distances between centres of detectors in the T10 beamline. US and DS refer to upstream and downstream, respectively.

Points	Distance between centres
Beam monitor – *S1*	(0.2882 ± 0.0014) m
$S1 - S2$	(1.4194 ± 0.0014) m
$S1 - S3$	(10.7562 ± 0.0014) m
S3 – TPC US side	(1.322 ± 0.002) m
TPC DS side – *S4*	(0.917 ± 0.002) m
$S2 - S4$	(12.6510 ± 0.0014) m

Chapter 6.

Test Beam Flux Measurements

6.1. Time of Flight analysis

A particle of mass m and momentum p travelling over a distance d will traverse that distance in a time

$$t = d\sqrt{\frac{m^2}{p^2} + \frac{1}{c^2}} \tag{6.1}$$

where c is the speed of light in a vacuum. Therefore, particles with smaller mass or greater momentum cross the same distance in a shorter time. Consequently, in a beam composed of a number of different particles of the same momenta, such as the beam at the Proton Synchrotron at CERN, the mass of a particle can be determined by measuring this time of flight, t.

As an example, a charged pion with a momentum of 0.8 GeV/c will have a time of flight from *S1* to *S3* (a distance of 10.8 m) of 37 ns, while a proton with identical momentum will have a time of flight of 55 ns. For the same two particles travelling between *S2* and *S4* (a distance of 12.7 m), the charged pion would have a time of flight of 43 ns and the proton would again have a longer time of flight of 65 ns. The predicted times of flight for a number of different particles across the $S1 - S3$ distance and the $S2 - S4$ distance are shown in figures 6.1 and 6.2, respectively.

Varying the number of acrylic moderator blocks placed in the beamline, changes the profile of the beam and consequently the time of flight distribution. Figure 6.3 shows the time of flight spectrum recorded in the *S3* timing point as the number of these moderator blocks was changed. The earlier peak is formed by MIPs, while the peak

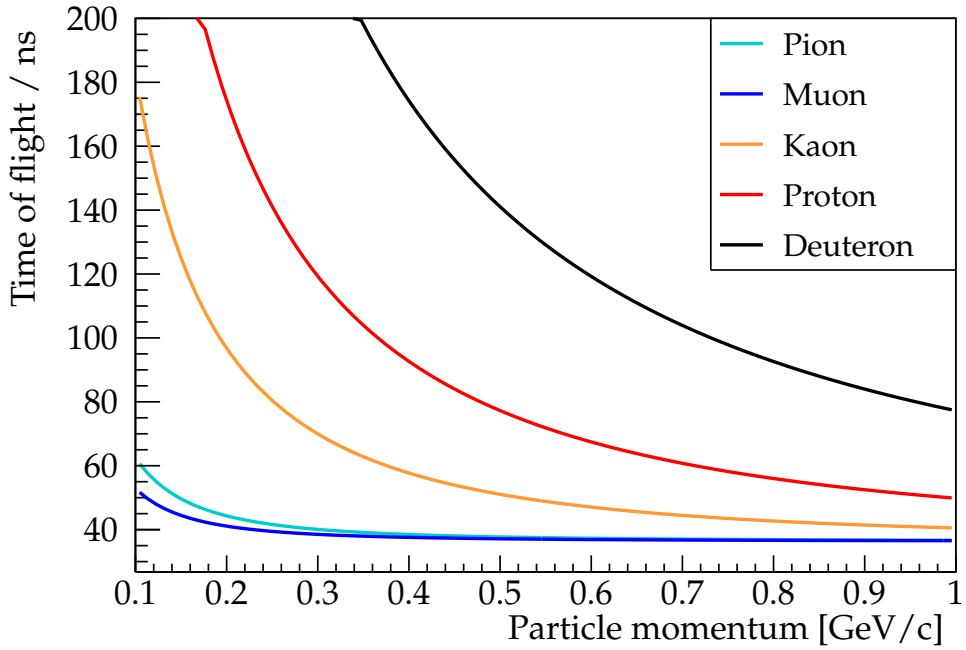

Figure 6.1.: Calculated time of flight between *S1* and *S3* for different particle species as a function of particle momentum.

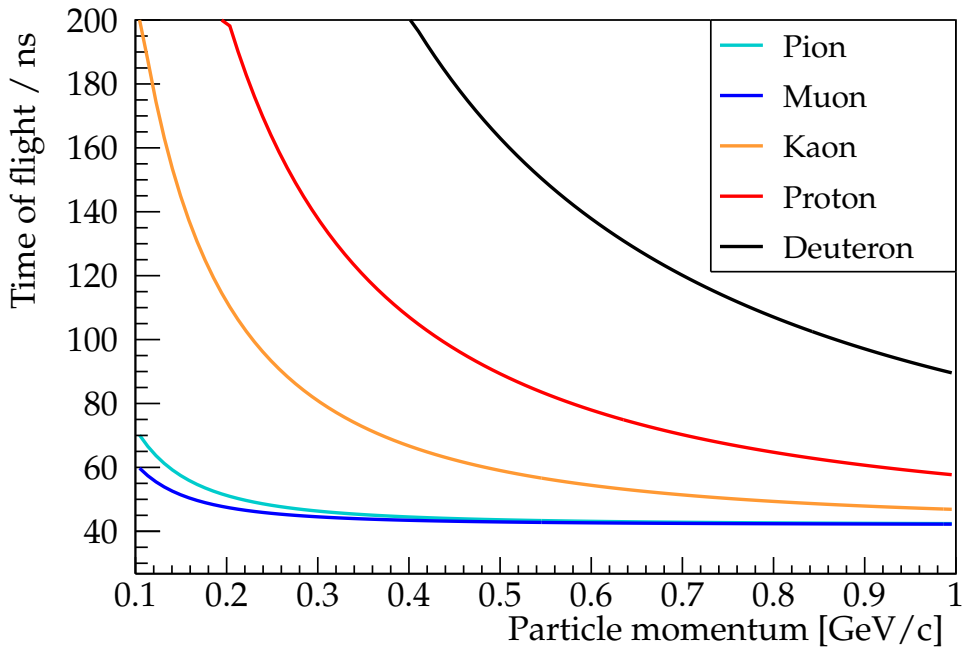

Figure 6.2.: Calculated time of flight between *S2* and *S4* for different particle species as a function of particle momentum.

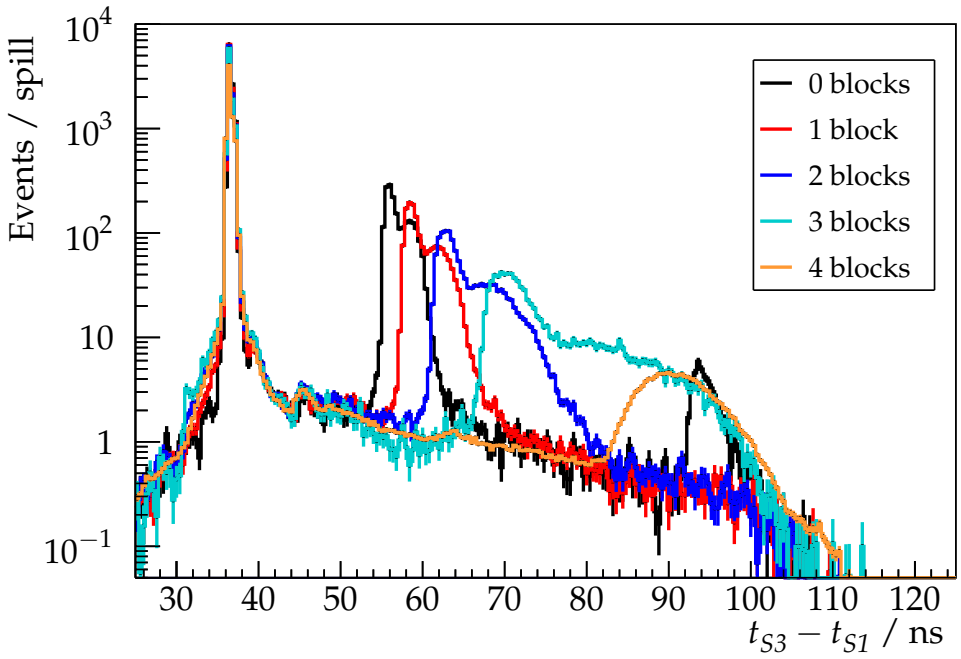

Figure 6.3.: *S3* time of flight spectra for different moderator block configurations.

at higher values of $S3 - S1$ corresponds to protons. In the black curve, which shows the 0 block data, a deuteron peak can be seen centered at 95 ns. The timing ranges for particle species selection are chosen using the analytic expectations shown in Figure 6.1. The proton peaks show a double peak feature, with a smaller delayed peak closely following the main proton peak; this feature appeared after the beam was steered so that the full 2.5 degree off-axis angle could be achieved and is due to a portion of beam scattering in the steering magnets, leading to the slower peak. The part of the beam which does not impinge on the steering magnets produces the quicker proton peak in the spectrum. Figure 6.4, left and right, shows the proton peak for the unsteered beam and the double peak structure is not present.

In order to calculate the correct time of flight, timing delays caused by cabling and equipment are taken into account and subtracted. The method used to correct the measurements of the time of flight between *S1* and *S3*, and *S2* and *S4* is identical. The initial recorded time, t_i, is either t_{S1} or t_{S2} while the final recorded time, t_f is then t_{S3} or t_{S4} respectively.

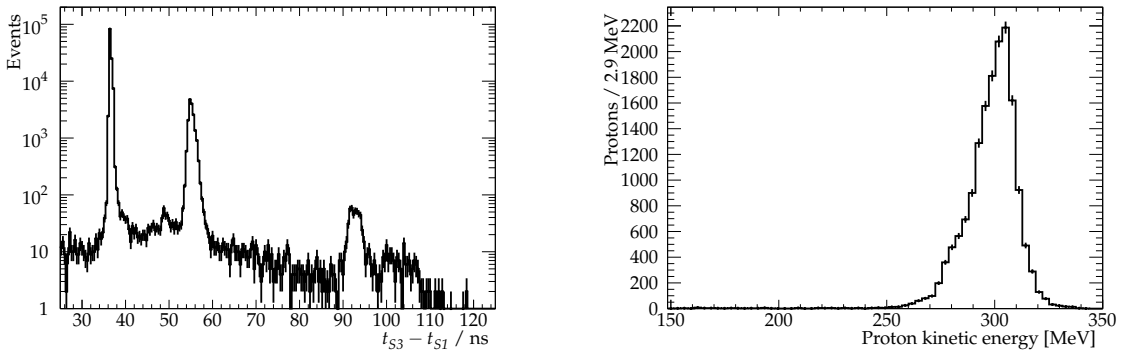

Figure 6.4.: Measurements of the unmoderated and unbent T10 beam over a baseline of 10.8 m for a selected beam momentum of 0.8 GeV/c. Measurements are made in the *S3* detector. The peak between 50 ns and 60 ns is produced by protons. Left: Time of flight spectrum. Right: Measured kinetic energy of protons.

A signal measured in the same DAQ from the more upstream counters (*S1* or *S2*) is recorded at a time

$$t_{i,\,\mathrm{rec}} = t_i + t_{i,\,\mathrm{delay}}\,, \tag{6.2}$$

while a signal measured in the detector walls (*S3* or *S4*) which occurs at a true time t_f is recorded as happening at a time

$$t_{f,\,\mathrm{rec}} = t_f + t_{f,\,\mathrm{delay}}\,, \tag{6.3}$$

where $t_{f,\,\mathrm{delay}}$ and $t_{i,\,\mathrm{delay}}$ are the total delays caused by cabling and equipment between the respective detectors and the DAQ. Therefore, the true time of flight, $t_f - t_i$, is given by

$$t_f - t_i = t_{f,\,\mathrm{rec}} - t_{i,\,\mathrm{rec}} - \left(t_{f,\,\mathrm{delay}} - t_{i,\,\mathrm{delay}}\right)\,, \tag{6.4}$$

where $t_{f,\,\mathrm{delay}} - t_{i,\,\mathrm{delay}}$ must be determined. The determination of $t_{f,\,\mathrm{delay}} - t_{i,\,\mathrm{delay}}$ is performed by fitting a Gaussian to the peak corresponding to faster particles observed in the 0 block data which is considered to have been produced by MIPs.

A charged pion with a momentum of 0.8 GeV/c has a speed of 0.985c and therefore traverses the distance between *S2* and *S4* (12.7 m) in a time of 42.6 ns. Fitting a Gaussian to the data, the mean of the MIP peak lies at (86.31 ± 0.019) ns. Substituting this value for $t_{S4,\,\mathrm{rec}} - t_{S2,\,\mathrm{rec}}$ in equation 6.4 gives a value for $t_{S4,\,\mathrm{delay}} - t_{S2,\,\mathrm{delay}}$ of 43.7 ns. This shift is applied to all measured times, in order to arrive at a final value of

$t_{S4} - t_{S2}$ used in the analysis. The process is repeated for the upstream wall, *S3* data, which is found to require a timing shift of 65.0 ns.

For runs without any moderator placed in the beamline, the mass distribution of particles is shown in figure 6.5. This distribution is produced by converting the time difference between *S3* and *S1* counters corresponding to a given particle to mass. Starting from the equation for relativistic momentum

$$p = \gamma m v \,, \tag{6.5}$$

where m is the mass of the particle, v is the speed of particle and γ is the Lorentz factor. Squaring and rearranging this expression gives

$$m^2 = \frac{p^2}{\gamma^2 v^2} \,, \tag{6.6}$$

where the Lorentz factor can be expanded to give

$$m^2 = p^2 \left(\frac{1}{v^2} - \frac{1}{c^2} \right) \,, \tag{6.7}$$

where c is the speed of light in a vacuum. Expressing v as the distance between *S1* and *S3* ($x_{S3} - x_{S1} = 10.9$ m) divided by the time difference between the *S1* and *S3* counters ($t_{S3} - t_{S1}$) gives

$$m^2 = p^2 \left(\left(\frac{t_{S3} - t_{S1}}{x_{S3} - x_{S1}} \cdot c \right)^2 - 1 \right) \,, \tag{6.8}$$

in natural units, where the particle momentum p is assumed to be 0.8 GeV/c. The true particle masses in figure 6.5 are indicated by vertical arrows. Distinct peaks corresponding to protons and deuterons are clearly visible. The insert in the figure shows the zoomed in region close to 0, showing the masses of MIPs.

For data collected by *S3*, both signal amplitude and timing cuts were used to differentiate protons and MIPs. Figure 6.6 shows an example of the signal size recorded in one of the SiPMs on one of the scintillator bars against the measured value of $t_{S3} - t_{S1}$. At the beam energies in question, the protons typically deposit more energy in the detector due to their higher mass, resulting in greater observed amplitudes. Therefore, in order to reduce the number of background events in the proton sample, a selection criterion of a minimum required signal amplitude is used. This cut varies with

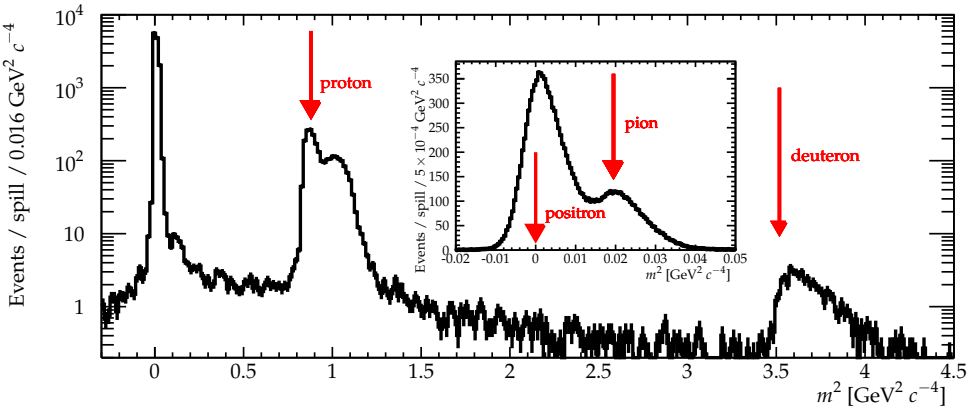

Figure 6.5.: Reconstructed mass spectrum of the beam contents with 0 moderator blocks calculated from the upstream time of flight wall. The time difference between *S3* and *S1* was used to calculate mass. Red arrows show the predicted mass squared of particles given a momentum of 0.8 GeV/c. The inset figure shows the area around 0 mass in greater detail.

each SiPM, and is determined from such distributions as those shown in figure 6.6. Overall, the signal amplitude cut values vary from 0.125 V to 0.3 V. Particles for which 35.75 ns $< t_{S3} - t_{S1} <$ 37.75 ns are identified as MIPs. Particles which pass the amplitude cut and for which 53 ns $< t_{S3} - t_{S1} <$ 115 ns are identified as protons. The upper bound of this timing cut is reduced to 80 ns for the unmoderated sample in order to exclude deuterons.

A correction must be applied to the upstream ToF DAQ (*S1*, *S2* and *S3*) to account for its large dead time. The $S1 \cap S2$ signal is digitised by both the upstream and downstream ToF DAQ. The dead time of the downstream ToF DAQ is found to be negligible. A linear relationship between the number of $S1 \cap S2$ signals measured in each DAQ is determined for each moderator block sample. Therefore, events measured in the upstream ToF DAQ are weighted, such that the number of $S1 \cap S2$ signals measured in the upstream and downstream ToF DAQs are approximately equal.

Figure 6.7 shows the time of flight spectrum varying with changing number of moderator blocks as recorded by *S4*. This spectrum is given by the difference in time between observation of a coincidence in the *S1* and *S2* timing points and a signal being recorded in *S4* (the definition of an *S4* signal is given above).

In addition, the reconstructed mass distribution for particles travelling between *S2* and *S4* is given in figure 6.8. The distribution is again produced using equation 6.8. In this case, $x_{S4} - x_{S2} = 12.7$ m. In contrast to the same distribution produced for

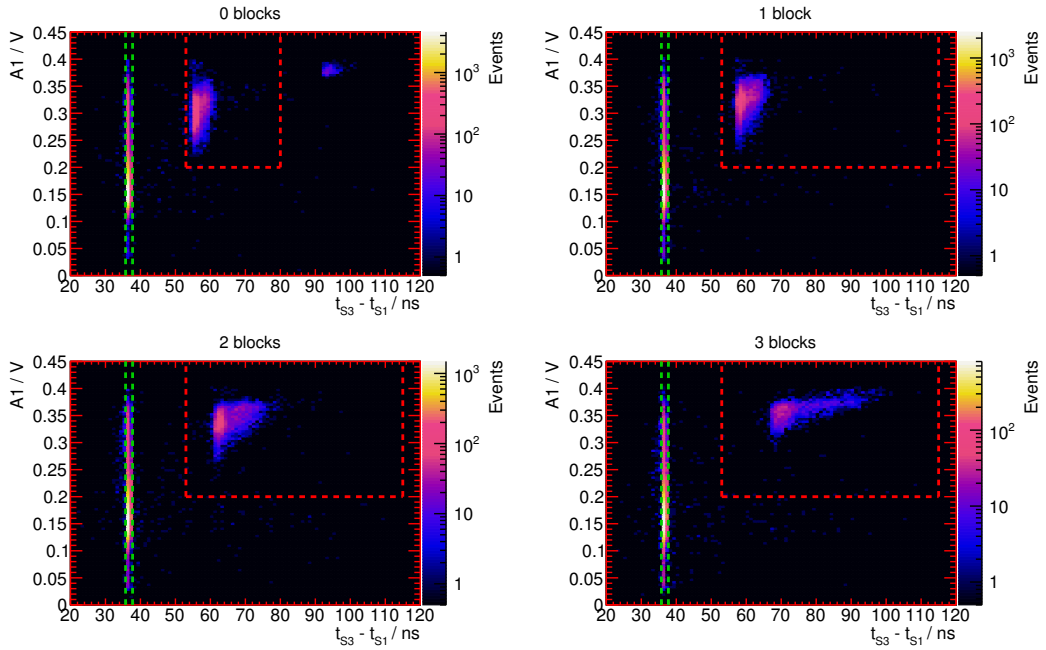

Figure 6.6.: Examples of SiPM signal amplitude against the time of flight from *S1* to *S3* for different numbers of moderator blocks from 0 to 3. The voltage recorded in the SiPM is labelled as A1. The red dashed line shows the amplitude cut used for that SiPM. The population corresponding to the enclosed areas in red dashed rectangles is that of protons. The population corresponding to the enclosed areas in green dashed rectangles is that of MIPs.

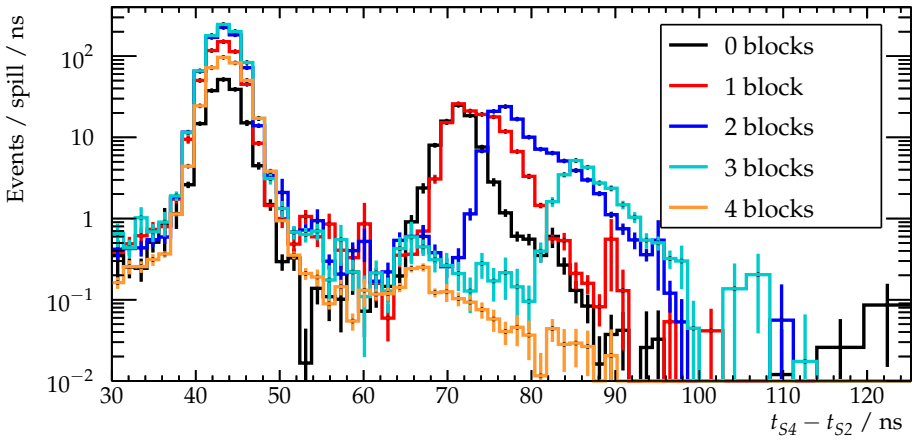

Figure 6.7.: *S4* time of flight spectra for different numbers of moderator blocks. In the case of each configuration, a flat background has been fit to and subtracted from the data. Furthermore, a correction has been made for the differing efficiencies of the various bars and for the variation in efficiency as a function of position along the bar. As in the case of *S3*, a proton peak and a MIP peak are observed.

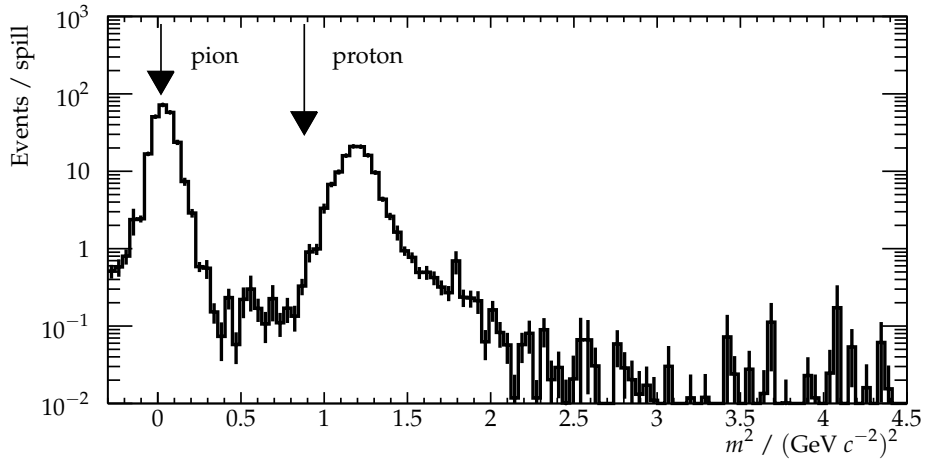

Figure 6.8.: Reconstructed mass spectrum for the data taken without moderator blocks calculated from the downstream time of flight wall. The spectrum was determined using the time difference between *S4* and *S2*. Vertical arrows show the calculated predicted position of particles.

particles travelling from *S1* to *S3* as shown in 6.5, no deuteron peak can be seen. This is a consequence of the attenuation of deuterons within the walls of the TPC. Additionally, the predicted proton position does not line up perfectly with the measured proton position. This is also due to the effect of the TPC, which lies upstream of *S4*: Protons passing through the TPC walls lose energy, resulting in their having less momentum than the original 0.8 GeV/c beam. In turn, this results in protons having a larger reconstructed mass than predicted. The displacement of the proton mass peak in Figure 6.8 is consistent with the expected energy loss in the vessel walls. This consistency is shown with MC studies in Section 6.2.3. These MC studies also show that, at the energies used in this study, approximately 40% of protons which impinge on the vessel stop within it.

A correction is made for the variation in particle detection efficiency between the bars and for the variation in this efficiency as a function of the position along each bar. This correction is performed using the cosmic ray flux. It is assumed that the flux of cosmic rays passing through each part of *S4* is equal. Each *S4* bar is divided into 7 cm segments for analysis, and the number of cosmic rays passing through each segment is measured by assuming that all signals occurring outside of beam spills are produced by cosmic rays. The efficiency is then found from this distribution by normalising the bin with the highest number of cosmic ray signals to 1. This efficiency is highest around the middle of the bars (70 cm) because of the requirement that coincident

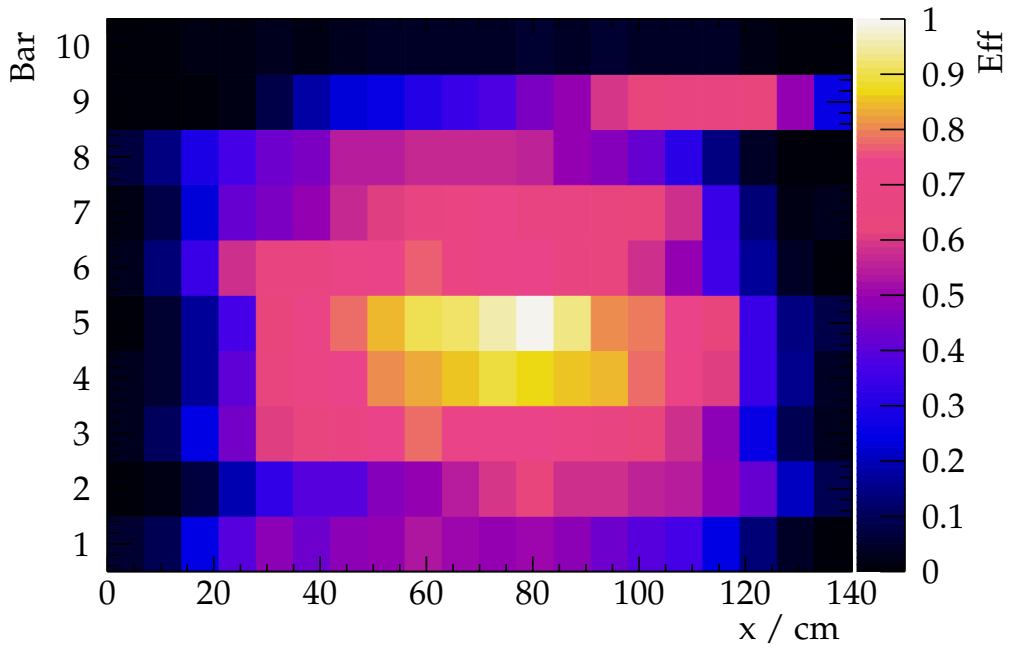

Figure 6.9.: Relative detection efficiency of *S4* as a function of bar number and position along each bar calculated from cosmic ray data. The efficiency of bar 10 is very low, so it was excluded from the data analysis.

signals are observed in both PMTs on a given bar in order for a hit to be recorded. An example of one of these distributions is shown in Figure 6.9. Events are then weighted according to the bar in which they are observed and their measured position along this bar. The weight applied is the inverse of the value shown on the z-axis of Figure 6.9. Additionally, a further weight is applied to all *S4* events of 1.25. This weight is derived from tests performed on the *S4* bars with a ^{90}Sr source. Using this source, it was determined that the maximum measured rate of signals produced by the ^{90}Sr source was equal to 0.8 of the true rate.

Informed by figure 6.7, protons and MIPs are differentiated with timing cuts. The particles in the earlier timing window (those for which $t_{S4} - t_{S2} < 51$ ns and $t_{S4} - t_{S2} > 36$ ns) are designated to be MIPs while those in the later timing window (those for which $t_{S4} - t_{S2} < 285$ ns and $t_{S4} - t_{S2} > 62$ ns) are designated to be protons. These timing cuts are chosen by fitting a sum of signal and background functions to the time of flight spectra shown in figure 6.7. The signal functions are treated as Gaussians while the background is taken to be flat. An example of this is shown in figure 6.10. The background rates for each sample are shown in Table 6.1. These backgrounds have been subtracted from the totals shown in section 6.2.2. The backgrounds follow

Table 6.1.: Background rates for the time of flight spectra measured in *S4*. To convert these to the number of expected background events in a spill, the rate is multiplied by the size of the timing window for either MIPs or protons.

Number of moderator blocks	Background / Events $\times$ spill^{-1} $\times$ ns^{-1}
0	0.037 ± 0.004
1	0.066 ± 0.005
2	0.165 ± 0.007
3	0.124 ± 0.009
4	0.085 ± 0.002

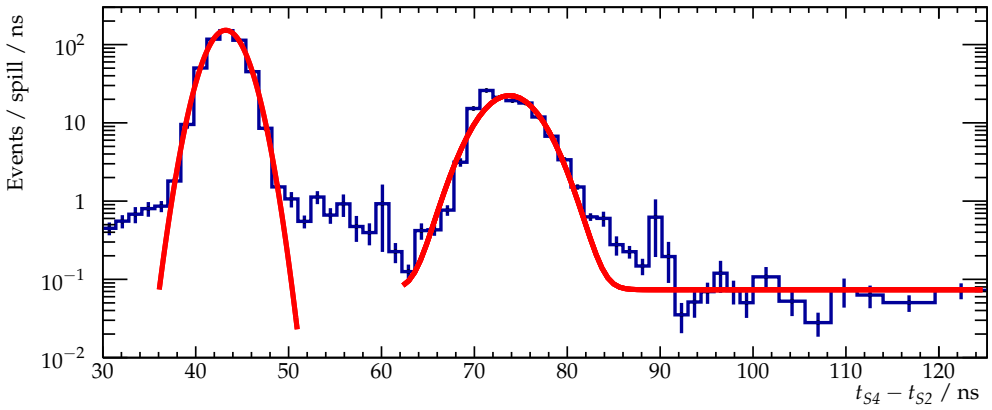

Figure 6.10.: Time of flight spectrum observed in *S4*: a combined signal and background function (red) has been fit to the data.

the same pattern as the total measured *S4* particle rates (as in section 6.2.2). The background rate initially increases with the addition of more moderator blocks then decreases for the 3 and 4 moderator block configurations. The ratio of the rate of signal protons to the background rate falls with the addition of moderator blocks. This is due to increased scattering from the moderator blocks which causes more particles to strike *S4* without passing through *S2*. This leads to an increase in false coincidences which contribute to the background rate.

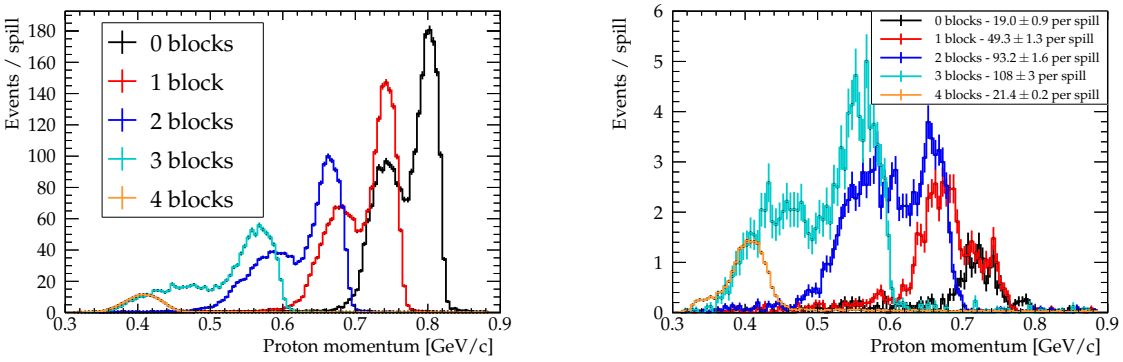

Figure 6.11.: Proton momentum spectrum as measured in *S3*. Left: all protons. Right: the subset of protons passing through the HPTPC drift volume.

6.2. Beam flux measurement

6.2.1. Flux measurements with S3

The time of flight systems are at an off-axis angle with respect to the beam axis (see table 5.2 for values) in order to increase the relative low-momentum proton flux in the most relevant range for neutrino experiments. This is quantified in terms of the two off-axis angles which are defined according to section 5.3.1.

The momentum of protons measured by *S3* is shown in figure 6.11. The momentum of particles determined to be protons was successfully reduced with increasing numbers of moderator blocks, with the range falling from 0.65-0.85 GeV/c for the unmoderated beam, to 0.30-0.45 GeV/c for 4 acrylic blocks.

Figure 6.11, right, shows the momentum spectrum of only those protons arriving at the HPTPC vessel. The angular range of the TPC is provided in table 5.2. It can be observed that the flux of low momentum protons (those with a momentum of less than 0.4 GeV/c) reaching the TPC was increased from negligible in the 0, 1, and 2 block cases to (9.65 ± 0.13) per spill for the 4 block case.

Figure 6.12 shows the kinetic energy distribution of protons at *S3* reaching the time projection chamber. A comparison of figure 6.12 with the generator comparison in figure 3.10 shows that for the case of four moderator blocks, the kinetic energy of protons incident upon the TPC is just above the 50 MeV region in which the different neutrino interaction generators are discrepant. These protons lose more energy within the walls of the HPTPC vessel, resulting in a non-zero flux of protons below 50 MeV within the TPC.

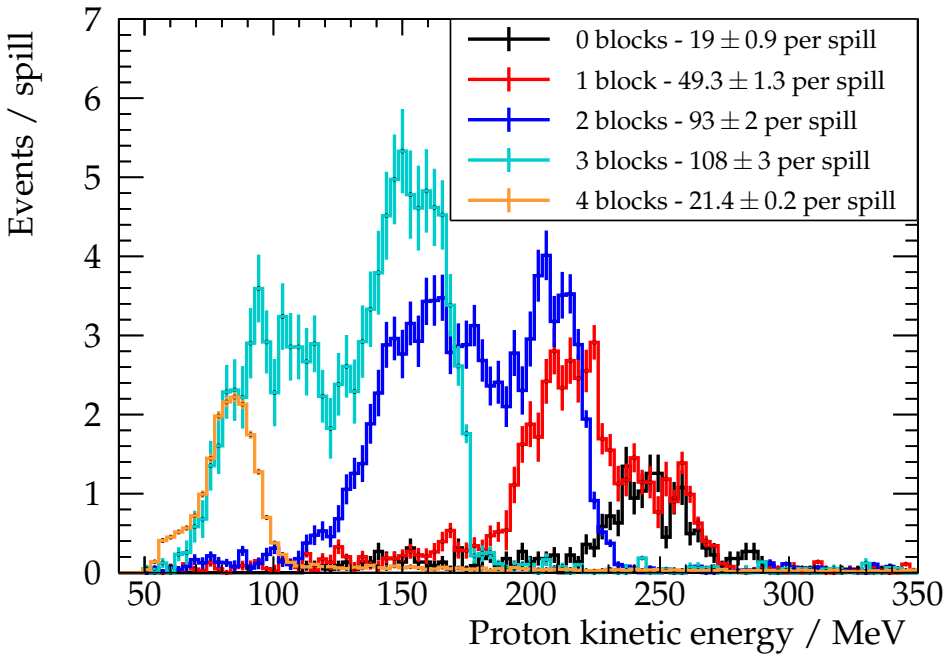

Figure 6.12.: Proton kinetic energy spectrum as measured in *S3* for only those protons passing through the HPTPC drift volume.

The combination of the use of moderator blocks and the positioning of the TPC in an off-axis position also changed the multiplicity of protons passing through the TPC. Figure 6.11, right, shows the addition of 1, 2, and 3 moderator blocks increasing the number of protons passing through the TPC from (19.0 ± 0.9) per spill in the unmoderated case to (108 ± 3) per spill in the 3 block case. However, the addition of the fourth moderator block removes almost all protons with energy above 100 MeV passing through the TPC, leaving (21.4 ± 0.2) per spill.

The distribution as a function of off-axis angle of MIPs and protons recorded by *S3* is shown in figure 6.13. In both cases, the peak beam intensity falls and broadens in θ with the increasing number of moderator blocks. At angles further from the true beam axis, the number of MIPs and protons is increased with an increasing number of moderator blocks. The active TPC region lies within this off-axis area. The particle spread for unmoderated data was unexpected, as the beam was already diffuse; the peak in both figures for 0 blocks was already broad, due to beam steering scattering that led to the double peak structure for protons seen in figures 6.3 and 6.5. Therefore the addition of 3 or 4 moderator blocks caused overscattering of protons to occur, and the number of protons reaching *S3* fell faster than the number of MIPs. For the

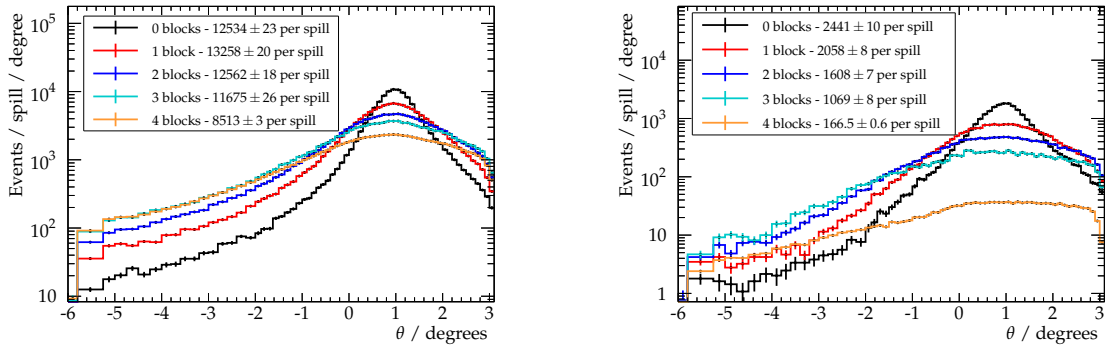

Figure 6.13.: Distribution of hits in *S3*. The hits are measured from *S1* and shown as a function of the horizontal off-axis angle, and for varying numbers of moderator blocks. No coincident hit in *S2* is required. Left: minimum ionizing particles. Right: protons.

unsteered and unmoderated beam, the horizontal and vertical FWHM are 9.6 cm and 11.0 cm, respectively. The horizontal FWHM for the steered beam (still without moderator blocks), the FWHM is 16.8 cm.

Figure 6.14 shows the proton-MIP ratio measured in *S3* as a function of the nominal off-axis angle, horizontally and vertically respectively, and for the different numbers of moderator blocks. For 0, 1, 2, and 3 moderator blocks the ratio falls to a minimum at approximately 1° with respect to the nominal beam axis. This corresponds to the true beam centre.

The peak at lower values of θ shifts to progressively smaller values of θ as more moderator blocks are added (from approximately $\theta = 1^\circ$ from the beam centre for 0 blocks up to approximately $\theta = 3^\circ$ from the beam centre for the 3 block case). At most values of θ, the proton/MIP ratio falls with the addition of more moderator blocks due to the overscattering of protons, particularly with 4 moderator blocks, which occurred due to the unmoderated beam being broader than expected. Thus, reducing the kinetic energy of the protons below 100 MeV/c came at the cost of reducing the purity of the proton beam.

The momentum of these particles is further reduced as they pass through the steel walls of the vessel on their path to the active TPC region.

6.2.2. Flux measurements with S4

Figure 6.15, left, shows the flux of particles identified as MIPs in *S4*. This flux is shown as as a function of the angle in the $x - y$ plane (figure 5.7 gives the definitions of these

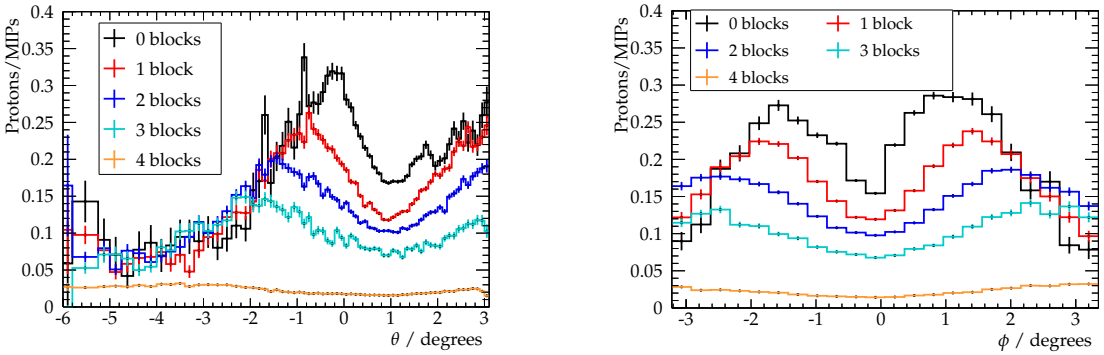

Figure 6.14.: Proton-MIP ratio in *S3* as measured from *S1*, as a function of off-axis angle and for varying numbers of moderator blocks. Left: horizontal angle. Right: vertical angle. The TPC spans horizontal angles 0.4–2.6° and vertical angles -2.6–+2.6° off the nominal beam axis.

coordinates) for varying numbers of moderator blocks from 0 to 4. For every set of moderator blocks, the peak flux of MIP events occurs at a value of θ between -1° and -2°. Similarly the number of proton events per spill, shown in figure 6.15, right, peaks at approximately -2°.

The angular overlap of *S2* and *S4* influences the exact position of the peak. Figure 5.9 demonstrates that, when observed from *S1*, a limited area of *S4* is shadowed by the active area of *S2*. Given the requirement that a signal must be observed in *S2*, all of the events that are observed in *S4* must be from this region of overlap.

Figure 6.15, left, also shows that initially, an increasing number of moderator blocks results in an increased total MIP flux through *S4*. This is because both *S2* and *S4* are positioned off-axis, so the unmoderated beam particles do not strike these detectors. Due to scattering processes in the moderator, a greater number of MIPs are incident upon *S2* and *S4*, with more scattering occurring with greater numbers of moderator blocks. However, with the fourth moderator block the flux of MIPs is seen to fall. Similarly, with the addition of the first two moderator blocks, the proton flux shown in Figure 6.15, right, initially sees an increase in the total number of events in *S4*. However, with three and four moderator blocks, the total number of protons observed in *S4* falls. The initial proton flux increase is similar to that for the MIP flux, with increased scattering causing more protons to pass through the off-axis *S2* and *S4* detectors. The subsequent decrease is due to the larger loss of energy of the protons in the thicker moderator. In turn, this leads to attenuation of protons in the pressure vessel resulting in fewer observed events in *S4*.

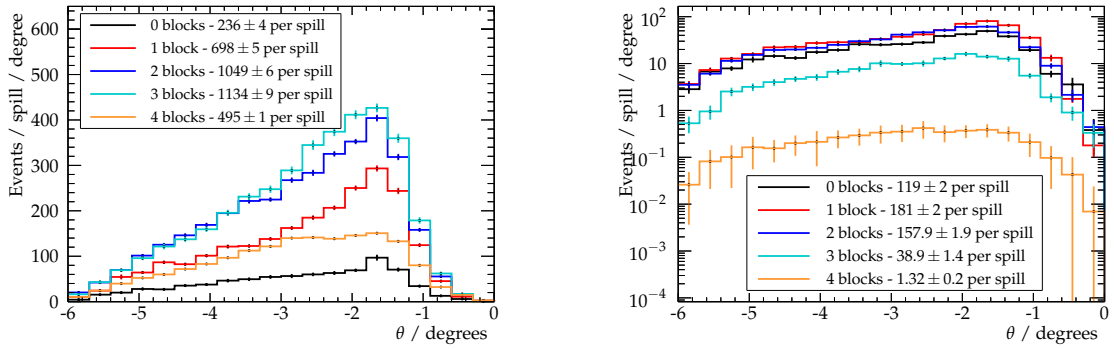

Figure 6.15.: Distribution of hits in *S4* as a function of the horizontal off-axis angle and the number of moderator blocks. Left: minimum ionizing particles. Right: protons.

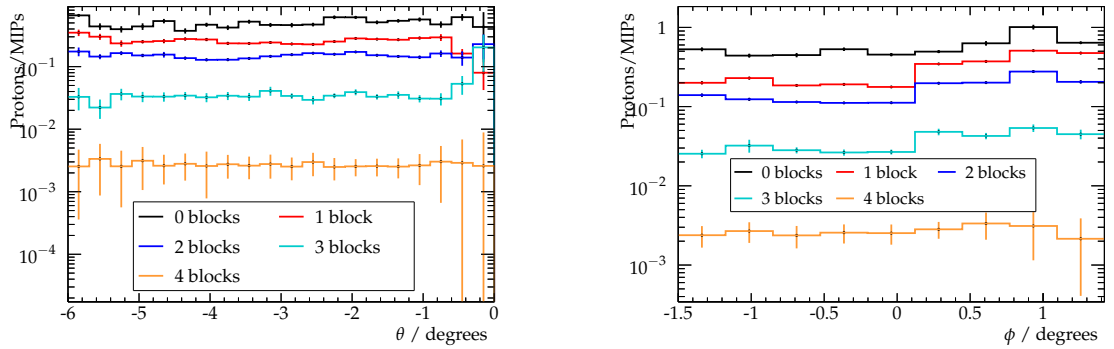

Figure 6.16.: Proton-MIP ratio in *S4* as a function of off-axis angle and for varying numbers of moderator blocks. Left: horizontal off-axis angle. Right: vertical off-axis angle.

Figure 6.16 shows ratio of protons to MIPs as a function of the number of moderator blocks and the two off-axis angles. For each moderator block configuration, figure 6.16, left, shows that the ratio remains flat as a function of θ. With the addition of moderator blocks, the ratio reduces from its highest level at 0.5 for the 0 block case down to 0.002 for the 4 block.

Similarly, figure 6.16, right, shows the proton-MIP ratio falling with the addition of moderator blocks. For every different configuration, the ratio is flat as a function ϕ. For the 4 block configuration, the value of the proton-MIP ratio is approximately 0.01 at all values of ϕ. As previously discussed, this is due to the attenuation of low energy protons within the walls of the pressure vessel.

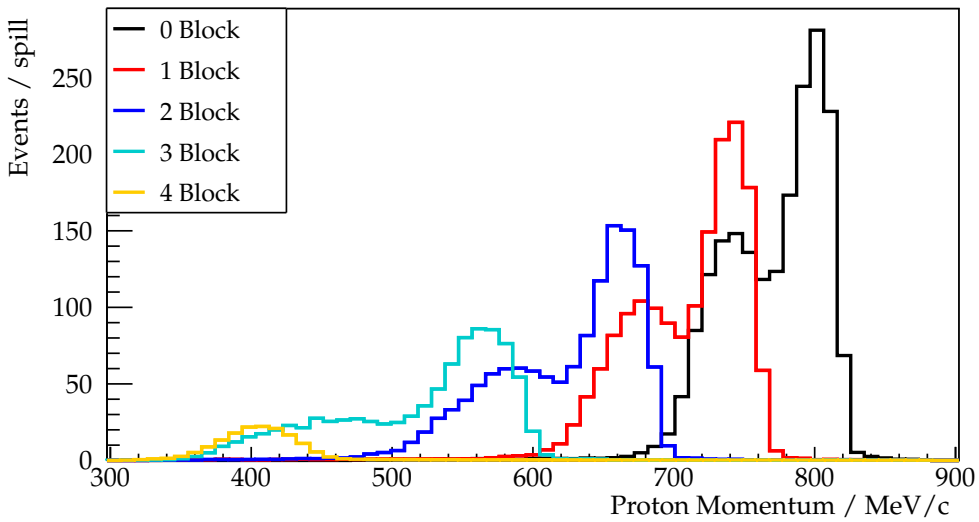

Figure 6.17.: Initial momentum profile of the simulation of protons at the *S3* wall in the direction of the TPC.

6.2.3. Monte Carlo studies

In order to determine the flux of protons reaching the active region of the TPC, and verify the dead time and other corrections, a Monte Carlo study was performed. Due to the lack of a full picture of the initial beam profile, most critically the initial spread of the beam without moderation being unknown, the method of simulation had to be modified from that used for the previous studies described in 5.2. As the initial beam characteristics were not fully known over the course of the beam test, the decision was made not to simulate the initial beam profile at the entrance to T10. Instead particle positions and momenta were drawn from the *S3* distributions shown in figure 6.11. Particle direction was calculated from the position in *S3*, to the position of the end of *S2* or *S1* depending on the actual coincidence requirement. To differentiate protons from MIPs, the same timing and amplitude cuts described in section 6.1 were applied. The initial simulation profile is constructed identically from the momentum profile shown in figure 6.11.

The vessel, doors, and TPC active region were modelled in GDML relative to the positions of *S3* and *S4*, and the simulated protons are propagated through the vessel. The momentum profile of simulated protons reaching the *S4* wall is shown in figure 6.18. A minimum cut is set at the momentum threshold of S4 of 140 MeV/c. The simulation shows a significant reduction in momentum in *S4* as compared with *S3*, as most particles have travelled through both steel walls of the TPC vessel. In

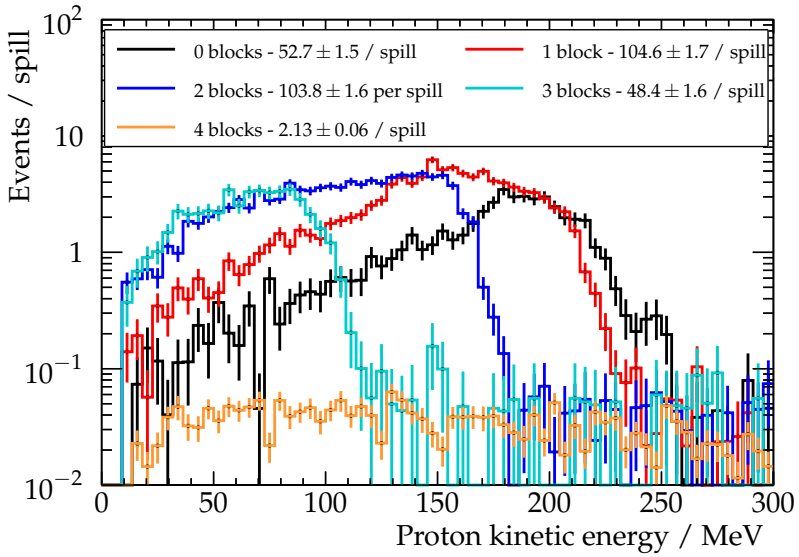

Figure 6.18.: Energy profile of simulated protons that reach *S4* with a kinetic energy greater than the detection threshold of 10 MeV.

Table 6.2.: Ratio of protons reaching *S4* to protons reaching *S3* for changing moderator block number in simulation and data. The combined statistical and systematic errors are shown.

Number of moderator blocks	Monte Carlo	Data	Data/MC
0	0.027 ± 0.003	0.049 ± 0.007	1.8 ± 0.3
1	0.067 ± 0.005	0.088 ± 0.013	1.3 ± 0.2
2	0.084 ± 0.007	0.098 ± 0.015	1.2 ± 0.2
3	0.055 ± 0.010	0.036 ± 0.006	0.7 ± 0.2
4	0.0115 ± 0.0010	0.0079 ± 0.0016	0.7 ± 0.2

particular, in the case of 4 moderator blocks, very few particles have survived through the second vessel wall to reach *S4* at all. The ratio of number of protons reaching *S4* to those reaching *S3* is shown for both simulation and data in table 6.2, which includes the statistical and systematic errors in each case.

The systematic uncertainty on the number of protons measured in *S3* and *S4* is calculated for both data and MC, with a breakdown shown in table 6.3. The equivalent uncertainty on the MC simulation is determined through studies varying the geometric initial conditions of the simulation, including the position of the *S1* and *S2* detectors. These variations cause changes in the intial kinematics of the propagated

protons. Additionally, a study was performed with 1 cm of additional acrylic in the beamline, as a proxy for the uncertainty on other pieces of light material in the beam facility. These calculated errors represent geometric sources of uncertainty in the MC simulation.

For the data, the uncertainty on the overall efficiency of *S3* is calculated by taking the $\pm 1\sigma$ uncertainty on the fitted linear relationship between $S1 \cap S2$ signals in the upstream and downstream ToF DAQs (see section 6.1) and calculating the fractional change this causes in the *S3* proton count.

The uncertainty on the overall efficiency of *S4* is calculated from the calibration tests performed on the *S4* bars with a ^{90}Sr source, as discussed in section 6.1. The overall efficiency factor of 0.8 was calculated using data taken with a significantly different readout to that used in the beam test and therefore is subject to variation. The spread in maximum bar efficiencies measured in these ^{90}Sr source tests for the various *S4* bars is used as the systematic uncertainty on the overall *S4* efficiency.

The size of the *S4* angular correction systematic uncertainty on the data is determined by varying the number of horizontal bins in figure 6.9 from 20 to 10. The uncertainty on the *S4* background subtraction is determined by the change in the number of protons, when varying the fitted flat background by one standard deviation. This has a larger effect in the 4 block case because of the very small number of protons detected in *S4* relative to the background.

The ratio of number of protons reaching *S4* to those reaching *S3* is shown for both simulation and data in Table 6.2, which includes the total statistical and systematic error in each case. The agreement shown relative to the uncertainty provided by the beam test setup provides strong evidence that the efficiency corrections described in Section 6.1 are justified.

The number of simulated particles that penetrate the active area of the TPC are shown in figure 6.19, left and right, as a function of the momentum and kinetic energy respectively. Comparing figure 6.19, right, with the motivational plot shown in figure 3.10, it is clear that it was only possible to access the low momentum region of interest due to the off axis and moderator technique. This method was therefore successful in lowering the proton energy to the necessary extent. The number of protons reaching the active area of the TPC was (6.97 ± 0.11) per spill for 4 moderator blocks, compared with (12.6 ± 0.7) per spill without moderation. For 4 moderator blocks, (5.56 ± 0.10) of

Table 6.3.: Breakdown of systematic errors for data and simulation. The values shown are the percentage error on the *S4* proton count with the exception of the uncertainty on the efficiency of *S3*, which is the percentage error in the *S3* proton count. All uncertainties are treated as uncorrelated. $n_{S4,\,MC}$ refers to the number of protons reaching *S4* in simulations

Monte Carlo					
	Number of moderator blocks				
	0	1	2	3	4
Systematic uncertainty on $n_{S4,\,MC}$	9.5%	8.0%	8.5%	17%	8.0%
Data					
	Number of moderator blocks				
Source of systematic error	0	1	2	3	4
Absolute efficiency of *S3*	1.1%	11.4%	7.0%	11.4%	4.9%
Absolute efficiency of *S4*	11.0%	11.0%	11.0%	11.0%	11.0%
S4 angular correction	2.9%	1.5%	6.7%	8.2%	4.1%
S4 background uncertainty	0.18%	0.16%	1.1%	1.4%	8.1%
Total	11.5%	16.0%	14.7%	18.3%	18.9%

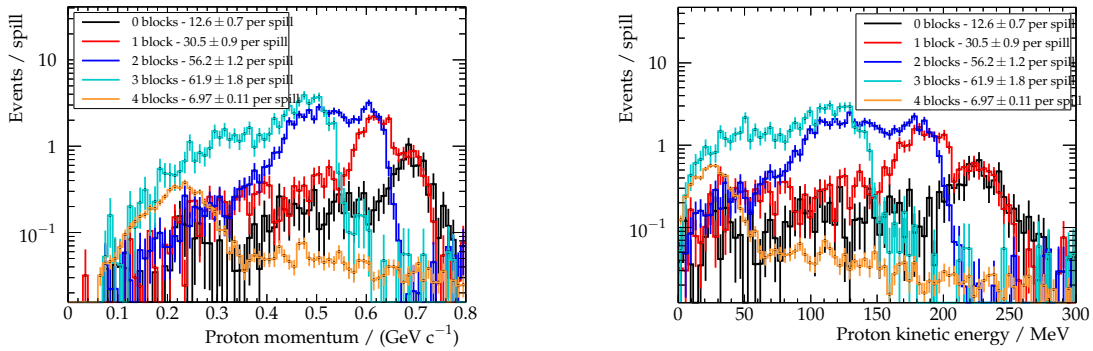

Figure 6.19.: Kinematic profiles of simulated protons reaching the active region of the TPC. Left: momentum profile. Right: energy profile.

those protons had energies below 100 MeV. These values were calibrated with the full comparison between data and simulation.

6.3. CCD analysis

6.3.1. Calibration sources

A significant component of the HPTPC prototype was the use of optical readout in addition to charge readout. As described in subsection 3.3.6, four CCD cameras imaged a quadrant of the amplification region each, through quartz windows.

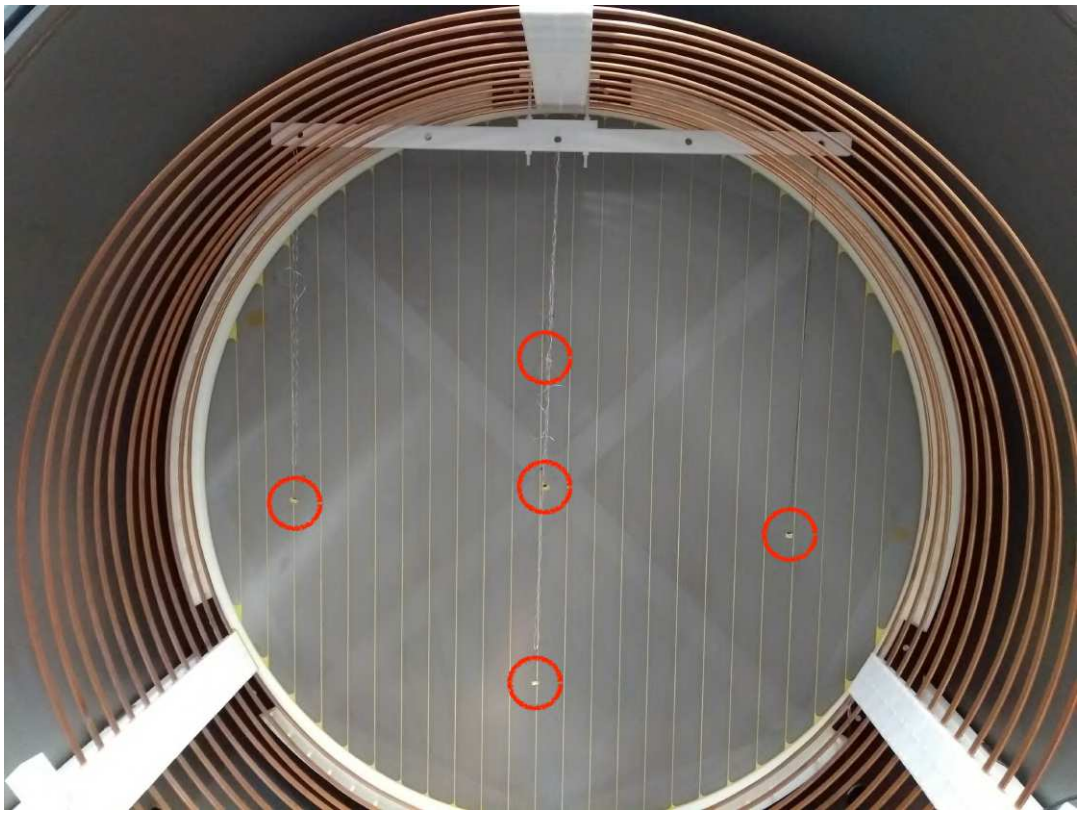

Figure 6.20.: Cross-sectional view of the TPC prototype. The locations of the ^{241}Am sources are marked by circles. Figure taken from [67].

In order to calibrate the optical readout process, five ^{241}Am calibration sources were attached to the prototype. The position of these sources is shown in figure 6.20. The source positions were chosen such that each source would be visible in two cameras, with the central source positioned in the overlap region of the view of all four cameras.

The process of taking camera images was as follows: first the cameras were cooled to between -25°C and -30°C in order to reduce the total noise. Then in order to remove any time dependent dark noise, a number of bias frames are taken with the camera shutters closed. These are averaged and subtracted from the exposure frames. The bias frames are taken regularly and subtracted only from images in the same

run and therefore similar conditions. This additionally reduces the effect of other noise sources that are time dependent. These effects include cosmic muons passing through a camera chip causing individual pixels to remain saturated for some time, and the readout electronics producing heat the longer they have been active. The shutter of the bottom right camera was broken, meaning that bias frames were not taken in darkness. One further noise reduction effort is required: a number of pixels in a CCD may always register as hot. This can occur for a number of reasons including defects in the silicon and faulty connections. Therefore, the bias frames are cleaned, removing any anomalously charged pixels. Each pixel of each bias frame is compared to the same pixel in the proceeding bias frame, and if the reading has changed by an uncharacteristically large amount, the value of the pixel is set to that of the previous image.

Four CCD images showing the ^{241}Am source are shown in figure 6.21. All five sources are clearly visible against the noise background in positions corresponding to those shown circled in figure 6.20. The top right quadrant differs in intensity because the top right CCD camera had a different conversion gain compared with the other three. The broken shutter for the bottom right camera caused the sources to be visible in bias frames as well as exposure frames. Therefore following bias subtraction, the sources are no longer visible in that quadrant. The images shown were taken in pure Argon at an absolute pressure of 3 bar, with an exposure time of 200 s.

6.3.2. Clustering algorithm

In order to improve event detection in CCD images, a clustering algorithm was developed. Following cleaning of the images, pixels are clustered in order to identify regions of the image where activity significantly higher than the background is observed. A hierarchical clustering algorithm is used, and the distance between pixels a and b, in the algorithm is defined as:

$$d_{ab} = min\left(|x_a - x_b|, |y_a - y_b|\right). \tag{6.9}$$

Four parameters, namely SEED_THRESHOLD, SKIRT_THRESHOLD, MAX_GAP and MIN_CLUSTER_SIZE are used in the algorithm which is defined as:

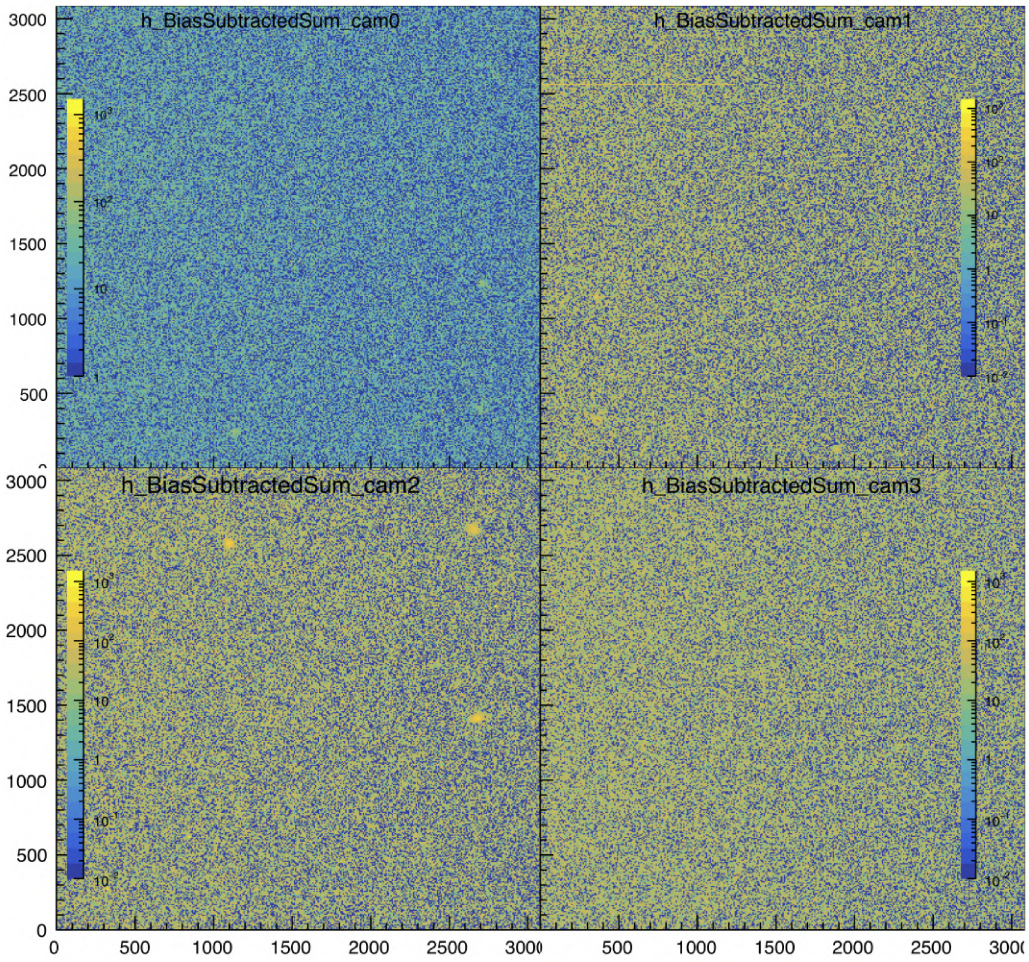

Figure 6.21.: Light yield from the five calibration sources imaged by the CCD cameras. The intensity of the image in the top left frame differs from the other three frames, because the corresponding camera has a different conversion gain. The ^{241}Am sources are visible against the background noise in the top left, top right, and bottom left cameras. In the bottom right image, where bias subtraction was not performed, the sources are not visible. Figure taken from [67].

- The highest valued unclustered pixel in the image is considered. If the pixel's value is less than the SEED_THRESHOLD or if there are no unclustered pixels go directly to the final step. Otherwise add the pixel to the current cluster.

- All unclustered pixels within a distance of MAX_GAP+1 of any pixel in the current cluster are considered. All of these pixels with a value above SKIRT_THRESHOLD are added to the cluster.

- Repeat the previous step until such a time as there are no pixels above threshold close enough. Then the cluster is complete, and a new cluster is started by returning to the start of the algorithm.
- All clusters containing fewer than MIN_CLUSTER_SIZE pixels are removed. Subsequently algorithm terminates.

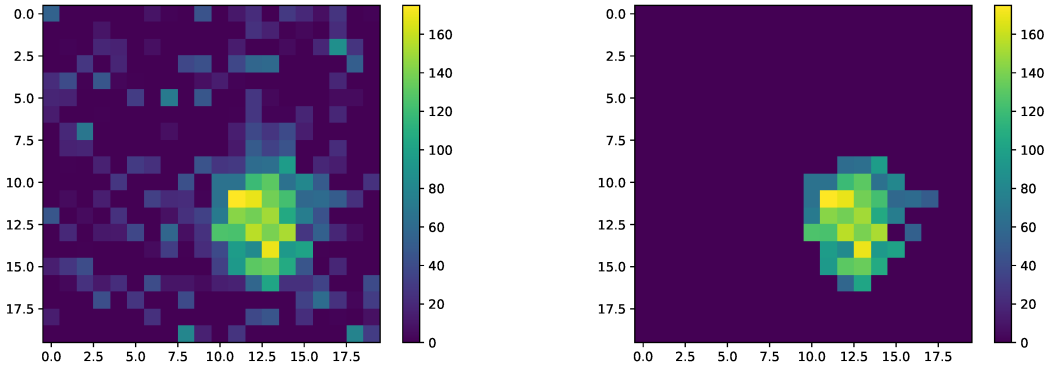

Figure 6.22.: Effect of the clustering algorithm on light from a single ^{241}Am source. Left: the image prior to application of the clustering algorithm. Right: the result of the algorithm's application. Figure taken from [67].

Application of the algorithm to an image of one single ^{241}Am source is shown in figure 6.22. The clustering identifies the source and removes the background noise. The analysis of data from the beam test, which makes use of this clustering method, is ongoing.

Chapter 7.

Nucleon FSI in NEUT

7.1. The nucleon cascade in NEUT

NEUT simulates nucleon cascades using a semi-classical intra-nuclear cascade model. The simulation model is described in detail in section 4.3. The cascade is split into a finite number of individual steps through the nucleus, with the nucleon either undergoing an interaction, or surviving onto the next cascade step undisturbed. These final state interactions are split into 3 main categories:

- Elastic interactions including charge exchange
- Single pion production
- Double pion production

Whether an interaction occurs at any step along the cascade and what type of interaction occurs is determined by the throw of random numbers scaled to the probability of interaction types. The cascade continues until the nucleon and any daughter particles have interacted or escaped the nucleon by moving beyond a defined maximum radius. A schematic of a nucleon cascade is shown in figure 7.1.

7.1.1. Introduction of nucleon dials to NEUT

The FSI model can be parameterised by a number of scaling factors. In this work, four variable scaling factors or "dials" have been introduced to NEUT and are listed in table 7.1.

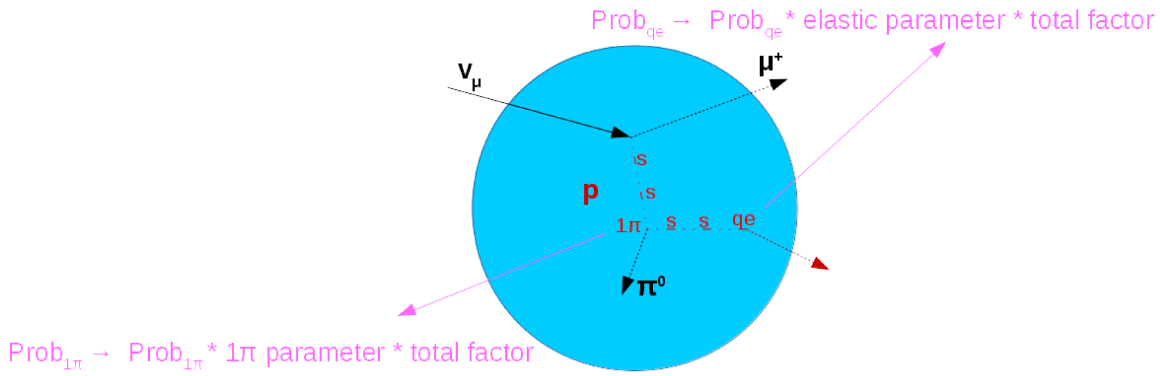

Figure 7.1.: Schematic of the nucleon cascade. The movement of the nucleon through the nucleus is divided into small steps, at which survival or other interactions may occur. In the schematic, s represents a survival, qe represents a quasi-elastic interaction, and 1pi represents a single pion production. The individual interaction probabilities are governed by the multiplicative nucleon FSI factors.

Table 7.1.: Names and brief descriptions of each of the four nucleon FSI scaling factors

Parameter	Description
XNUCFACT	Scales total interaction probability
XNUCELAFACT	Scales elastic interaction probability
XNUCSPIFACT	Scales single pion production probability
XNUCDPIFACT	Scales double pion production probability

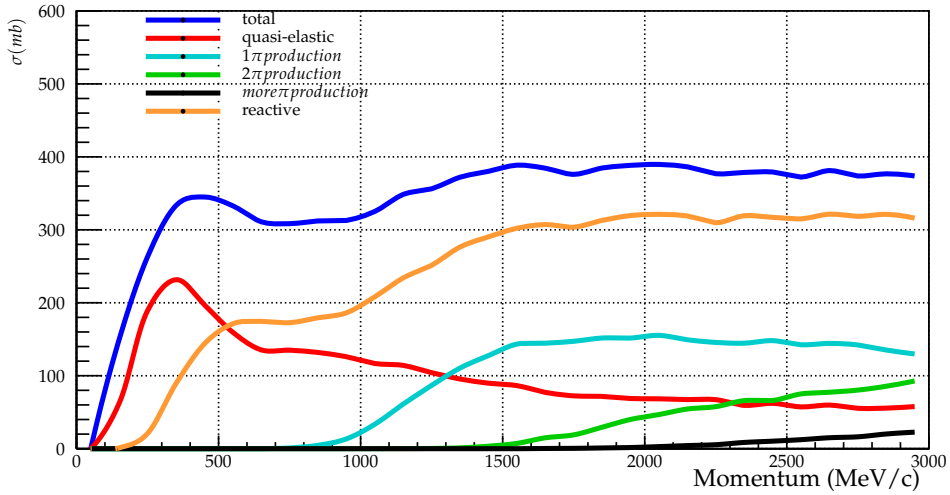

Figure 7.2.: Simulated interaction cross-sections as a function of true initial nucleon momentum from neutrino interactions on carbon. The reactive cross-section is defined as the total minus the quasi-elastic cross-section.

Three of the variable factors directly multiply the probability of the three categories of interaction type described in the section 7.1: elastic, single pion production, and double pion production. One further factor multiplies the probability of all three interaction types equally. While the total probability factor was previously implemented in NEUT, the three individual interaction factors were implemented in NEUT for the first time along with tunable dials to vary them as a part of this work. These dials can now be varied to affect the nucleon cascade probabilities in NEUT simulations.

An example of the simulated distribution of nucleon interactions with all four dials set to the nominal value of 1 is shown in figure 7.2.

The cross-section of different interaction channels is shown as a function of the momentum of an outgoing nucleon from a neutrino interaction. The initial momenta are drawn from actual T2K energies. In contrast to the nucleon dials above, the definitions of these channels correspond not to true step-level information but simply to final state particles. The definitions of the channels are as follows:

- Quasi-elastic scattering: Precisely 1 nucleon in the final state, and 0 pions.
- Reactive: quasi-elastic distribution subtracted from the total distribution. Pion production channels are a subset of this channel.
- Single pion channel: only 1 pion in the final state.

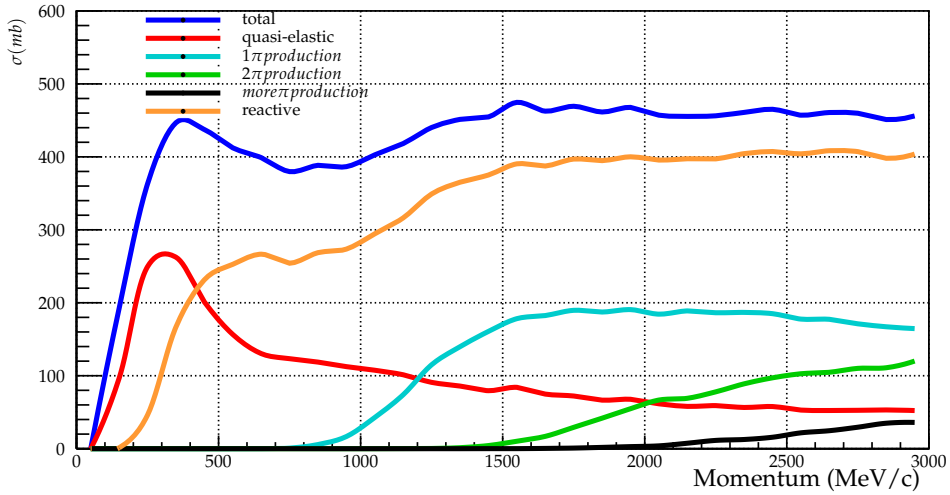

Figure 7.3.: Simulated interaction cross-sections as a function of true outgoing nucleon momentum from neutrino interactions on carbon for a total interaction dial value of 1.5.

- Double pion chanel: only 2 pions in the final state.
- More pion channel: more than 2 pions in the final state.

Therefore if at a single step in a cascade 2 pions are produced, but only 1 pion survives to the final state, the cascade would be recorded in the single pion channel.

Varying the values of the nucleon FSI dial governing the probability of all interaction types changes each of the cross-sections. For a variation of the total interaction probability dial of a factor 1.5 and 0.5, the resultant cross-sections are shown in figures 7.3 and 7.4 respectively. Increasing the dial value increases the cross-section for all interaction channels. The quasi-elastic channel is particularly strongly affected in the low momentum region for two reasons: the majority of elastic interactions occur in this region, while above the pion production threshold, increasing the total interaction probability also increases the probability of producing pions. The other channels are increased relatively uniformly. Similarly, a reduction in the value of the total interaction dial reduces the cross-section in each channel.

Varying the dials corresponding to specific interaction types changes the interaction channel cross-sections dissimilarly. Five variations are shown for each dial with dial values of: 0.5, 0.75, 1, 1.25, and 1.5. The impact of varying the elastic dial is shown in figure 7.5. The cross-section of the quasi-elastic channel is strongly affected in the low momentum region where elastic interactions dominate. The reactive channel is

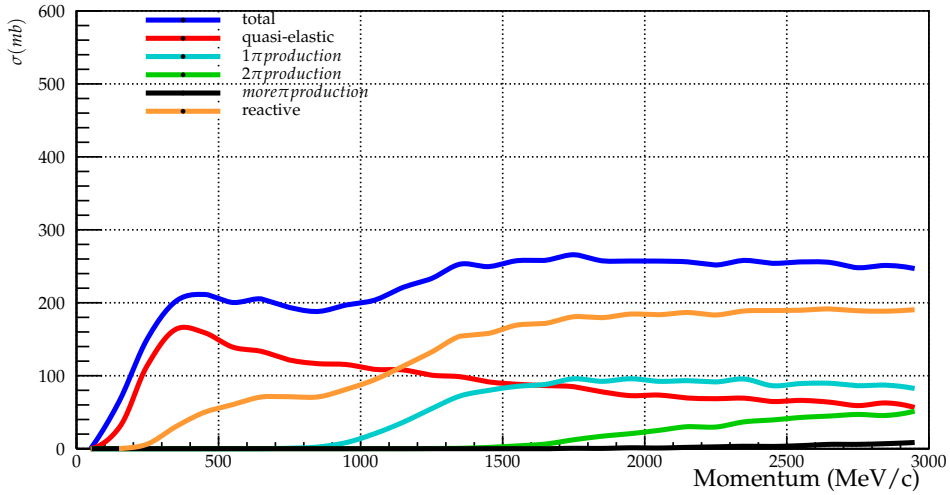

Figure 7.4.: Simulated interaction cross-sections as a function of true outgoing nucleon momentum from neutrino interactions on carbon. For a total interaction dial value of 0.5.

also strongly affected below the pion production limit. The single and double pion channels are largely unaffected.

The impact of varying the single pion dial is shown in figure 7.6. Variations of this dial strongly affect the single pion channel, with the cross-section increasing with dial value. Below the pion production limit, all the channels are entirely unaffected, and the quasi-elastic channel is largely unaffected at higher momenta as well. The two pion channel, while not as strong as the single pion channel, does see some variation in the same direction as the single pion distribution. This is because cascades with multiple single pion production vertices are recorded in the two pion channel if two survive to the final state.

Lastly, the effect of varying the double pion dial is shown in figure 7.7. Like the single pion dial, varying this dial sees no effect below the pion production limit in any cross-section. The two pion channel is strongly affected. The single pion channel is weakly affected, due to cascades in which a double pion production occurs, but one pion does not survive to the final state. However, the effect of the double pion dial on the single pion cross-section is much weaker than that of the single pion dial on the two pion production channel.

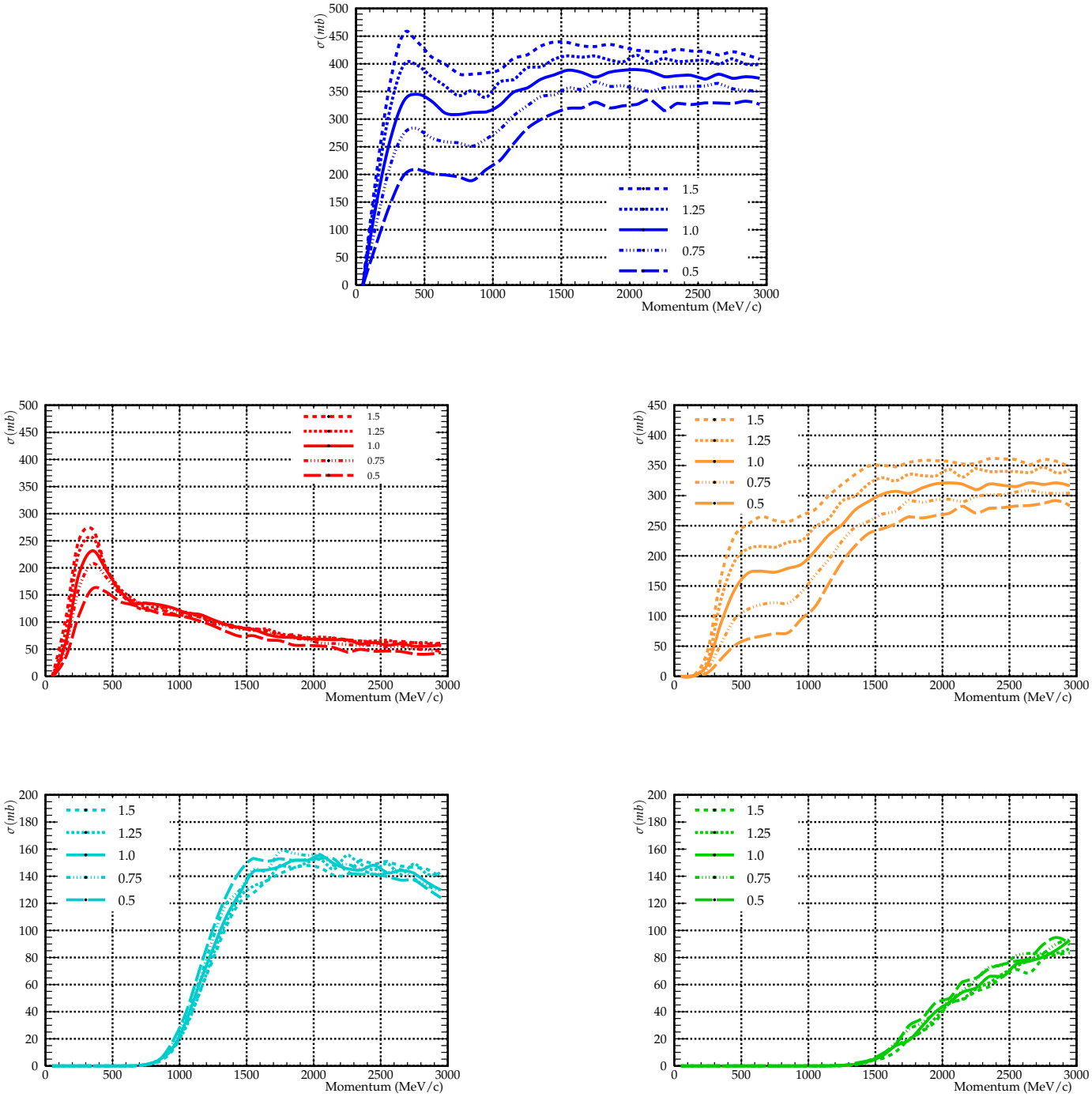

Figure 7.5.: Effect of different variations of the dial governing elastic interactions on the cross-sections of the total (blue), quasi-elastic (red), reactive (orange), single pion (cyan), and double pion (green) channels.

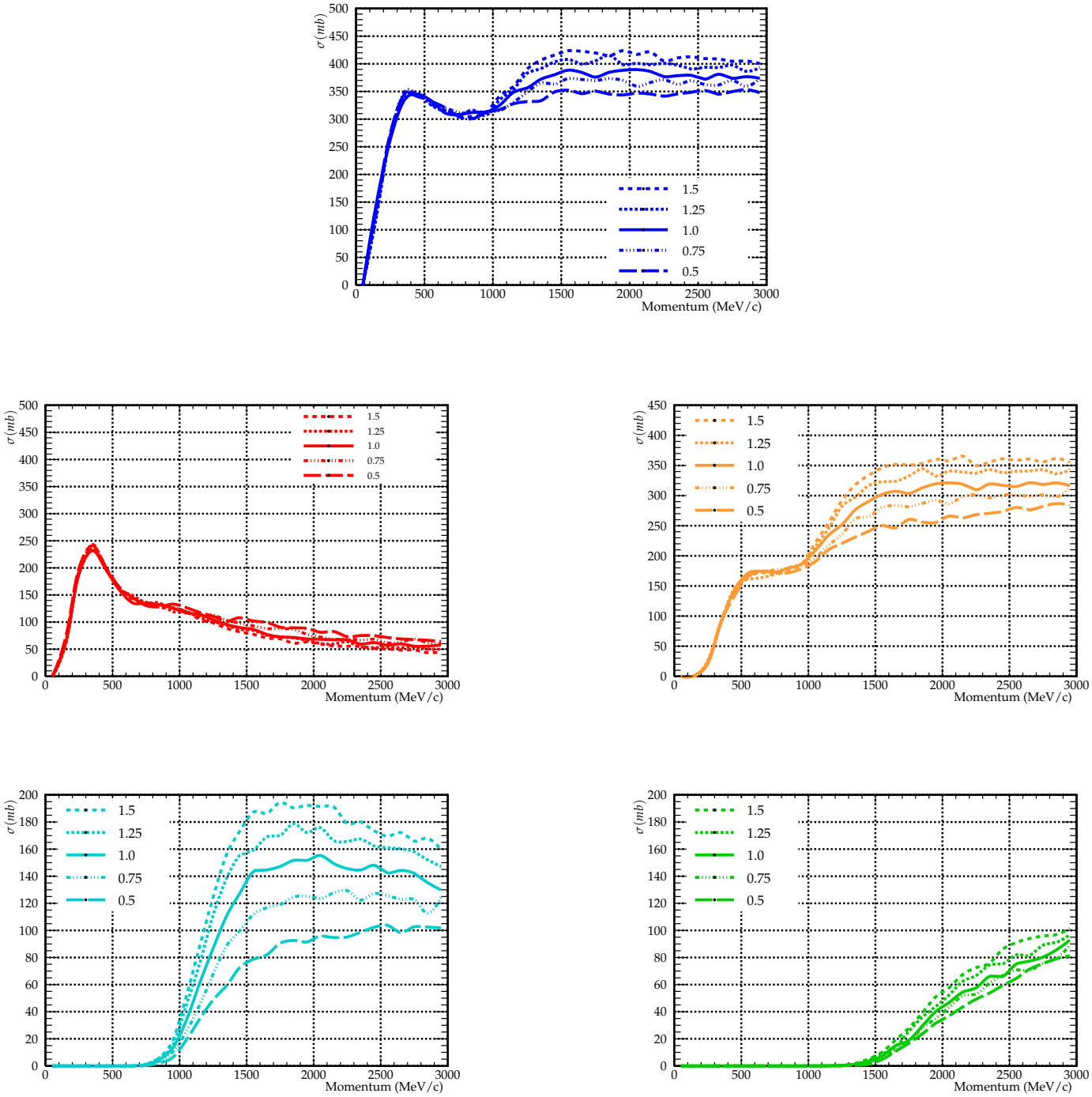

Figure 7.6.: Effect of different variations of the dial governing single pion production on the cross-sections of the total (blue), quasi-elastic (red), reactive (orange), single pion (cyan), and double pion (green) channels.

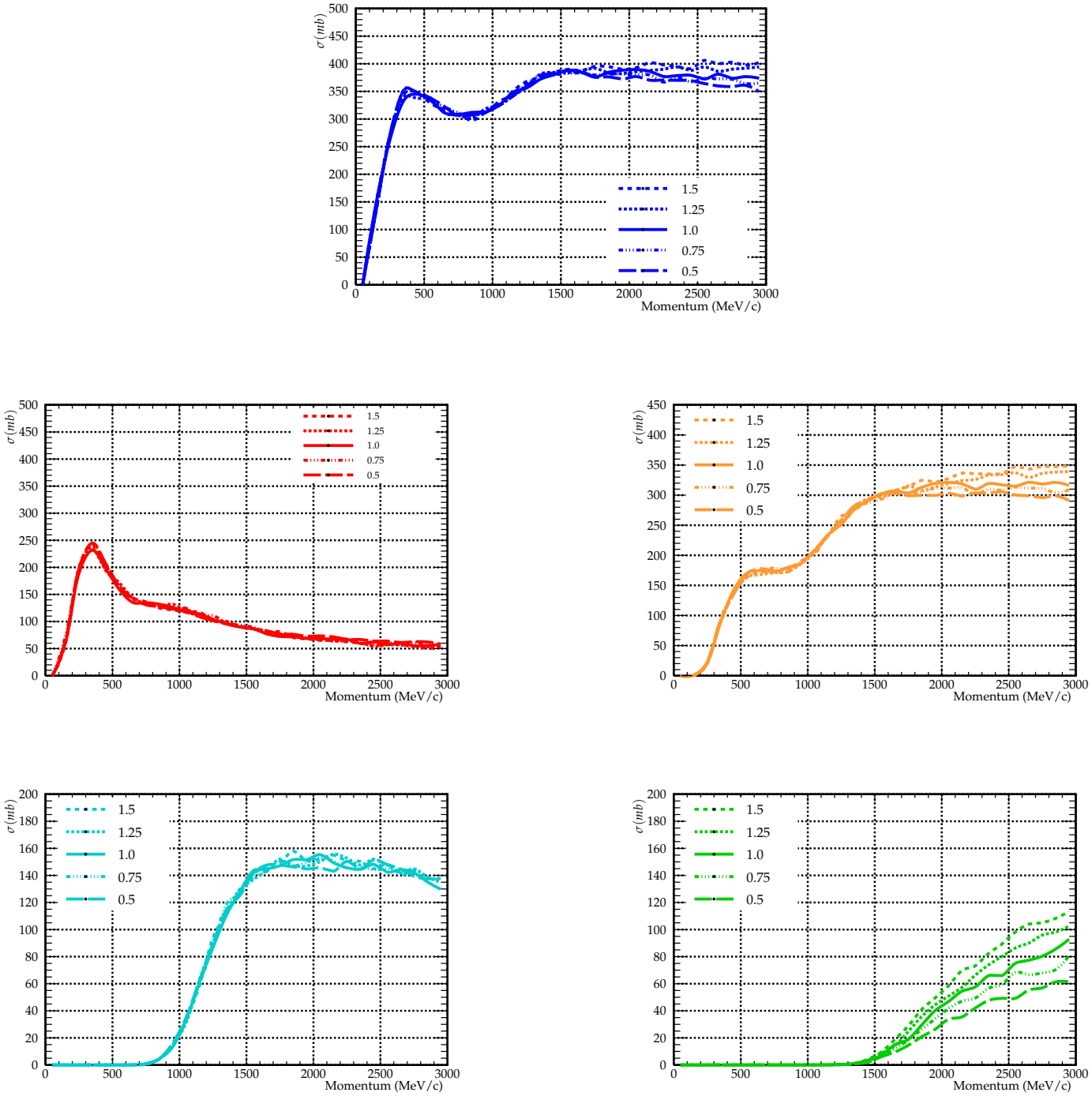

Figure 7.7.: Effect of different variations of the dial governing double pion production on the cross-sections of the total (blue), quasi-elastic (red), reactive (orange), single pion (cyan), and double pion (green) channels.

7.2. Reweighting the nucleon dials

In order to extract best-fit parameters from data, it is necessary to predict event distributions with different values of the model parameters. The simplest way of doing this is to rerun the entire MC simulation of the chosen model with varied input parameters. However this is typically prohibitively time-consuming. The efficient method, MC reweighting, is used to approximate a solution, by varying only the parts of the simulation that are significantly affected by the parameters in question. A more in depth explanation of the principles of re-weighting is provided in 4.4. In the case of cascade simulation of nucleon FSI, the reweighting process involves rerunning the nucleon cascade, without rerunning the rest of the MC simulation.

7.2.1. Previous reweighting attempts

Prior to this work, nucleon FSI reweighting had never been successfully performed in NEUT. A previous attempt to reweight the total interaction dial (the only nucleon FSI dial implemented in NEUT at the time) was made, but did not function correctly. That attempt involved calculating interaction probabilities within the cascade at every vertex, ie. at every step at which an interaction other than survival occurred. This attempt failed because interaction probabilities, while normalised to one another correctly, could not be normalised to the probability of survival. Thus, variation of the interaction dials incorrectly had no impact on the mean free path of interaction, and the reweighting of any cascade with more than a small number of vertices would fail catastrophically, even for small dial variations.

In this work, a successful reweighting process was established and validated for all 4 nucleon dials.

7.2.2. The novel reweighting process

The newly implemented reweighting process involves rerunning the nucleon cascade with adjusted FSI dial values without rerunning the entire NEUT MC. A schematic of the process is shown in figure 7.8. At generation time, the probability of each step along the cascade is recorded and the probability of the full cascade is recorded. To reweight, the cascade is rerun with the dial values changed, and the probability of the same interaction or survival occurring at each step is recalculated. The weight

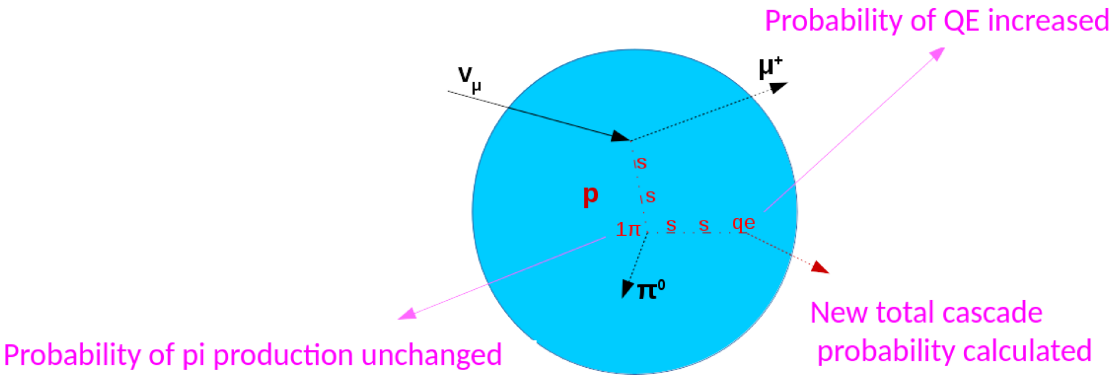

Figure 7.8.: Schematic of the reweighted nucleon cascade. In this example, the value of the dial governing quasi-elastic interactions has been increased, while the others have been held constant. The total probability of the cascade is recalculated.

is calculated as the ratio between the new cascade probability and the old cascade probability.

The crucial change to the unsuccessful prior attempt described in section 7.2.1 was to record information on the step level rather than vertex level. Interaction probabilities were passed between generation and reweighting at every step, including for survival steps. This allowed the different interaction type probabilities to be normalised, not just to one another, but also to the probability of a survival.

7.2.3. Validations of the reweighting

Before the reweighting method can be used in T2K analyses, it is crucial to demonstrate that it is functioning correctly. The criterion for successful reweighting is that the reweighting with given dial values should have an identical impact on various kinematic distributions to that of full regeneration with the same dial values. In the following section, various kinematic distributions are shown for an increase and decrease of the total interaction dial value.

The energy distribution of the leading energy final state nucleon in the cascade simulation is shown in figure 7.9. $E_{nucleon}$ represents the energy of the nucleon emitted from the neutrino interaction. The generated events with dials set to 1 is shown in black. The statistically independent regenerated events with the dial value changed are shown in red. In each case ten million events were generated. The reweighting of the nominal distribution to the changed dial value is shown in blue. It is clearly visible from the red and black lines that varying the dials changes the distribution -

increasing the dial causes an increase in the low energy region and a decrease in the high energy region. As each event has a single leading energy nucleon, the integral of the red and black curves is equal. For the decreased dial, the effect on the distribution is opposite - increase in the high and decrease in the low momentum regions respectively. In both cases, the blue reweighted distribution closely matches the regenerated distribution of the same total dial value, demonstrating that the weighting correctly approximates fully regenerating the simulation. For each of the variations, a residual plot of $\frac{Reweighted-regenerated}{regenerated}$ is also given. The error is largest on those data points where the cross-section is close to 0. Over the full range, the points are consistent with 0, showing good agreement between regeneration and reweighting. The agreement between the regenerated and reweighted lines has a $\frac{\chi^2}{NDF}$ value of 1.08 for the increase and 0.804 for the decrease in dial value respectively, where NDF is the number of degrees of freedom.

The angular distribution of the same leading energy nucleons is shown in figure 7.10. In this plot θ represents the angle of the nucleon emitted from the neutrino interaction. As with the energy distribution, the blue reweighted curve matches the black regenerated curve across the full $\cos(\theta)$ range, although the difference is less clear than in figure 7.9 as the difference between the regenerated sets is smaller. Again the residual plots show that within statistical error there is very strong agreement between reweighting and regenerating. The value of $\frac{\chi^2}{NDF}$ between reweighted and regenerated is 0.699 for the increased dial and 0.755 for the decreased dial.

For a clearer picture, it is possible to extend the figures to include all final state nucleons - not just the leading energy nucleons. The energy distributions and angular distributions for all nucleons leaving the nucleus are shown in figures 7.11 and 7.12 respectively. Even taking into account all final state nucleons, the reweighting is able to match the regenerated profile across the full spectrum. Now the total cross-section of events no longer has to be identical for the different data sets, as events producing more or fewer nucleons may be weighted by different amounts. The successful operation of the reweighting on the angular distribution is therefore clearer in figure 7.12 than figure 7.10. For the case of all particles, as for the case of leading order particles, the residual plots show the agreement between reweighting and regenerating is within statistical error across the full kinematic range. The $\frac{\chi^2}{NDF}$ values are 1.37 and 1.20, respectively for the increased and decreased dial in figure 7.11 and 0.88 and 1.04 for the increased and decreased dial in figure 7.12.

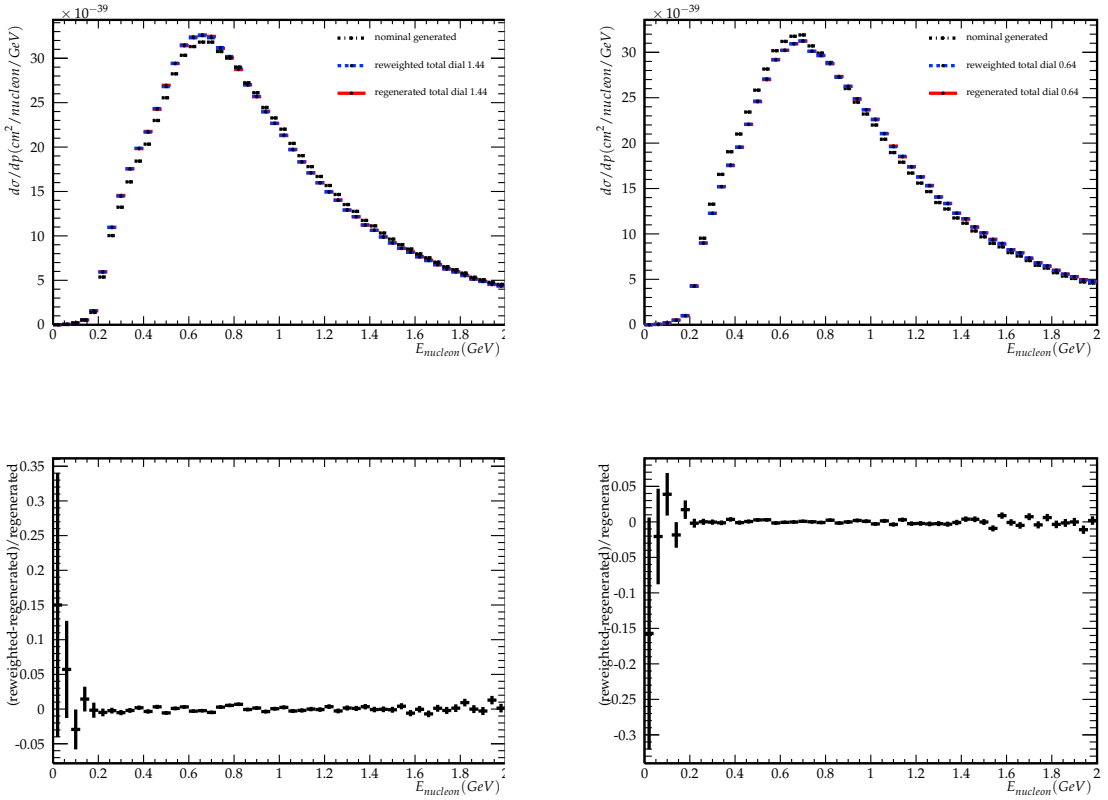

Figure 7.9.: Energy distribution for reweighting the total interaction dial to values of 1.44, top left, and 0.64 top right. Only the leading order final state nucleon is shown. The distribution generated with nominal dial values is shown in black, the distribution reweighted to changed dial values in blue, and the regenerated distribution with those dial values in red. Statistical errors are shown as a vertical error band, but in the case of some bins are too small to be visible due to the large number of events contributing to the data points. Bottom left and right: residual plots for these dial variations are shown.

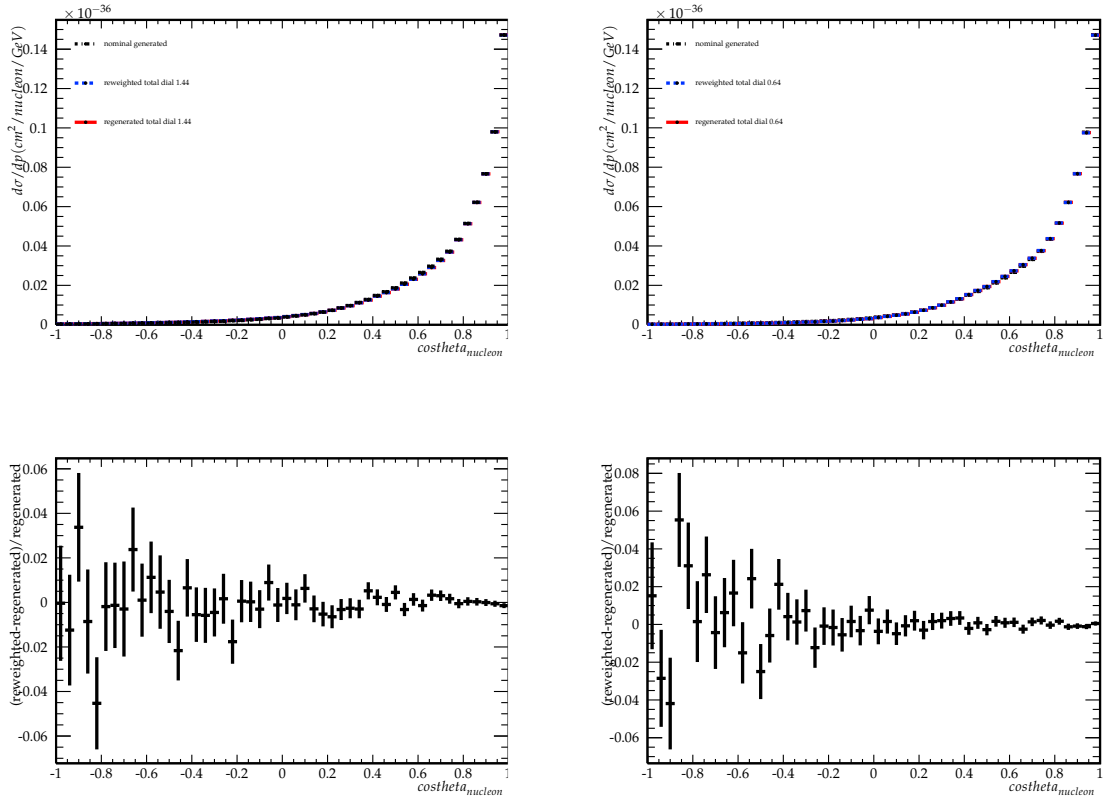

Figure 7.10.: Angular distribution for reweighting the total interaction dial to values of 1.44, top left, and 0.64, top right. Only the leading order final state nucleon is shown. The distribution generated with nominal dial values is shown in black, the distribution reweighted to changed dial values in blue, and the regenerated distribution with those dial values in red. Statistical errors are shown as a vertical error band, but in the case of some bins are too small to be visible due to the large number of events contributing to the data points. Bottom left and right: residual plots for these dial variations are shown.

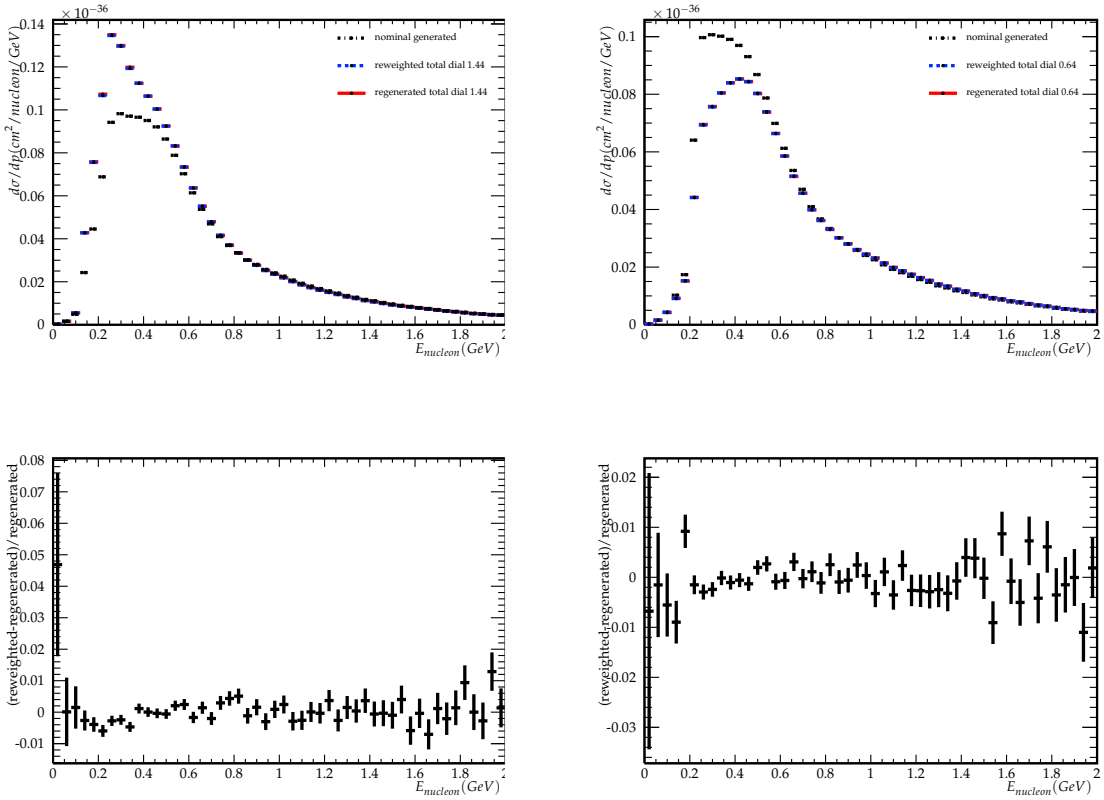

Figure 7.11.: Energy distribution for reweighting the total interaction dial to values of 1.44, top left, and 0.64, top right. All final state nucleons are included. The distribution generated with nominal dial values is shown in black, the distribution reweighted to changed dial values in blue, and the regenerated distribution with those dial values in red. Statistical errors are shown as a vertical error band, but in the case of some bins are too small to be visible due to the large number of events contributing to the data points. Bottom left and right: residual plots for these dial variations are shown.

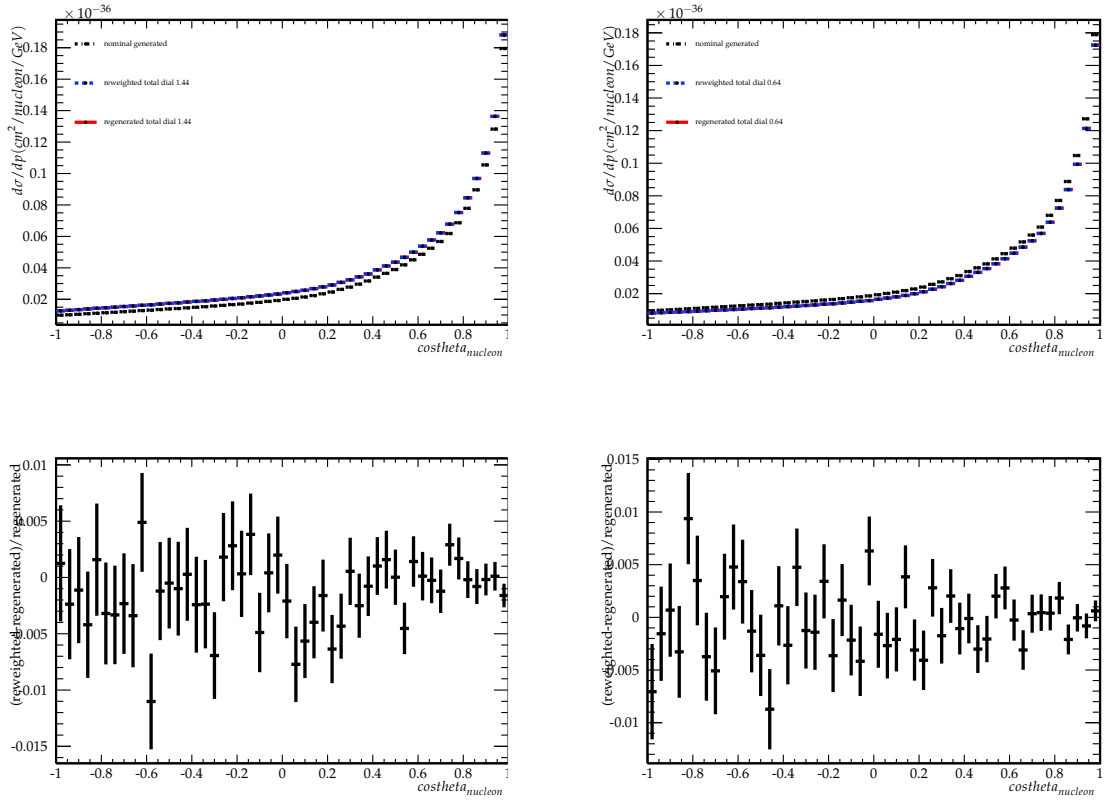

Figure 7.12.: Angular distribution for reweighting the total interaction dial to values of 1.44, top left, and 0.64, top right. All final state nucleons are included. The distribution generated with nominal dial values is shown in black, the distribution reweighted to changed dial values in blue, and the regenerated distribution with those dial values in red. Statistical errors are shown as a vertical error band, but in the case of some bins are too small to be visible due to the large number of events contributing to the data points. Bottom left and right: residual plots for these dial variations are shown.

It is also crucial that the reweighting process does not impact the parts of the code that should not be affected by changes in interaction probability in the nucleon cascade. This can be demonstrated by examining the kinematic distributions of final state leptons, which should not be affected at all. The energy distribution for all final state leptons is shown in figures 7.13. In this case, all three lines corresponding to nominal generated, reweighted, and regenerated agree, demonstrating that the lepton distributions are unaffected by variation of the nucleon dials. The residual profiles show the agreement between reweighted and regenerated which have a $\frac{\chi^2}{NDF}$ value of 0.728 and 0.801 for increase and decreased dial variations respectively.

These plots outline the validation of the reweighting process, showing that the reweighting methods are working correctly. Many further validation plots are included in appendix A, for variation of different dials, split by particle and NEUT interaction mode.

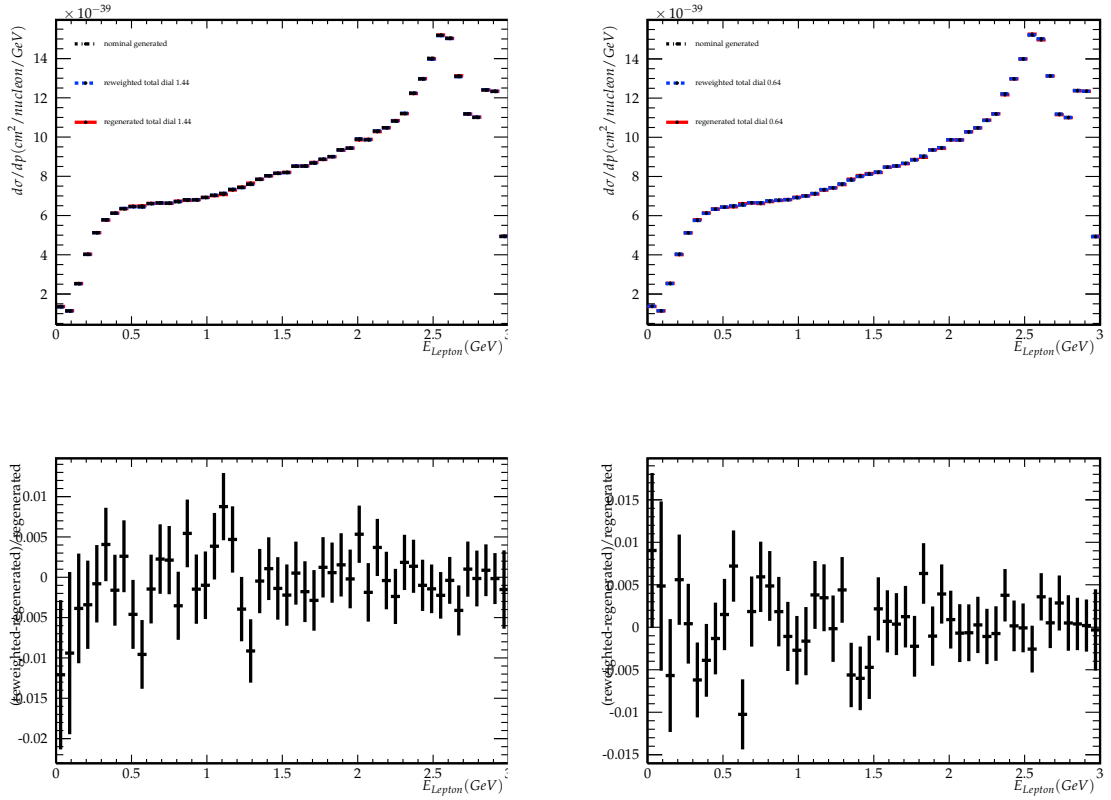

Figure 7.13.: Lepton energy distribution for reweighting the total interaction dial to values of 1.44, top left, and 0.64, top right. All final state leptons are included. The distribution generated with nominal dial values is shown in black, the distribution reweighted to changed dial values in blue, and the regenerated distribution with those dial values in red. Statistical errors are shown as a vertical error band, but in the case of some bins are too small to be visible due to the large number of events contributing to the data points. Bottom left and right: residual plots for these dial variations are shown.

7.2.4. Limitations of reweighting

The validations shown in the previous section demonstrate that the reweighting works successfully. However, the reweighting process does have fundamental limitations. Although for medium sized dial variations such as those shown above (or smaller), the reweighting shows excellent agreement with regeneration, for very large dial variations this ceases to be true. The energy profile for all particles with a variation in the total dial value of 400% is shown in figure 7.14. In contrast with the same plot for a dial variation of 144%, figure 7.9, the reweighting does not function correctly. Although the reweighting moves in the same direction away from the nominal curve towards the regenerated curve with higher dial values, it is not able to keep up. This is due to cascades with significant probability at more extreme interaction dial values not appearing in the original generated set at nominal dial values. It is therefore not possible to give these cascades weights, and as such they do not appear in the reweighted profile, while they do in the regenerated profile. The $\frac{\chi^2}{NDF}$ value of the agreement between regenerated and reweighted profiles in this case is 313.7, two orders of magnitude higher than the agreement for any of the previous smaller dial variations.

The problem can be seen most clearly by looking at the range of values of weights produced by the reweighting. The values of weights for reweighting to a total dial value of 1.44 is shown in figure 7.15, left, while the weights for a dial value of 4.00 are shown in figure 7.15, right. For 1.44, the weights form a distribution about 1, as each cascade in the nominal generated set also exists at the higher dial value with a modified probability. However for 4.00, there is a large peak at 0. In this case, a number of cascades that were possible at nominal values are not possible at all at the higher dial value, and as such are weighted down to 0. Therefore there is not a complete overlap between cascades at nominal and a dial value of 4.00. Rather, a number of cascades that appear in regenerating with a dial value of 4.00 do not appear in the nominal set. The reweighting only handles cascades that exist in the nominal, and is incapable of introducing these new cascades with a weight. Therefore the reweighting cannot keep up with generation at these extrema. The missing events in the reweighting (those weighted to 0) are the reason for the larger statistical errors in some bins in figure 7.14 This is a problem that is fundamental to reweighting. However, this problem only exists for extreme dial variations not required in any typical analyses. The range of dial values which have been shown to be possible include variation by a factor of 2, and

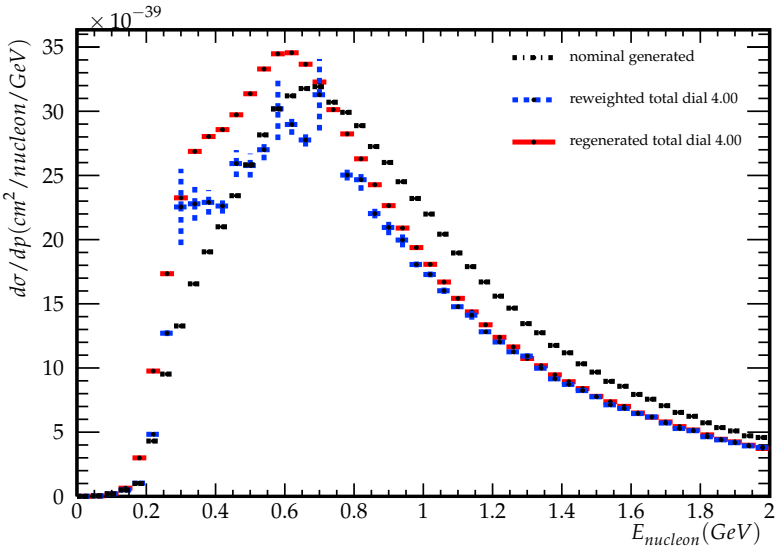

Figure 7.14.: Energy distribution for reweighting the total interaction dial to an extreme value of 4.00. Only the leading order final state nucleon is shown. The distribution generated with nominal dial values is shown in black, the distribution reweighted to changed dial values in blue, and the regenerated distribution with those dial values in red. Statistical errors are shown as a vertical error band, but in the case of some bins are too small to be visible due to the large number of events contributing to the data points.

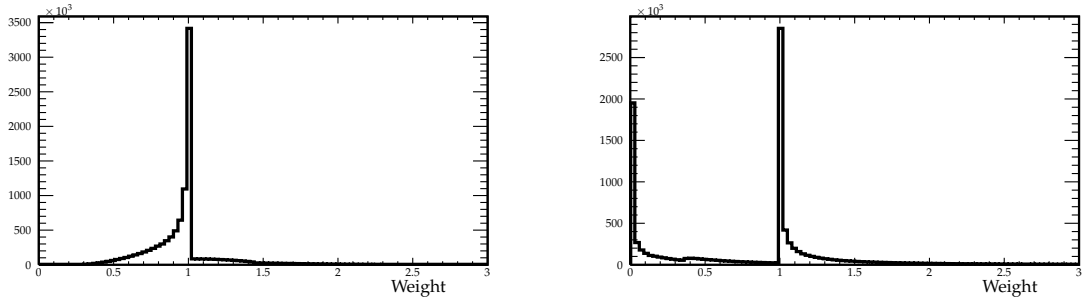

Figure 7.15.: Distribution of weights for dial variations. Left: small total dial variation of 1.44. Right: Large total dial variation of 4.00.

values higher than that may also be acceptable depending on the required agreement between regeneration and reweighting of a given analysis.

Table 7.2.: Time taken for reweighting nucleon dials vs regeneration. 100,000 events were generated and reweighted. Time for the full generation, the subset of time spent just in the nucleon cascade, and for reweighting are shown.

Process	Time required
Generation of 100k NEUT events	10 mins 44 s
Generation of 100k NEUT events (nucleon cascade only)	21.5s
Reweighting of 100k NEUT events	11.4s

7.2.5. Comparisons of speed of reweighting and regeneration

The primary purpose of reweighting is to provide a tool for analysers to investigate the effect of changing parameters in an analysis without the need to perform a full regeneration which is prohibitively slow. As such, in addition to correctly approximating generation, the reweighting process must also show an improvement in speed over generation. Table 7.2 shows the difference in speed of running the generation and reweighting of the nucleon dials. Not only is there a large time saving, the reweighting even shows an improvement in speed by close to a factor of two on just the cascade portion of the code. This time saving makes it possible for the implementation of nucleon dials to have an impact, reducing systematic uncertainties in future T2K and Hyper-K analyses.

Chapter 8.

Conclusions and Outlook

Fundamental to future discovery in particle physics are both building detectors with novel sensitivity to provide data, and the underlying framework required to make full use of those data in modelling and simulation. In this thesis, related work in both of these areas has been presented.

A high pressure time projection chamber has sensitivity to low momentum hadrons not seen in liquid scintillator or water detectors. The building of a prototype HPTPC and operation in a test beam at the T10 beamline were detailed in this work. Techniques used to reduce the momentum of particles and change the ratio of protons to background MIPs are detailed, and a full analysis of time of flight measurements was made to characterise the beam impinging the TPC. Using moderator blocks and placing the detector off axis, an average energy reduction from 0.3 GeV with 0 moderator blocks to 0.1 GeV with 4 moderator blocks was achieved. Simulations of the beam test concluded that with 4 moderator blocks an average of 5.6 ± 0.1 protons with energies below 100 MeV reached the active TPC region, and the simulations were validated with comparisons to the time of flight data. Analysis of the results from the TPC prototype are ongoing, including results of optical readout. This optical readout was shown to work on calibration sources, with methods successfully applied to improve event detection. The HPTPC prototype will be tested again at FermiLab in the coming year, and makes up a part of the official design of the next generation experiment, DUNE.

The sensitivity to very low momentum hadrons from neutrino interactions that an HPTPC would provide will allow better modelling of neutrino interactions which informs neutrino interaction generators. Improving handling of nucleon systematics in generators is therefore a crucial step in reducing systematics in future neutrino

analyses. Four dials governing nucleon final state interactions were added to NEUT, the primary generator of the T2K experiment. A reweighting method was written, and it was validated that the method works for moderate dial variations. These validations include showing reweighted cross-sections well approximate regnerated cross-sections with the same dial values, for a range of nucleon kinematics. It was also shown that lepton kinematics are not affected by the nucleon dial. These dials, and the reweighting structure to support them are now being made available in NEUT for use by analysers, providing a reduction in uncertainty due to nucleon final state interactions in various analyses. This will be particularly valuable as neutrino oscillation enters the precision era and a new generation of neutrino experiments with ever increasing statistics require ever improved systematics.

Appendix A.

Validation plots

This appendix includes all validation plots corresponding to the work described in chapter 7. Plots are shown for an increase to 1.44 and decrease to 0.64 of each of the four nucleon dials: total dial, elastic dial, single pion dial, and double pion dial. In each case plots of energy and angle are shown for both the leading order particle, and all final state particles, as well as a residual plot comparing reweighting and regenerating in each case. In addition to validation plots for all neutrino events, specific subsections corresponding to specific NEUT Modes are shown. These are NEUT Mode 1 (CCQE), NEUT Mode 2 (2p2h), and NEUT Mode 11 (resonance pion production). In each case the full kinematic distribution is shown for nucleons, protons, neutrons, pions, and leptons.

A.1. Total Dial: varied up to 1.44

Energy plot: Leading Energy Nucleon: Neut Mode =AllModesCombined

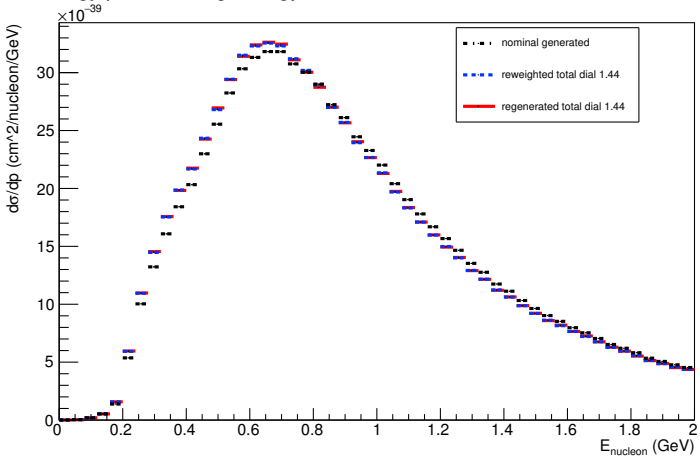

Energy plot: Every FSI Nucleon: Neut Mode =AllModesCombined

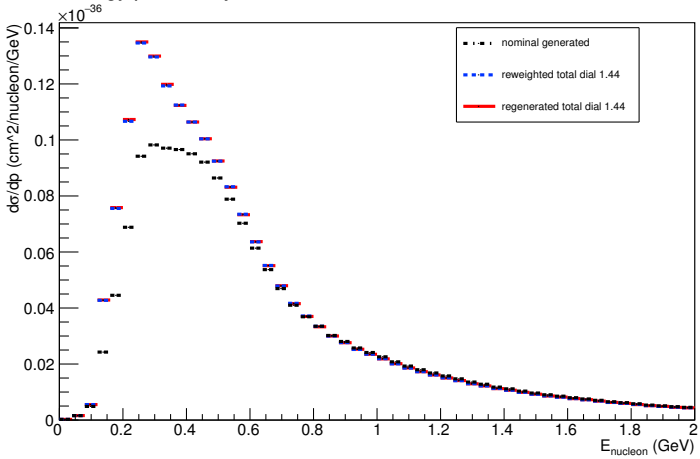

Energy plot: Leading Energy Nucleon: Neut Mode =AllModesCombined

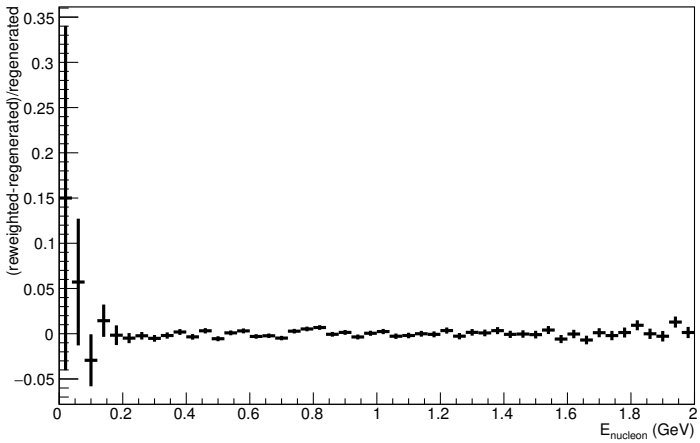

Energy plot: Every FSI Nucleon: Neut Mode =AllModesCombined

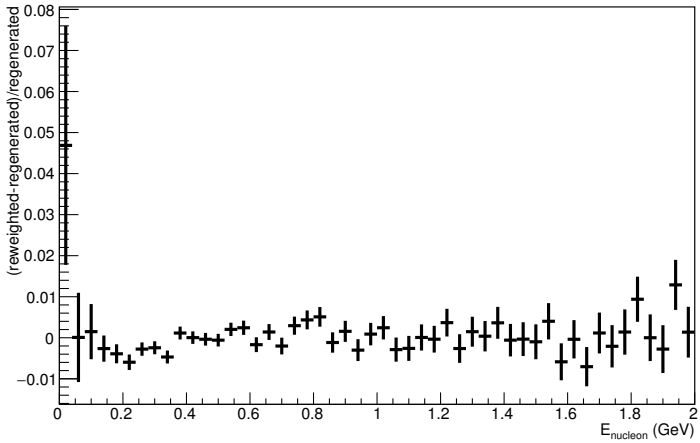

Angle plot: Leading Energy Nucleon: Neut Mode =AllModesCombined

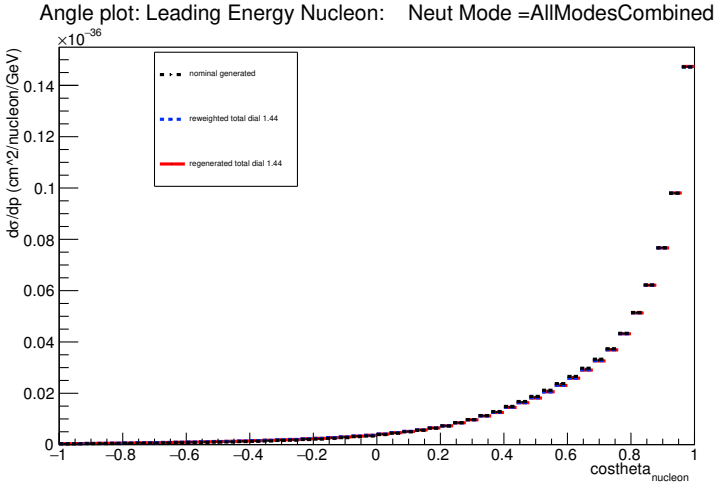

Angle plot: Every FSI Nucleon: Neut Mode =AllModesCombined

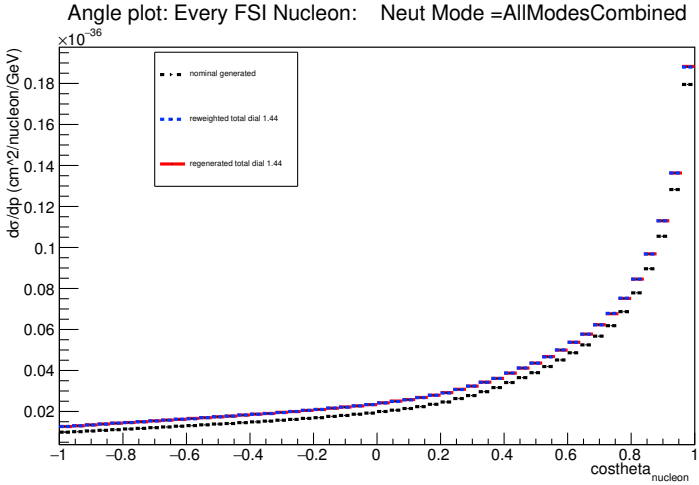

Angle plot: Leading Energy Nucleon: Neut Mode =AllModesCombined

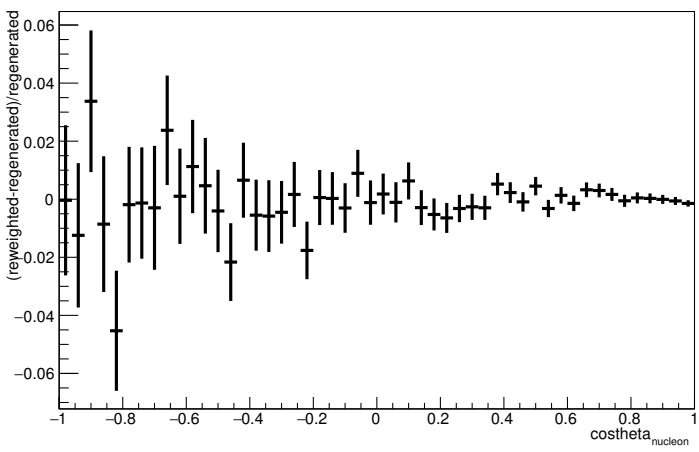

Angle plot: Every FSI Nucleon: Neut Mode =AllModesCombined

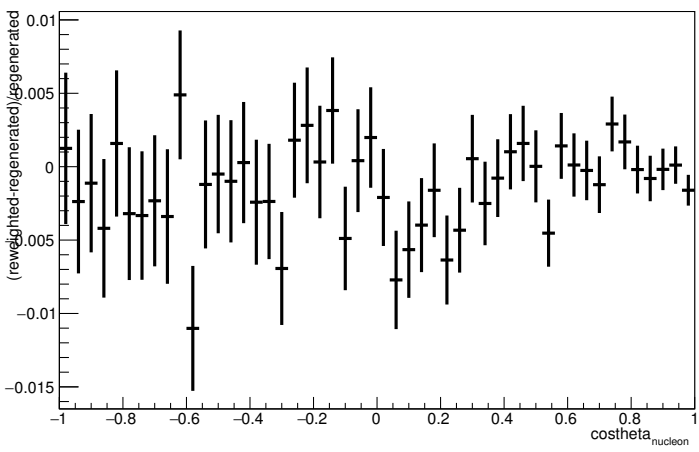

Energy plot: Leading Energy Proton: Neut Mode =AllModesCombined

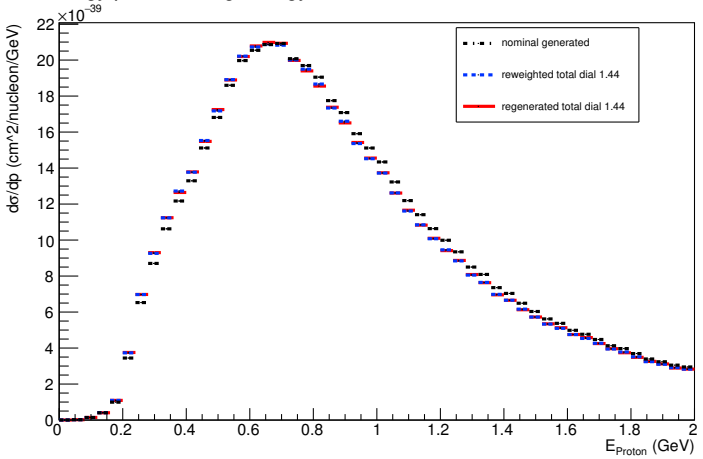

Energy plot: Every FSI Proton: Neut Mode =AllModesCombined

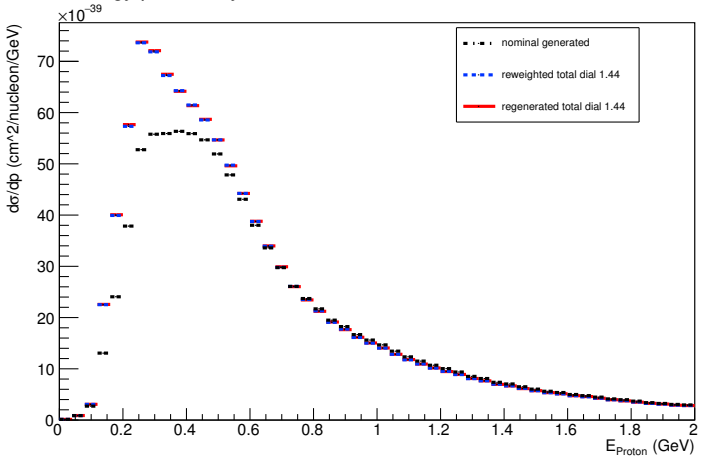

Energy plot: Leading Energy Proton: Neut Mode =AllModesCombined

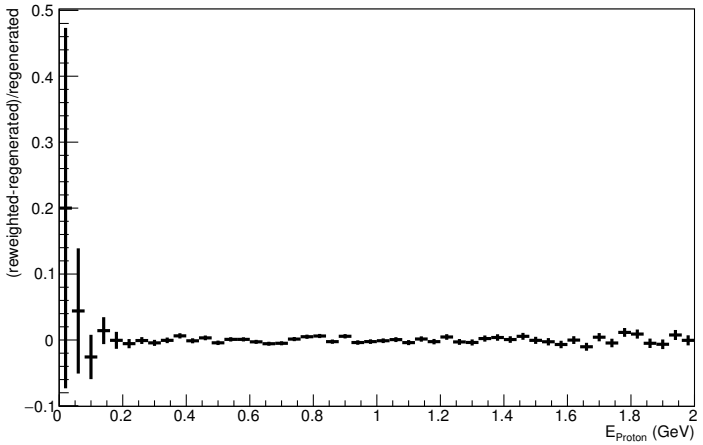

Energy plot: Every FSI Proton: Neut Mode =AllModesCombined

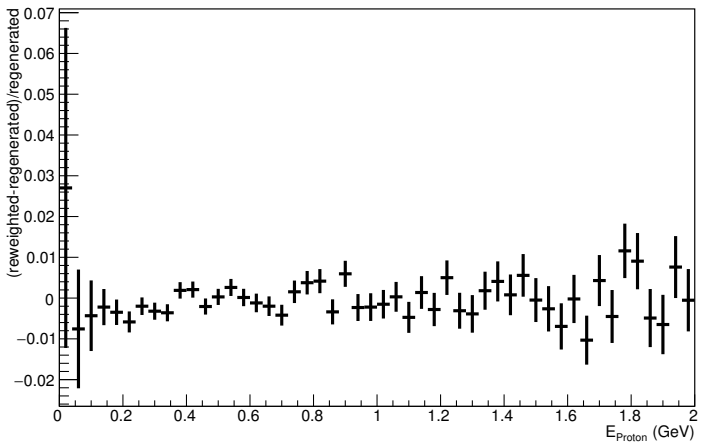

Angle plot: Leading Energy Proton: Neut Mode =AllModesCombined

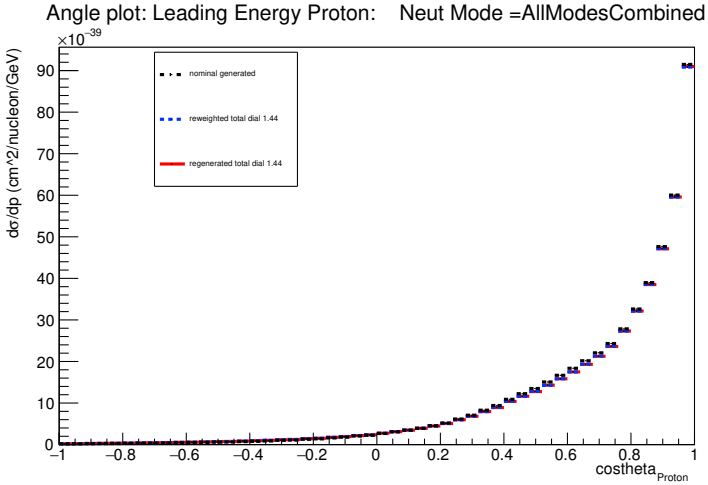

Angle plot: Every FSI Proton: Neut Mode =AllModesCombined

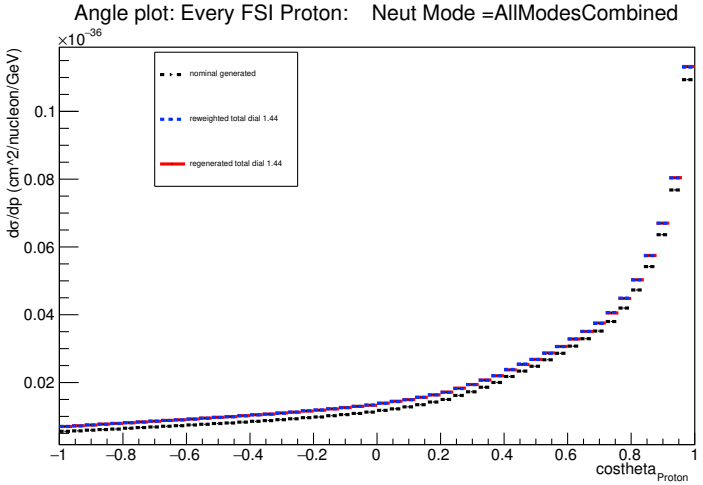

Angle plot: Leading Energy Proton: Neut Mode =AllModesCombined

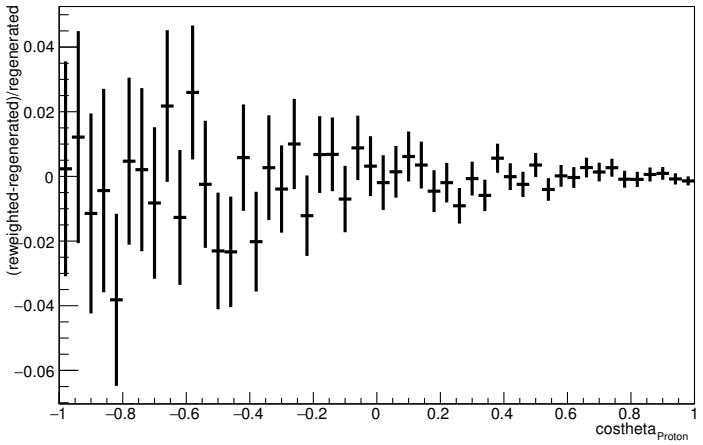

Angle plot: Every FSI Proton: Neut Mode =AllModesCombined

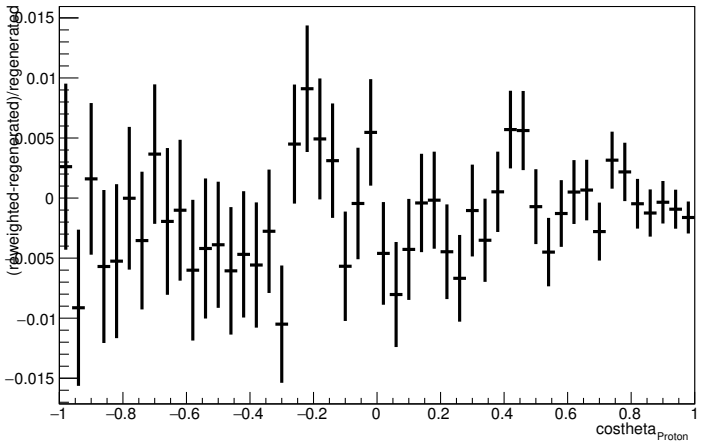

Energy plot: Leading Energy Neutron: Neut Mode =AllModesCombined

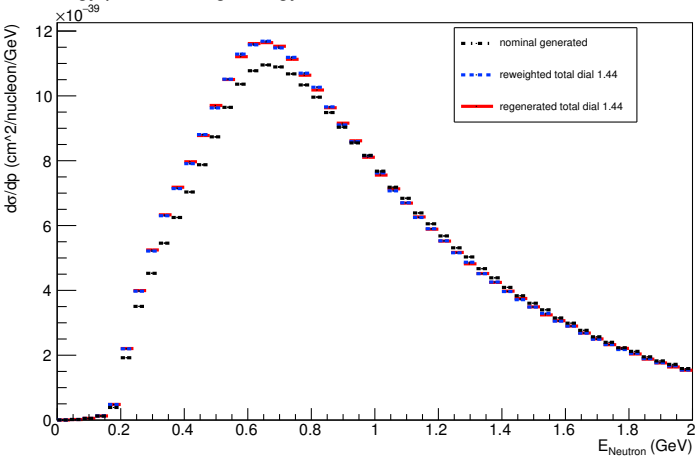

Energy plot: Every FSI Neutron: Neut Mode =AllModesCombined

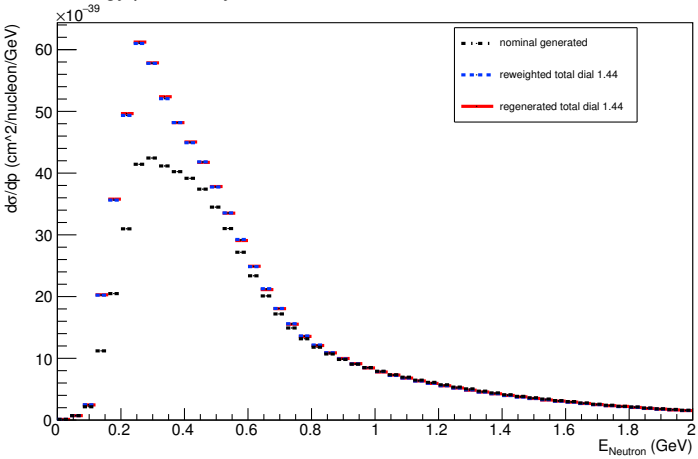

Energy plot: Leading Energy Neutron: Neut Mode =AllModesCombined

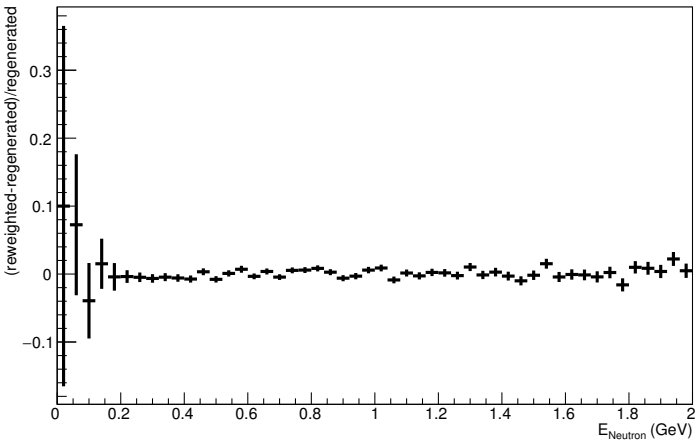

Energy plot: Every FSI Neutron: Neut Mode =AllModesCombined

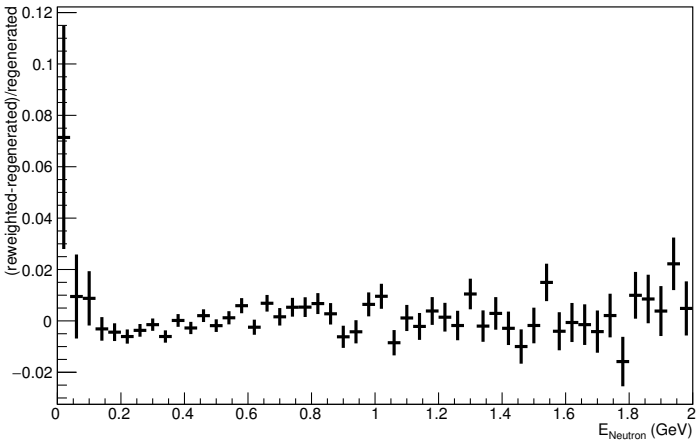

Angle plot: Leading Energy Neutron: Neut Mode =AllModesCombined

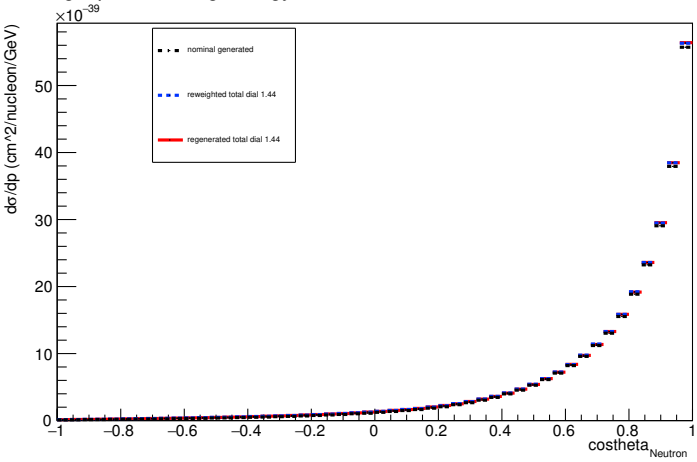

Angle plot: Every FSI Neutron: Neut Mode =AllModesCombined

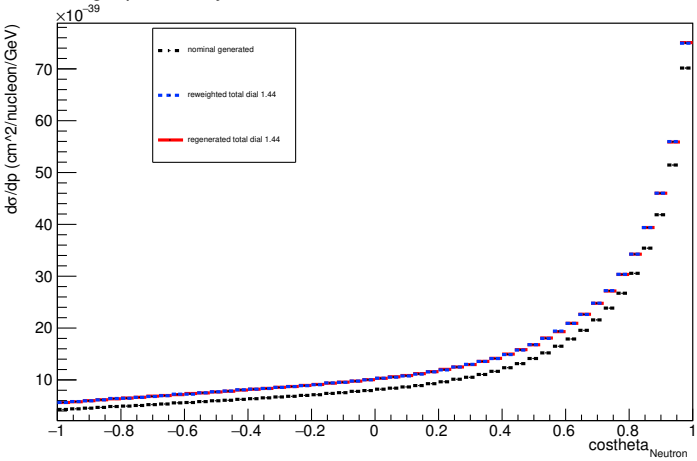

Angle plot: Leading Energy Neutron: Neut Mode =AllModesCombined

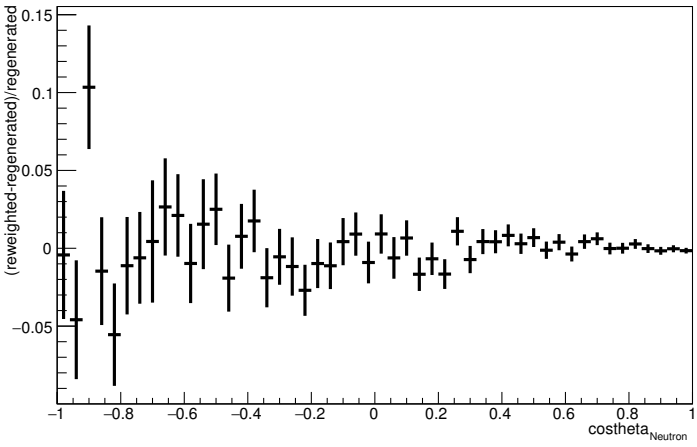

Angle plot: Every FSI Neutron: Neut Mode =AllModesCombined

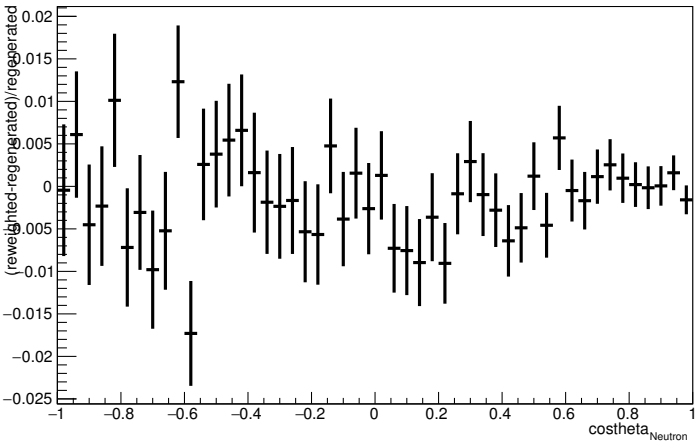

Energy plot: Leading Energy Lepton: Neut Mode =AllModesCombined

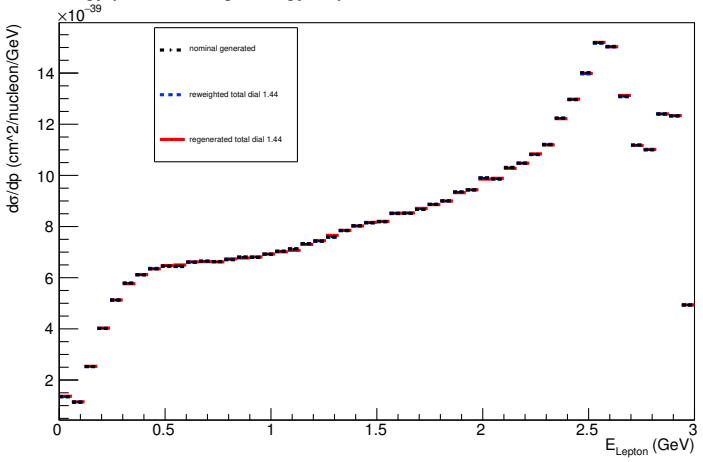

Angle plot: Leading Energy Lepton: Neut Mode =AllModesCombined

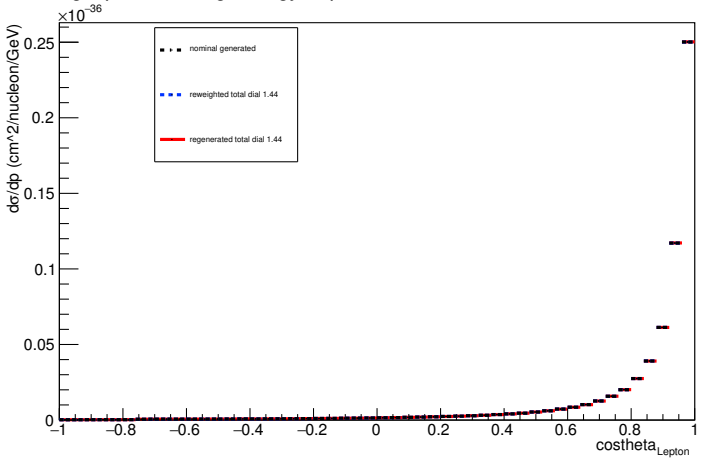

Energy plot: Leading Energy Lepton: Neut Mode =AllModesCombined

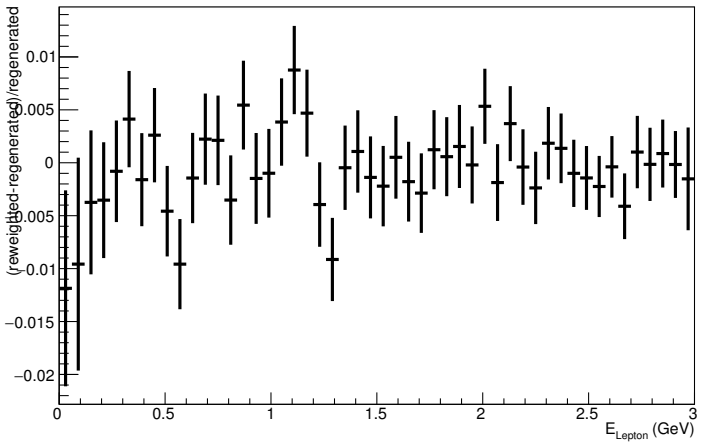

Angle plot: Leading Energy Lepton: Neut Mode =AllModesCombined

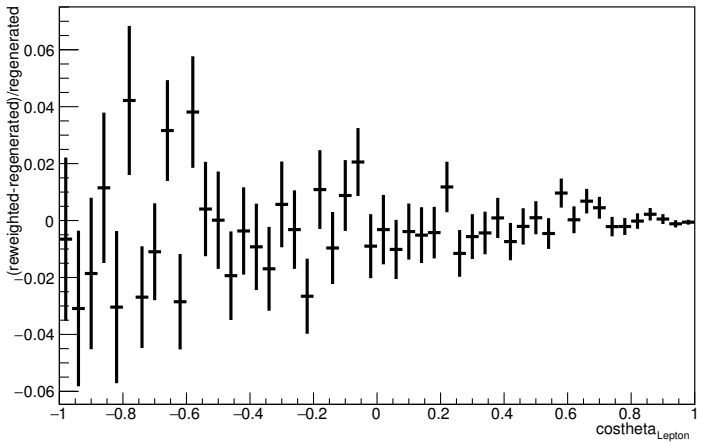

Energy plot: Leading Energy Pion: Neut Mode =AllModesCombined

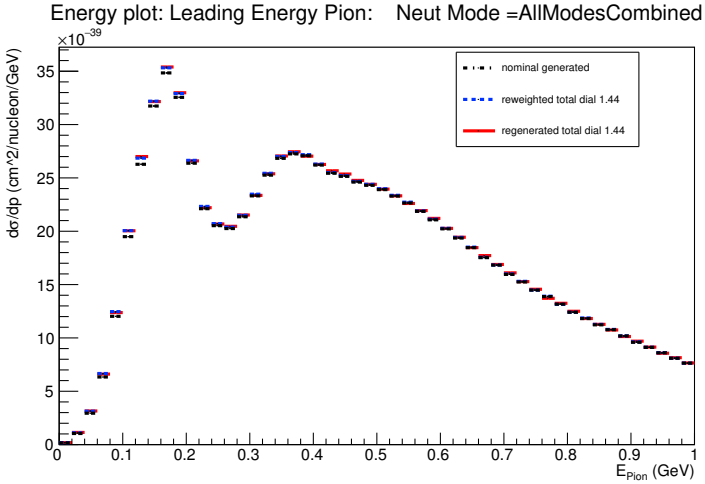

Energy plot: Every FSI Pion: Neut Mode =AllModesCombined

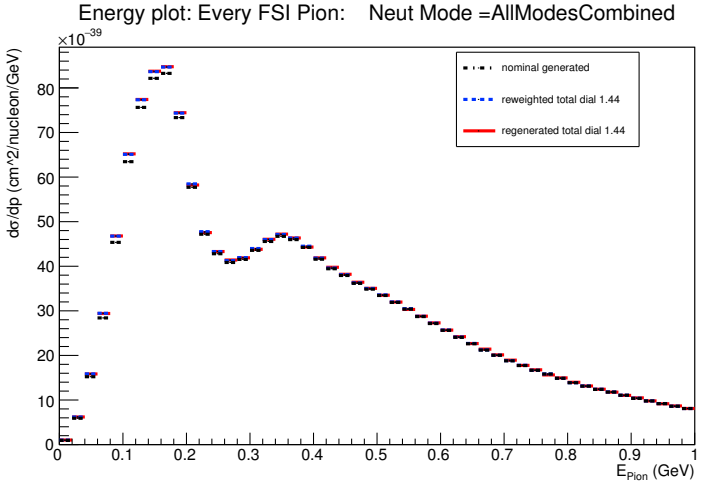

Energy plot: Leading Energy Pion: Neut Mode =AllModesCombined

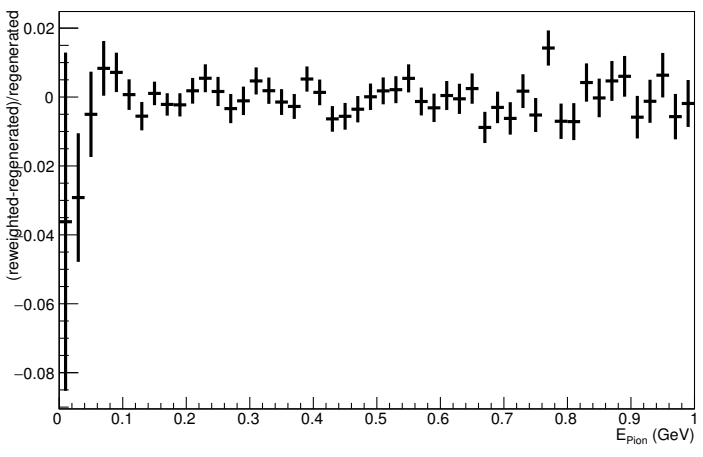

Energy plot: Every FSI Pion: Neut Mode =AllModesCombined

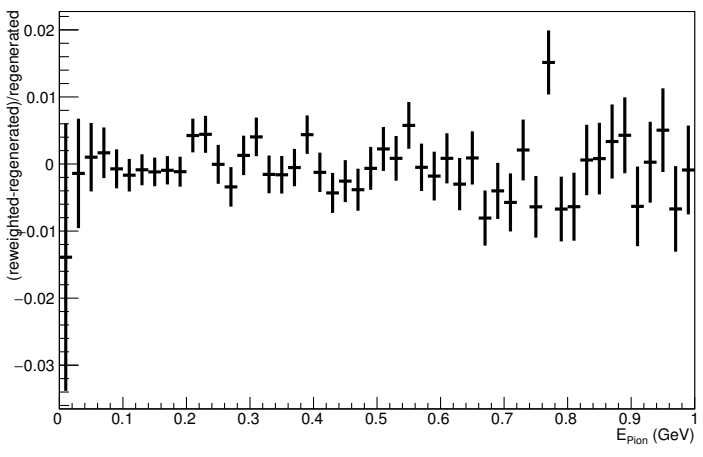

Angle plot: Leading Energy Pion: Neut Mode =AllModesCombined

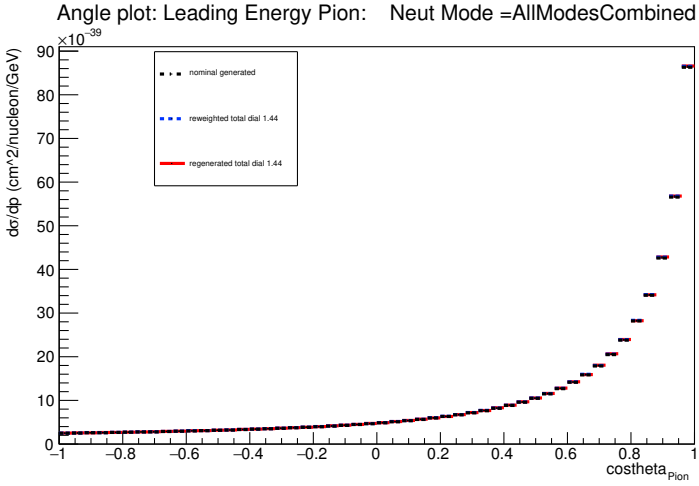

Angle plot: Every FSI Pion: Neut Mode =AllModesCombined

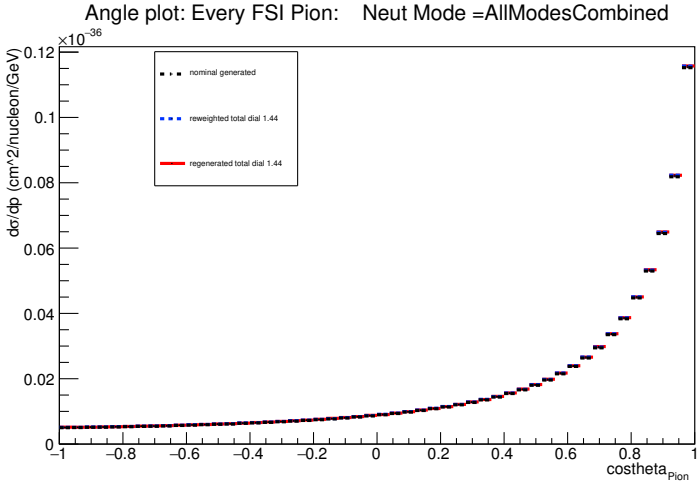

Angle plot: Leading Energy Pion: Neut Mode =AllModesCombined

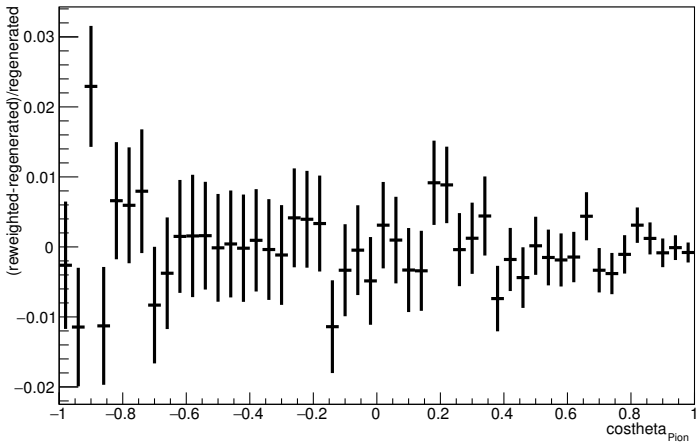

Angle plot: Every FSI Pion: Neut Mode =AllModesCombined

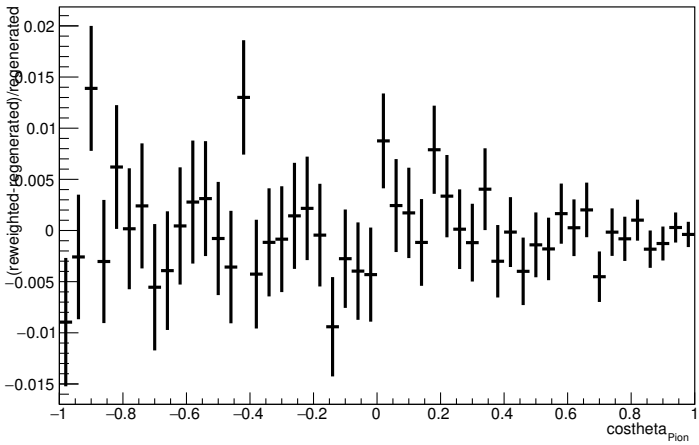

Energy plot: Leading Energy Nucleon: Neut Mode =1

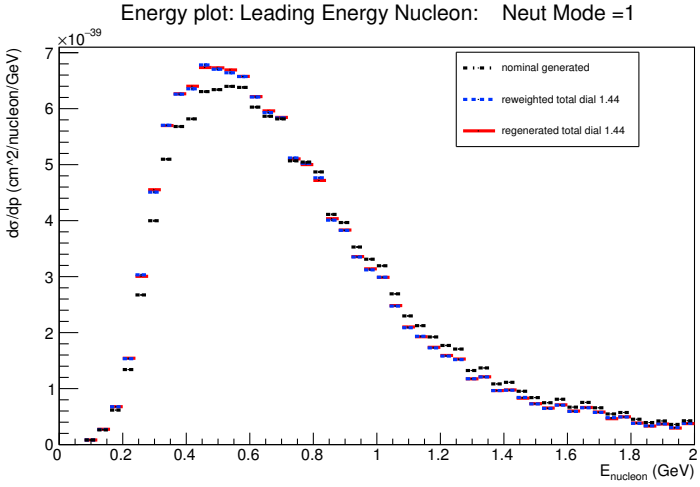

Energy plot: Every FSI Nucleon: Neut Mode =1

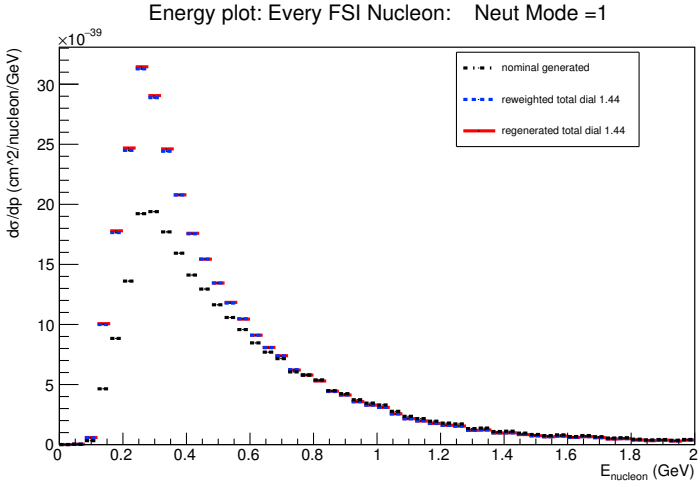

Energy plot: Leading Energy Nucleon: Neut Mode =1

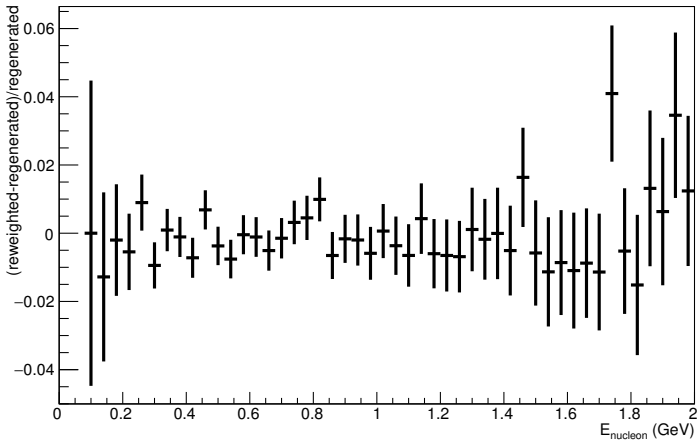

Energy plot: Every FSI Nucleon: Neut Mode =1

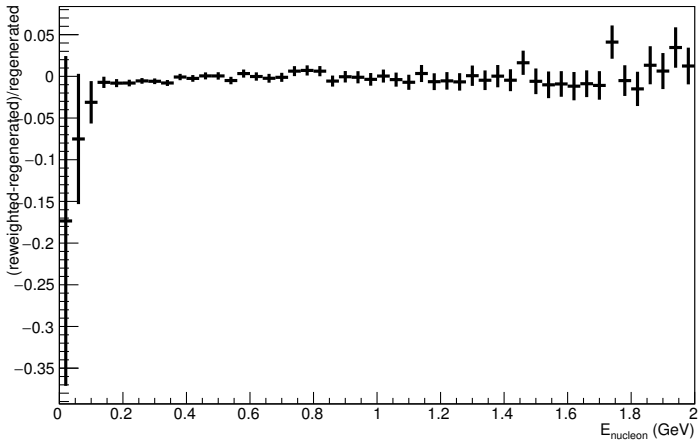

Angle plot: Leading Energy Nucleon: Neut Mode =1

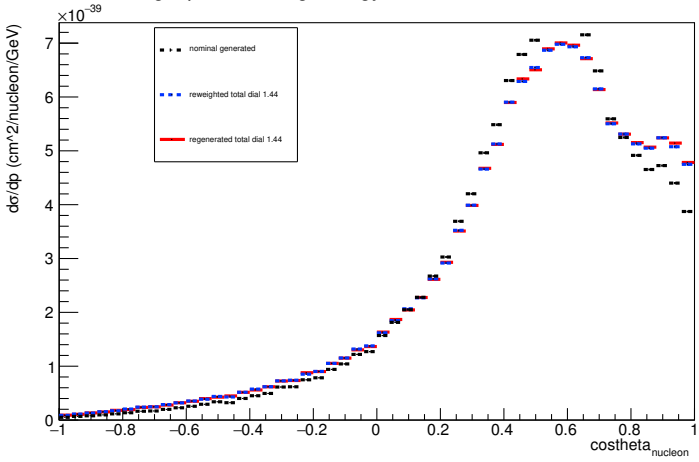

Angle plot: Every FSI Nucleon: Neut Mode =1

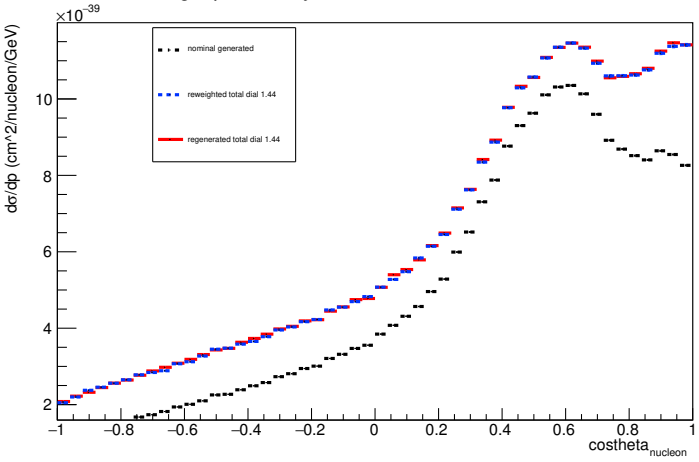

Angle plot: Leading Energy Nucleon: Neut Mode =1

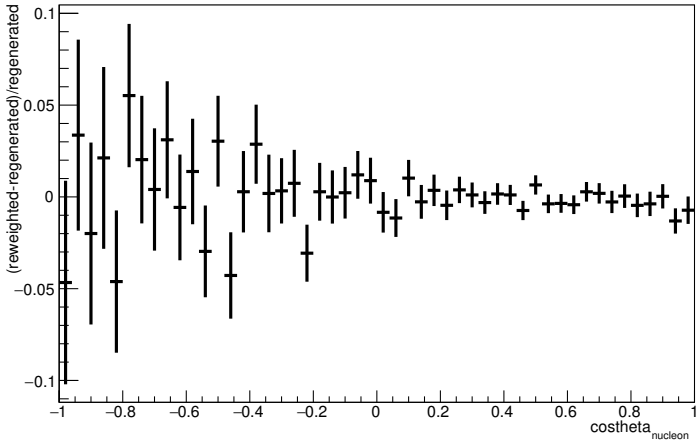

Angle plot: Every FSI Nucleon: Neut Mode =1

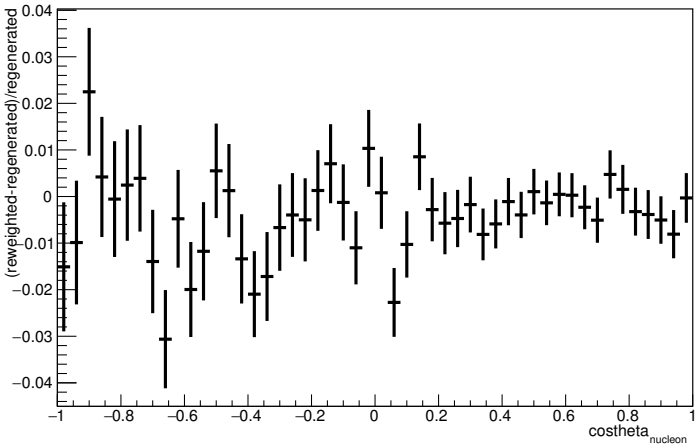

Energy plot: Leading Energy Proton: Neut Mode =1

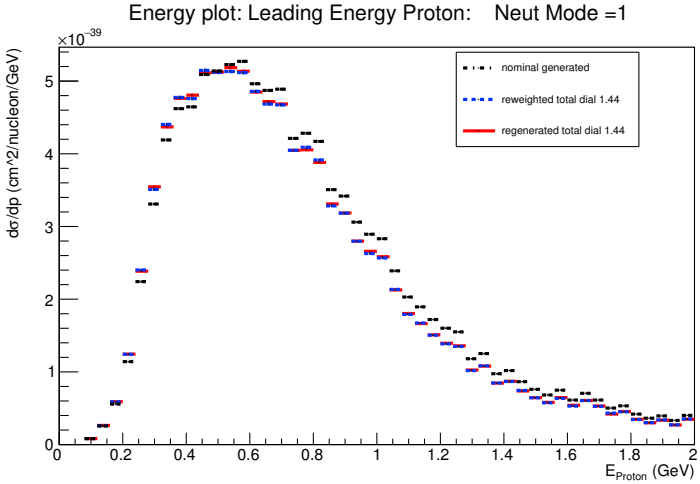

Energy plot: Every FSI Proton: Neut Mode =1

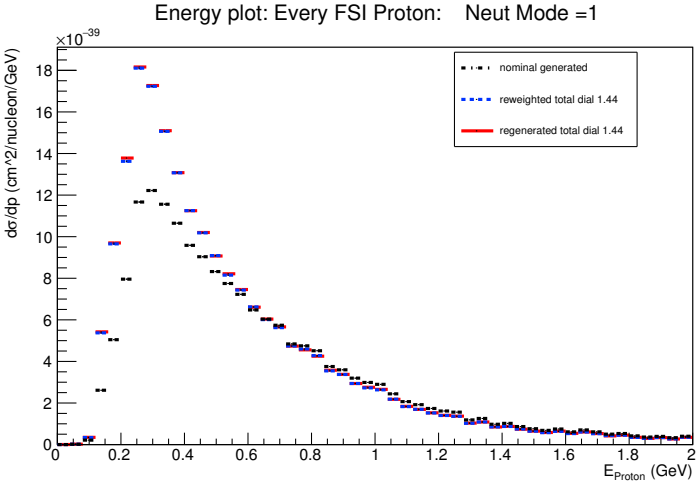

Energy plot: Leading Energy Proton: Neut Mode =1

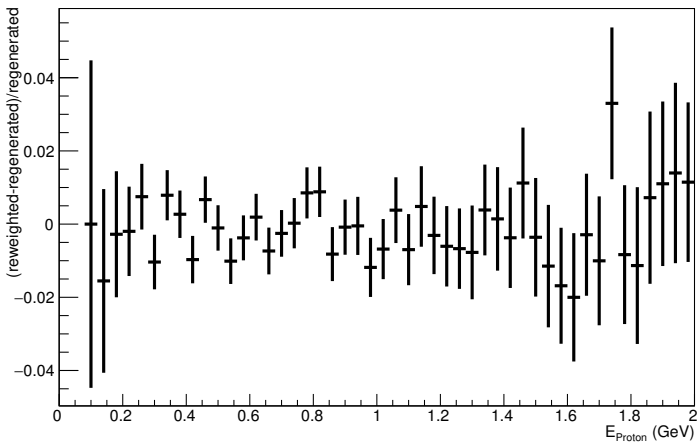

Energy plot: Every FSI Proton: Neut Mode =1

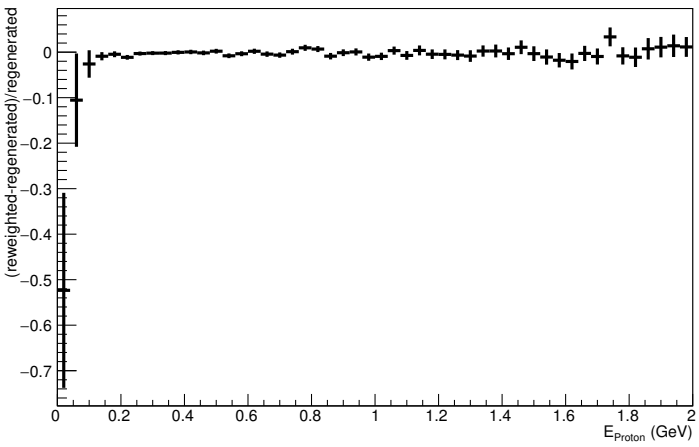

Angle plot: Leading Energy Proton: Neut Mode =1

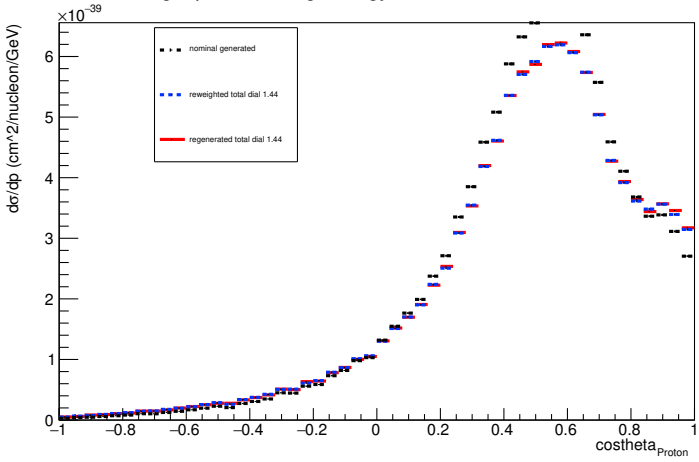

Angle plot: Every FSI Proton: Neut Mode =1

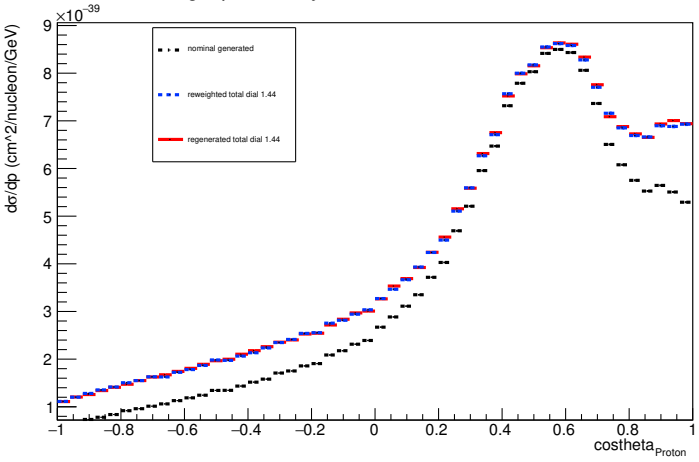

Angle plot: Leading Energy Proton: Neut Mode =1

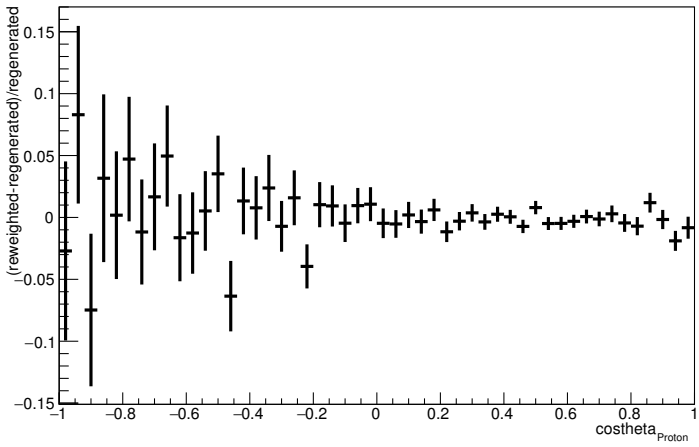

Angle plot: Every FSI Proton: Neut Mode =1

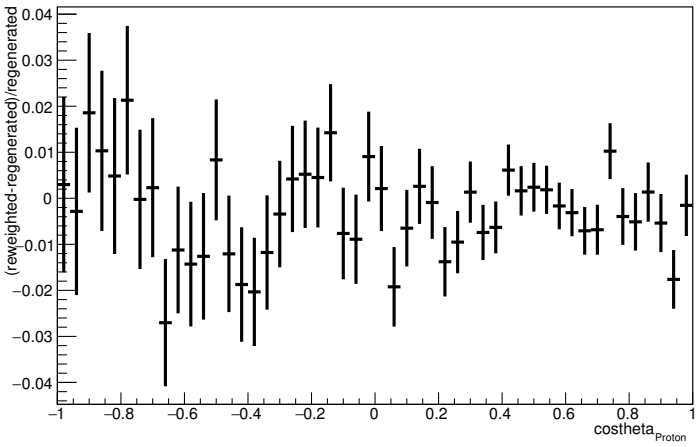

Energy plot: Leading Energy Neutron: Neut Mode =1

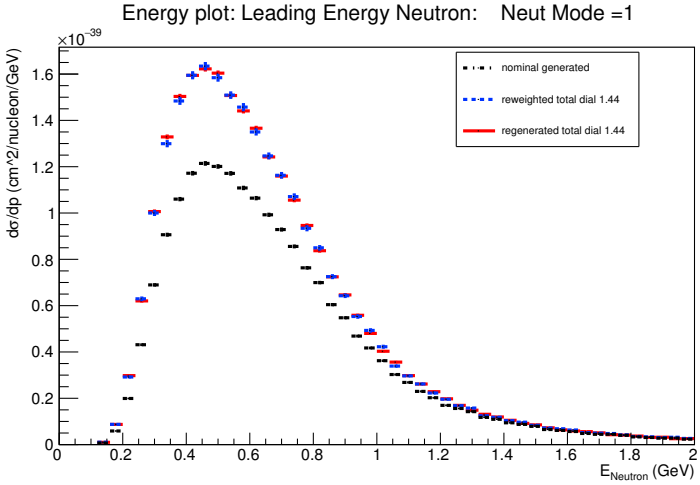

Energy plot: Every FSI Neutron: Neut Mode =1

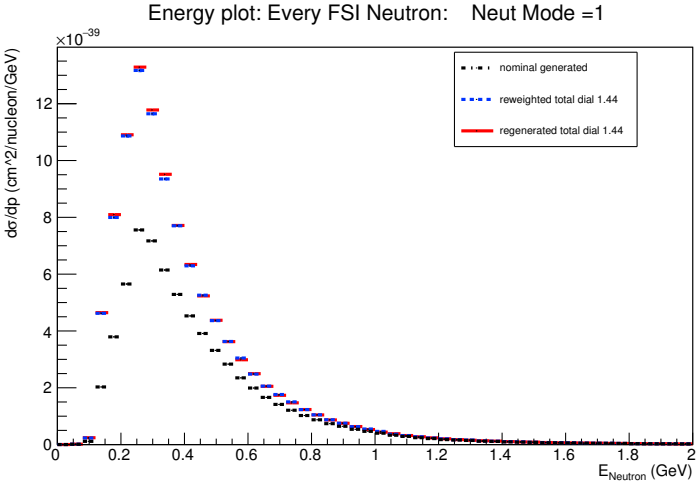

Energy plot: Leading Energy Neutron: Neut Mode =1

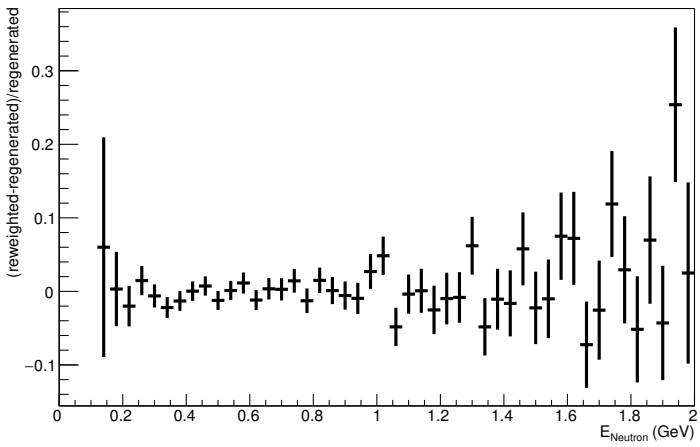

Energy plot: Every FSI Neutron: Neut Mode =1

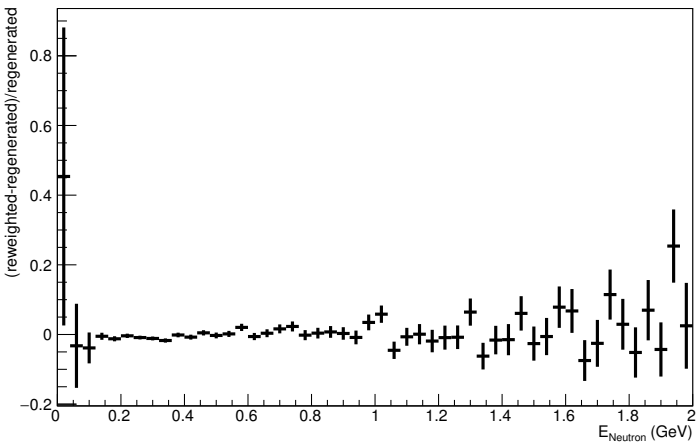

Angle plot: Leading Energy Neutron: Neut Mode =1

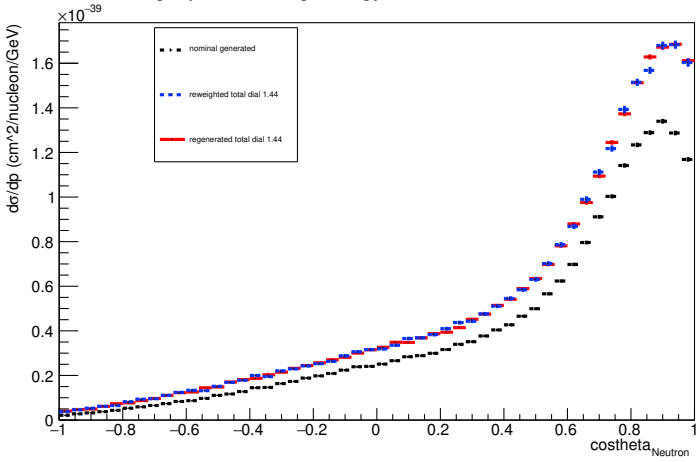

Angle plot: Every FSI Neutron: Neut Mode =1

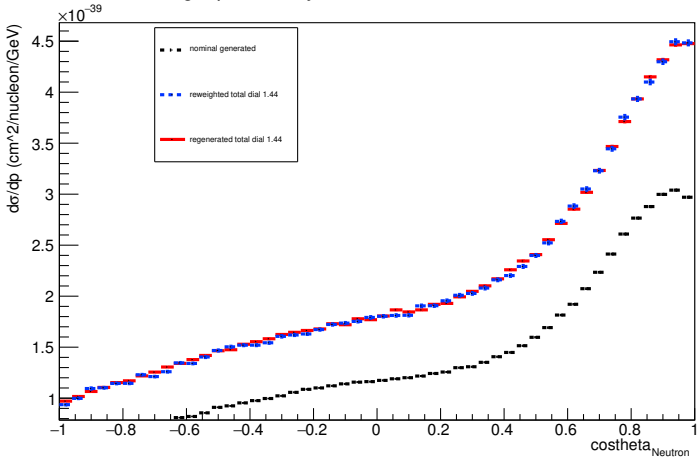

Angle plot: Leading Energy Neutron: Neut Mode =1

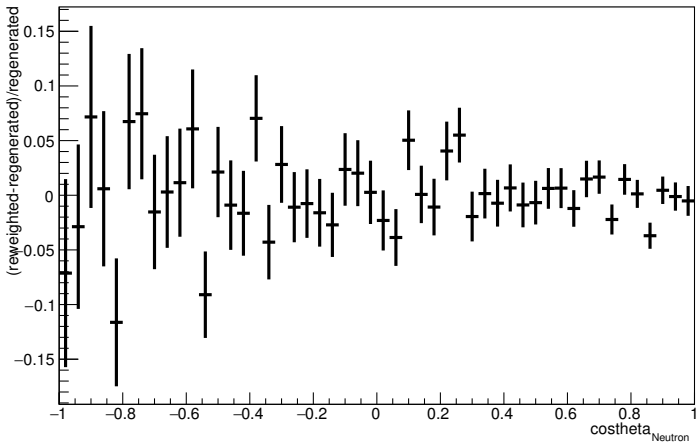

Angle plot: Every FSI Neutron: Neut Mode =1

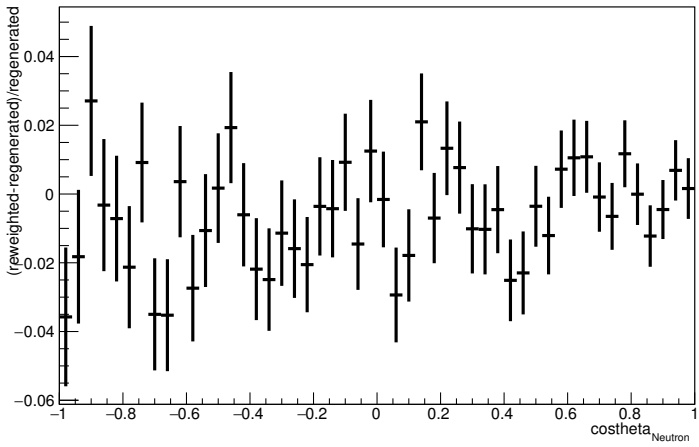

Energy plot: Leading Energy Lepton: Neut Mode =1

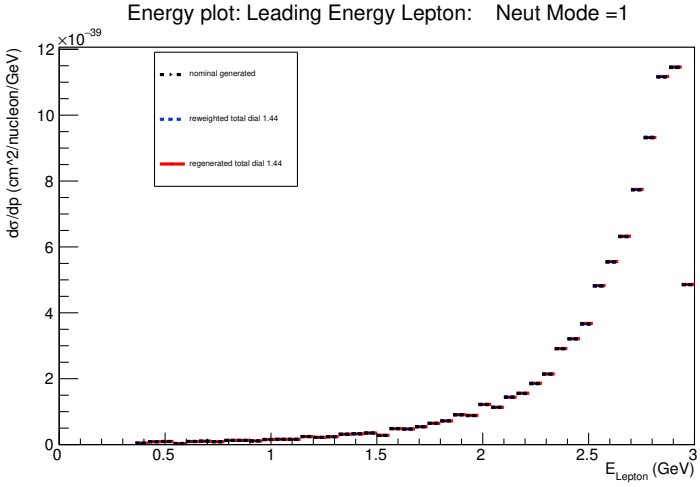

Angle plot: Leading Energy Lepton: Neut Mode =1

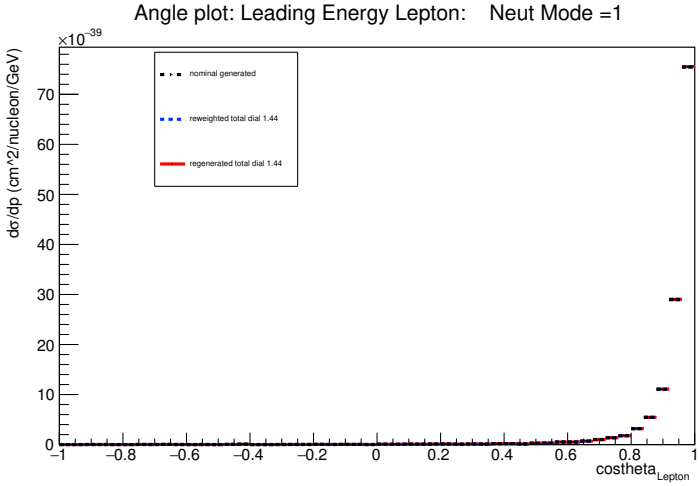

Energy plot: Leading Energy Lepton: Neut Mode =1

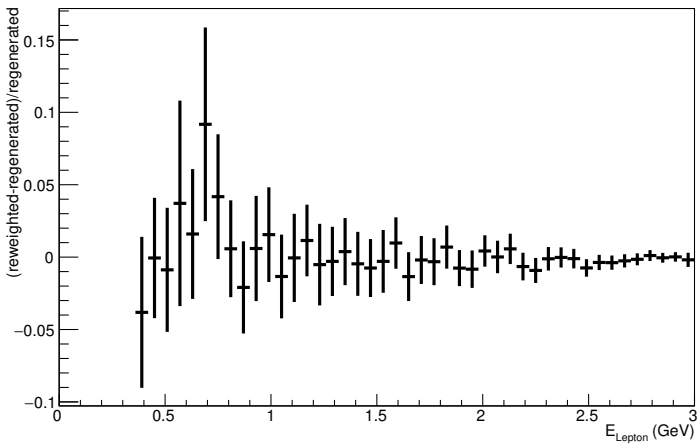

Angle plot: Leading Energy Lepton: Neut Mode =1

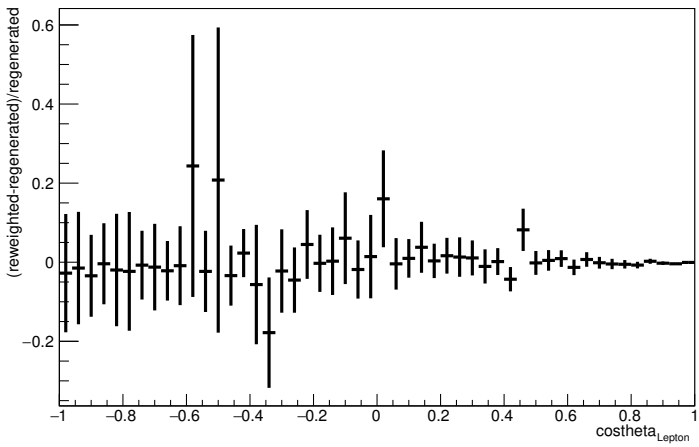

Energy plot: Leading Energy Pion: Neut Mode =1

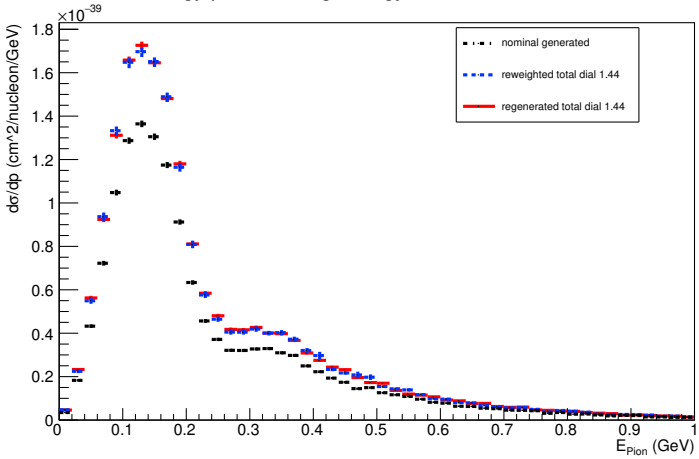

Energy plot: Every FSI Pion: Neut Mode =1

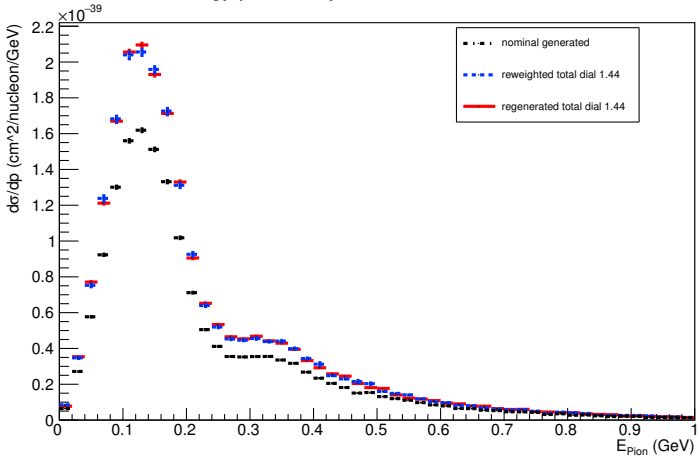

Energy plot: Leading Energy Pion: Neut Mode =1

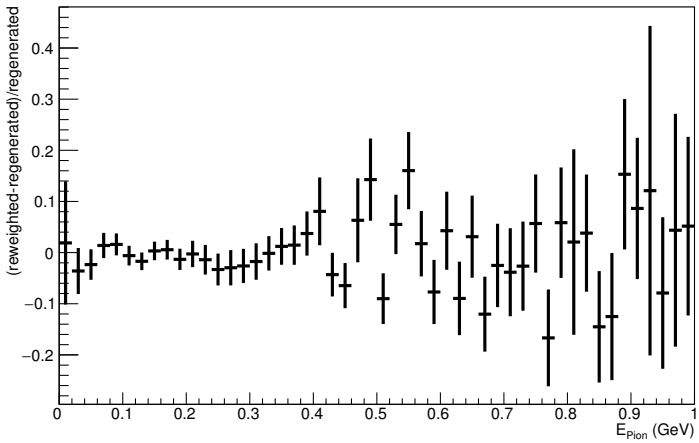

Energy plot: Every FSI Pion: Neut Mode =1

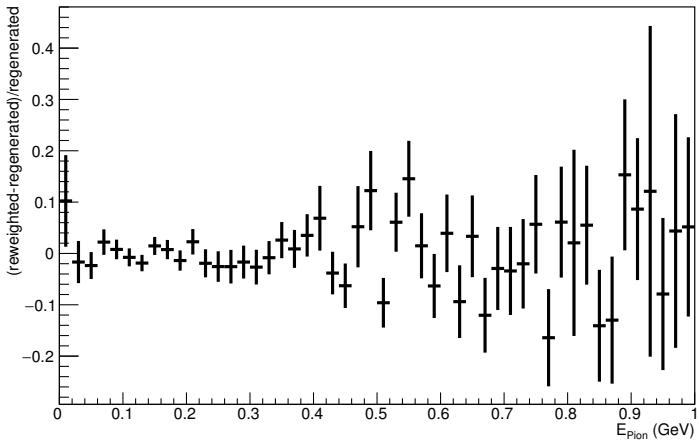

Angle plot: Leading Energy Pion: Neut Mode =1

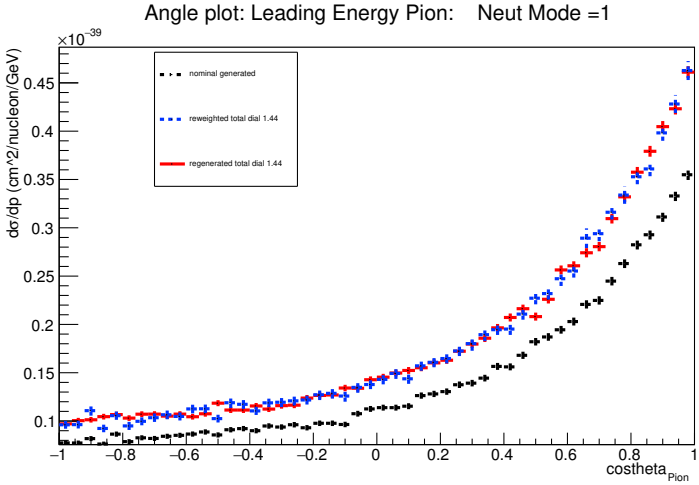

Angle plot: Every FSI Pion: Neut Mode =1

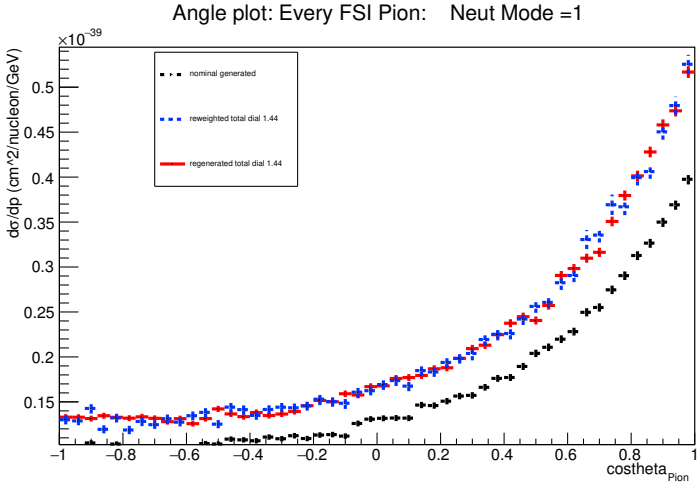

Angle plot: Leading Energy Pion: Neut Mode =1

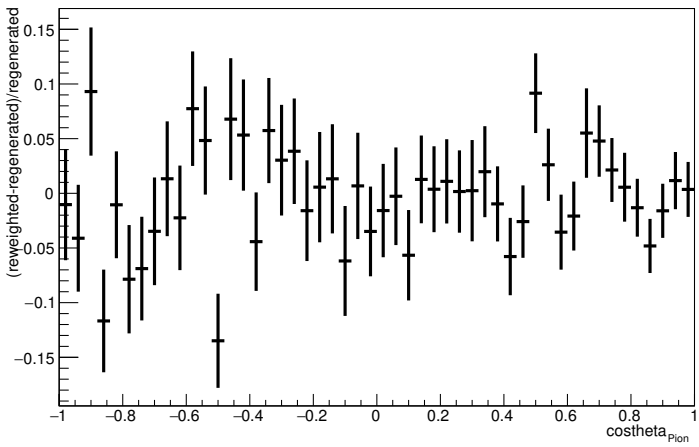

Angle plot: Every FSI Pion: Neut Mode =1

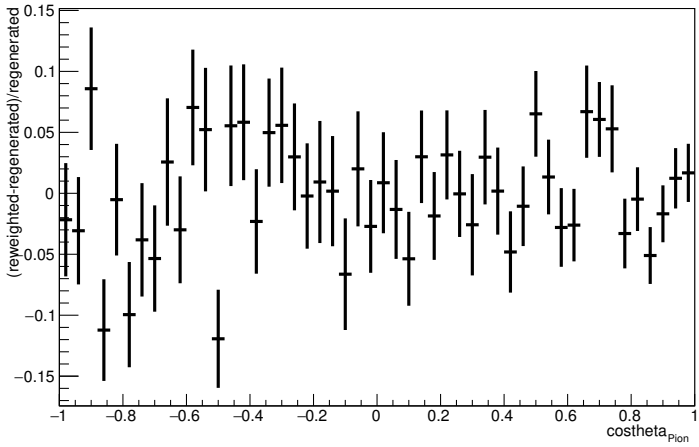

Energy plot: Leading Energy Nucleon: Neut Mode =2

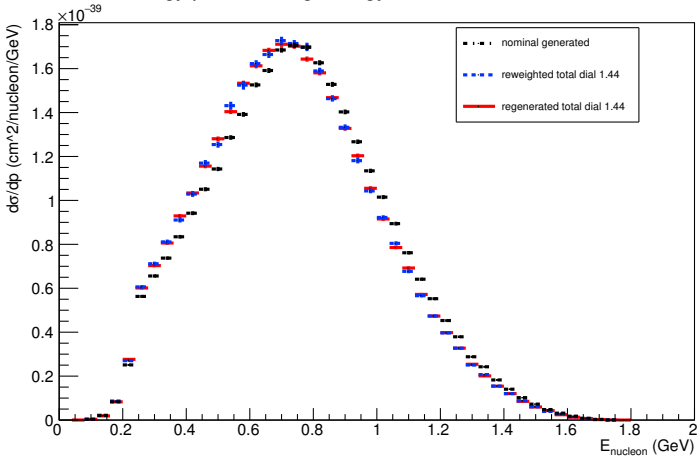

Energy plot: Every FSI Nucleon: Neut Mode =2

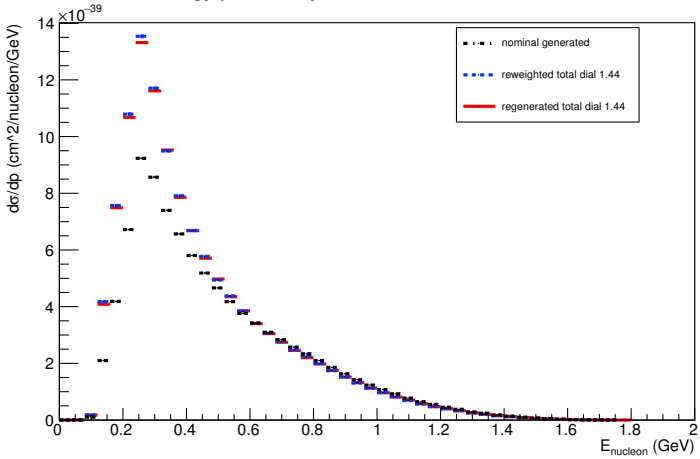

Energy plot: Leading Energy Nucleon: Neut Mode =2

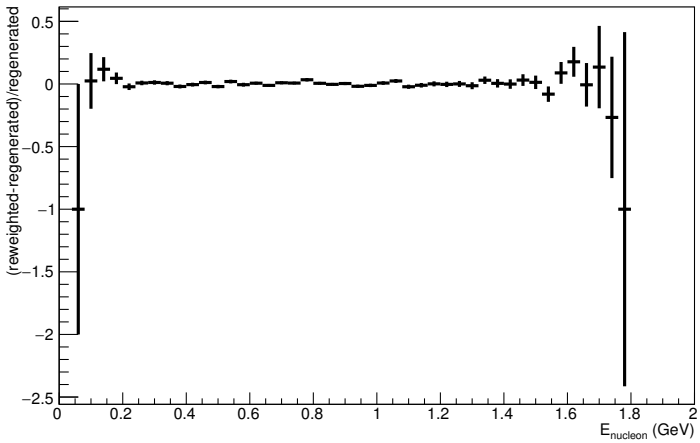

Energy plot: Every FSI Nucleon: Neut Mode =2

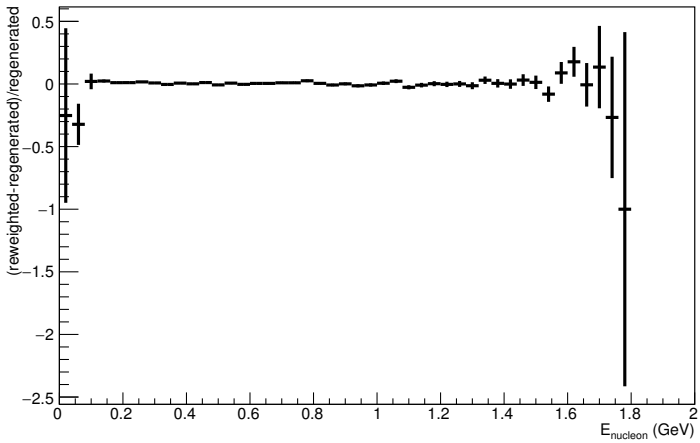

Angle plot: Leading Energy Nucleon: Neut Mode =2

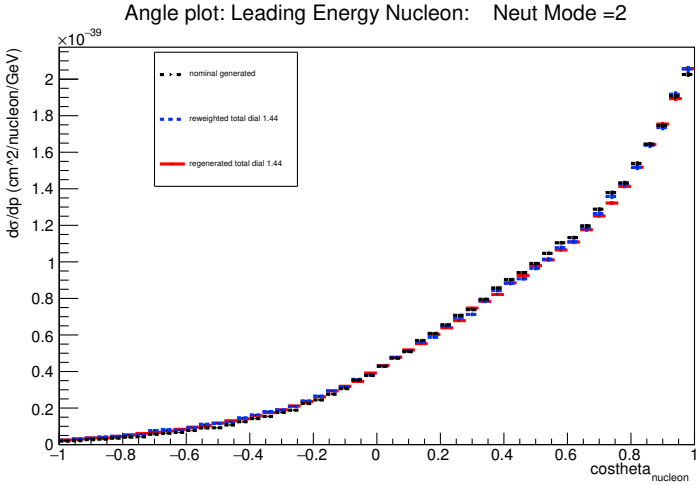

Angle plot: Every FSI Nucleon: Neut Mode =2

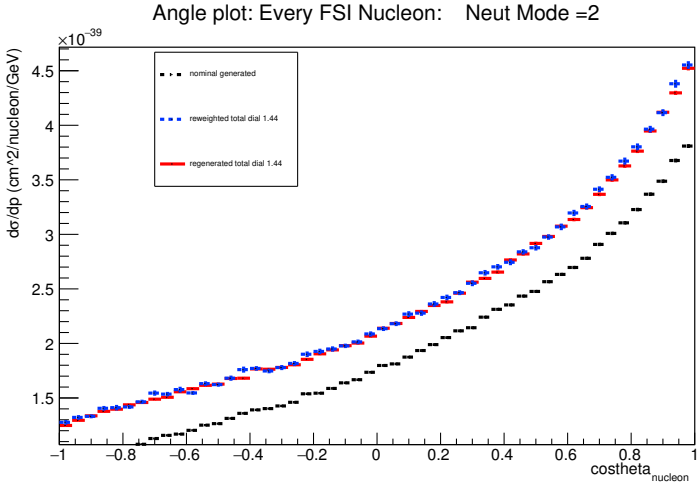

Angle plot: Leading Energy Nucleon: Neut Mode =2

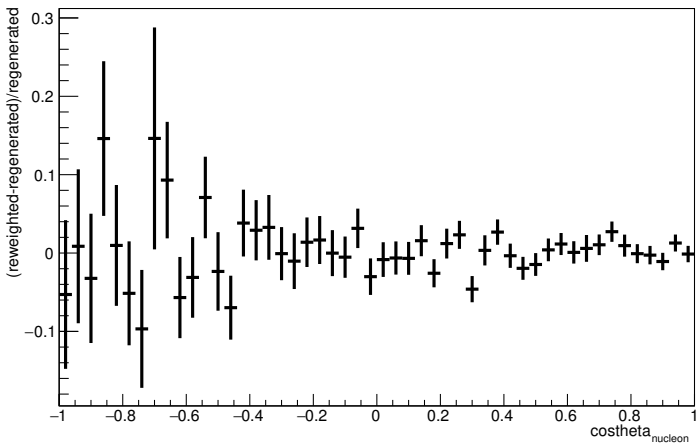

Angle plot: Every FSI Nucleon: Neut Mode =2

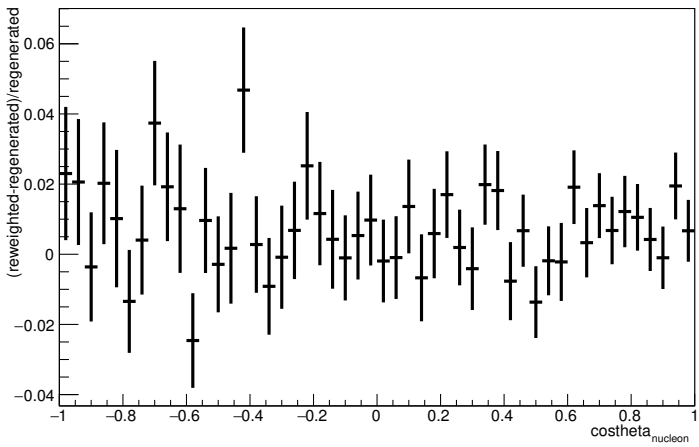

Energy plot: Leading Energy Proton: Neut Mode =2

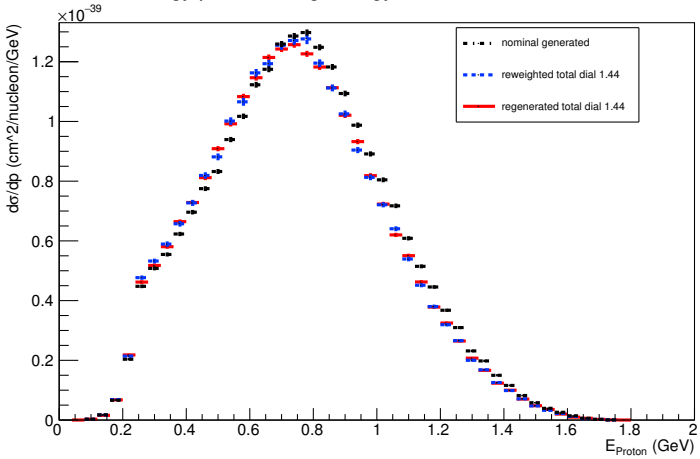

Energy plot: Every FSI Proton: Neut Mode =2

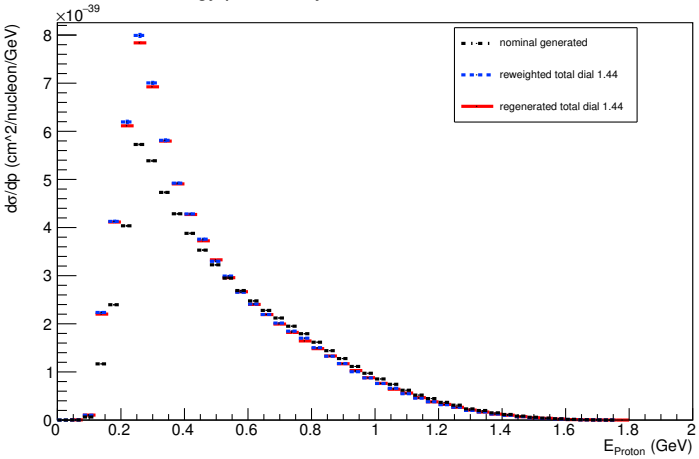

Energy plot: Leading Energy Proton: Neut Mode =2

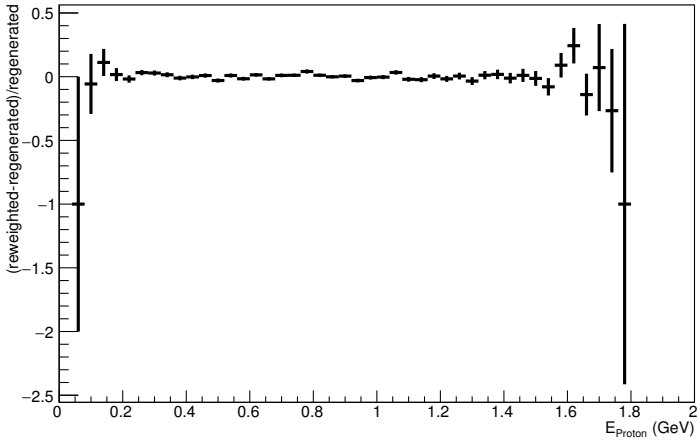

Energy plot: Every FSI Proton: Neut Mode =2

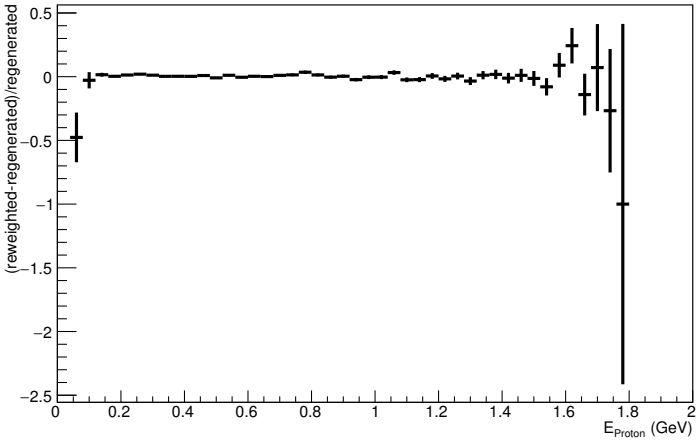

Angle plot: Leading Energy Proton: Neut Mode =2

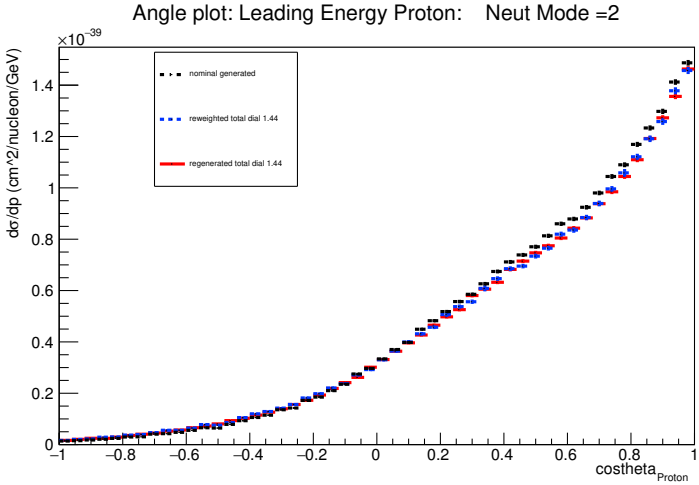

Angle plot: Every FSI Proton: Neut Mode =2

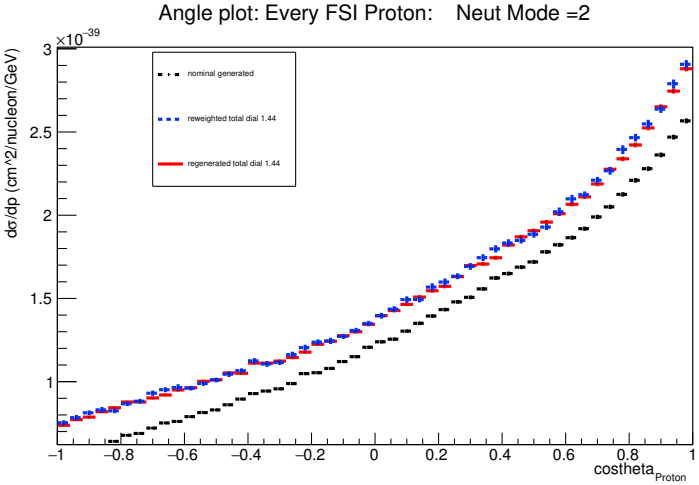

Angle plot: Leading Energy Proton: Neut Mode =2

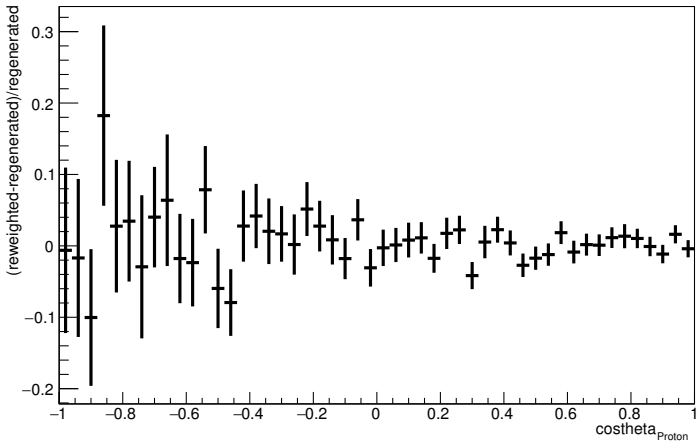

Angle plot: Every FSI Proton: Neut Mode =2

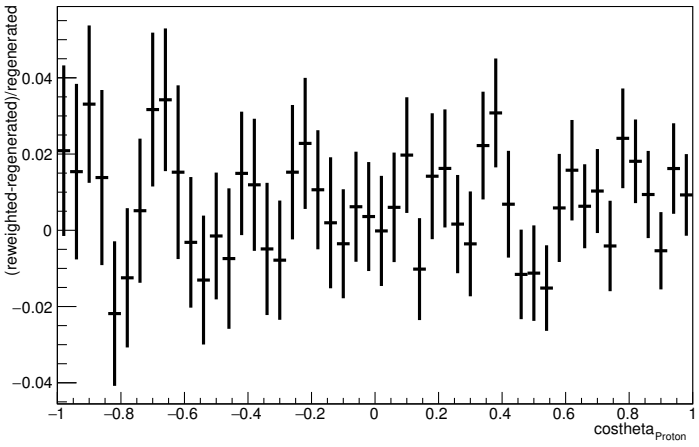

Energy plot: Leading Energy Neutron: Neut Mode =2

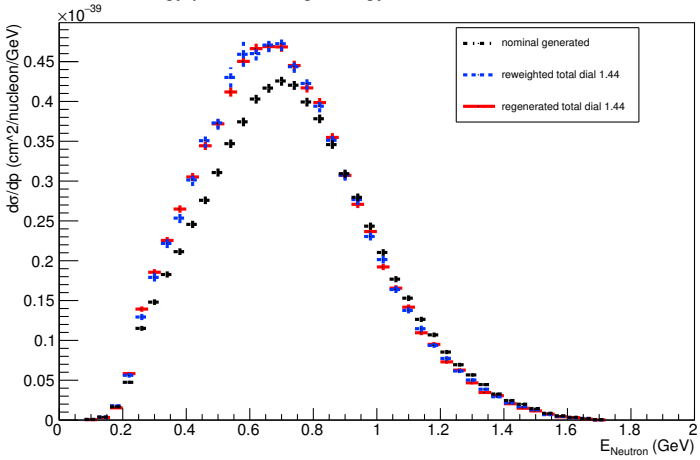

Energy plot: Every FSI Neutron: Neut Mode =2

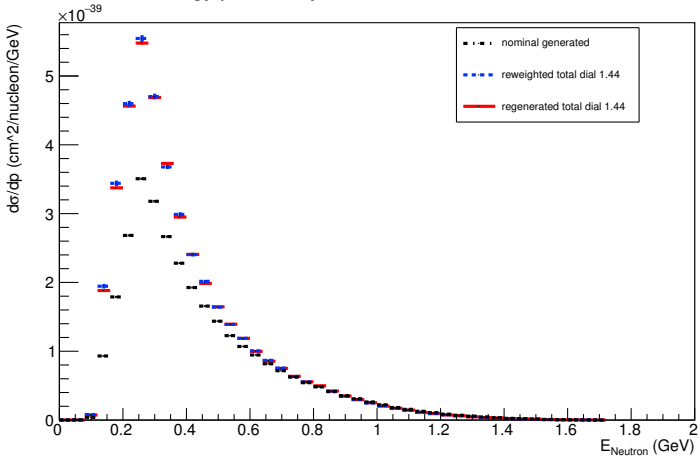

Energy plot: Leading Energy Neutron: Neut Mode =2

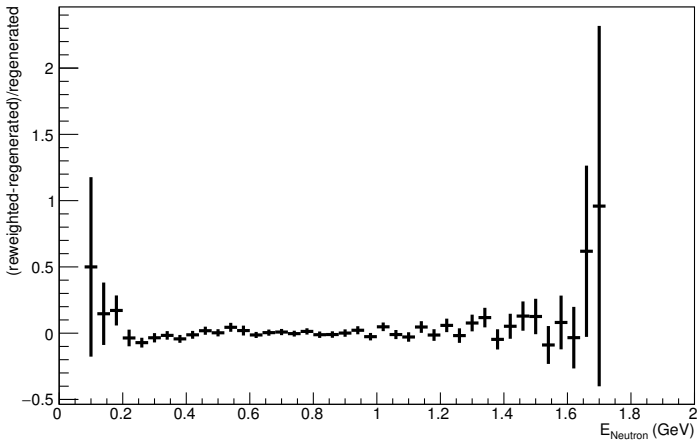

Energy plot: Every FSI Neutron: Neut Mode =2

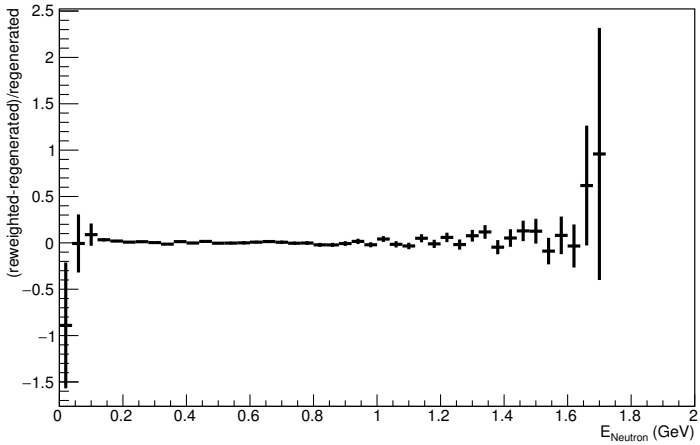

Angle plot: Leading Energy Neutron: Neut Mode =2

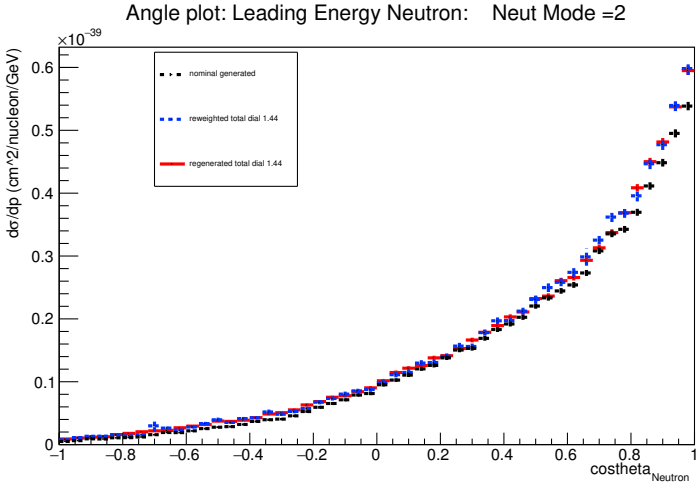

Angle plot: Every FSI Neutron: Neut Mode =2

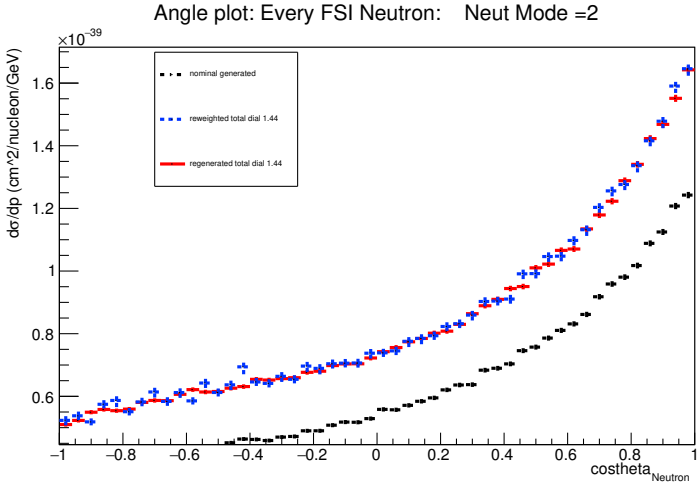

Angle plot: Leading Energy Neutron: Neut Mode =2

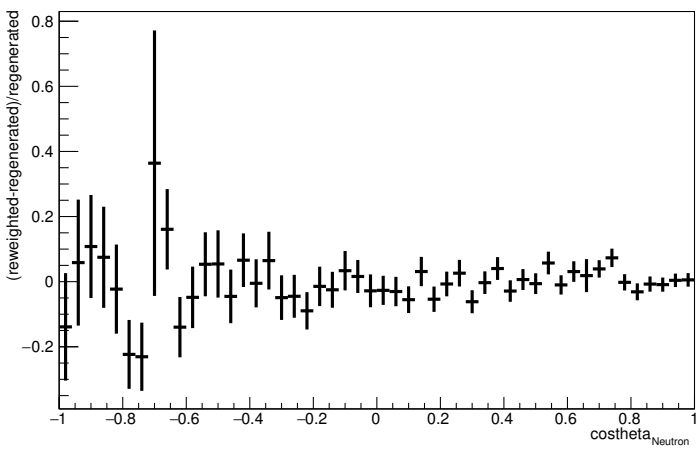

Angle plot: Every FSI Neutron: Neut Mode =2

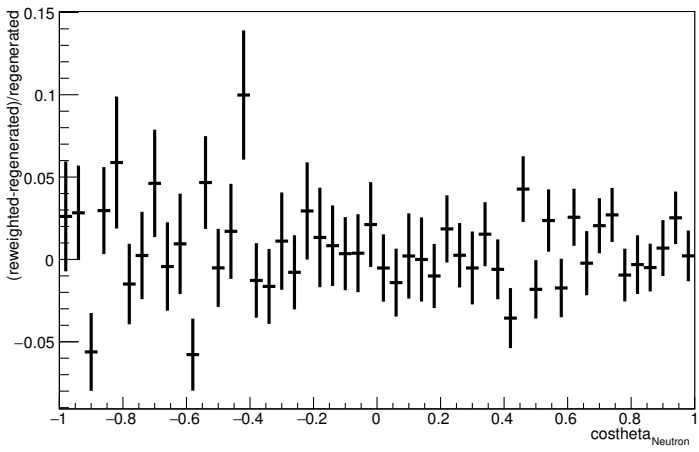

Energy plot: Leading Energy Lepton: Neut Mode =2

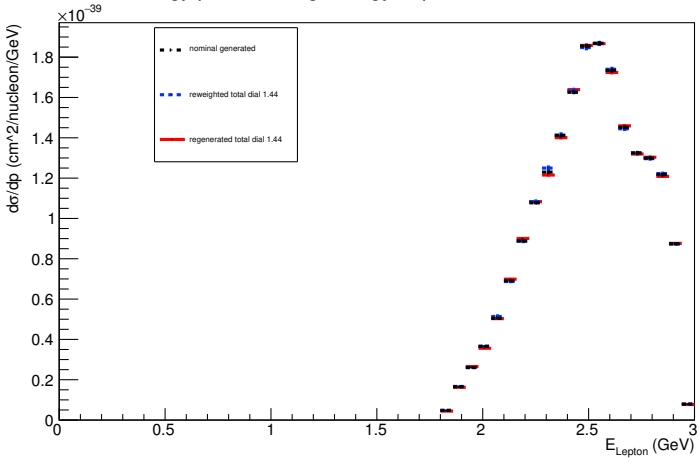

Angle plot: Leading Energy Lepton: Neut Mode =2

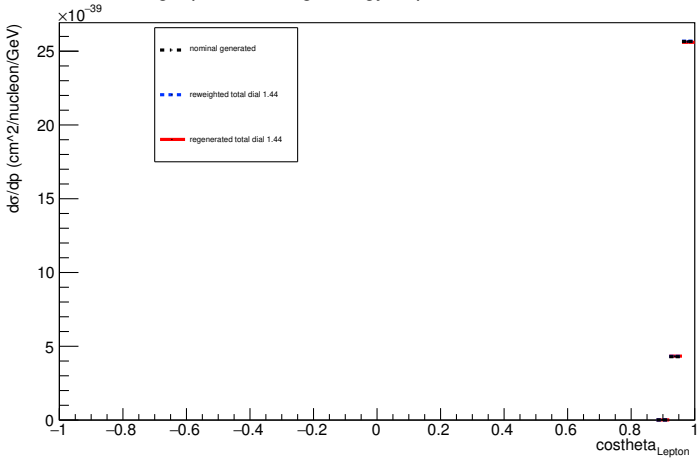

Energy plot: Leading Energy Lepton: Neut Mode =2

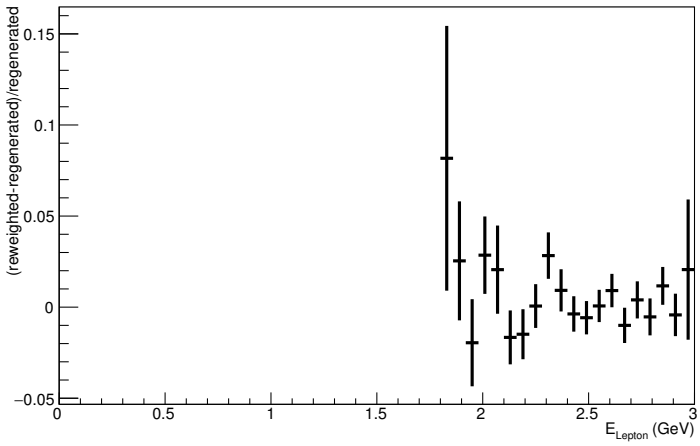

Angle plot: Leading Energy Lepton: Neut Mode =2

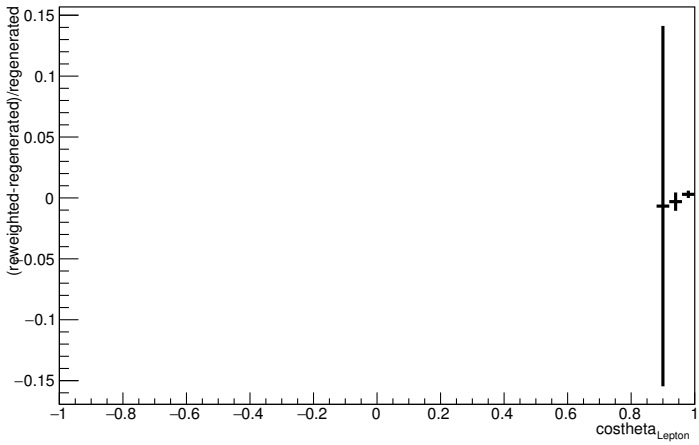

Energy plot: Leading Energy Pion: Neut Mode =2

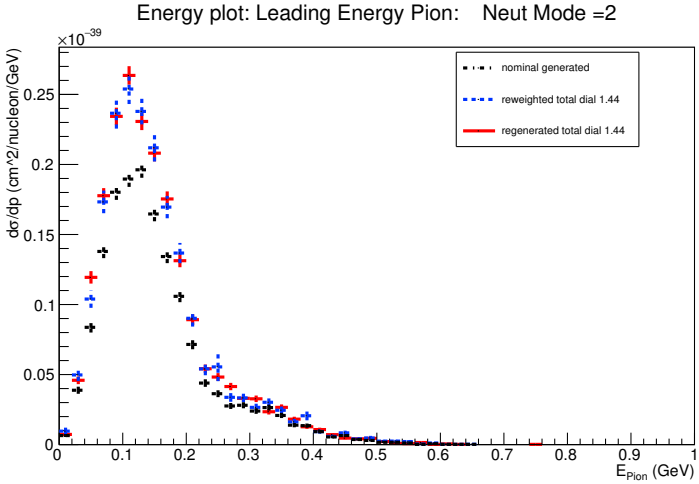

Energy plot: Every FSI Pion: Neut Mode =2

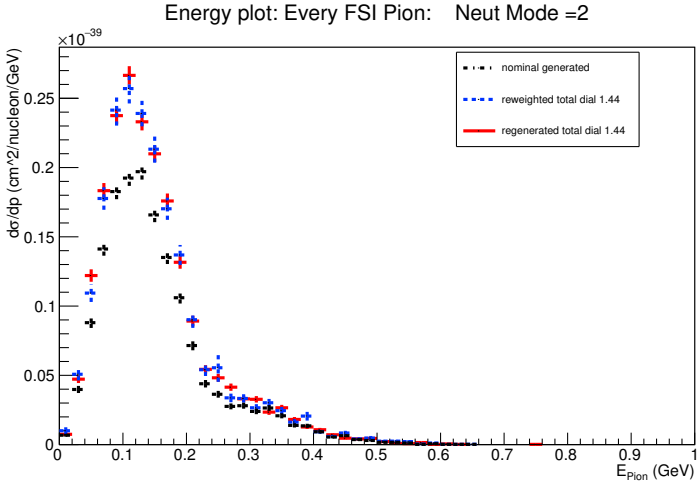

Energy plot: Leading Energy Pion: Neut Mode =2

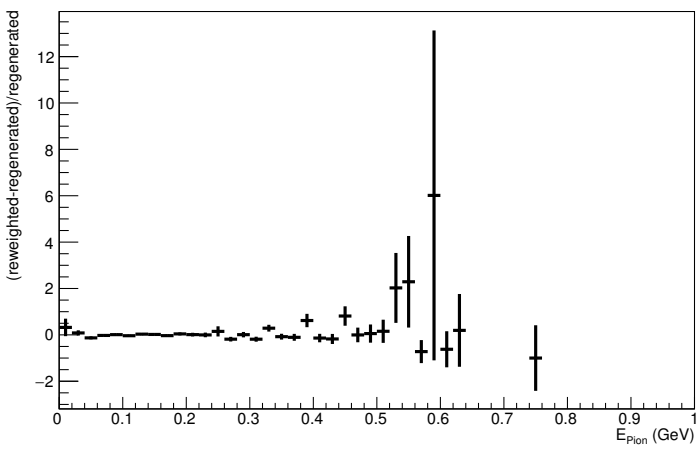

Energy plot: Every FSI Pion: Neut Mode =2

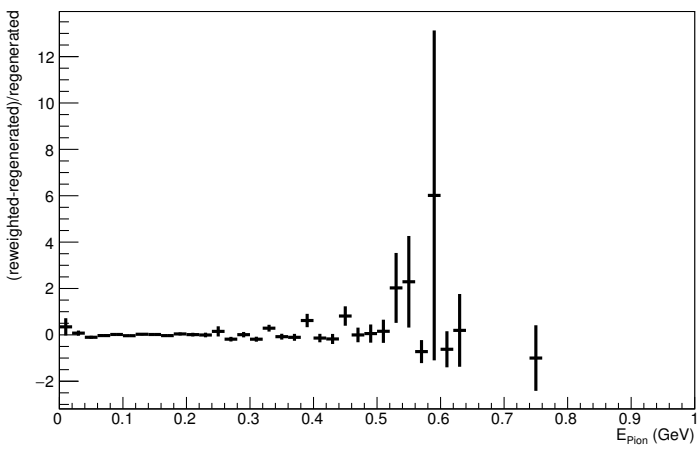

Angle plot: Leading Energy Pion: Neut Mode =2

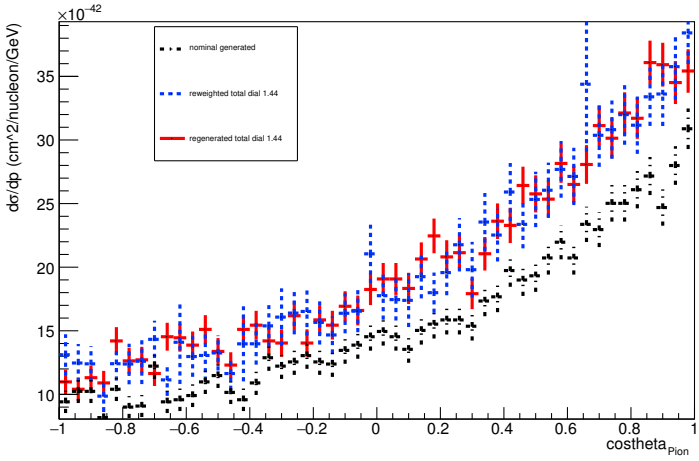

Angle plot: Every FSI Pion: Neut Mode =2

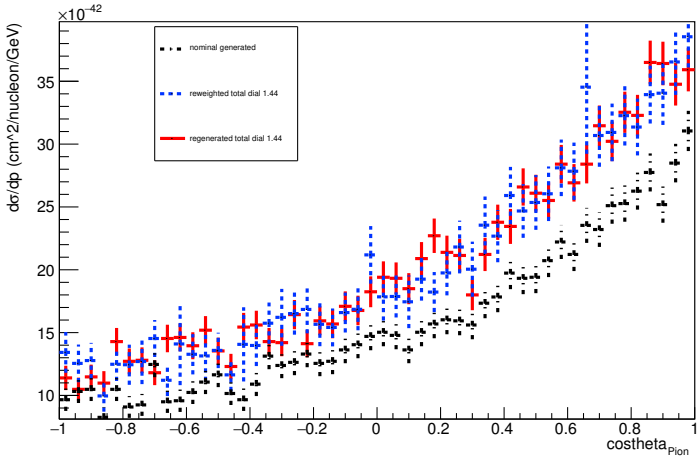

Angle plot: Leading Energy Pion: Neut Mode =2

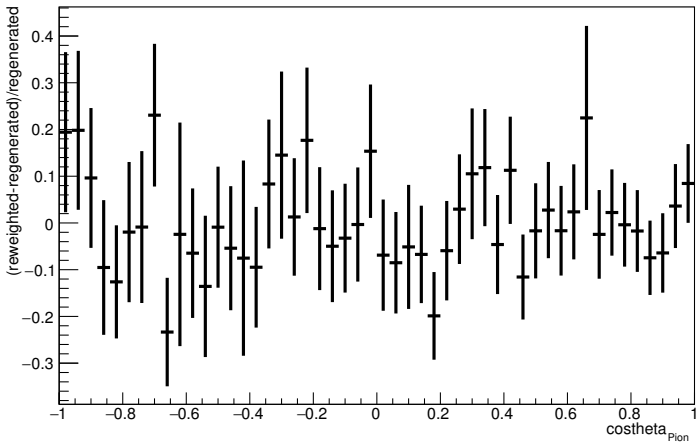

Angle plot: Every FSI Pion: Neut Mode =2

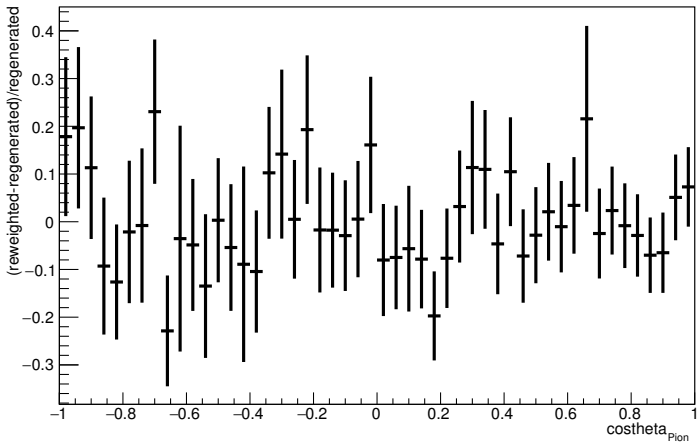

Energy plot: Leading Energy Nucleon: Neut Mode =11

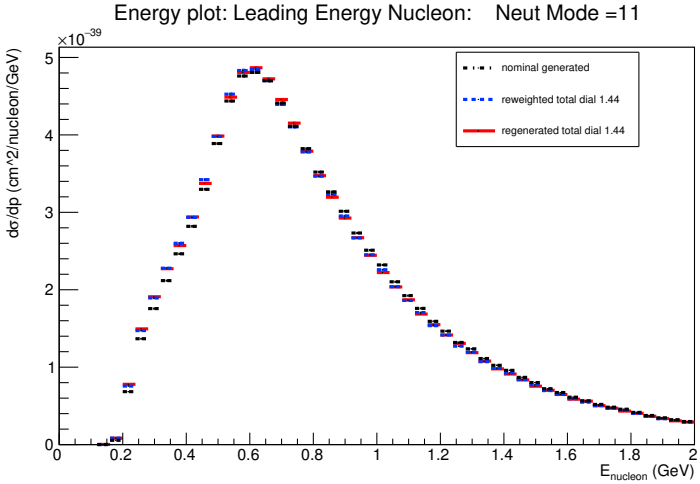

Energy plot: Every FSI Nucleon: Neut Mode =11

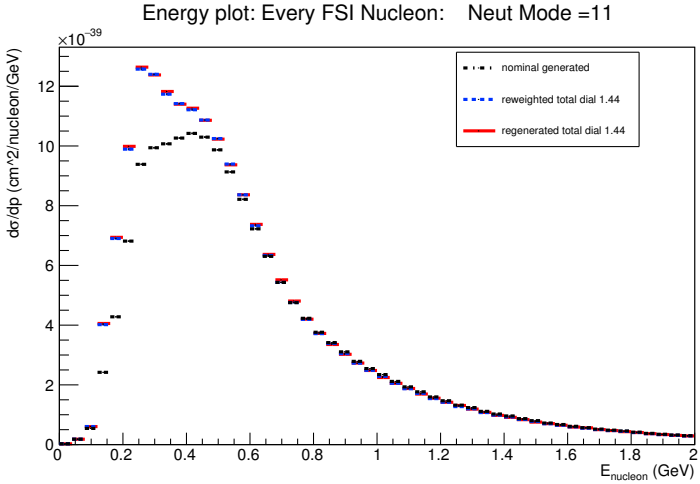

Energy plot: Leading Energy Nucleon: Neut Mode =11

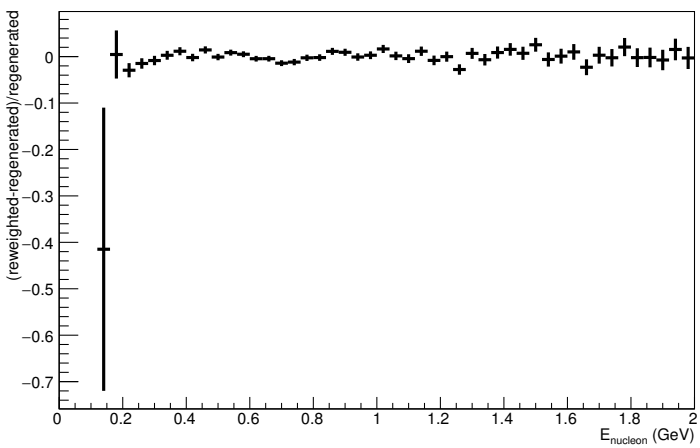

Energy plot: Every FSI Nucleon: Neut Mode =11

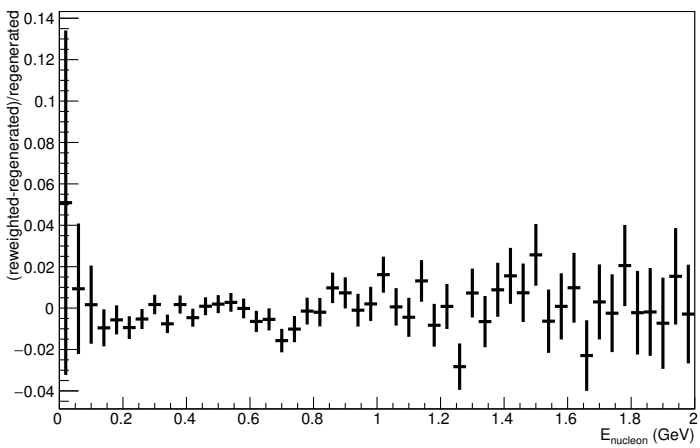

Angle plot: Leading Energy Nucleon: Neut Mode =11

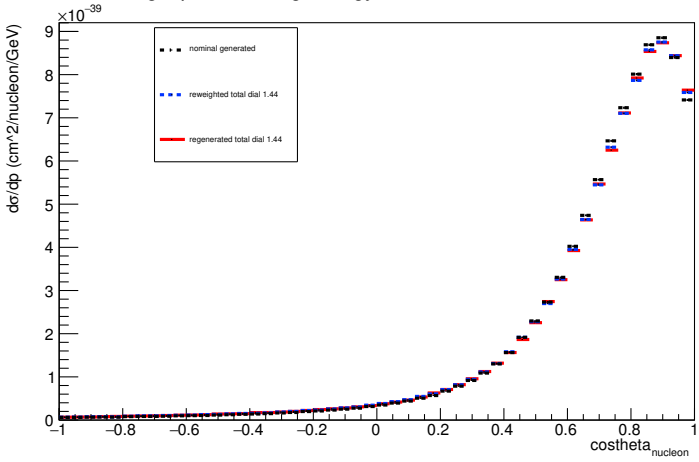

Angle plot: Every FSI Nucleon: Neut Mode =11

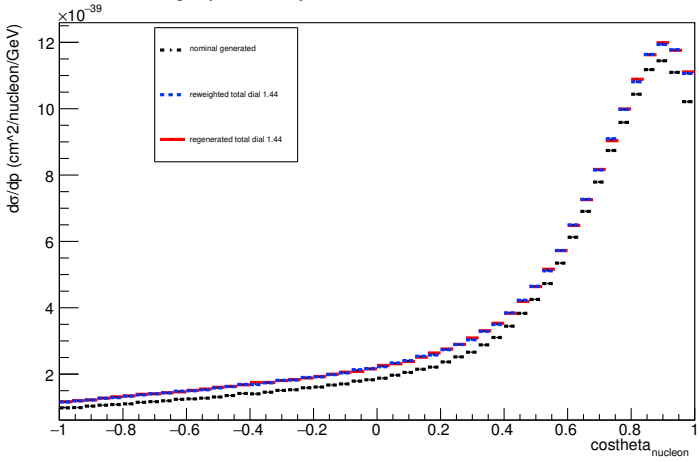

Angle plot: Leading Energy Nucleon: Neut Mode =11

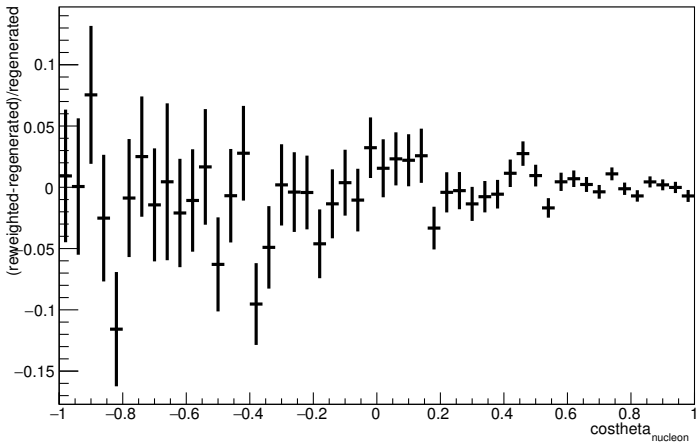

Angle plot: Every FSI Nucleon: Neut Mode =11

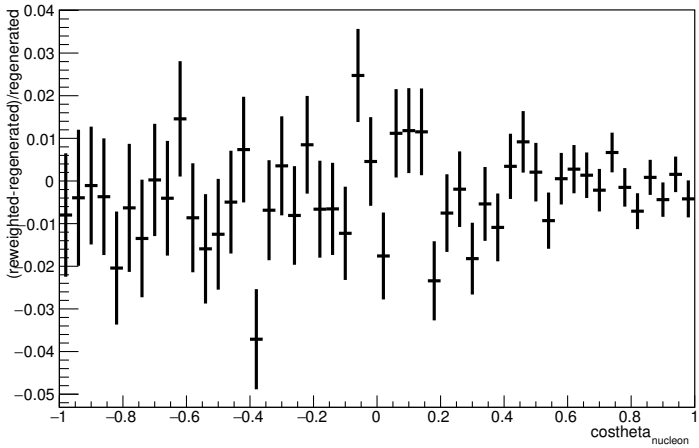

Energy plot: Leading Energy Proton: Neut Mode =11

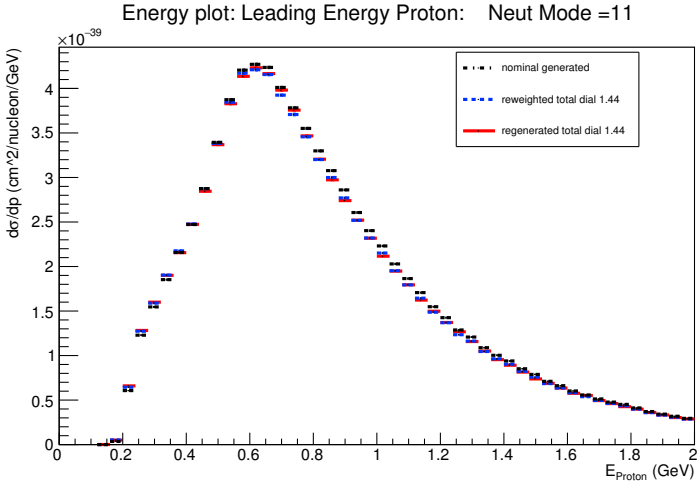

Energy plot: Every FSI Proton: Neut Mode =11

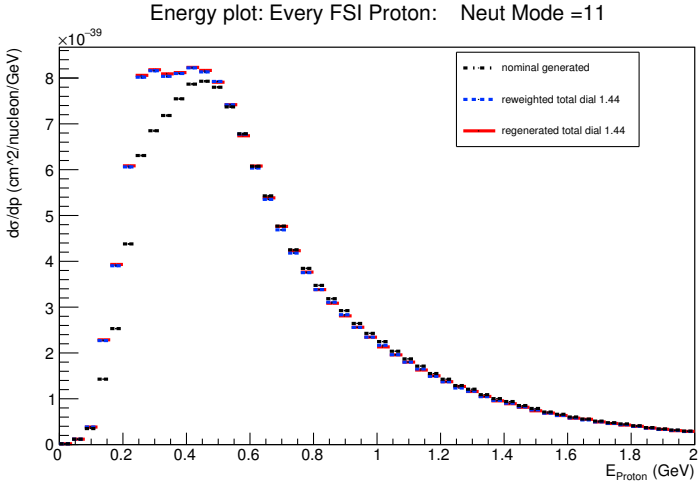

Energy plot: Leading Energy Proton: Neut Mode =11

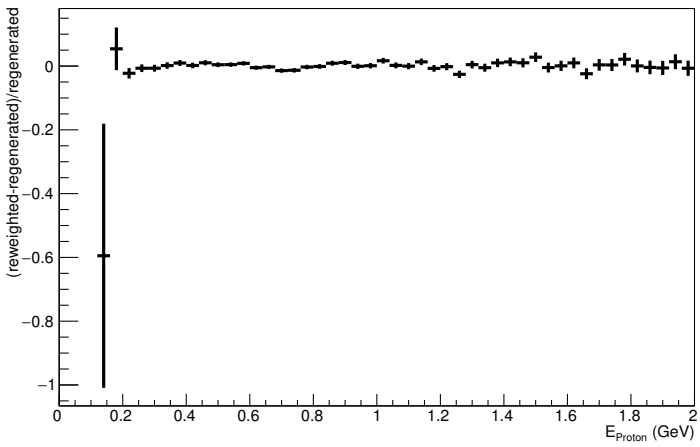

Energy plot: Every FSI Proton: Neut Mode =11

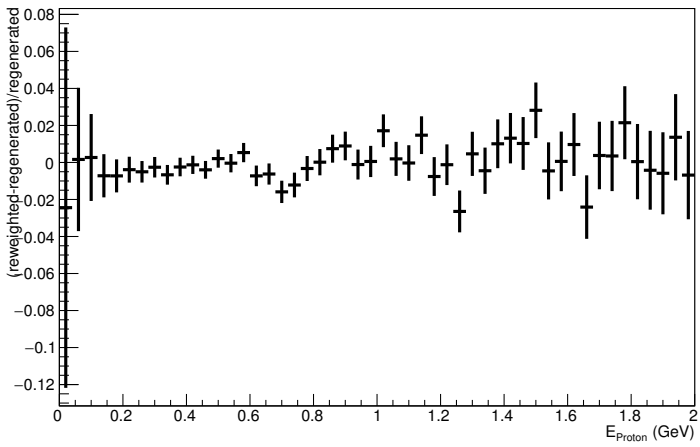

Angle plot: Leading Energy Proton: Neut Mode =11

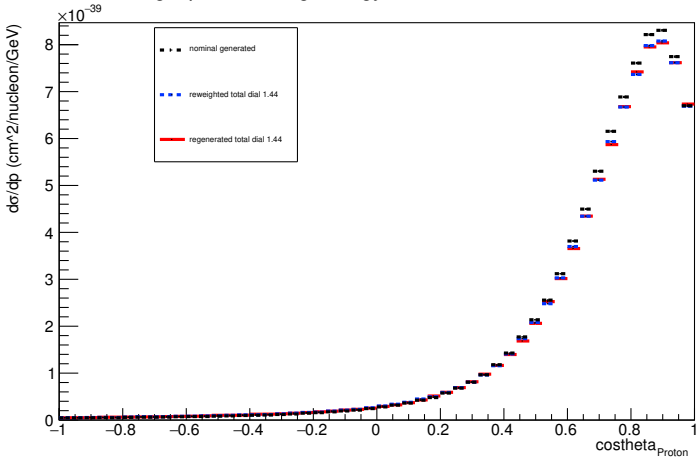

Angle plot: Every FSI Proton: Neut Mode =11

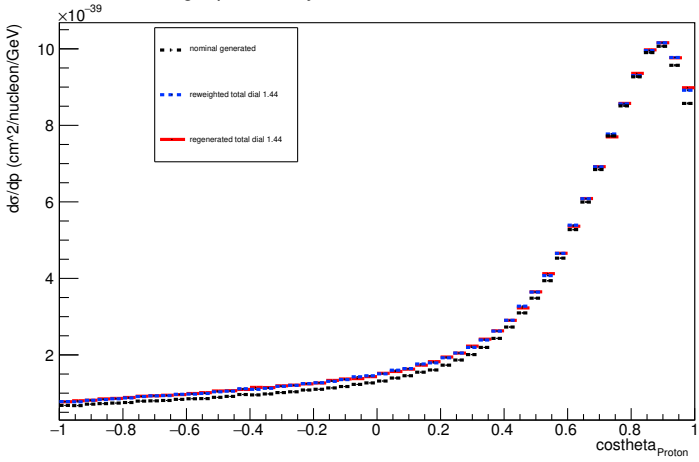

Angle plot: Leading Energy Proton: Neut Mode =11

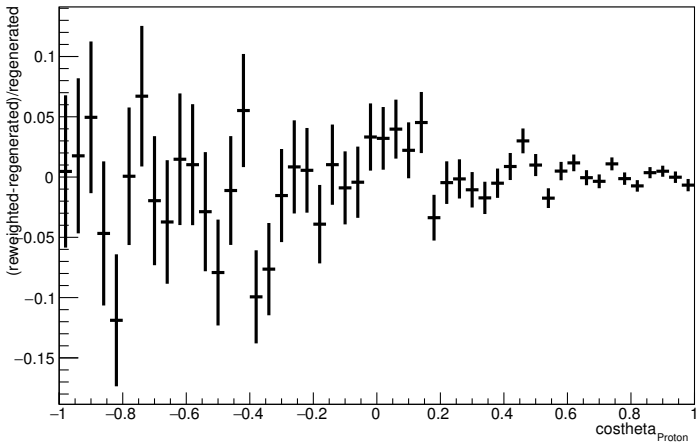

Angle plot: Every FSI Proton: Neut Mode =11

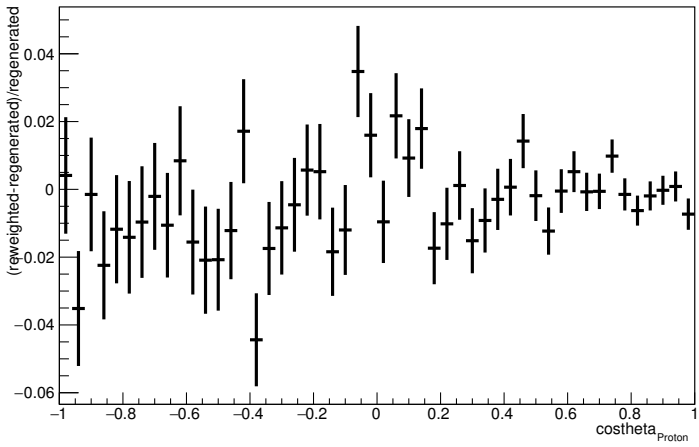

Energy plot: Leading Energy Neutron: Neut Mode =11

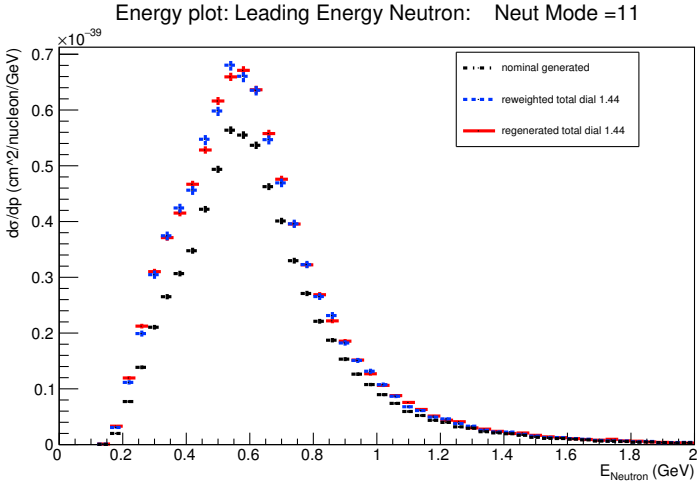

Energy plot: Every FSI Neutron: Neut Mode =11

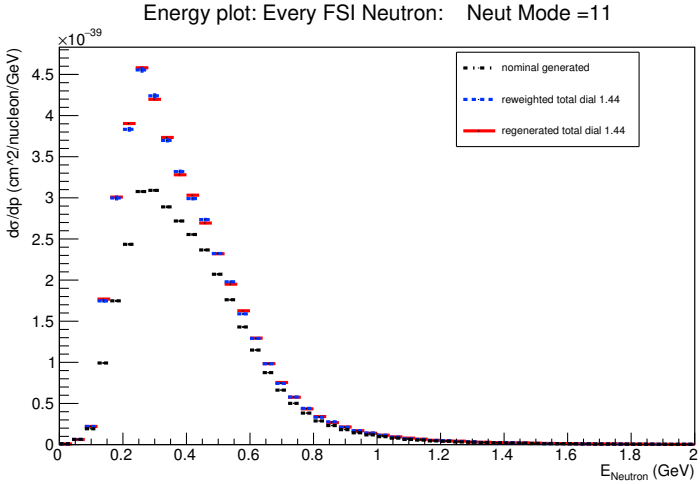

Energy plot: Leading Energy Neutron: Neut Mode =11

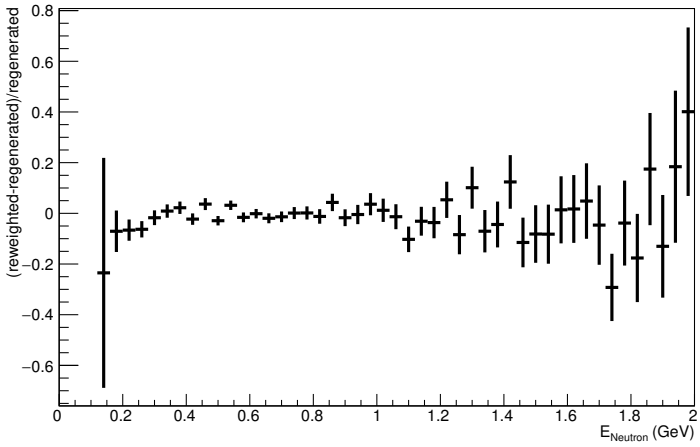

Energy plot: Every FSI Neutron: Neut Mode =11

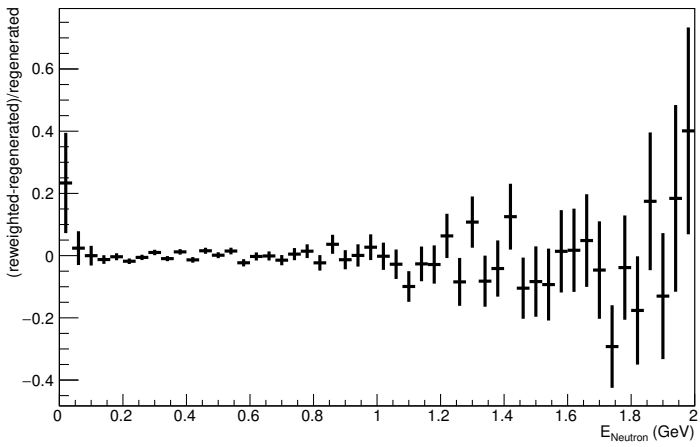

Angle plot: Leading Energy Neutron: Neut Mode =11

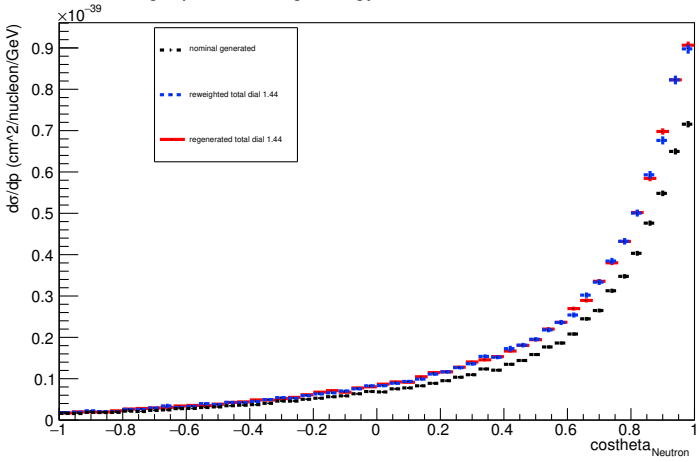

Angle plot: Every FSI Neutron: Neut Mode =11

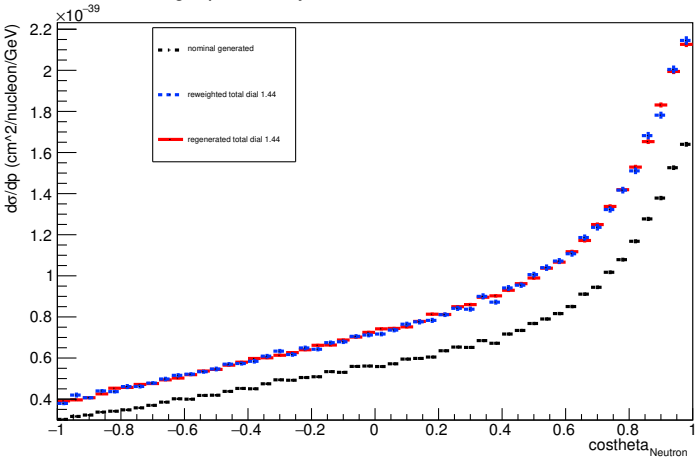

Angle plot: Leading Energy Neutron: Neut Mode =11

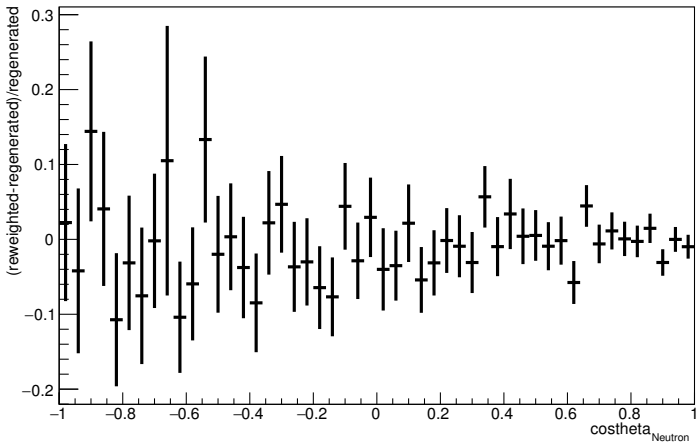

Angle plot: Every FSI Neutron: Neut Mode =11

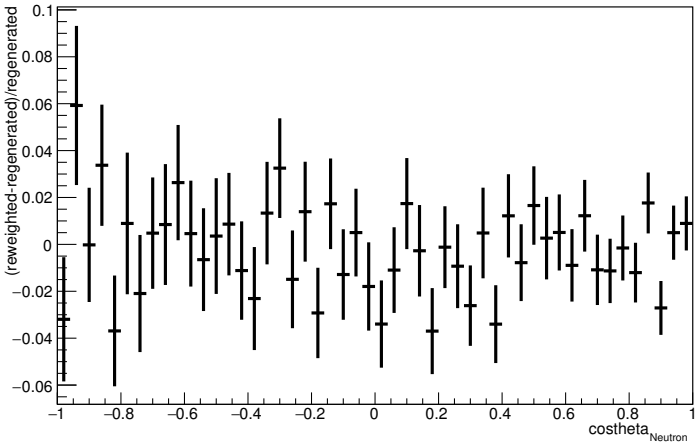

Energy plot: Leading Energy Lepton: Neut Mode =11

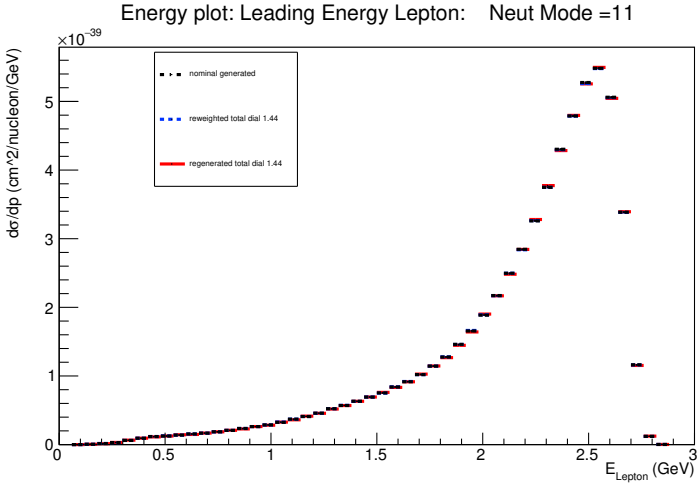

Angle plot: Leading Energy Lepton: Neut Mode =11

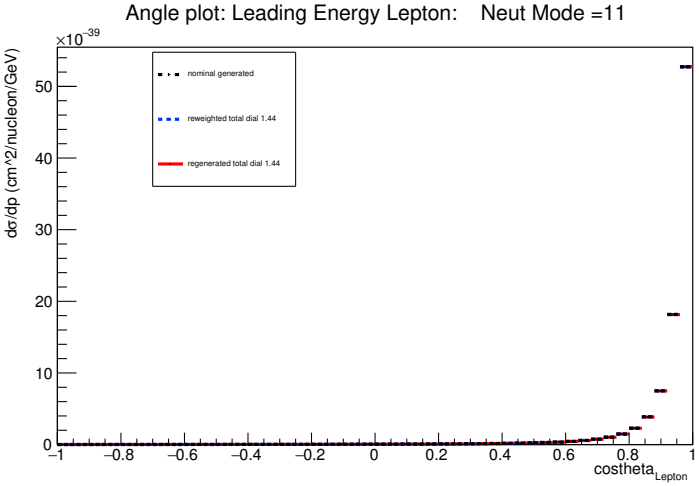

Energy plot: Leading Energy Lepton: Neut Mode =11

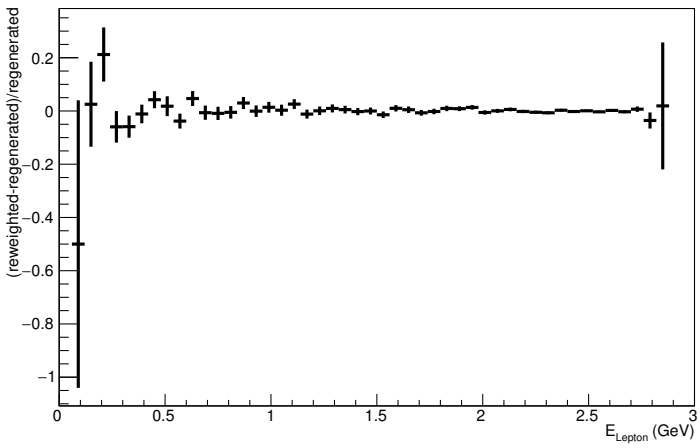

Angle plot: Leading Energy Lepton: Neut Mode =11

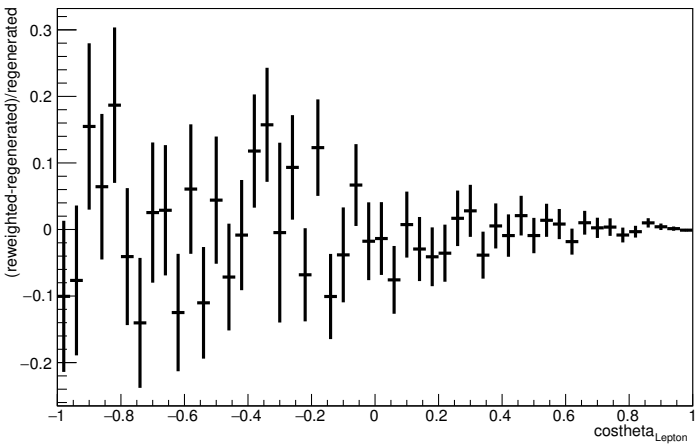

Energy plot: Leading Energy Pion: Neut Mode =11

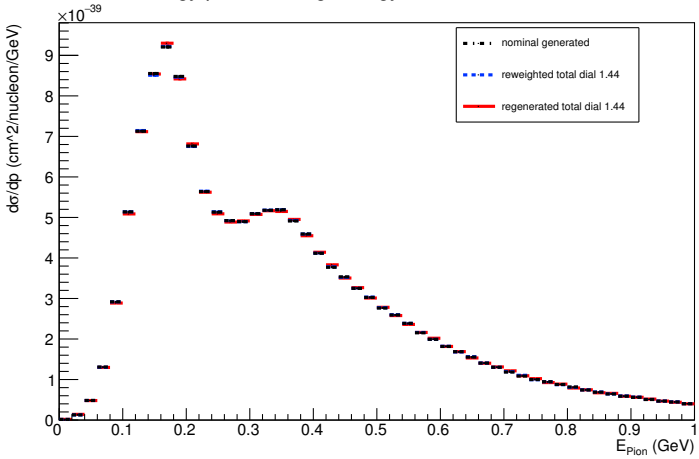

Energy plot: Every FSI Pion: Neut Mode =11

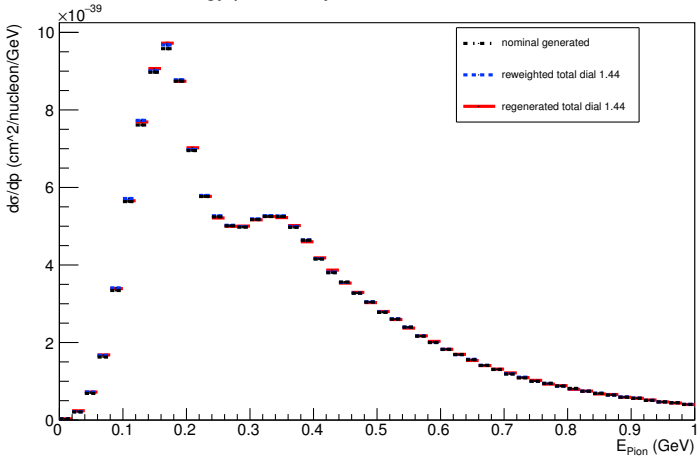

Energy plot: Leading Energy Pion: Neut Mode =11

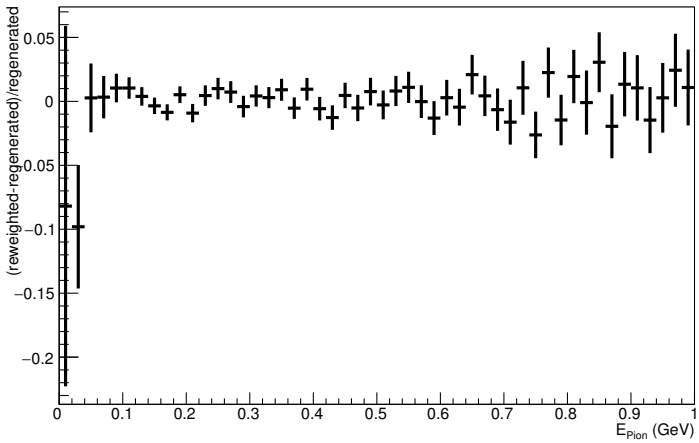

Energy plot: Every FSI Pion: Neut Mode =11

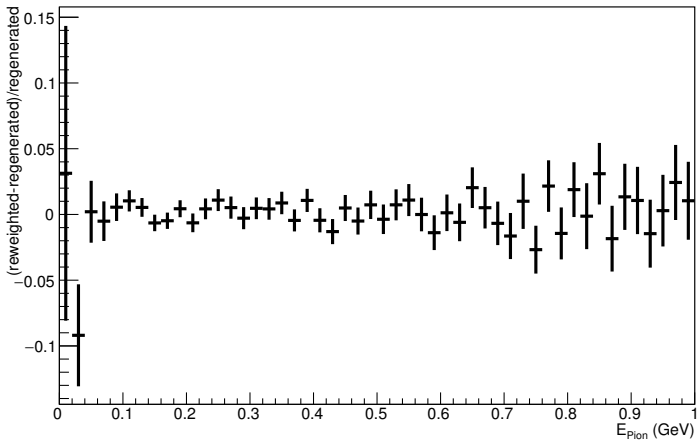

Angle plot: Leading Energy Pion: Neut Mode =11

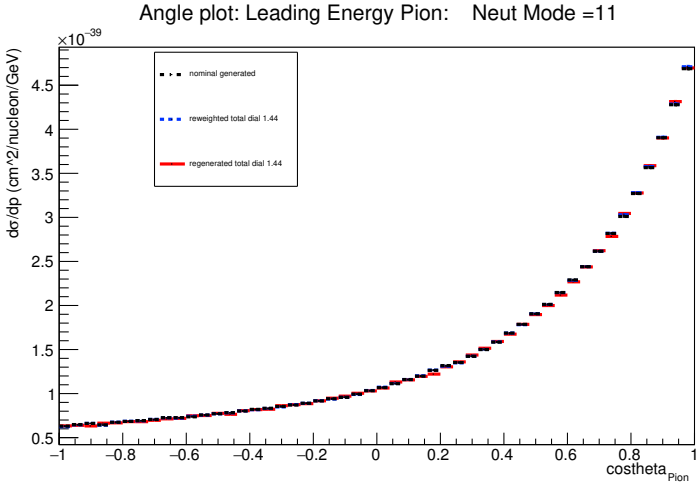

Angle plot: Every FSI Pion: Neut Mode =11

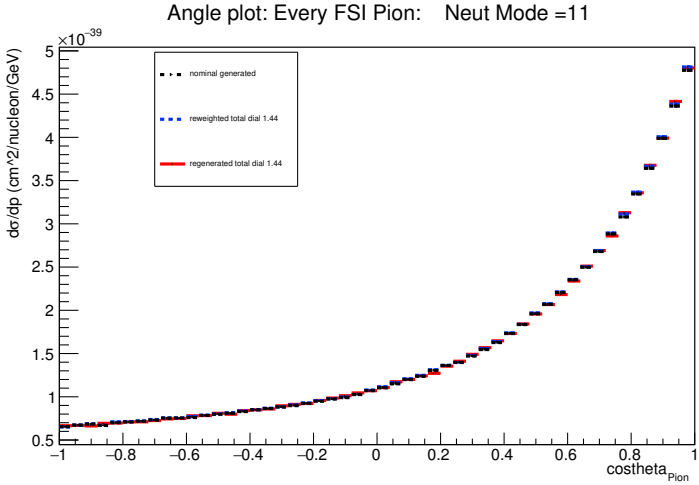

Angle plot: Leading Energy Pion: Neut Mode =11

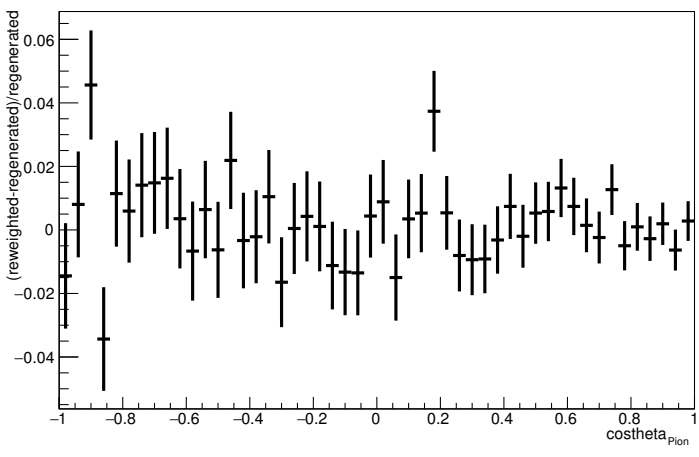

Angle plot: Every FSI Pion: Neut Mode =11

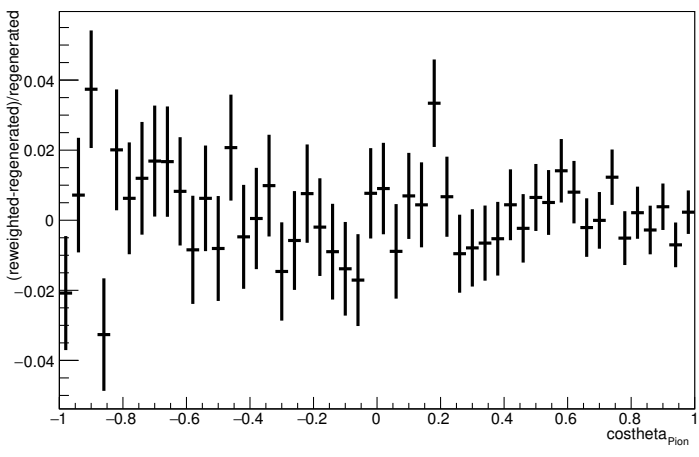

A.2. Total Dial: varied down to 0.64

Energy plot: Leading Energy Nucleon: Neut Mode =AllModesCombined

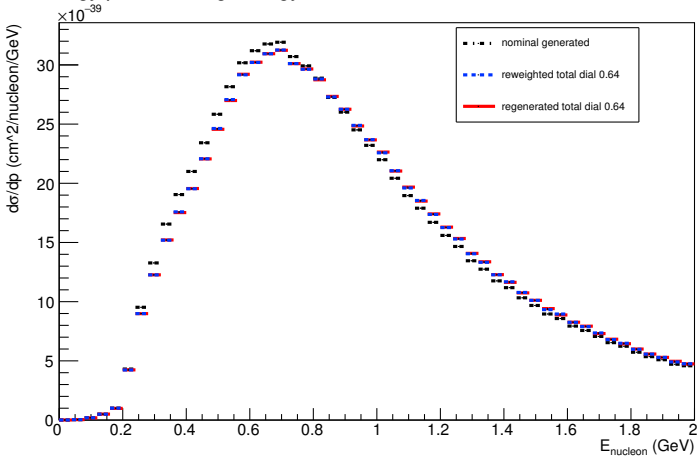

Energy plot: Every FSI Nucleon: Neut Mode =AllModesCombined

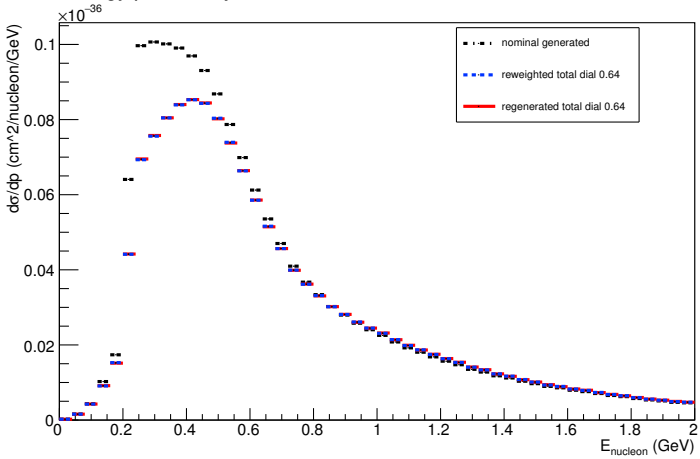

Energy plot: Leading Energy Nucleon: Neut Mode =AllModesCombined

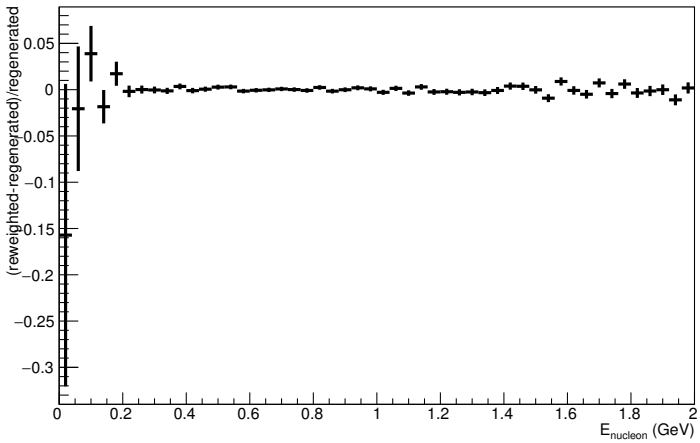

Energy plot: Every FSI Nucleon: Neut Mode =AllModesCombined

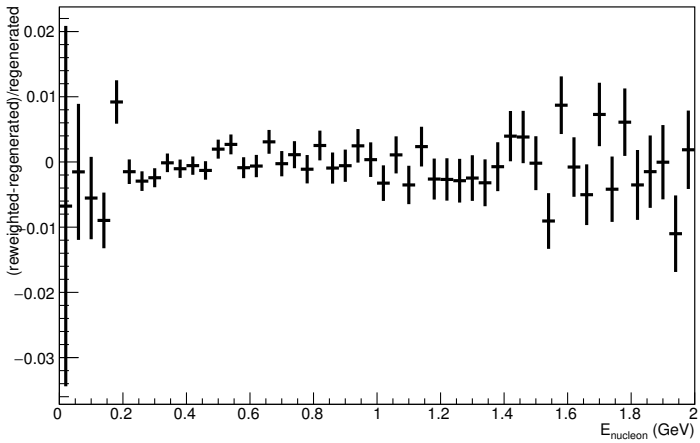

Angle plot: Leading Energy Nucleon: Neut Mode =AllModesCombined

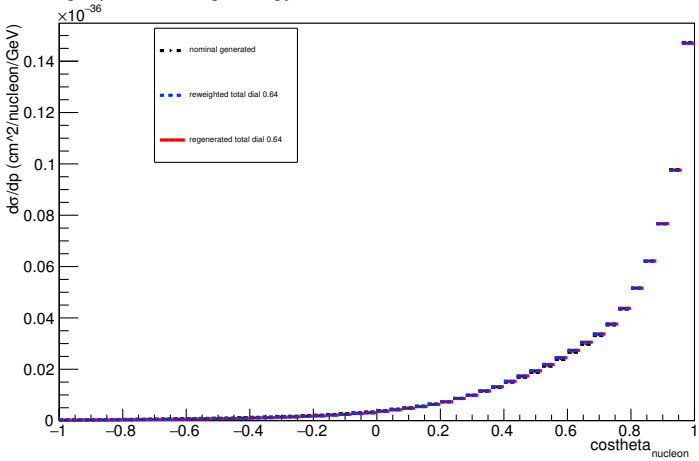

Angle plot: Every FSI Nucleon: Neut Mode =AllModesCombined

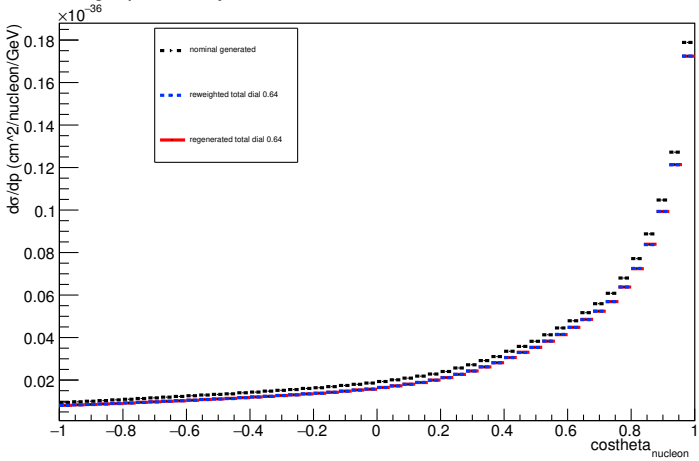

Angle plot: Leading Energy Nucleon: Neut Mode =AllModesCombined

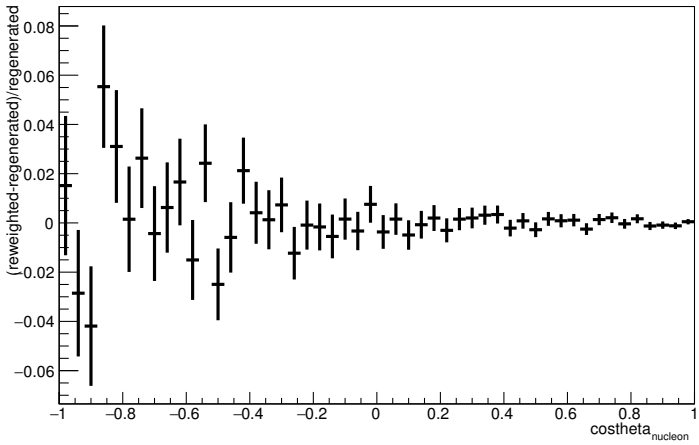

Angle plot: Every FSI Nucleon: Neut Mode =AllModesCombined

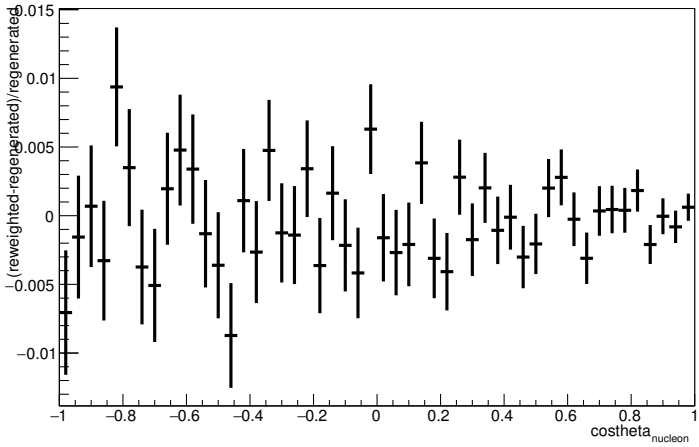

Energy plot: Leading Energy Proton: Neut Mode =AllModesCombined

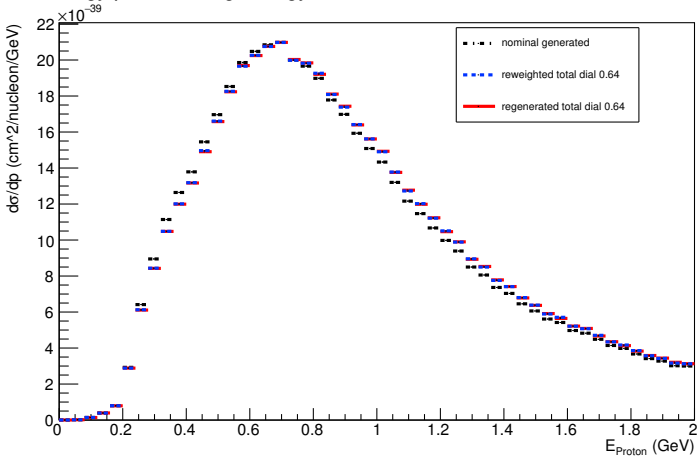

Energy plot: Every FSI Proton: Neut Mode =AllModesCombined

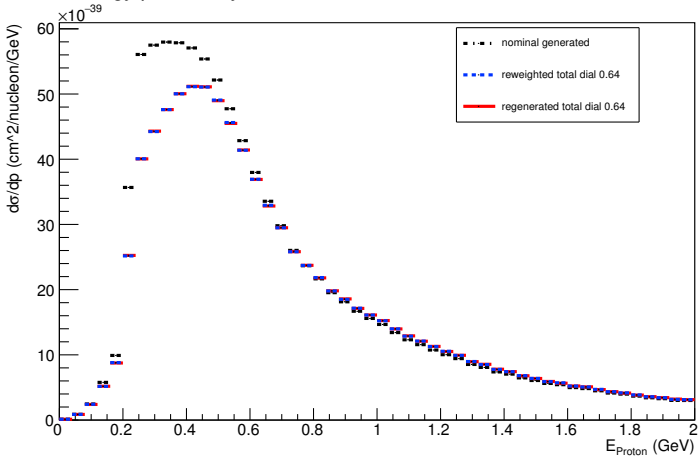

Energy plot: Leading Energy Proton: Neut Mode =AllModesCombined

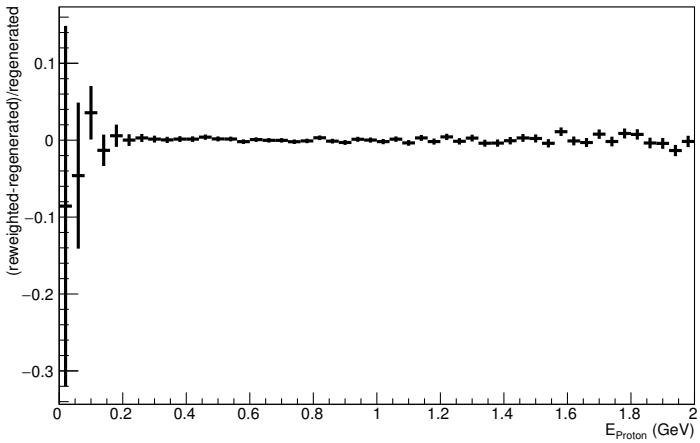

Energy plot: Every FSI Proton: Neut Mode =AllModesCombined

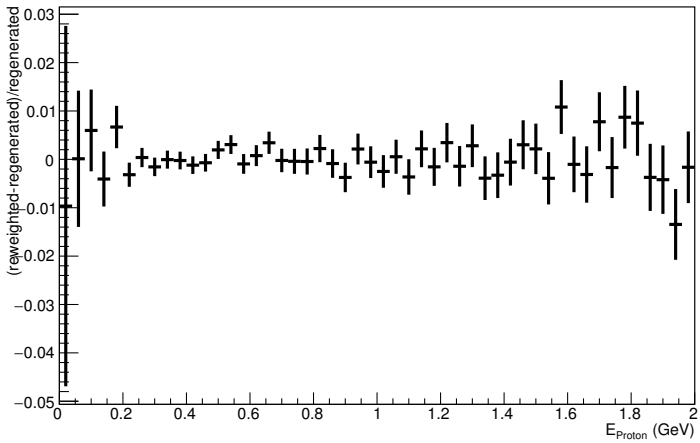

Angle plot: Leading Energy Proton: Neut Mode =AllModesCombined

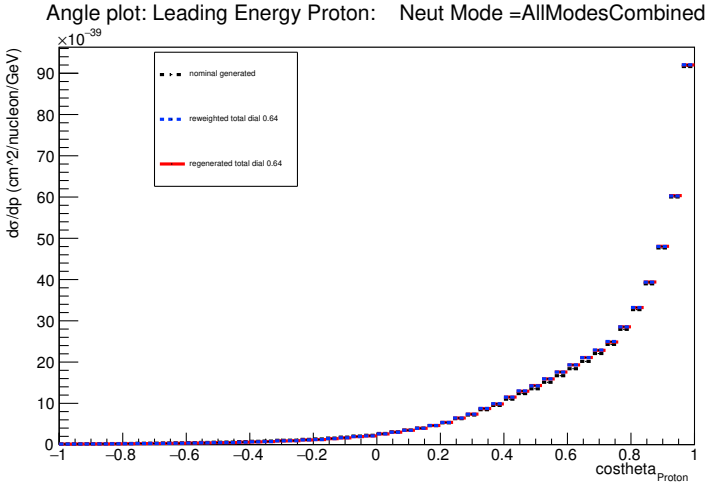

Angle plot: Every FSI Proton: Neut Mode =AllModesCombined

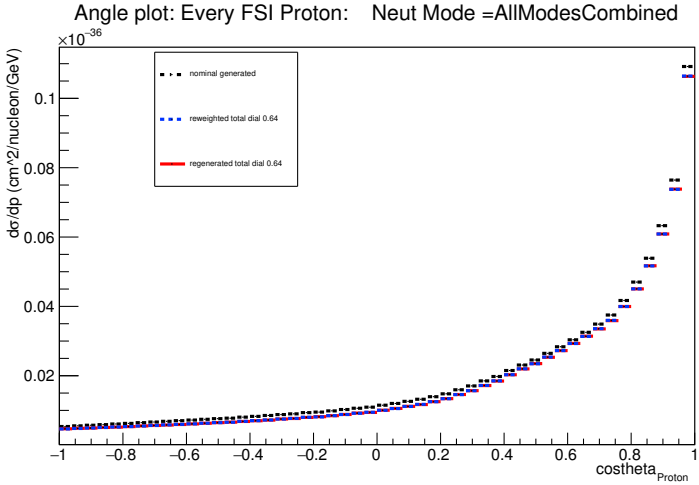

Angle plot: Leading Energy Proton: Neut Mode =AllModesCombined

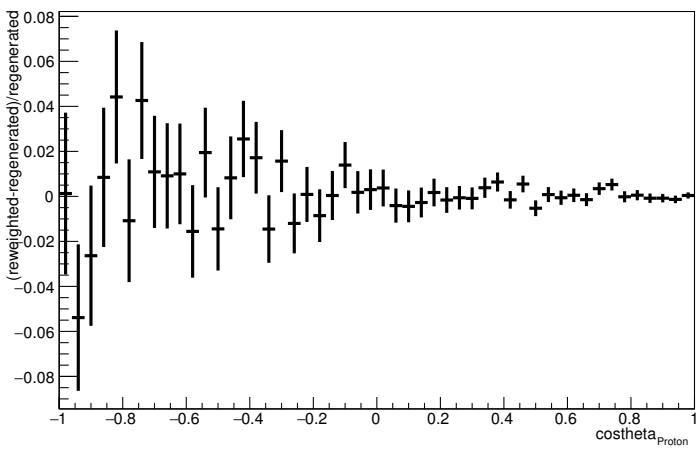

Angle plot: Every FSI Proton: Neut Mode =AllModesCombined

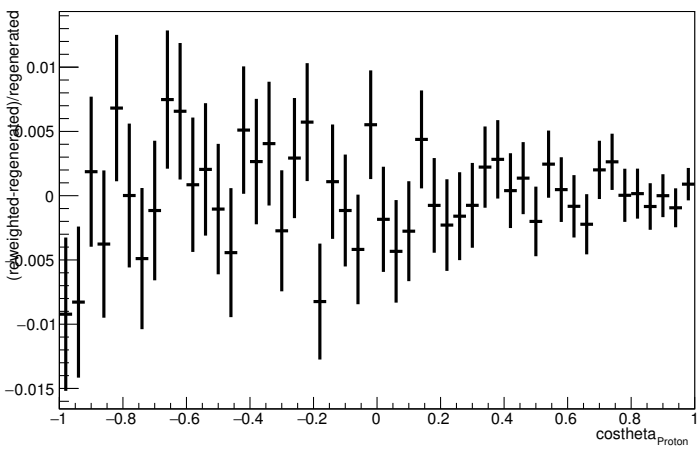

Energy plot: Leading Energy Neutron: Neut Mode =AllModesCombined

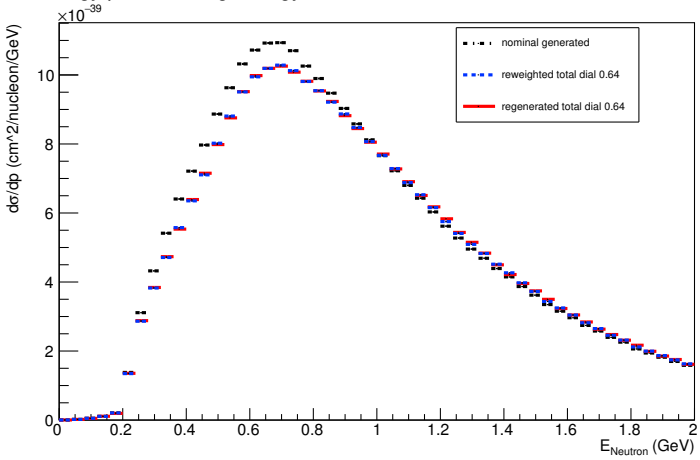

Energy plot: Every FSI Neutron: Neut Mode =AllModesCombined

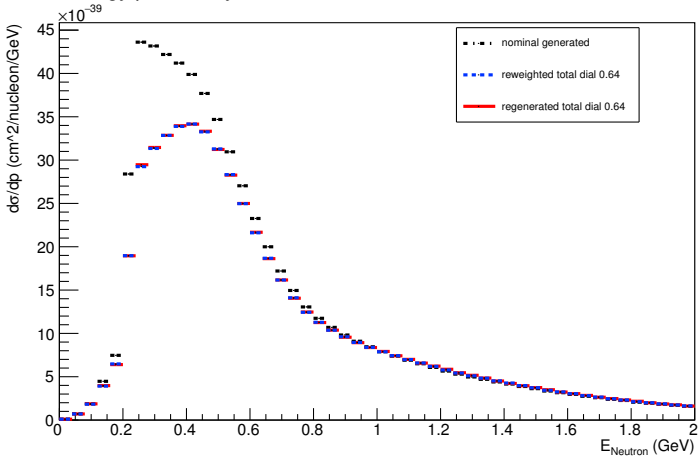

Energy plot: Leading Energy Neutron: Neut Mode =AllModesCombined

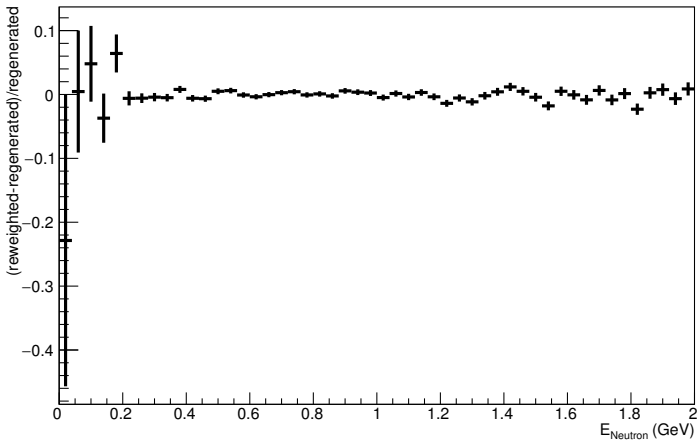

Energy plot: Every FSI Neutron: Neut Mode =AllModesCombined

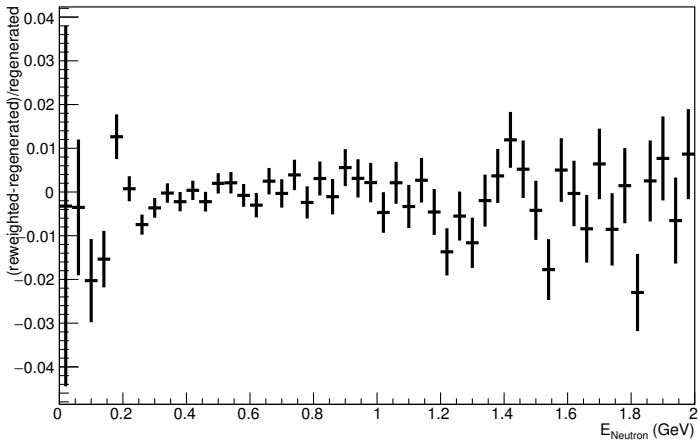

Angle plot: Leading Energy Neutron: Neut Mode =AllModesCombined

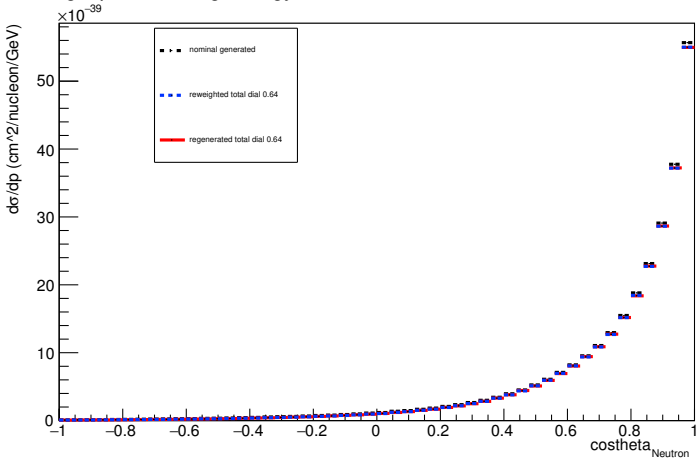

Angle plot: Every FSI Neutron: Neut Mode =AllModesCombined

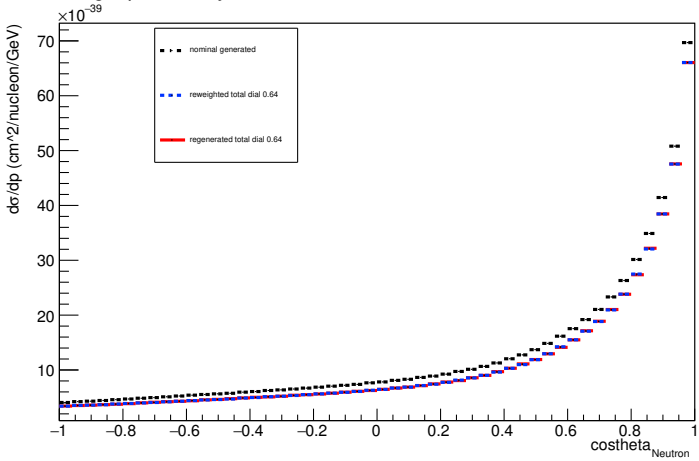

Angle plot: Leading Energy Neutron: Neut Mode =AllModesCombined

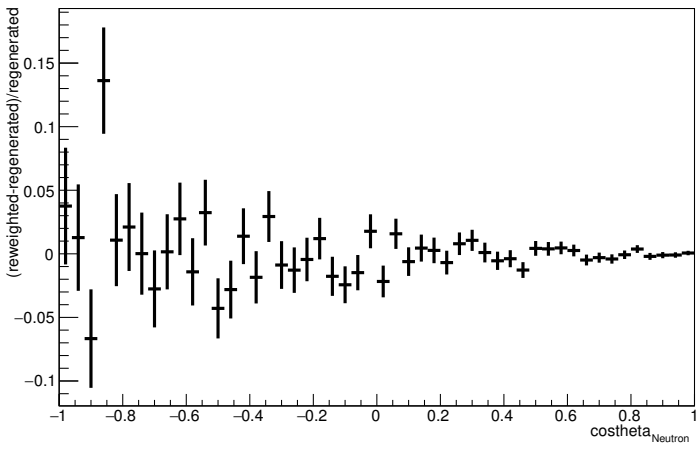

Angle plot: Every FSI Neutron: Neut Mode =AllModesCombined

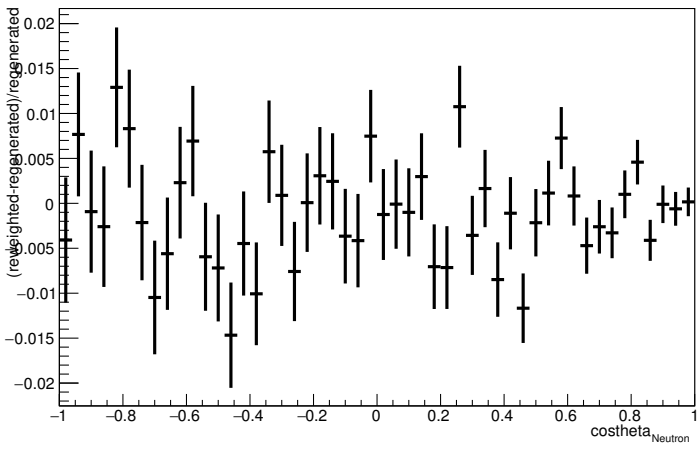

Energy plot: Leading Energy Lepton: Neut Mode =AllModesCombined

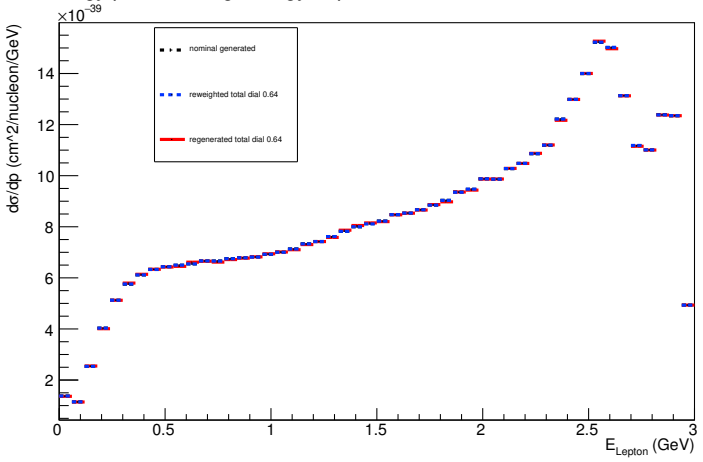

Angle plot: Leading Energy Lepton: Neut Mode =AllModesCombined

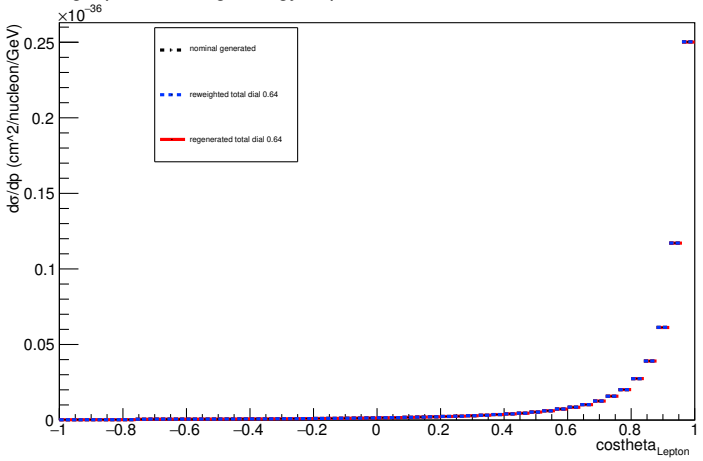

Energy plot: Leading Energy Lepton: Neut Mode =AllModesCombined

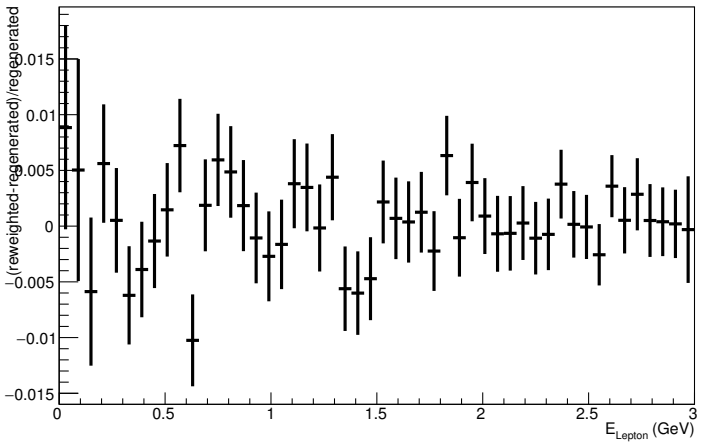

Angle plot: Leading Energy Lepton: Neut Mode =AllModesCombined

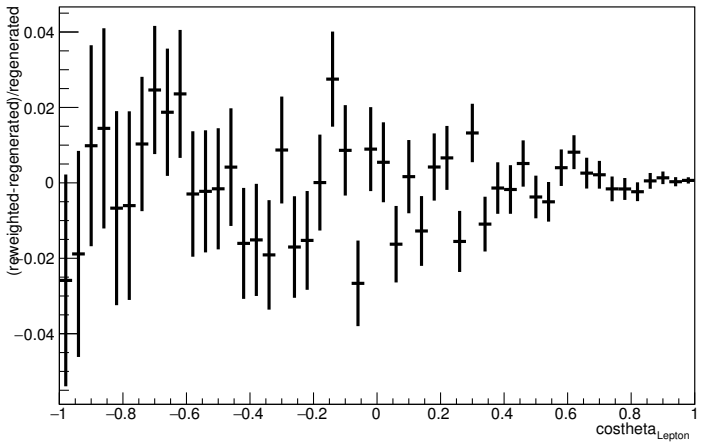

Energy plot: Leading Energy Pion: Neut Mode =AllModesCombined

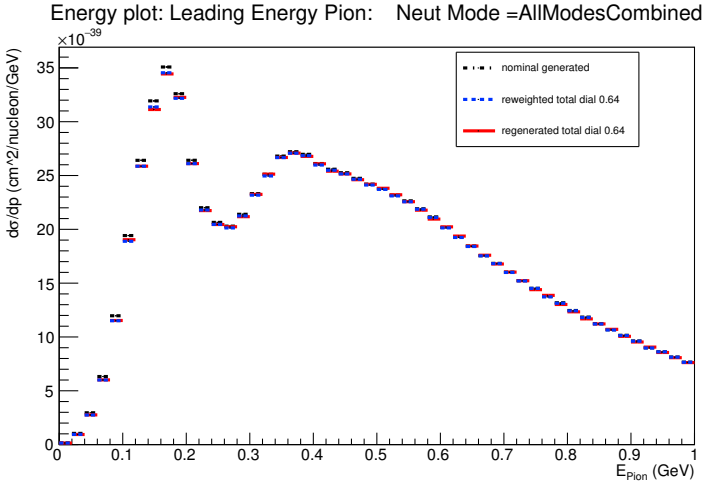

Energy plot: Every FSI Pion: Neut Mode =AllModesCombined

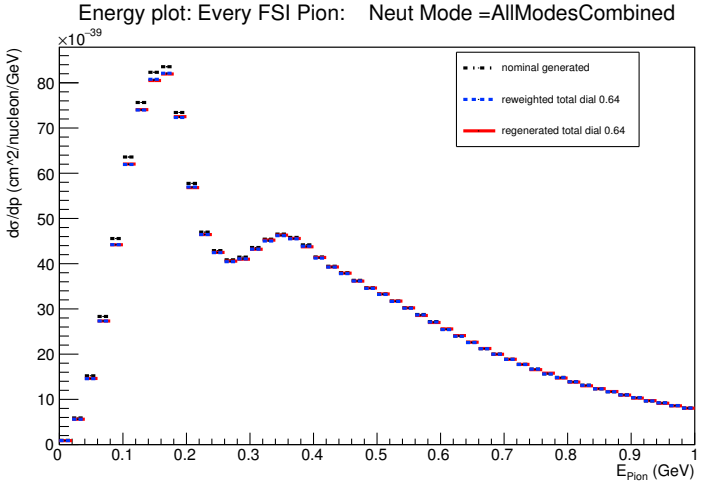

Energy plot: Leading Energy Pion: Neut Mode =AllModesCombined

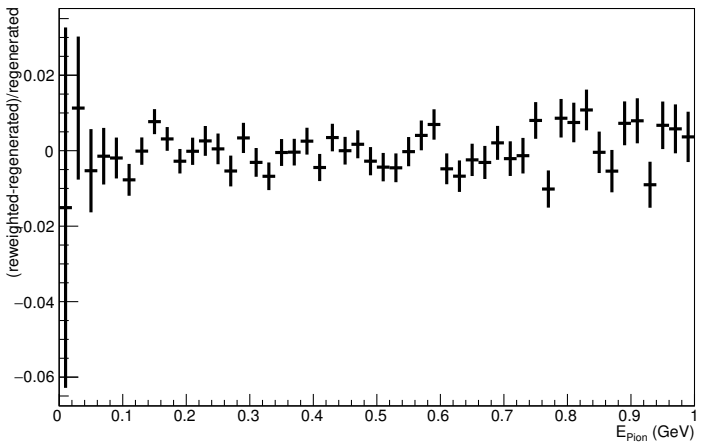

Energy plot: Every FSI Pion: Neut Mode =AllModesCombined

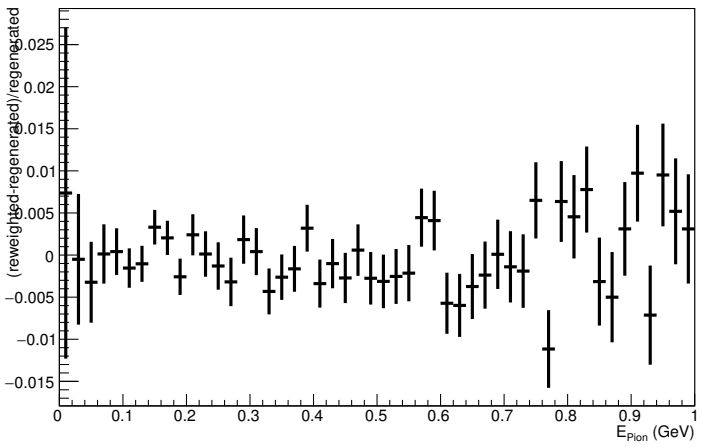

Angle plot: Leading Energy Pion: Neut Mode =AllModesCombined

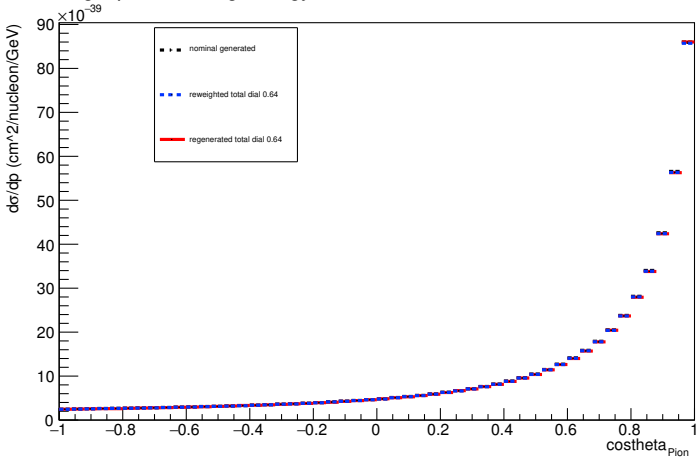

Angle plot: Every FSI Pion: Neut Mode =AllModesCombined

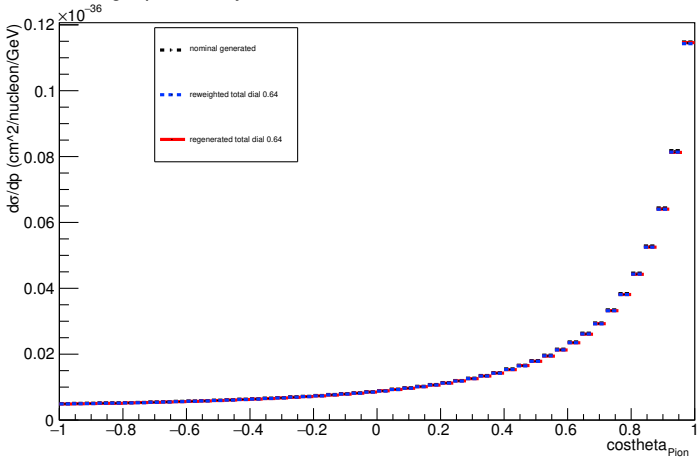

Angle plot: Leading Energy Pion: Neut Mode =AllModesCombined

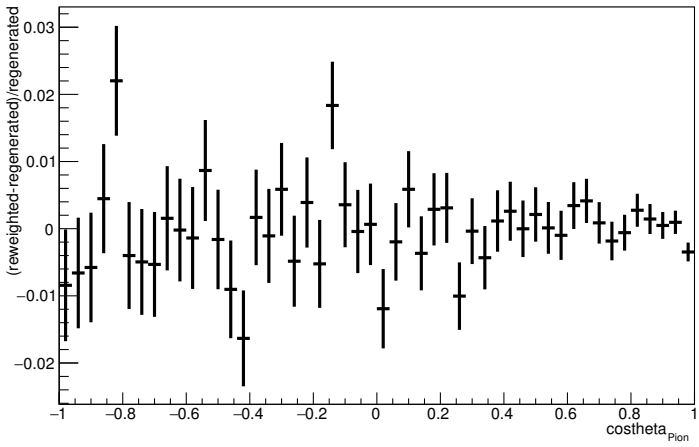

Angle plot: Every FSI Pion: Neut Mode =AllModesCombined

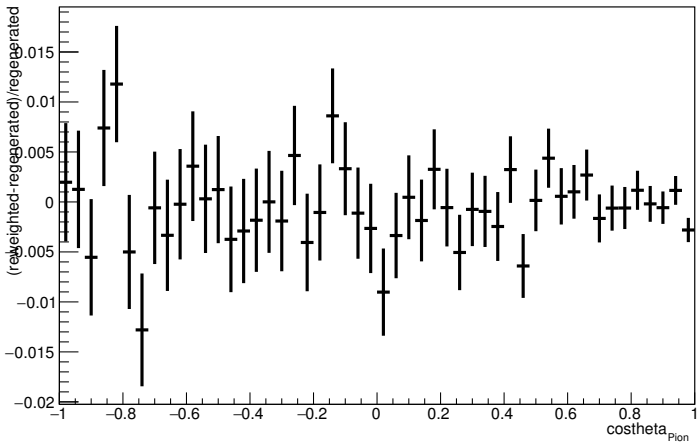

Energy plot: Leading Energy Nucleon: Neut Mode =1

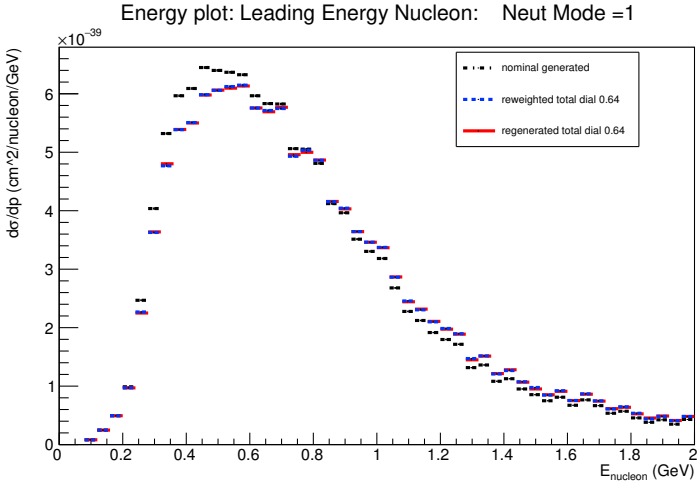

Energy plot: Every FSI Nucleon: Neut Mode =1

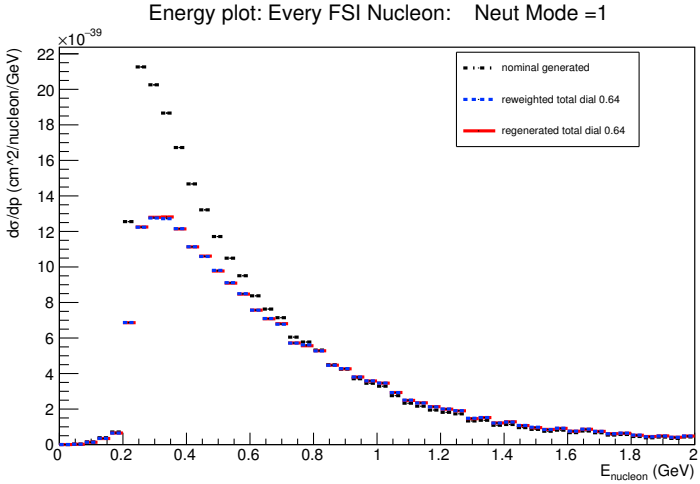

Energy plot: Leading Energy Nucleon: Neut Mode =1

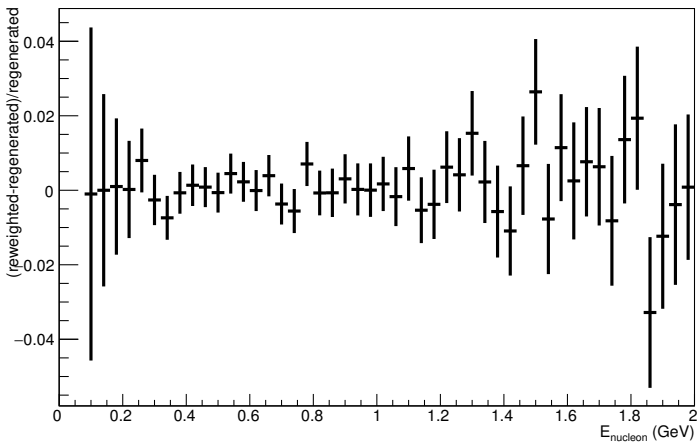

Energy plot: Every FSI Nucleon: Neut Mode =1

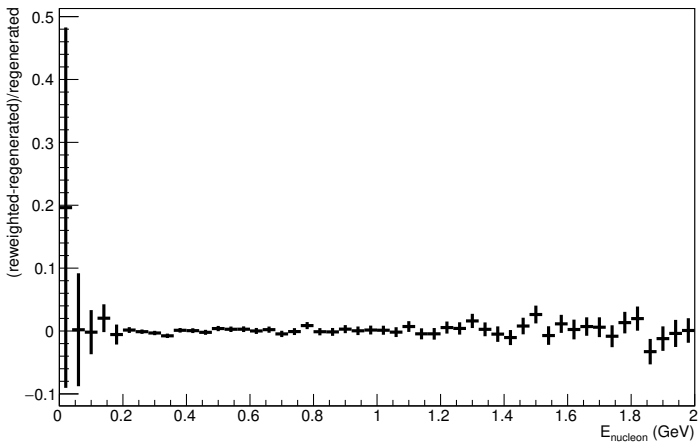

Angle plot: Leading Energy Nucleon: Neut Mode =1

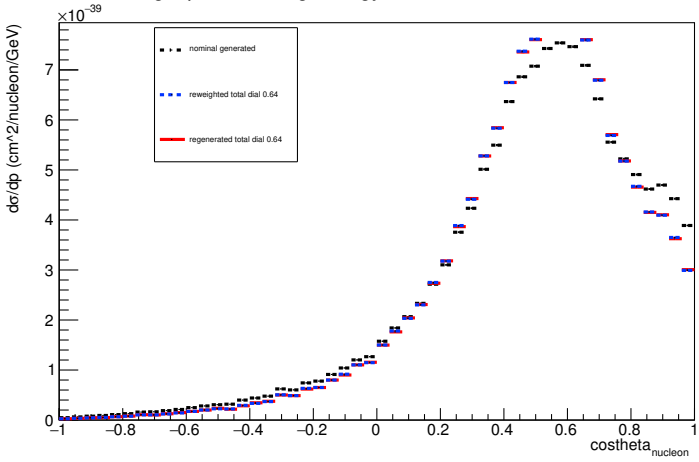

Angle plot: Every FSI Nucleon: Neut Mode =1

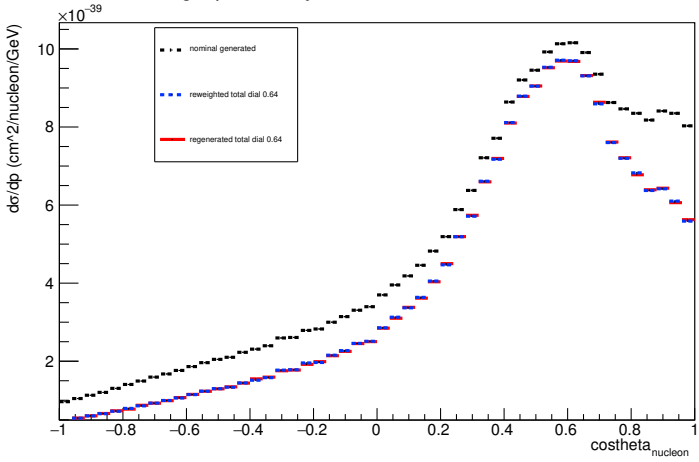

Angle plot: Leading Energy Nucleon: Neut Mode =1

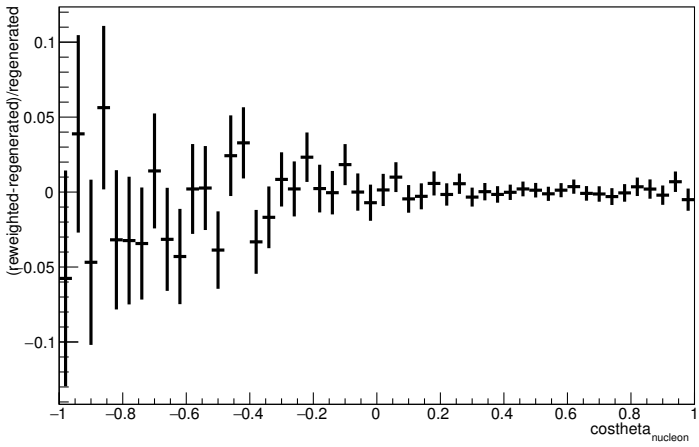

Angle plot: Every FSI Nucleon: Neut Mode =1

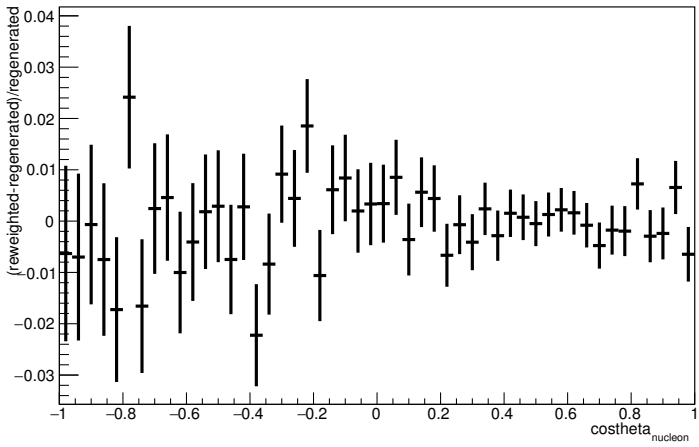

Energy plot: Leading Energy Proton: Neut Mode =1

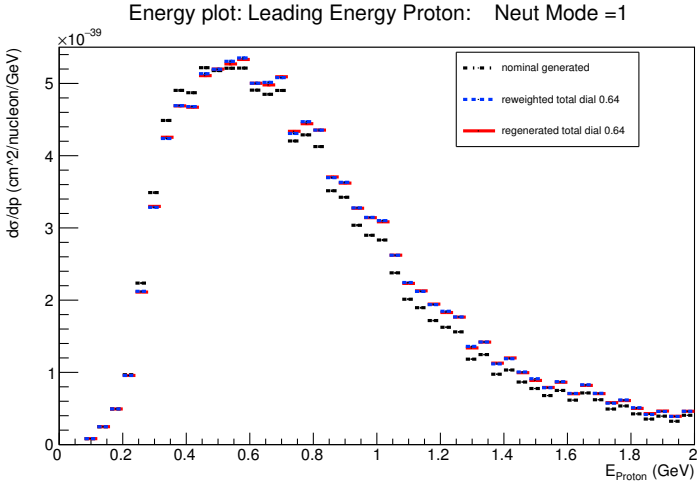

Energy plot: Every FSI Proton: Neut Mode =1

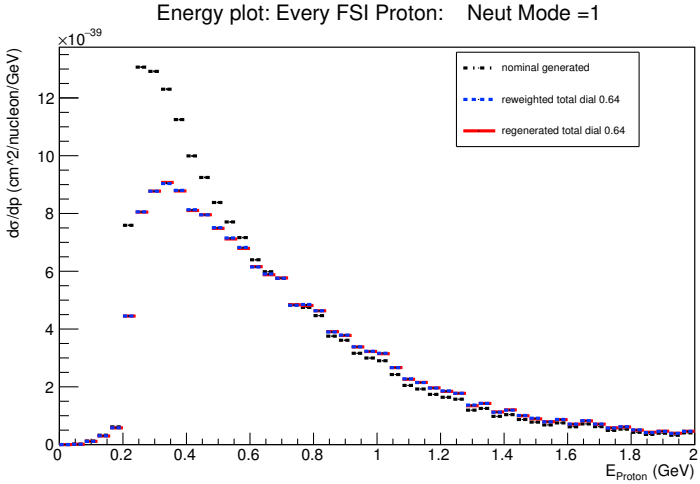

Energy plot: Leading Energy Proton: Neut Mode =1

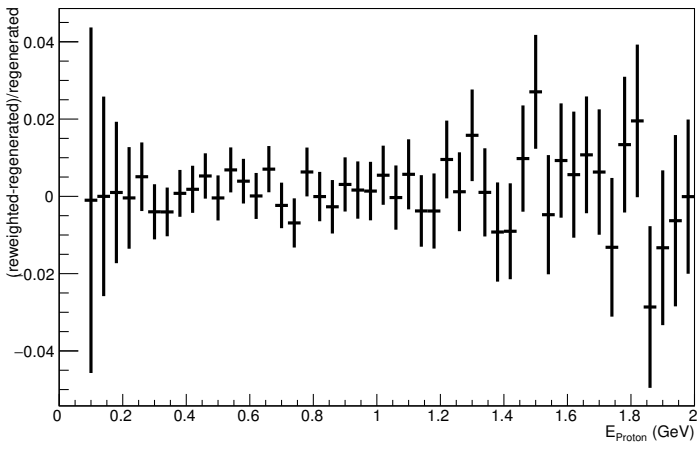

Energy plot: Every FSI Proton: Neut Mode =1

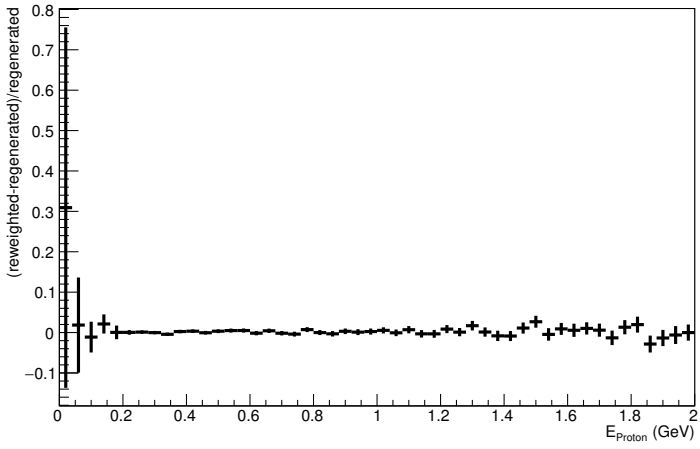

Angle plot: Leading Energy Proton: Neut Mode =1

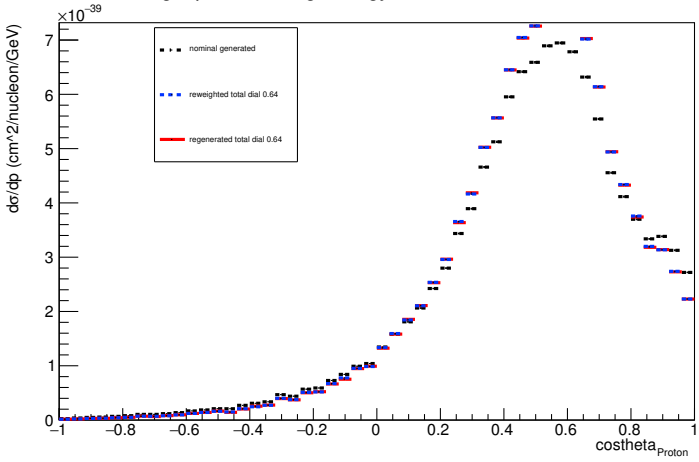

Angle plot: Every FSI Proton: Neut Mode =1

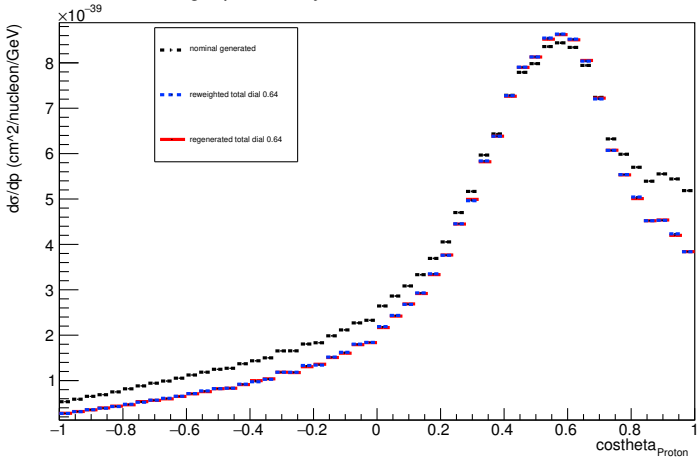

Angle plot: Leading Energy Proton: Neut Mode =1

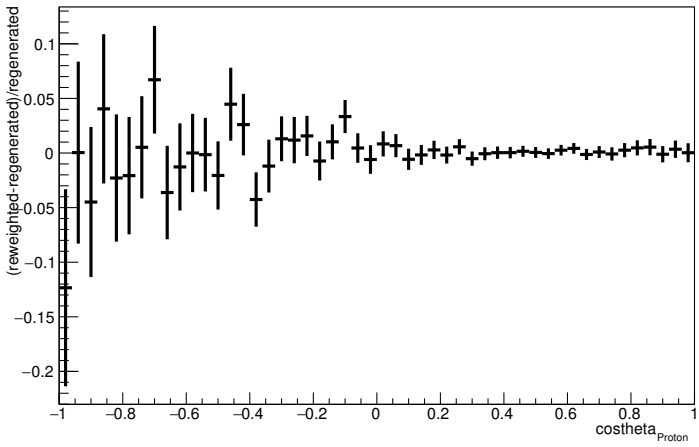

Angle plot: Every FSI Proton: Neut Mode =1

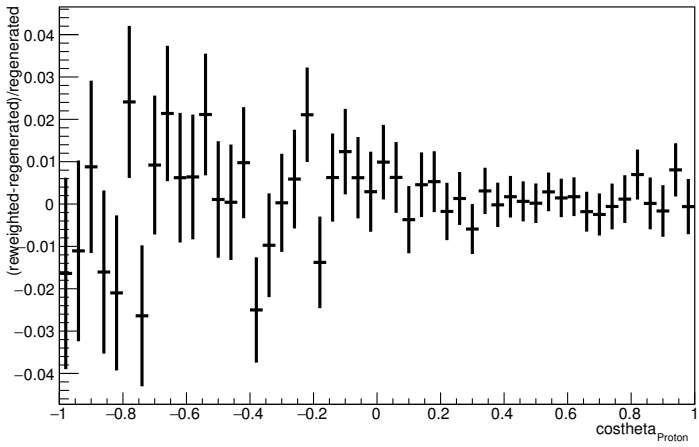

Energy plot: Leading Energy Neutron: Neut Mode =1

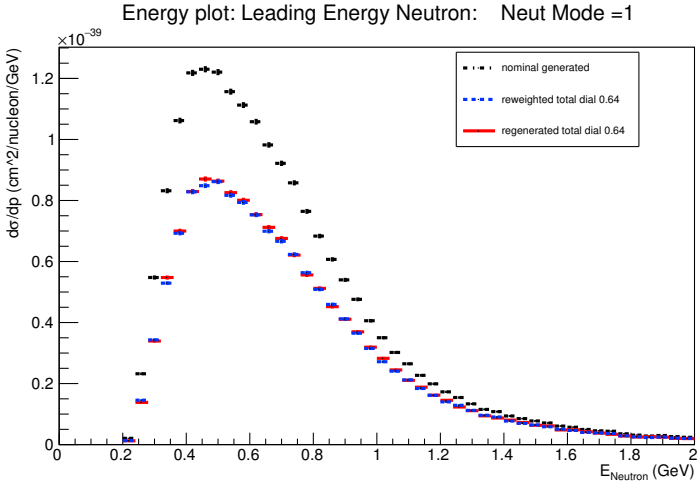

Energy plot: Every FSI Neutron: Neut Mode =1

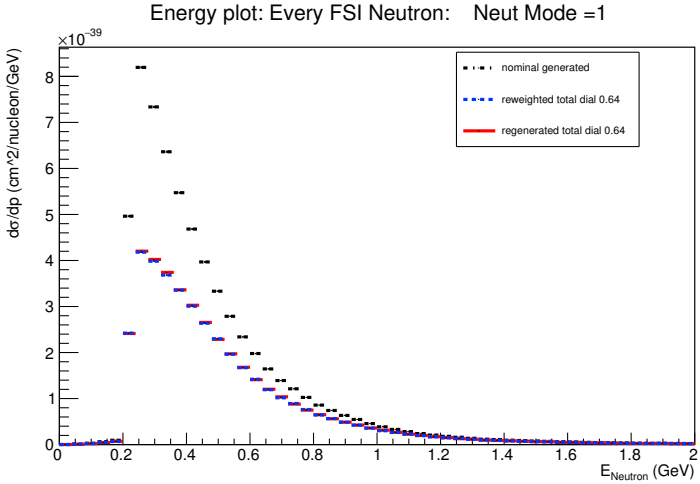

Energy plot: Leading Energy Neutron: Neut Mode =1

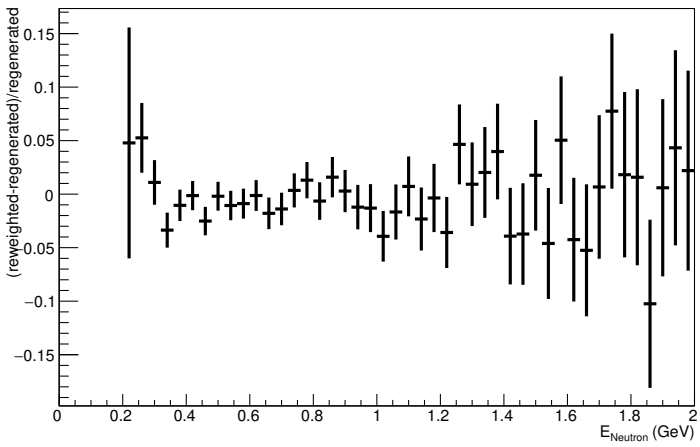

Energy plot: Every FSI Neutron: Neut Mode =1

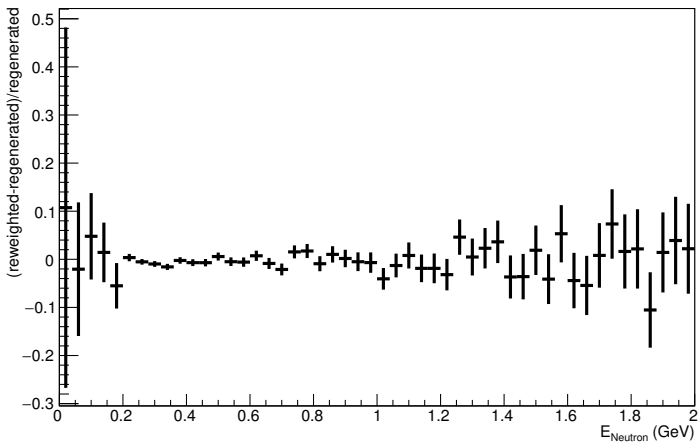

Angle plot: Leading Energy Neutron: Neut Mode =1

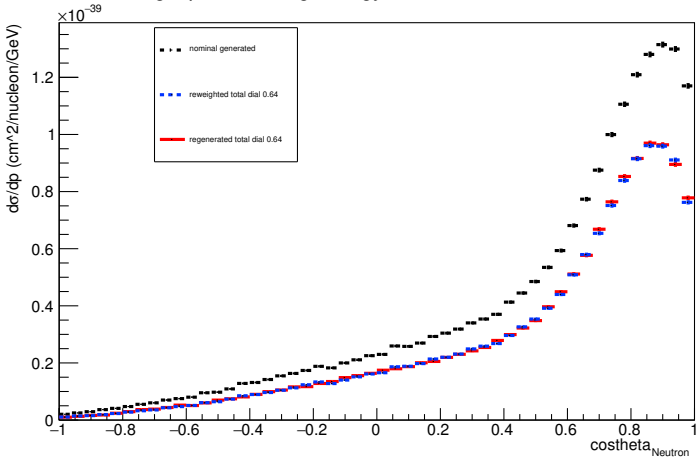

Angle plot: Every FSI Neutron: Neut Mode =1

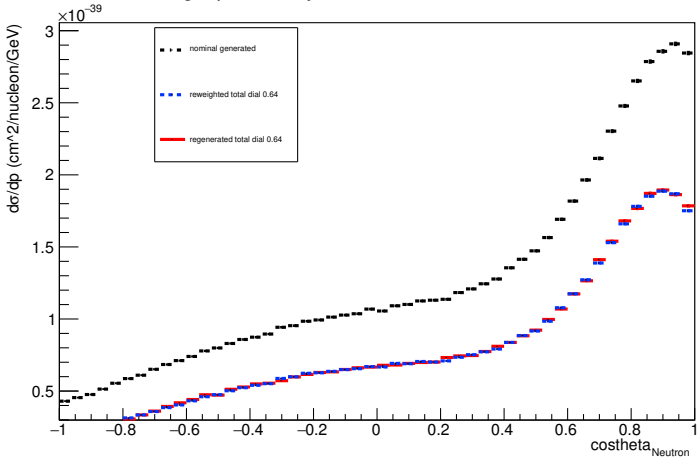

Angle plot: Leading Energy Neutron: Neut Mode =1

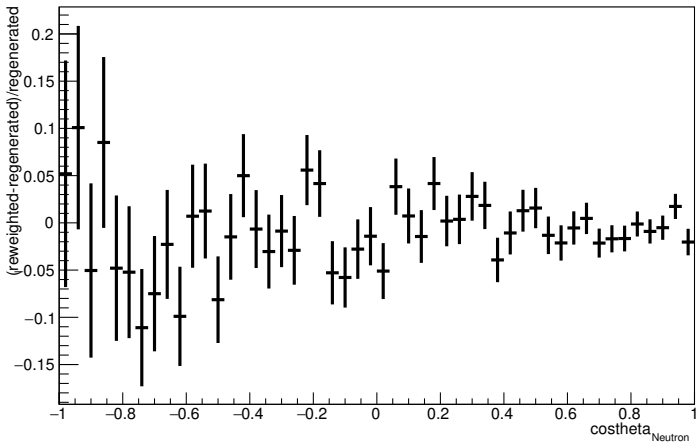

Angle plot: Every FSI Neutron: Neut Mode =1

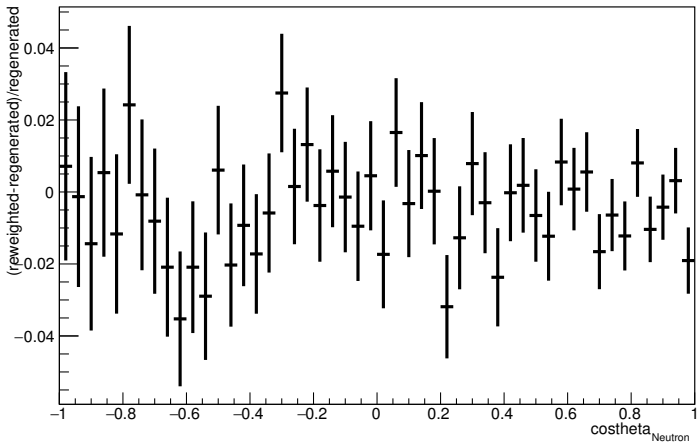

Energy plot: Leading Energy Lepton: Neut Mode =1

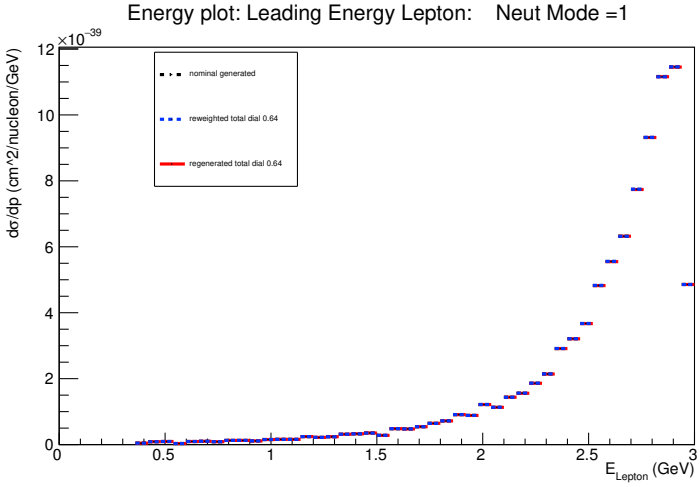

Angle plot: Leading Energy Lepton: Neut Mode =1

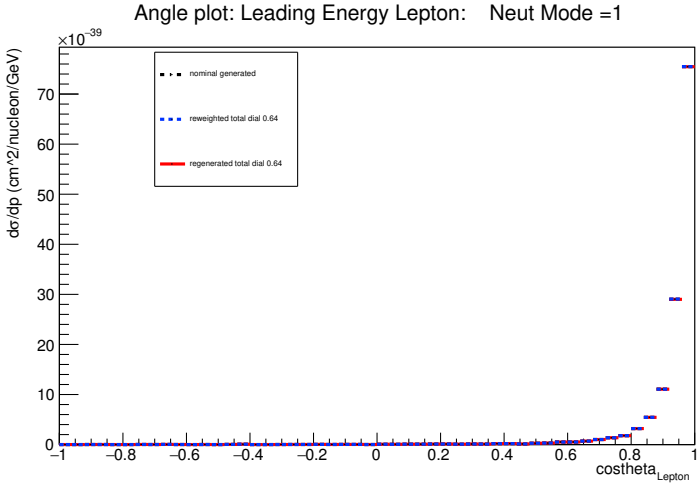

Energy plot: Leading Energy Lepton: Neut Mode =1

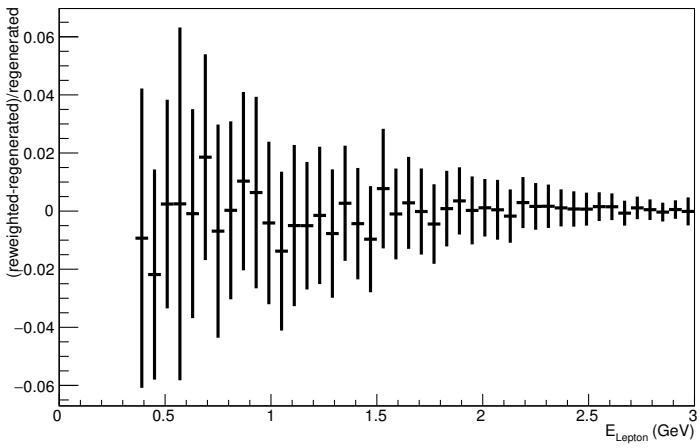

Angle plot: Leading Energy Lepton: Neut Mode =1

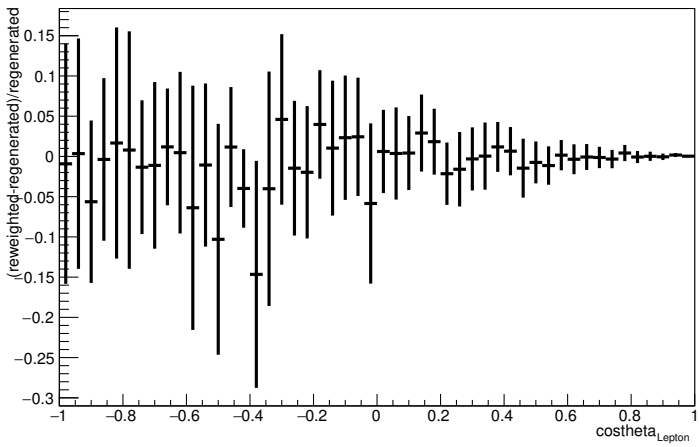

Energy plot: Leading Energy Pion: Neut Mode =1

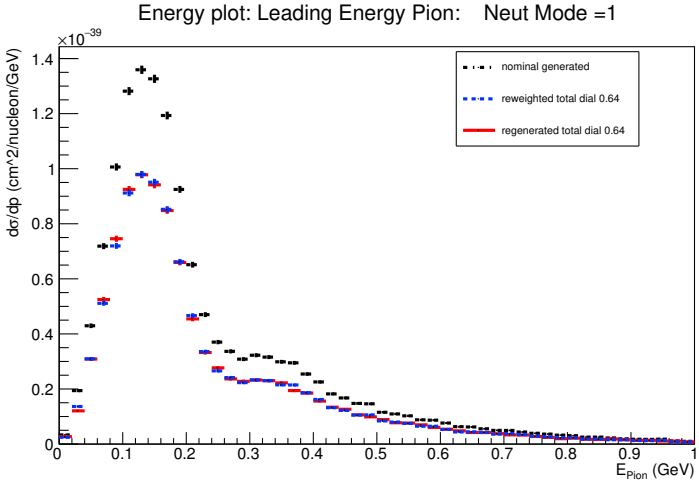

Energy plot: Every FSI Pion: Neut Mode =1

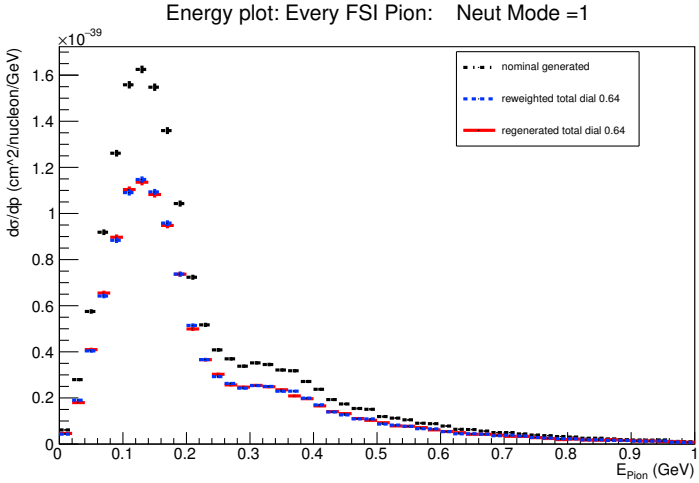

Energy plot: Leading Energy Pion: Neut Mode =1

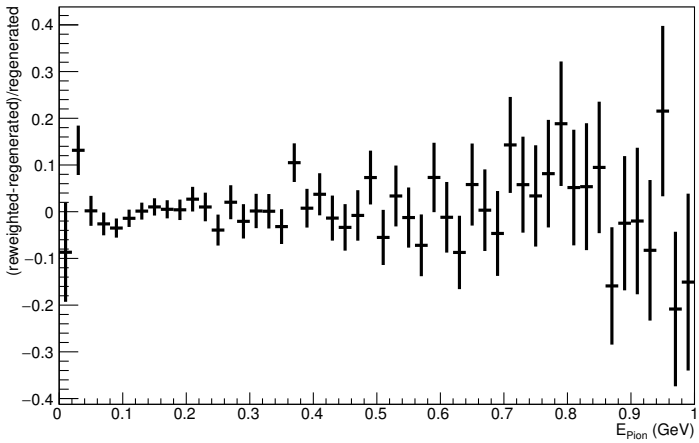

Energy plot: Every FSI Pion: Neut Mode =1

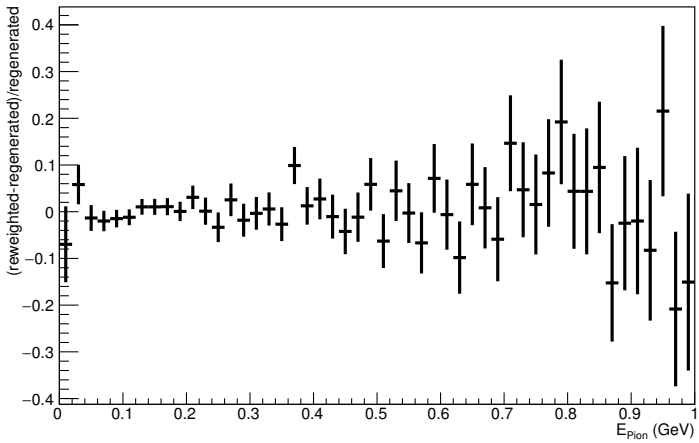

Angle plot: Leading Energy Pion: Neut Mode =1

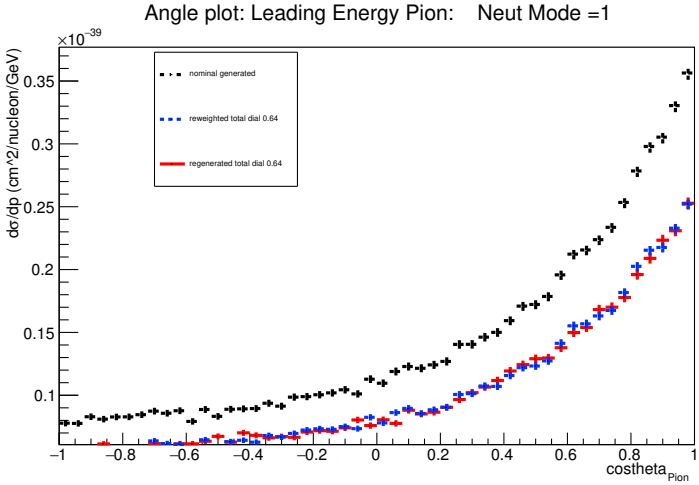

Angle plot: Every FSI Pion: Neut Mode =1

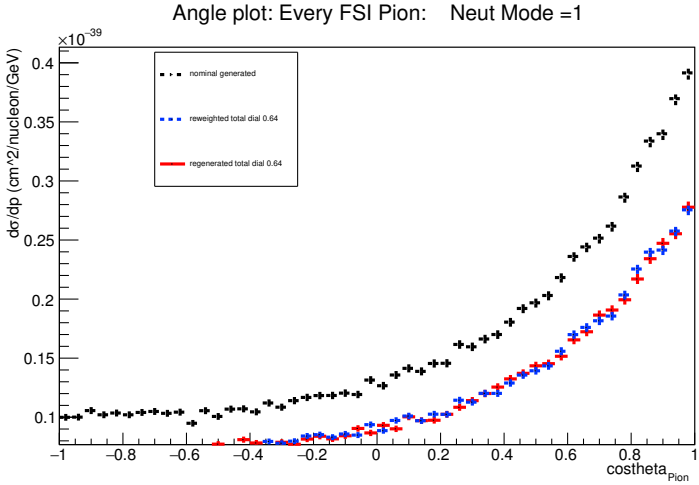

Angle plot: Leading Energy Pion: Neut Mode =1

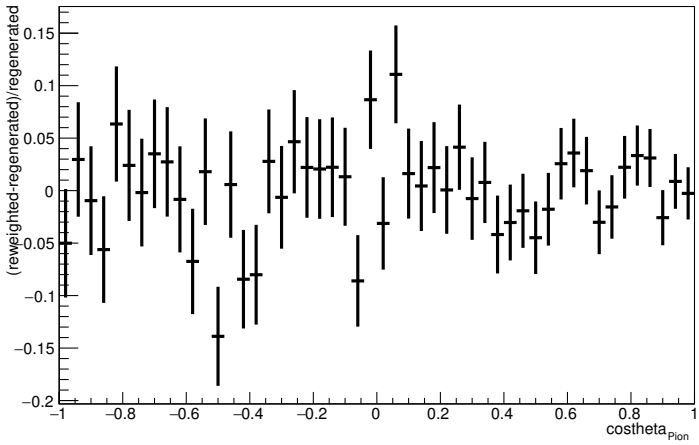

Angle plot: Every FSI Pion: Neut Mode =1

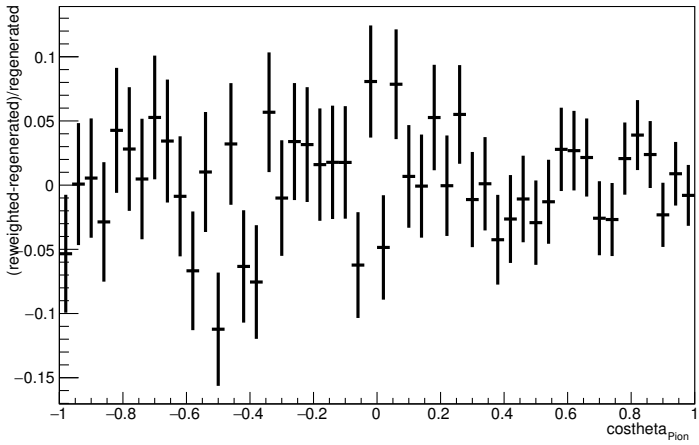

Energy plot: Leading Energy Nucleon: Neut Mode =2

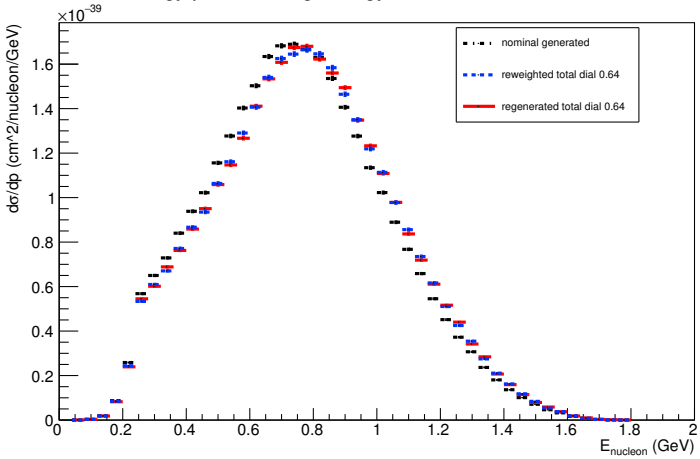

Energy plot: Every FSI Nucleon: Neut Mode =2

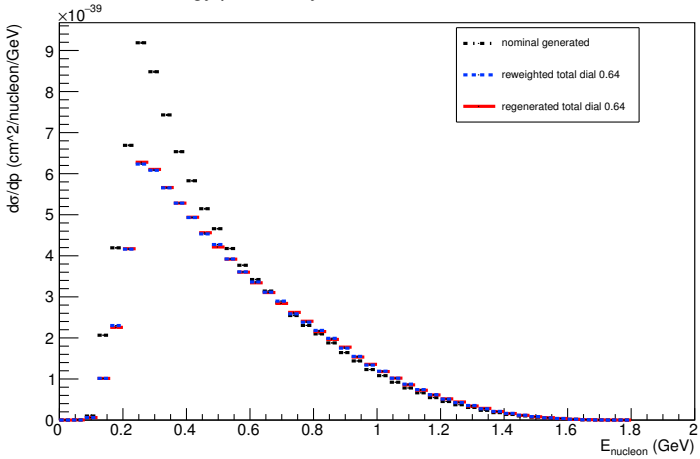

Energy plot: Leading Energy Nucleon: Neut Mode =2

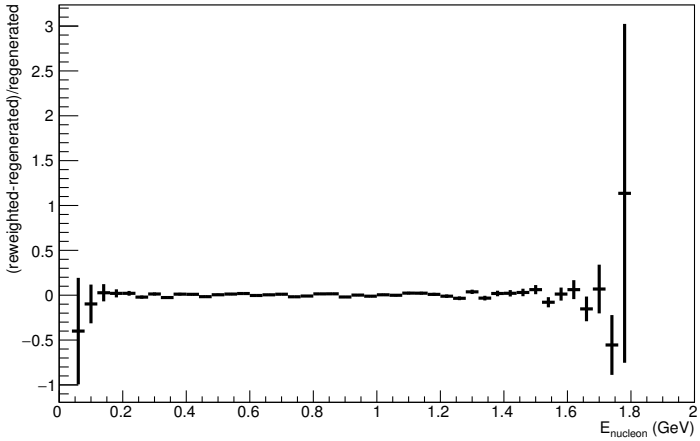

Energy plot: Every FSI Nucleon: Neut Mode =2

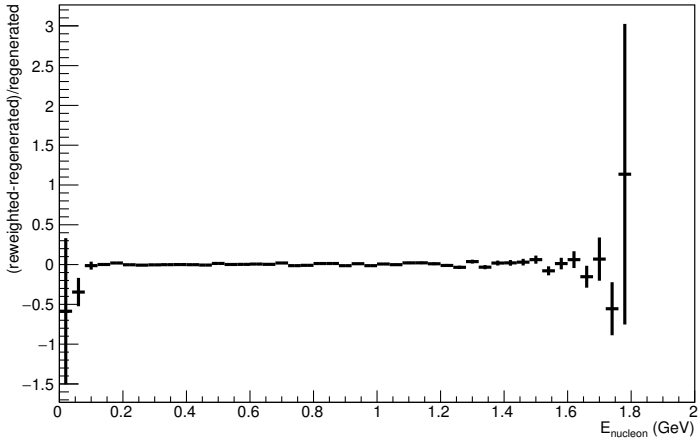

Angle plot: Leading Energy Nucleon: Neut Mode =2

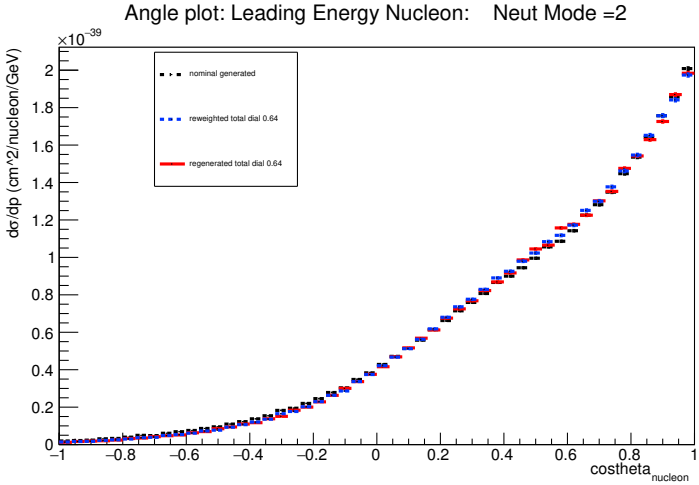

Angle plot: Every FSI Nucleon: Neut Mode =2

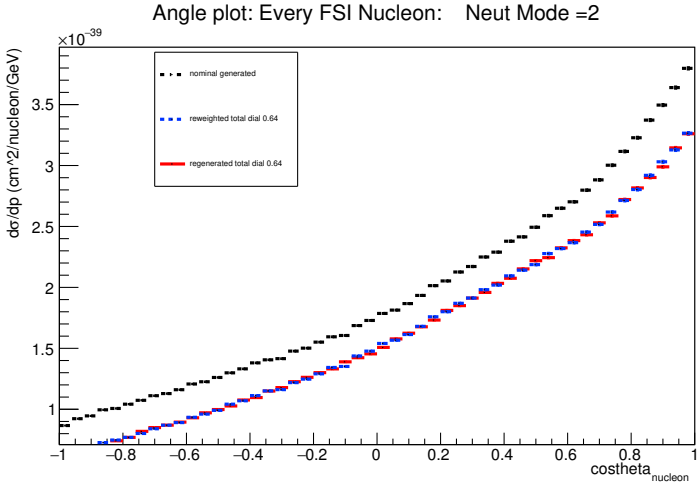

Angle plot: Leading Energy Nucleon: Neut Mode =2

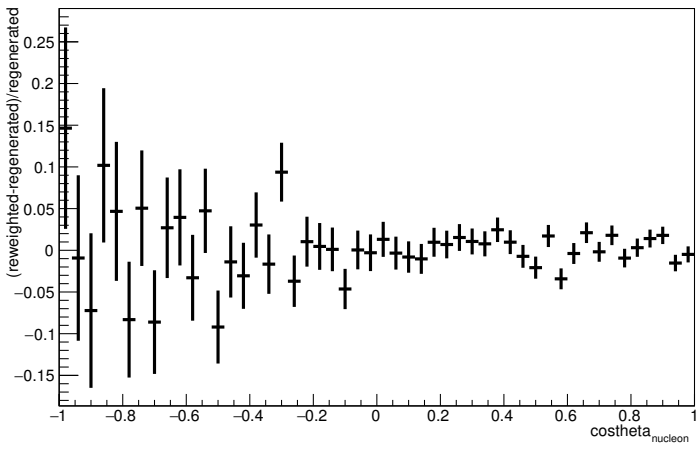

Angle plot: Every FSI Nucleon: Neut Mode =2

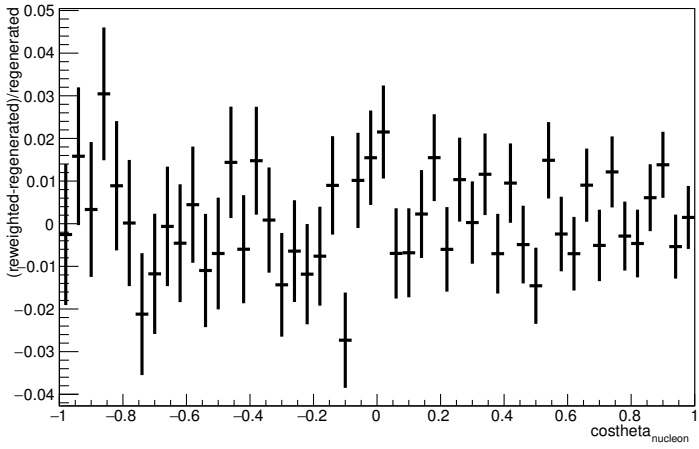

Energy plot: Leading Energy Proton: Neut Mode =2

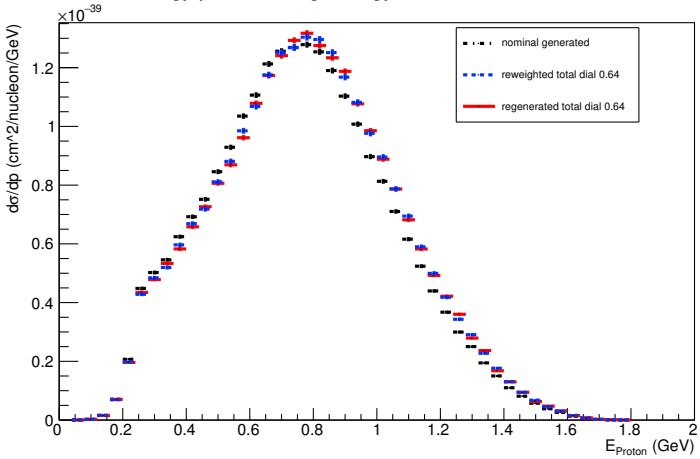

Energy plot: Every FSI Proton: Neut Mode =2

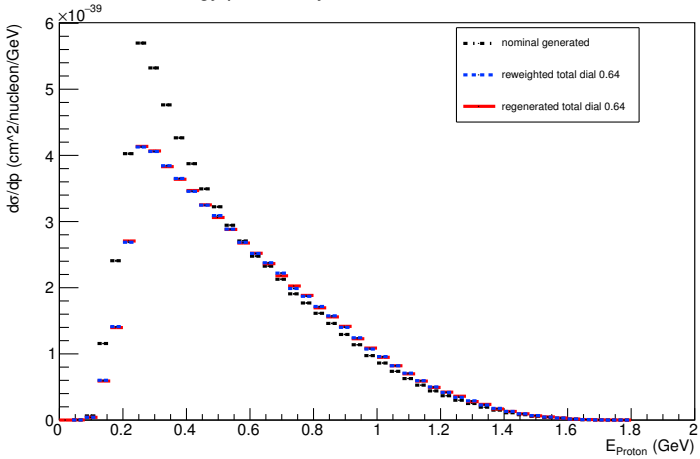

Energy plot: Leading Energy Proton: Neut Mode =2

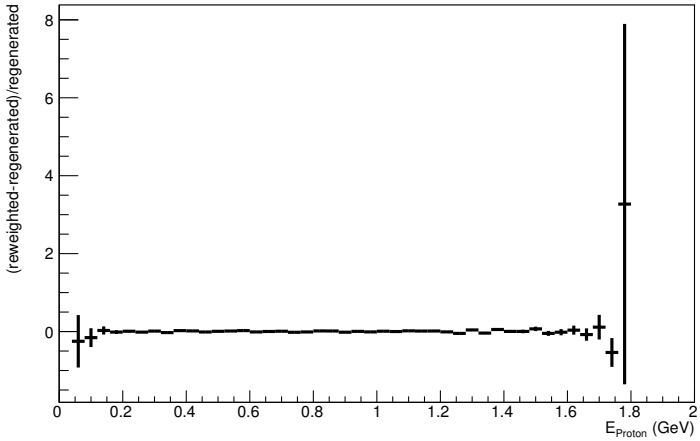

Energy plot: Every FSI Proton: Neut Mode =2

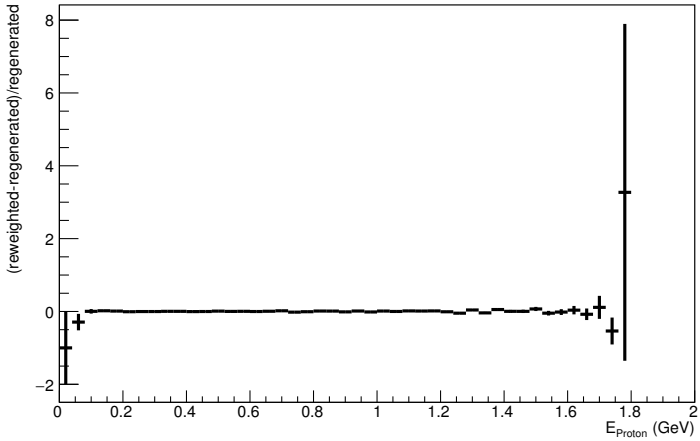

Angle plot: Leading Energy Proton: Neut Mode =2

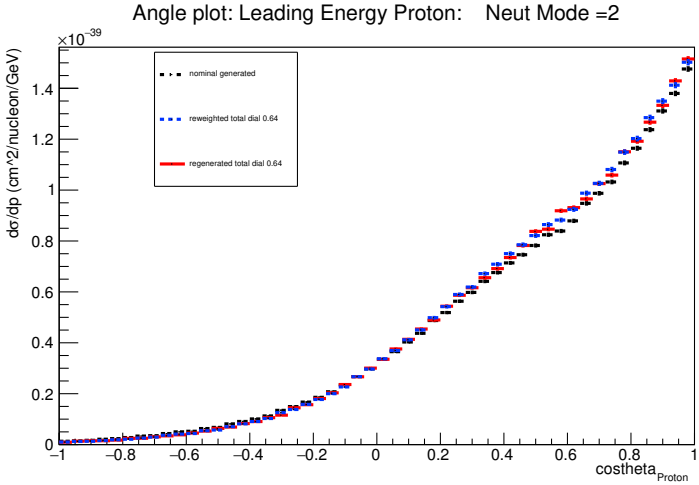

Angle plot: Every FSI Proton: Neut Mode =2

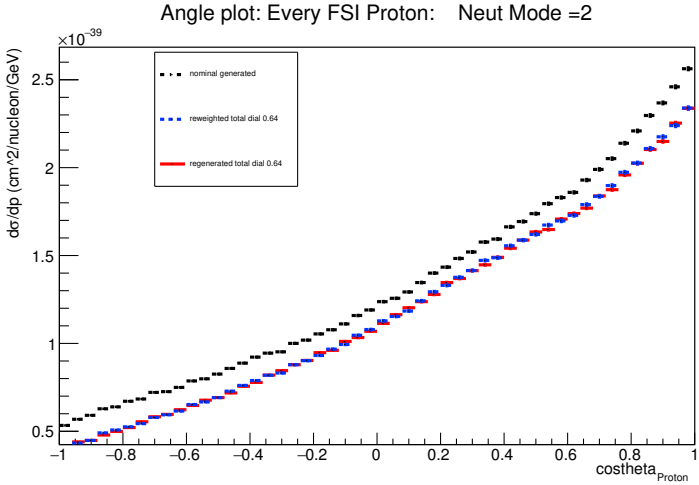

Angle plot: Leading Energy Proton: Neut Mode =2

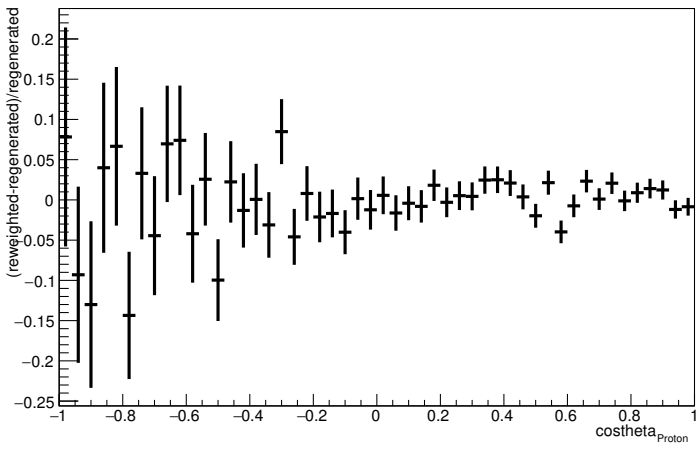

Angle plot: Every FSI Proton: Neut Mode =2

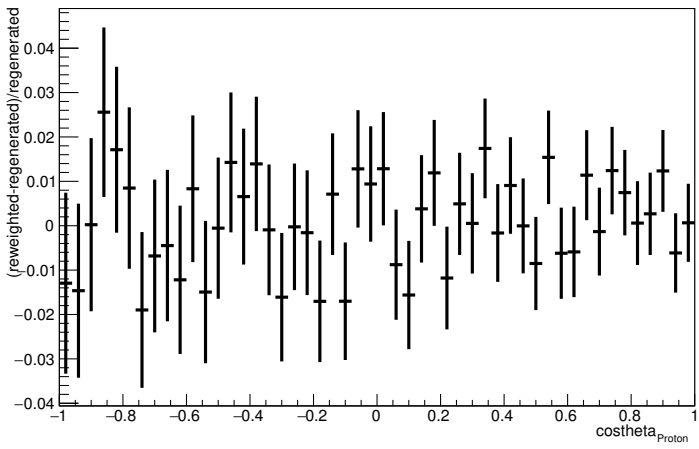

Energy plot: Leading Energy Neutron: Neut Mode =2

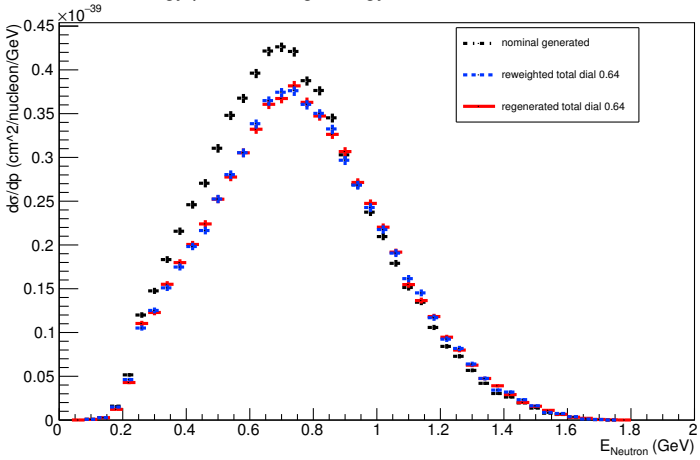

Energy plot: Every FSI Neutron: Neut Mode =2

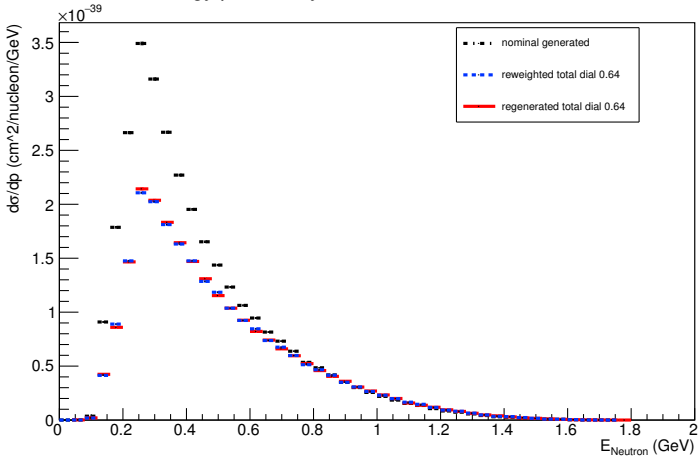

Energy plot: Leading Energy Neutron: Neut Mode =2

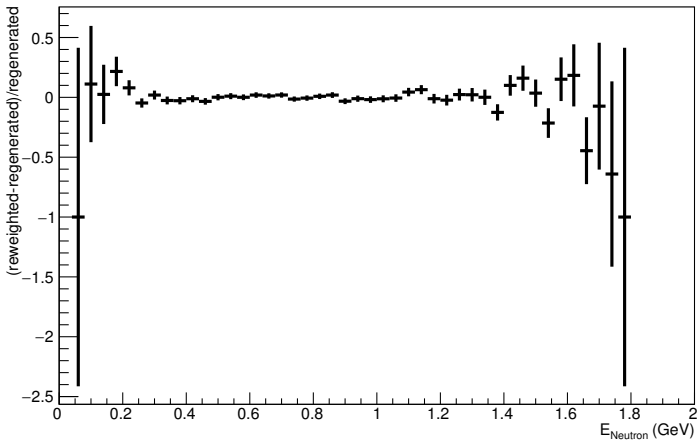

Energy plot: Every FSI Neutron: Neut Mode =2

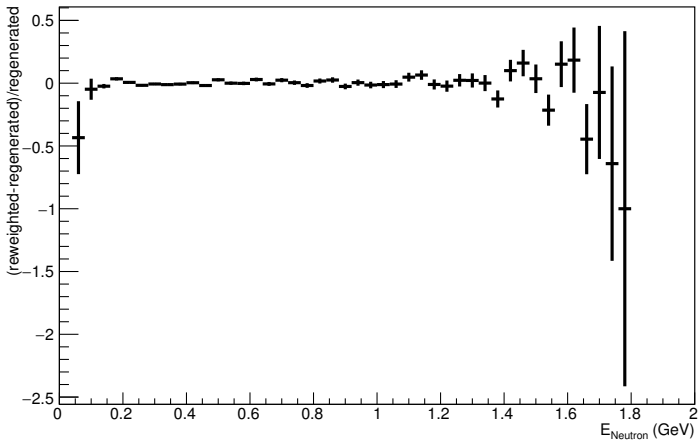

Angle plot: Leading Energy Neutron: Neut Mode =2

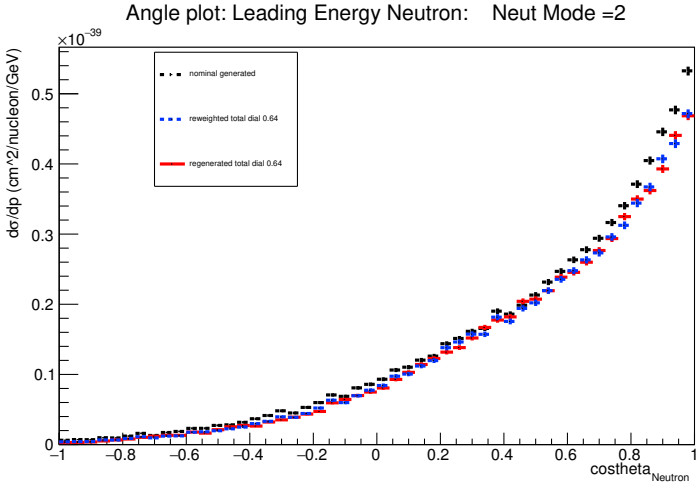

Angle plot: Every FSI Neutron: Neut Mode =2

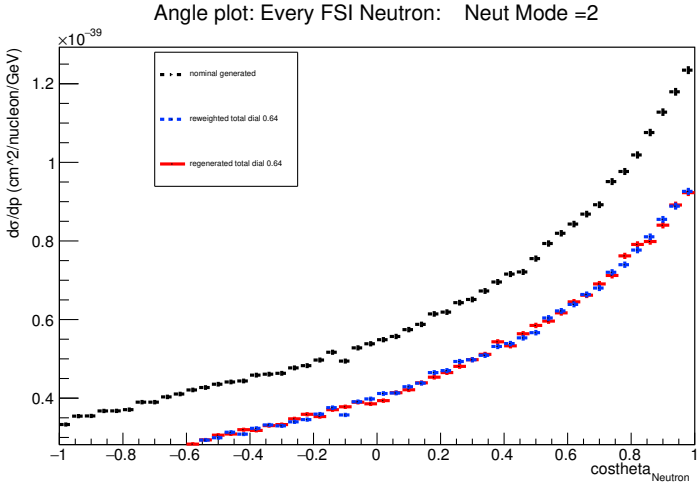

Angle plot: Leading Energy Neutron: Neut Mode =2

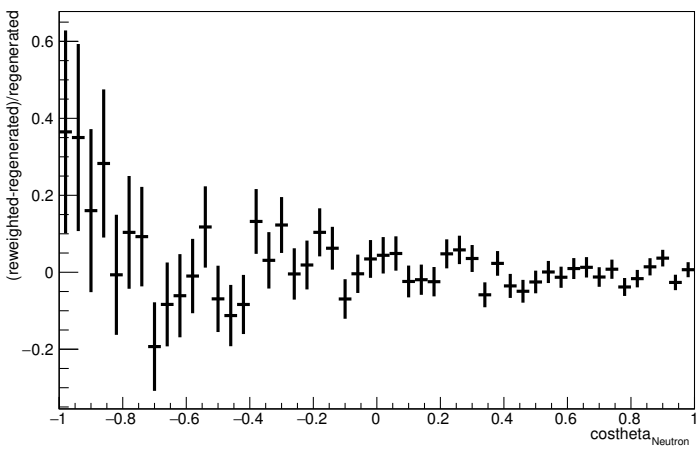

Angle plot: Every FSI Neutron: Neut Mode =2

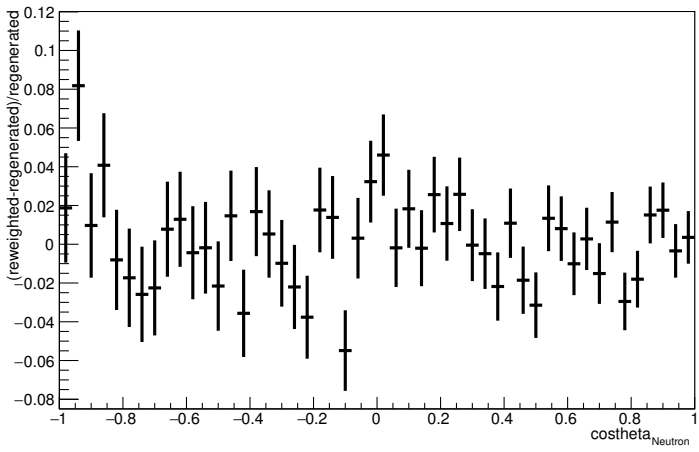

Energy plot: Leading Energy Lepton: Neut Mode =2

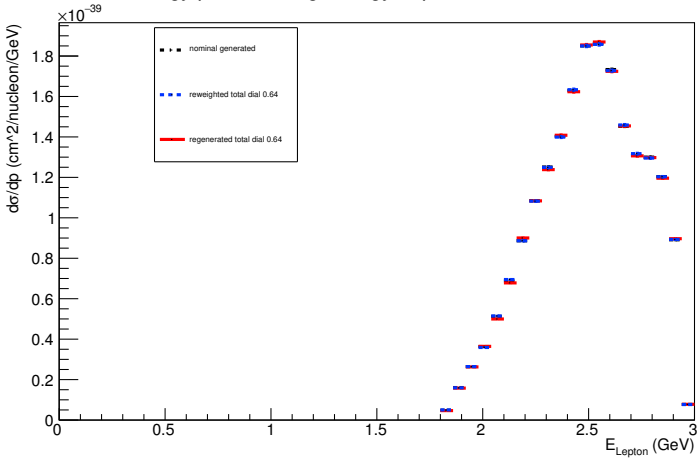

Angle plot: Leading Energy Lepton: Neut Mode =2

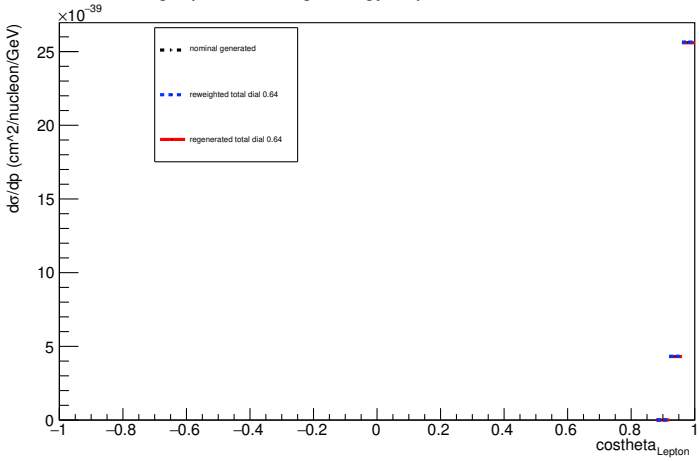

Energy plot: Leading Energy Lepton: Neut Mode =2

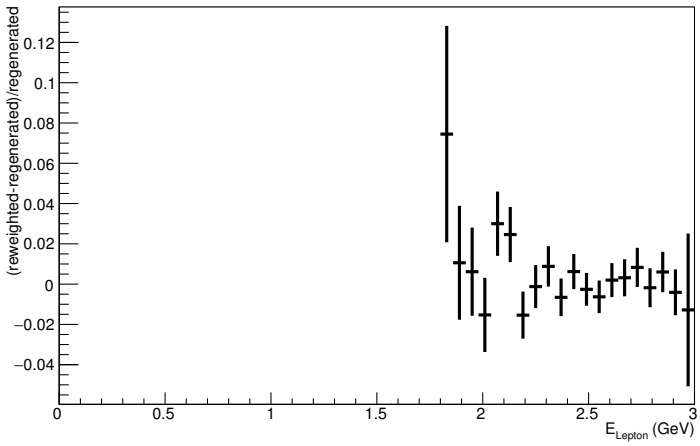

Angle plot: Leading Energy Lepton: Neut Mode =2

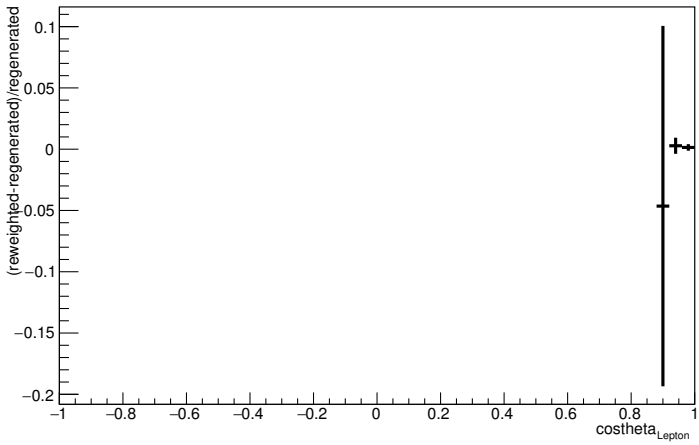

Energy plot: Leading Energy Pion: Neut Mode =2

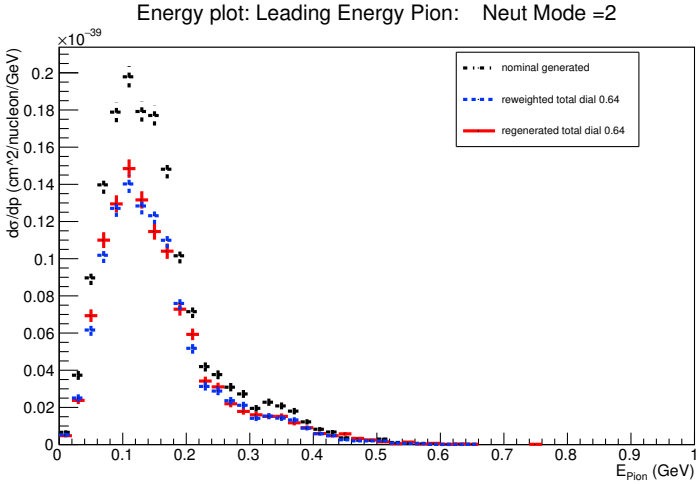

Energy plot: Every FSI Pion: Neut Mode =2

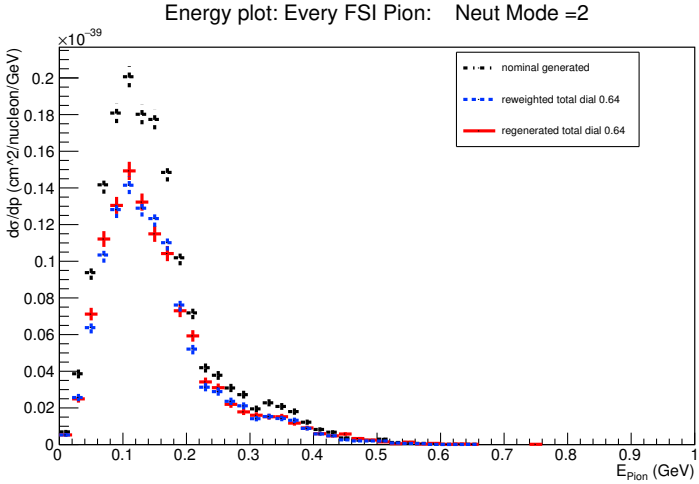

Energy plot: Leading Energy Pion: Neut Mode =2

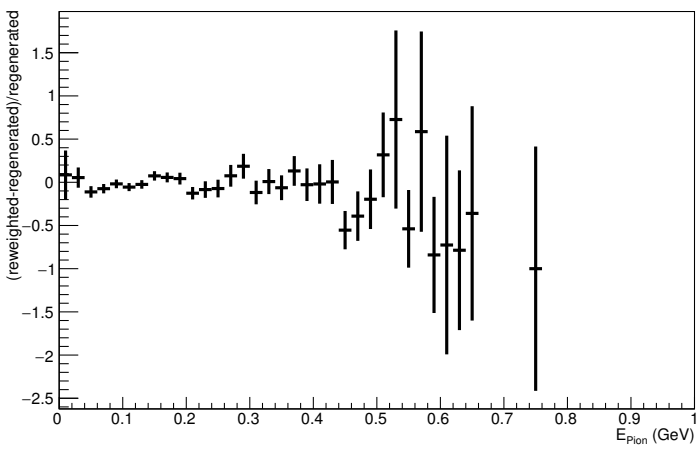

Energy plot: Every FSI Pion: Neut Mode =2

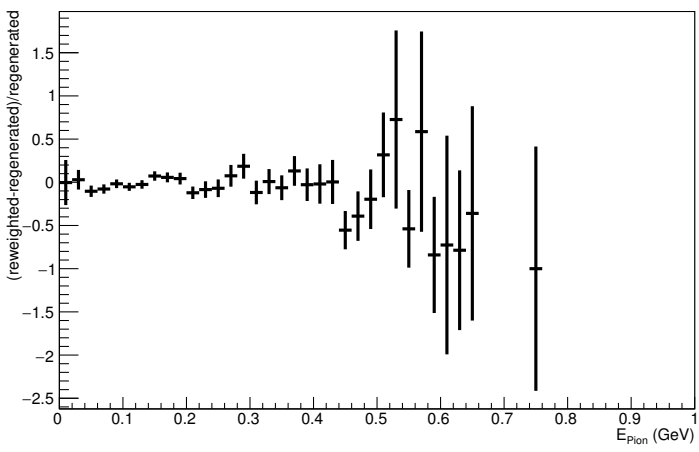

Angle plot: Leading Energy Pion: Neut Mode =2

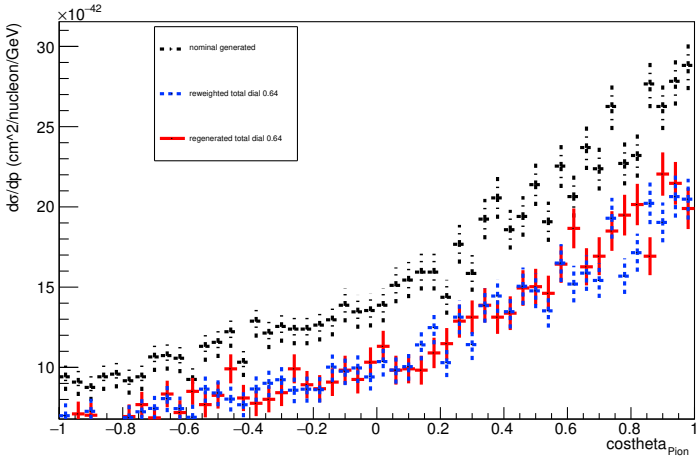

Angle plot: Every FSI Pion: Neut Mode =2

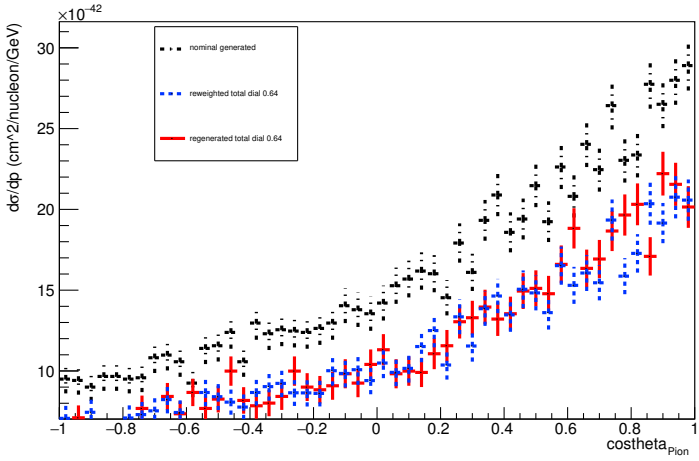

Angle plot: Leading Energy Pion: Neut Mode =2

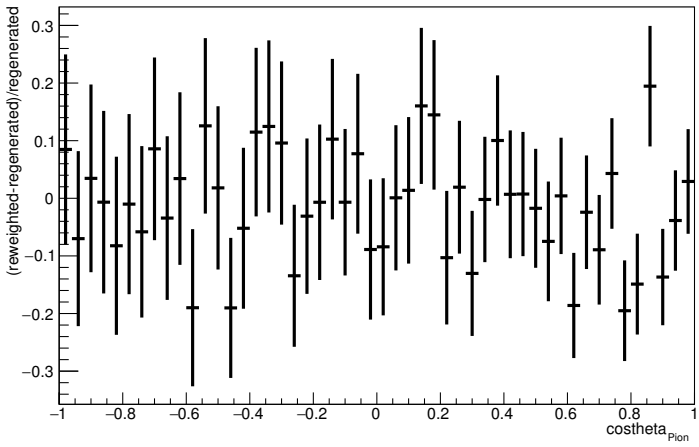

Angle plot: Every FSI Pion: Neut Mode =2

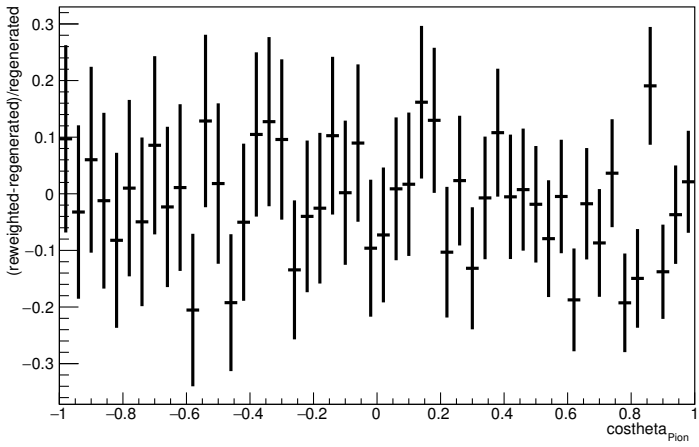

Energy plot: Leading Energy Nucleon: Neut Mode =11

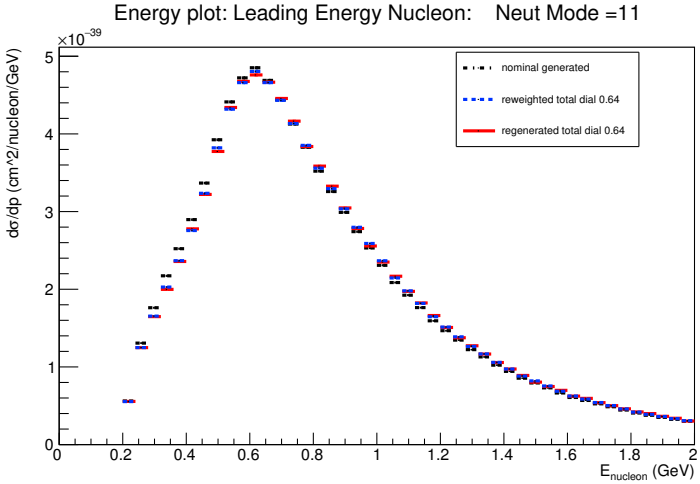

Energy plot: Every FSI Nucleon: Neut Mode =11

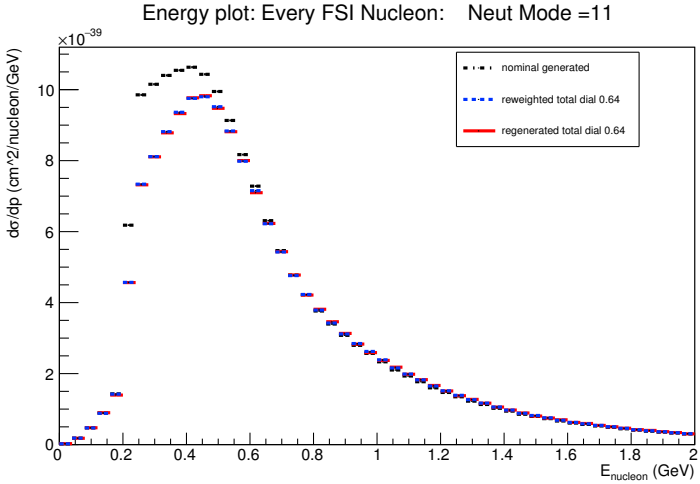

Energy plot: Leading Energy Nucleon: Neut Mode =11

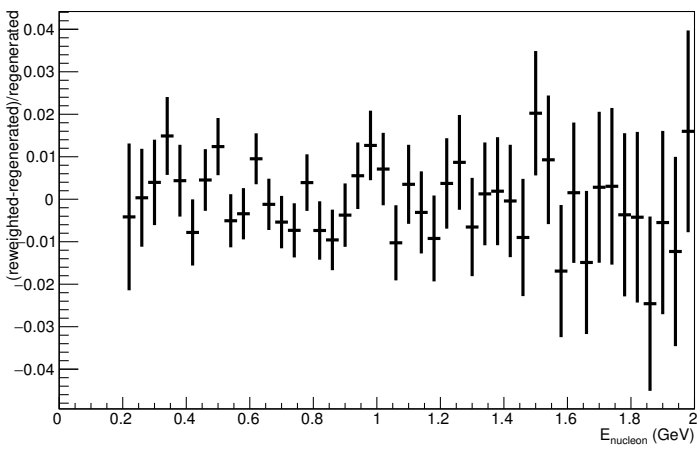

Energy plot: Every FSI Nucleon: Neut Mode =11

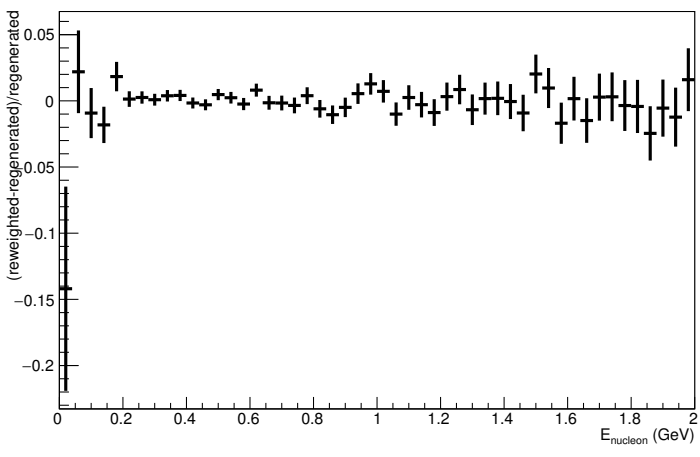

Angle plot: Leading Energy Nucleon: Neut Mode =11

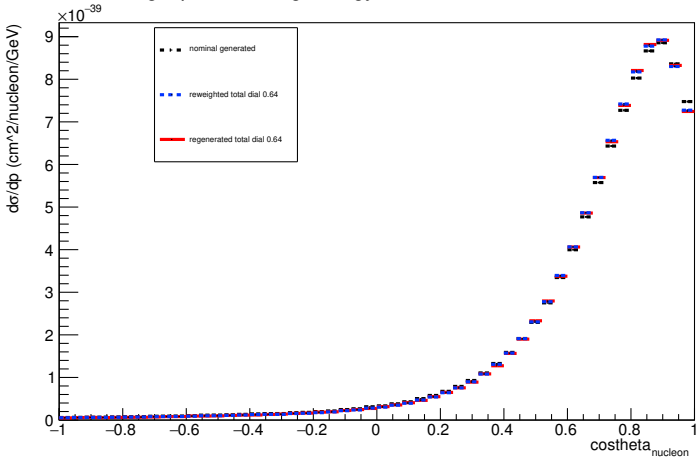

Angle plot: Every FSI Nucleon: Neut Mode =11

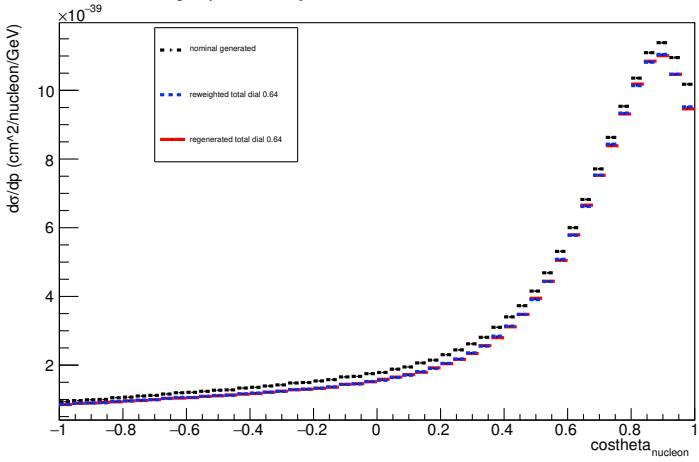

Angle plot: Leading Energy Nucleon: Neut Mode =11

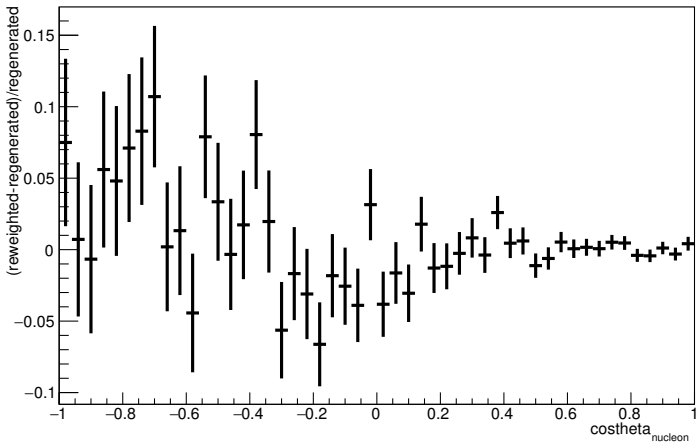

Angle plot: Every FSI Nucleon: Neut Mode =11

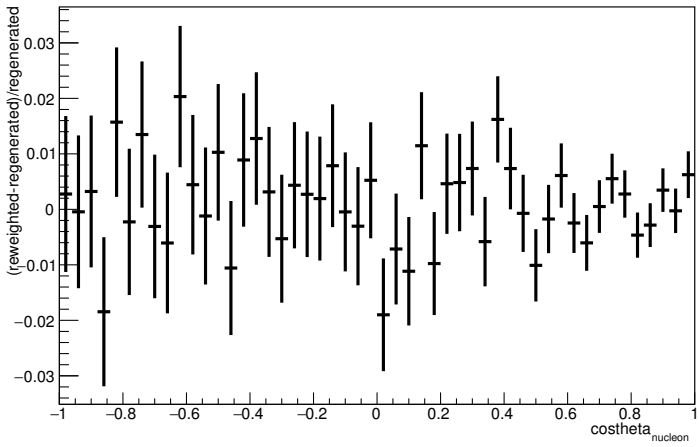

Energy plot: Leading Energy Proton: Neut Mode =11

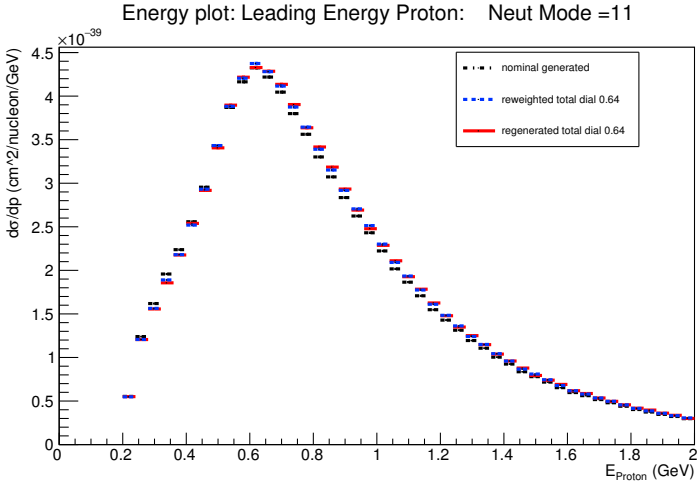

Energy plot: Every FSI Proton: Neut Mode =11

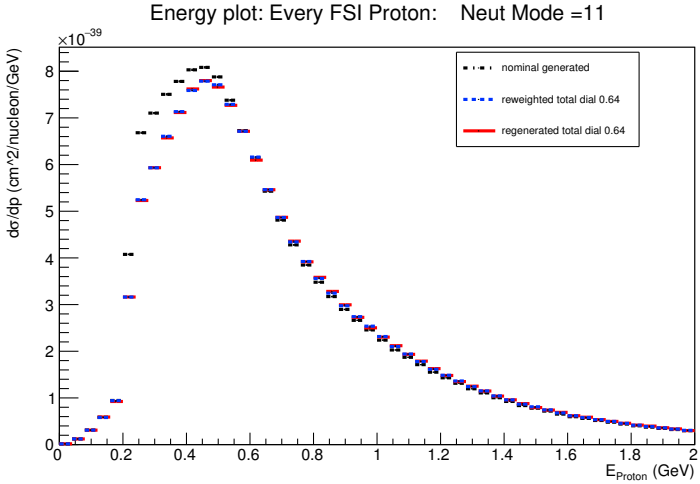

Energy plot: Leading Energy Proton: Neut Mode =11

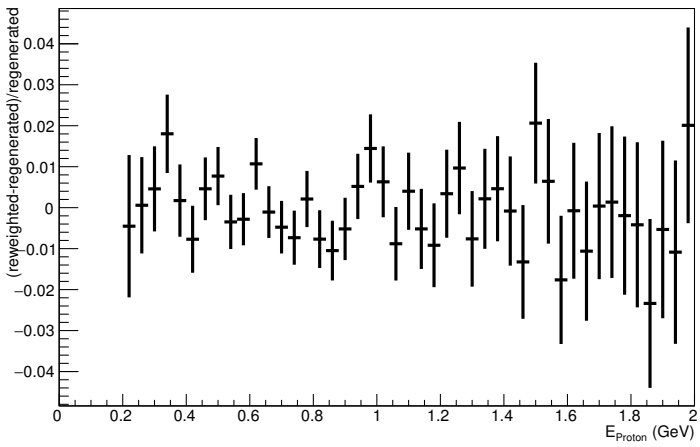

Energy plot: Every FSI Proton: Neut Mode =11

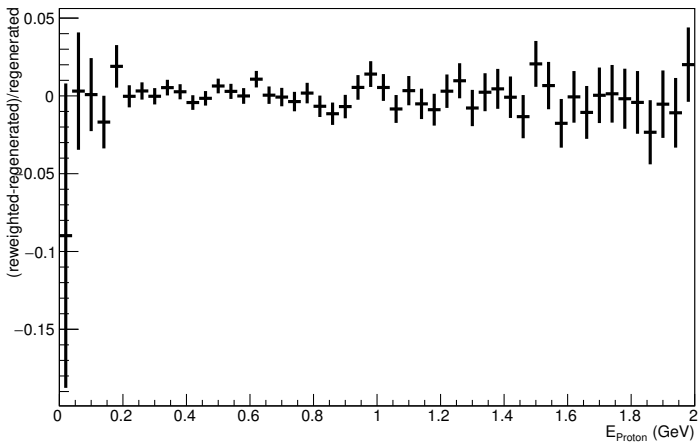

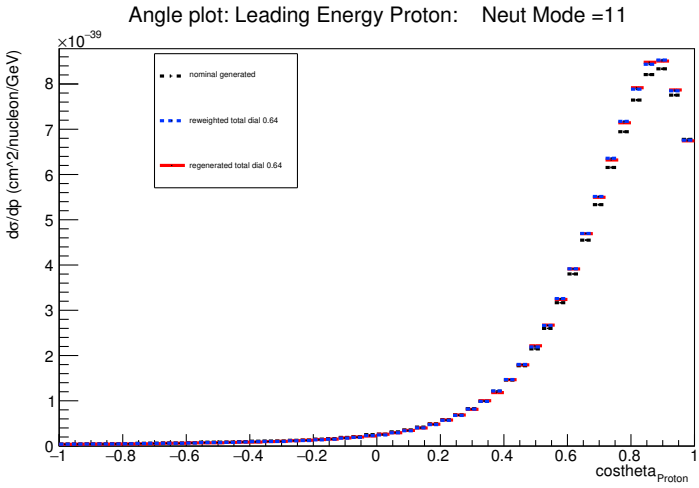
Angle plot: Leading Energy Proton: Neut Mode =11
nominal generated
reweighted total dial 0.64
regenerated total dial 0.64
dσ/dp (cm^2/nucleon/GeV)
costheta_Proton

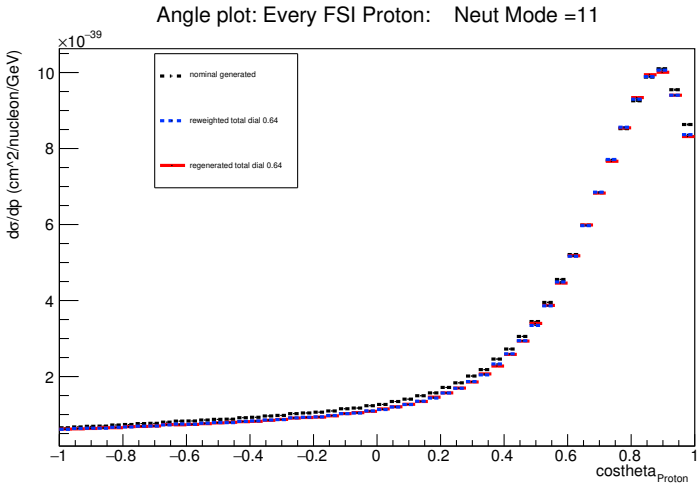
Angle plot: Every FSI Proton: Neut Mode =11
nominal generated
reweighted total dial 0.64
regenerated total dial 0.64
dσ/dp (cm^2/nucleon/GeV)
costheta_Proton

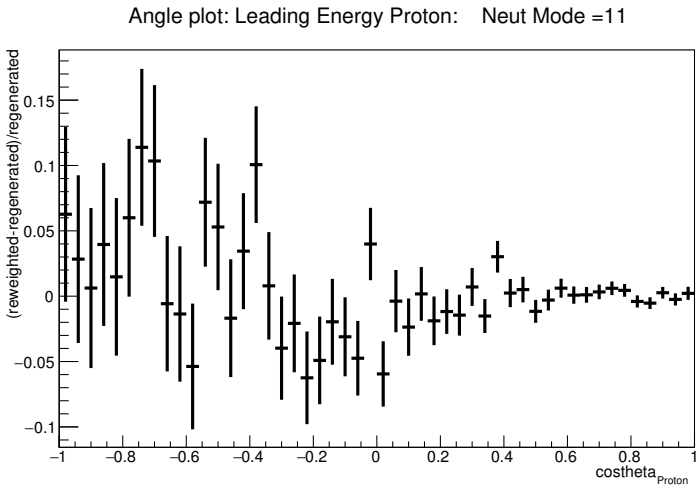
Angle plot: Leading Energy Proton: Neut Mode =11
(reweighted-regenerated)/regenerated
costheta_Proton

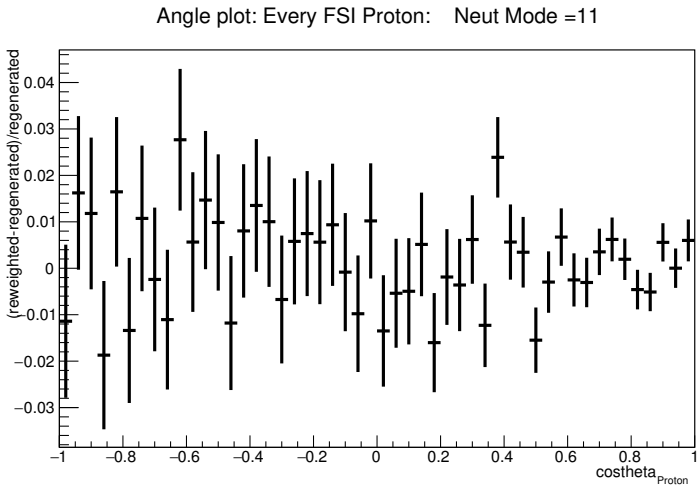
Angle plot: Every FSI Proton: Neut Mode =11
(reweighted-regenerated)/regenerated
costheta_Proton

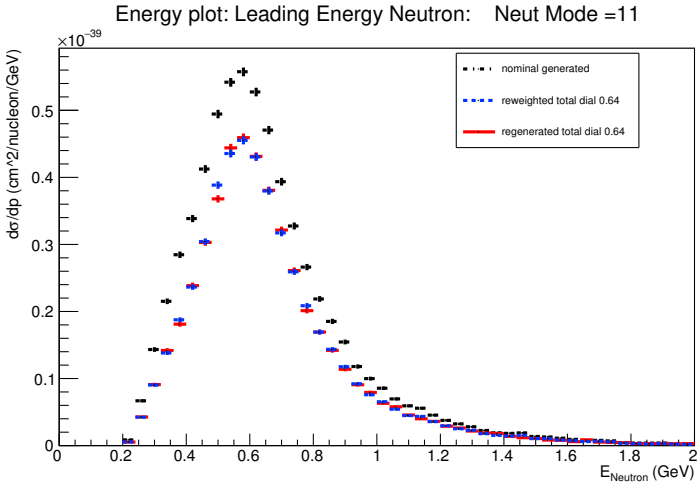
Energy plot: Leading Energy Neutron: Neut Mode =11
nominal generated
reweighted total dial 0.64
regenerated total dial 0.64
dσ/dp (cm^2/nucleon/GeV)
E_Neutron (GeV)

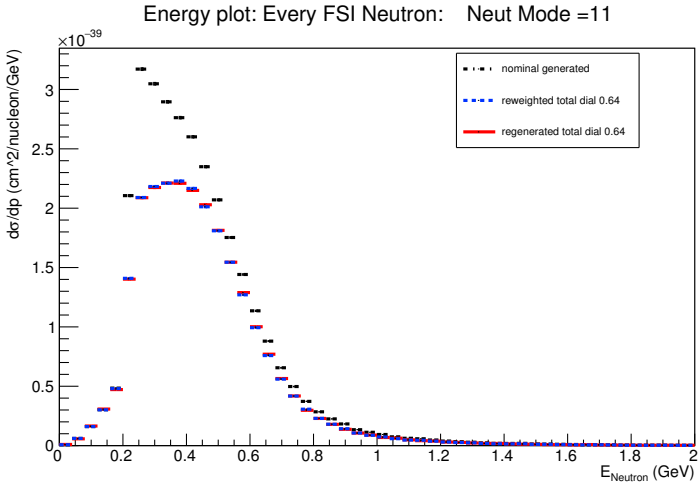
Energy plot: Every FSI Neutron: Neut Mode =11
nominal generated
reweighted total dial 0.64
regenerated total dial 0.64
dσ/dp (cm^2/nucleon/GeV)
E_Neutron (GeV)

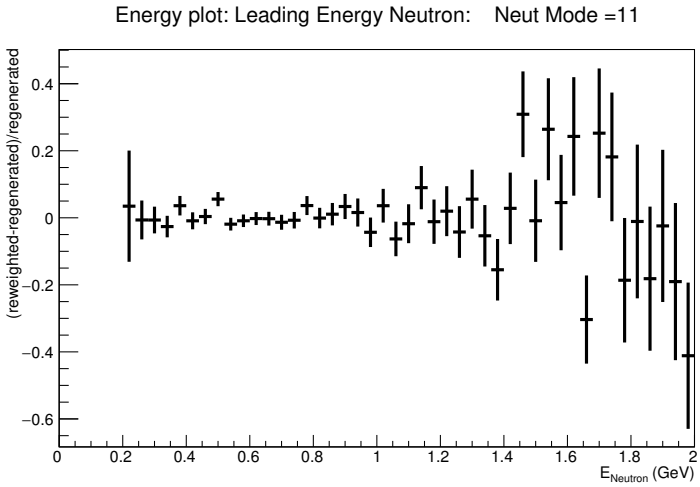
Energy plot: Leading Energy Neutron: Neut Mode =11
(reweighted-regenerated)/regenerated
E_Neutron (GeV)

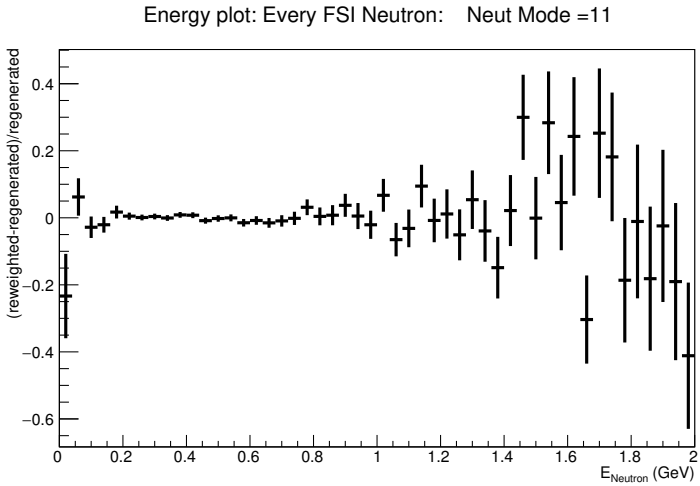
Energy plot: Every FSI Neutron: Neut Mode =11
(reweighted-regenerated)/regenerated
E_Neutron (GeV)

Angle plot: Leading Energy Neutron: Neut Mode =11

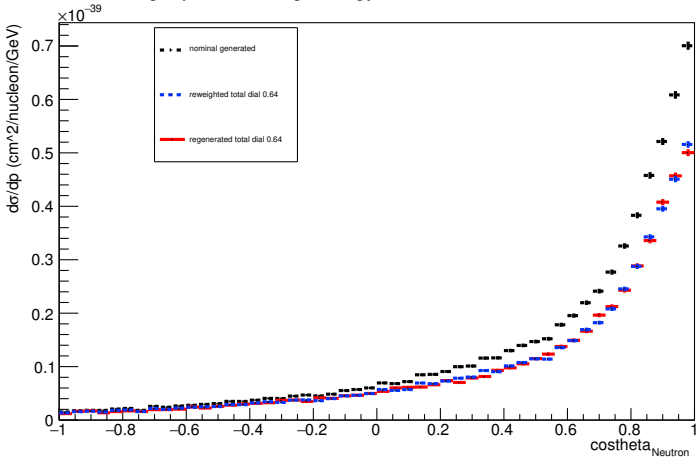

Angle plot: Every FSI Neutron: Neut Mode =11

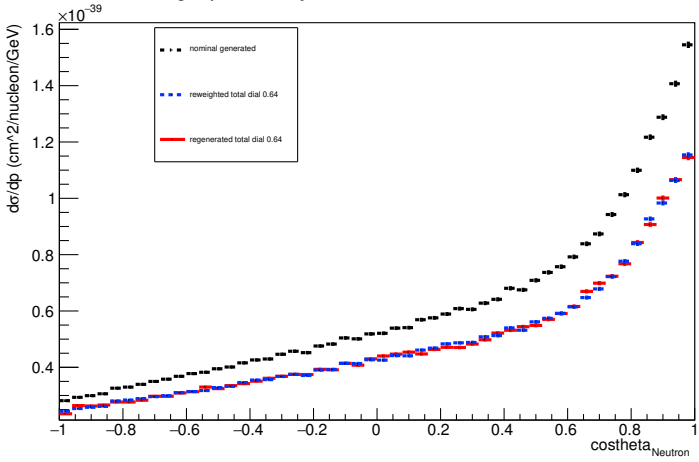

Angle plot: Leading Energy Neutron: Neut Mode =11

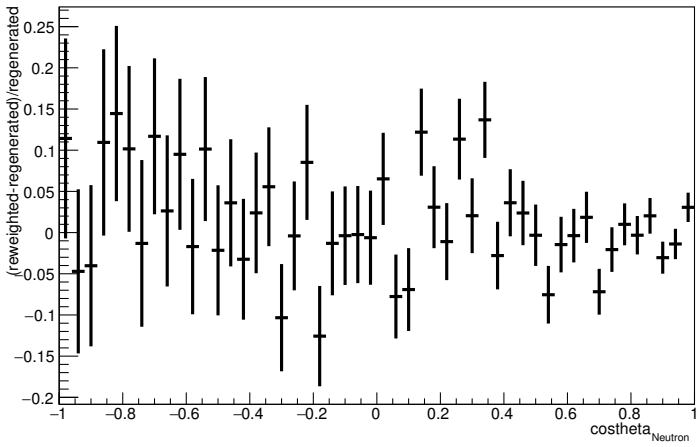

Angle plot: Every FSI Neutron: Neut Mode =11

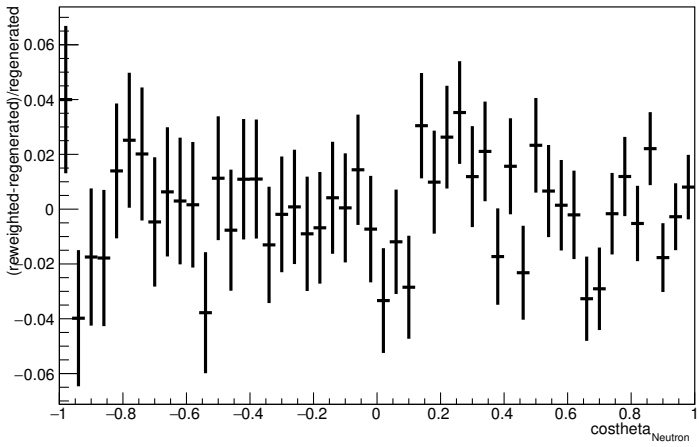

Energy plot: Leading Energy Lepton: Neut Mode =11

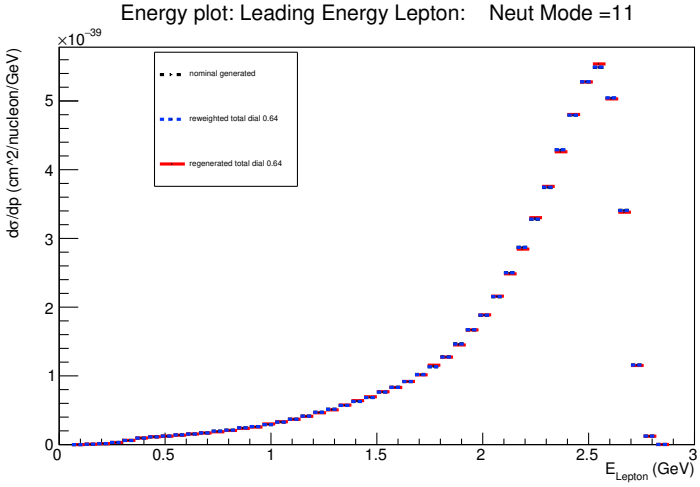

Angle plot: Leading Energy Lepton: Neut Mode =11

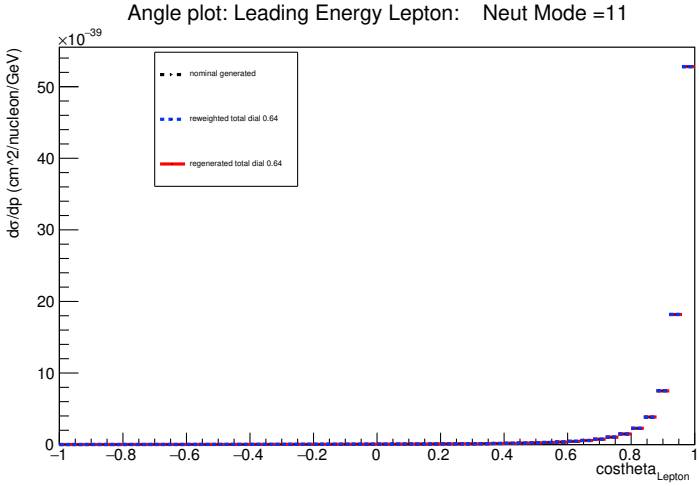

Energy plot: Leading Energy Lepton: Neut Mode =11

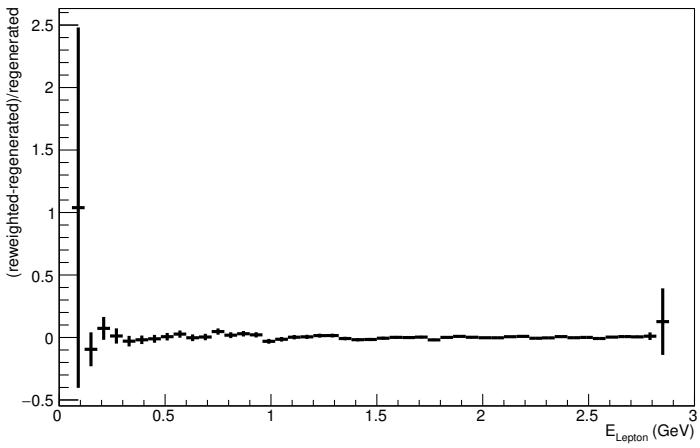

Angle plot: Leading Energy Lepton: Neut Mode =11

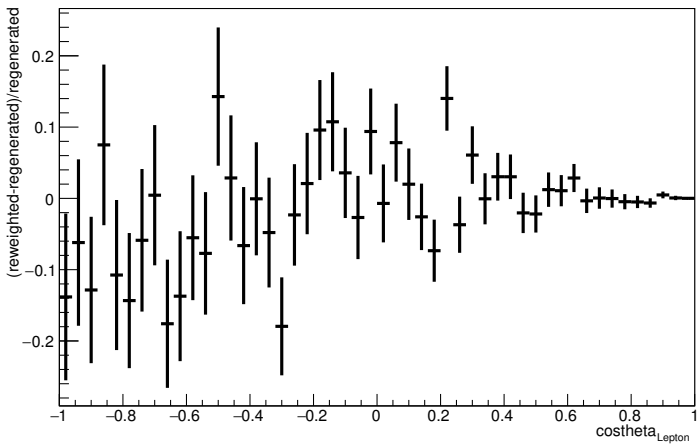

Energy plot: Leading Energy Pion: Neut Mode =11

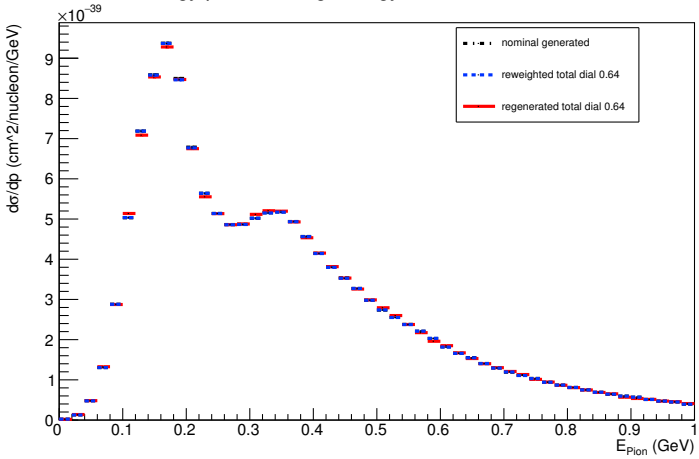

Energy plot: Every FSI Pion: Neut Mode =11

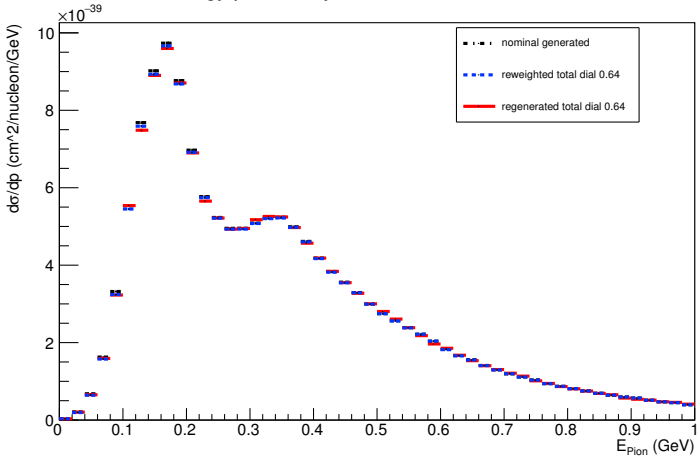

Energy plot: Leading Energy Pion: Neut Mode =11

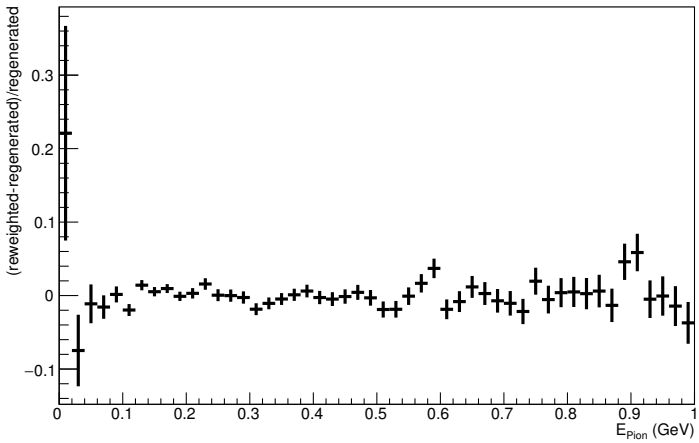

Energy plot: Every FSI Pion: Neut Mode =11

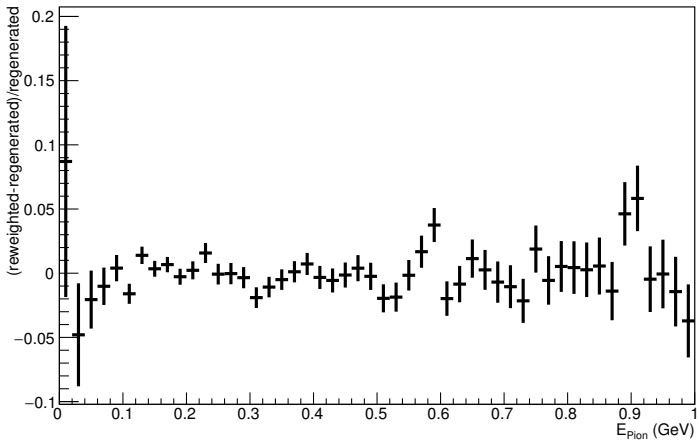

Angle plot: Leading Energy Pion: Neut Mode =11

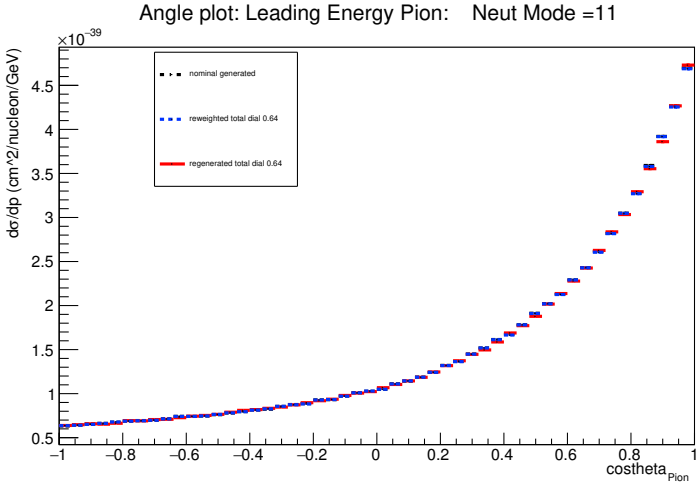

Angle plot: Every FSI Pion: Neut Mode =11

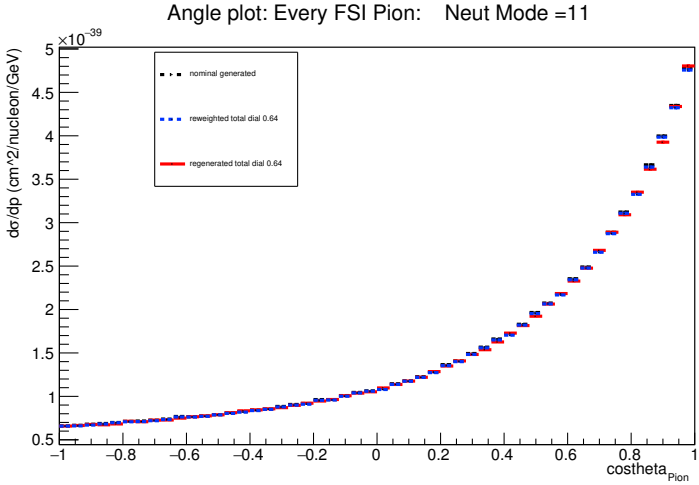

Angle plot: Leading Energy Pion: Neut Mode =11

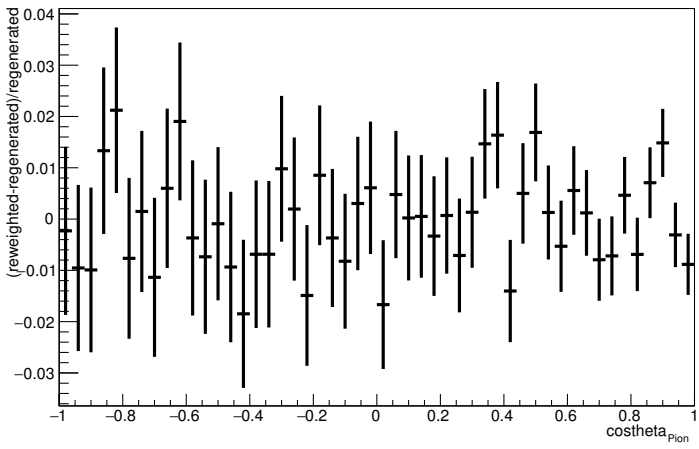

Angle plot: Every FSI Pion: Neut Mode =11

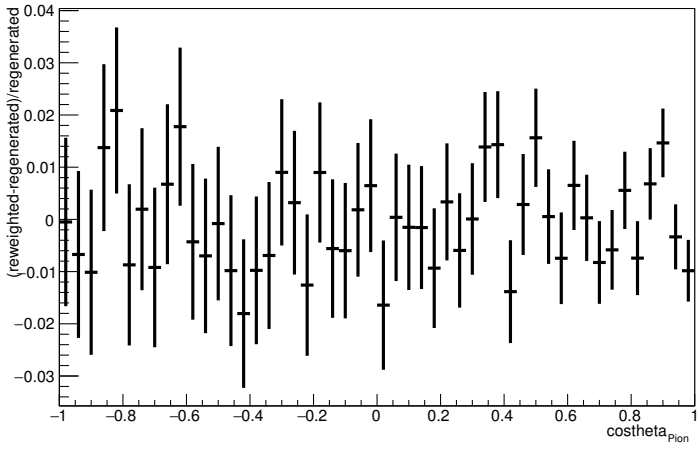

A.3. Elastic Dial: varied up to 1.44

Energy plot: Leading Energy Nucleon: Neut Mode =AllModesCombined

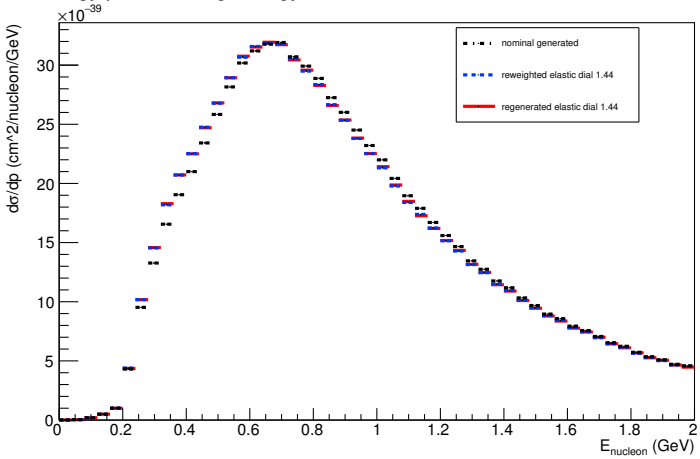

Energy plot: Every FSI Nucleon: Neut Mode =AllModesCombined

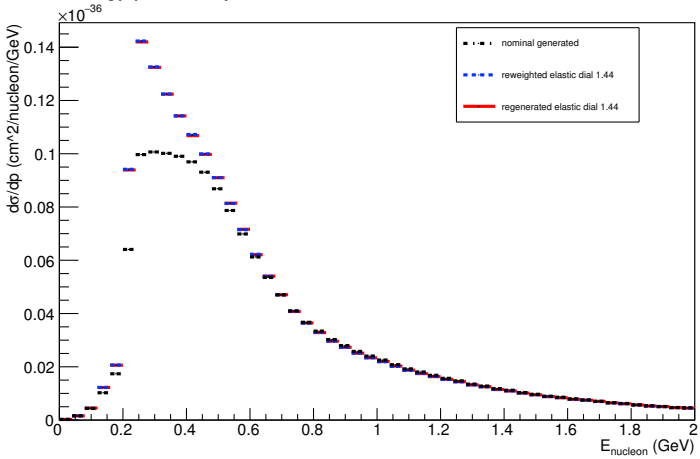

Energy plot: Leading Energy Nucleon: Neut Mode =AllModesCombined

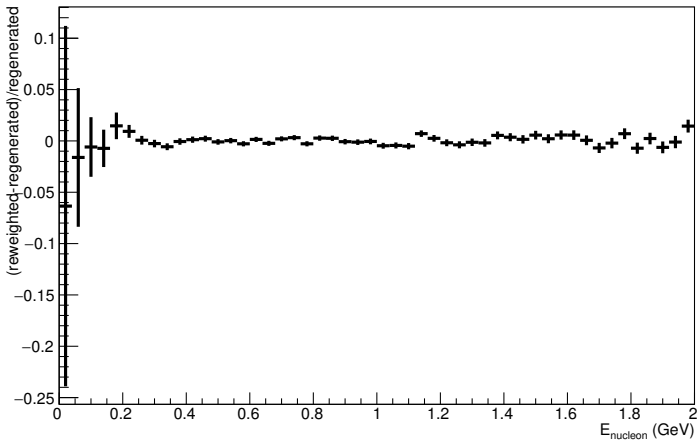

Energy plot: Every FSI Nucleon: Neut Mode =AllModesCombined

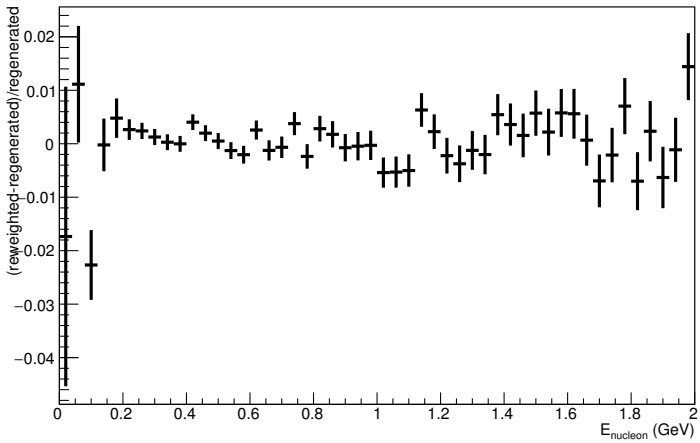

Angle plot: Leading Energy Nucleon: Neut Mode =AllModesCombined

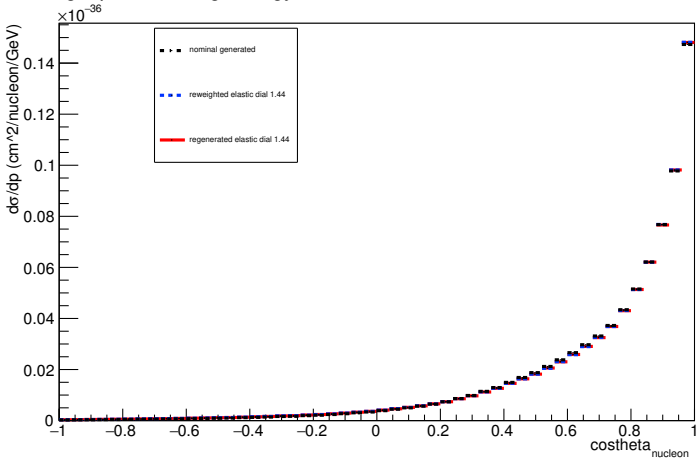

Angle plot: Every FSI Nucleon: Neut Mode =AllModesCombined

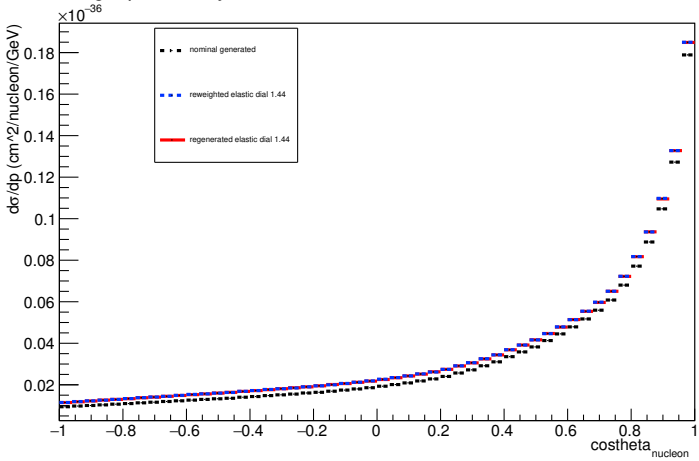

Angle plot: Leading Energy Nucleon: Neut Mode =AllModesCombined

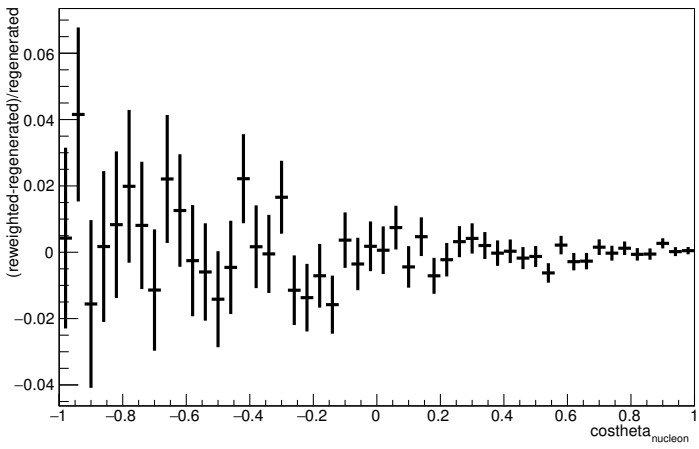

Angle plot: Every FSI Nucleon: Neut Mode =AllModesCombined

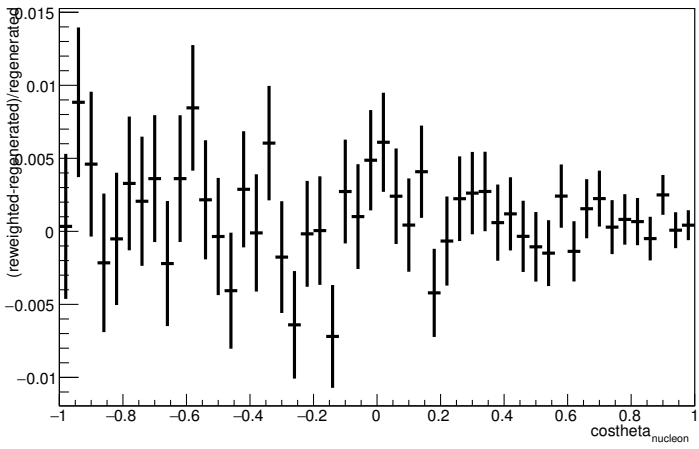

Energy plot: Leading Energy Proton: Neut Mode =AllModesCombined

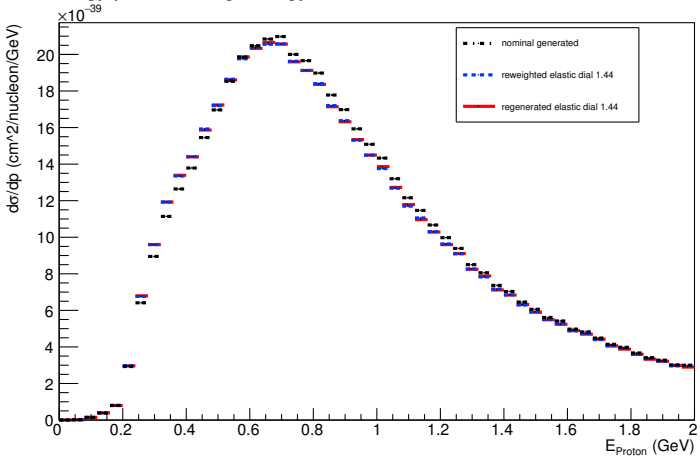

Energy plot: Every FSI Proton: Neut Mode =AllModesCombined

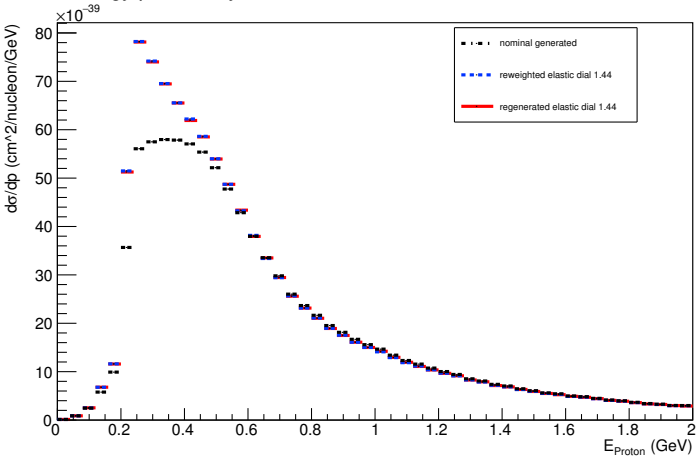

Energy plot: Leading Energy Proton: Neut Mode =AllModesCombined

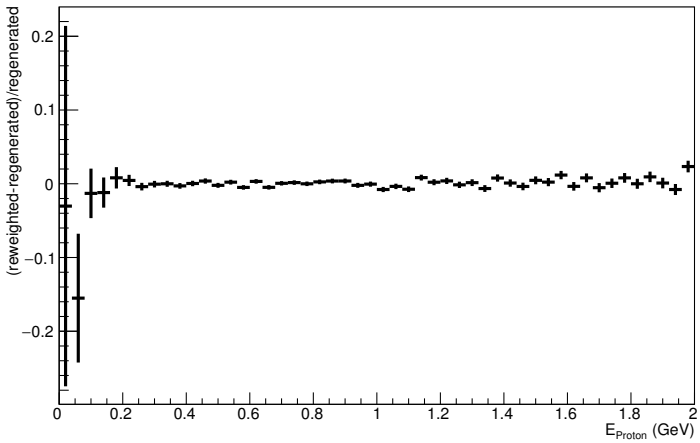

Energy plot: Every FSI Proton: Neut Mode =AllModesCombined

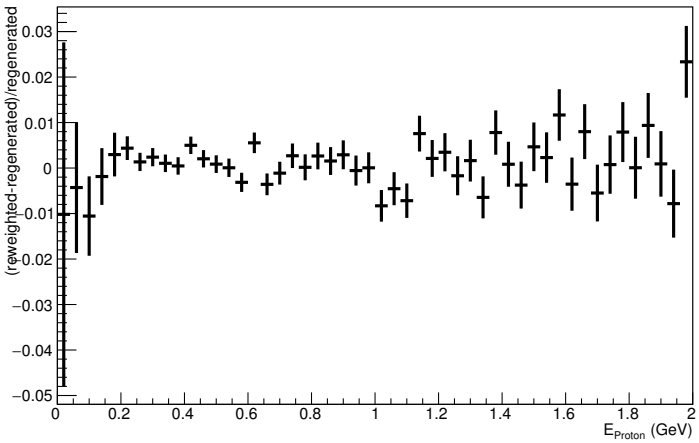

Angle plot: Leading Energy Proton: Neut Mode =AllModesCombined

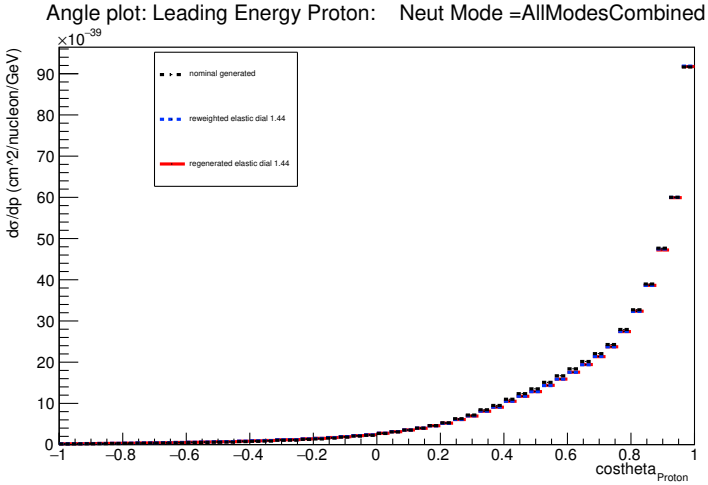

Angle plot: Every FSI Proton: Neut Mode =AllModesCombined

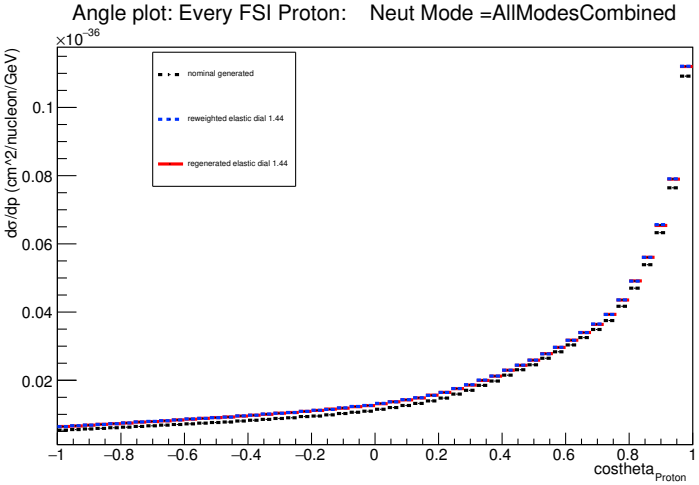

Angle plot: Leading Energy Proton: Neut Mode =AllModesCombined

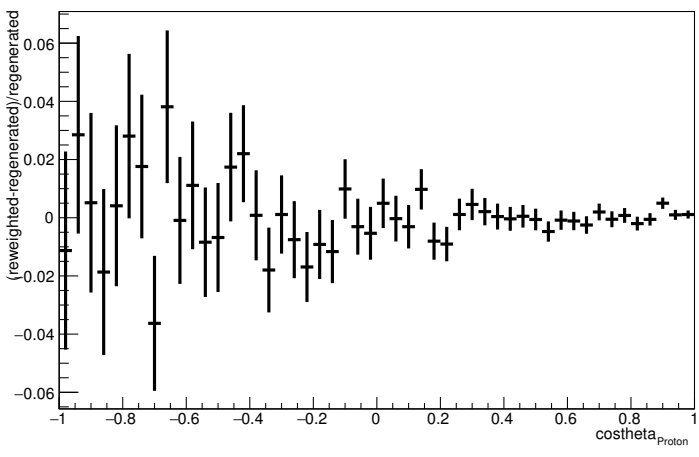

Angle plot: Every FSI Proton: Neut Mode =AllModesCombined

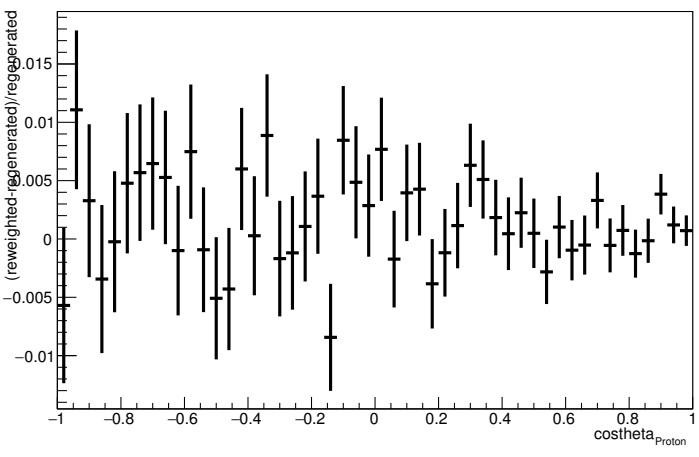

Energy plot: Leading Energy Neutron: Neut Mode =AllModesCombined

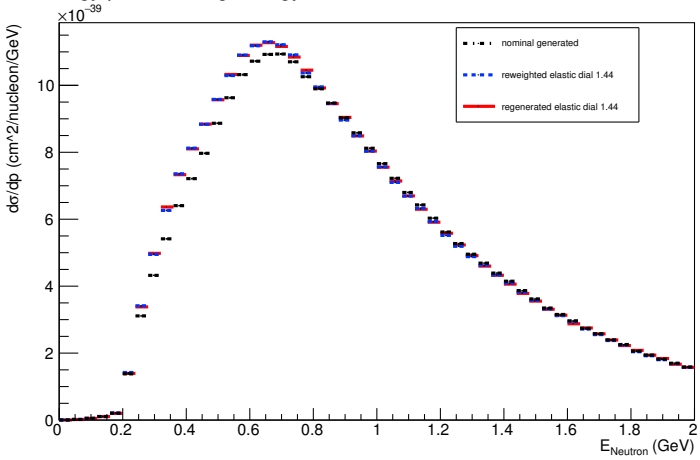

Energy plot: Every FSI Neutron: Neut Mode =AllModesCombined

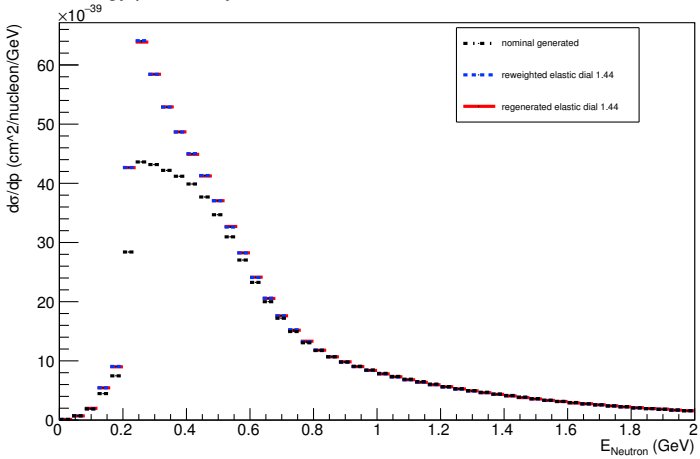

Energy plot: Leading Energy Neutron: Neut Mode =AllModesCombined

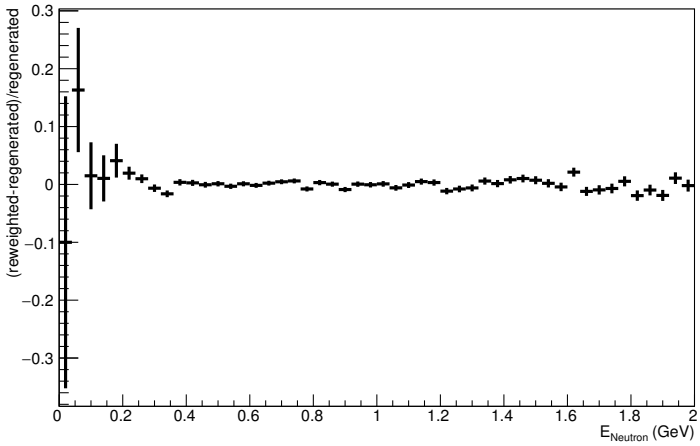

Energy plot: Every FSI Neutron: Neut Mode =AllModesCombined

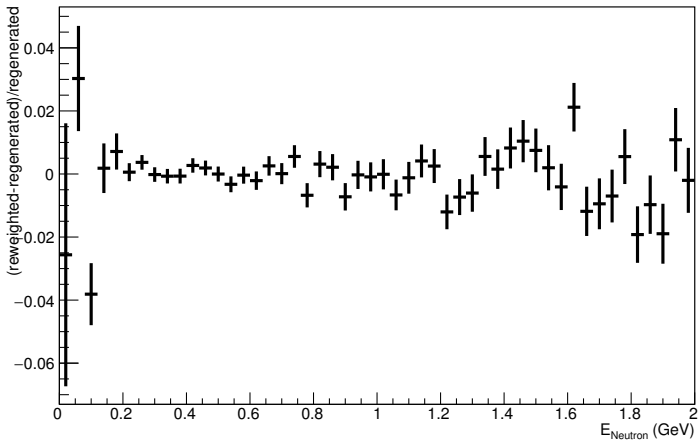

Angle plot: Leading Energy Neutron: Neut Mode =AllModesCombined

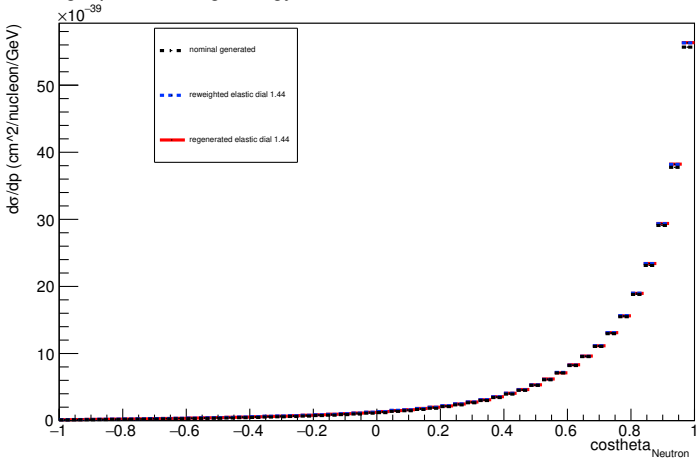

Angle plot: Every FSI Neutron: Neut Mode =AllModesCombined

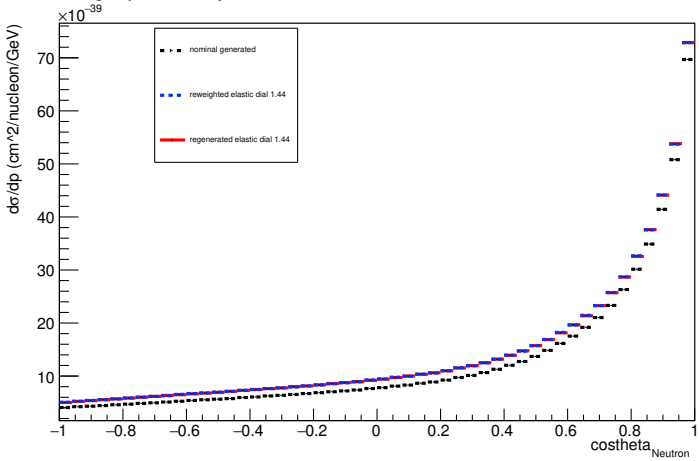

Angle plot: Leading Energy Neutron: Neut Mode =AllModesCombined

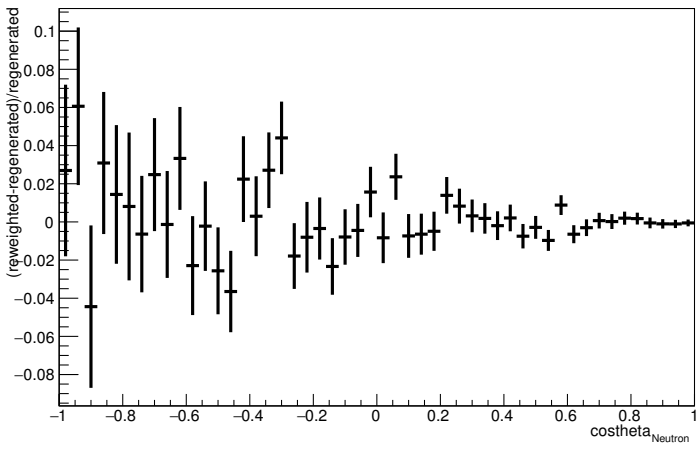

Angle plot: Every FSI Neutron: Neut Mode =AllModesCombined

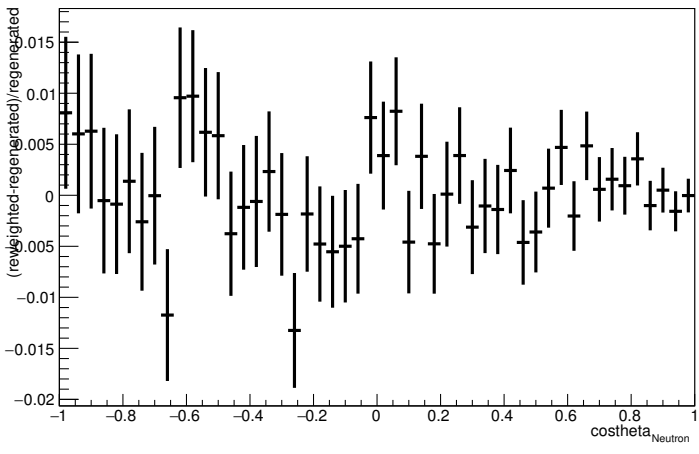

Energy plot: Leading Energy Lepton: Neut Mode =AllModesCombined

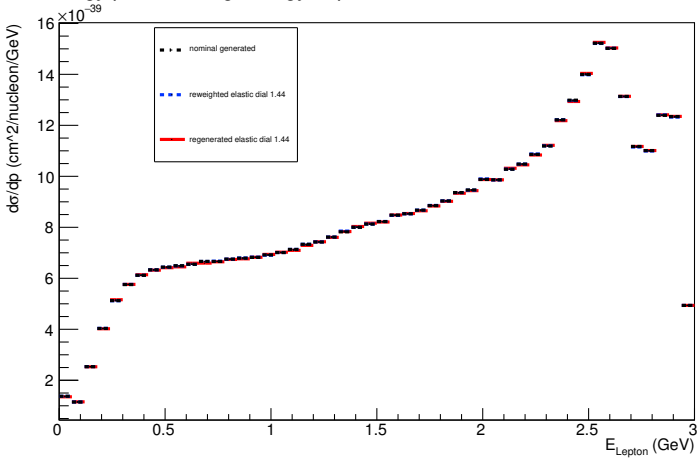

Angle plot: Leading Energy Lepton: Neut Mode =AllModesCombined

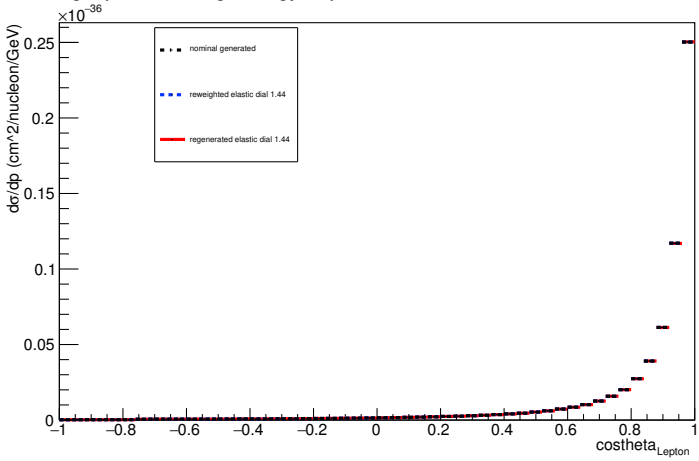

Energy plot: Leading Energy Lepton: Neut Mode =AllModesCombined

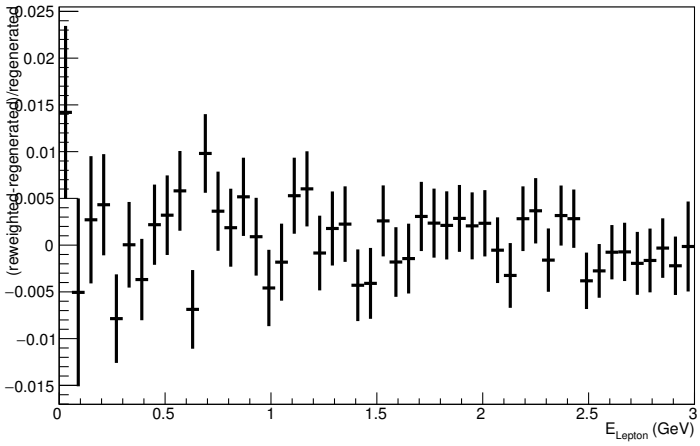

Angle plot: Leading Energy Lepton: Neut Mode =AllModesCombined

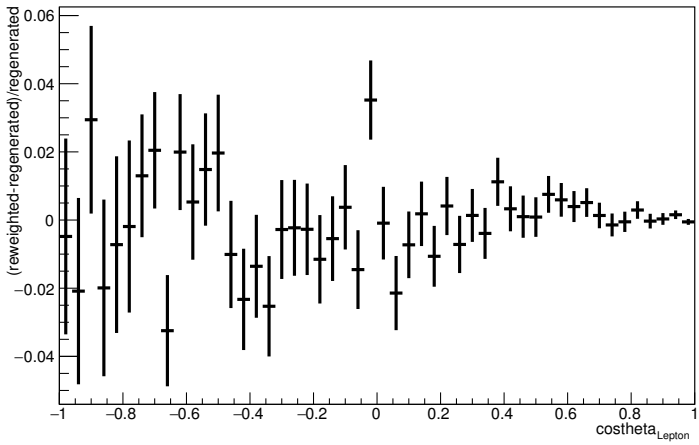

Energy plot: Leading Energy Pion: Neut Mode =AllModesCombined

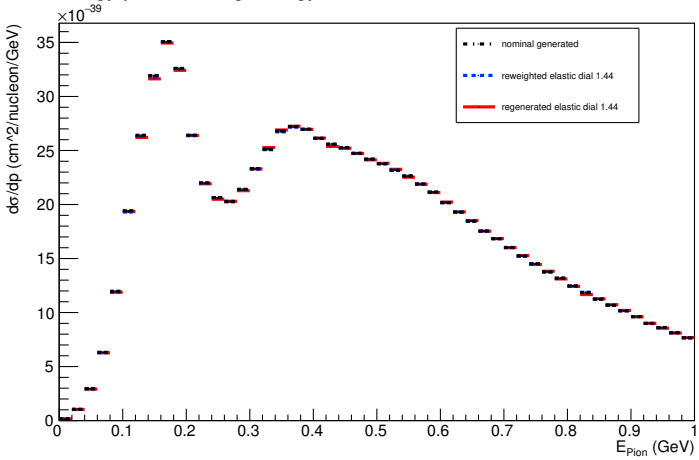

Energy plot: Every FSI Pion: Neut Mode =AllModesCombined

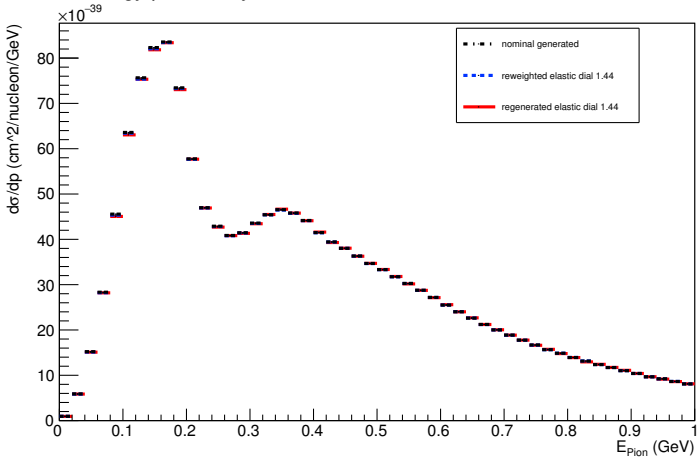

Energy plot: Leading Energy Pion: Neut Mode =AllModesCombined

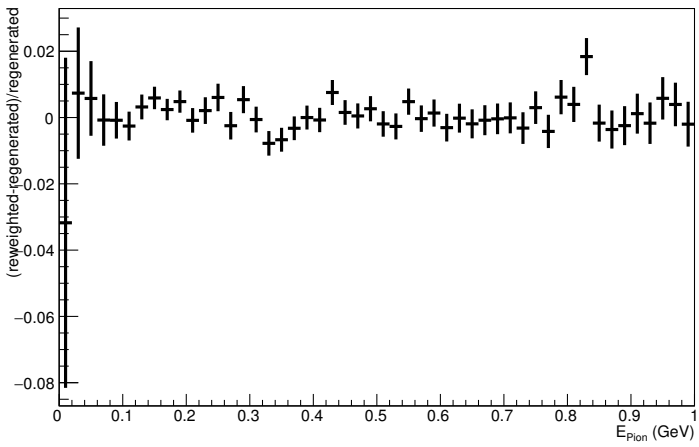

Energy plot: Every FSI Pion: Neut Mode =AllModesCombined

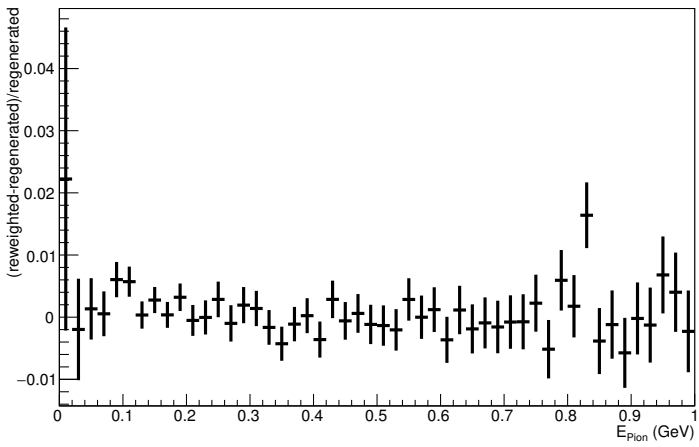

Angle plot: Leading Energy Pion: Neut Mode =AllModesCombined

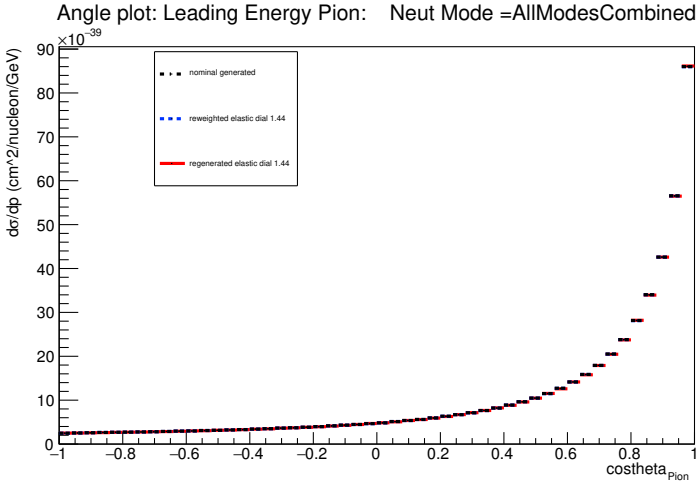

Angle plot: Every FSI Pion: Neut Mode =AllModesCombined

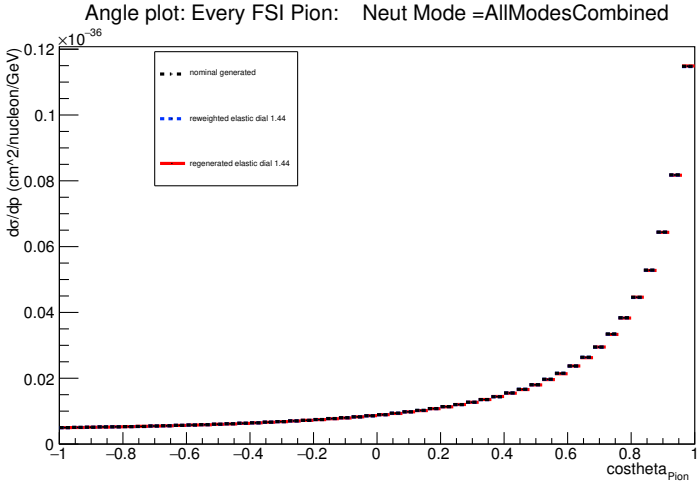

Angle plot: Leading Energy Pion: Neut Mode =AllModesCombined

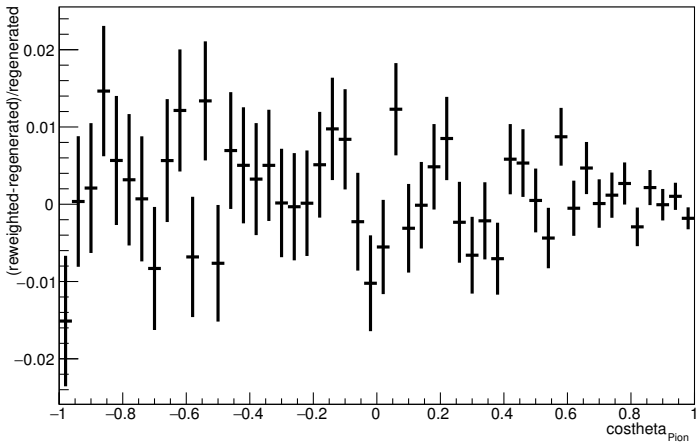

Angle plot: Every FSI Pion: Neut Mode =AllModesCombined

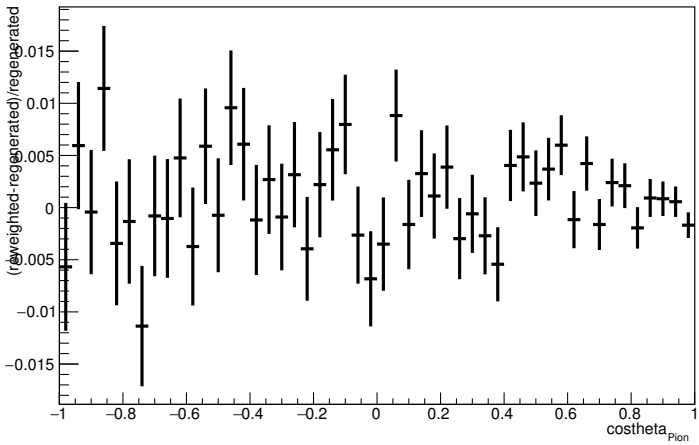

Energy plot: Leading Energy Nucleon: Neut Mode =1

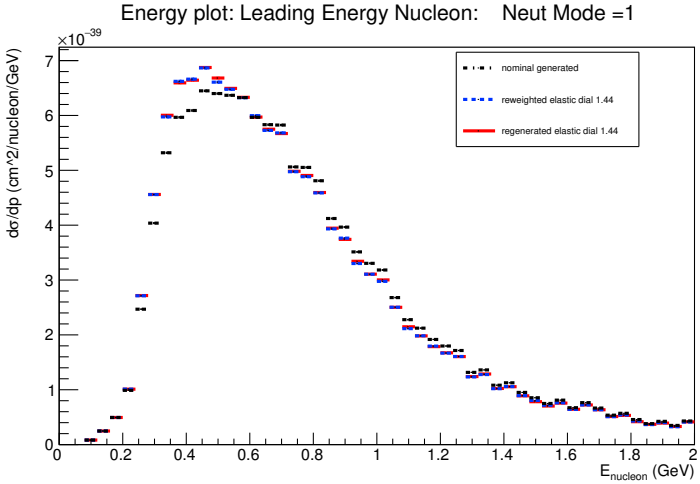

Energy plot: Every FSI Nucleon: Neut Mode =1

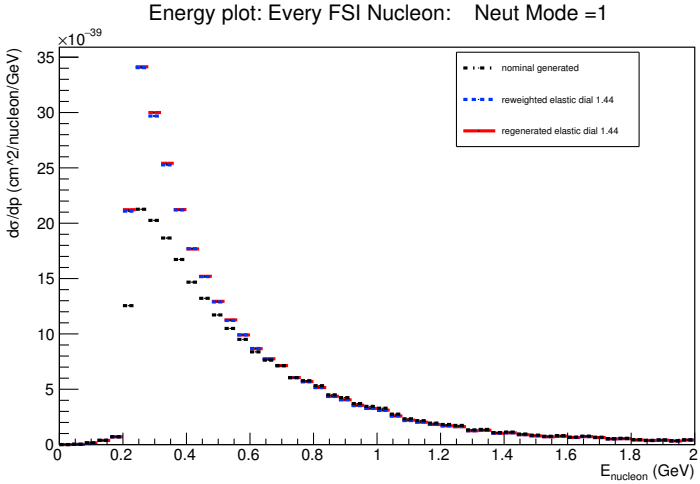

Energy plot: Leading Energy Nucleon: Neut Mode =1

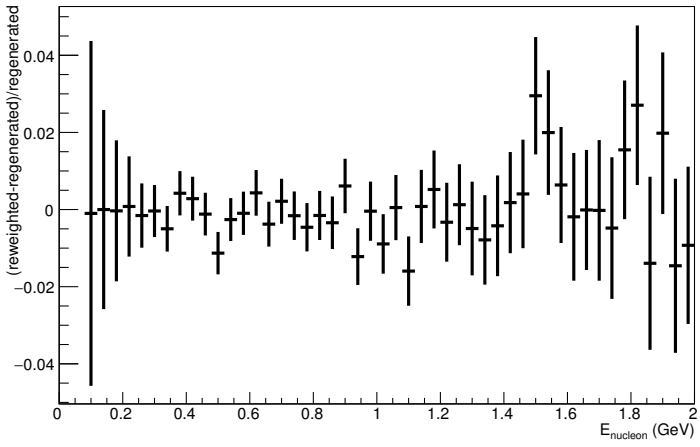

Energy plot: Every FSI Nucleon: Neut Mode =1

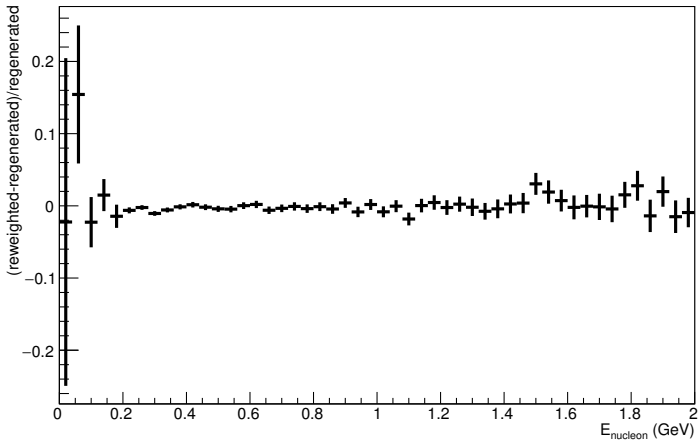

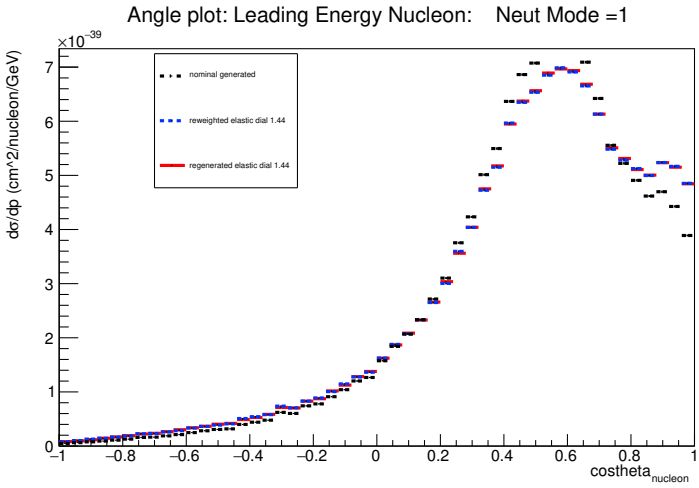
Angle plot: Leading Energy Nucleon: Neut Mode =1
nominal generated
reweighted elastic dial 1.44
regenerated elastic dial 1.44
dσ/dp (cm^2/nucleon/GeV)
costheta_nucleon

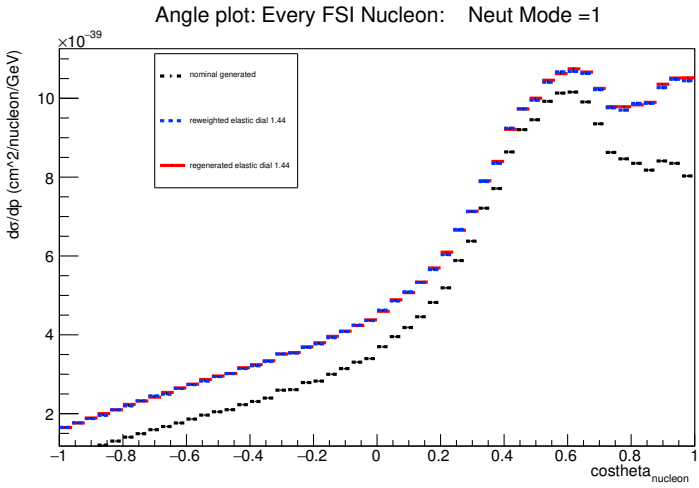
Angle plot: Every FSI Nucleon: Neut Mode =1
nominal generated
reweighted elastic dial 1.44
regenerated elastic dial 1.44
dσ/dp (cm^2/nucleon/GeV)
costheta_nucleon

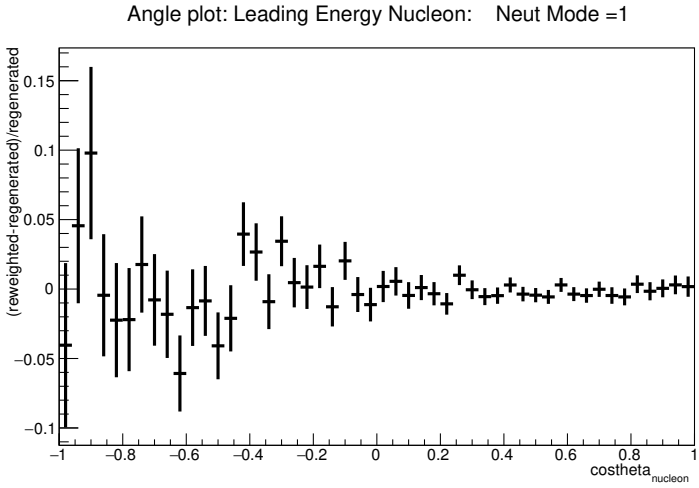
Angle plot: Leading Energy Nucleon: Neut Mode =1
(reweighted-regenerated)/regenerated
costheta_nucleon

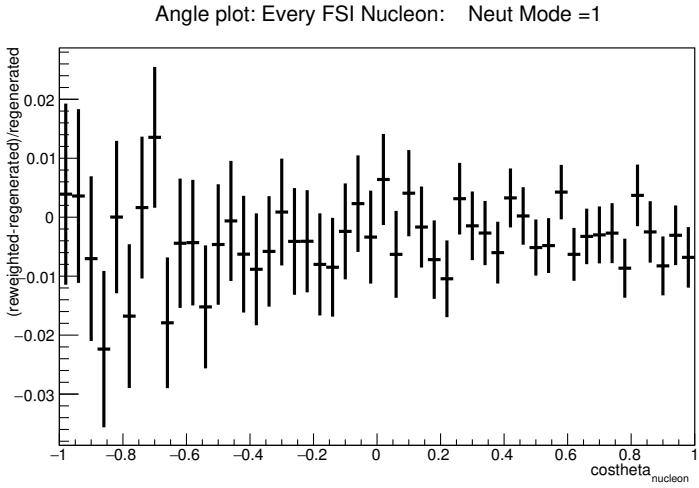
Angle plot: Every FSI Nucleon: Neut Mode =1
(reweighted-regenerated)/regenerated
costheta_nucleon

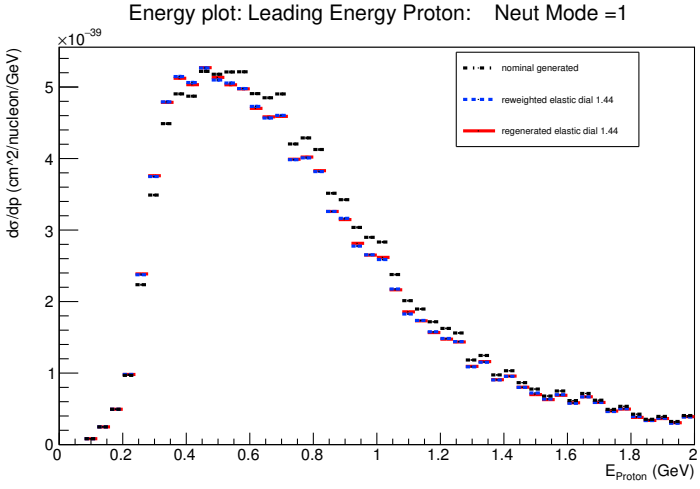
Energy plot: Leading Energy Proton: Neut Mode =1
nominal generated
reweighted elastic dial 1.44
regenerated elastic dial 1.44
dσ/dp (cm^2/nucleon/GeV)
E_Proton (GeV)

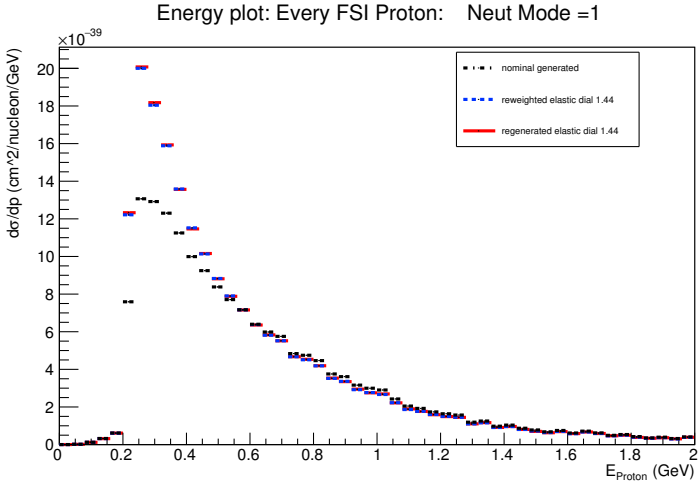
Energy plot: Every FSI Proton: Neut Mode =1
nominal generated
reweighted elastic dial 1.44
regenerated elastic dial 1.44
dσ/dp (cm^2/nucleon/GeV)
E_Proton (GeV)

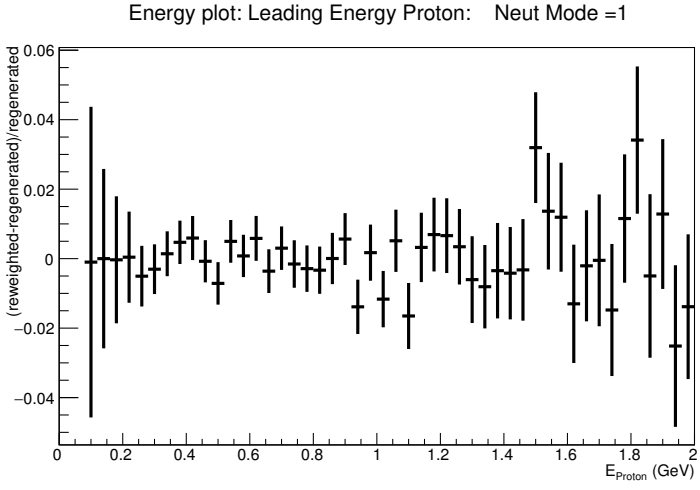
Energy plot: Leading Energy Proton: Neut Mode =1
(reweighted-regenerated)/regenerated
E_Proton (GeV)

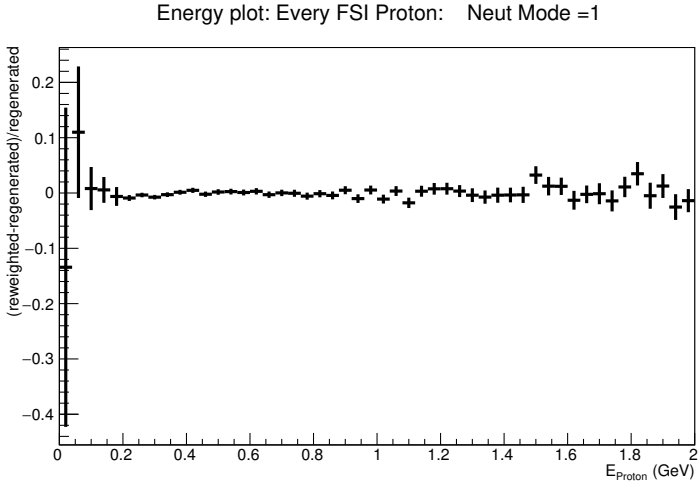
Energy plot: Every FSI Proton: Neut Mode =1
(reweighted-regenerated)/regenerated
E_Proton (GeV)

Angle plot: Leading Energy Proton: Neut Mode =1

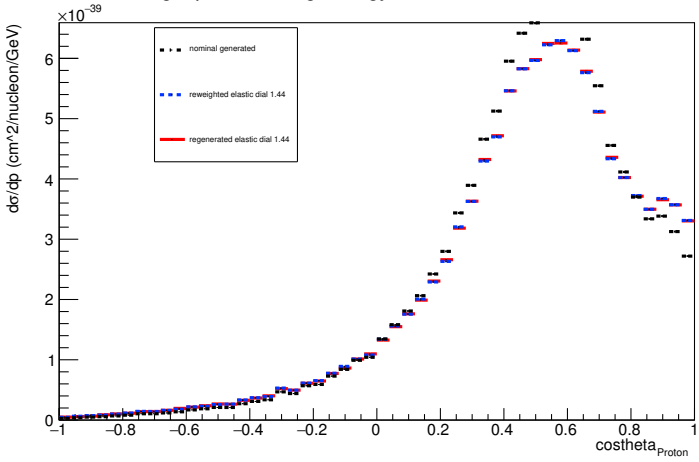

Angle plot: Every FSI Proton: Neut Mode =1

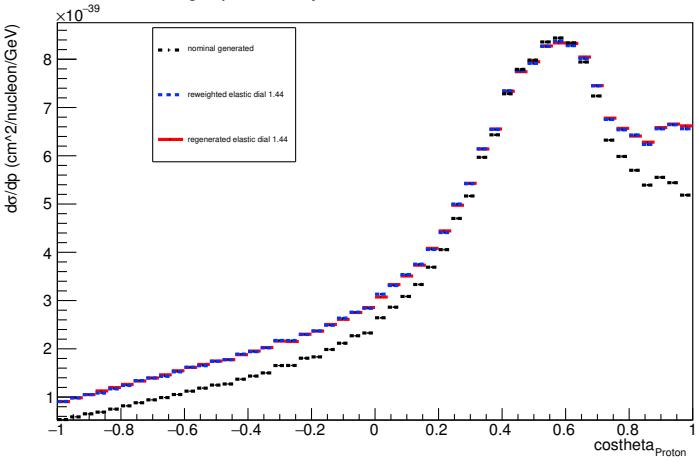

Angle plot: Leading Energy Proton: Neut Mode =1

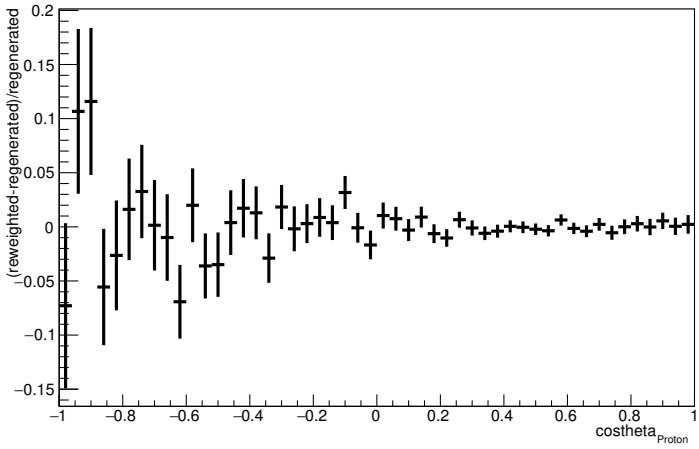

Angle plot: Every FSI Proton: Neut Mode =1

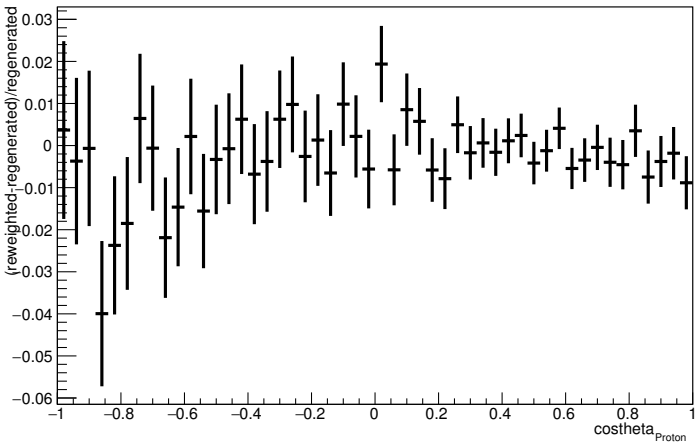

Energy plot: Leading Energy Neutron: Neut Mode =1

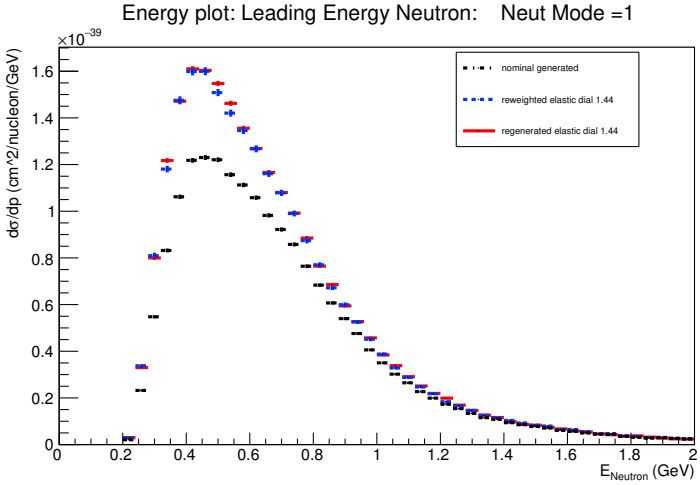

Energy plot: Every FSI Neutron: Neut Mode =1

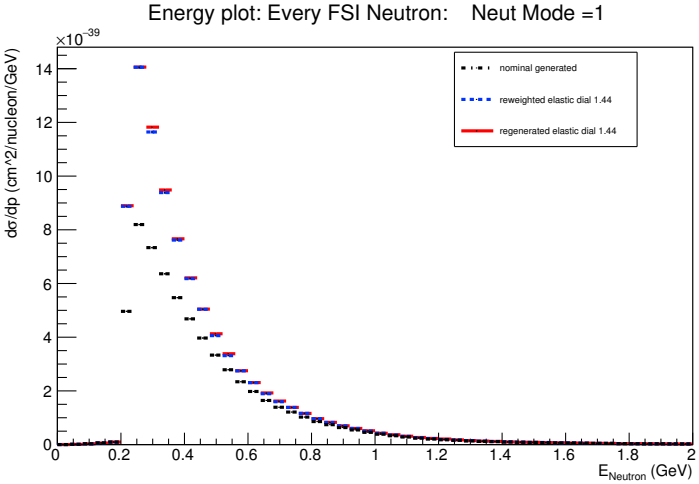

Energy plot: Leading Energy Neutron: Neut Mode =1

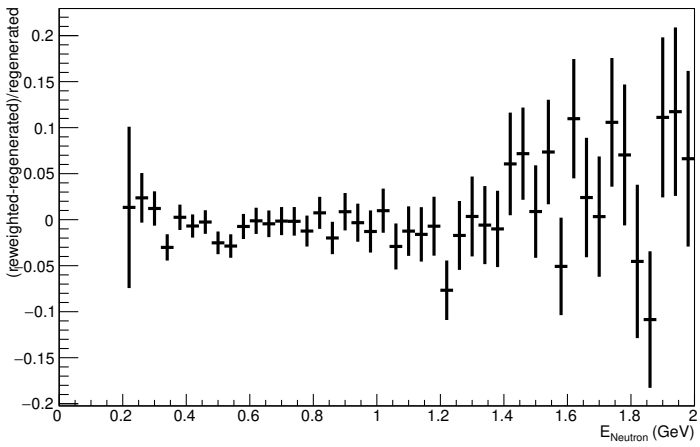

Energy plot: Every FSI Neutron: Neut Mode =1

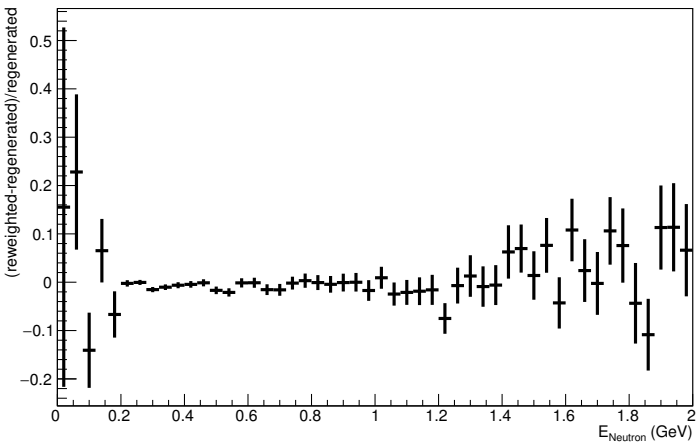

Angle plot: Leading Energy Neutron: Neut Mode =1

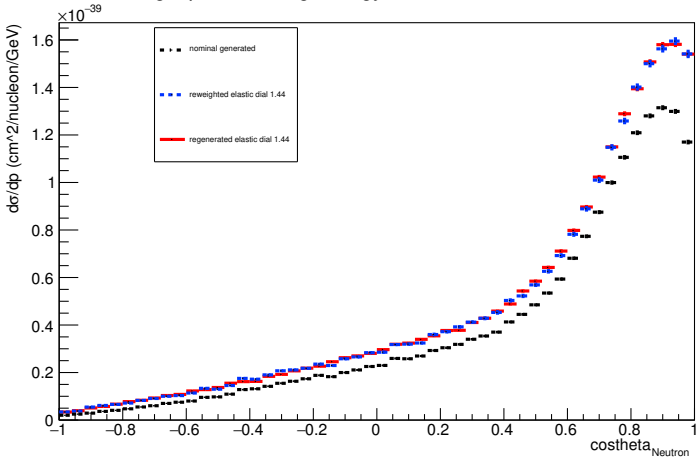

Angle plot: Every FSI Neutron: Neut Mode =1

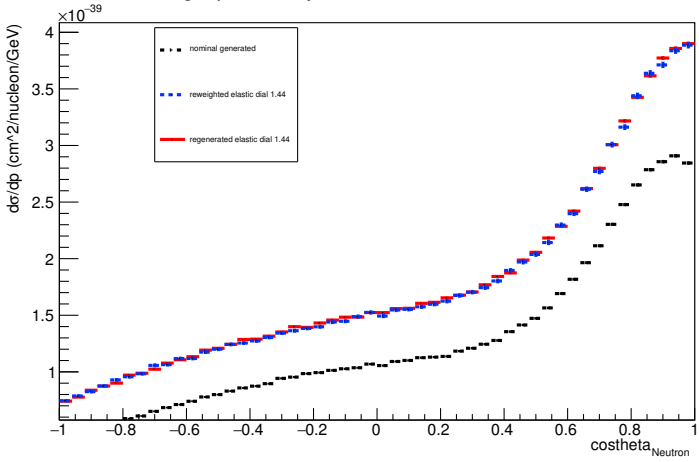

Angle plot: Leading Energy Neutron: Neut Mode =1

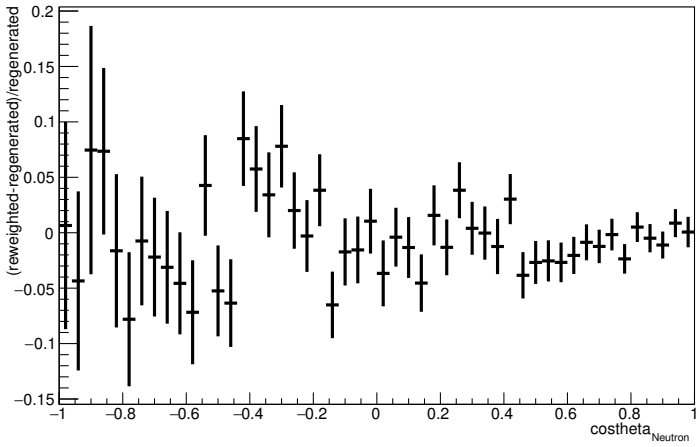

Angle plot: Every FSI Neutron: Neut Mode =1

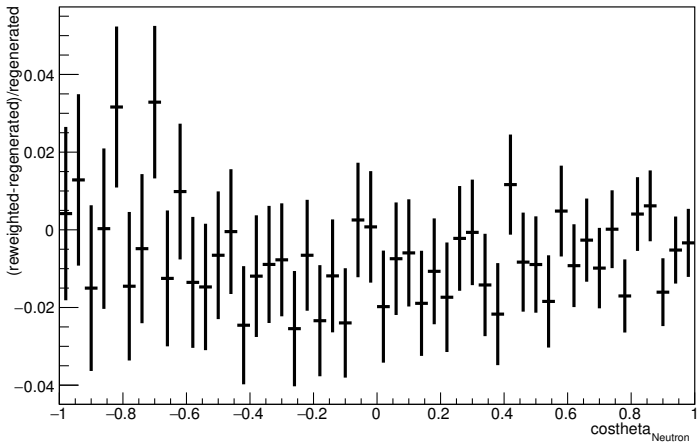

Energy plot: Leading Energy Lepton: Neut Mode =1

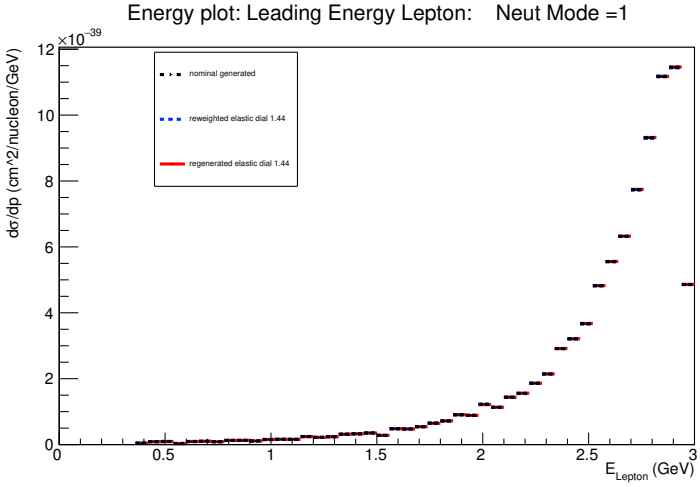

Angle plot: Leading Energy Lepton: Neut Mode =1

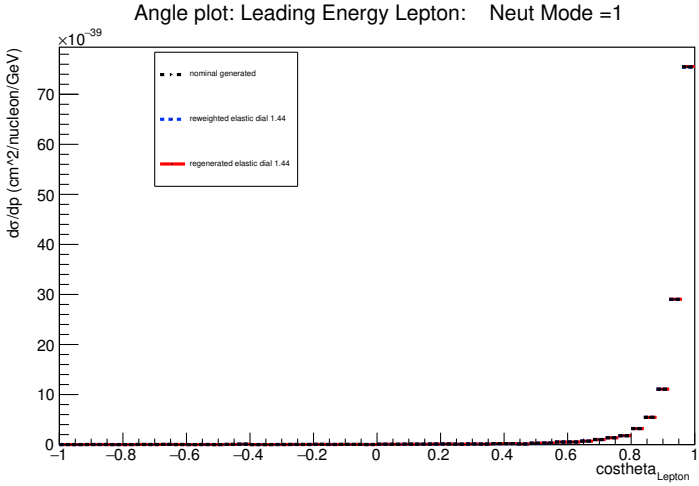

Energy plot: Leading Energy Lepton: Neut Mode =1

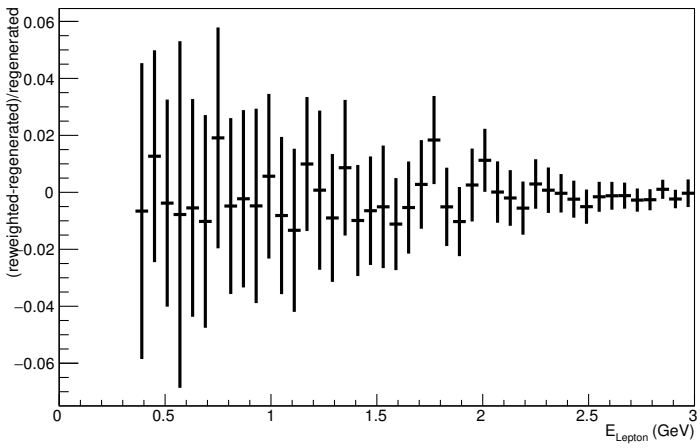

Angle plot: Leading Energy Lepton: Neut Mode =1

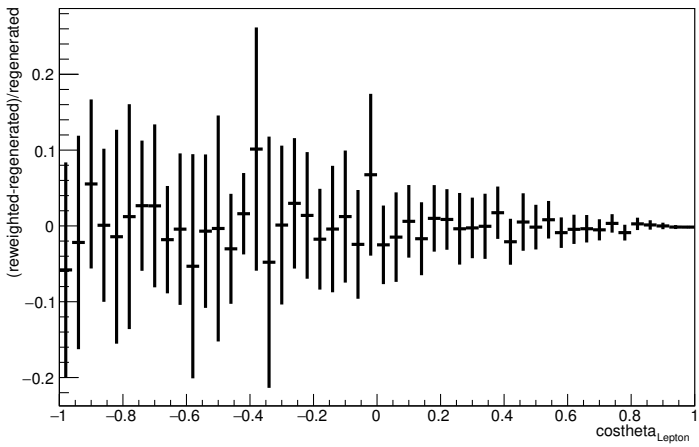

Energy plot: Leading Energy Pion: Neut Mode =1

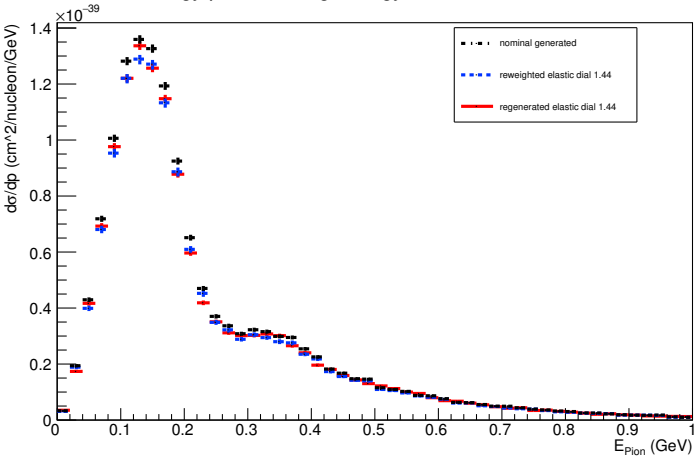

Energy plot: Every FSI Pion: Neut Mode =1

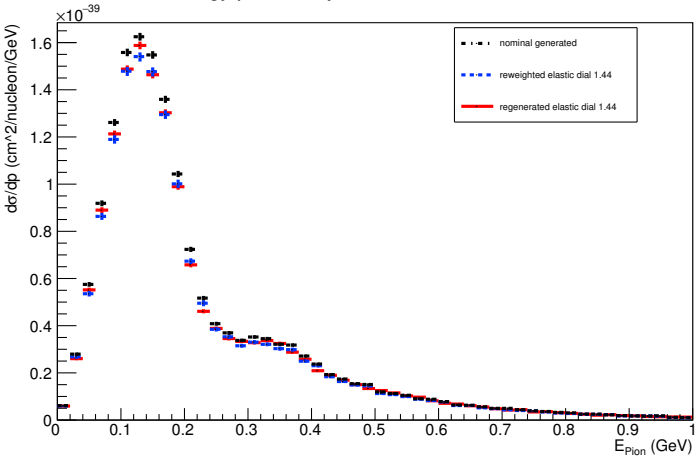

Energy plot: Leading Energy Pion: Neut Mode =1

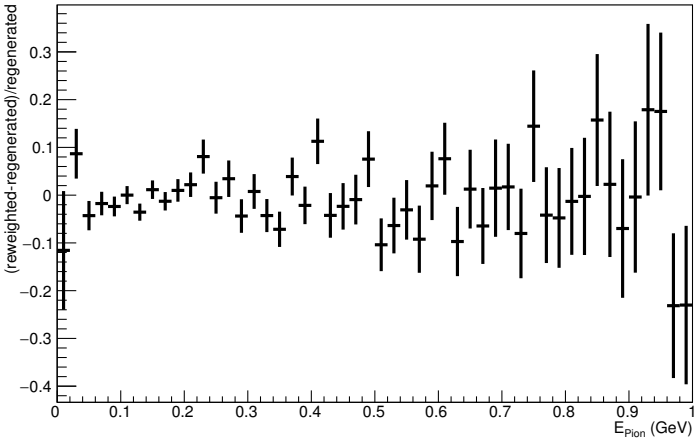

Energy plot: Every FSI Pion: Neut Mode =1

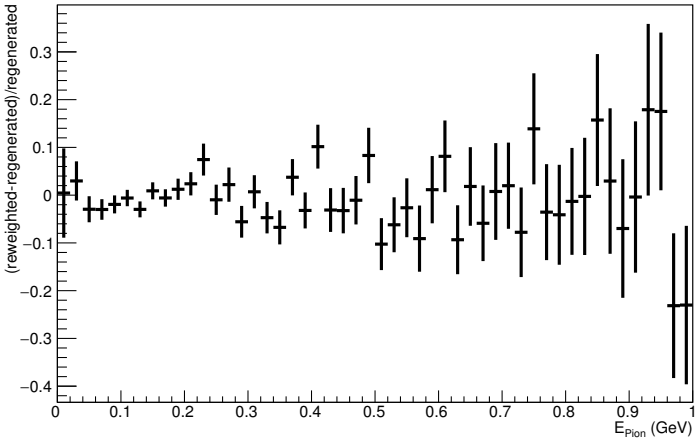

Angle plot: Leading Energy Pion: Neut Mode =1

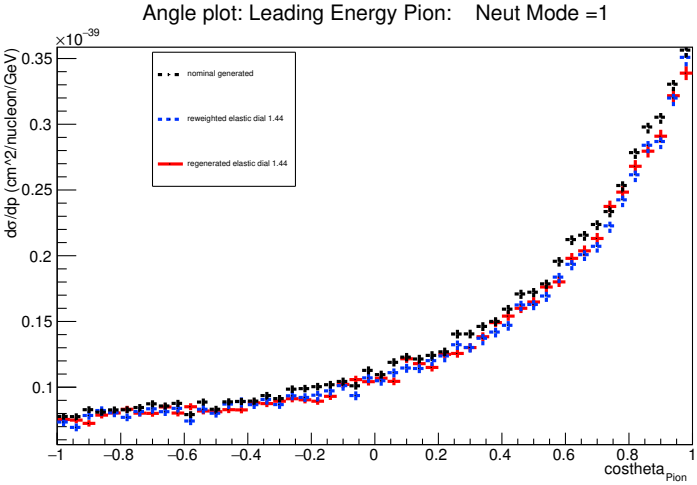

Angle plot: Every FSI Pion: Neut Mode =1

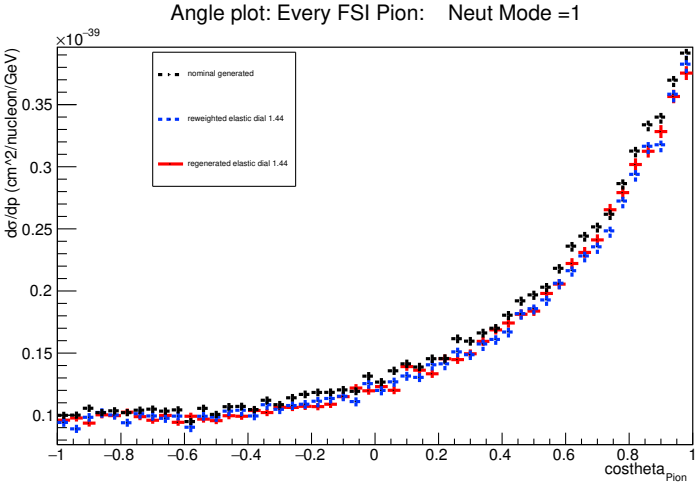

Angle plot: Leading Energy Pion: Neut Mode =1

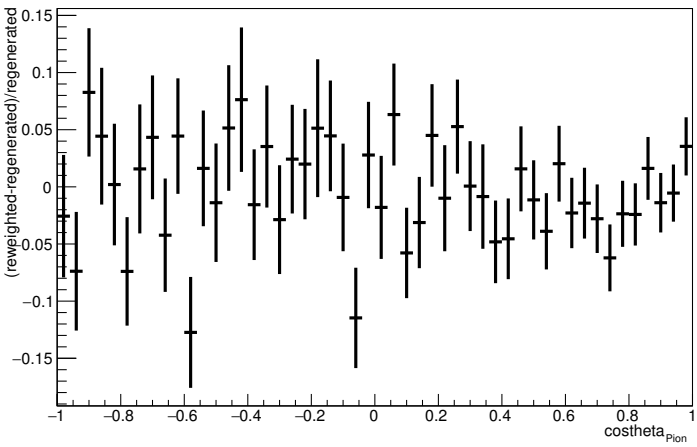

Angle plot: Every FSI Pion: Neut Mode =1

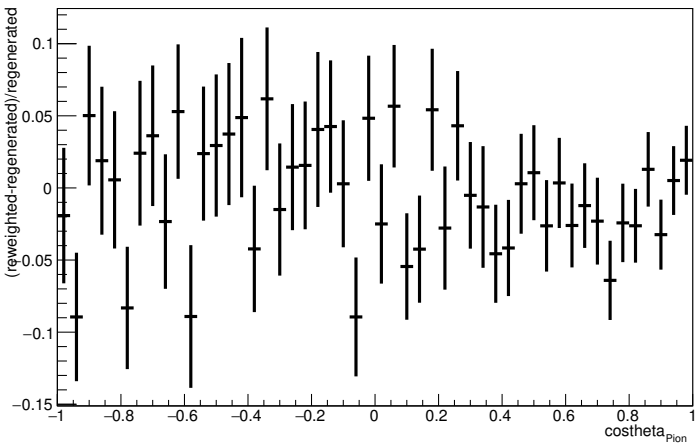

Energy plot: Leading Energy Nucleon: Neut Mode =2

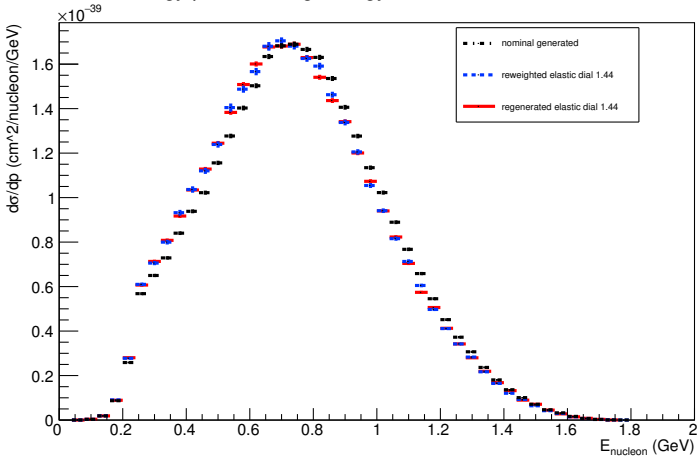

Energy plot: Every FSI Nucleon: Neut Mode =2

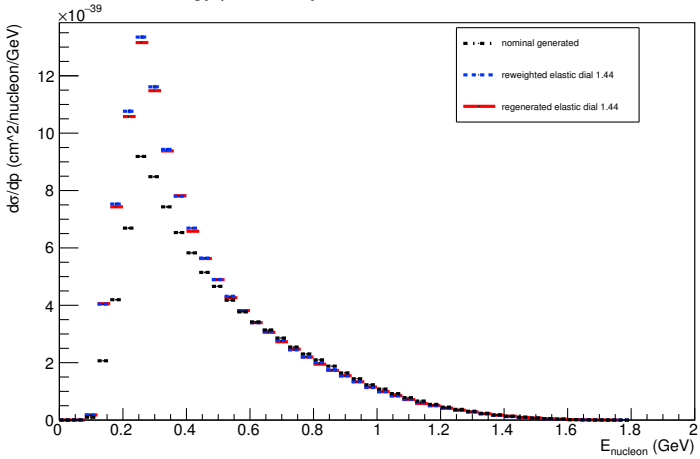

Energy plot: Leading Energy Nucleon: Neut Mode =2

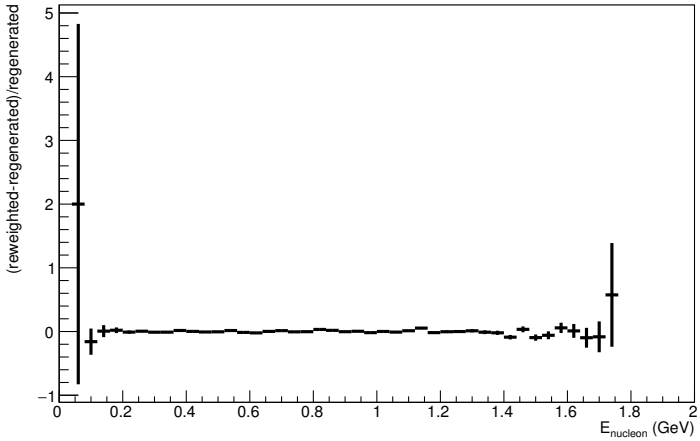

Energy plot: Every FSI Nucleon: Neut Mode =2

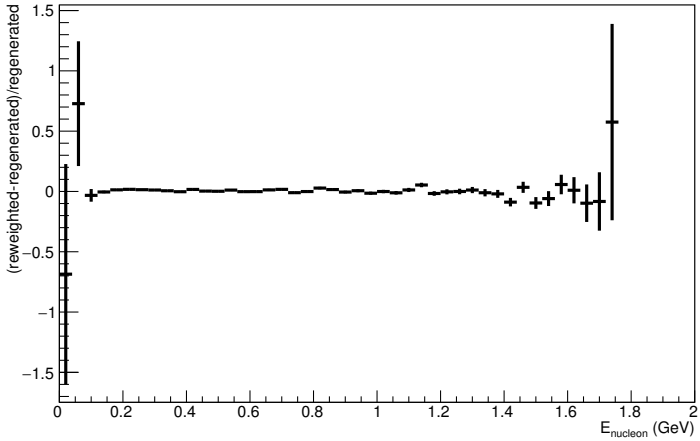

Angle plot: Leading Energy Nucleon: Neut Mode =2

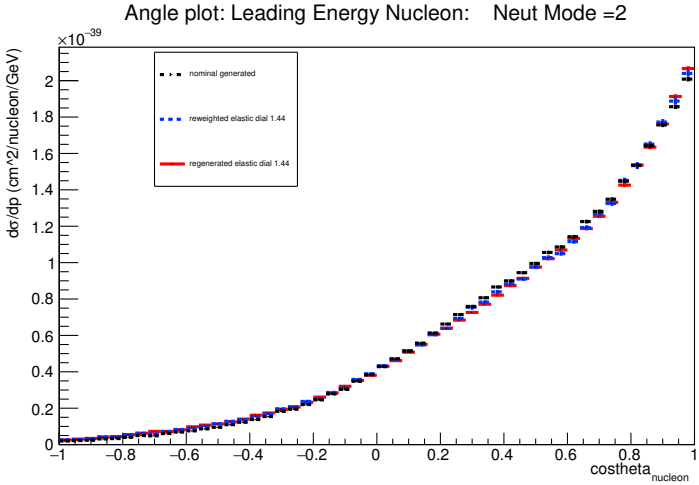

Angle plot: Every FSI Nucleon: Neut Mode =2

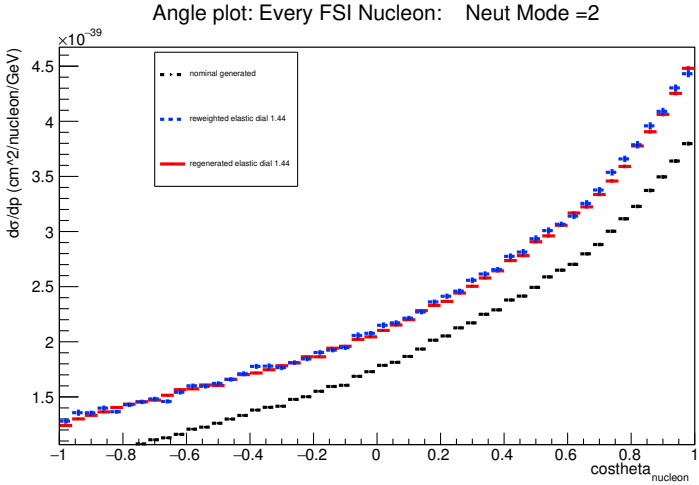

Angle plot: Leading Energy Nucleon: Neut Mode =2

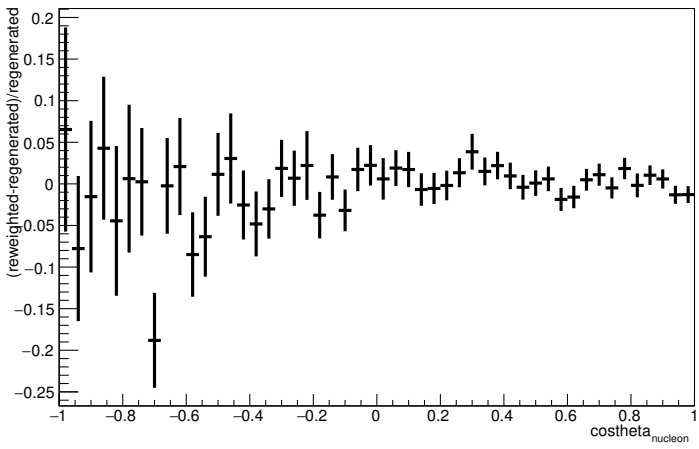

Angle plot: Every FSI Nucleon: Neut Mode =2

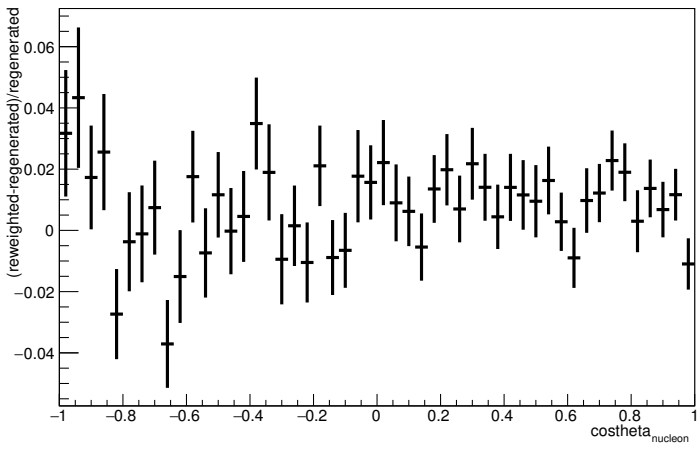

Energy plot: Leading Energy Proton: Neut Mode =2

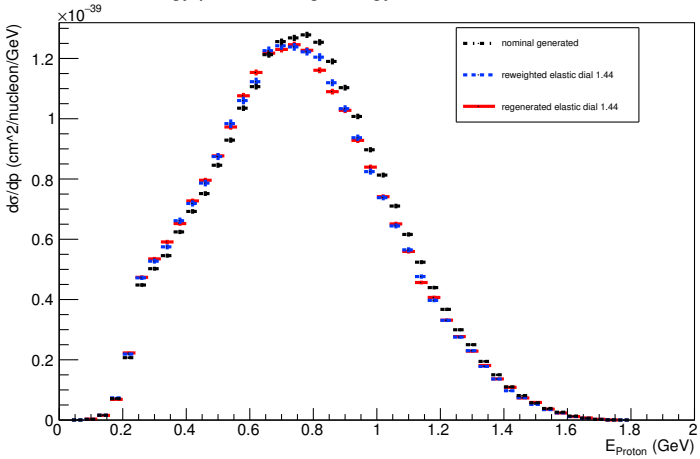

Energy plot: Every FSI Proton: Neut Mode =2

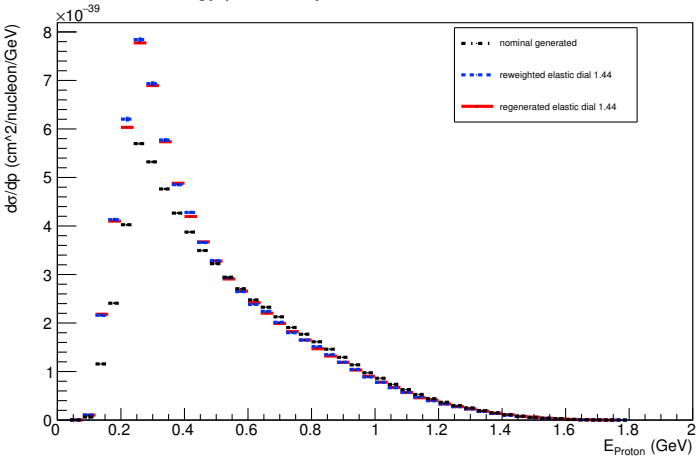

Energy plot: Leading Energy Proton: Neut Mode =2

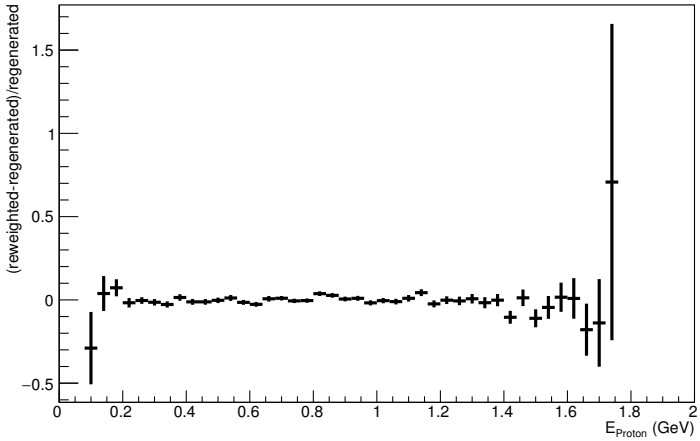

Energy plot: Every FSI Proton: Neut Mode =2

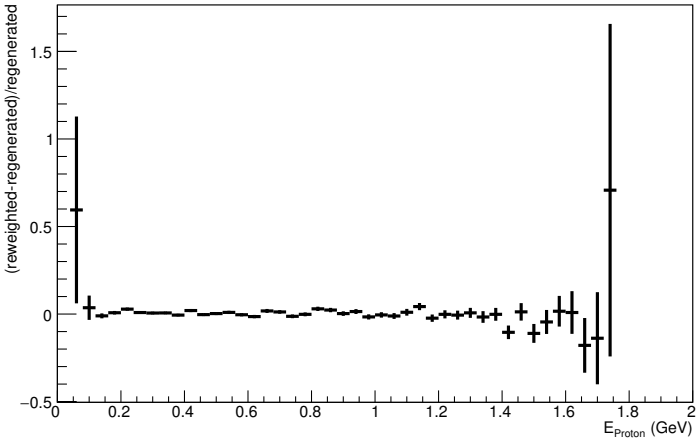

Angle plot: Leading Energy Proton: Neut Mode =2

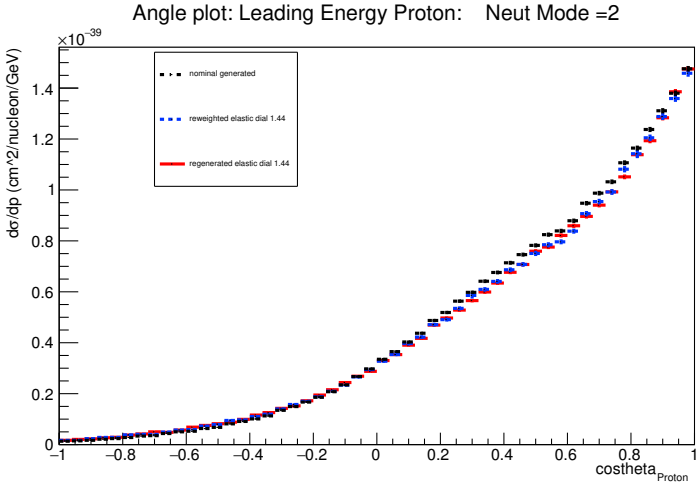

Angle plot: Every FSI Proton: Neut Mode =2

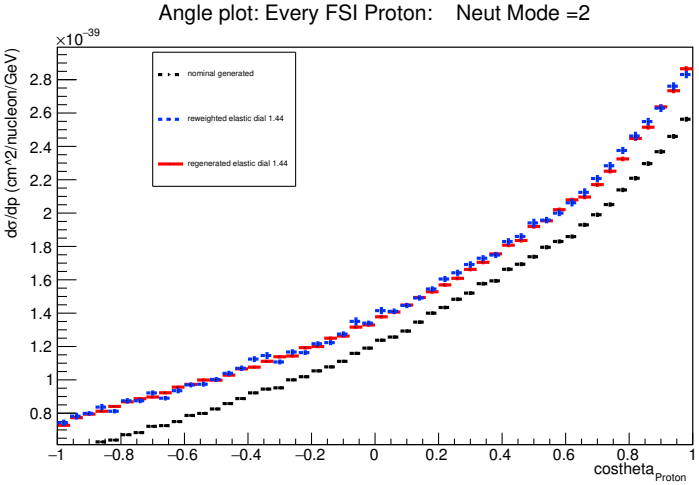

Angle plot: Leading Energy Proton: Neut Mode =2

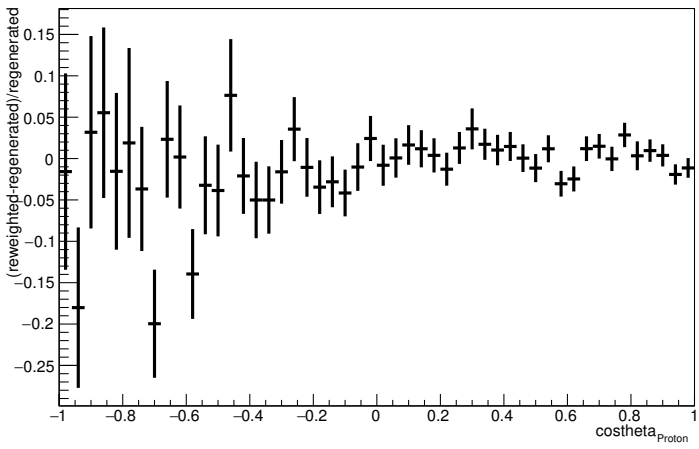

Angle plot: Every FSI Proton: Neut Mode =2

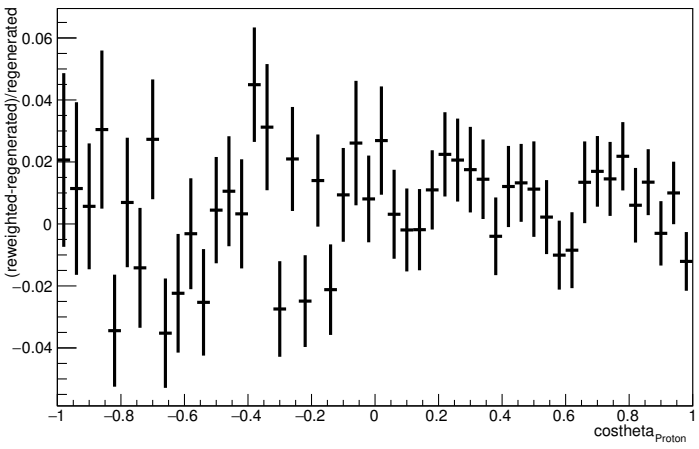

Energy plot: Leading Energy Neutron: Neut Mode =2

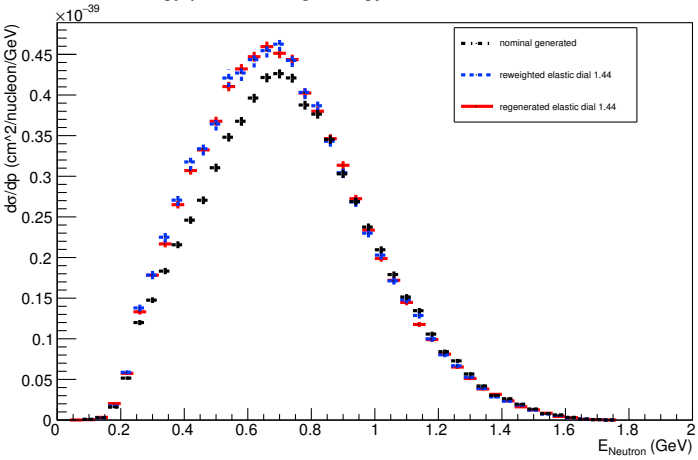

Energy plot: Every FSI Neutron: Neut Mode =2

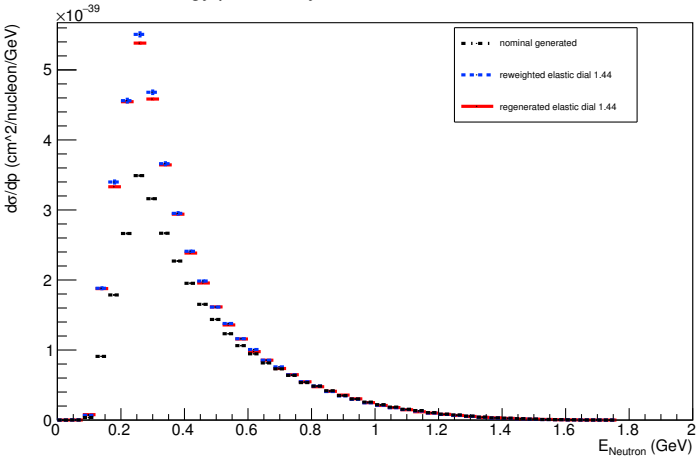

Energy plot: Leading Energy Neutron: Neut Mode =2

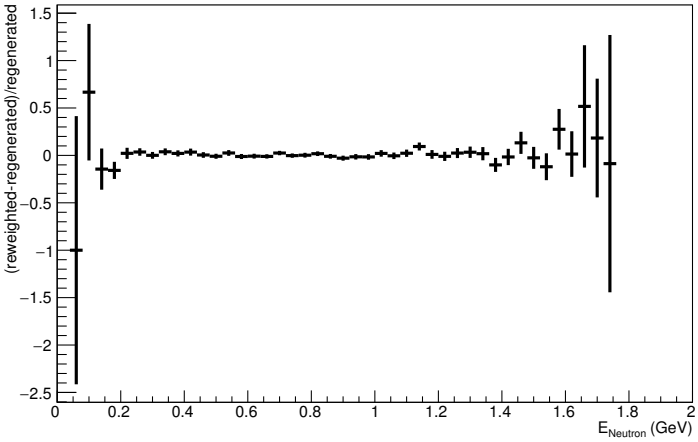

Energy plot: Every FSI Neutron: Neut Mode =2

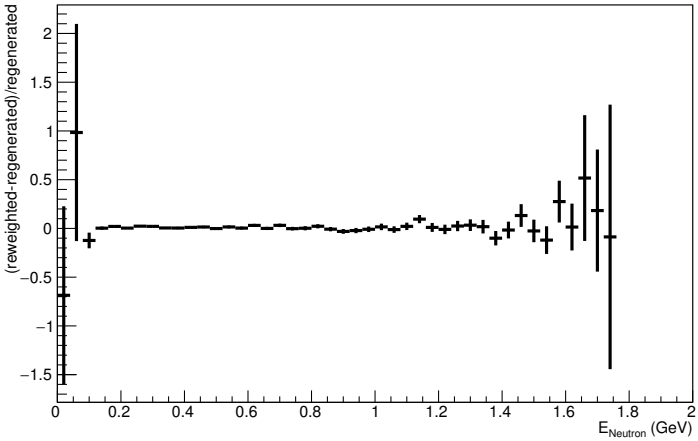

Angle plot: Leading Energy Neutron: Neut Mode =2

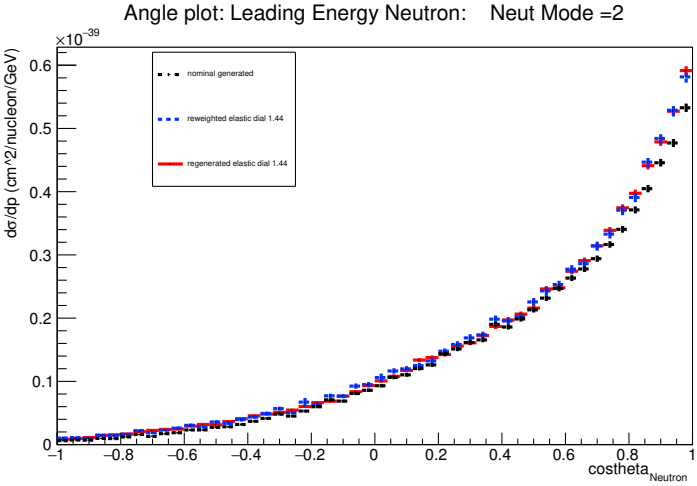

Angle plot: Every FSI Neutron: Neut Mode =2

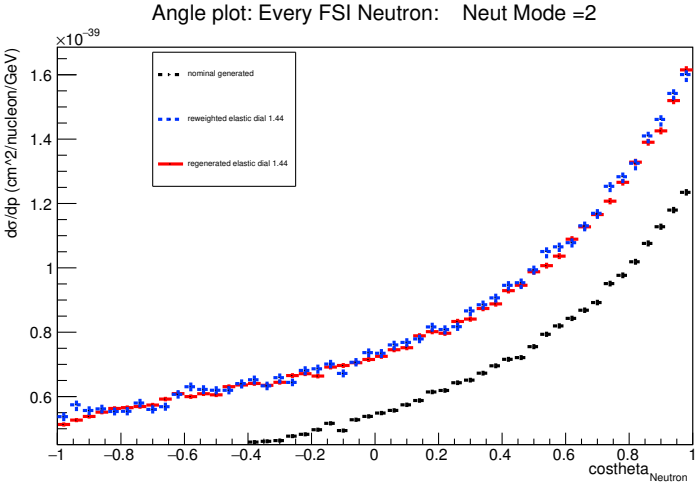

Angle plot: Leading Energy Neutron: Neut Mode =2

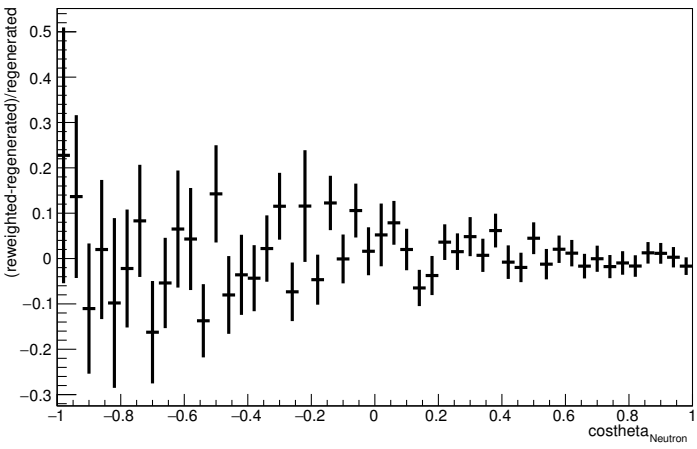

Angle plot: Every FSI Neutron: Neut Mode =2

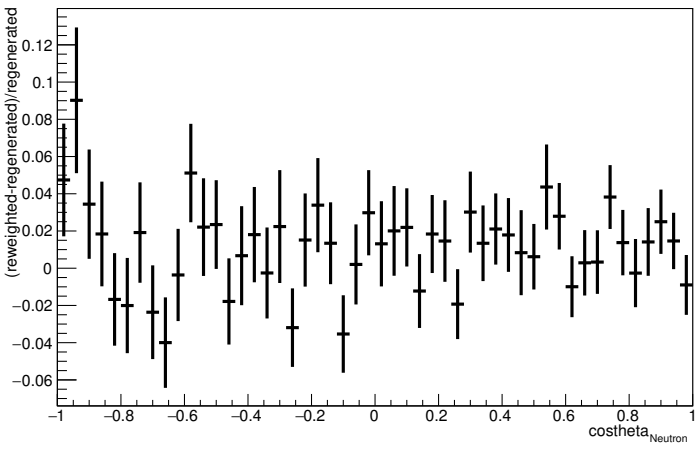

Energy plot: Leading Energy Lepton: Neut Mode =2

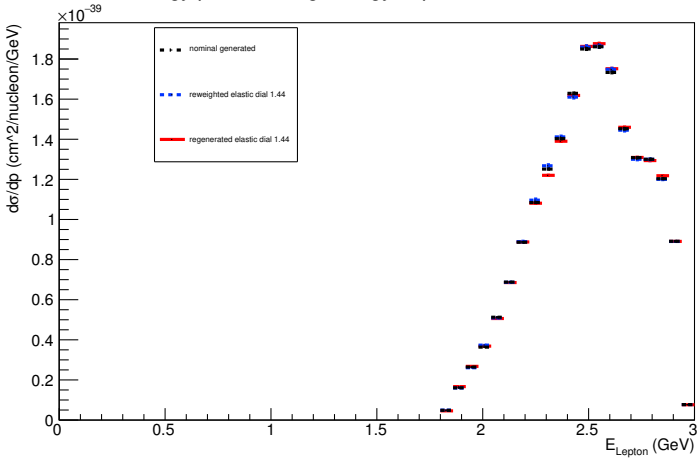

Angle plot: Leading Energy Lepton: Neut Mode =2

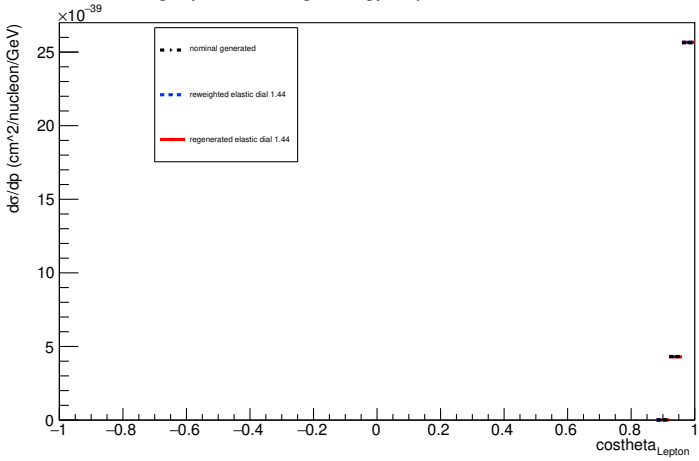

Energy plot: Leading Energy Lepton: Neut Mode =2

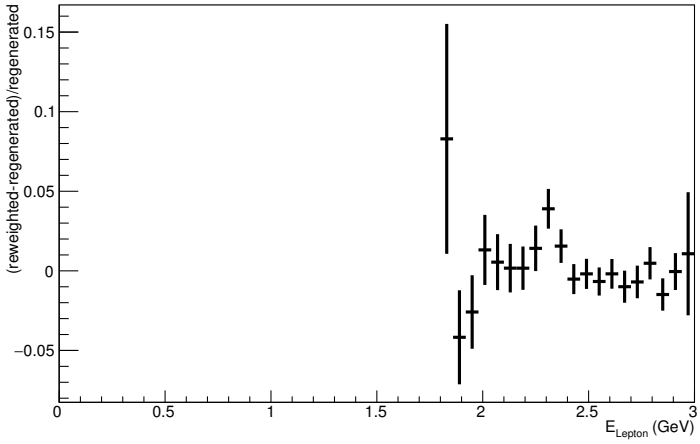

Angle plot: Leading Energy Lepton: Neut Mode =2

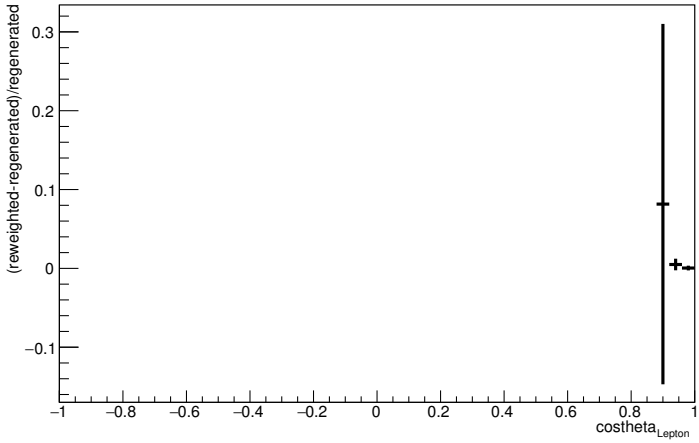

Energy plot: Leading Energy Pion: Neut Mode =2

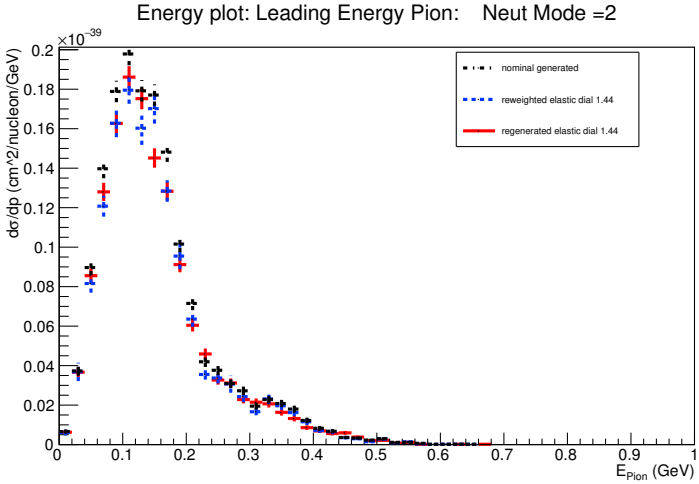

Energy plot: Every FSI Pion: Neut Mode =2

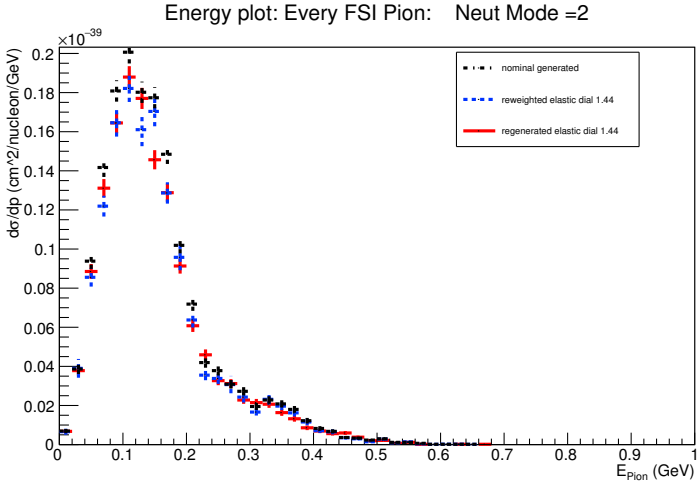

Energy plot: Leading Energy Pion: Neut Mode =2

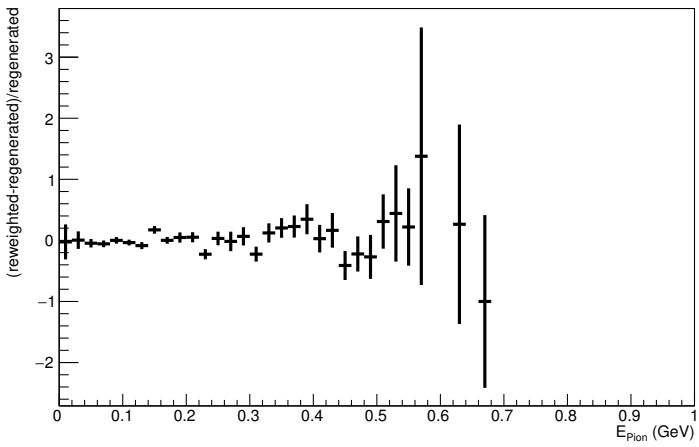

Energy plot: Every FSI Pion: Neut Mode =2

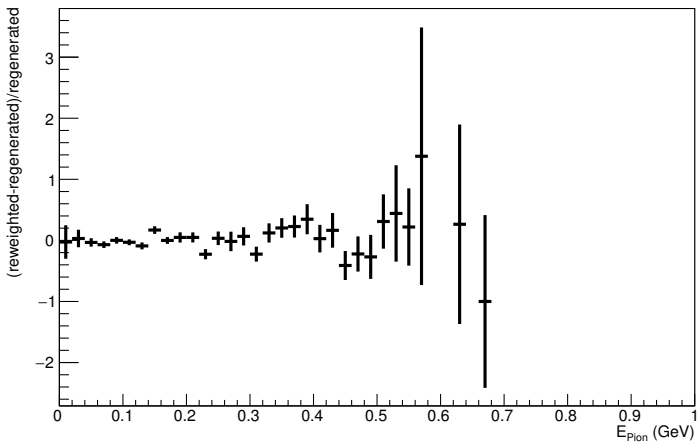

Angle plot: Leading Energy Pion: Neut Mode =2

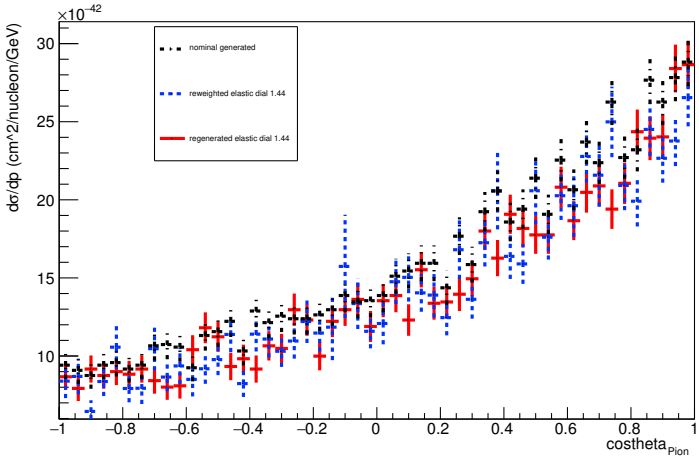

Angle plot: Every FSI Pion: Neut Mode =2

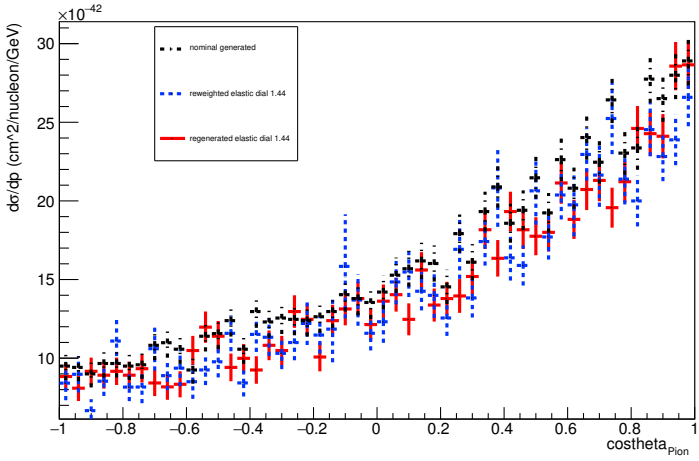

Angle plot: Leading Energy Pion: Neut Mode =2

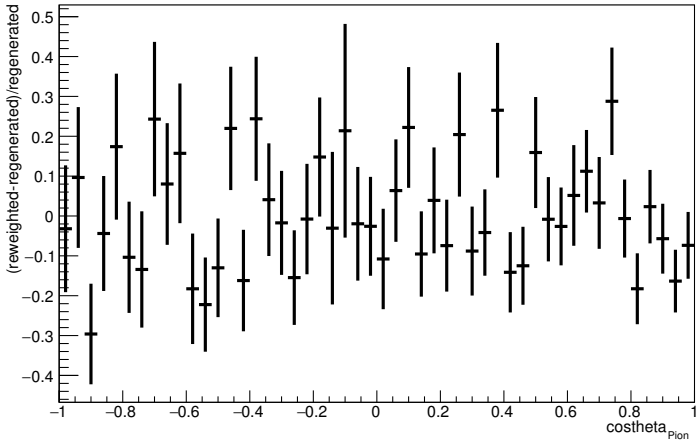

Angle plot: Every FSI Pion: Neut Mode =2

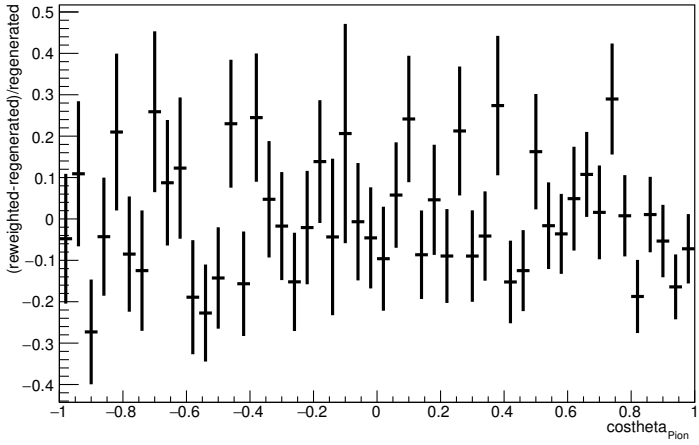

Energy plot: Leading Energy Nucleon: Neut Mode =11

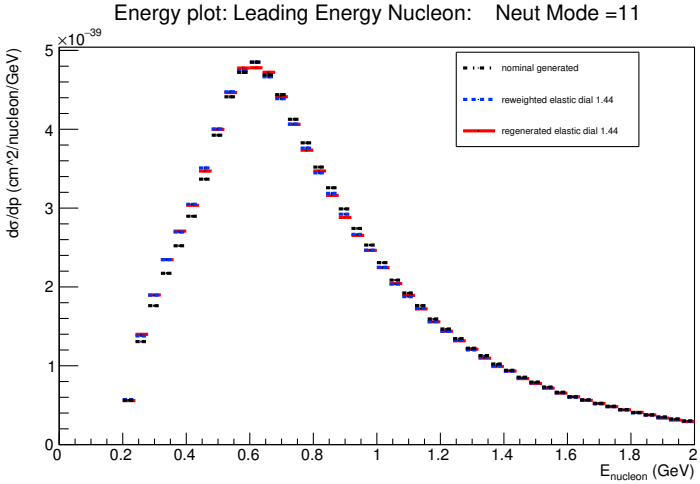

Energy plot: Every FSI Nucleon: Neut Mode =11

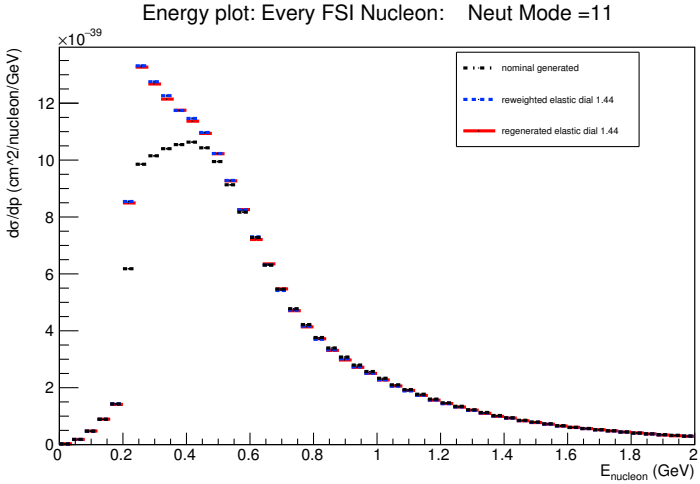

Energy plot: Leading Energy Nucleon: Neut Mode =11

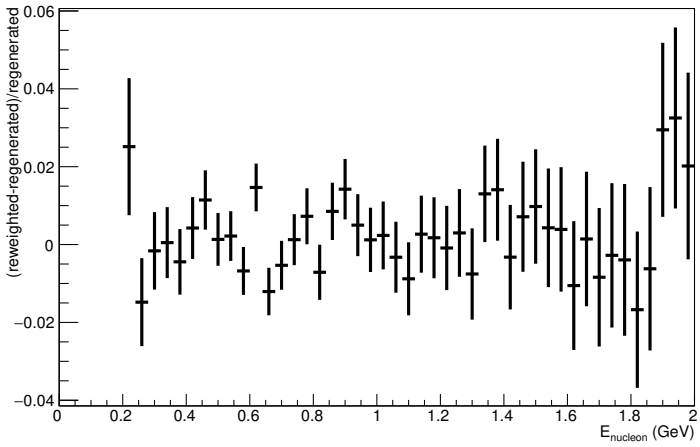

Energy plot: Every FSI Nucleon: Neut Mode =11

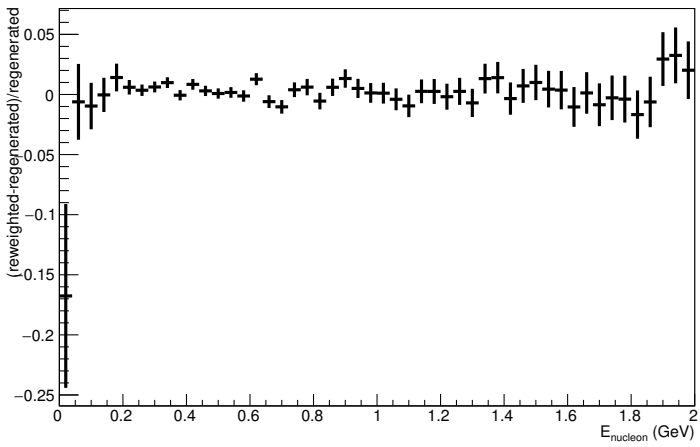

Angle plot: Leading Energy Nucleon: Neut Mode =11

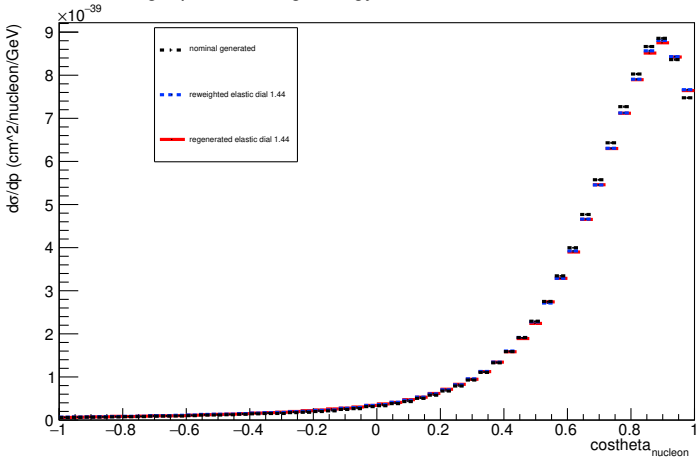

Angle plot: Every FSI Nucleon: Neut Mode =11

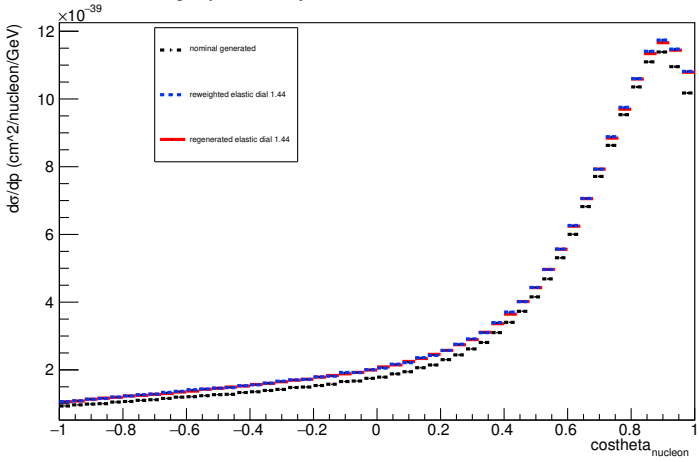

Angle plot: Leading Energy Nucleon: Neut Mode =11

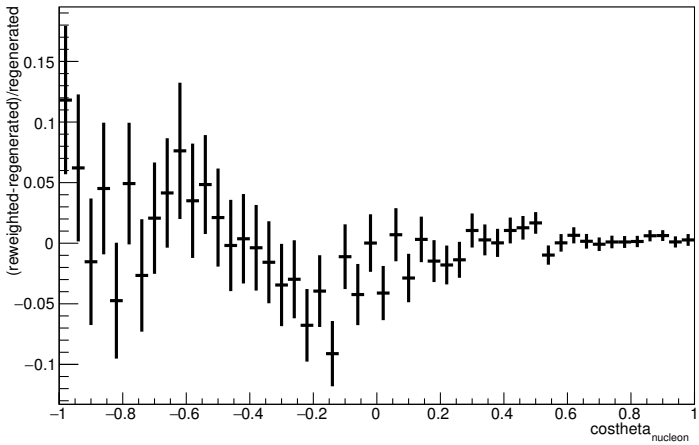

Angle plot: Every FSI Nucleon: Neut Mode =11

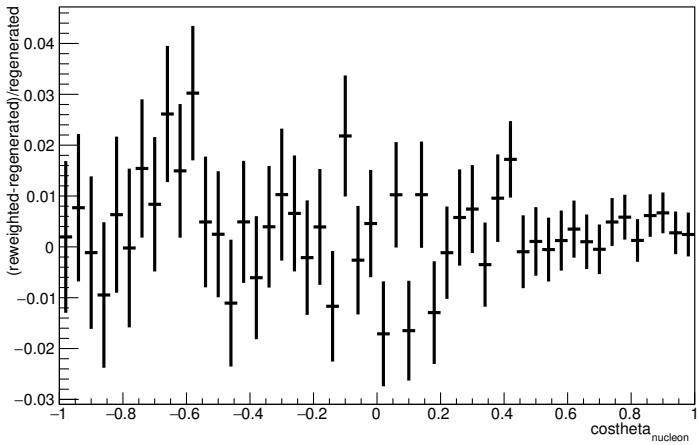

Energy plot: Leading Energy Proton: Neut Mode =11

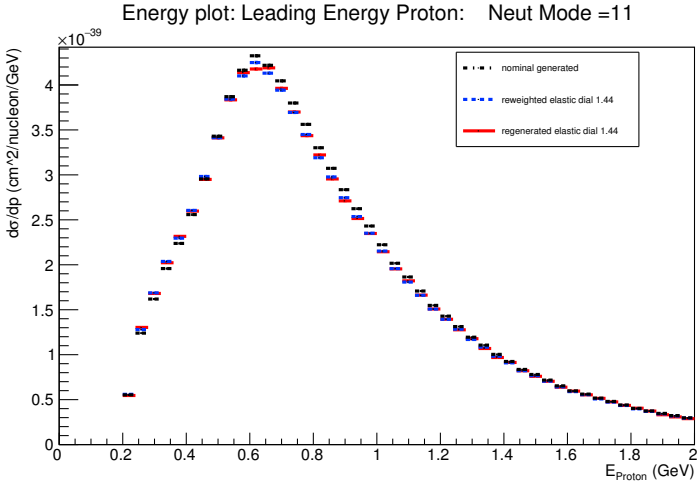

Energy plot: Every FSI Proton: Neut Mode =11

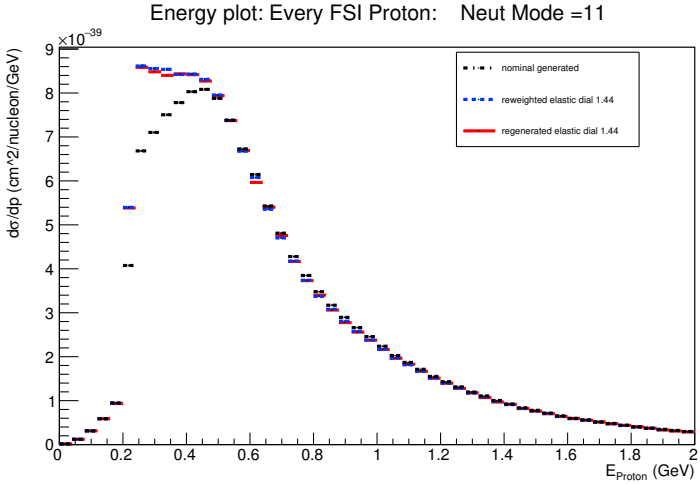

Energy plot: Leading Energy Proton: Neut Mode =11

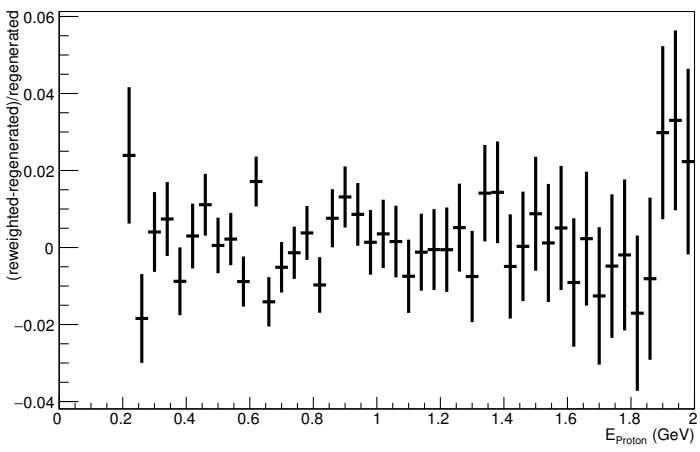

Energy plot: Every FSI Proton: Neut Mode =11

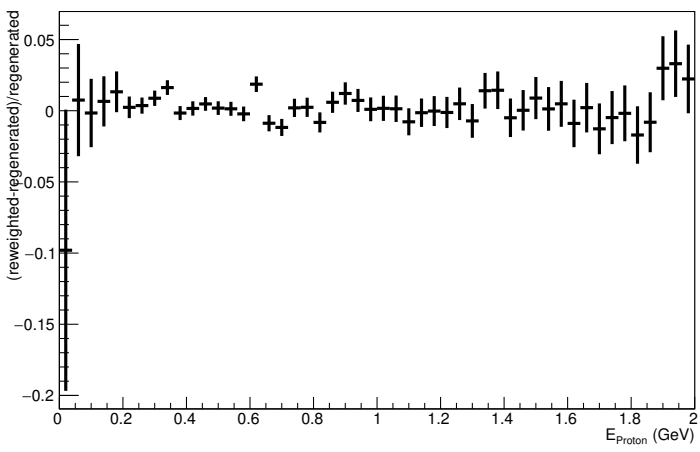

Angle plot: Leading Energy Proton: Neut Mode =11

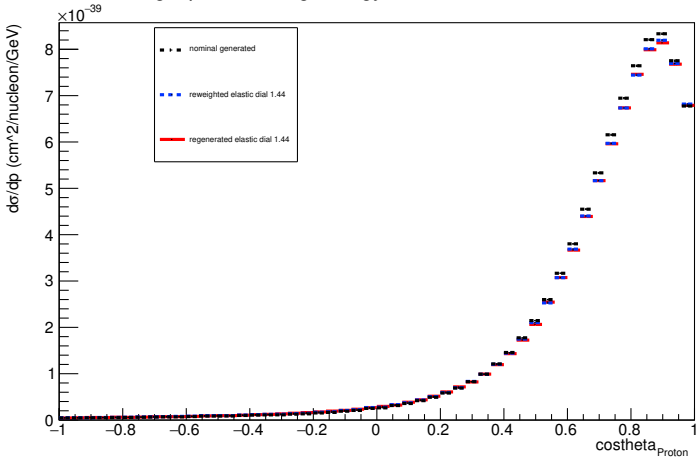

Angle plot: Every FSI Proton: Neut Mode =11

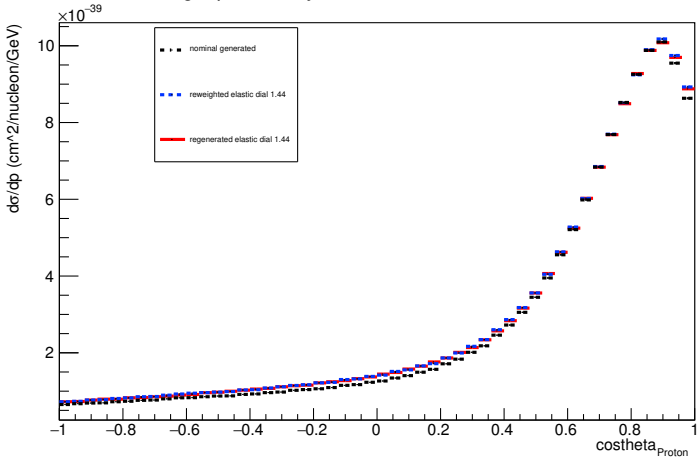

Angle plot: Leading Energy Proton: Neut Mode =11

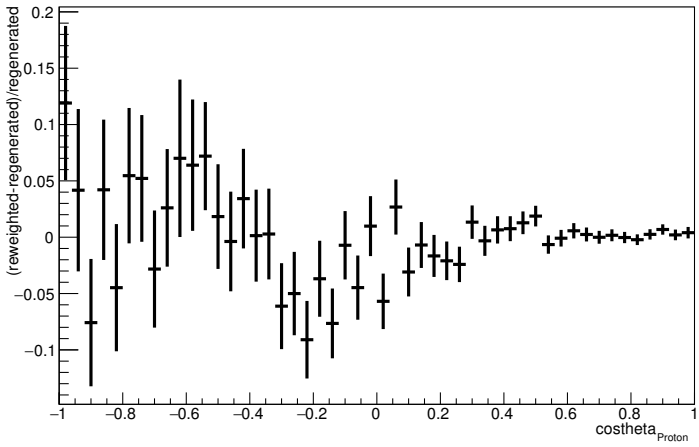

Angle plot: Every FSI Proton: Neut Mode =11

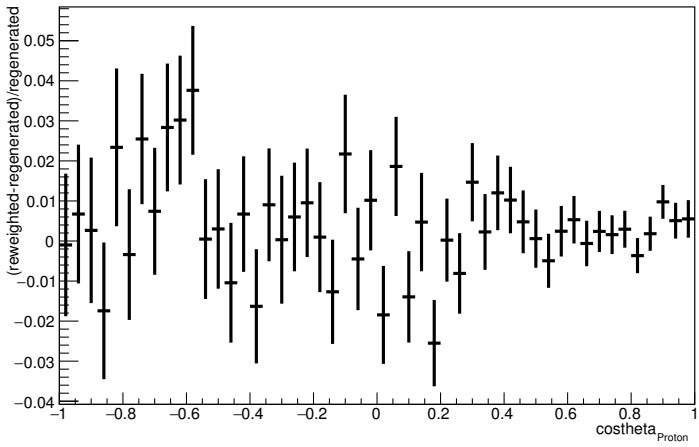

Energy plot: Leading Energy Neutron: Neut Mode =11

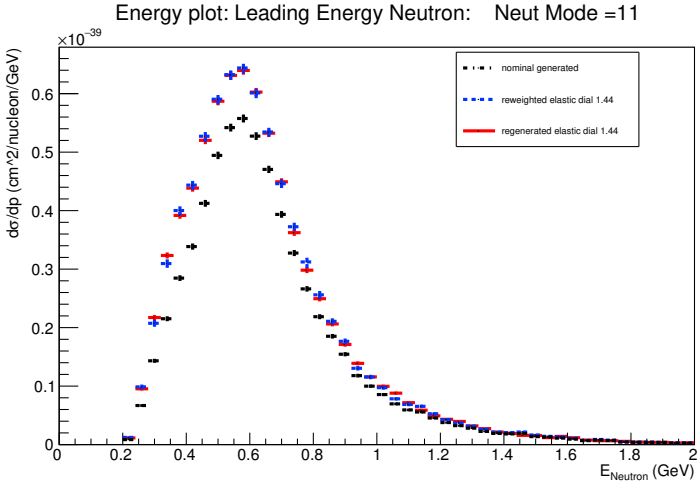

Energy plot: Every FSI Neutron: Neut Mode =11

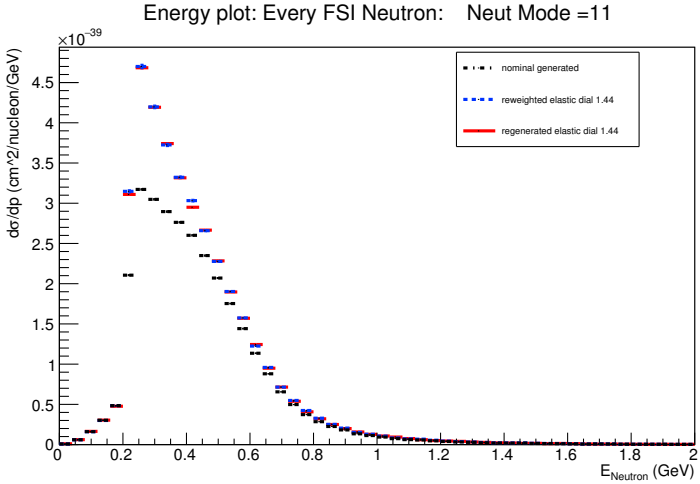

Energy plot: Leading Energy Neutron: Neut Mode =11

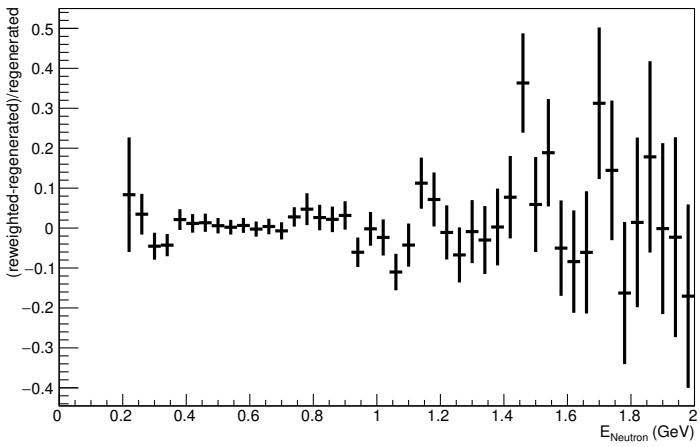

Energy plot: Every FSI Neutron: Neut Mode =11

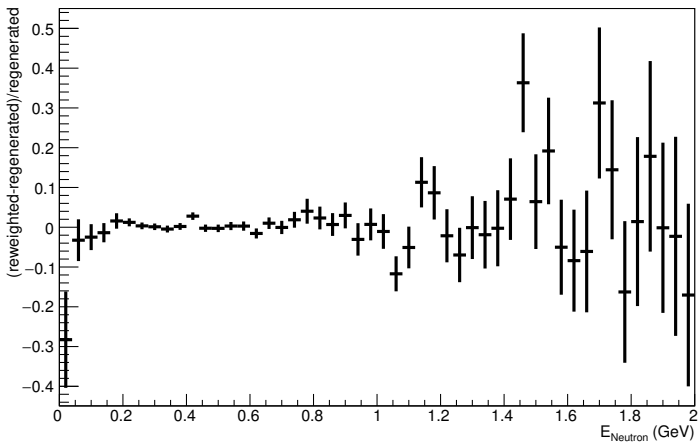

Angle plot: Leading Energy Neutron: Neut Mode =11

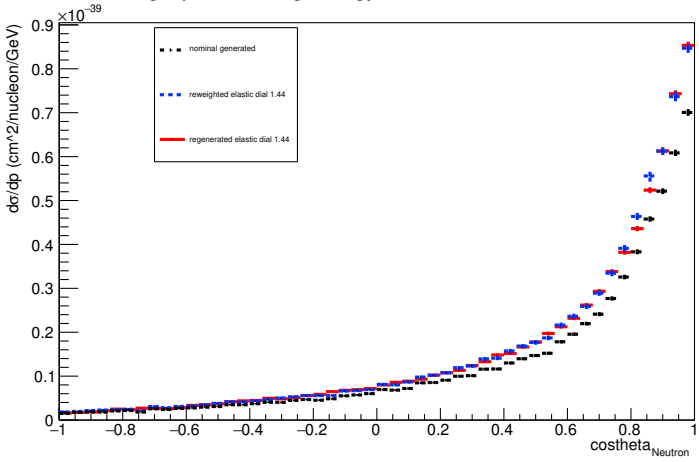

Angle plot: Every FSI Neutron: Neut Mode =11

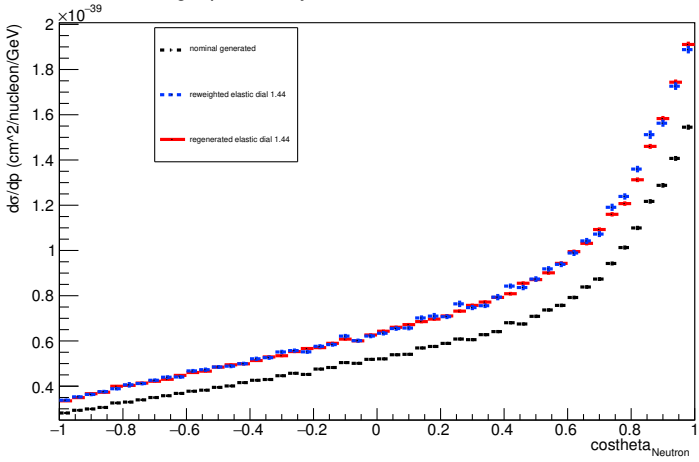

Angle plot: Leading Energy Neutron: Neut Mode =11

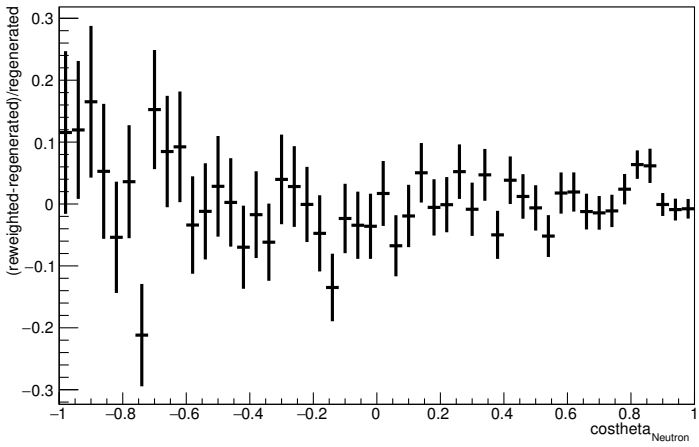

Angle plot: Every FSI Neutron: Neut Mode =11

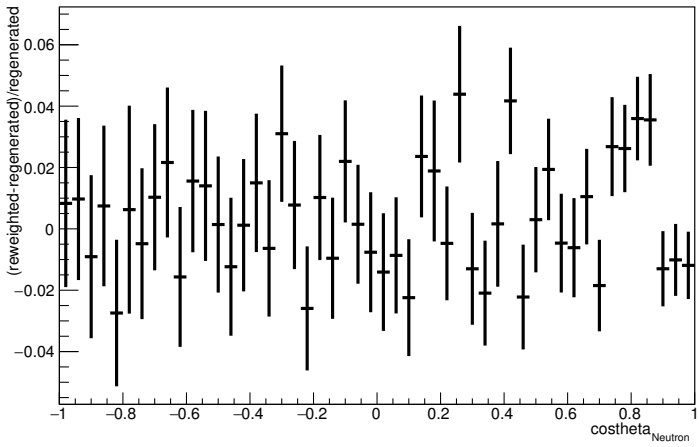

Energy plot: Leading Energy Lepton: Neut Mode =11

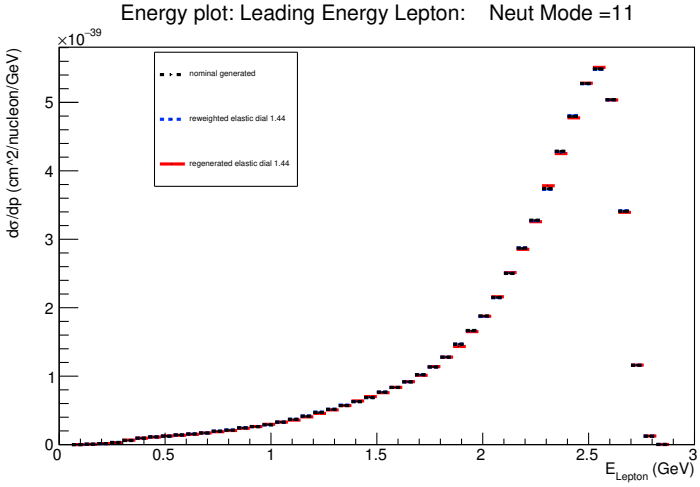

Angle plot: Leading Energy Lepton: Neut Mode =11

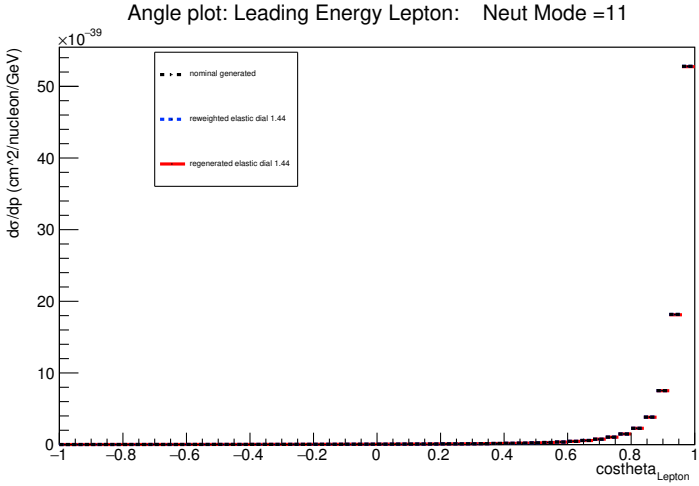

Energy plot: Leading Energy Lepton: Neut Mode =11

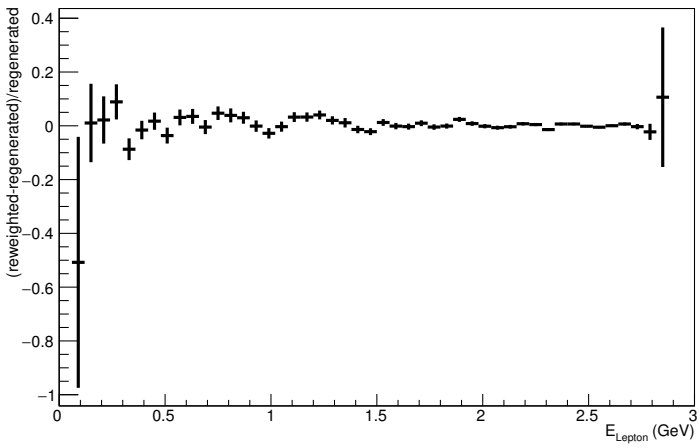

Angle plot: Leading Energy Lepton: Neut Mode =11

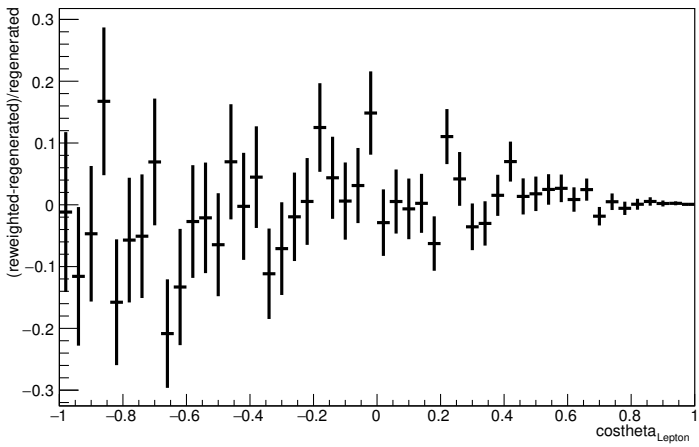

Energy plot: Leading Energy Pion: Neut Mode =11

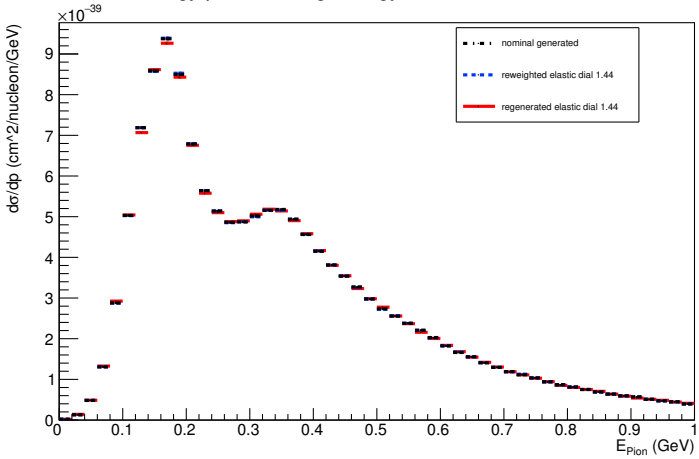

Energy plot: Every FSI Pion: Neut Mode =11

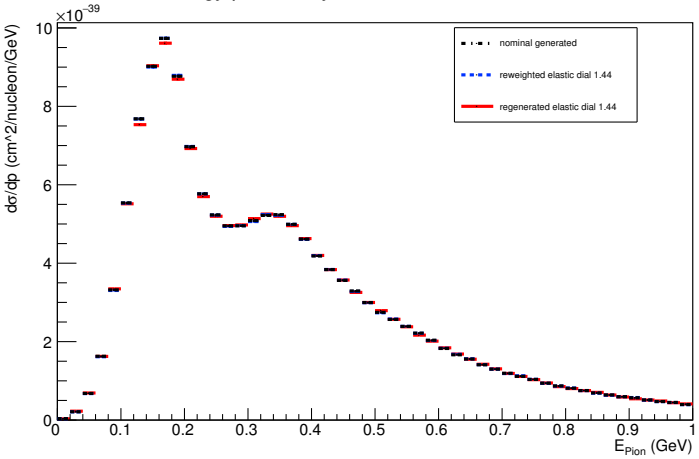

Energy plot: Leading Energy Pion: Neut Mode =11

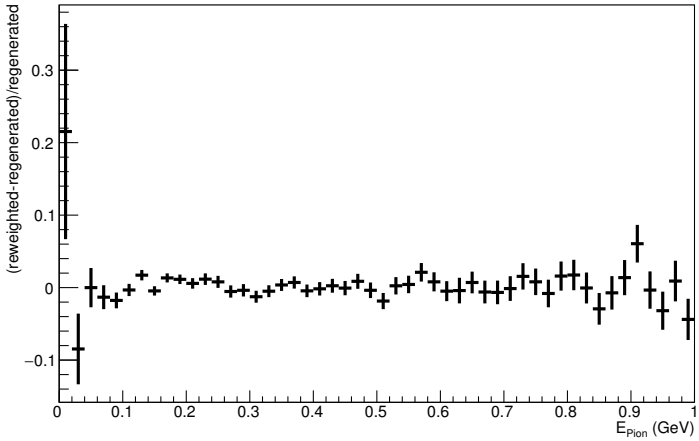

Energy plot: Every FSI Pion: Neut Mode =11

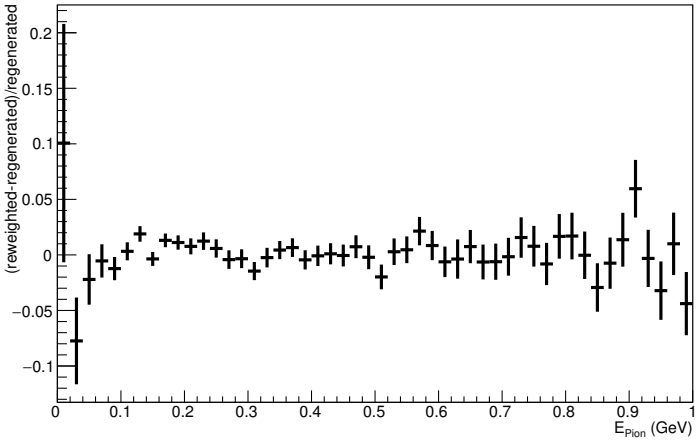

Angle plot: Leading Energy Pion: Neut Mode =11

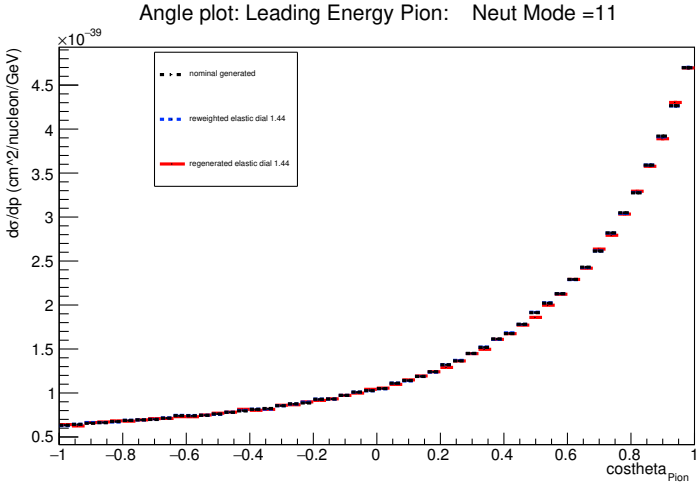

Angle plot: Every FSI Pion: Neut Mode =11

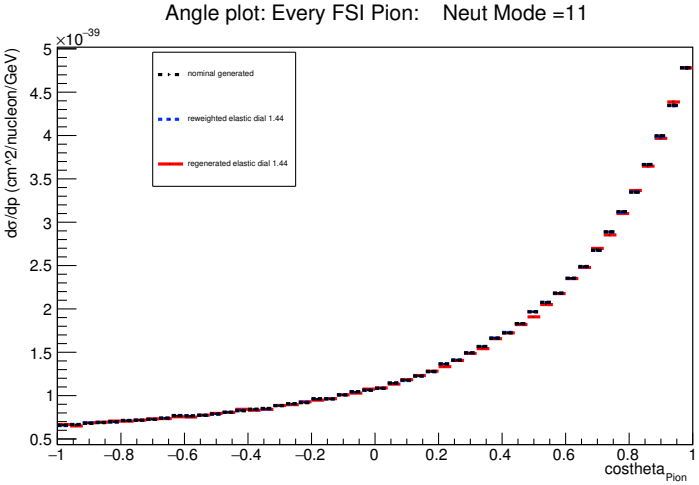

Angle plot: Leading Energy Pion: Neut Mode =11

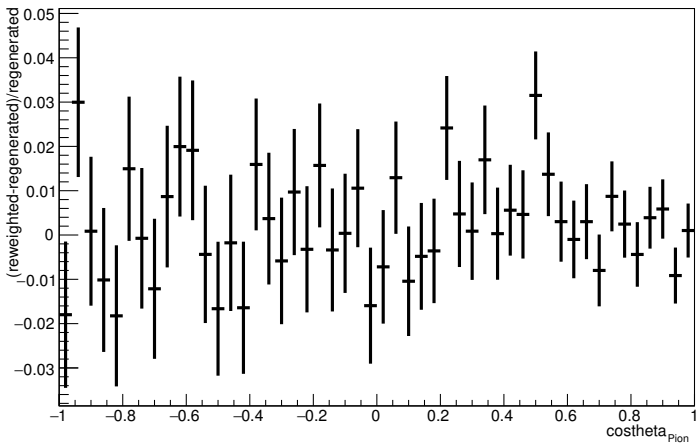

Angle plot: Every FSI Pion: Neut Mode =11

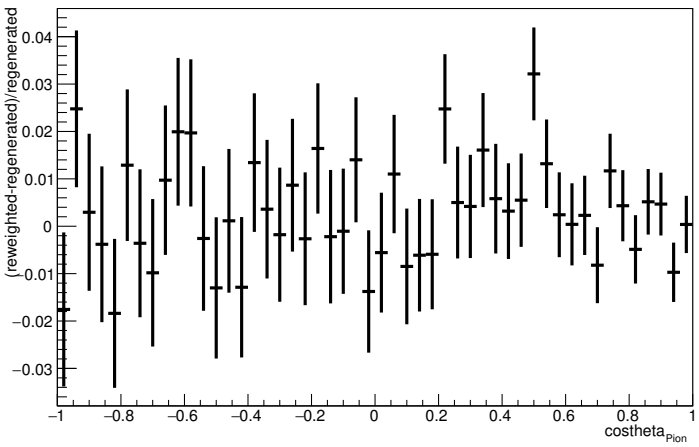

A.4. Elastic Dial: varied down to 0.64

Energy plot: Leading Energy Nucleon: Neut Mode =AllModesCombined

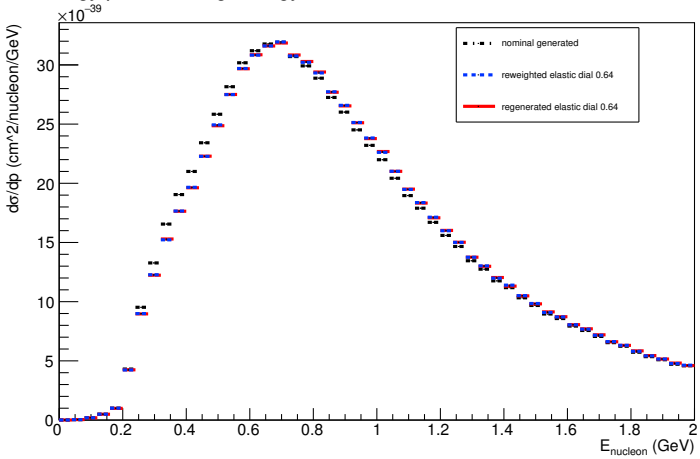

Energy plot: Every FSI Nucleon: Neut Mode =AllModesCombined

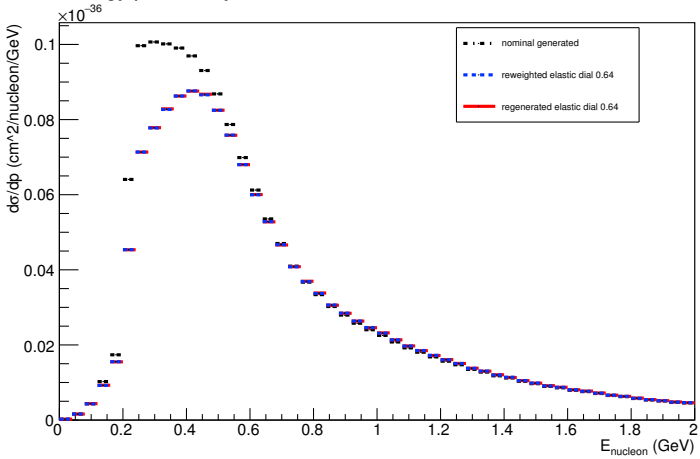

Energy plot: Leading Energy Nucleon: Neut Mode =AllModesCombined

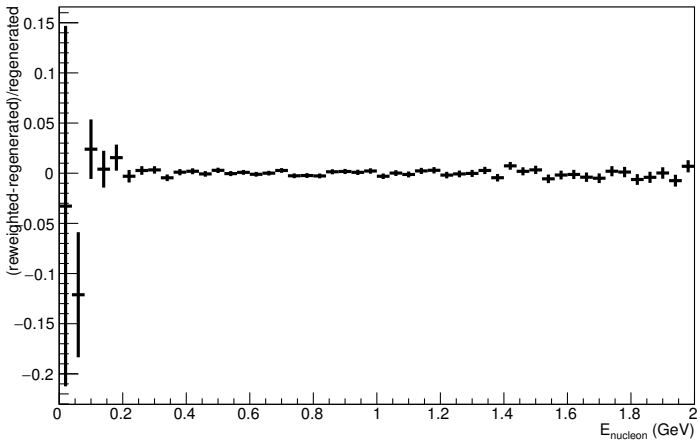

Energy plot: Every FSI Nucleon: Neut Mode =AllModesCombined

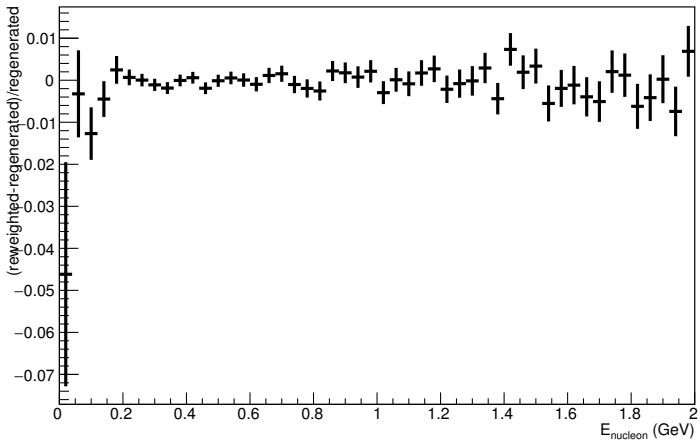

Angle plot: Leading Energy Nucleon: Neut Mode =AllModesCombined

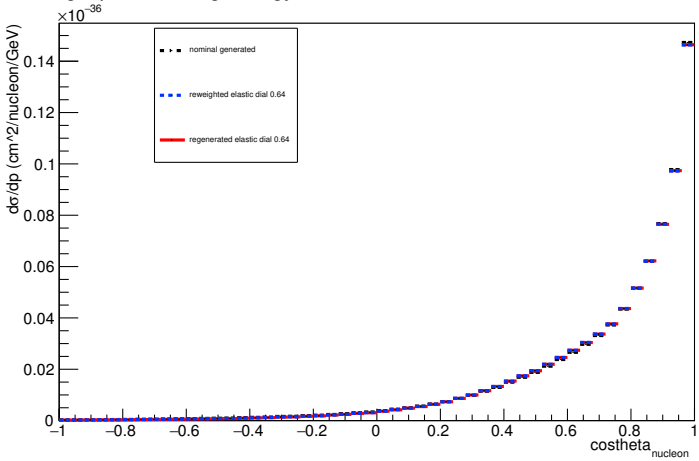

Angle plot: Every FSI Nucleon: Neut Mode =AllModesCombined

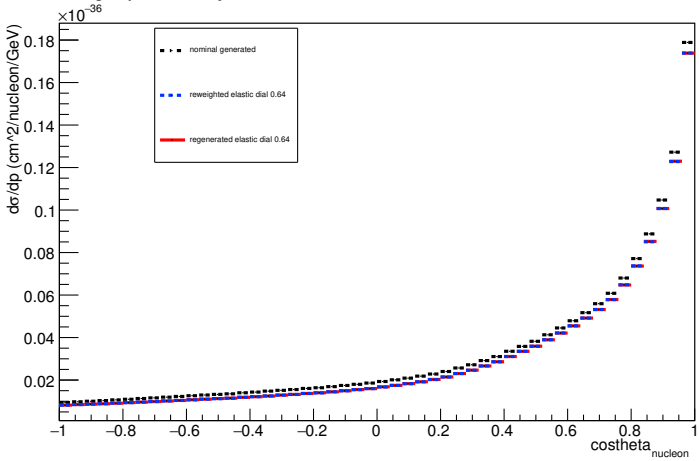

Angle plot: Leading Energy Nucleon: Neut Mode =AllModesCombined

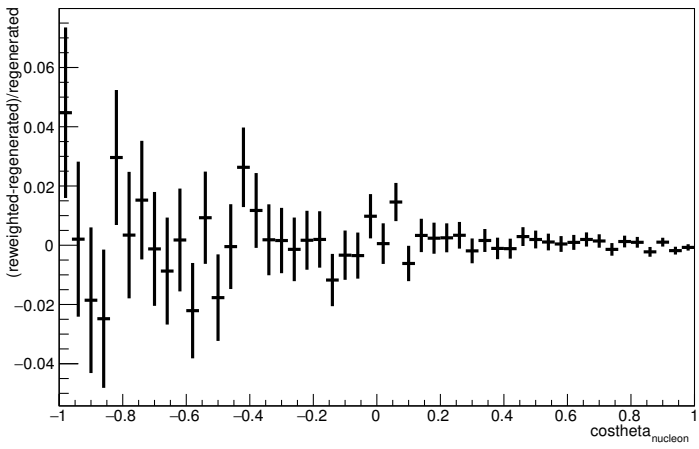

Angle plot: Every FSI Nucleon: Neut Mode =AllModesCombined

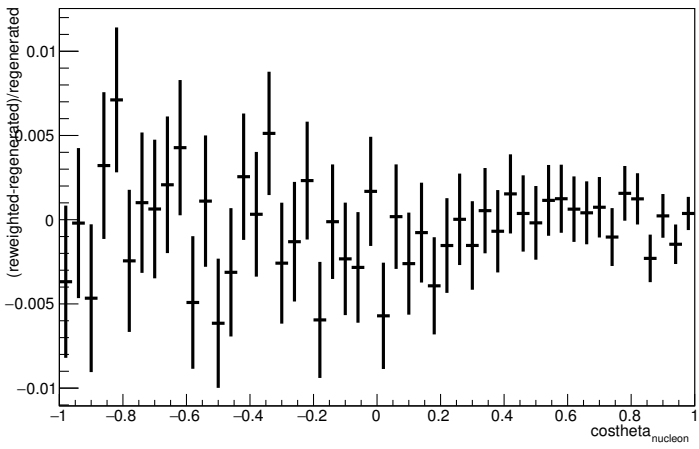

Energy plot: Leading Energy Proton: Neut Mode =AllModesCombined

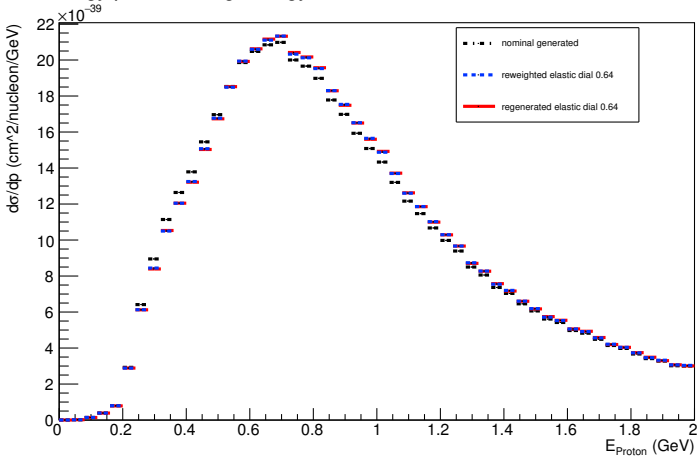

Energy plot: Every FSI Proton: Neut Mode =AllModesCombined

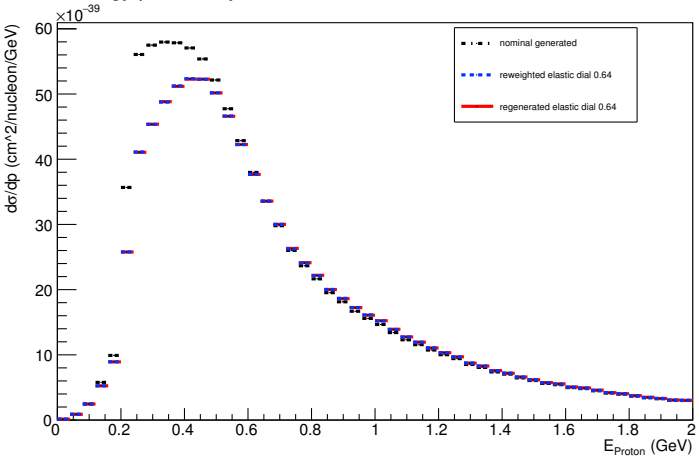

Energy plot: Leading Energy Proton: Neut Mode =AllModesCombined

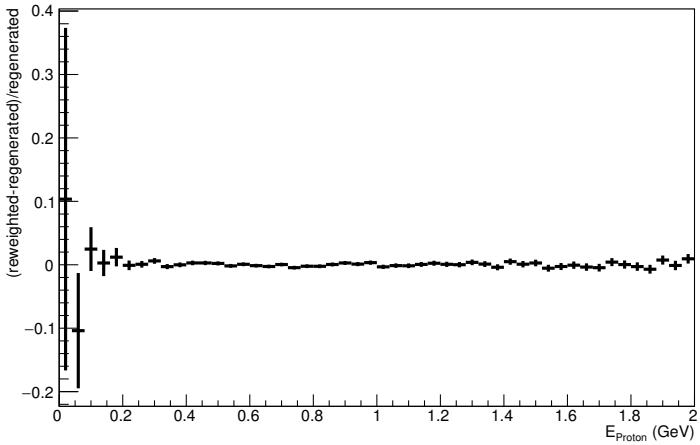

Energy plot: Every FSI Proton: Neut Mode =AllModesCombined

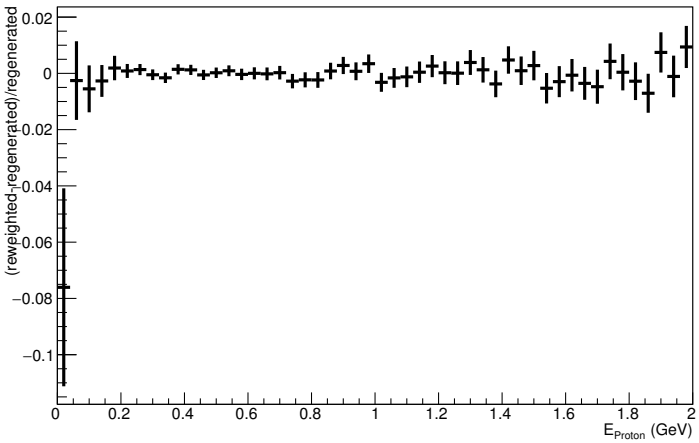

Angle plot: Leading Energy Proton: Neut Mode =AllModesCombined

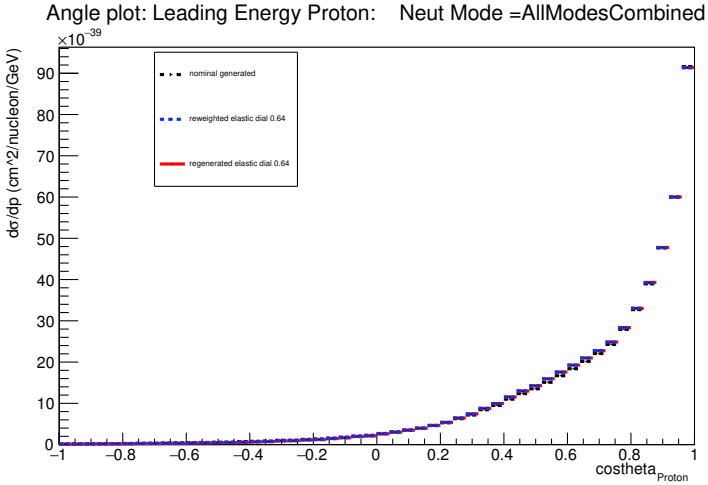

Angle plot: Every FSI Proton: Neut Mode =AllModesCombined

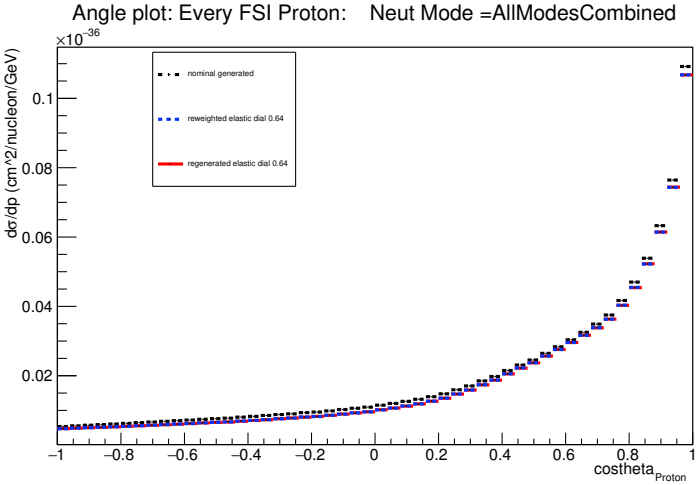

Angle plot: Leading Energy Proton: Neut Mode =AllModesCombined

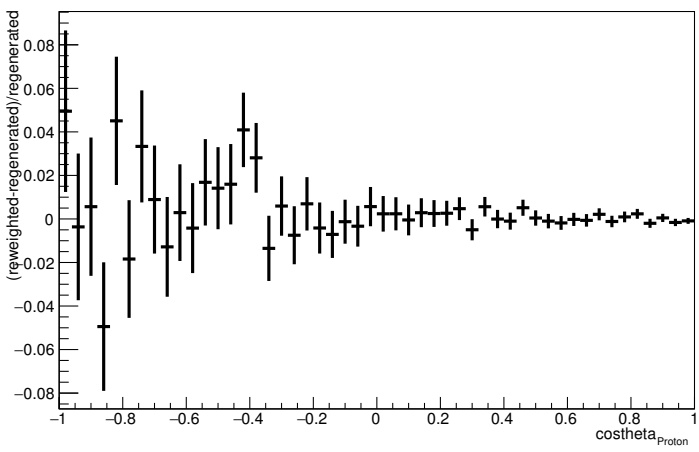

Angle plot: Every FSI Proton: Neut Mode =AllModesCombined

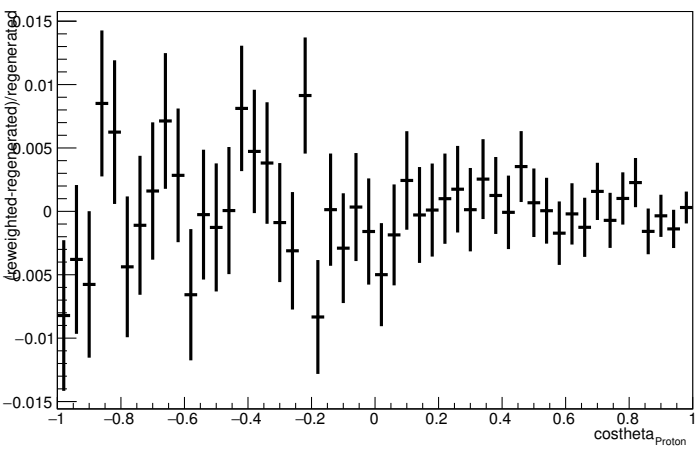

Energy plot: Leading Energy Neutron: Neut Mode =AllModesCombined

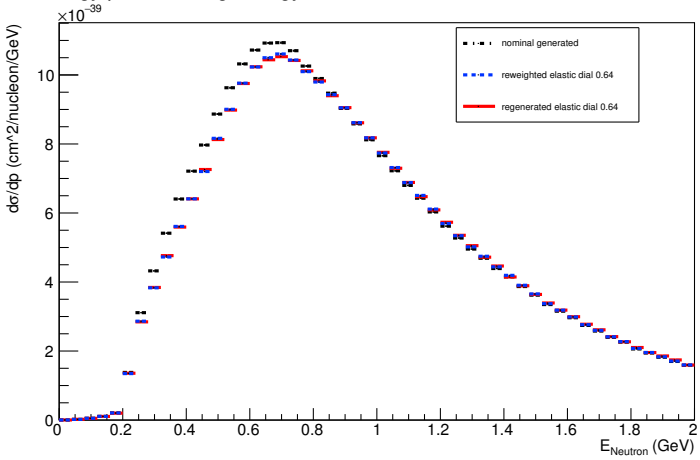

Energy plot: Every FSI Neutron: Neut Mode =AllModesCombined

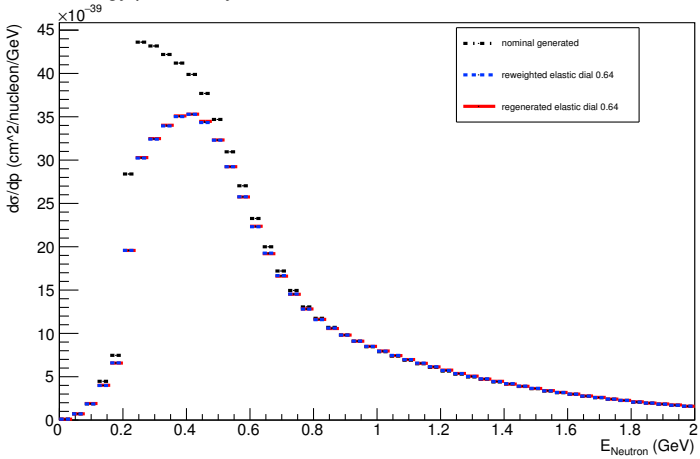

Energy plot: Leading Energy Neutron: Neut Mode =AllModesCombined

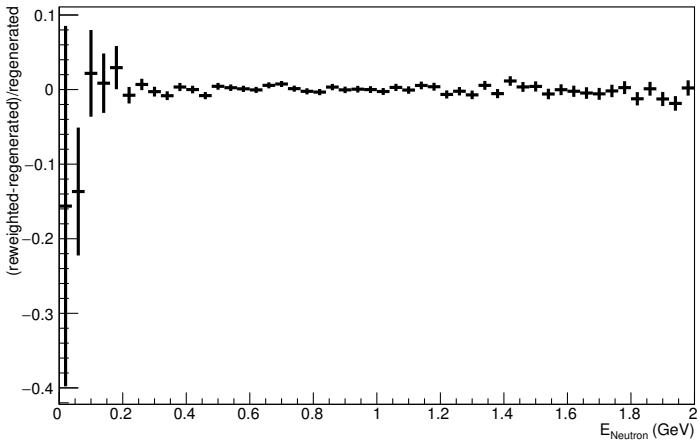

Energy plot: Every FSI Neutron: Neut Mode =AllModesCombined

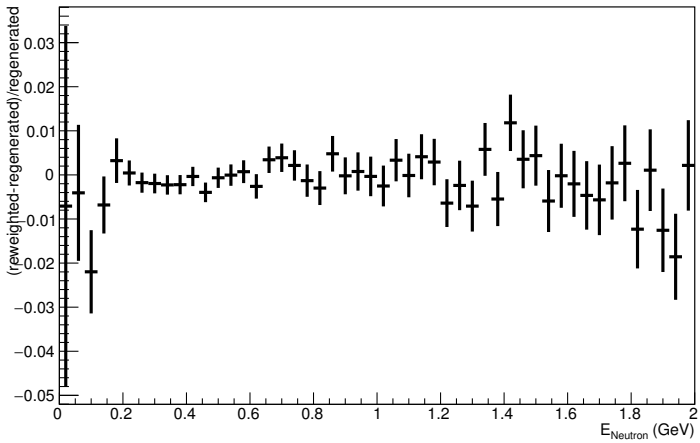

Angle plot: Leading Energy Neutron: Neut Mode =AllModesCombined

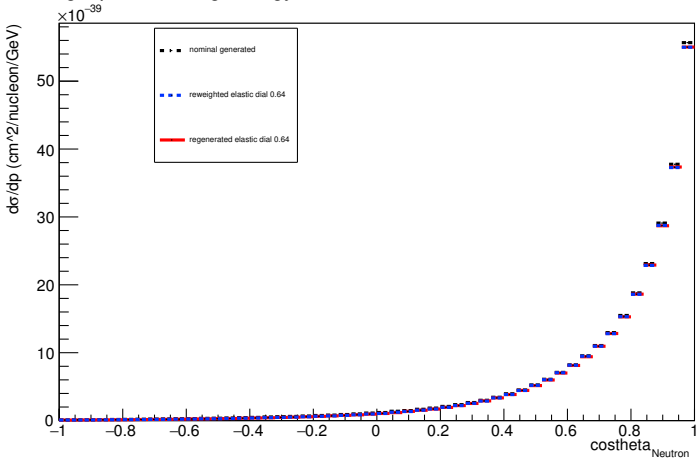

Angle plot: Every FSI Neutron: Neut Mode =AllModesCombined

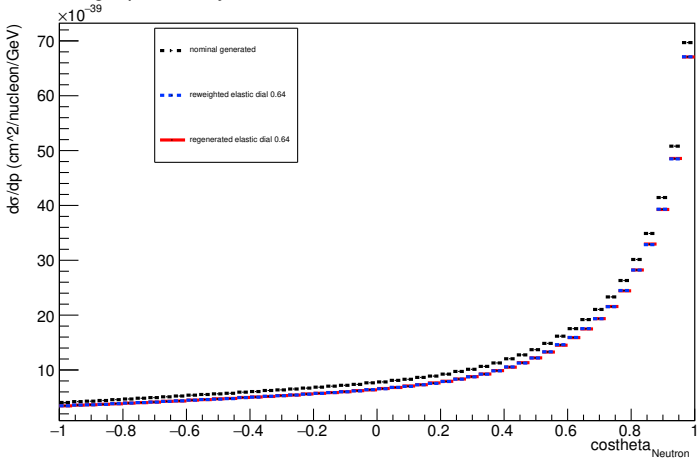

Angle plot: Leading Energy Neutron: Neut Mode =AllModesCombined

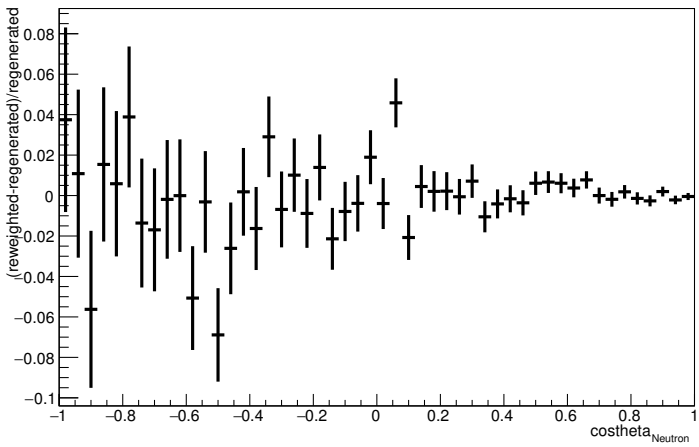

Angle plot: Every FSI Neutron: Neut Mode =AllModesCombined

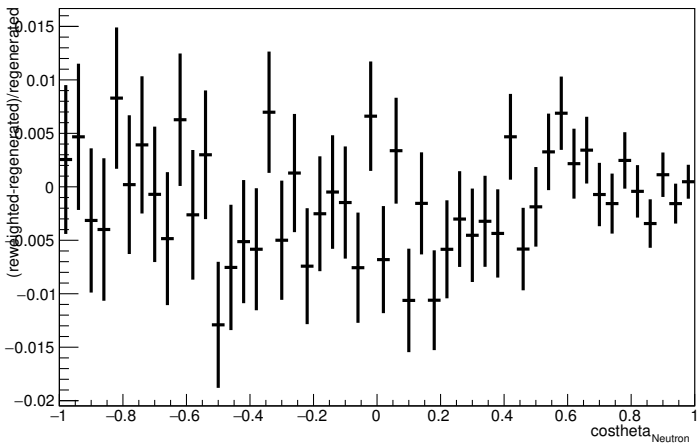

Energy plot: Leading Energy Lepton: Neut Mode =AllModesCombined

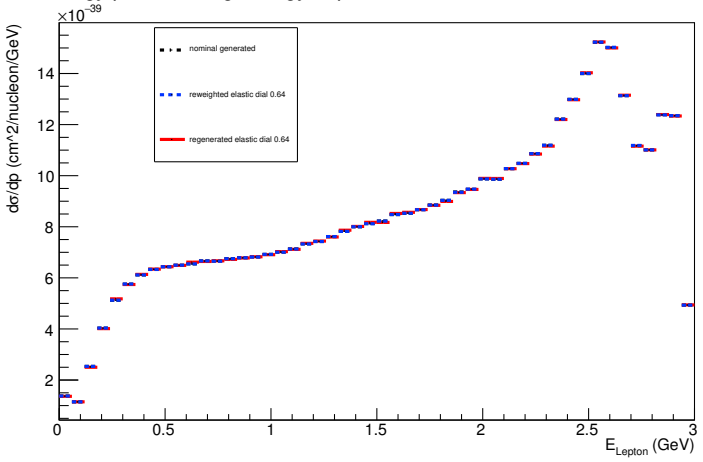

Angle plot: Leading Energy Lepton: Neut Mode =AllModesCombined

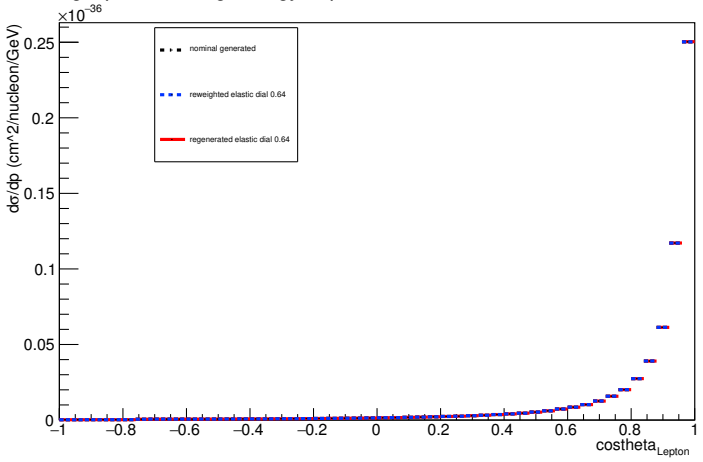

Energy plot: Leading Energy Lepton: Neut Mode =AllModesCombined

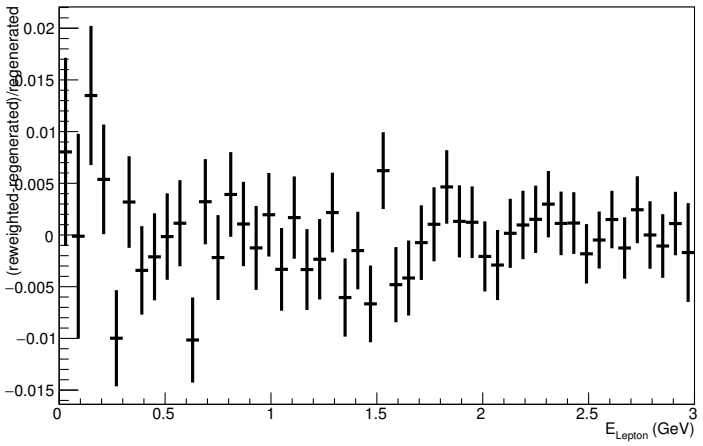

Angle plot: Leading Energy Lepton: Neut Mode =AllModesCombined

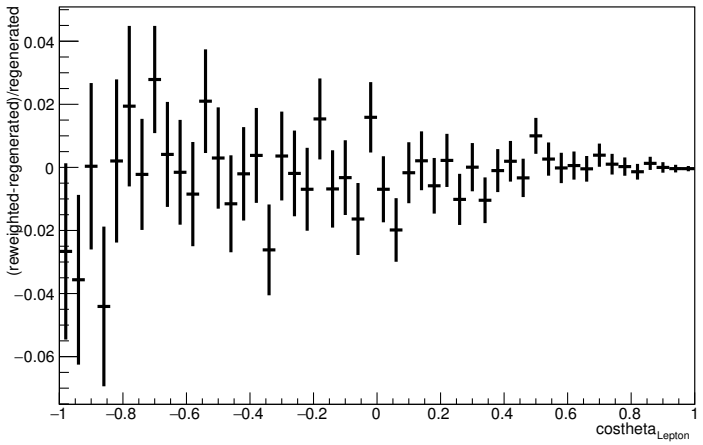

Energy plot: Leading Energy Pion: Neut Mode =AllModesCombined

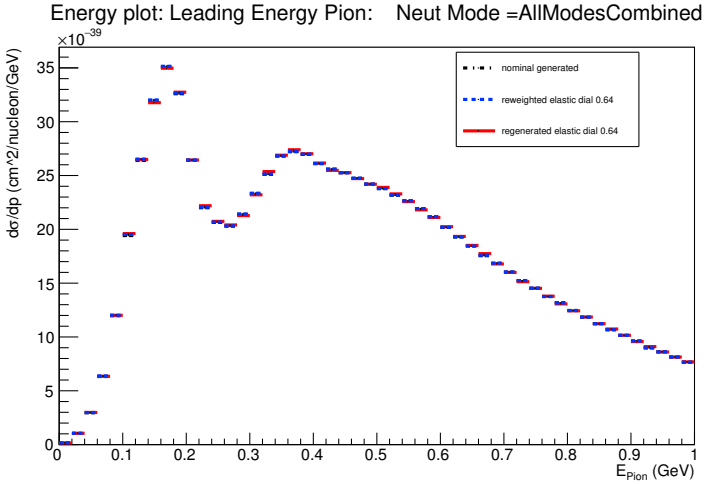

Energy plot: Every FSI Pion: Neut Mode =AllModesCombined

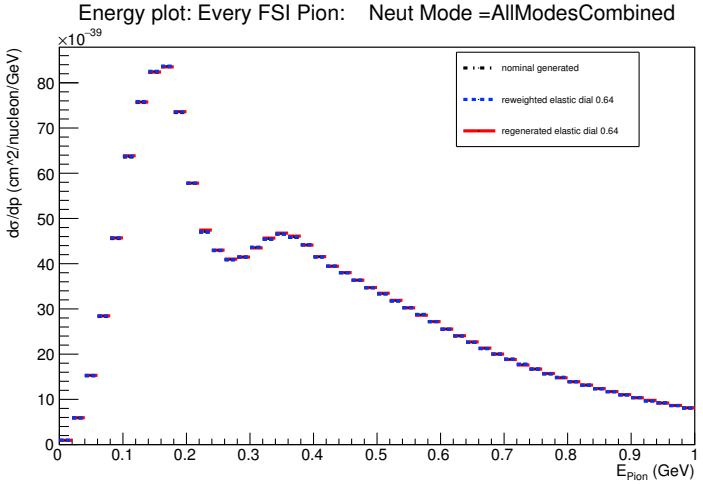

Energy plot: Leading Energy Pion: Neut Mode =AllModesCombined

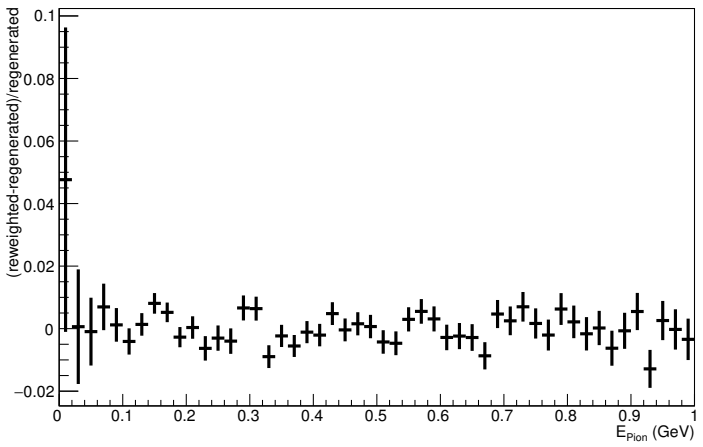

Energy plot: Every FSI Pion: Neut Mode =AllModesCombined

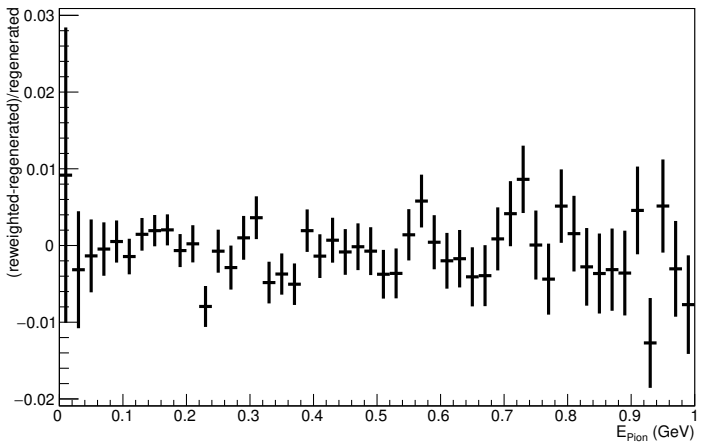

Angle plot: Leading Energy Pion: Neut Mode =AllModesCombined

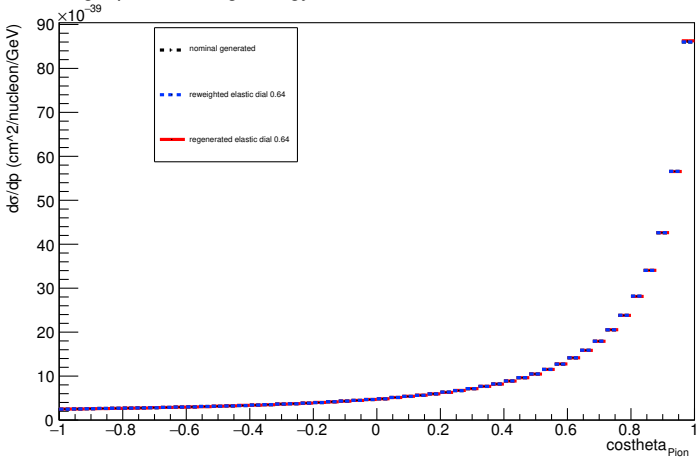

Angle plot: Every FSI Pion: Neut Mode =AllModesCombined

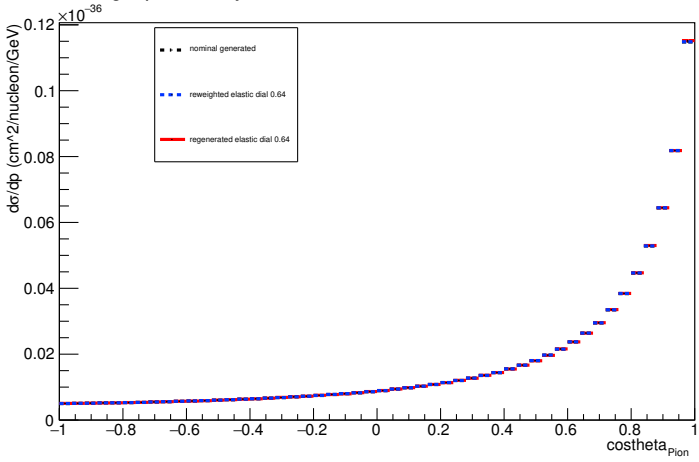

Angle plot: Leading Energy Pion: Neut Mode =AllModesCombined

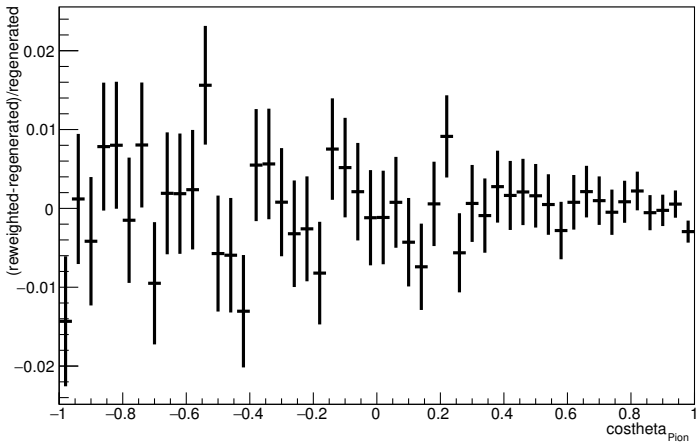

Angle plot: Every FSI Pion: Neut Mode =AllModesCombined

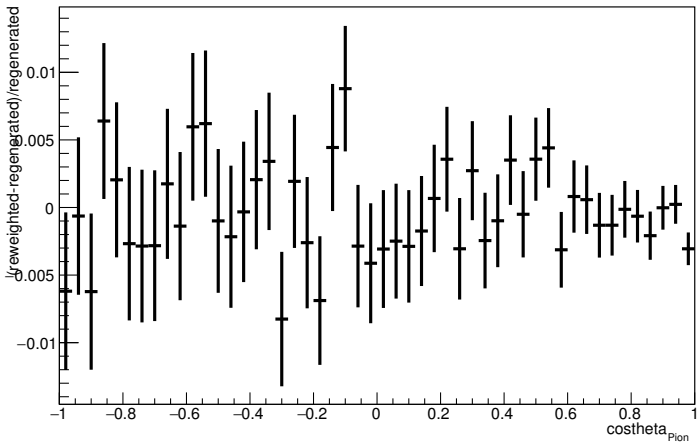

Energy plot: Leading Energy Nucleon: Neut Mode =1

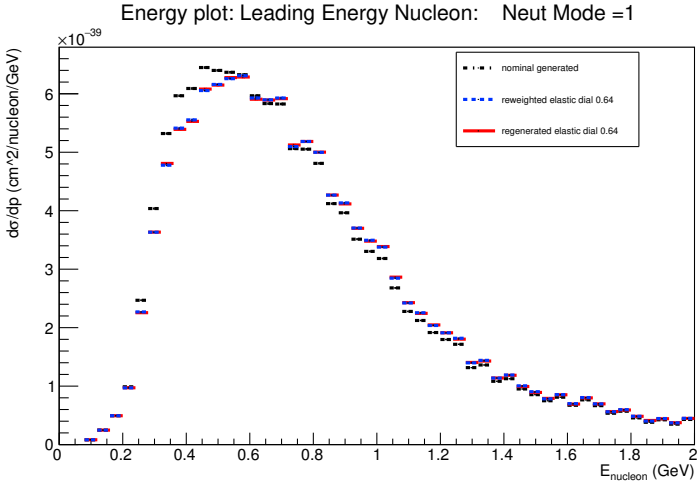

Energy plot: Every FSI Nucleon: Neut Mode =1

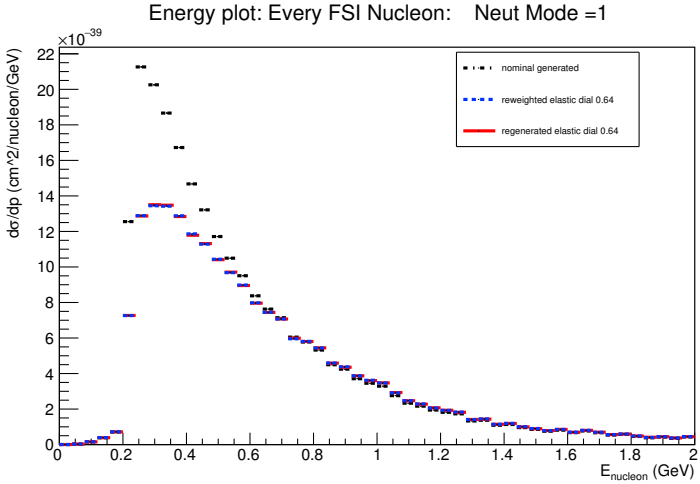

Energy plot: Leading Energy Nucleon: Neut Mode =1

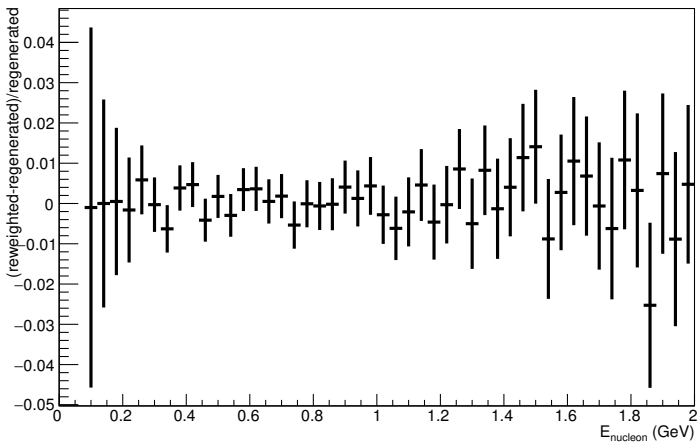

Energy plot: Every FSI Nucleon: Neut Mode =1

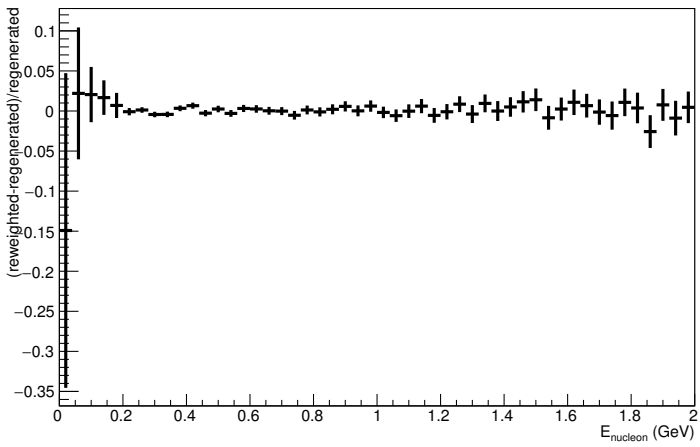

Angle plot: Leading Energy Nucleon: Neut Mode =1

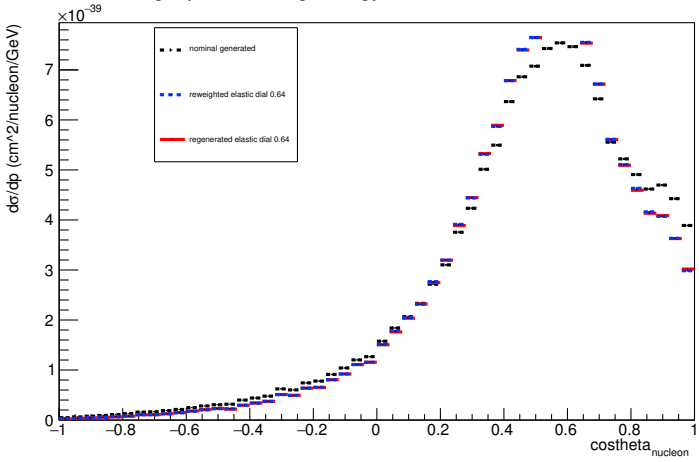

Angle plot: Every FSI Nucleon: Neut Mode =1

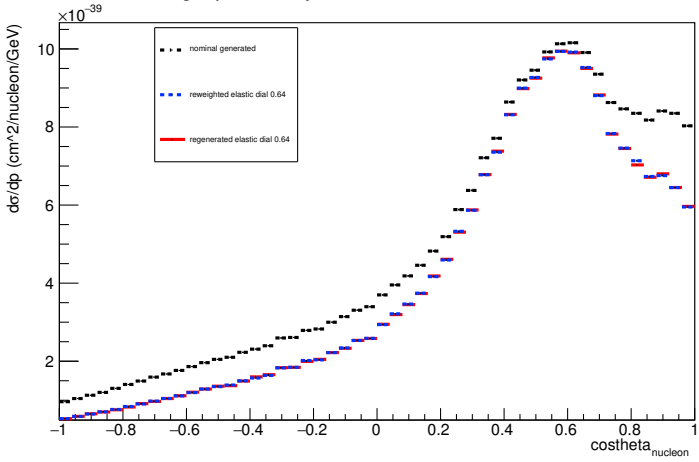

Angle plot: Leading Energy Nucleon: Neut Mode =1

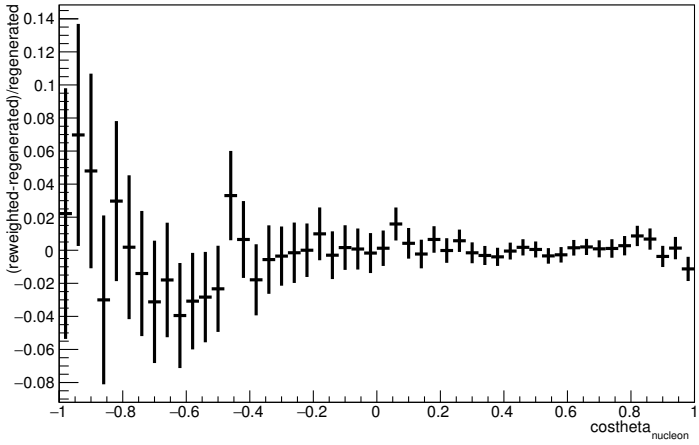

Angle plot: Every FSI Nucleon: Neut Mode =1

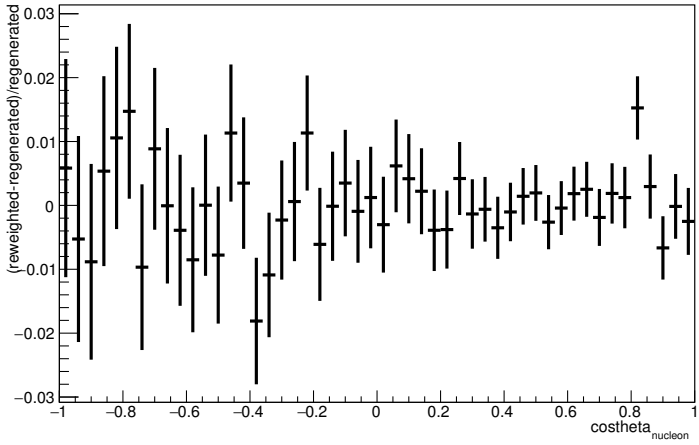

Energy plot: Leading Energy Proton: Neut Mode =1

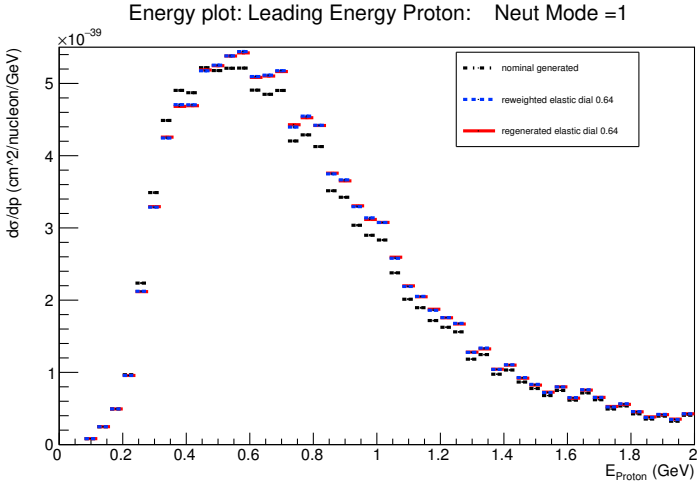

Energy plot: Every FSI Proton: Neut Mode =1

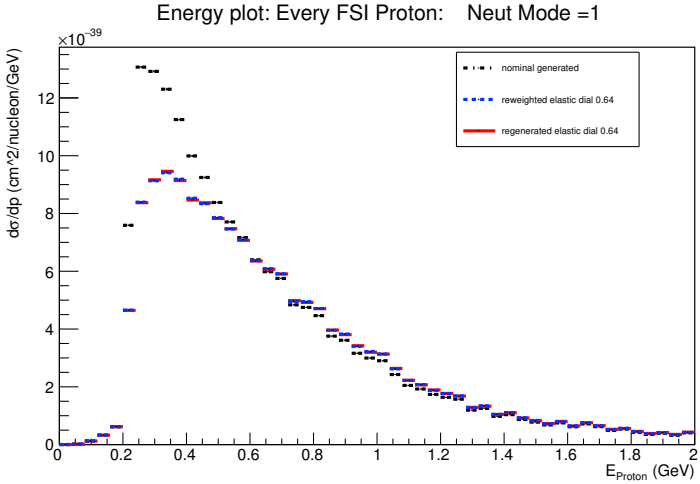

Energy plot: Leading Energy Proton: Neut Mode =1

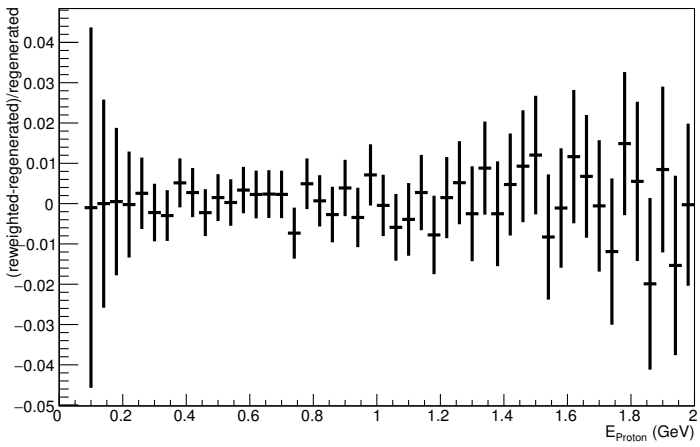

Energy plot: Every FSI Proton: Neut Mode =1

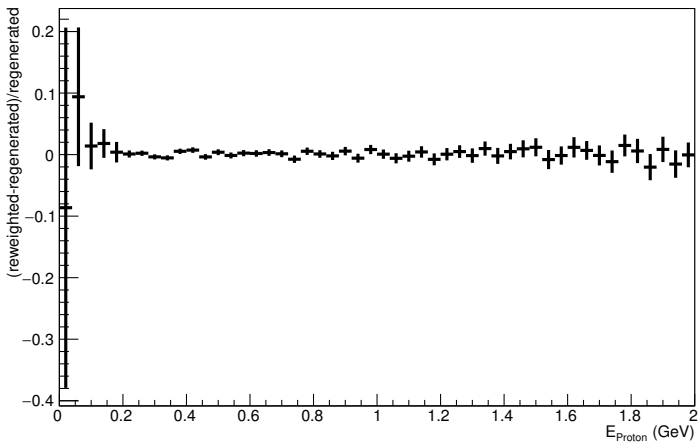

Angle plot: Leading Energy Proton: Neut Mode =1

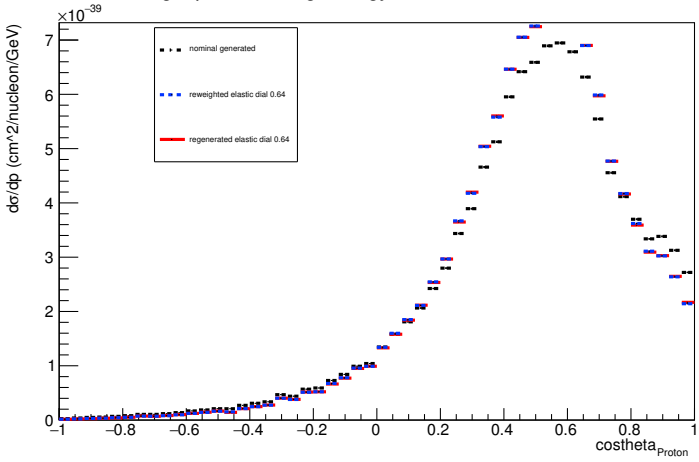

Angle plot: Every FSI Proton: Neut Mode =1

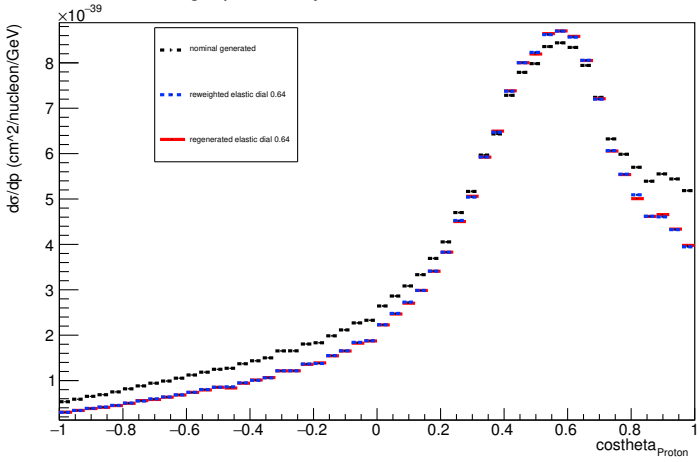

Angle plot: Leading Energy Proton: Neut Mode =1

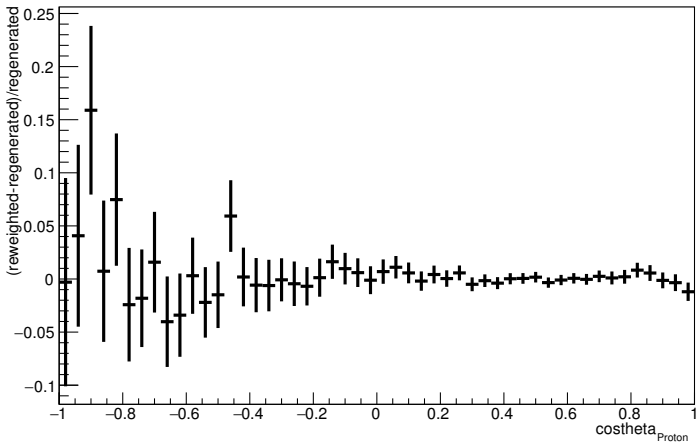

Angle plot: Every FSI Proton: Neut Mode =1

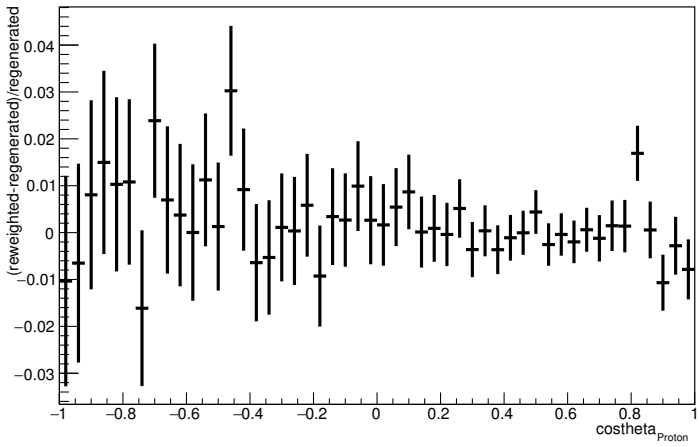

Energy plot: Leading Energy Neutron: Neut Mode =1

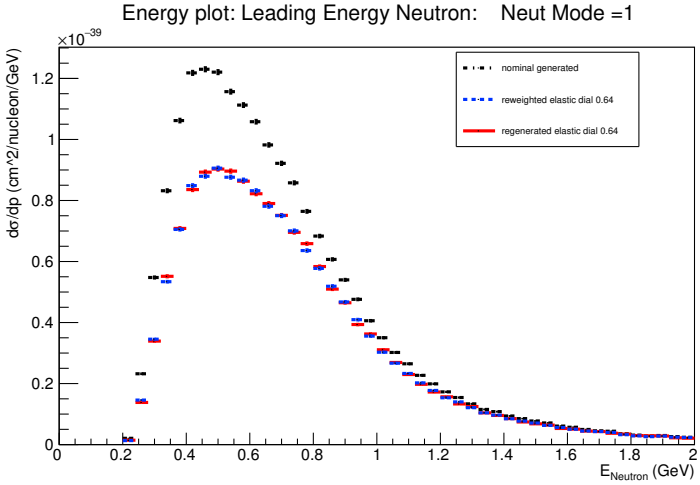

Energy plot: Every FSI Neutron: Neut Mode =1

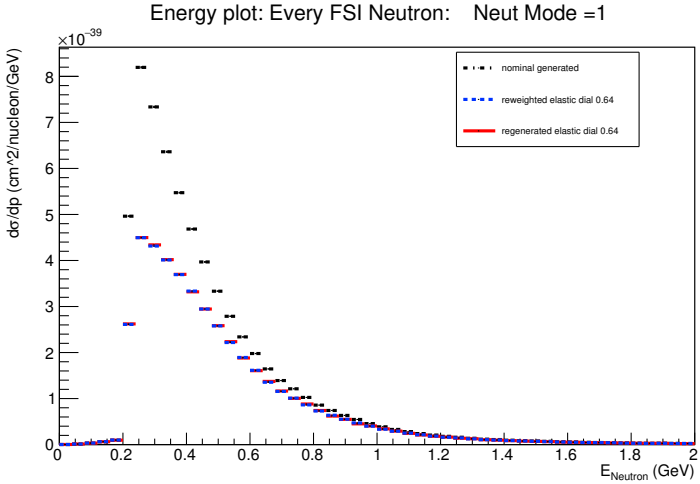

Energy plot: Leading Energy Neutron: Neut Mode =1

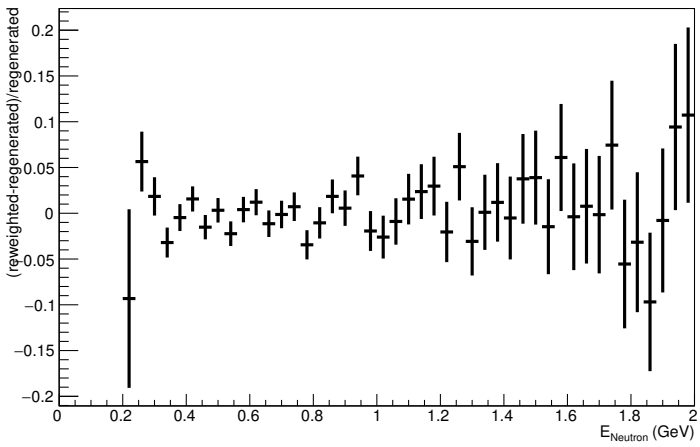

Energy plot: Every FSI Neutron: Neut Mode =1

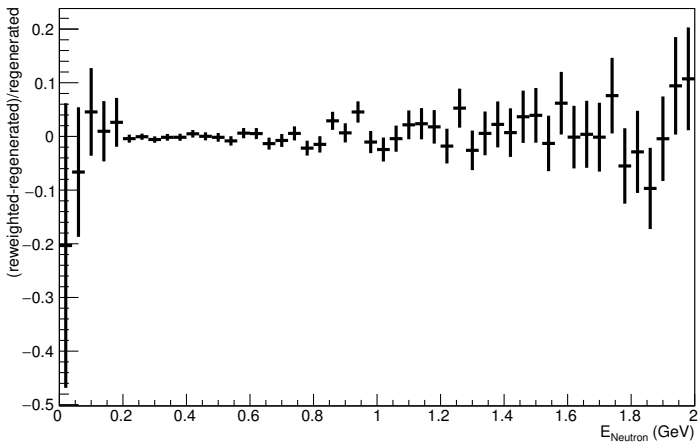

Angle plot: Leading Energy Neutron: Neut Mode =1

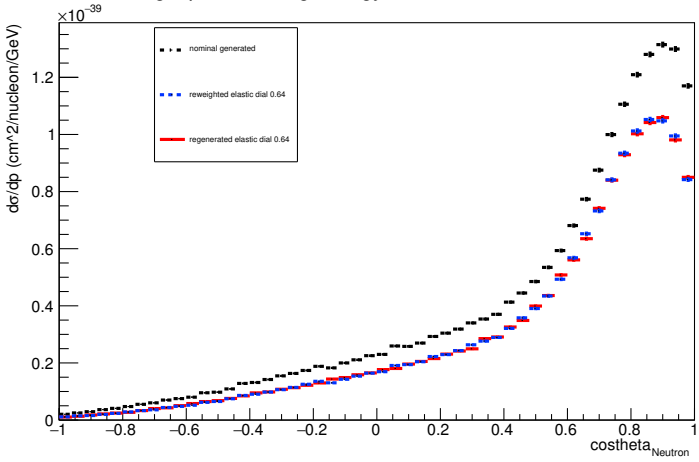

Angle plot: Every FSI Neutron: Neut Mode =1

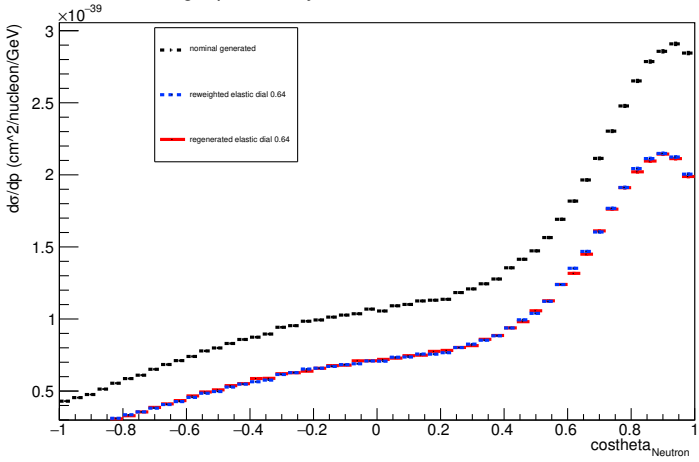

Angle plot: Leading Energy Neutron: Neut Mode =1

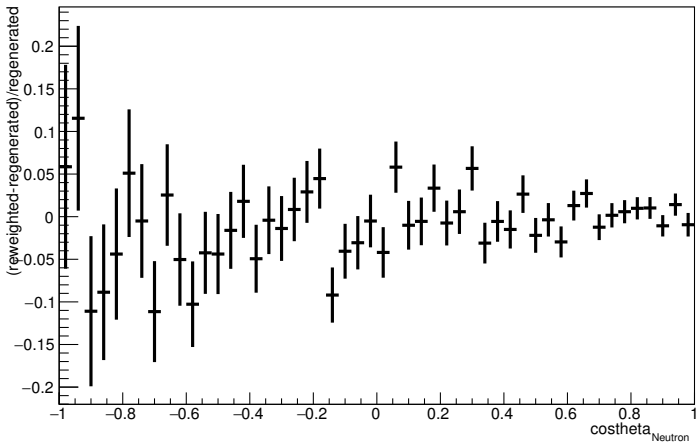

Angle plot: Every FSI Neutron: Neut Mode =1

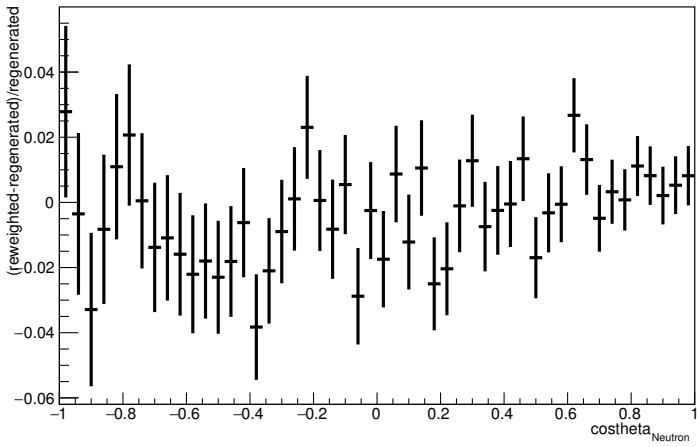

Energy plot: Leading Energy Lepton: Neut Mode =1

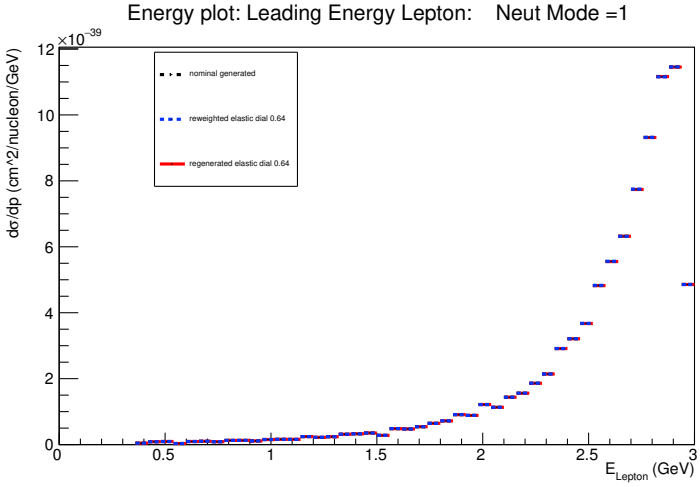

Angle plot: Leading Energy Lepton: Neut Mode =1

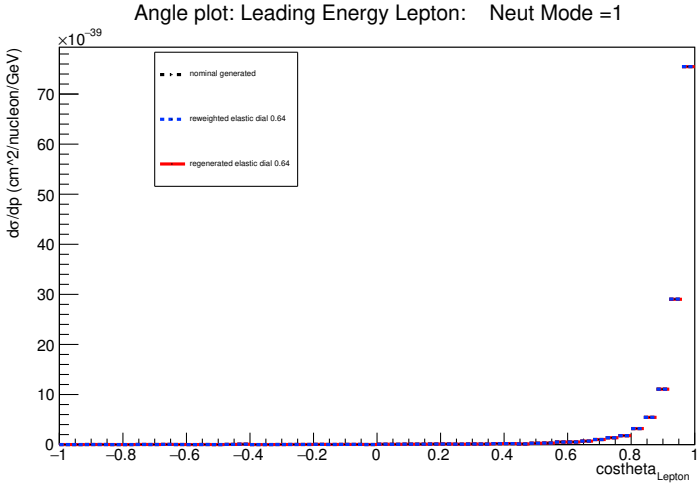

Energy plot: Leading Energy Lepton: Neut Mode =1

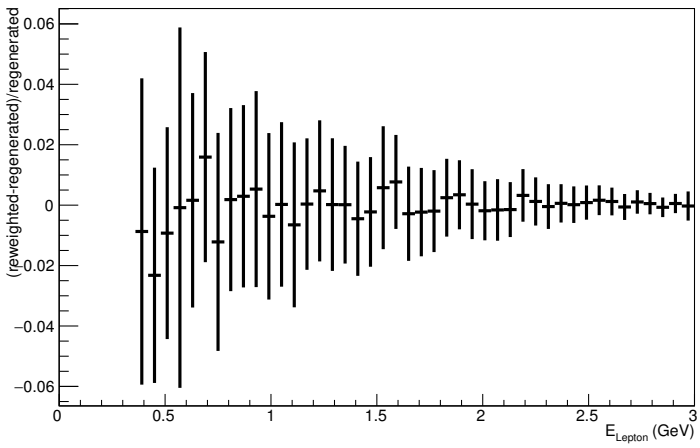

Angle plot: Leading Energy Lepton: Neut Mode =1

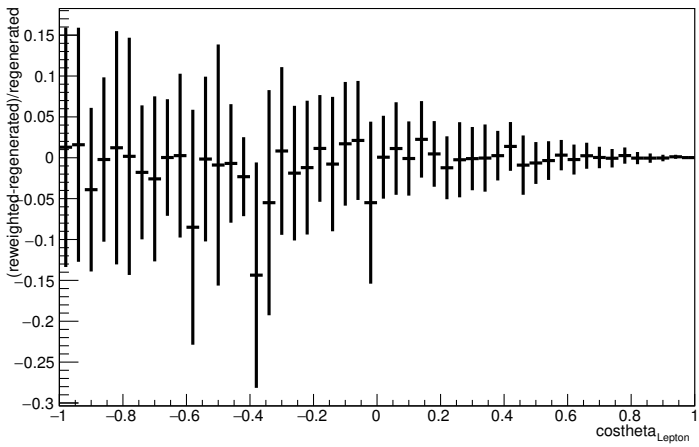

Energy plot: Leading Energy Pion: Neut Mode =1

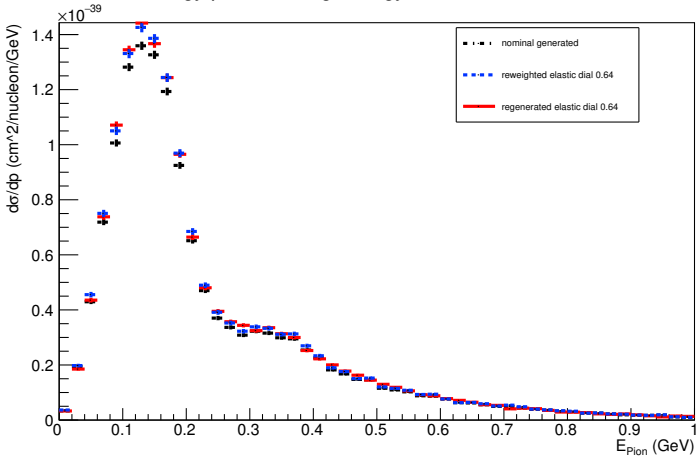

Energy plot: Every FSI Pion: Neut Mode =1

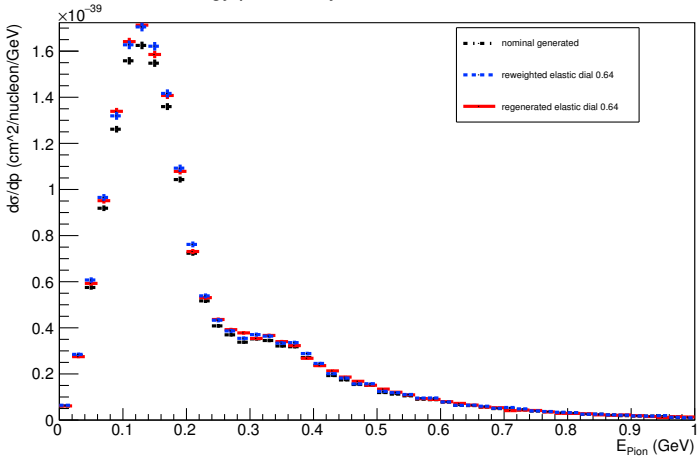

Energy plot: Leading Energy Pion: Neut Mode =1

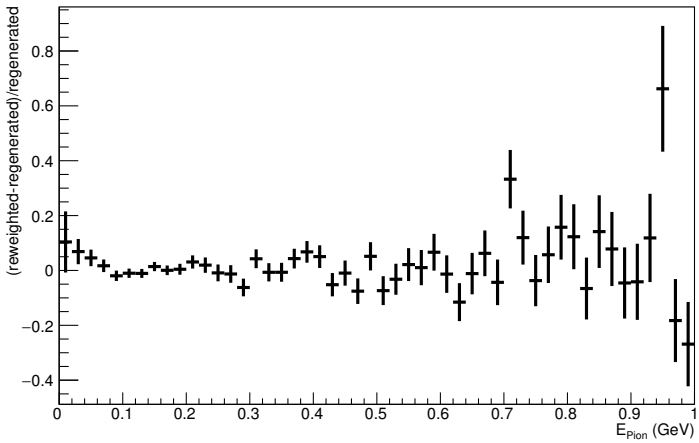

Energy plot: Every FSI Pion: Neut Mode =1

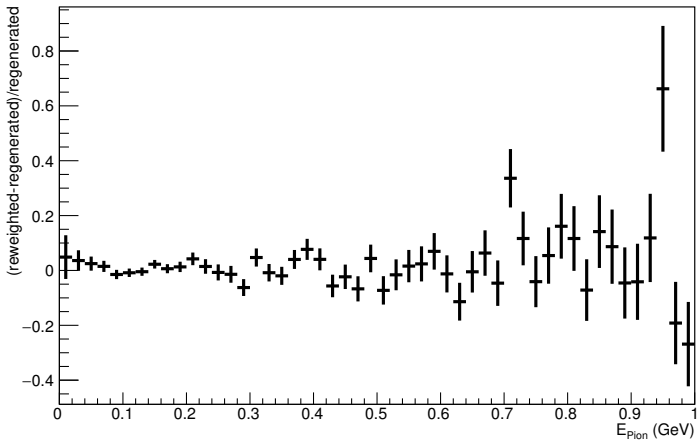

Angle plot: Leading Energy Pion: Neut Mode =1

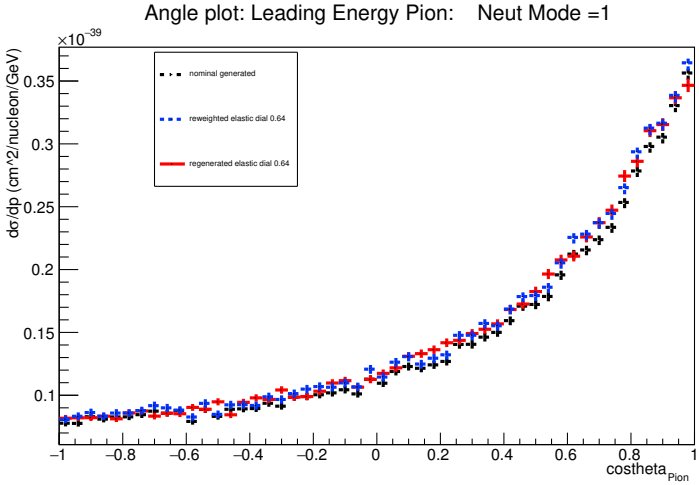

Angle plot: Every FSI Pion: Neut Mode =1

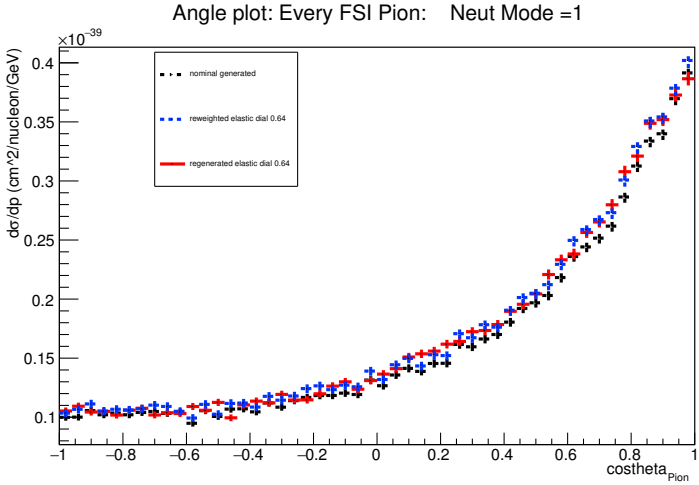

Angle plot: Leading Energy Pion: Neut Mode =1

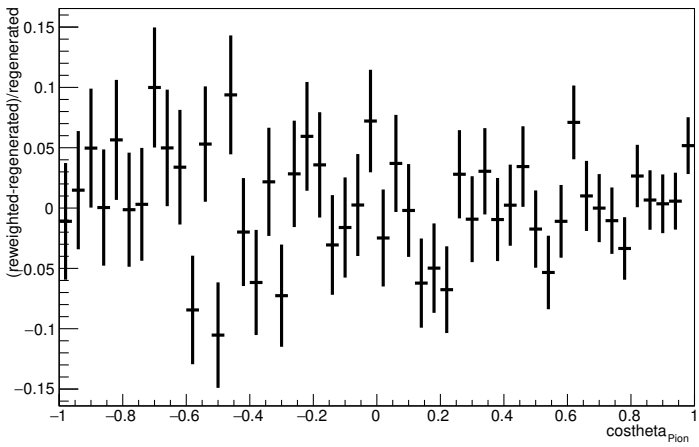

Angle plot: Every FSI Pion: Neut Mode =1

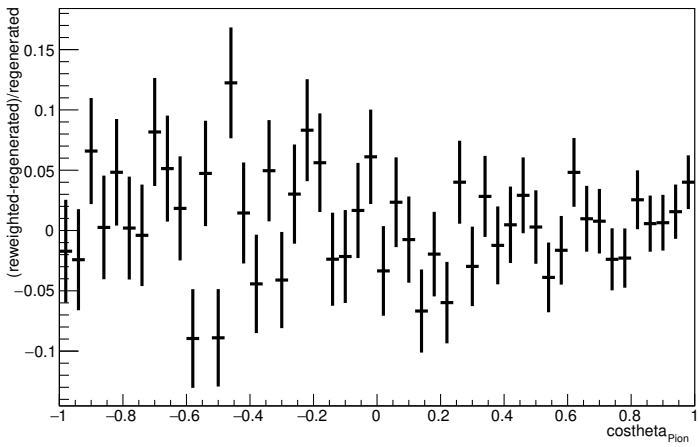

Energy plot: Leading Energy Nucleon: Neut Mode =2

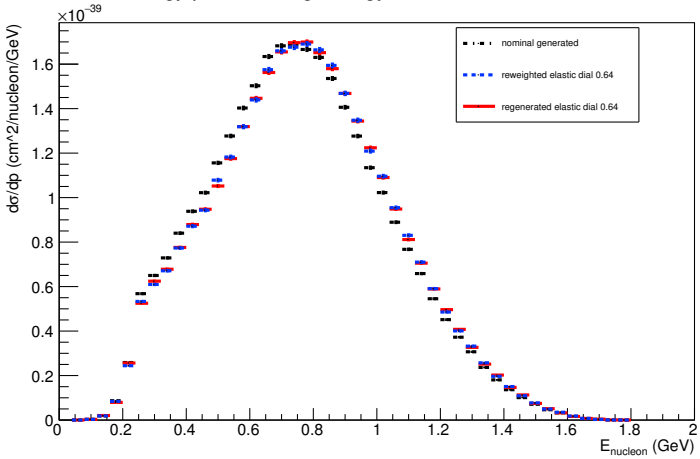

Energy plot: Every FSI Nucleon: Neut Mode =2

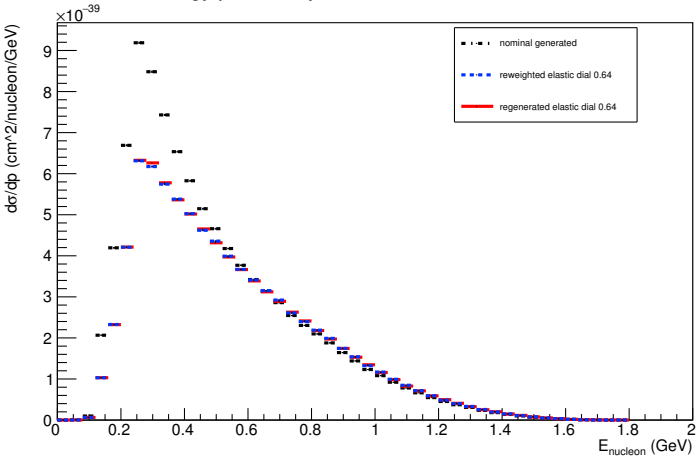

Energy plot: Leading Energy Nucleon: Neut Mode =2

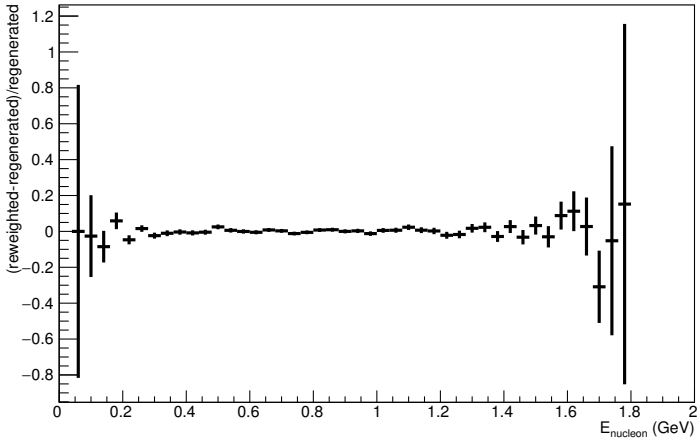

Energy plot: Every FSI Nucleon: Neut Mode =2

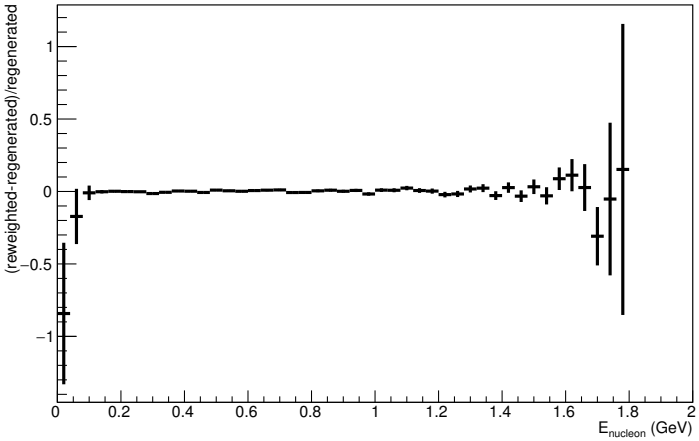

Angle plot: Leading Energy Nucleon: Neut Mode =2

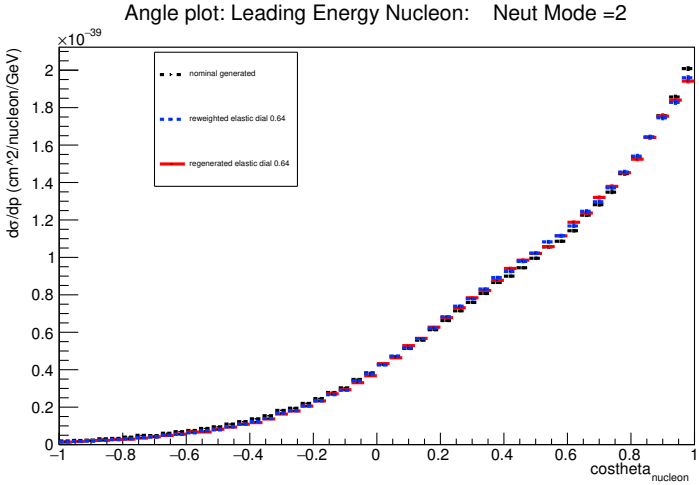

Angle plot: Every FSI Nucleon: Neut Mode =2

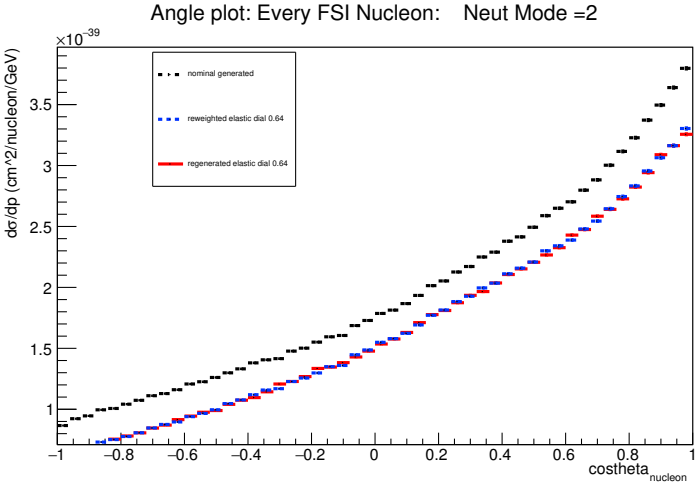

Angle plot: Leading Energy Nucleon: Neut Mode =2

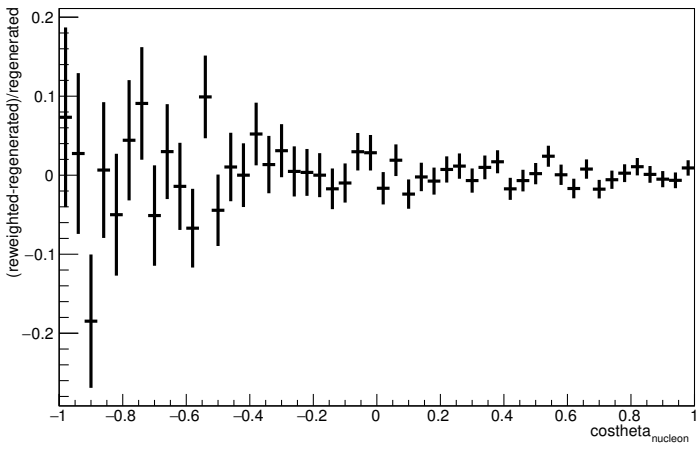

Angle plot: Every FSI Nucleon: Neut Mode =2

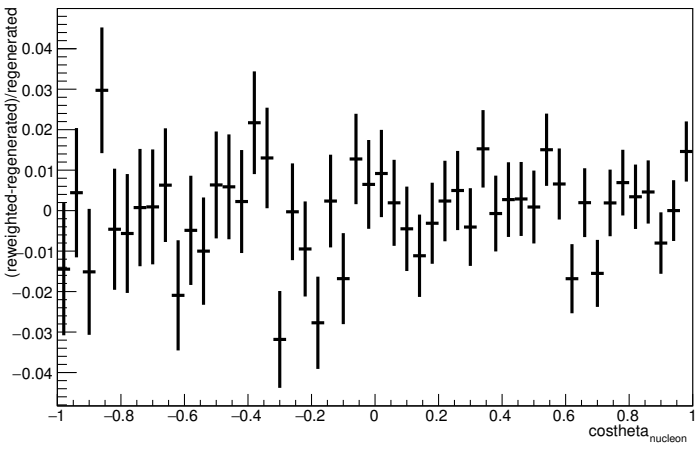

Energy plot: Leading Energy Proton: Neut Mode =2

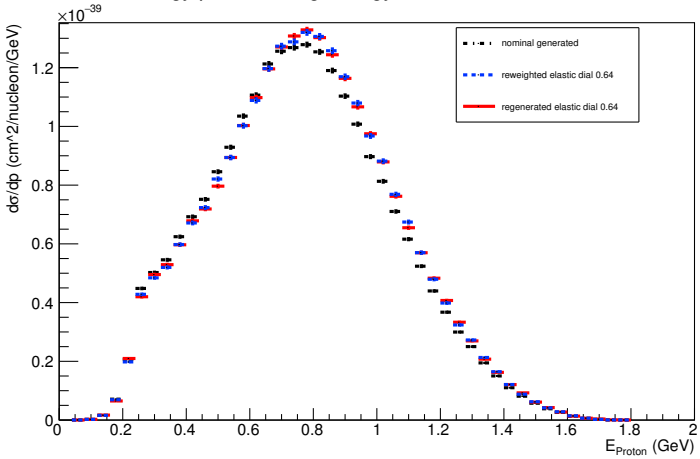

Energy plot: Every FSI Proton: Neut Mode =2

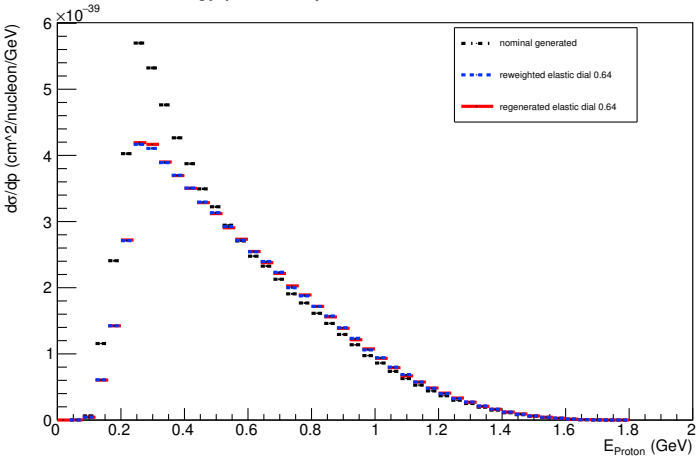

Energy plot: Leading Energy Proton: Neut Mode =2

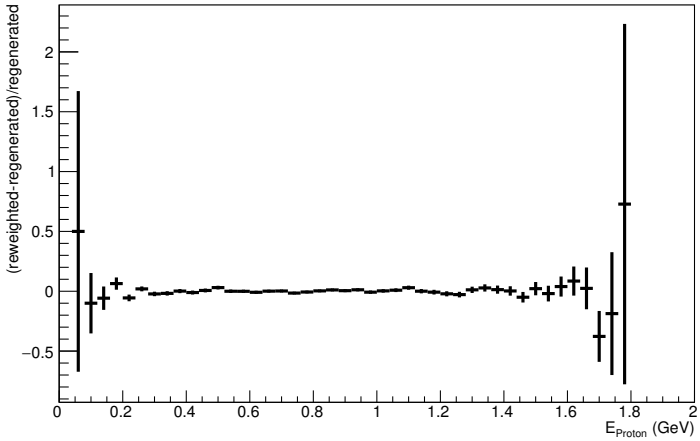

Energy plot: Every FSI Proton: Neut Mode =2

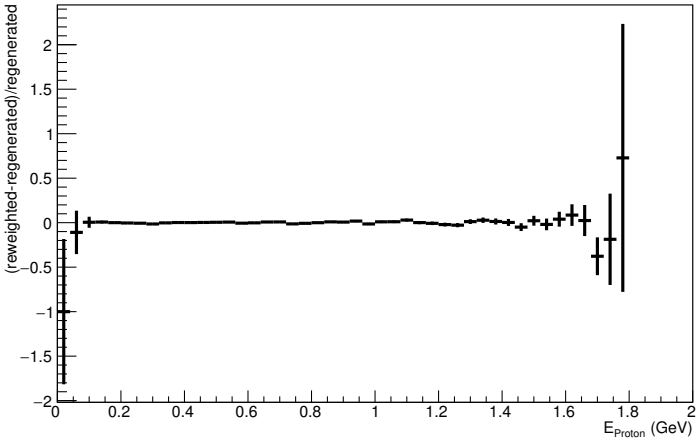

Angle plot: Leading Energy Proton: Neut Mode =2

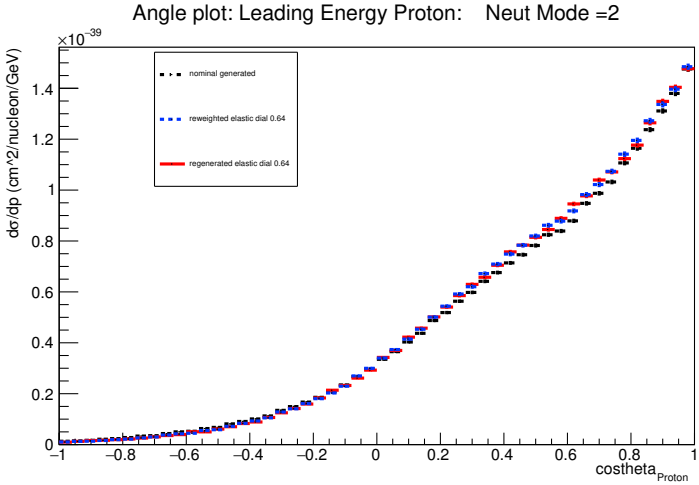

Angle plot: Every FSI Proton: Neut Mode =2

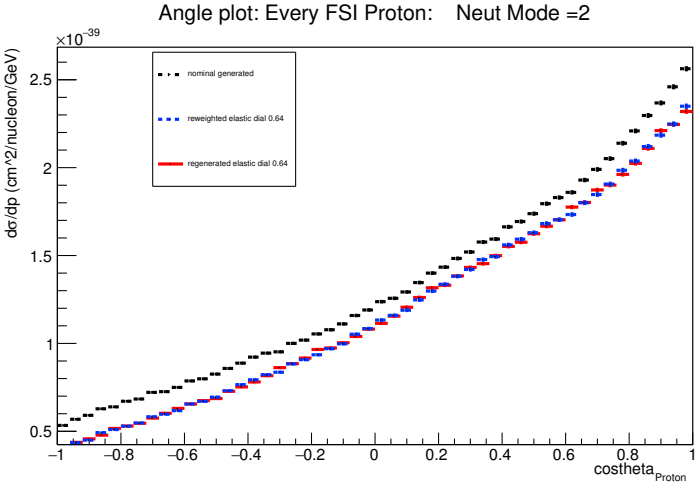

Angle plot: Leading Energy Proton: Neut Mode =2

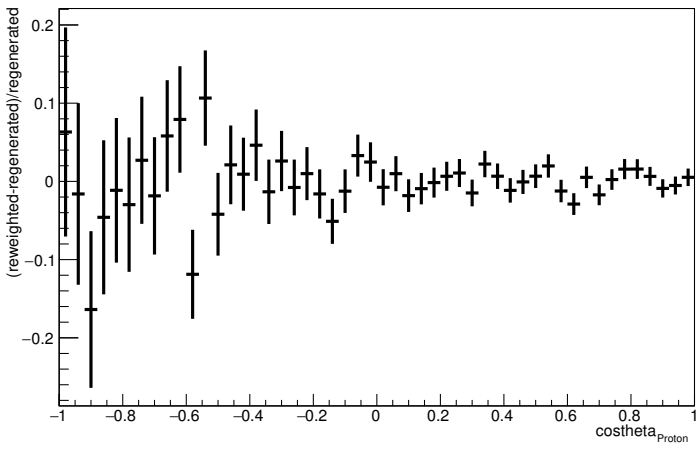

Angle plot: Every FSI Proton: Neut Mode =2

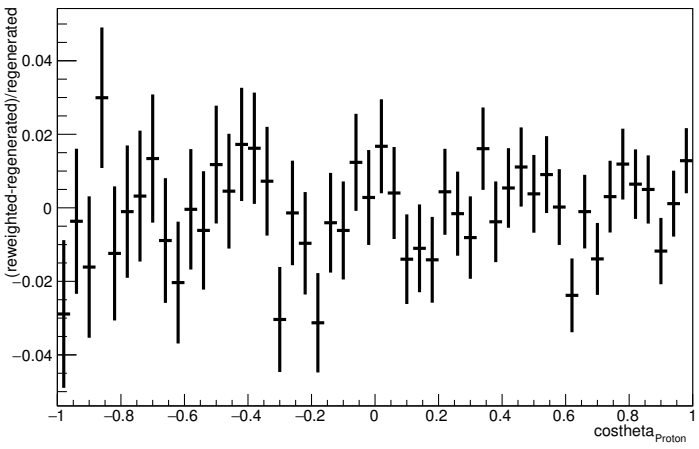

Energy plot: Leading Energy Neutron: Neut Mode =2

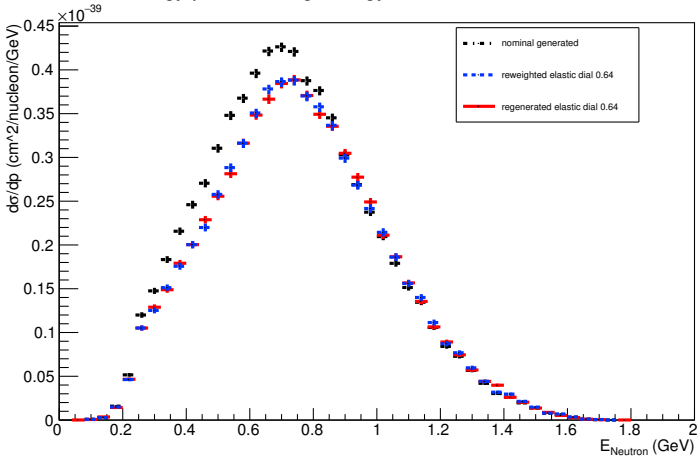

Energy plot: Every FSI Neutron: Neut Mode =2

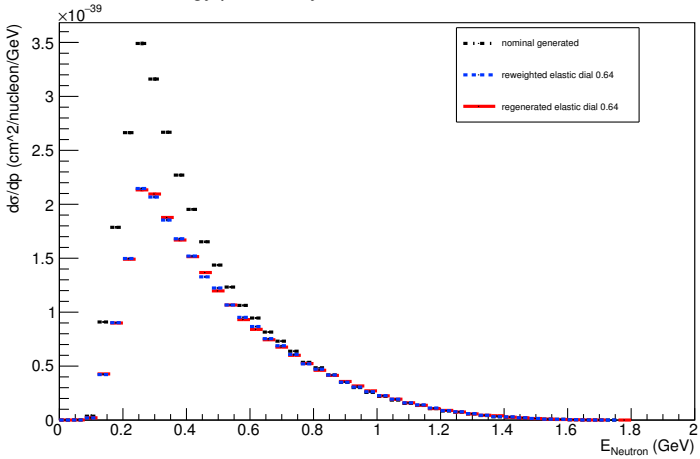

Energy plot: Leading Energy Neutron: Neut Mode =2

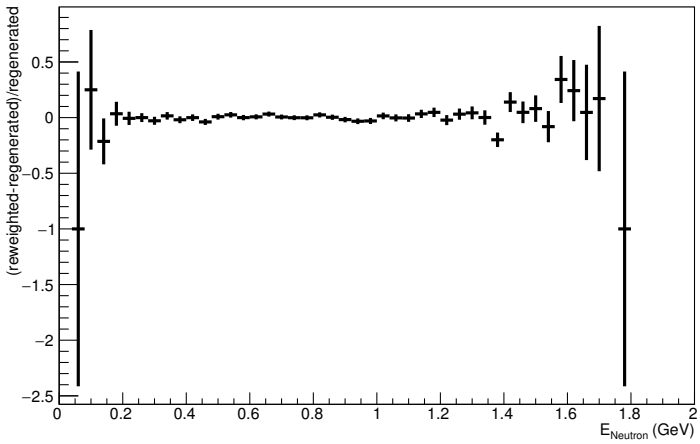

Energy plot: Every FSI Neutron: Neut Mode =2

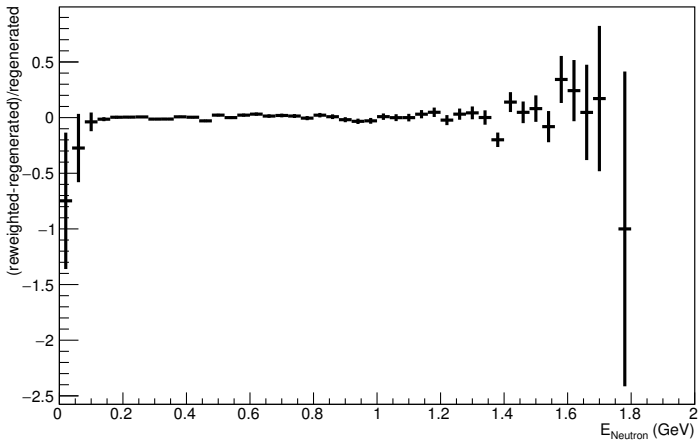

Angle plot: Leading Energy Neutron: Neut Mode =2

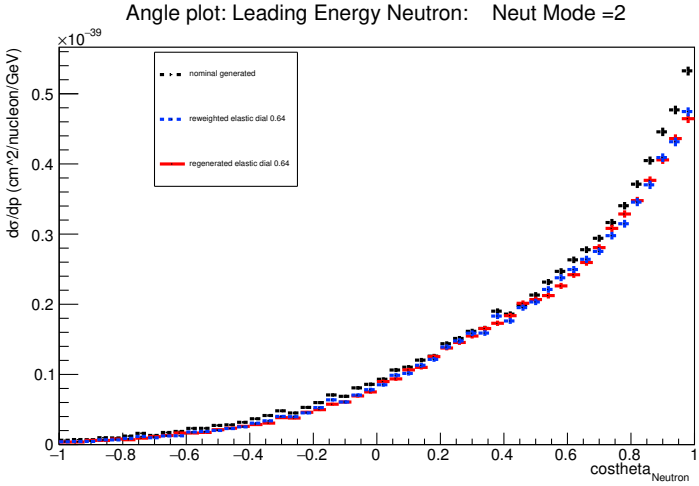

Angle plot: Every FSI Neutron: Neut Mode =2

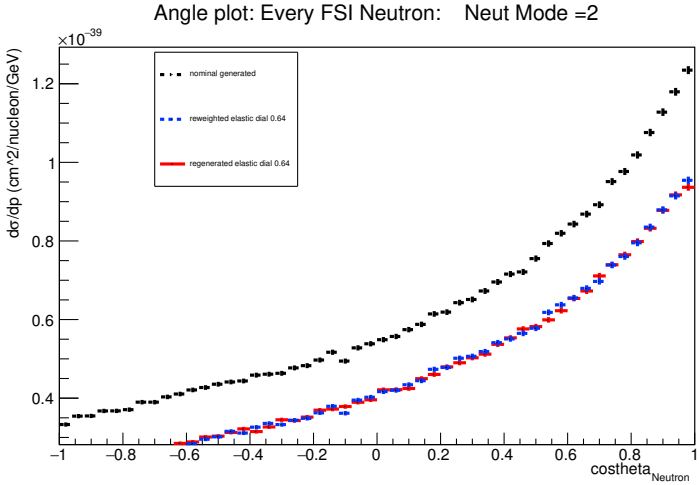

Angle plot: Leading Energy Neutron: Neut Mode =2

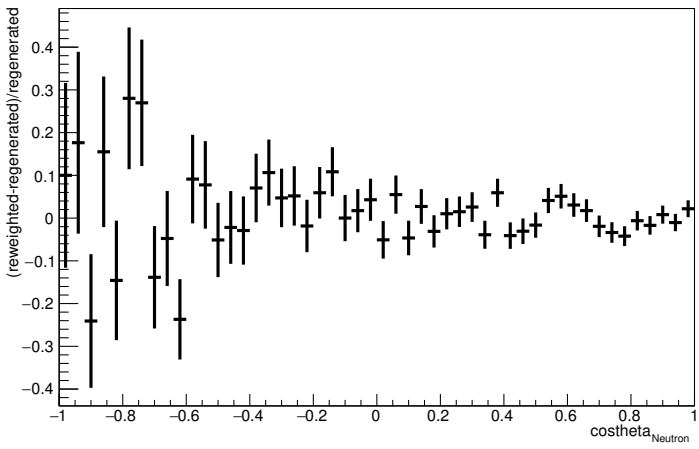

Angle plot: Every FSI Neutron: Neut Mode =2

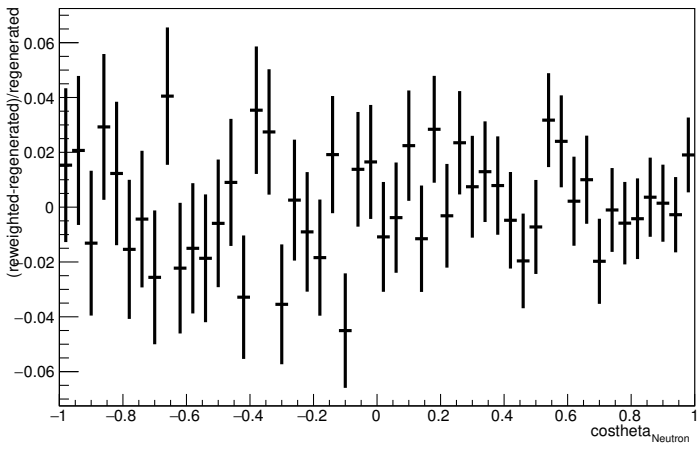

Energy plot: Leading Energy Lepton: Neut Mode =2

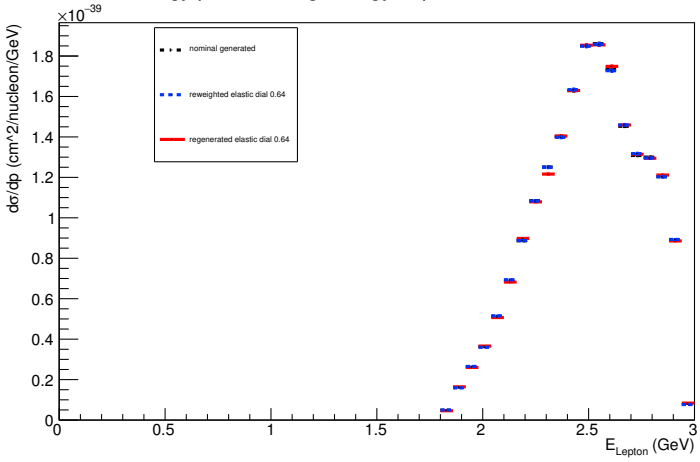

Angle plot: Leading Energy Lepton: Neut Mode =2

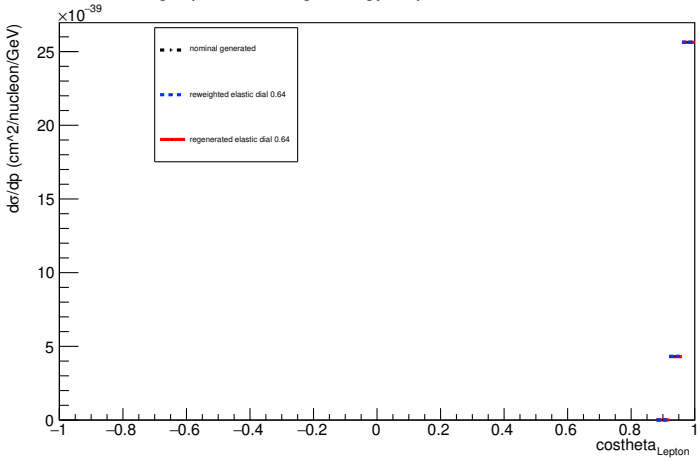

Energy plot: Leading Energy Lepton: Neut Mode =2

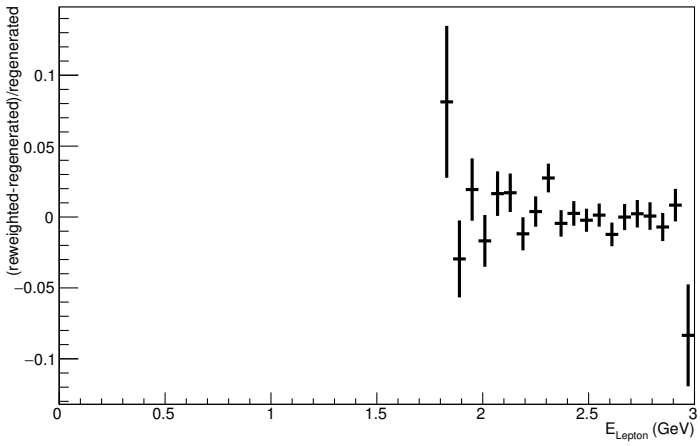

Angle plot: Leading Energy Lepton: Neut Mode =2

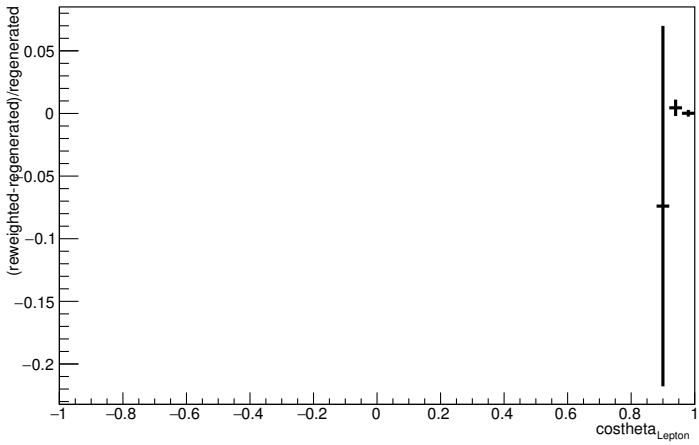

Energy plot: Leading Energy Pion: Neut Mode =2

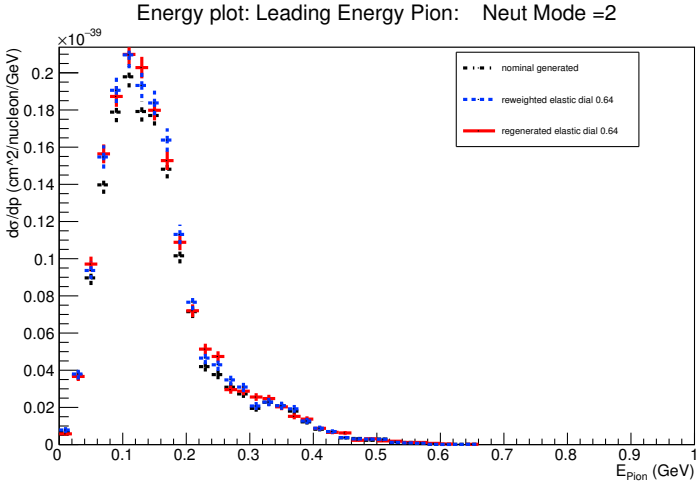

Energy plot: Every FSI Pion: Neut Mode =2

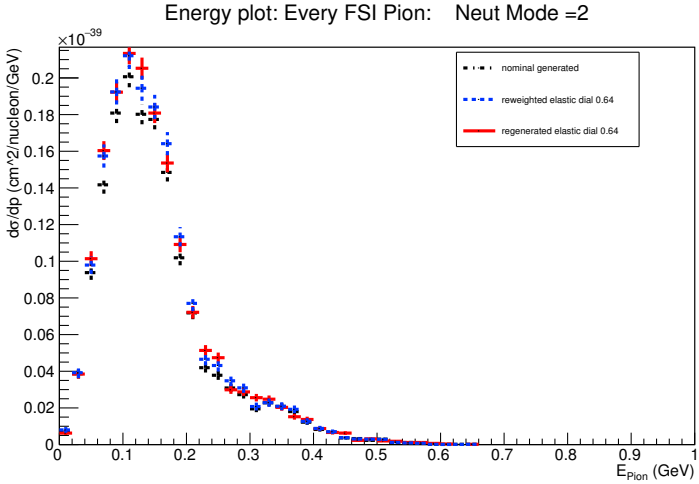

Energy plot: Leading Energy Pion: Neut Mode =2

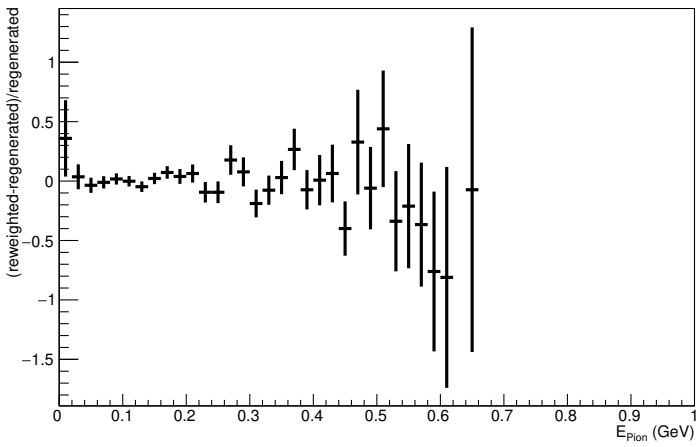

Energy plot: Every FSI Pion: Neut Mode =2

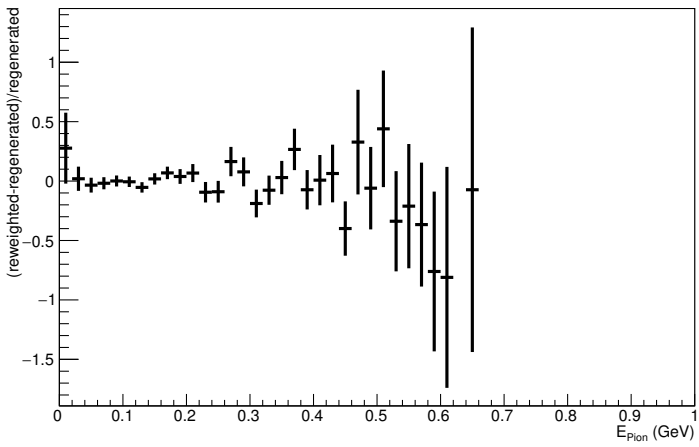

Angle plot: Leading Energy Pion: Neut Mode =2

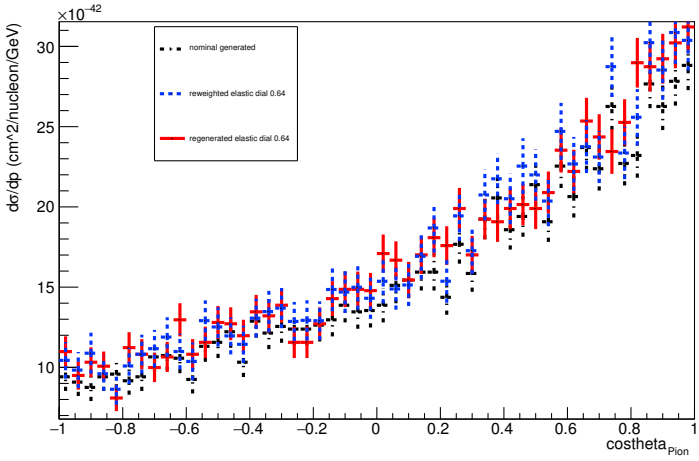

Angle plot: Every FSI Pion: Neut Mode =2

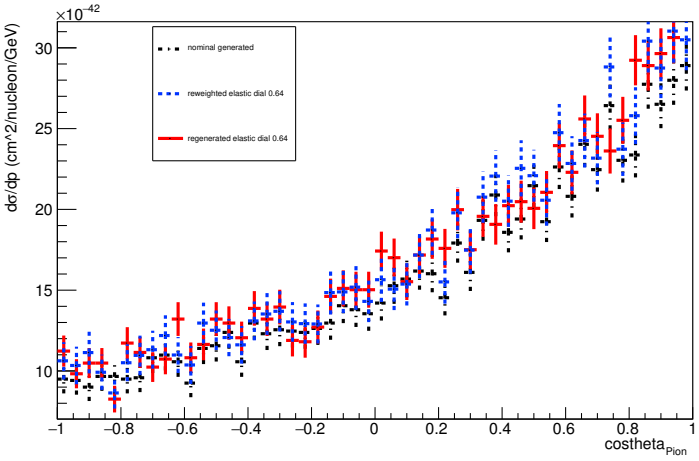

Angle plot: Leading Energy Pion: Neut Mode =2

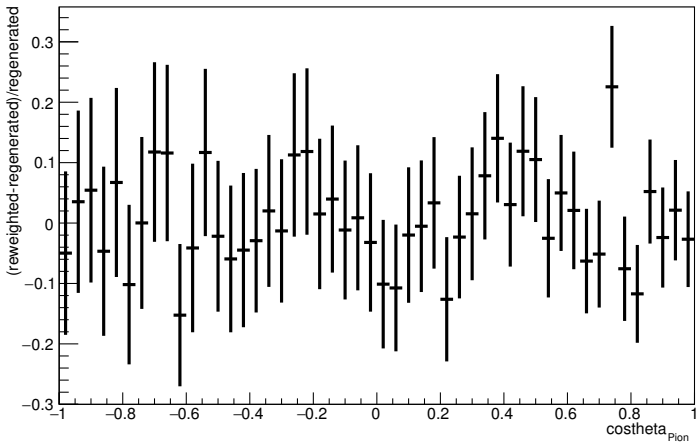

Angle plot: Every FSI Pion: Neut Mode =2

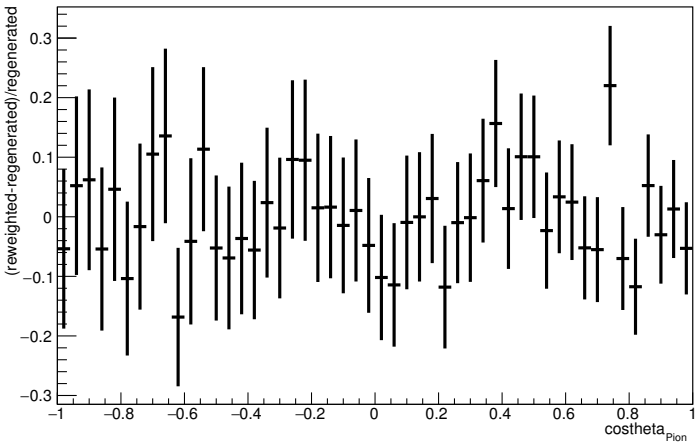

Energy plot: Leading Energy Nucleon: Neut Mode =11

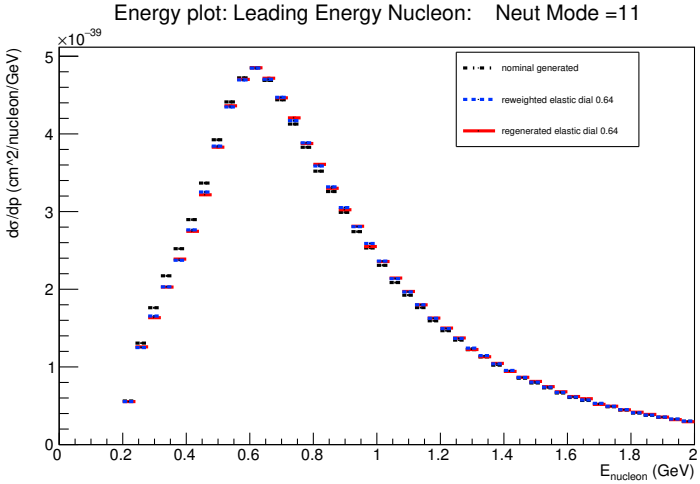

Energy plot: Every FSI Nucleon: Neut Mode =11

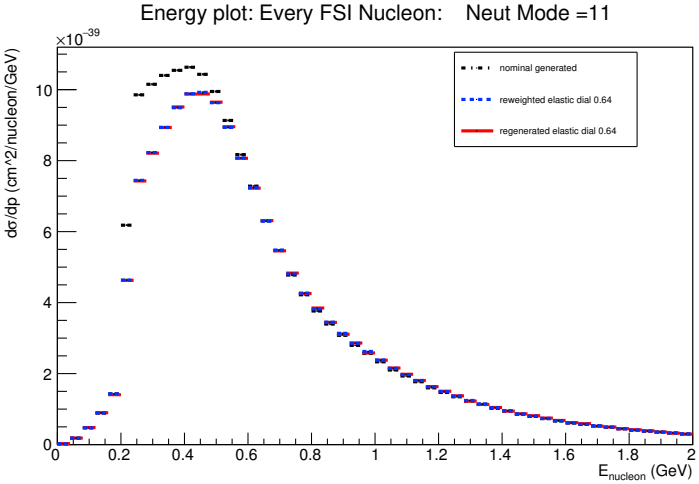

Energy plot: Leading Energy Nucleon: Neut Mode =11

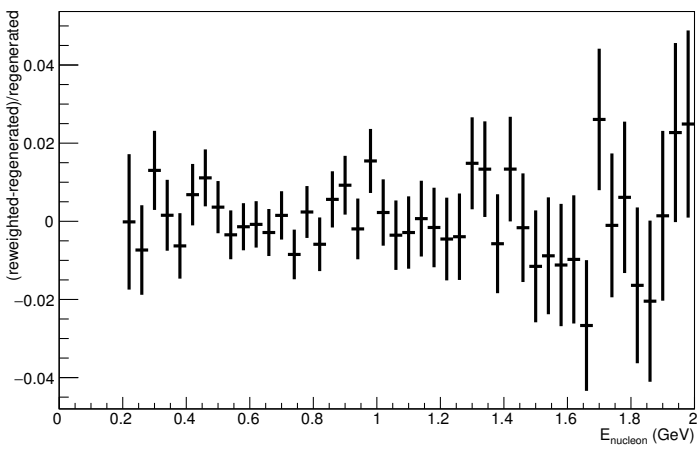

Energy plot: Every FSI Nucleon: Neut Mode =11

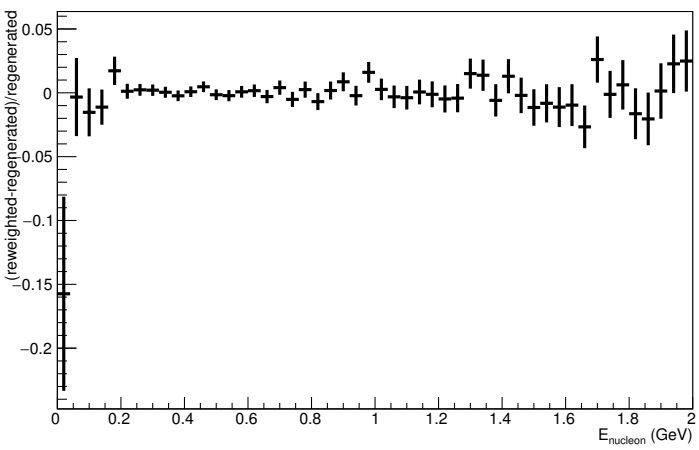

Angle plot: Leading Energy Nucleon: Neut Mode =11

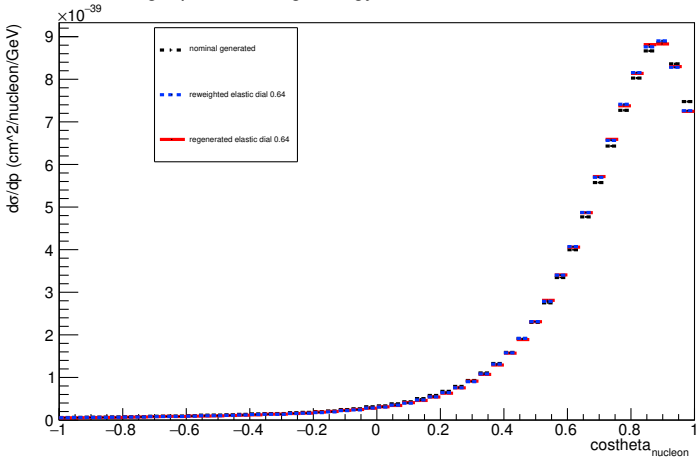

Angle plot: Every FSI Nucleon: Neut Mode =11

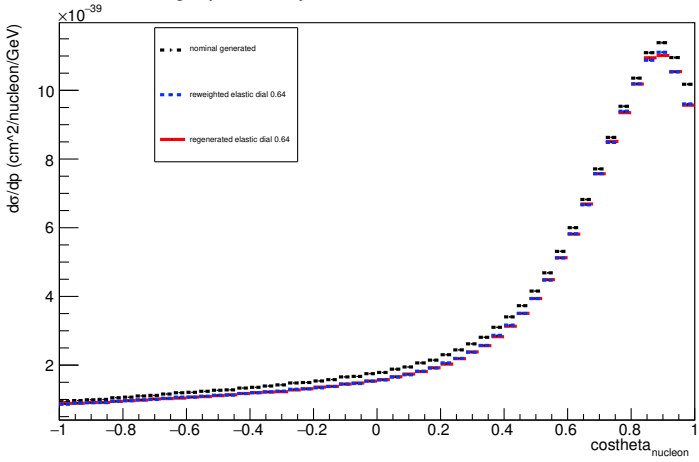

Angle plot: Leading Energy Nucleon: Neut Mode =11

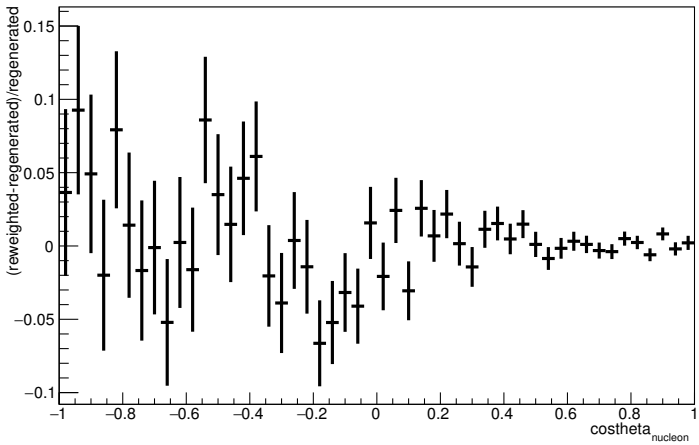

Angle plot: Every FSI Nucleon: Neut Mode =11

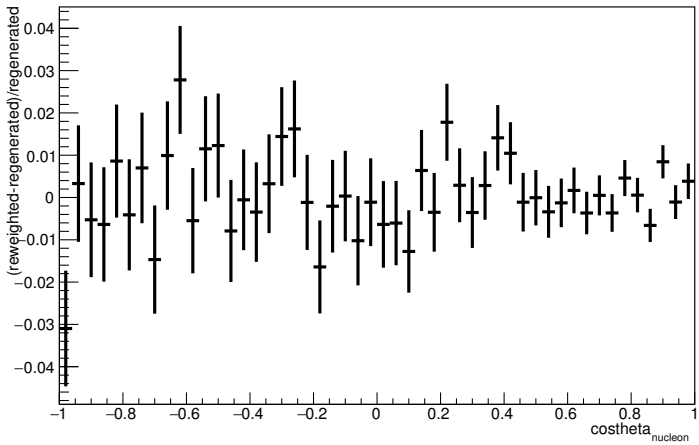

Energy plot: Leading Energy Proton: Neut Mode =11

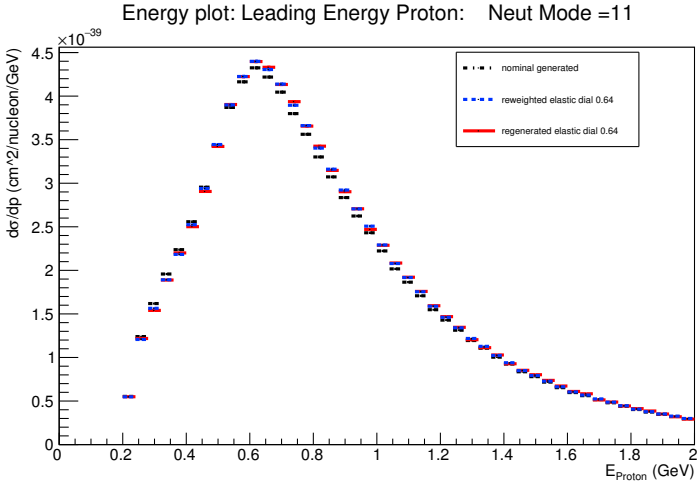

Energy plot: Every FSI Proton: Neut Mode =11

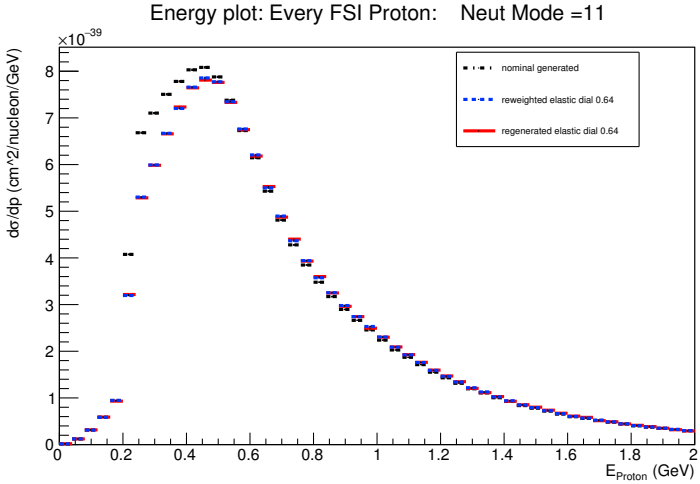

Energy plot: Leading Energy Proton: Neut Mode =11

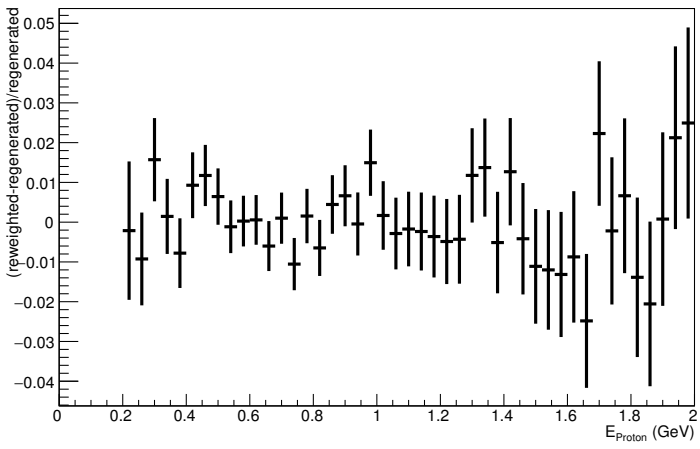

Energy plot: Every FSI Proton: Neut Mode =11

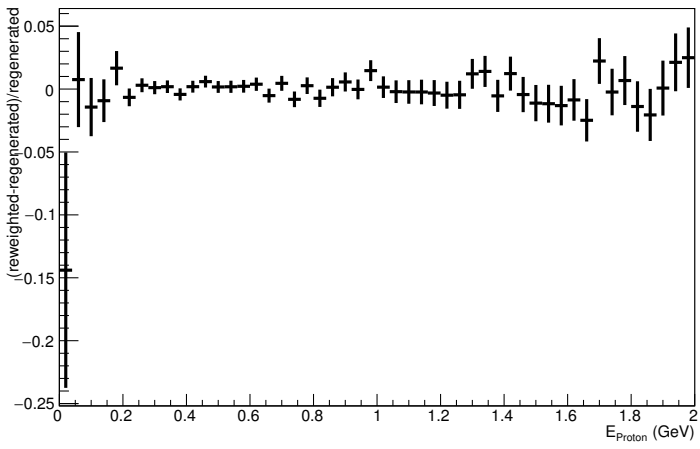

Angle plot: Leading Energy Proton: Neut Mode =11

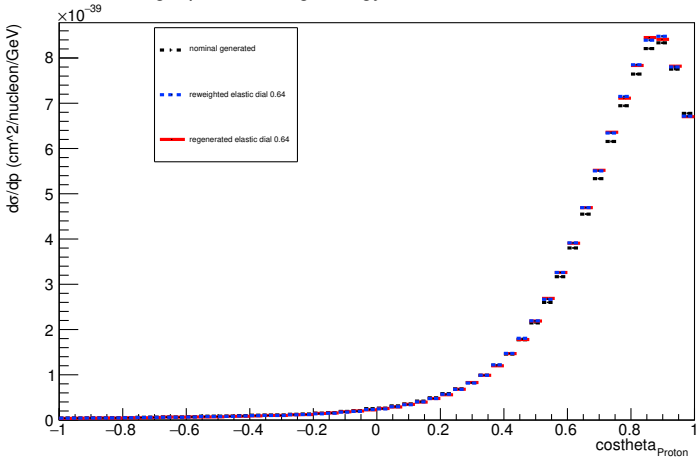

Angle plot: Every FSI Proton: Neut Mode =11

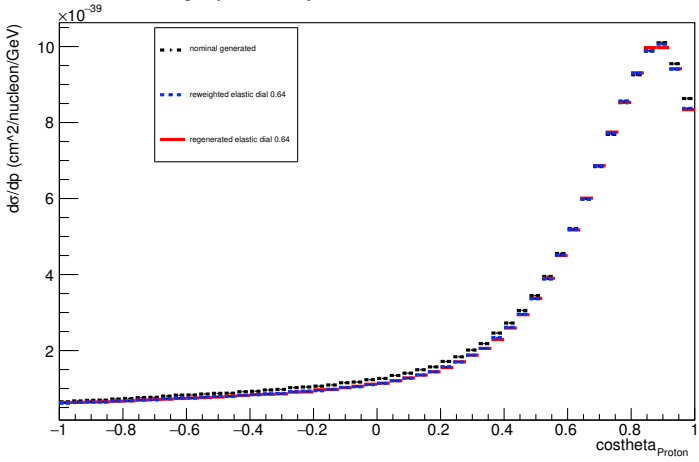

Angle plot: Leading Energy Proton: Neut Mode =11

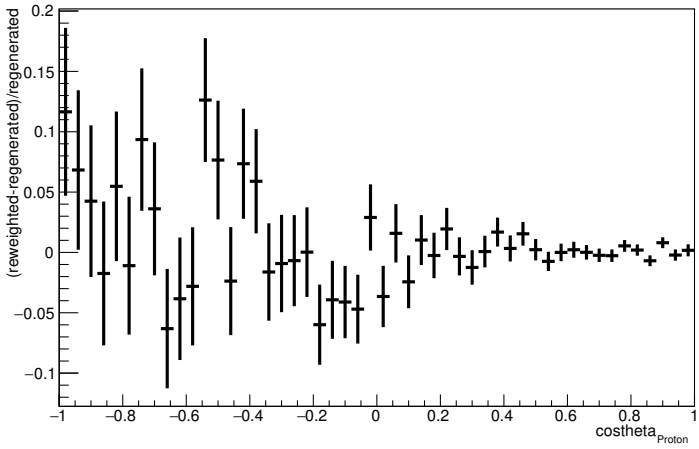

Angle plot: Every FSI Proton: Neut Mode =11

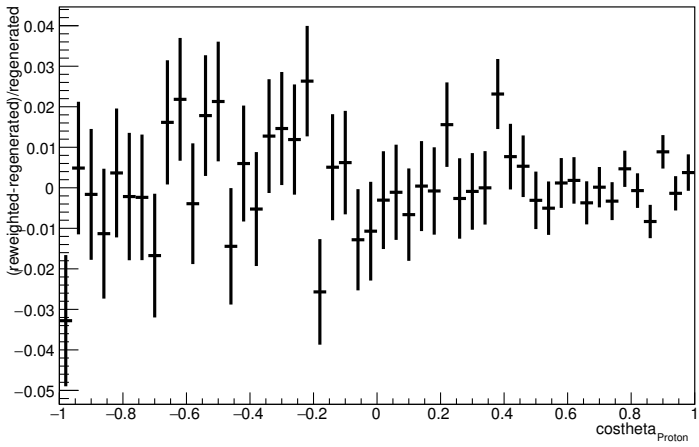

Energy plot: Leading Energy Neutron: Neut Mode =11

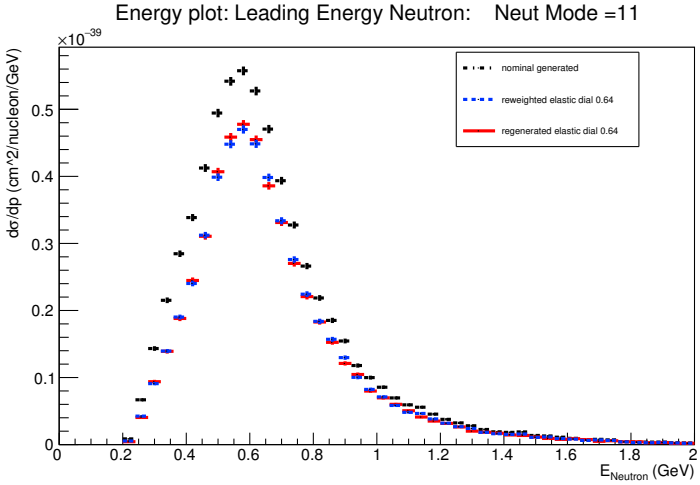

Energy plot: Every FSI Neutron: Neut Mode =11

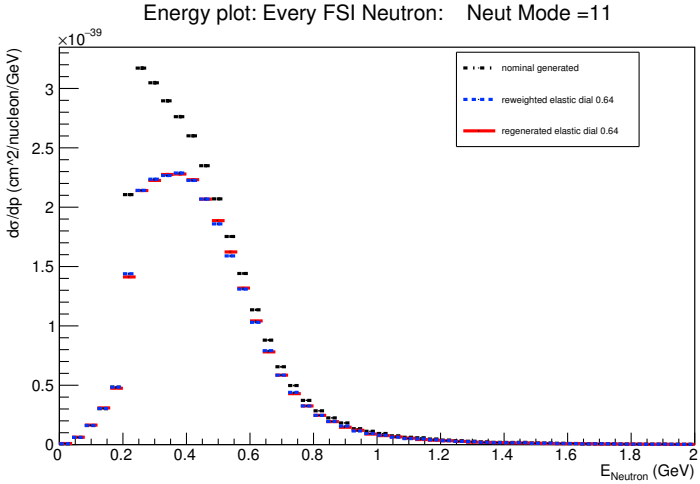

Energy plot: Leading Energy Neutron: Neut Mode =11

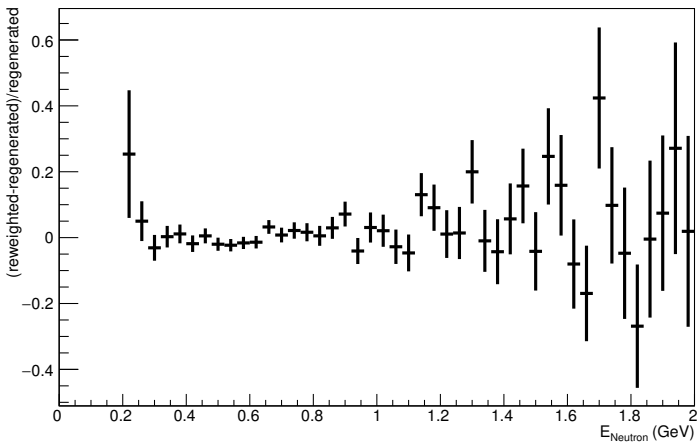

Energy plot: Every FSI Neutron: Neut Mode =11

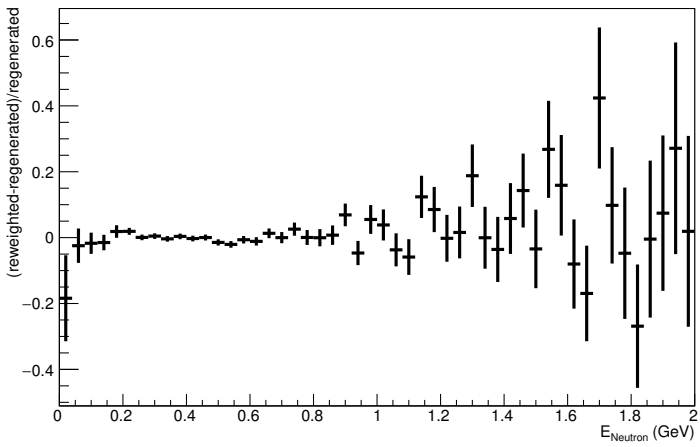

Angle plot: Leading Energy Neutron: Neut Mode =11

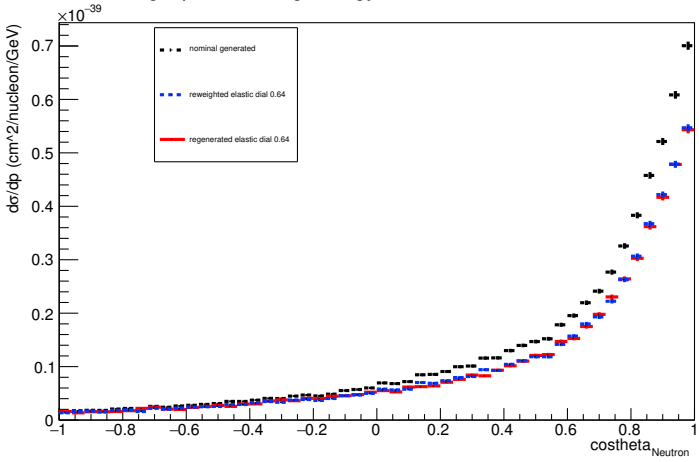

Angle plot: Every FSI Neutron: Neut Mode =11

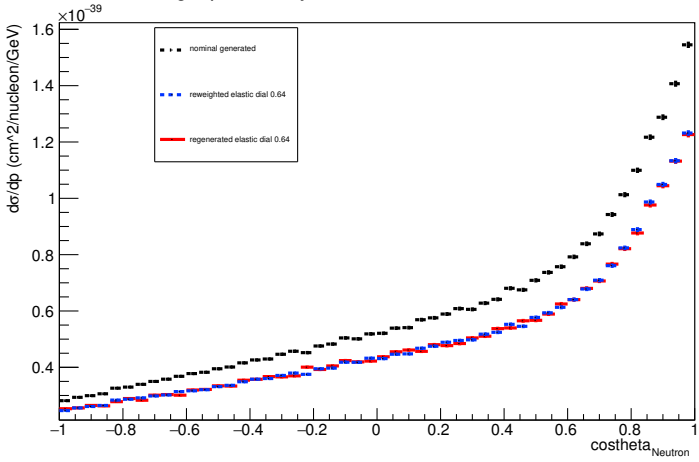

Angle plot: Leading Energy Neutron: Neut Mode =11

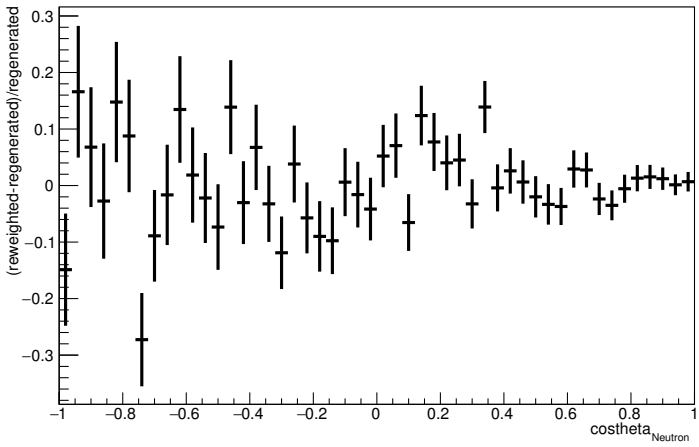

Angle plot: Every FSI Neutron: Neut Mode =11

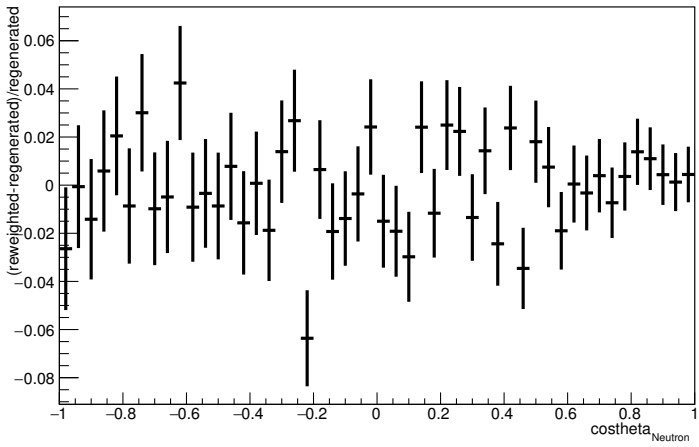

Energy plot: Leading Energy Lepton: Neut Mode =11

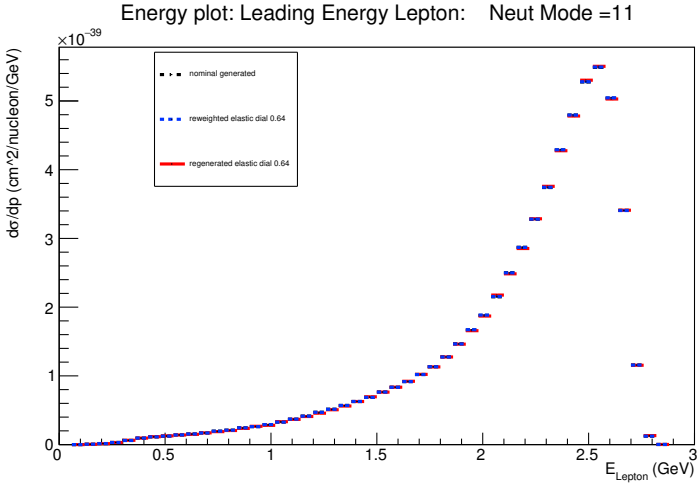

Angle plot: Leading Energy Lepton: Neut Mode =11

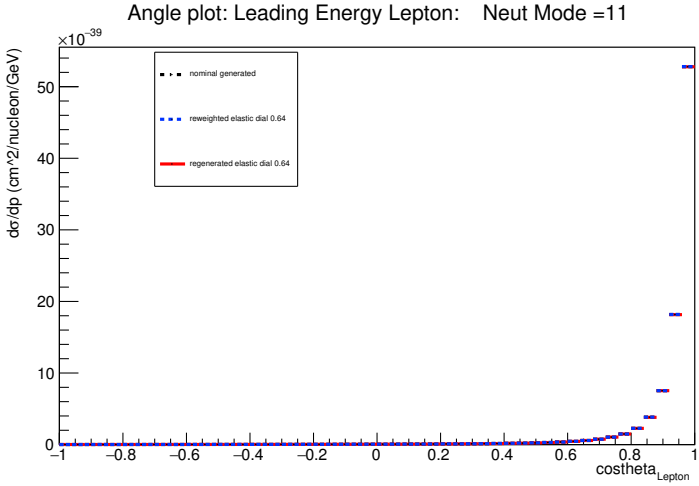

Energy plot: Leading Energy Lepton: Neut Mode =11

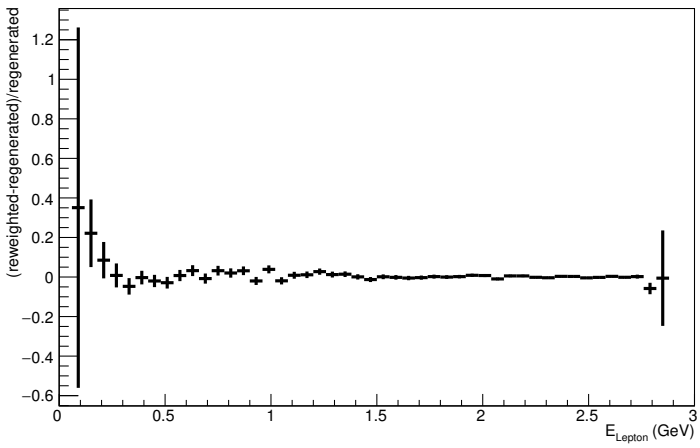

Angle plot: Leading Energy Lepton: Neut Mode =11

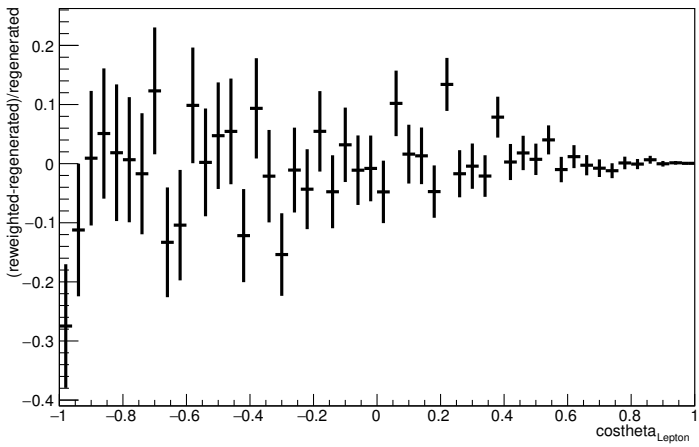

Energy plot: Leading Energy Pion: Neut Mode =11

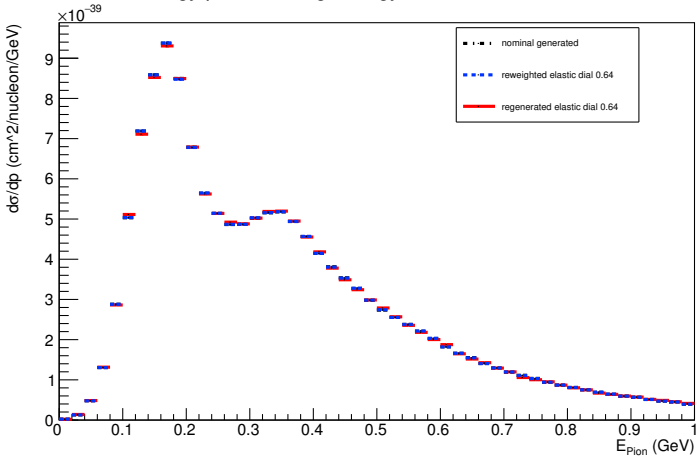

Energy plot: Every FSI Pion: Neut Mode =11

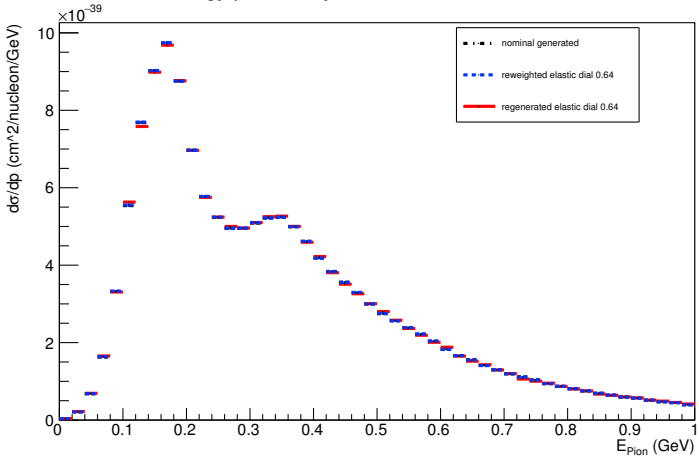

Energy plot: Leading Energy Pion: Neut Mode =11

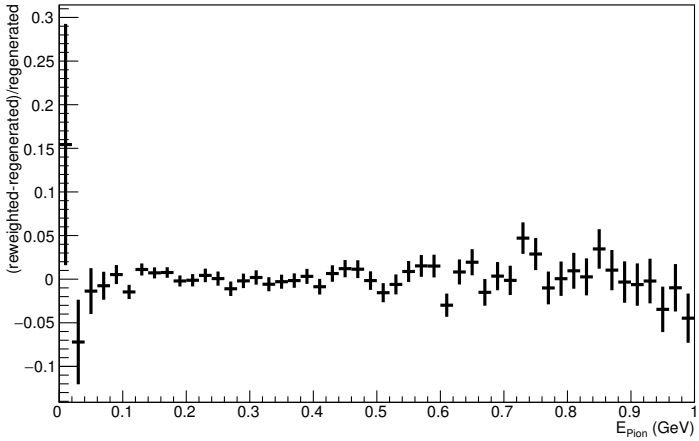

Energy plot: Every FSI Pion: Neut Mode =11

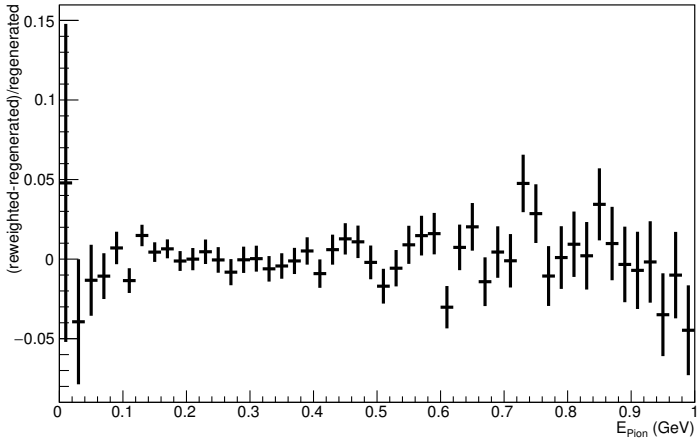

Angle plot: Leading Energy Pion: Neut Mode =11

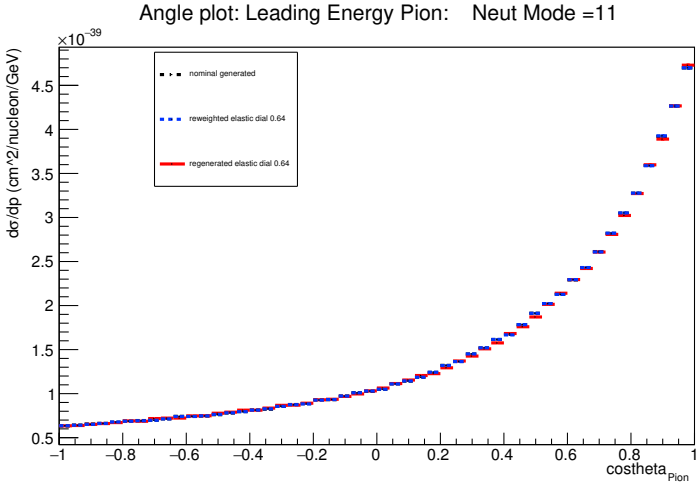

Angle plot: Every FSI Pion: Neut Mode =11

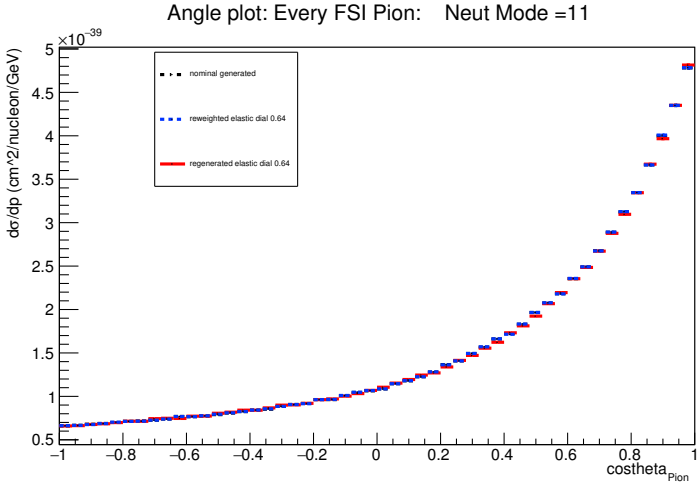

Angle plot: Leading Energy Pion: Neut Mode =11

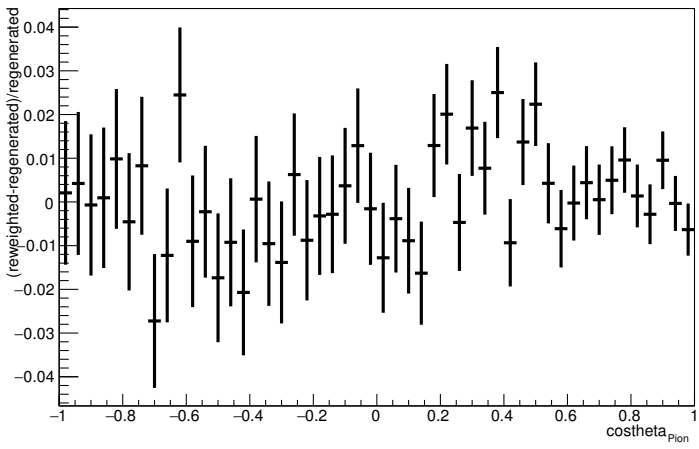

Angle plot: Every FSI Pion: Neut Mode =11

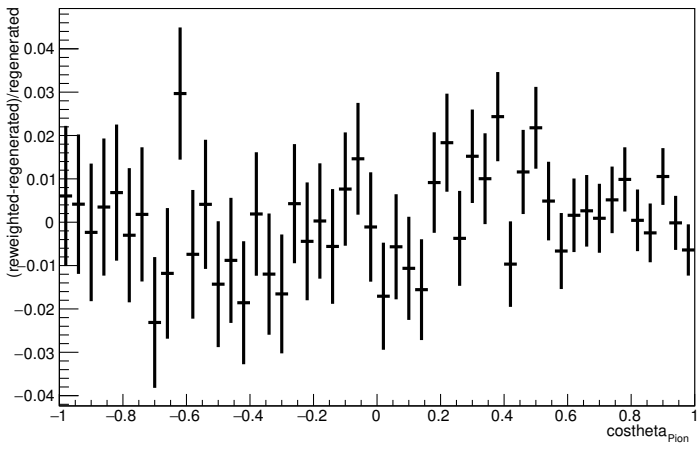

A.5. Single Pion Dial: varied up to 1.44

Energy plot: Leading Energy Nucleon: Neut Mode =AllModesCombined

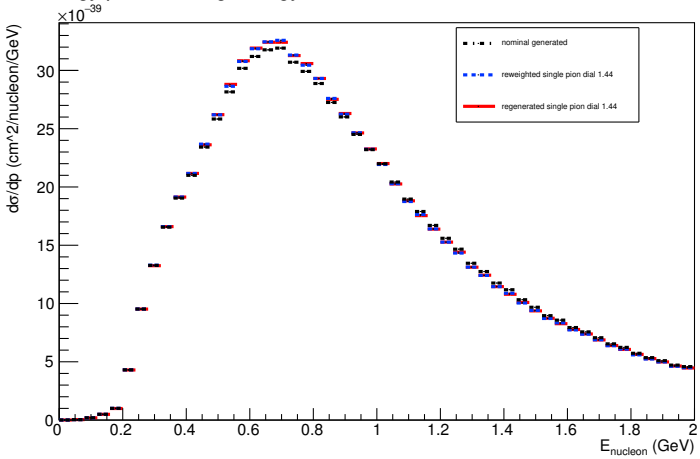

Energy plot: Every FSI Nucleon: Neut Mode =AllModesCombined

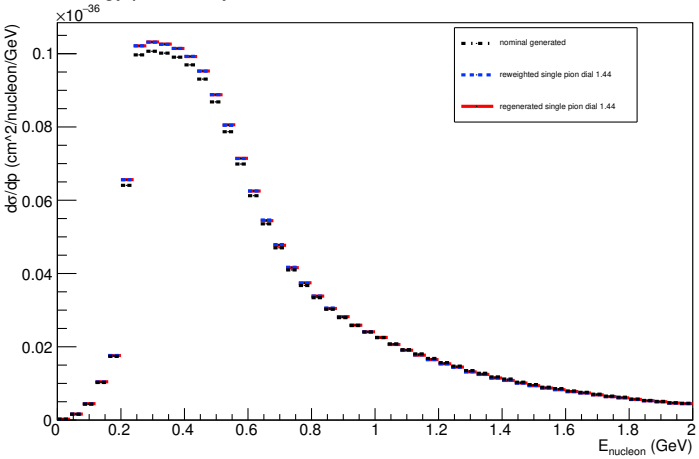

Energy plot: Leading Energy Nucleon: Neut Mode =AllModesCombined

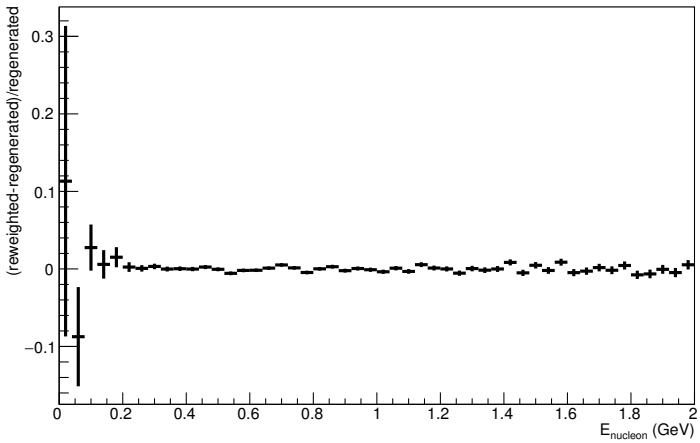

Energy plot: Every FSI Nucleon: Neut Mode =AllModesCombined

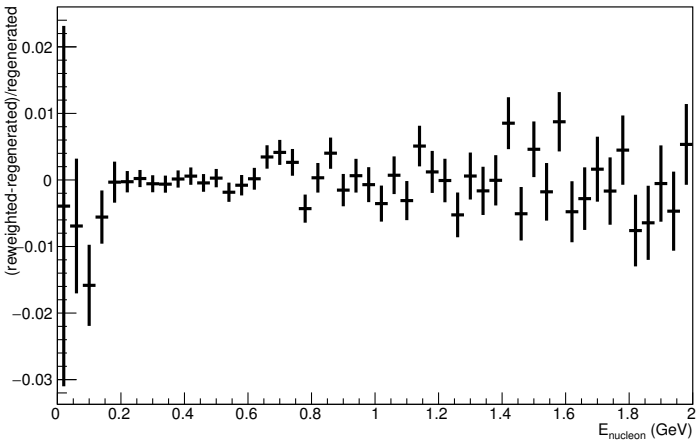

Angle plot: Leading Energy Nucleon: Neut Mode =AllModesCombined

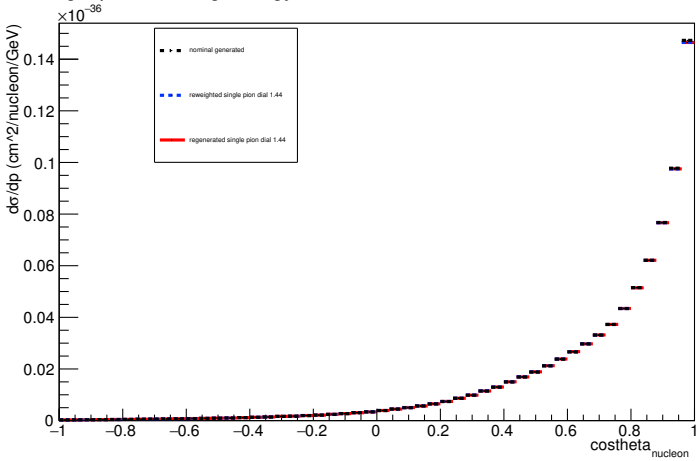

Angle plot: Every FSI Nucleon: Neut Mode =AllModesCombined

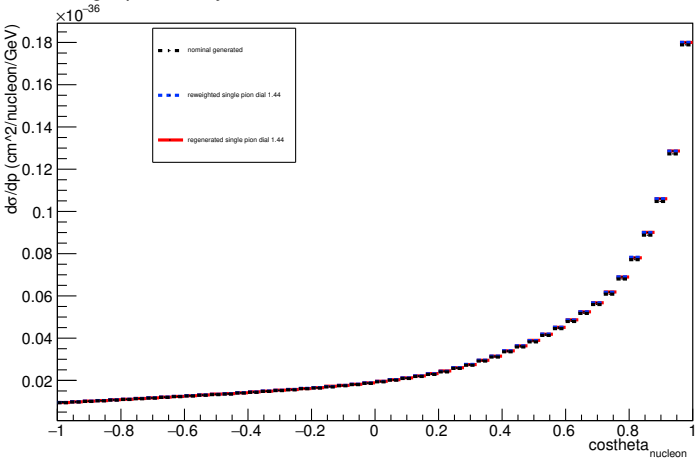

Angle plot: Leading Energy Nucleon: Neut Mode =AllModesCombined

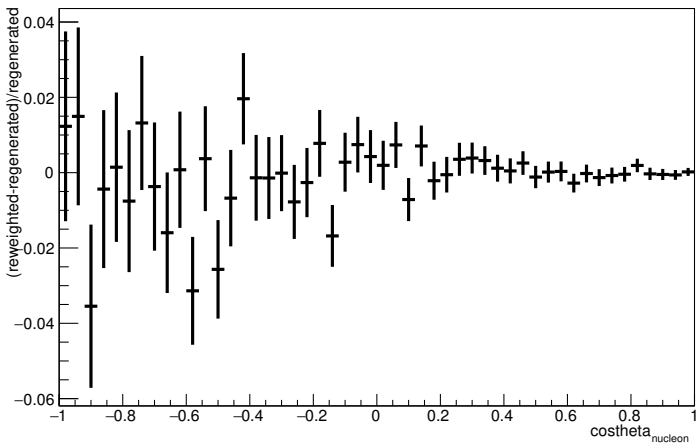

Angle plot: Every FSI Nucleon: Neut Mode =AllModesCombined

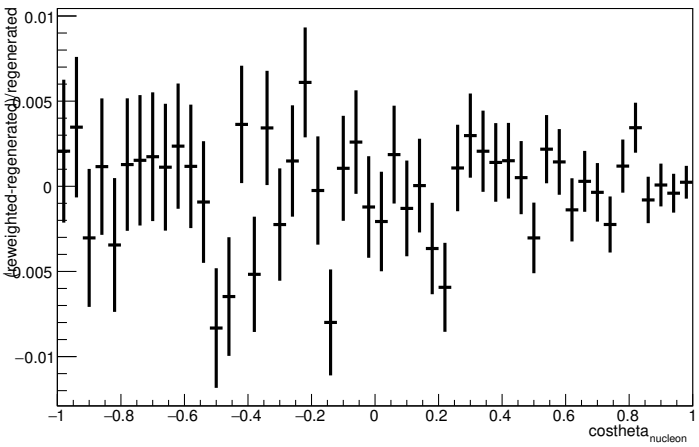

Energy plot: Leading Energy Proton: Neut Mode =AllModesCombined

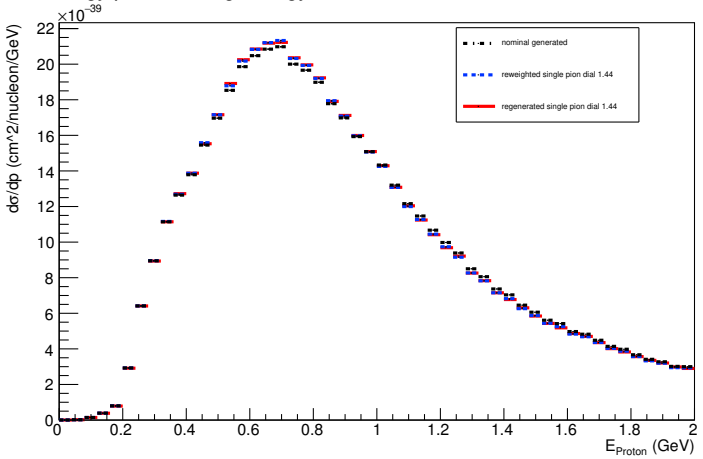

Energy plot: Every FSI Proton: Neut Mode =AllModesCombined

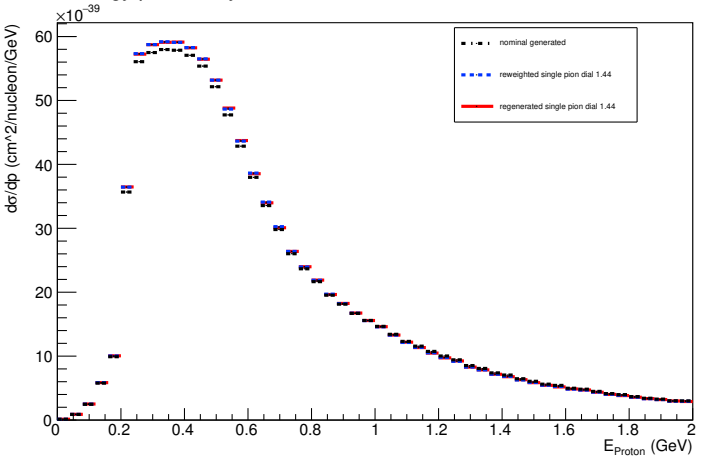

Energy plot: Leading Energy Proton: Neut Mode =AllModesCombined

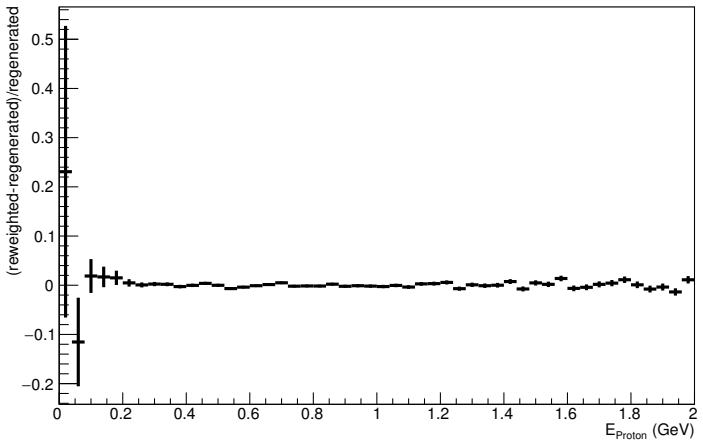

Energy plot: Every FSI Proton: Neut Mode =AllModesCombined

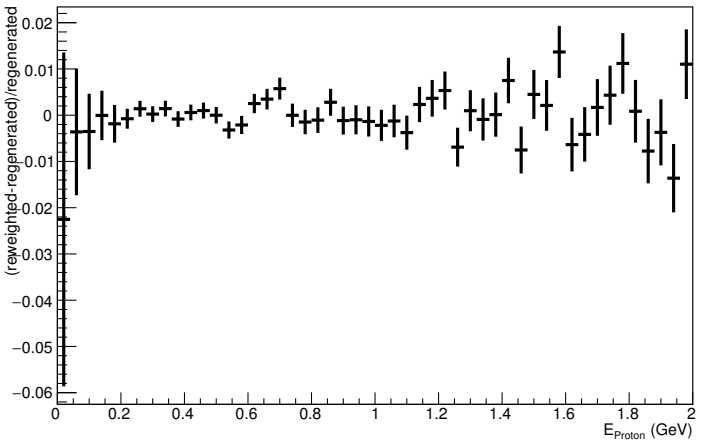

Angle plot: Leading Energy Proton: Neut Mode =AllModesCombined

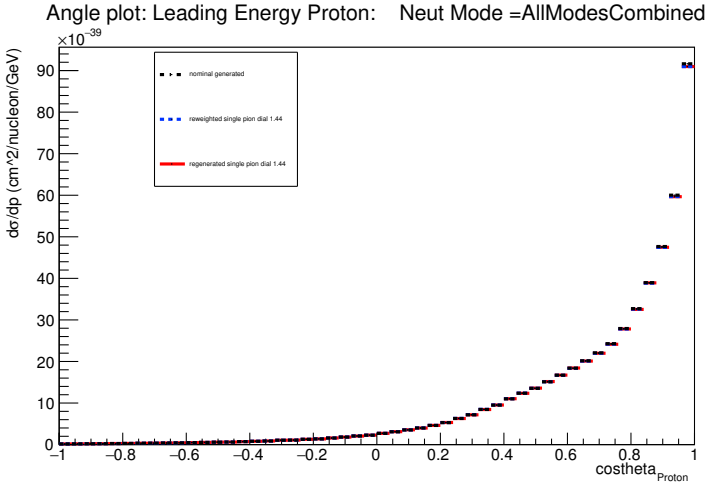

Angle plot: Every FSI Proton: Neut Mode =AllModesCombined

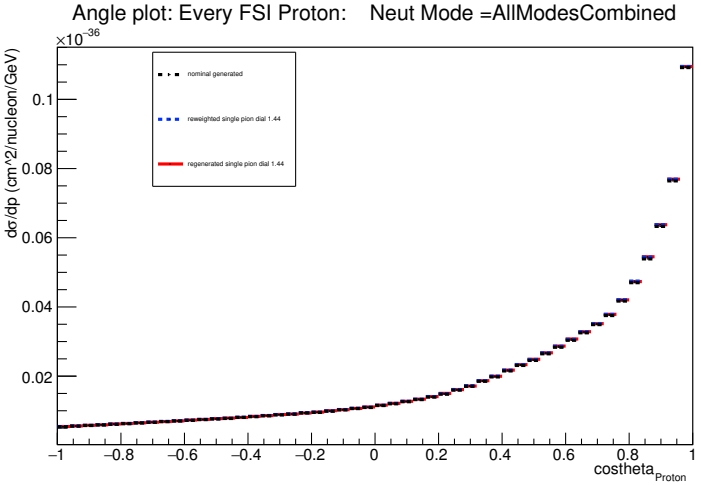

Angle plot: Leading Energy Proton: Neut Mode =AllModesCombined

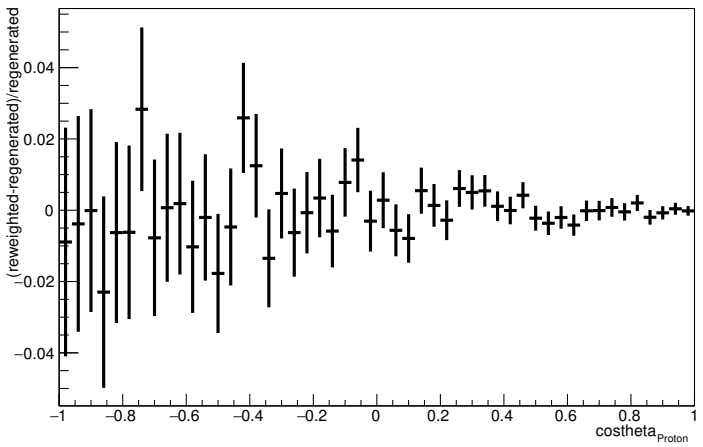

Angle plot: Every FSI Proton: Neut Mode =AllModesCombined

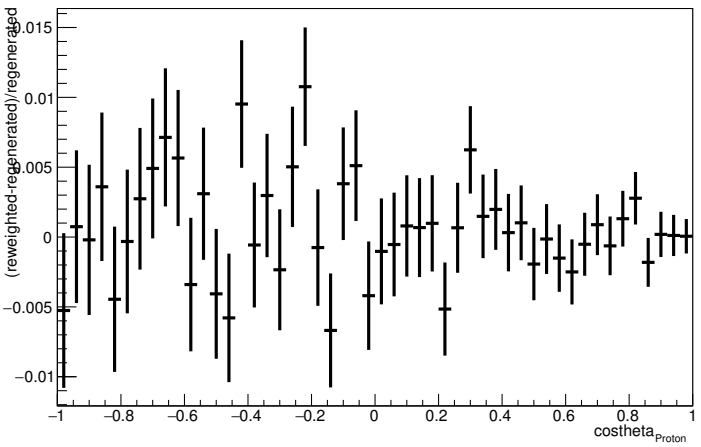

Energy plot: Leading Energy Neutron: Neut Mode =AllModesCombined

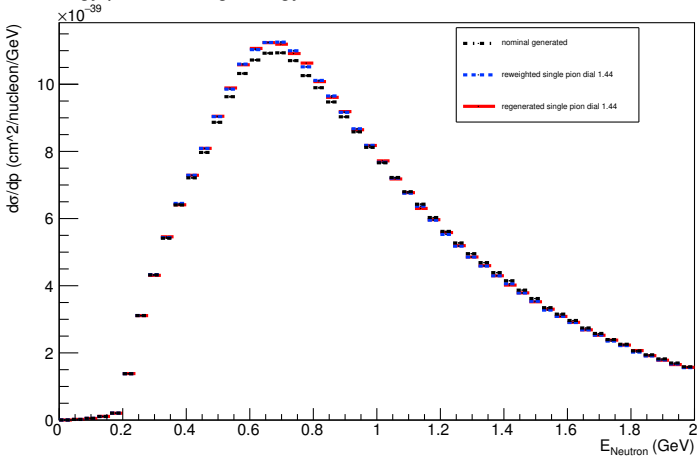

Energy plot: Every FSI Neutron: Neut Mode =AllModesCombined

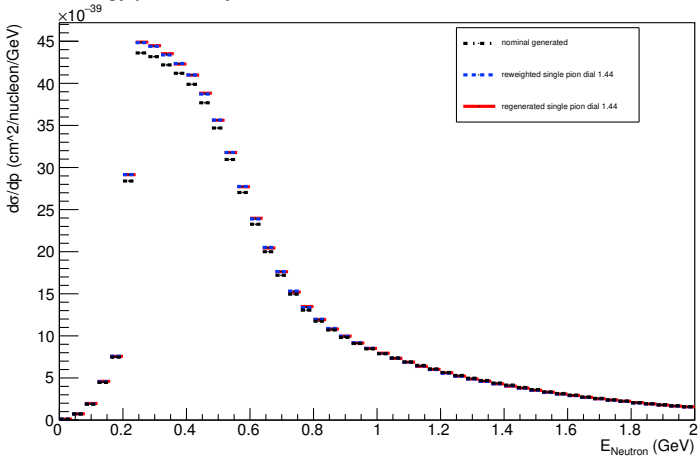

Energy plot: Leading Energy Neutron: Neut Mode =AllModesCombined

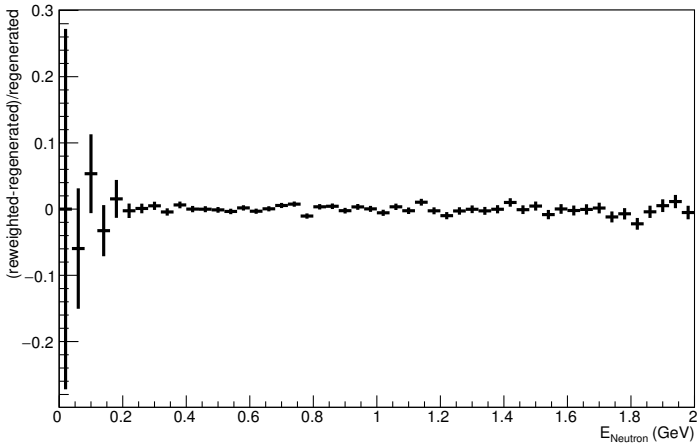

Energy plot: Every FSI Neutron: Neut Mode =AllModesCombined

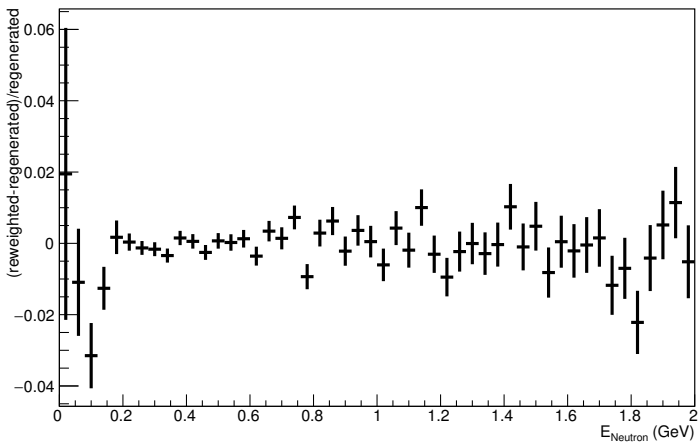

Angle plot: Leading Energy Neutron: Neut Mode =AllModesCombined

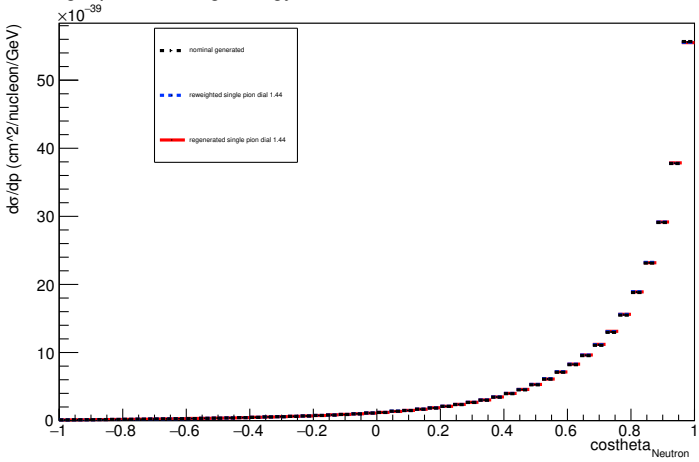

Angle plot: Every FSI Neutron: Neut Mode =AllModesCombined

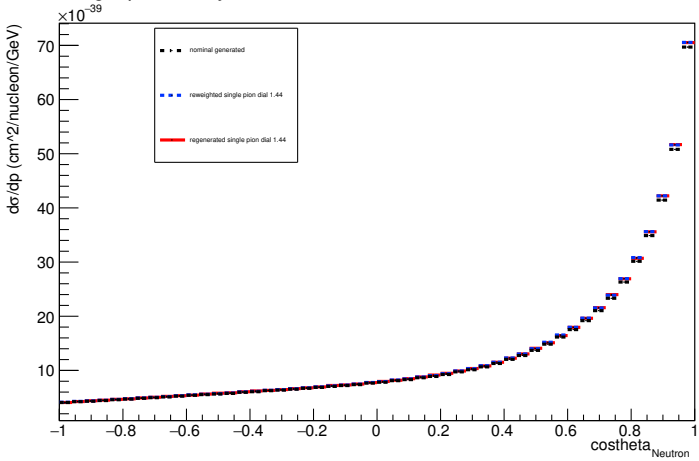

Angle plot: Leading Energy Neutron: Neut Mode =AllModesCombined

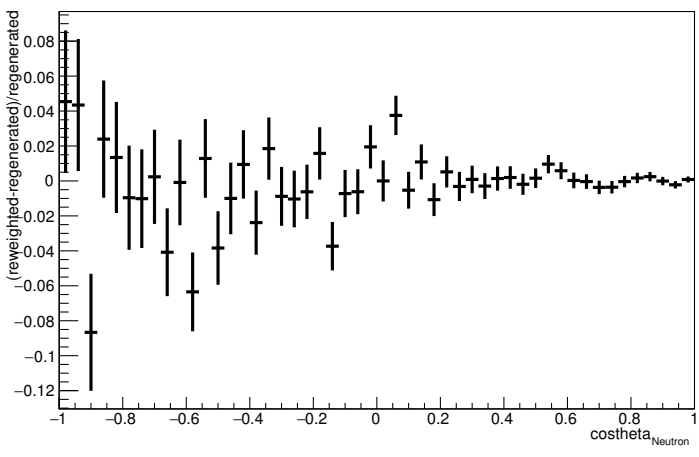

Angle plot: Every FSI Neutron: Neut Mode =AllModesCombined

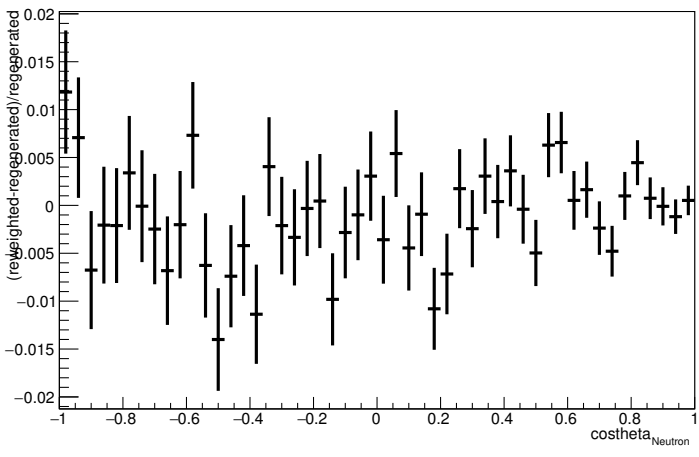

Energy plot: Leading Energy Lepton: Neut Mode =AllModesCombined

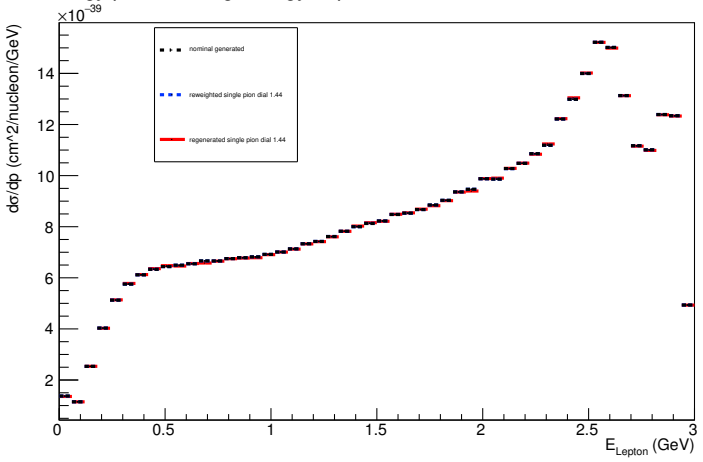

Angle plot: Leading Energy Lepton: Neut Mode =AllModesCombined

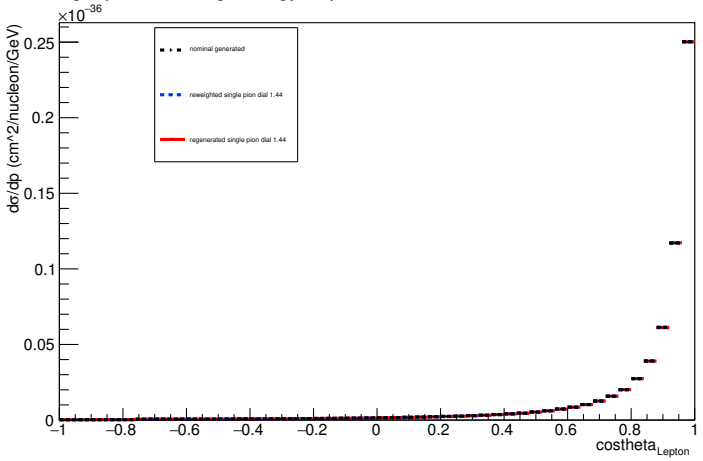

Energy plot: Leading Energy Lepton: Neut Mode =AllModesCombined

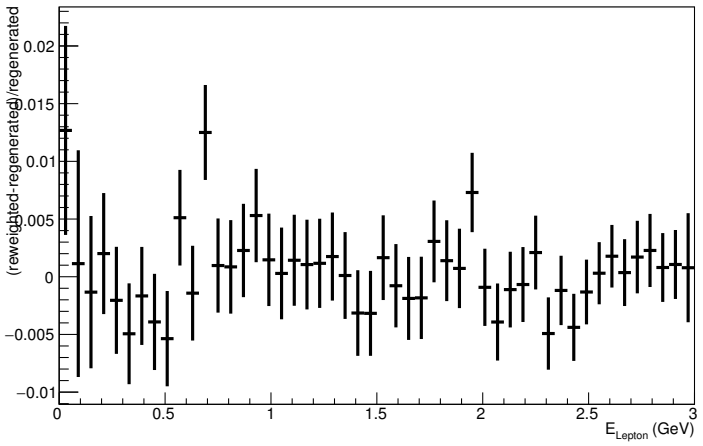

Angle plot: Leading Energy Lepton: Neut Mode =AllModesCombined

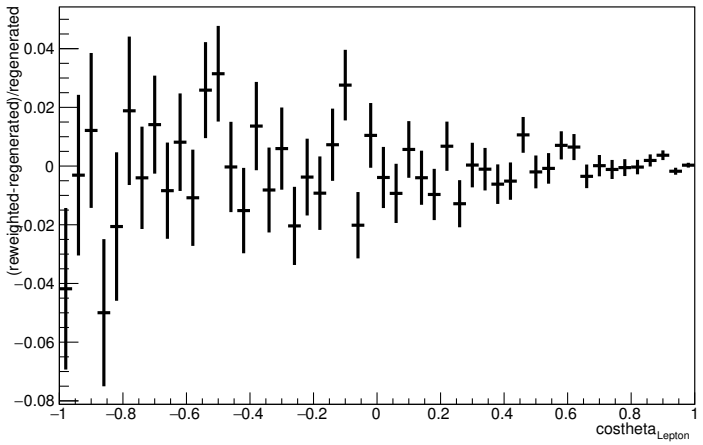

Energy plot: Leading Energy Pion: Neut Mode =AllModesCombined

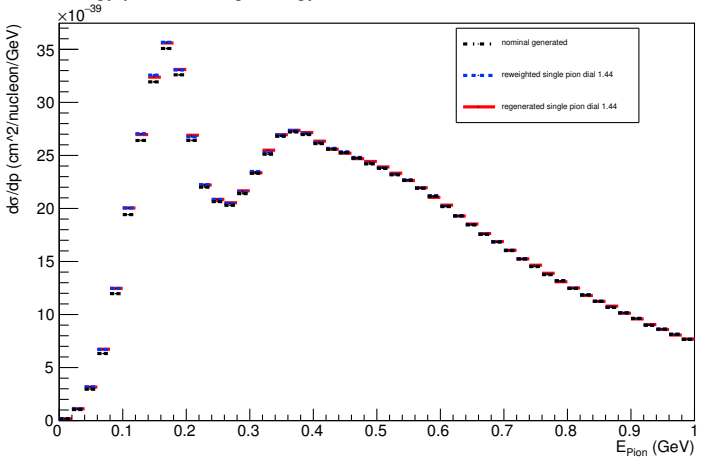

Energy plot: Every FSI Pion: Neut Mode =AllModesCombined

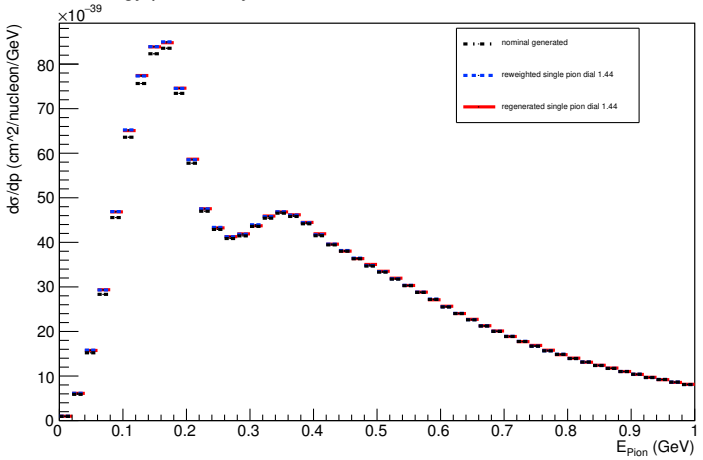

Energy plot: Leading Energy Pion: Neut Mode =AllModesCombined

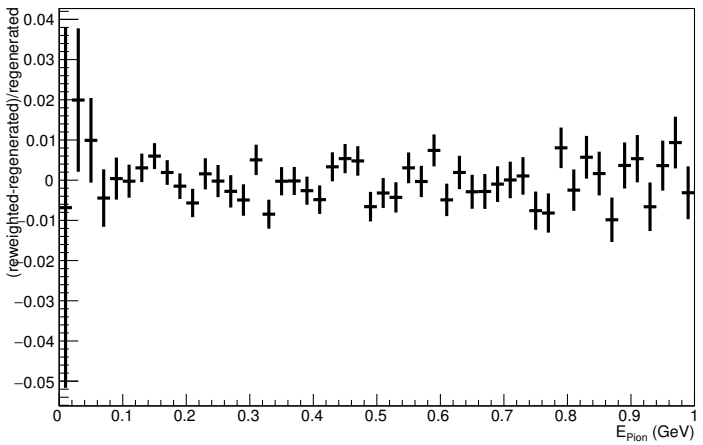

Energy plot: Every FSI Pion: Neut Mode =AllModesCombined

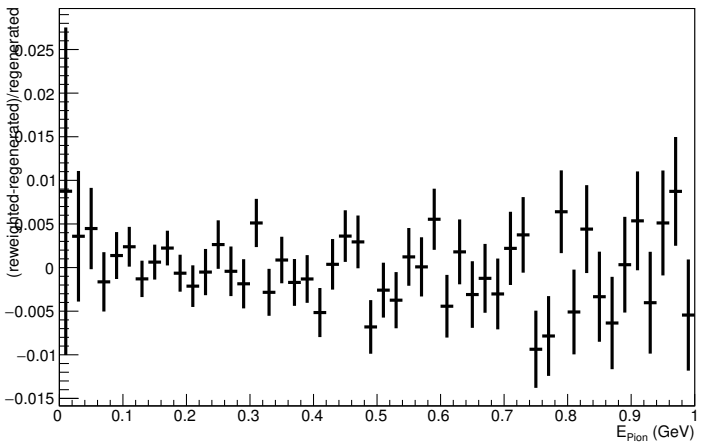

Angle plot: Leading Energy Pion: Neut Mode =AllModesCombined

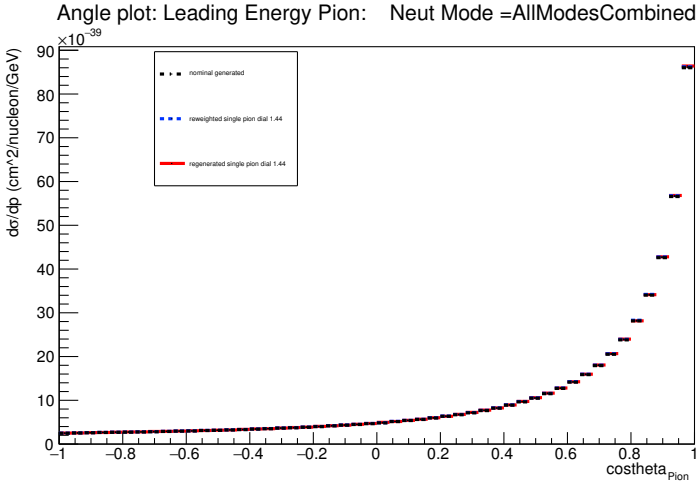

Angle plot: Every FSI Pion: Neut Mode =AllModesCombined

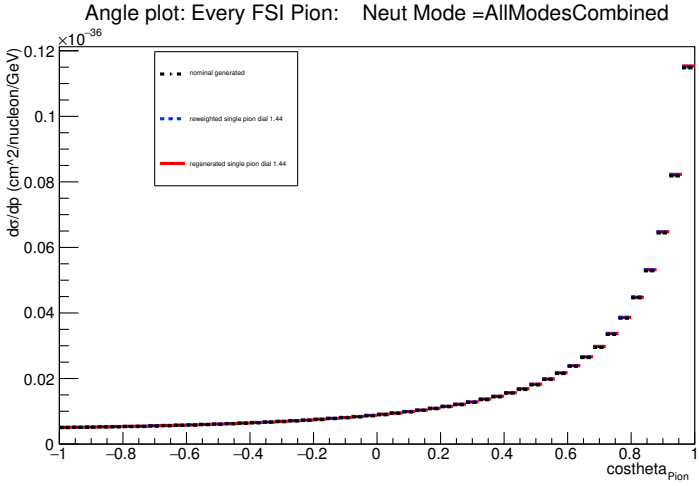

Angle plot: Leading Energy Pion: Neut Mode =AllModesCombined

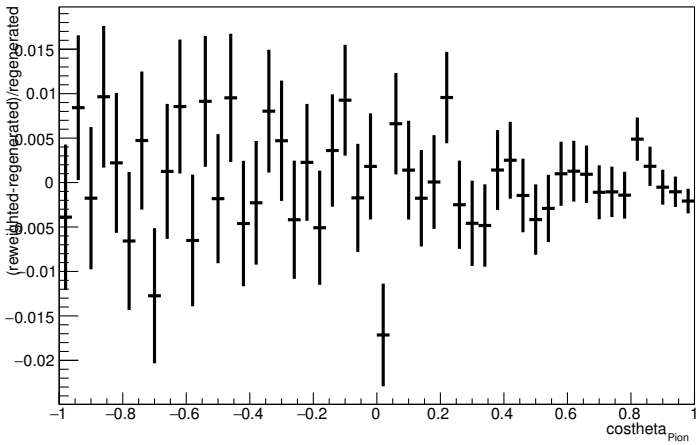

Angle plot: Every FSI Pion: Neut Mode =AllModesCombined

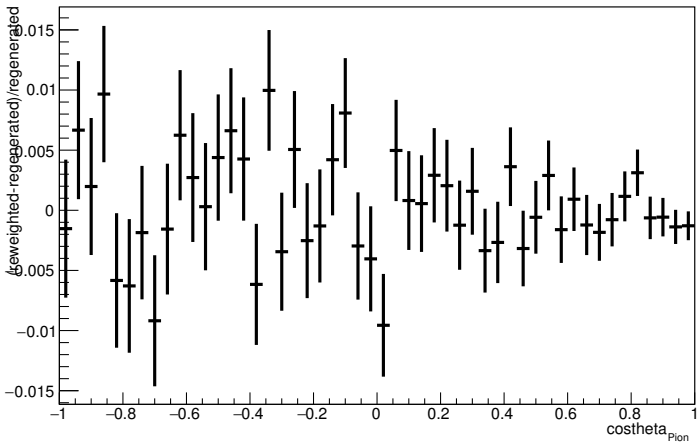

Energy plot: Leading Energy Nucleon: Neut Mode =1

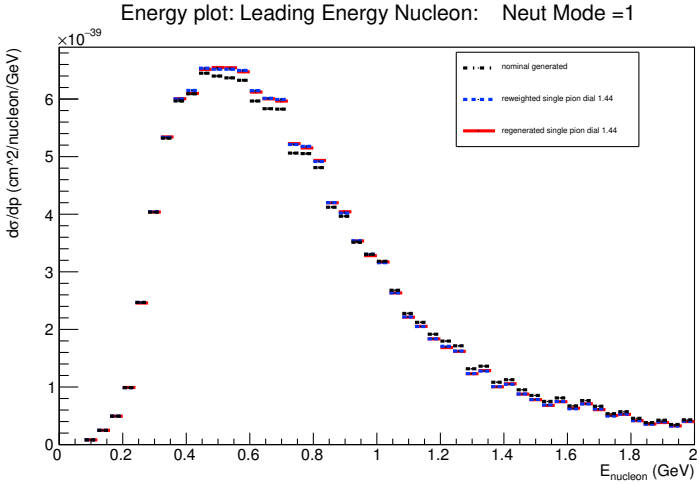

Energy plot: Every FSI Nucleon: Neut Mode =1

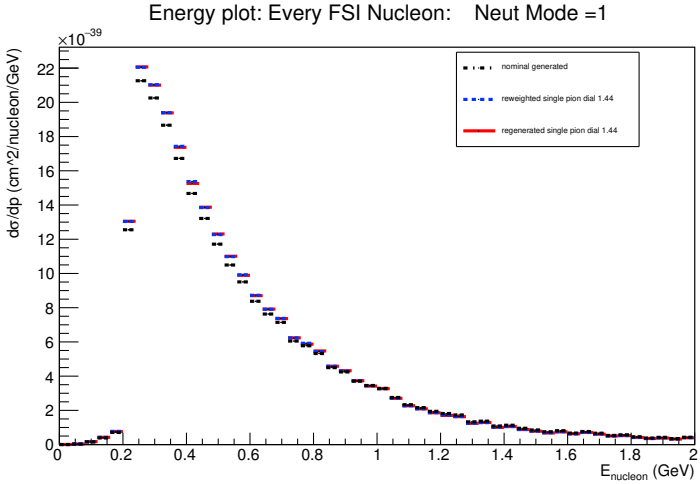

Energy plot: Leading Energy Nucleon: Neut Mode =1

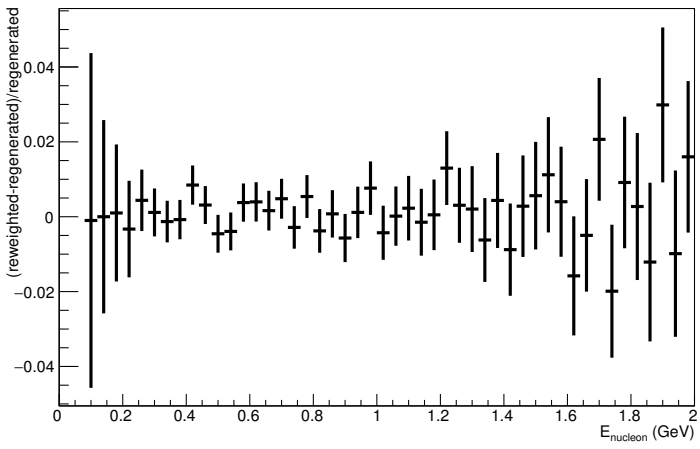

Energy plot: Every FSI Nucleon: Neut Mode =1

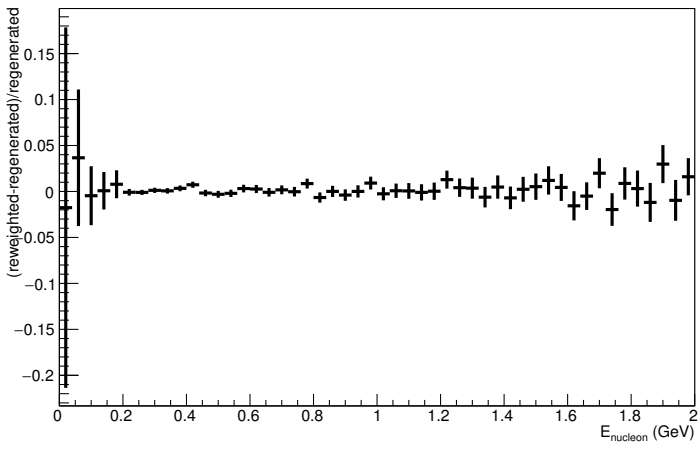

Angle plot: Leading Energy Nucleon: Neut Mode =1

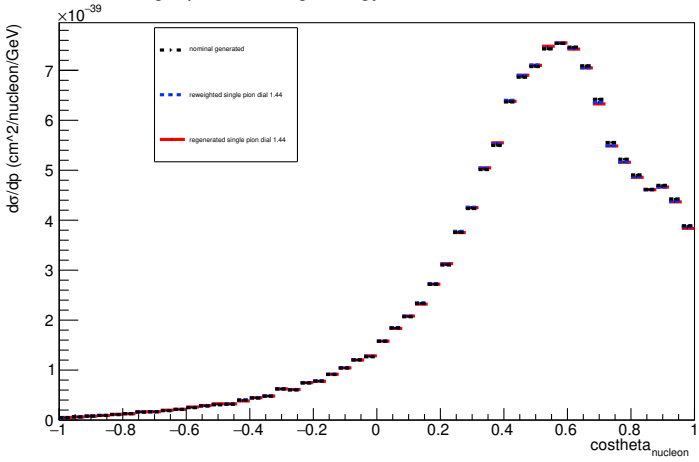

Angle plot: Every FSI Nucleon: Neut Mode =1

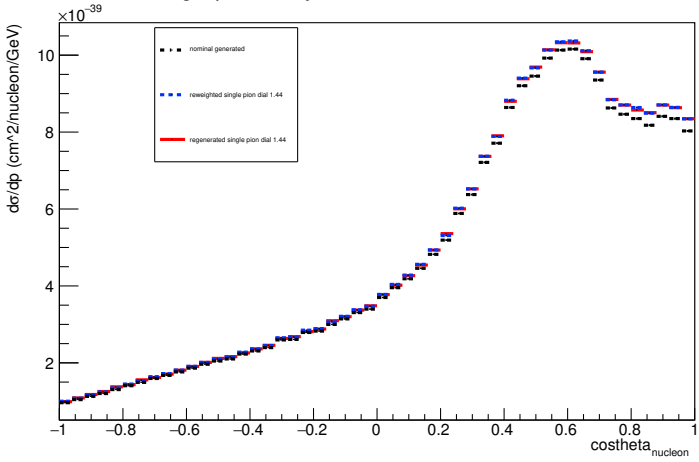

Angle plot: Leading Energy Nucleon: Neut Mode =1

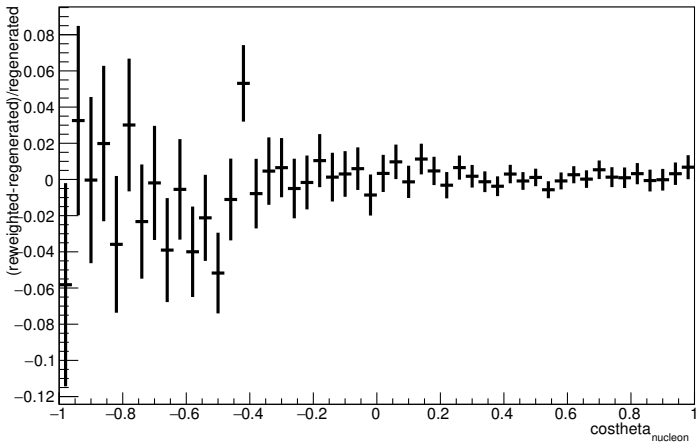

Angle plot: Every FSI Nucleon: Neut Mode =1

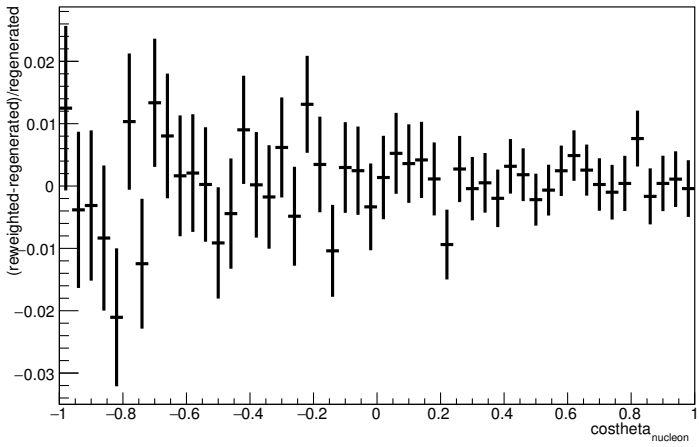

Energy plot: Leading Energy Proton: Neut Mode =1

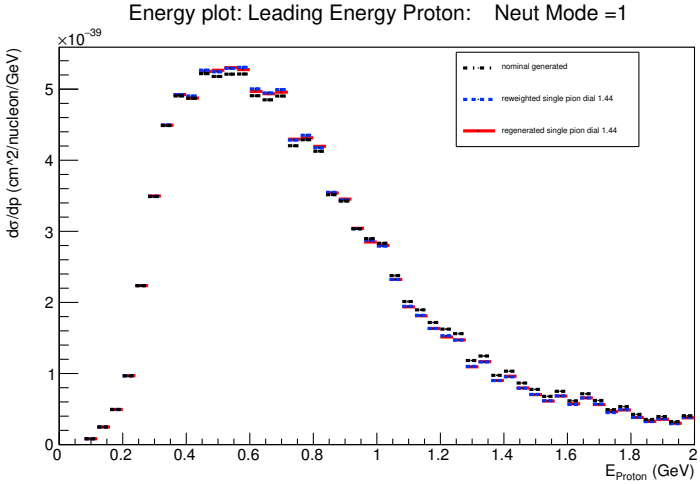

Energy plot: Every FSI Proton: Neut Mode =1

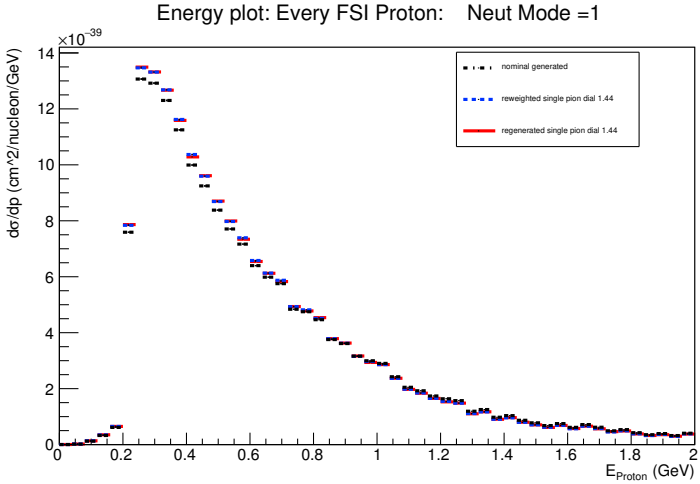

Energy plot: Leading Energy Proton: Neut Mode =1

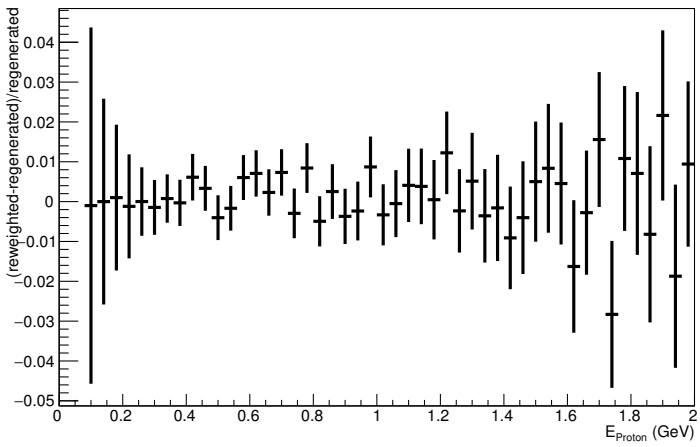

Energy plot: Every FSI Proton: Neut Mode =1

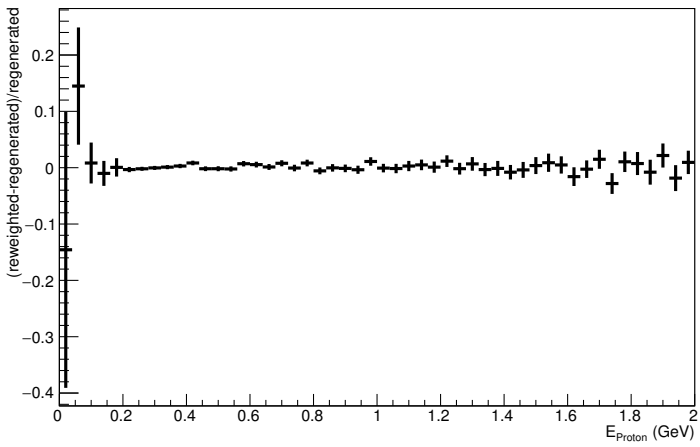

Angle plot: Leading Energy Proton: Neut Mode =1

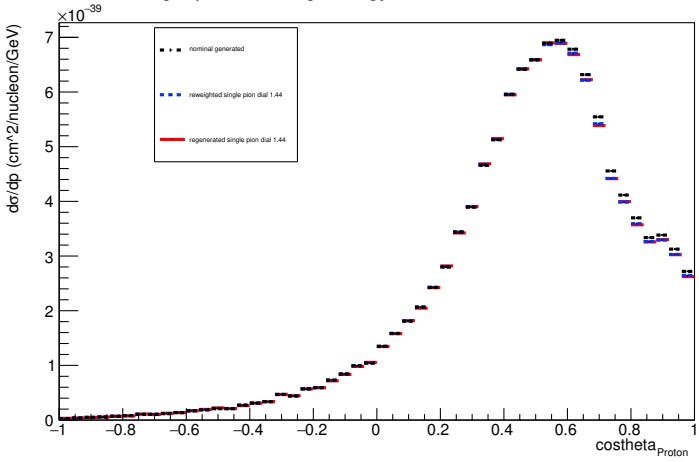

Angle plot: Every FSI Proton: Neut Mode =1

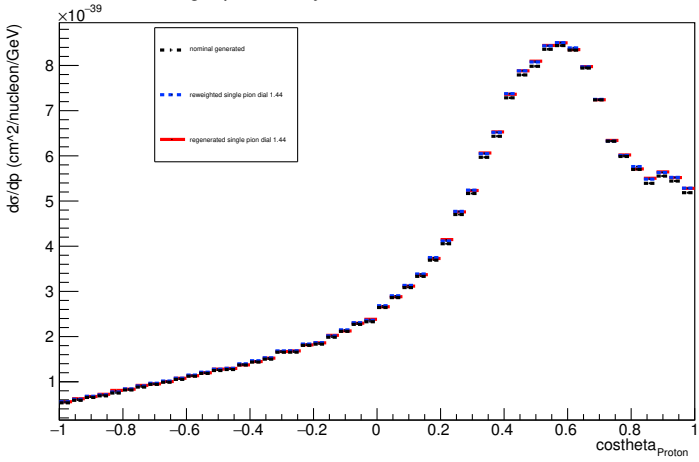

Angle plot: Leading Energy Proton: Neut Mode =1

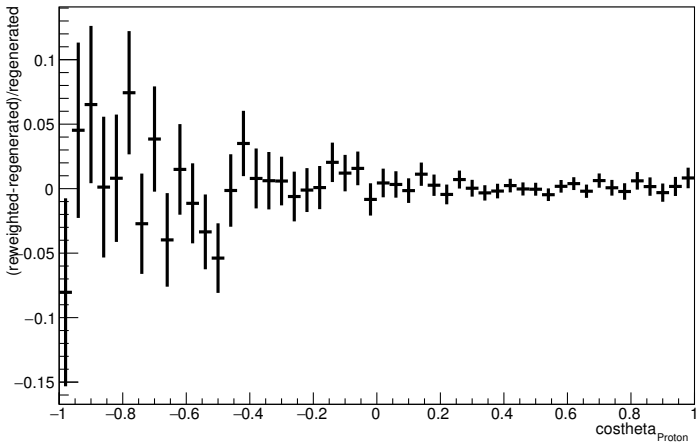

Angle plot: Every FSI Proton: Neut Mode =1

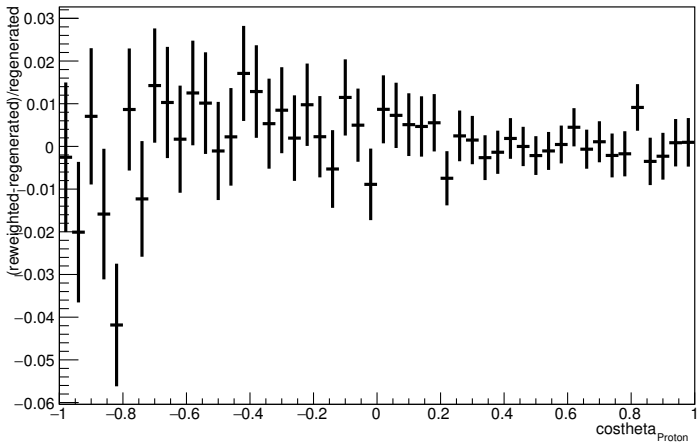

Energy plot: Leading Energy Neutron: Neut Mode =1

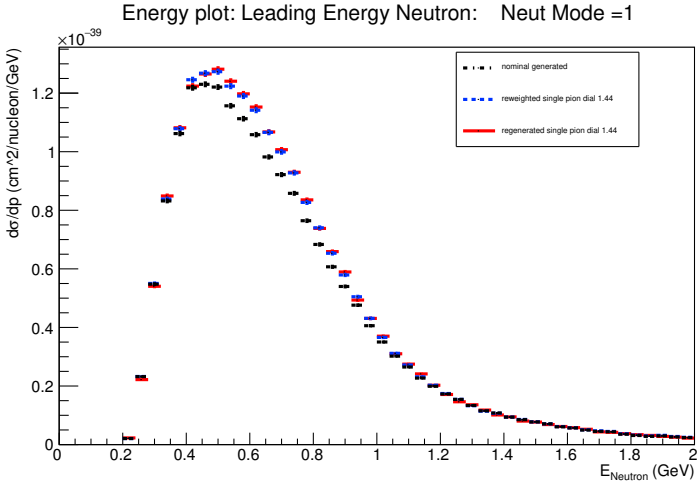

Energy plot: Every FSI Neutron: Neut Mode =1

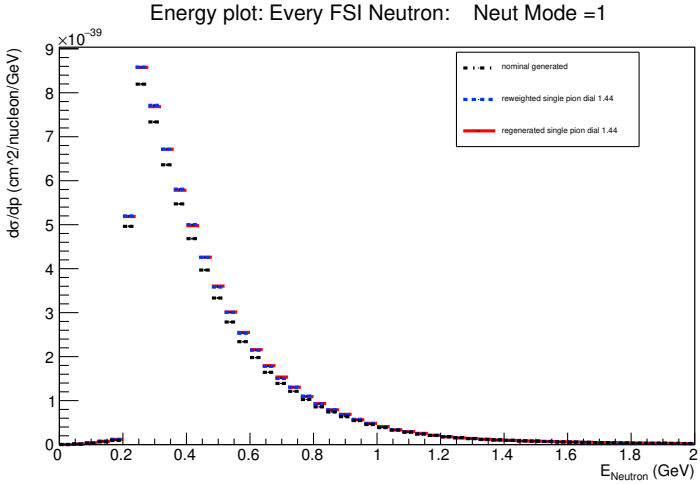

Energy plot: Leading Energy Neutron: Neut Mode =1

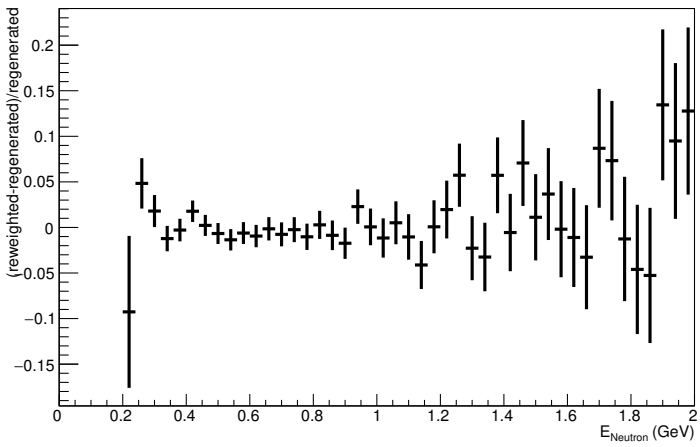

Energy plot: Every FSI Neutron: Neut Mode =1

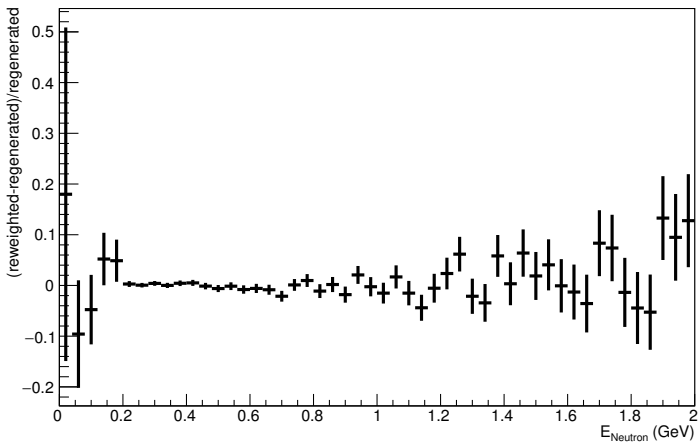

Angle plot: Leading Energy Neutron: Neut Mode =1

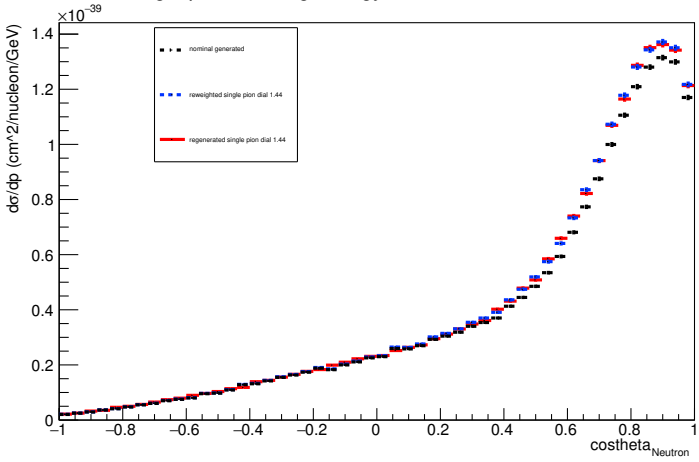

Angle plot: Every FSI Neutron: Neut Mode =1

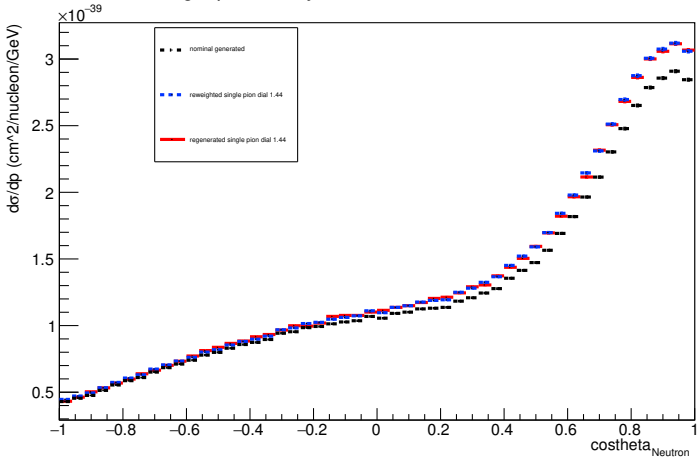

Angle plot: Leading Energy Neutron: Neut Mode =1

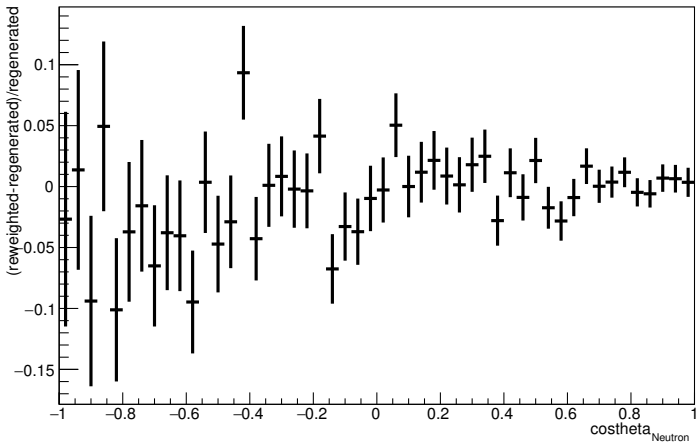

Angle plot: Every FSI Neutron: Neut Mode =1

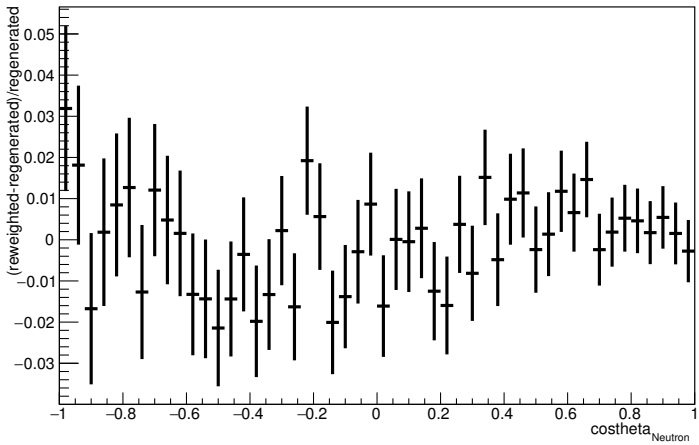

Energy plot: Leading Energy Lepton: Neut Mode =1

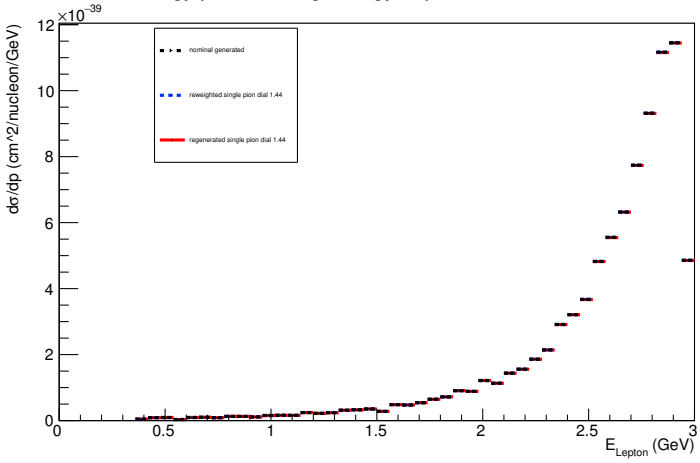

Angle plot: Leading Energy Lepton: Neut Mode =1

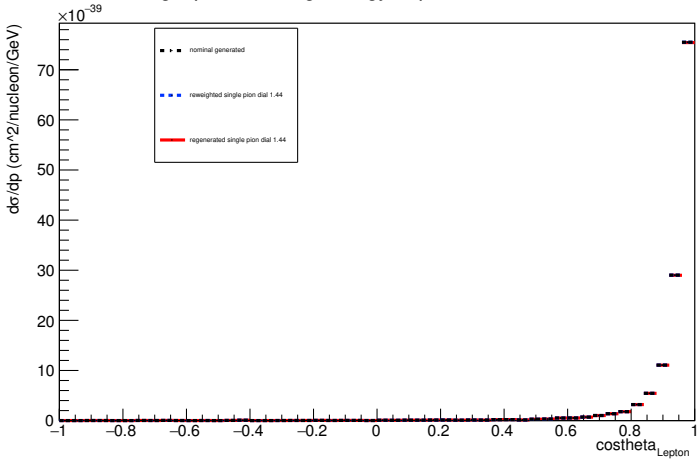

Energy plot: Leading Energy Lepton: Neut Mode =1

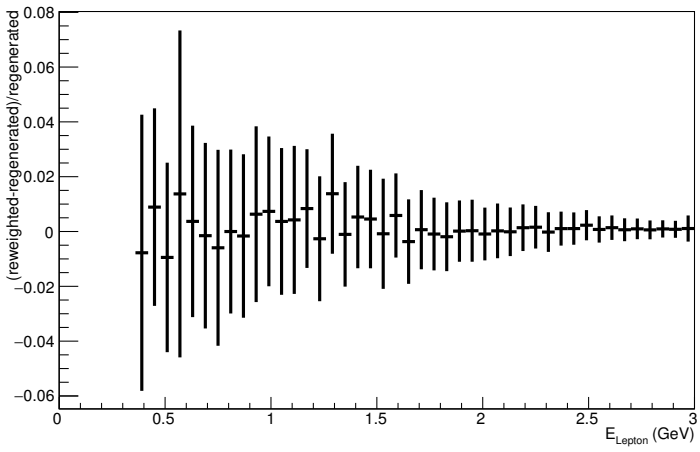

Angle plot: Leading Energy Lepton: Neut Mode =1

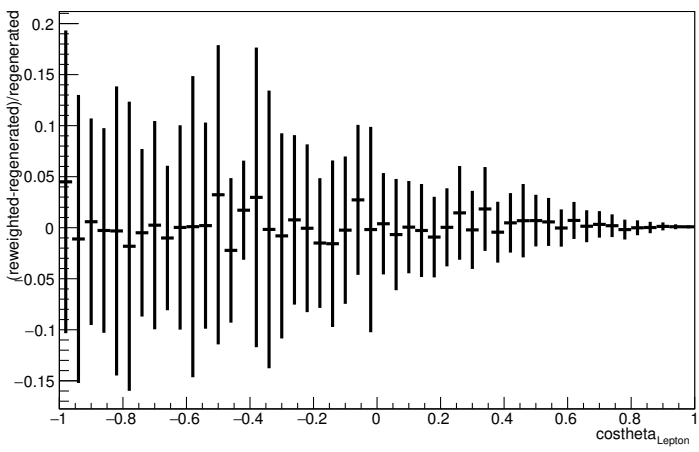

Energy plot: Leading Energy Pion: Neut Mode =1

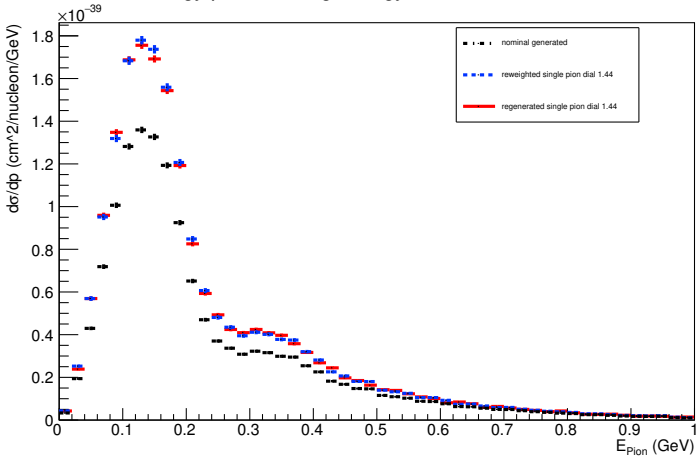

Energy plot: Every FSI Pion: Neut Mode =1

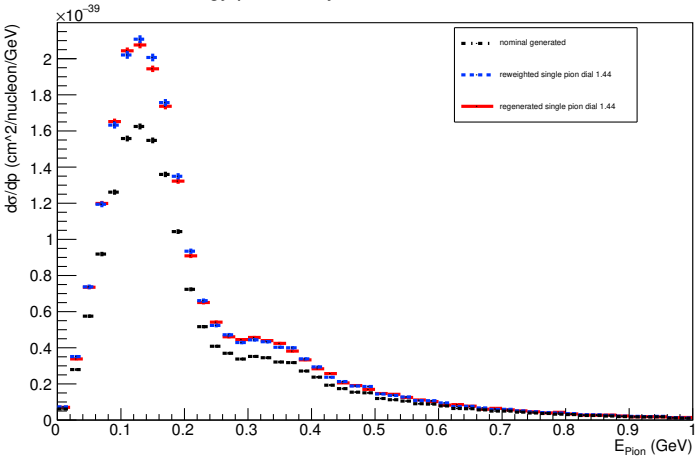

Energy plot: Leading Energy Pion: Neut Mode =1

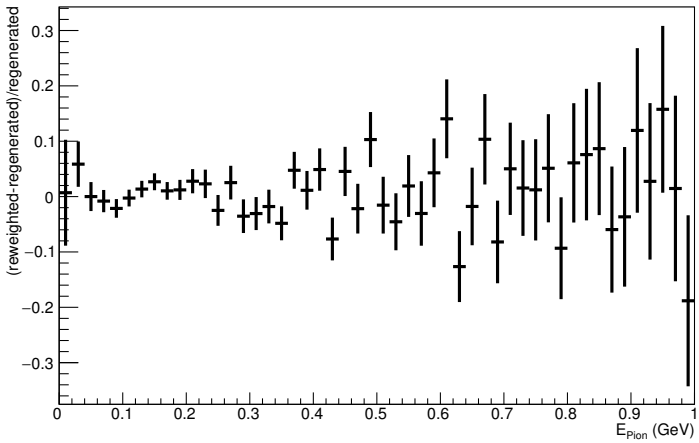

Energy plot: Every FSI Pion: Neut Mode =1

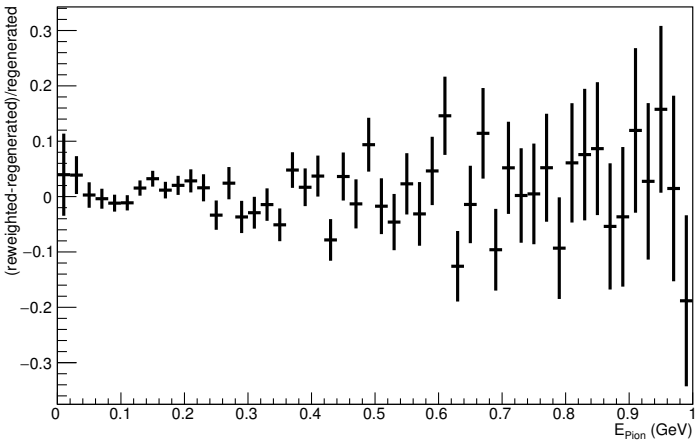

Angle plot: Leading Energy Pion: Neut Mode =1

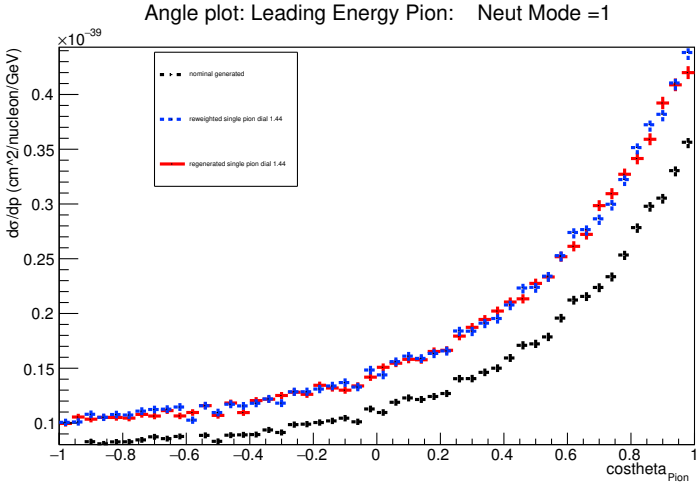

Angle plot: Every FSI Pion: Neut Mode =1

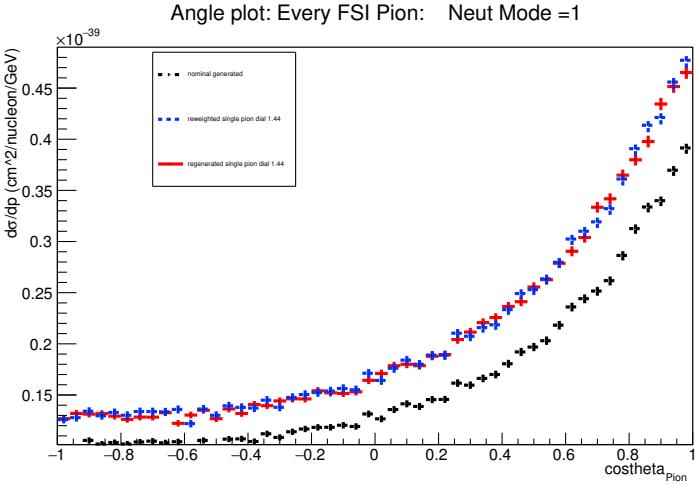

Angle plot: Leading Energy Pion: Neut Mode =1

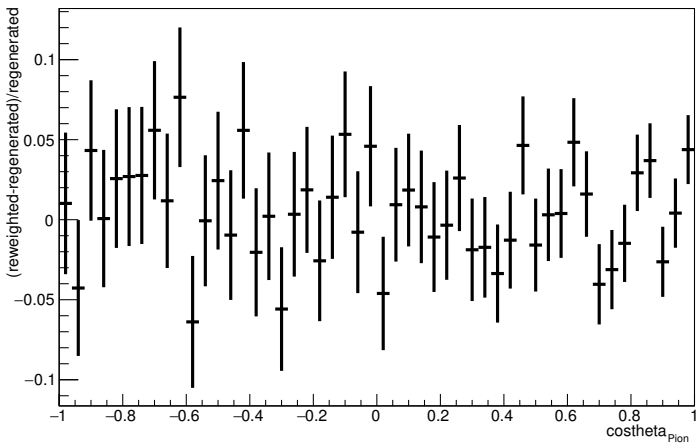

Angle plot: Every FSI Pion: Neut Mode =1

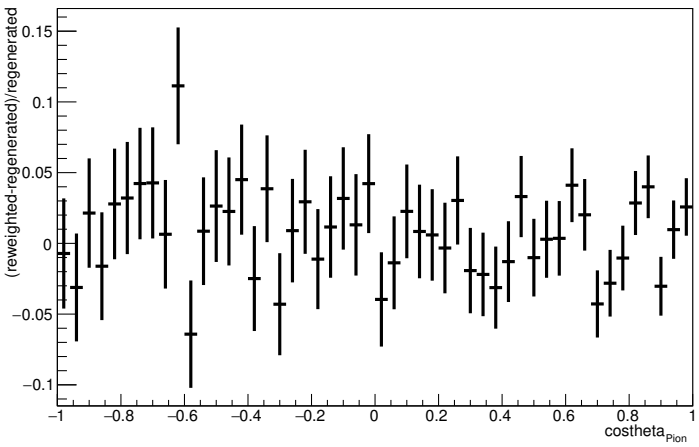

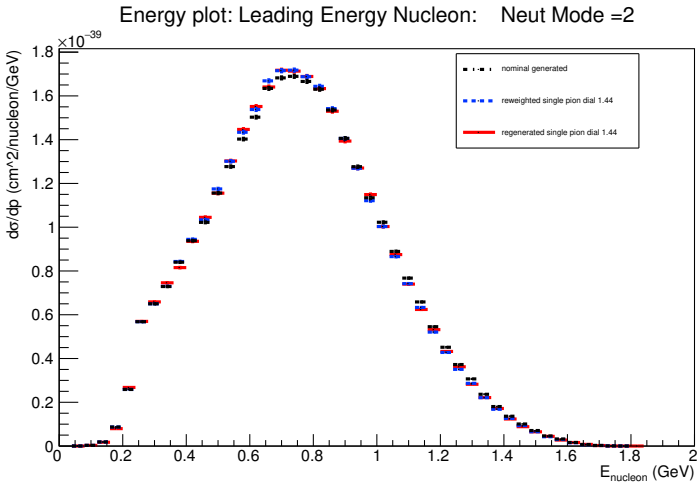
Energy plot: Leading Energy Nucleon: Neut Mode =2
dσ/dp (cm^2/nucleon/GeV)
×10^-39
nominal generated
reweighted single pion dial 1.44
regenerated single pion dial 1.44
E_nucleon (GeV)

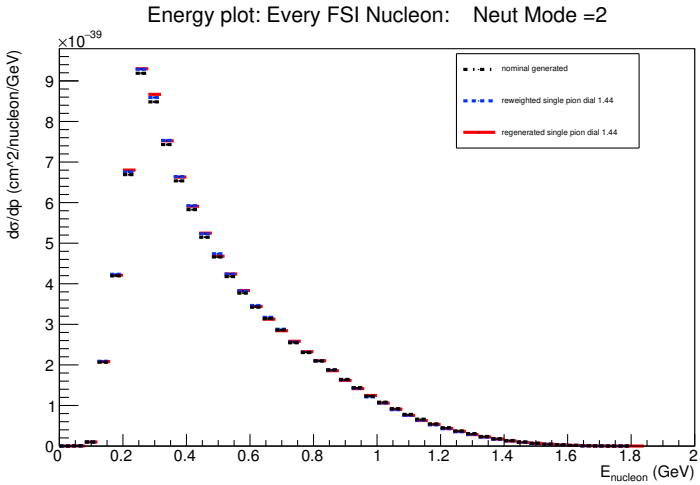
Energy plot: Every FSI Nucleon: Neut Mode =2
dσ/dp (cm^2/nucleon/GeV)
×10^-39
nominal generated
reweighted single pion dial 1.44
regenerated single pion dial 1.44
E_nucleon (GeV)

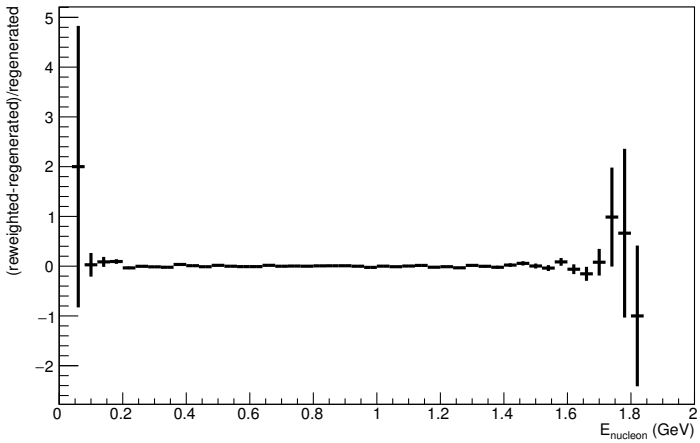
Energy plot: Leading Energy Nucleon: Neut Mode =2
(reweighted-regenerated)/regenerated
E_nucleon (GeV)

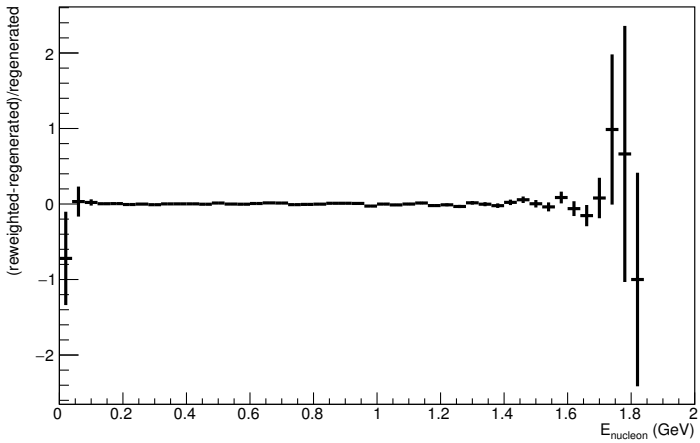
Energy plot: Every FSI Nucleon: Neut Mode =2
(reweighted-regenerated)/regenerated
E_nucleon (GeV)

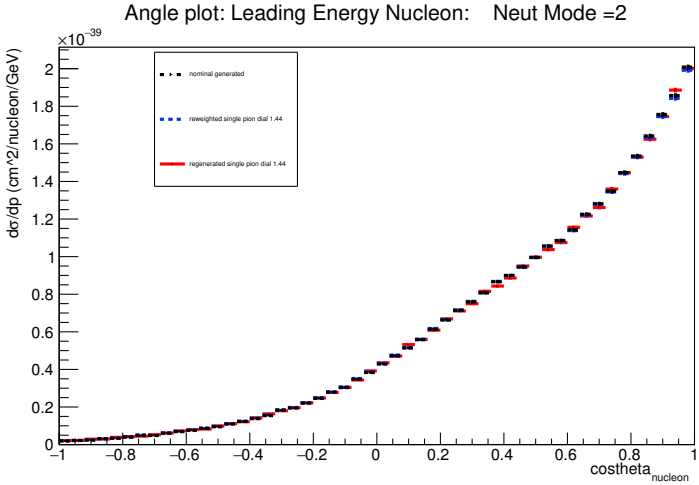
Angle plot: Leading Energy Nucleon: Neut Mode =2
dσ/dp (cm^2/nucleon/GeV)
×10^-39
nominal generated
reweighted single pion dial 1.44
regenerated single pion dial 1.44
costheta_nucleon

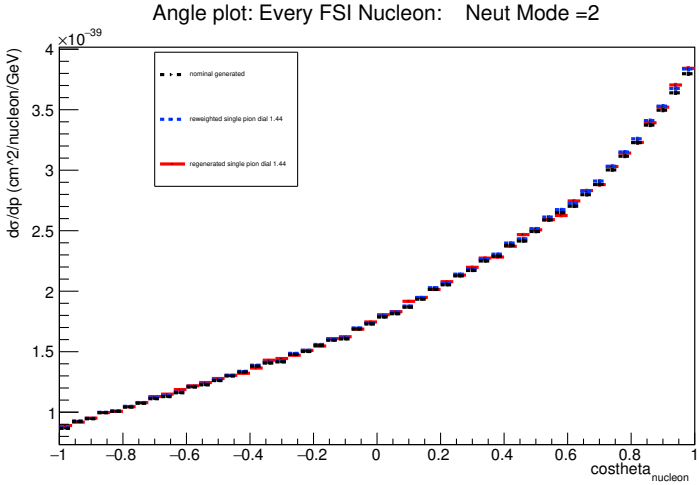
Angle plot: Every FSI Nucleon: Neut Mode =2
dσ/dp (cm^2/nucleon/GeV)
×10^-39
nominal generated
reweighted single pion dial 1.44
regenerated single pion dial 1.44
costheta_nucleon

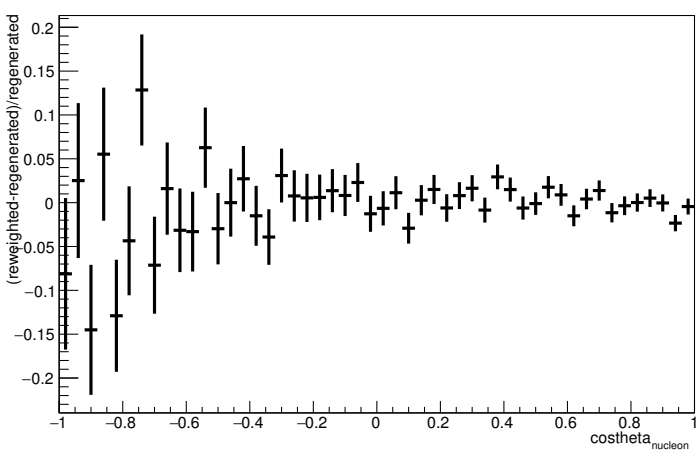
Angle plot: Leading Energy Nucleon: Neut Mode =2
(reweighted-regenerated)/regenerated
costheta_nucleon

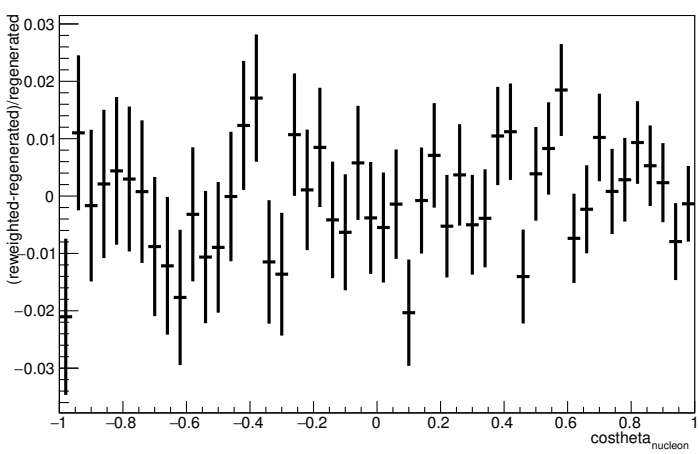
Angle plot: Every FSI Nucleon: Neut Mode =2
(reweighted-regenerated)/regenerated
costheta_nucleon

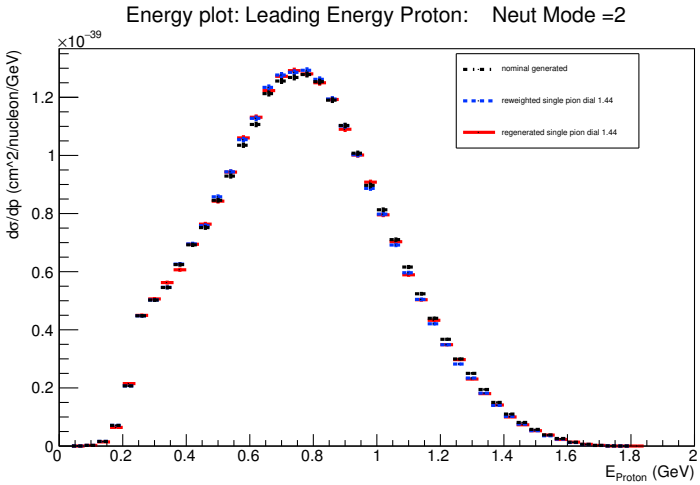
Energy plot: Leading Energy Proton: Neut Mode =2
×10^-39
dσ/dp (cm^2/nucleon/GeV)
nominal generated
reweighted single pion dial 1.44
regenerated single pion dial 1.44
E_Proton (GeV)

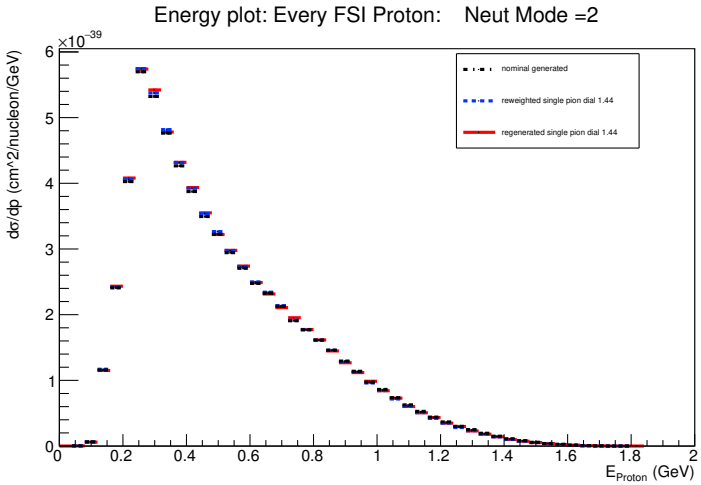
Energy plot: Every FSI Proton: Neut Mode =2
×10^-39
dσ/dp (cm^2/nucleon/GeV)
nominal generated
reweighted single pion dial 1.44
regenerated single pion dial 1.44
E_Proton (GeV)

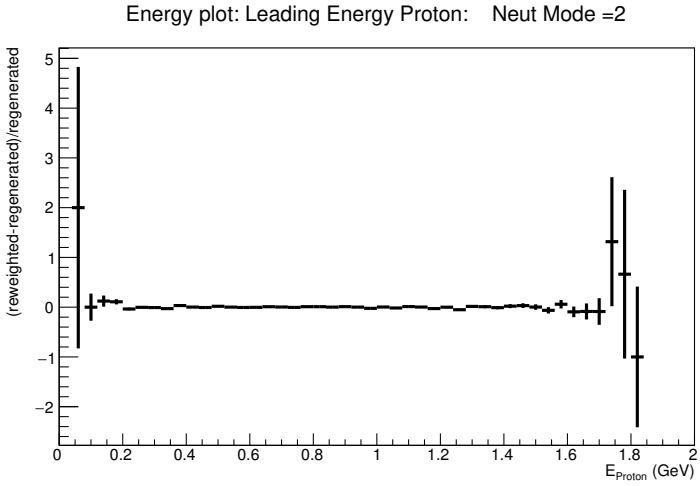
Energy plot: Leading Energy Proton: Neut Mode =2
(reweighted-regenerated)/regenerated
E_Proton (GeV)

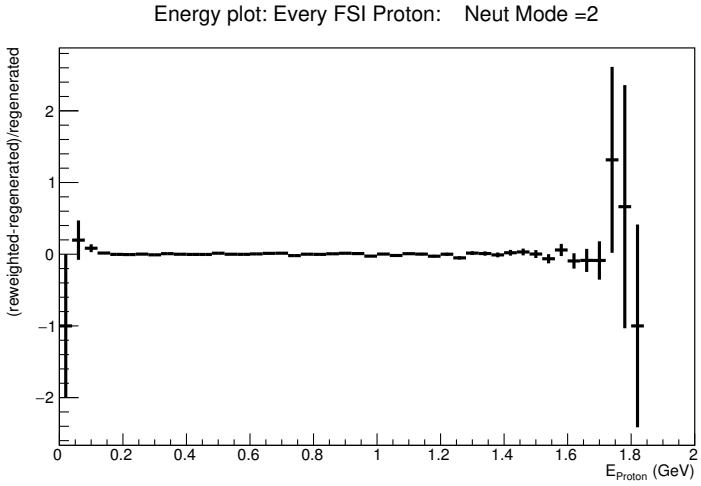
Energy plot: Every FSI Proton: Neut Mode =2
(reweighted-regenerated)/regenerated
E_Proton (GeV)

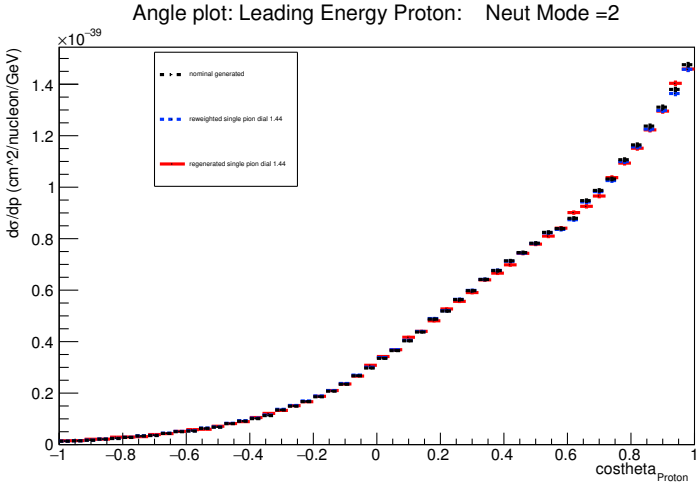
Angle plot: Leading Energy Proton: Neut Mode =2
×10^-39
dσ/dp (cm^2/nucleon/GeV)
nominal generated
reweighted single pion dial 1.44
regenerated single pion dial 1.44
costheta_Proton

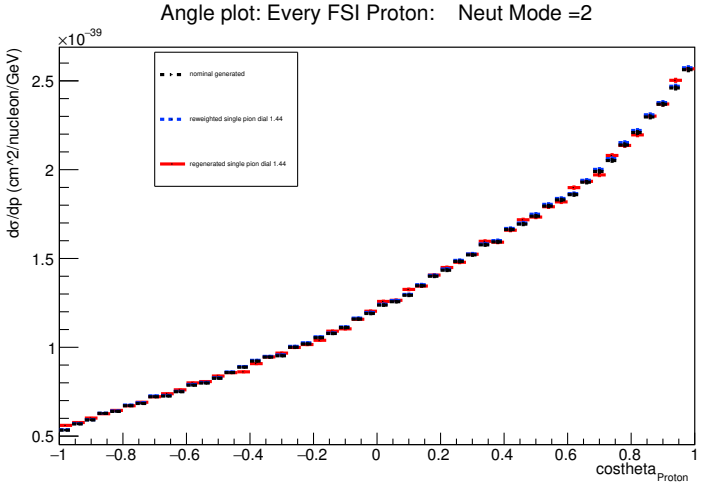
Angle plot: Every FSI Proton: Neut Mode =2
×10^-39
dσ/dp (cm^2/nucleon/GeV)
nominal generated
reweighted single pion dial 1.44
regenerated single pion dial 1.44
costheta_Proton

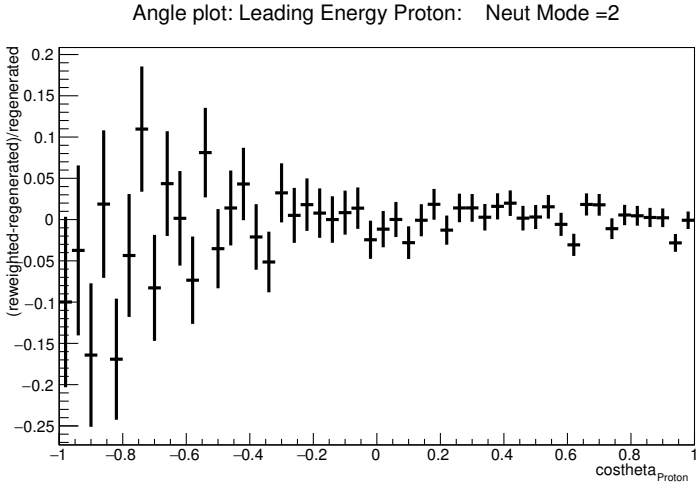
Angle plot: Leading Energy Proton: Neut Mode =2
(reweighted-regenerated)/regenerated
costheta_Proton

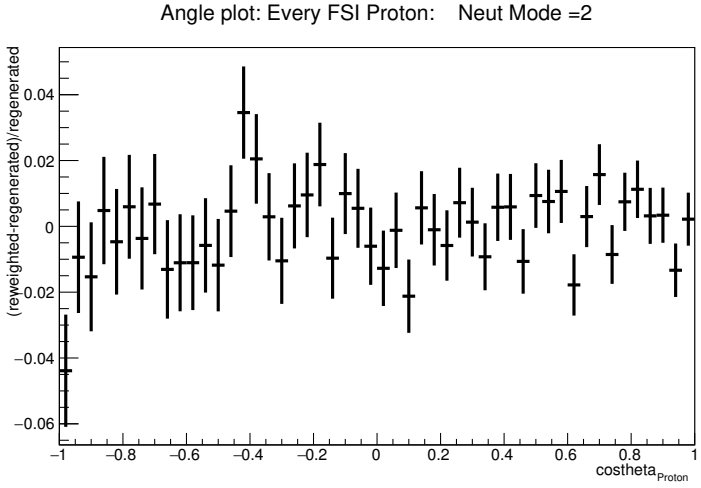
Angle plot: Every FSI Proton: Neut Mode =2
(reweighted-regenerated)/regenerated
costheta_Proton

Energy plot: Leading Energy Neutron: Neut Mode =2

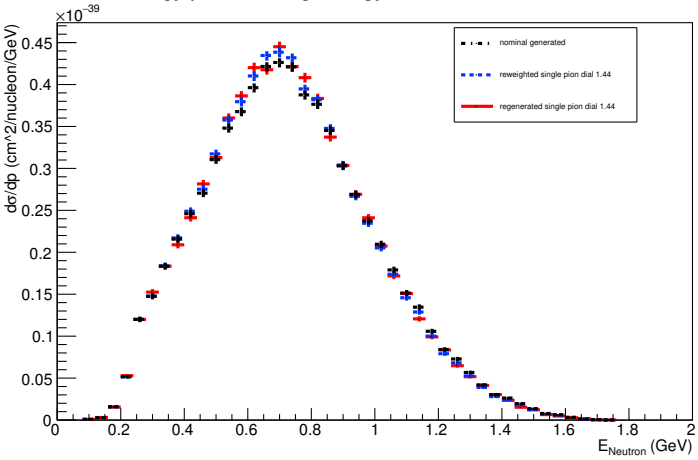

Energy plot: Every FSI Neutron: Neut Mode =2

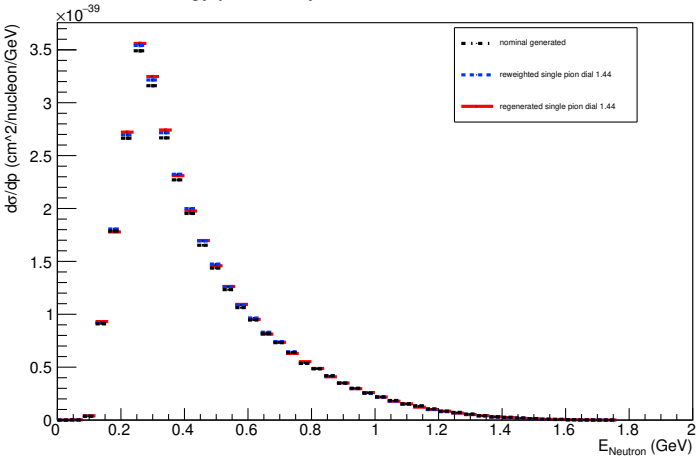

Energy plot: Leading Energy Neutron: Neut Mode =2

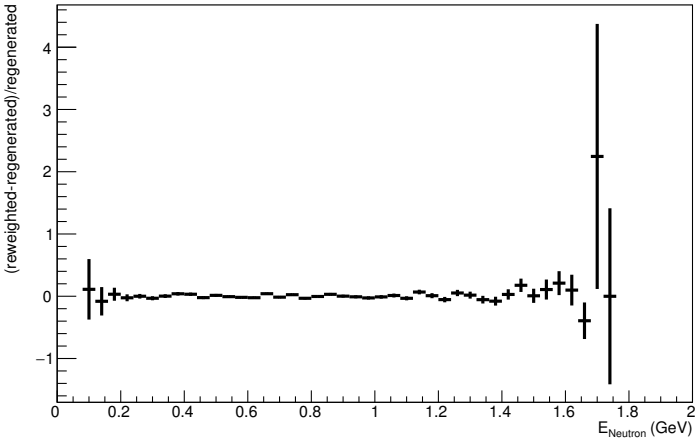

Energy plot: Every FSI Neutron: Neut Mode =2

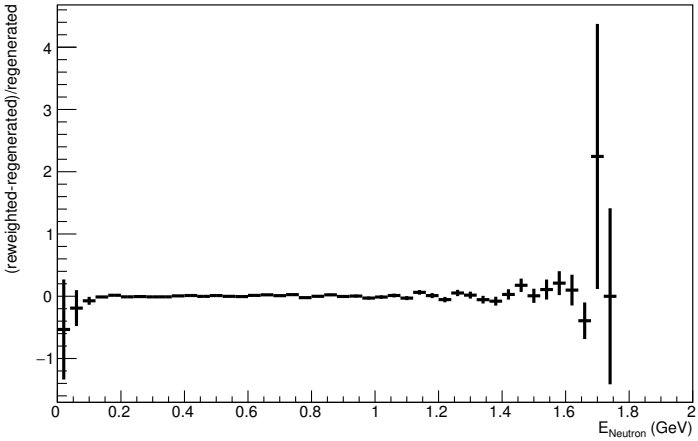

Angle plot: Leading Energy Neutron: Neut Mode =2

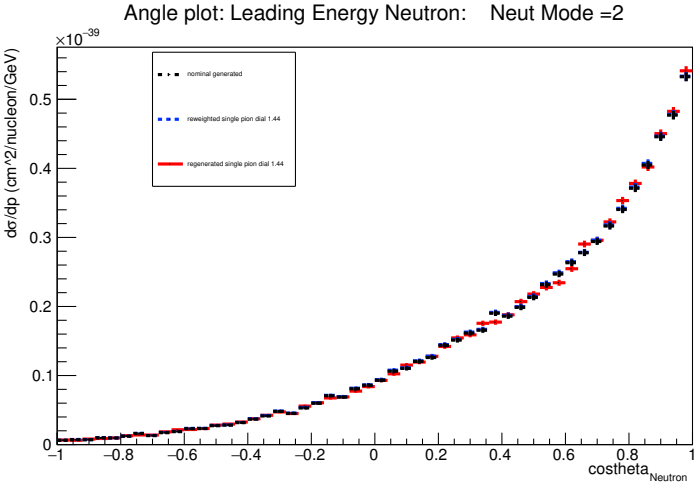

Angle plot: Every FSI Neutron: Neut Mode =2

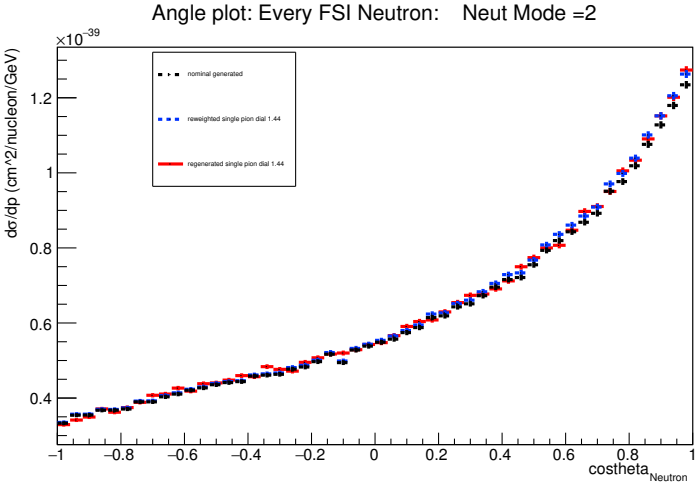

Angle plot: Leading Energy Neutron: Neut Mode =2

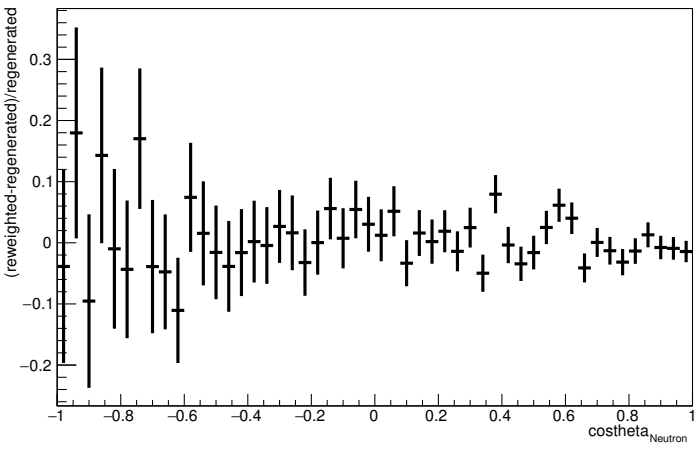

Angle plot: Every FSI Neutron: Neut Mode =2

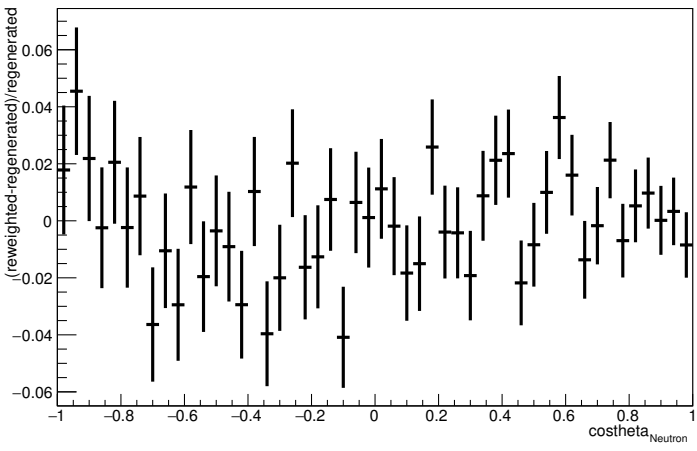

Energy plot: Leading Energy Lepton: Neut Mode =2

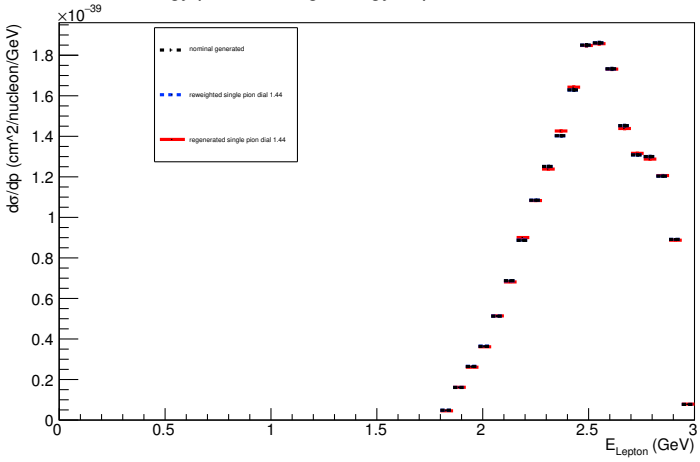

Angle plot: Leading Energy Lepton: Neut Mode =2

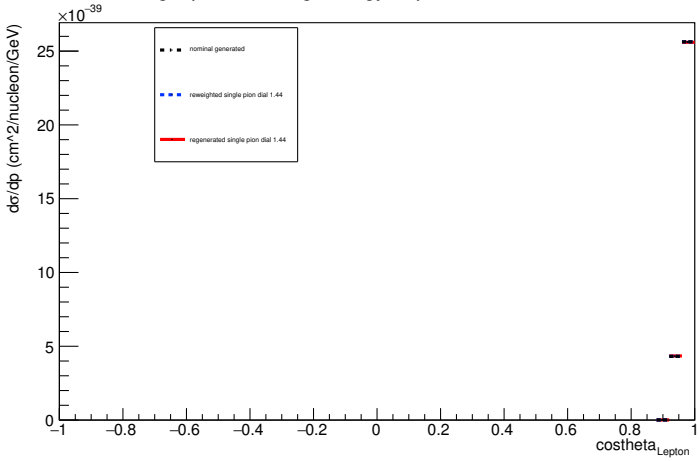

Energy plot: Leading Energy Lepton: Neut Mode =2

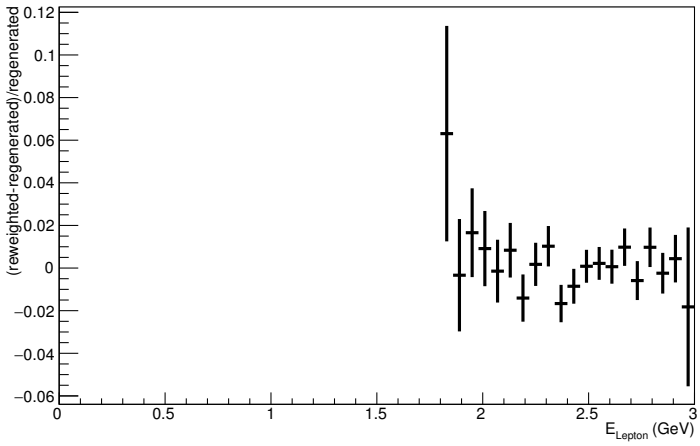

Angle plot: Leading Energy Lepton: Neut Mode =2

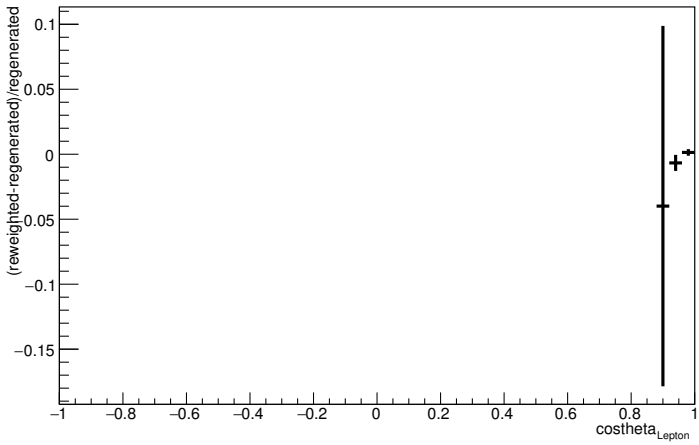

Energy plot: Leading Energy Pion: Neut Mode =2

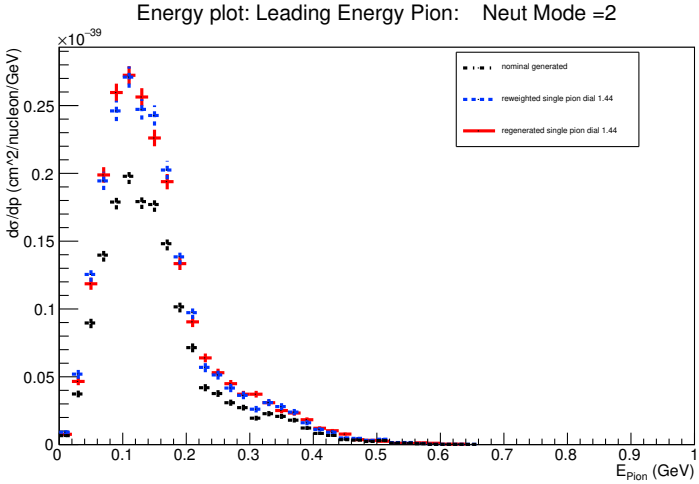

Energy plot: Every FSI Pion: Neut Mode =2

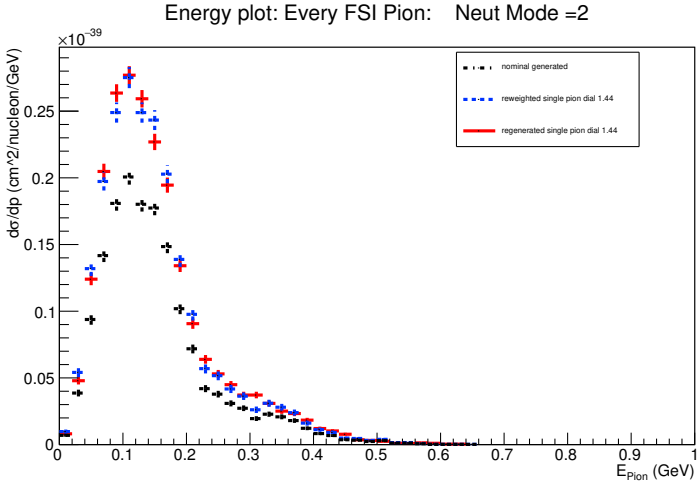

Energy plot: Leading Energy Pion: Neut Mode =2

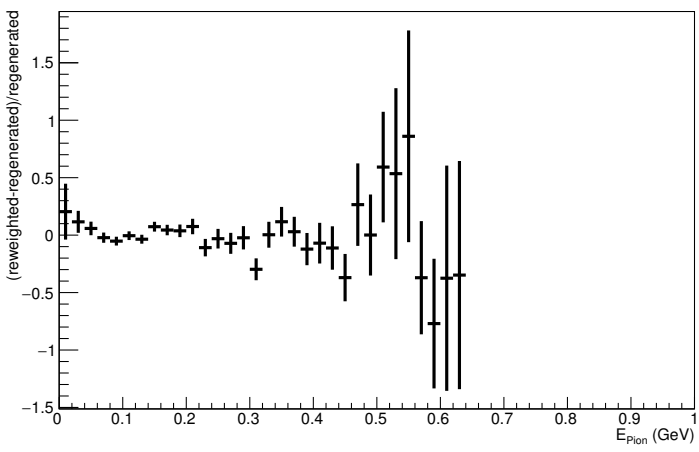

Energy plot: Every FSI Pion: Neut Mode =2

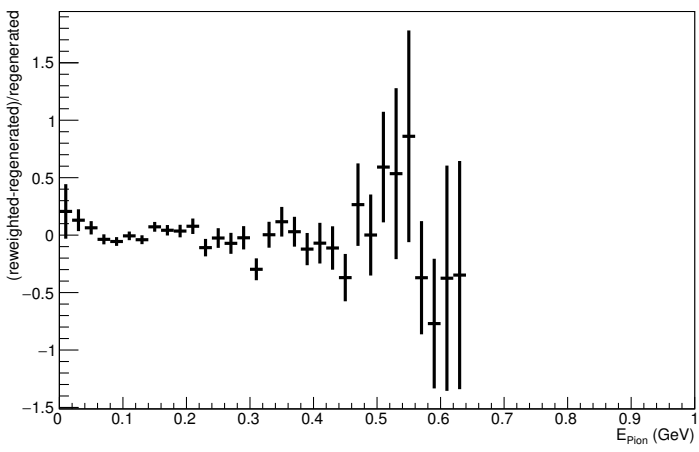

Angle plot: Leading Energy Pion: Neut Mode =2

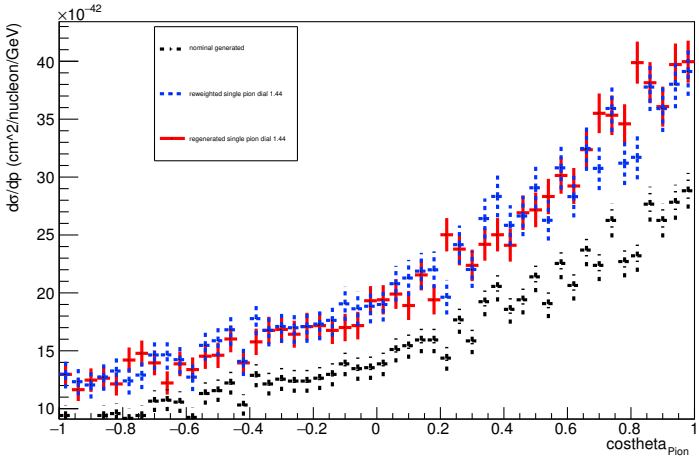

Angle plot: Every FSI Pion: Neut Mode =2

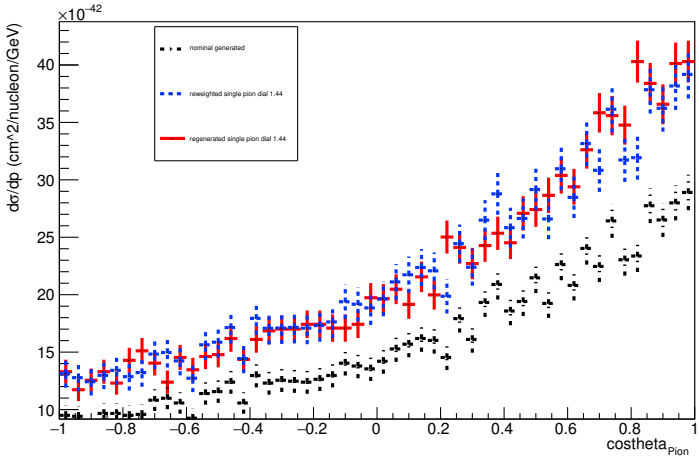

Angle plot: Leading Energy Pion: Neut Mode =2

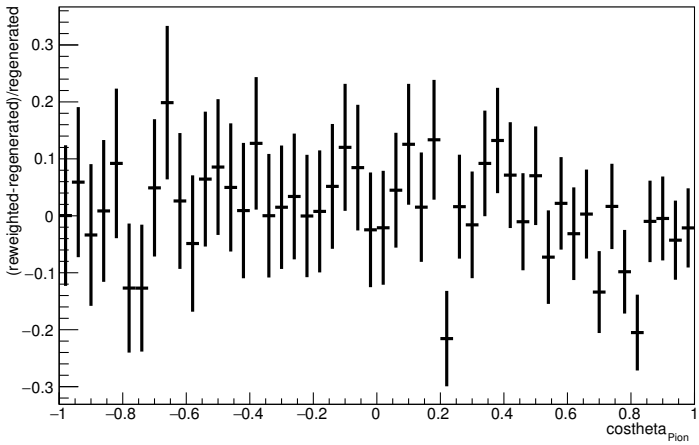

Angle plot: Every FSI Pion: Neut Mode =2

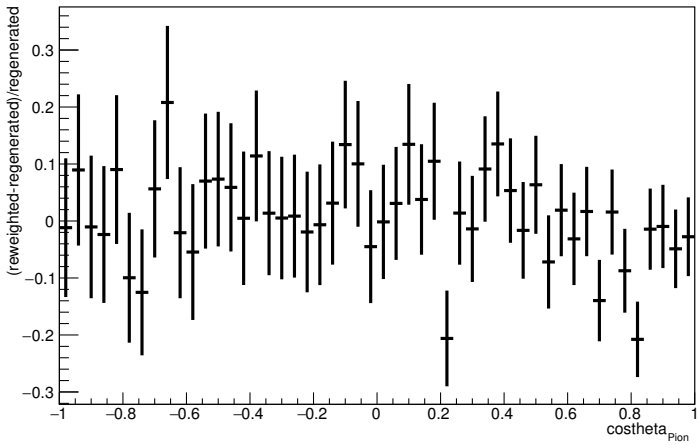

Energy plot: Leading Energy Nucleon: Neut Mode =11

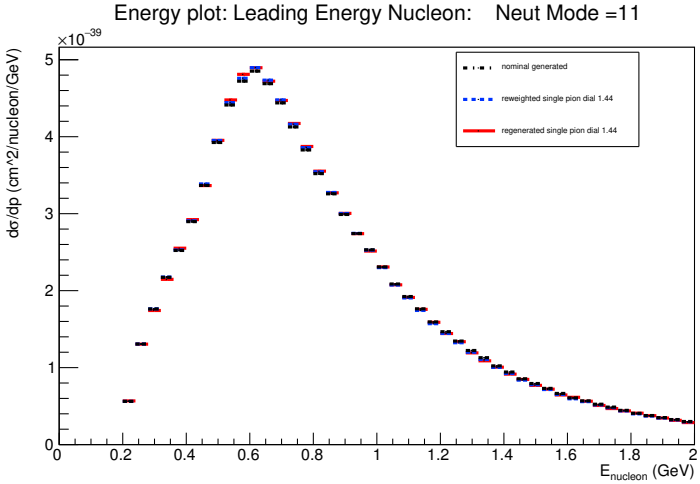

Energy plot: Every FSI Nucleon: Neut Mode =11

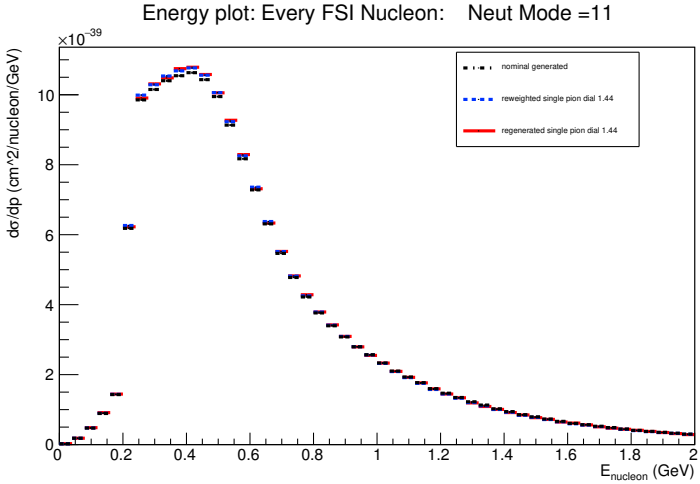

Energy plot: Leading Energy Nucleon: Neut Mode =11

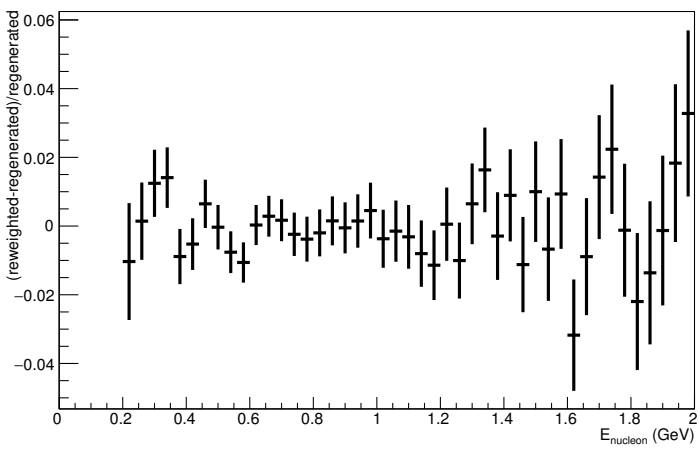

Energy plot: Every FSI Nucleon: Neut Mode =11

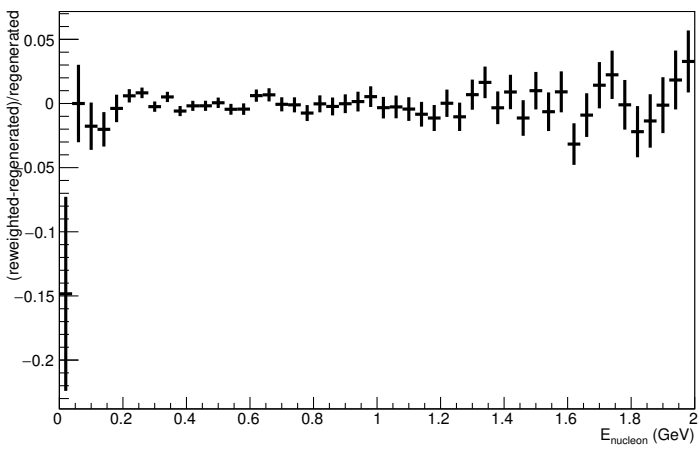

Angle plot: Leading Energy Nucleon: Neut Mode =11

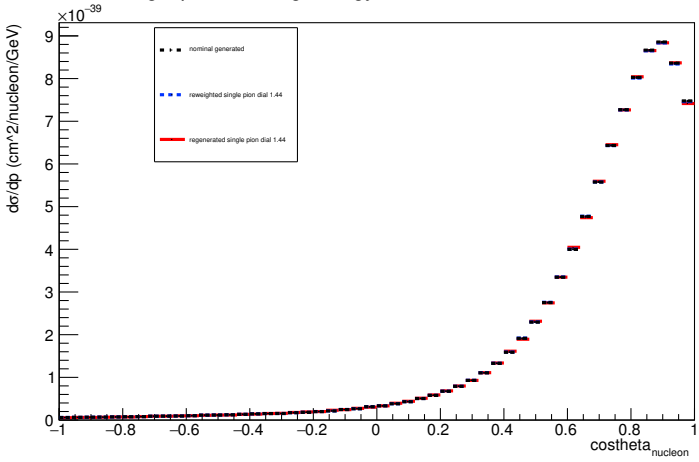

Angle plot: Every FSI Nucleon: Neut Mode =11

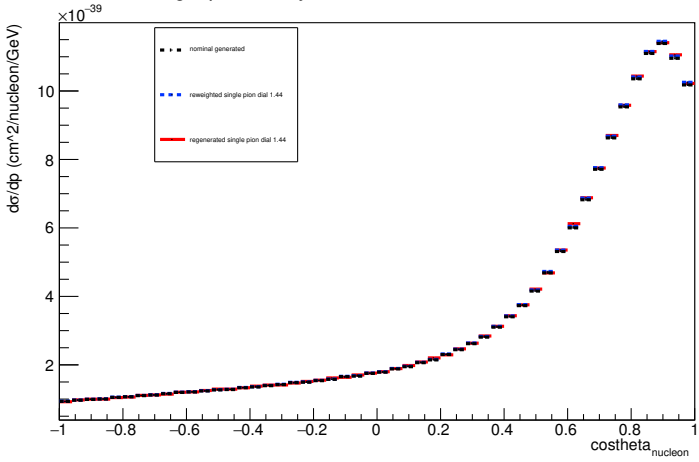

Angle plot: Leading Energy Nucleon: Neut Mode =11

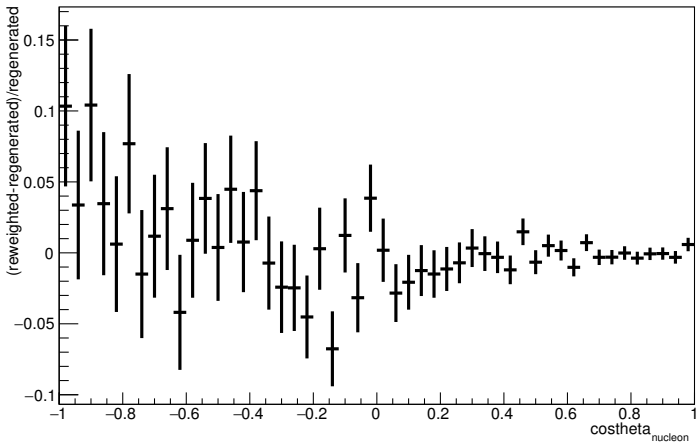

Angle plot: Every FSI Nucleon: Neut Mode =11

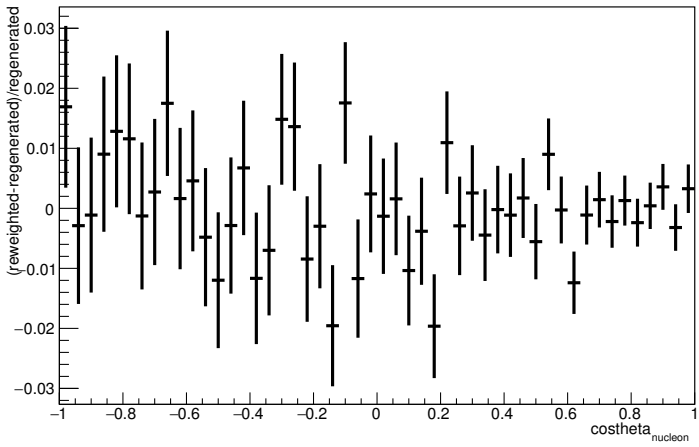

Energy plot: Leading Energy Proton: Neut Mode =11

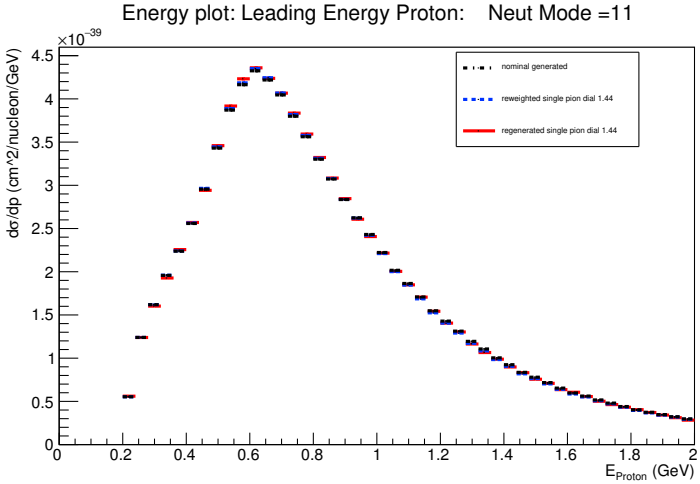

Energy plot: Every FSI Proton: Neut Mode =11

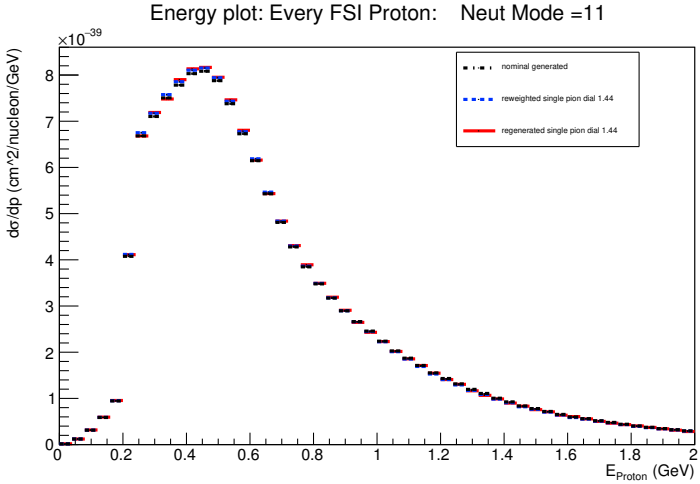

Energy plot: Leading Energy Proton: Neut Mode =11

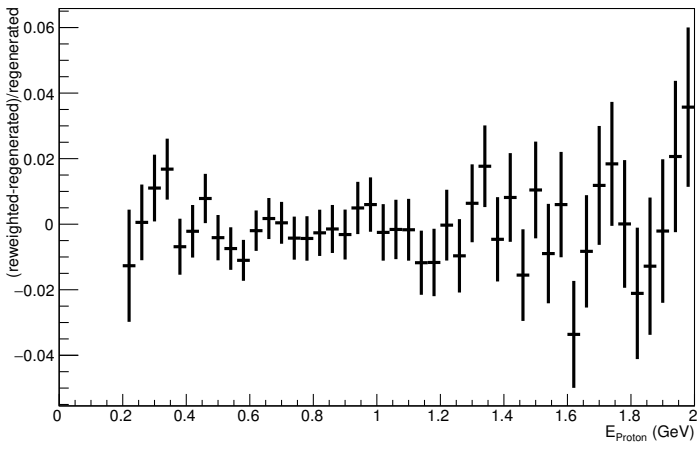

Energy plot: Every FSI Proton: Neut Mode =11

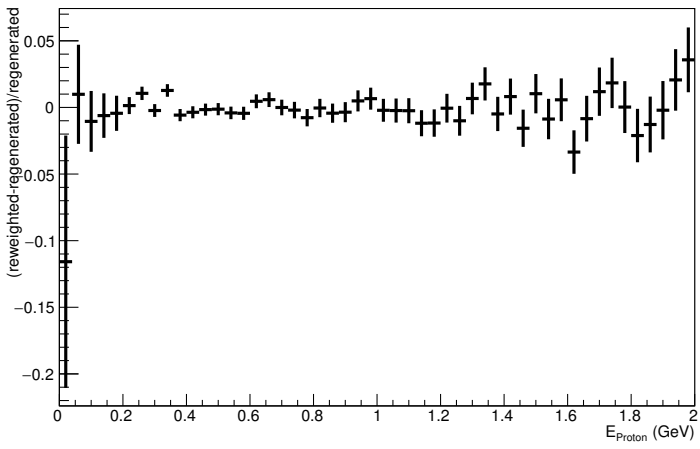

Angle plot: Leading Energy Proton: Neut Mode =11

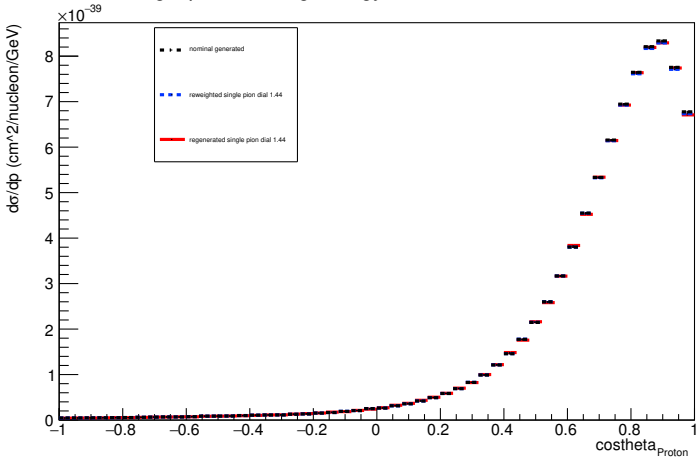

Angle plot: Every FSI Proton: Neut Mode =11

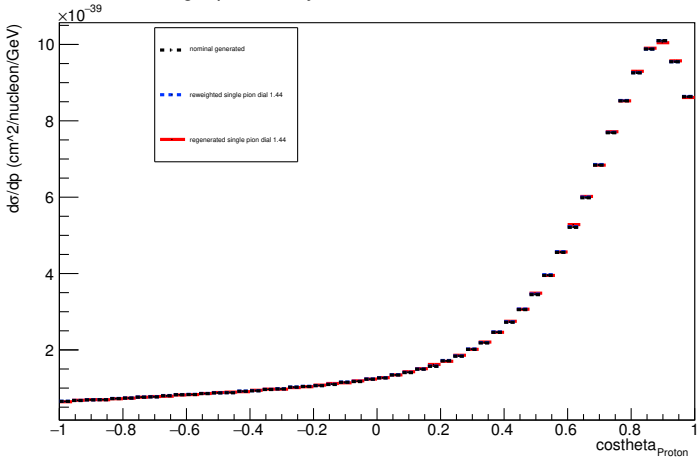

Angle plot: Leading Energy Proton: Neut Mode =11

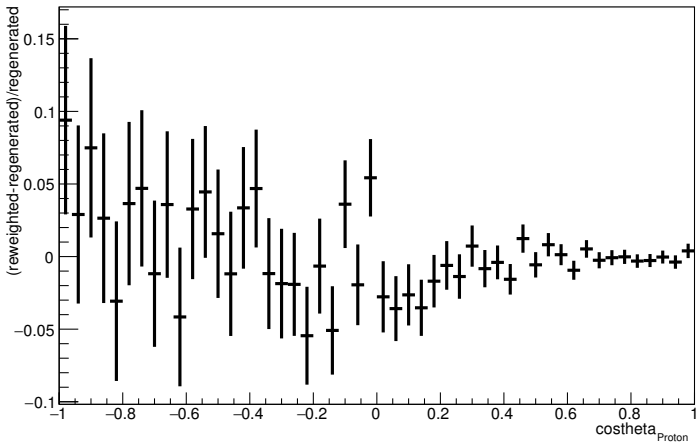

Angle plot: Every FSI Proton: Neut Mode =11

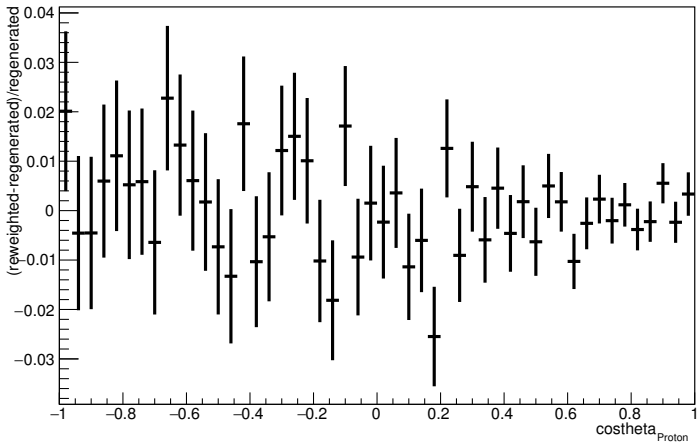

Energy plot: Leading Energy Neutron: Neut Mode =11

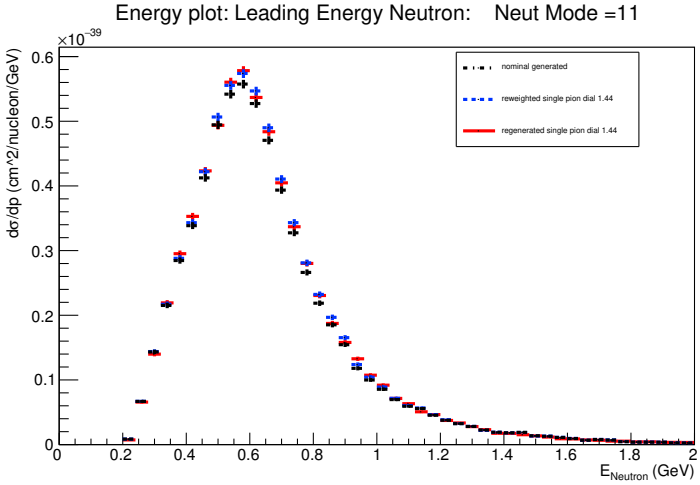

Energy plot: Every FSI Neutron: Neut Mode =11

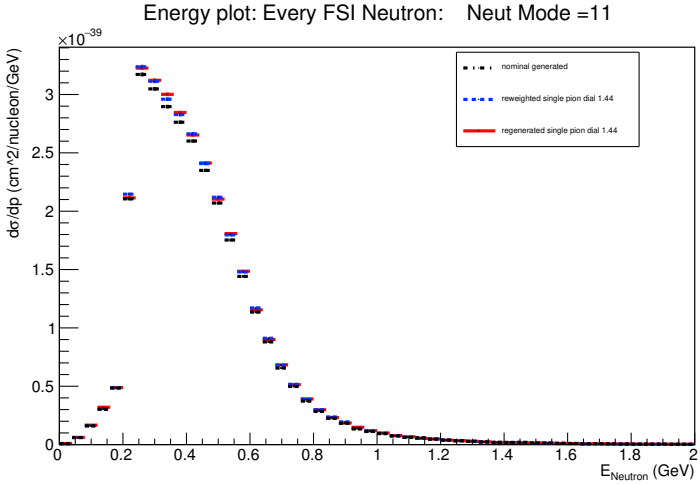

Energy plot: Leading Energy Neutron: Neut Mode =11

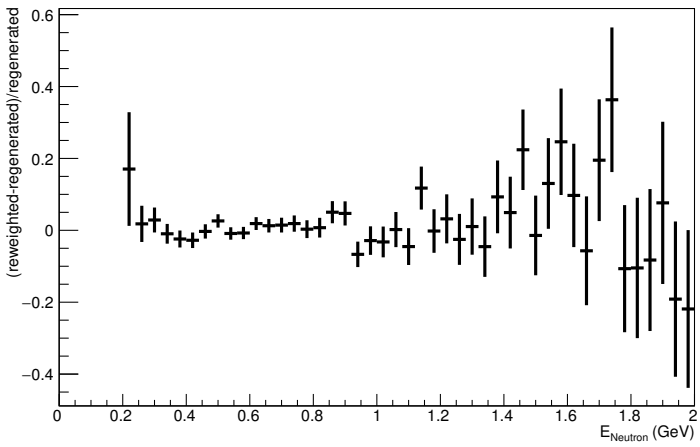

Energy plot: Every FSI Neutron: Neut Mode =11

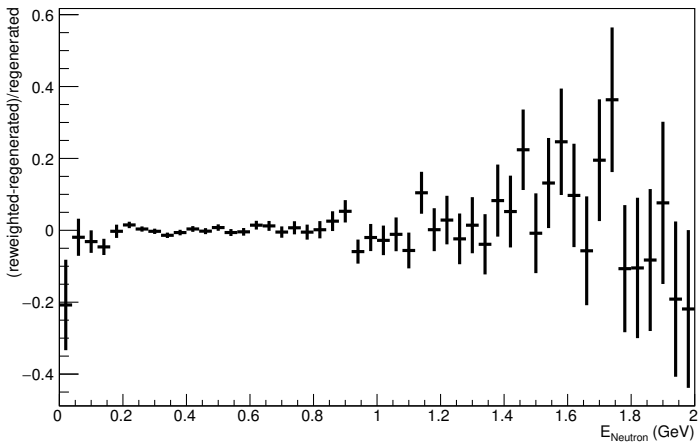

Angle plot: Leading Energy Neutron: Neut Mode =11

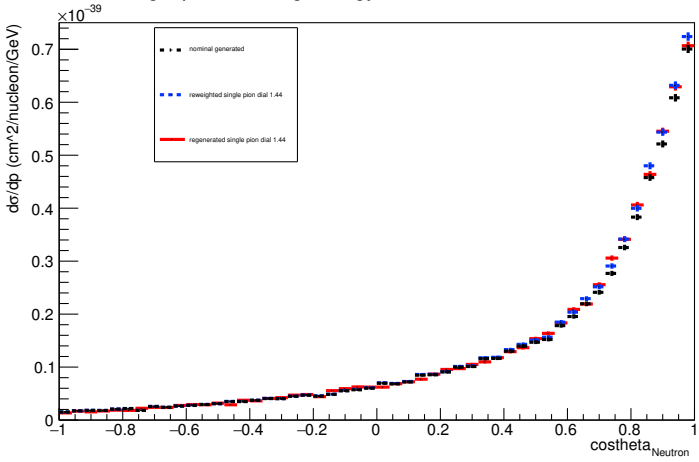

Angle plot: Every FSI Neutron: Neut Mode =11

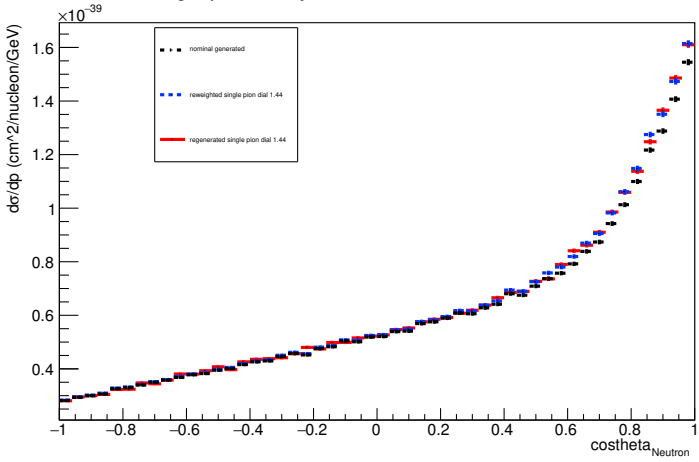

Angle plot: Leading Energy Neutron: Neut Mode =11

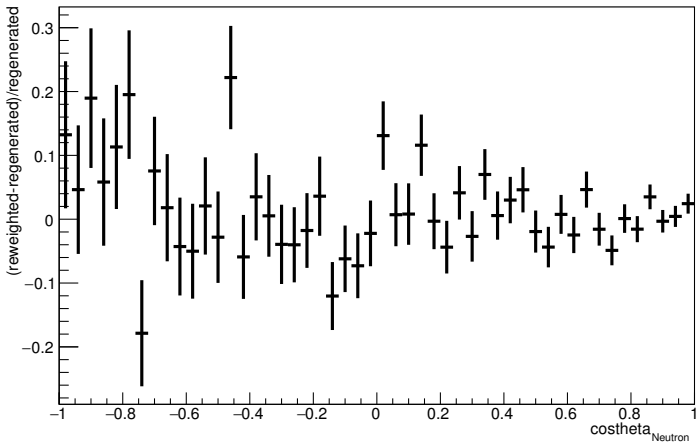

Angle plot: Every FSI Neutron: Neut Mode =11

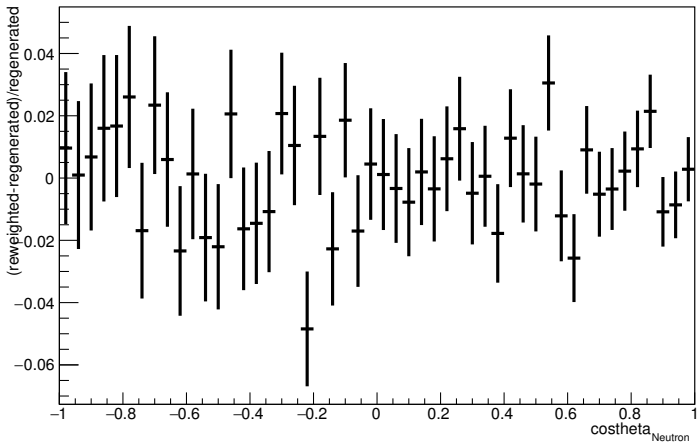

Energy plot: Leading Energy Lepton: Neut Mode =11

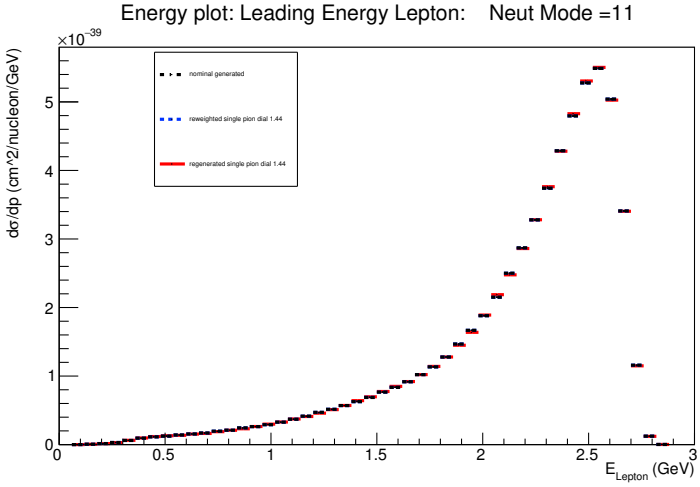

Angle plot: Leading Energy Lepton: Neut Mode =11

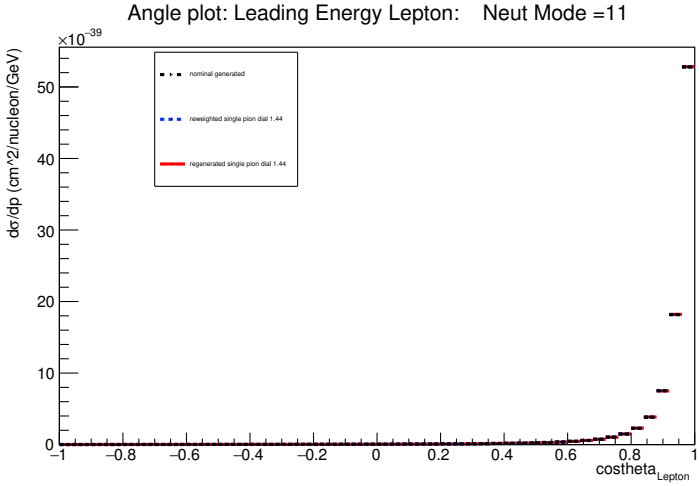

Energy plot: Leading Energy Lepton: Neut Mode =11

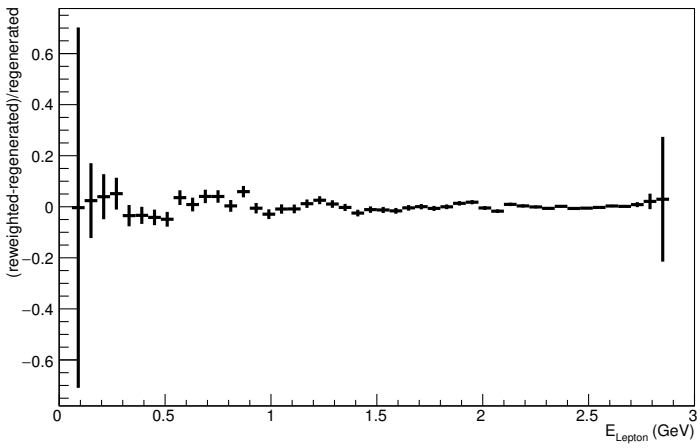

Angle plot: Leading Energy Lepton: Neut Mode =11

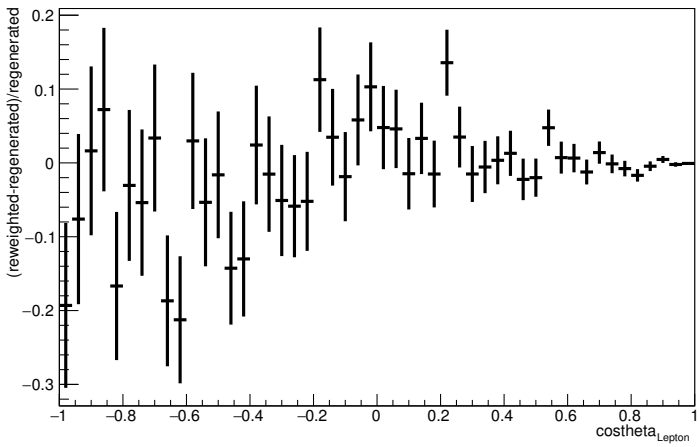

Energy plot: Leading Energy Pion: Neut Mode =11

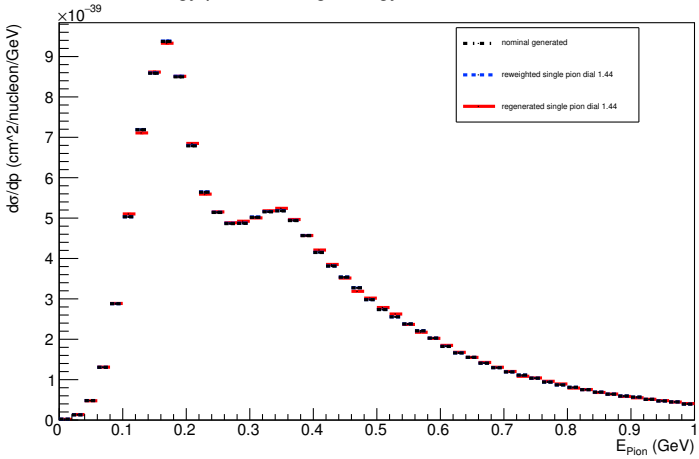

Energy plot: Every FSI Pion: Neut Mode =11

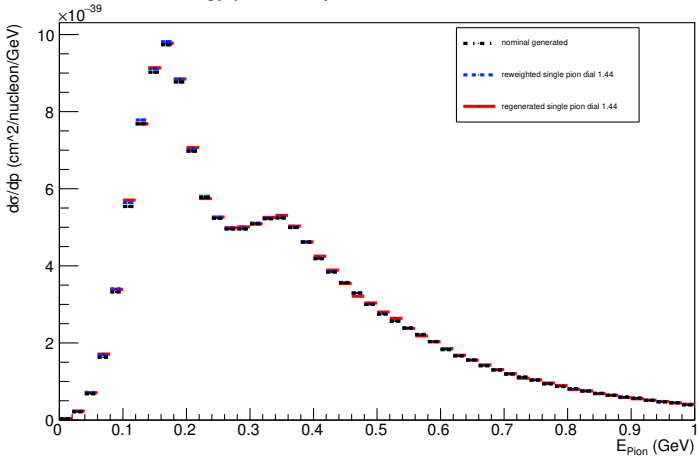

Energy plot: Leading Energy Pion: Neut Mode =11

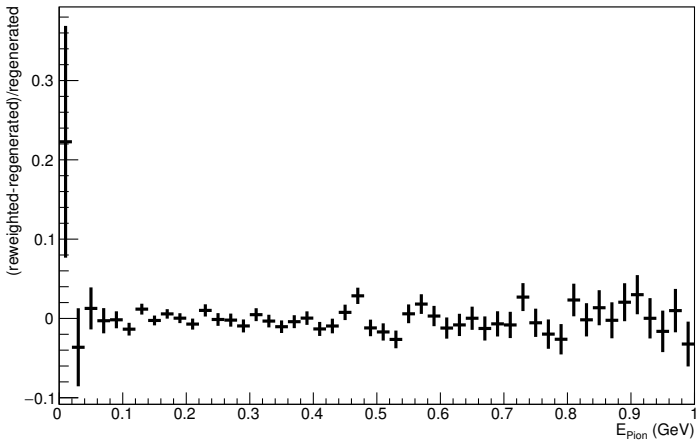

Energy plot: Every FSI Pion: Neut Mode =11

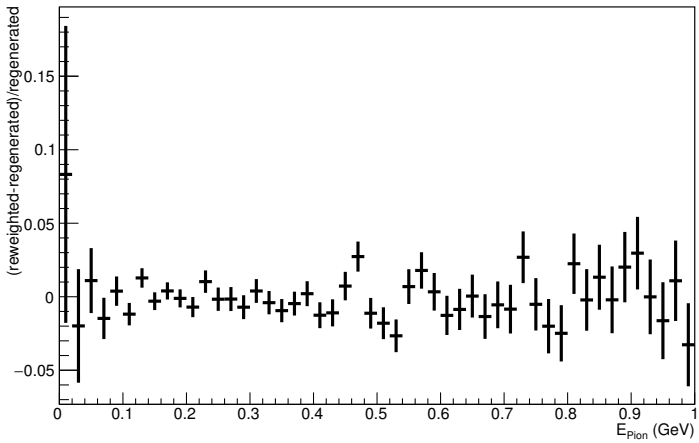

Angle plot: Leading Energy Pion: Neut Mode =11

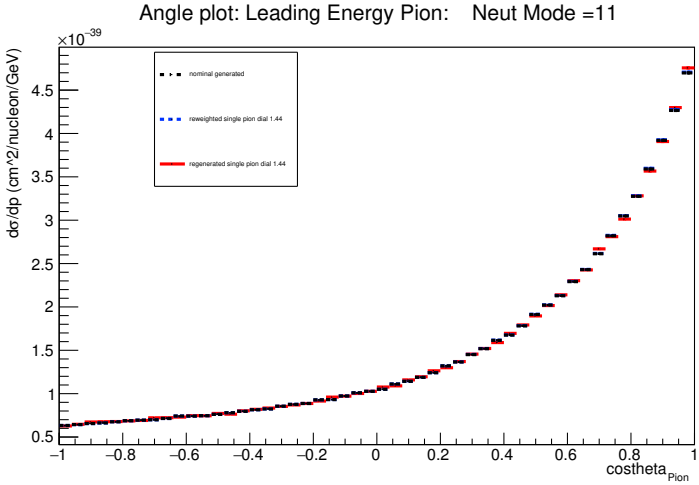

Angle plot: Every FSI Pion: Neut Mode =11

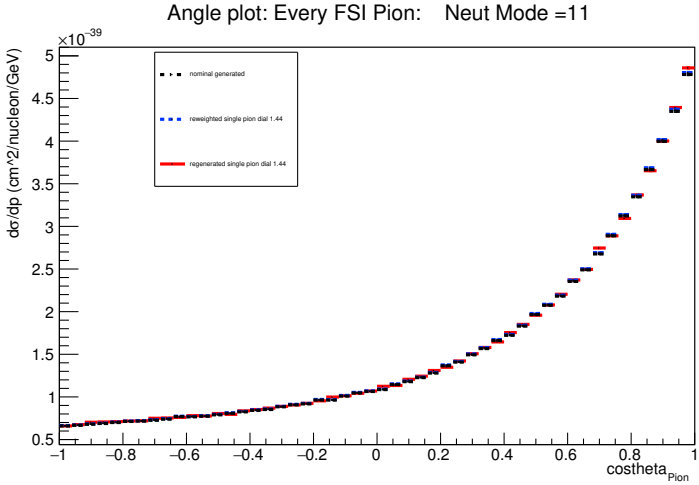

Angle plot: Leading Energy Pion: Neut Mode =11

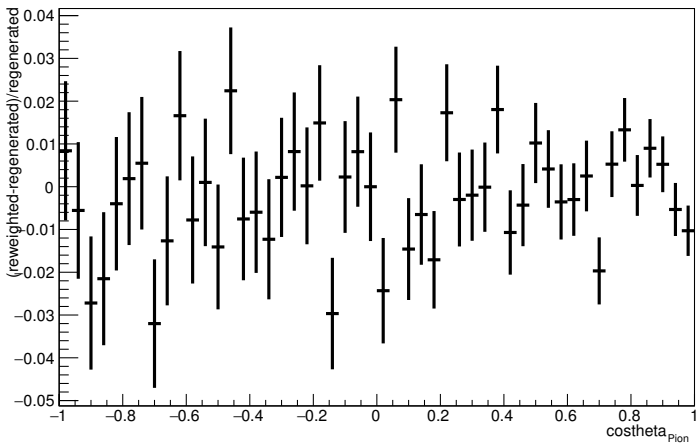

Angle plot: Every FSI Pion: Neut Mode =11

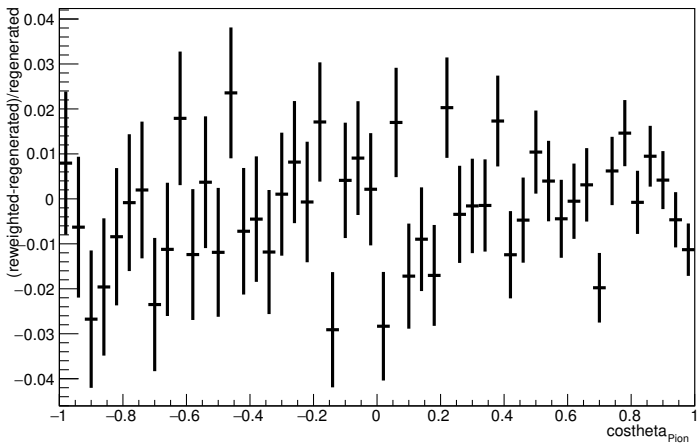

A.6. Single Pion Dial: varied down to 0.64

Energy plot: Leading Energy Nucleon: Neut Mode =AllModesCombined

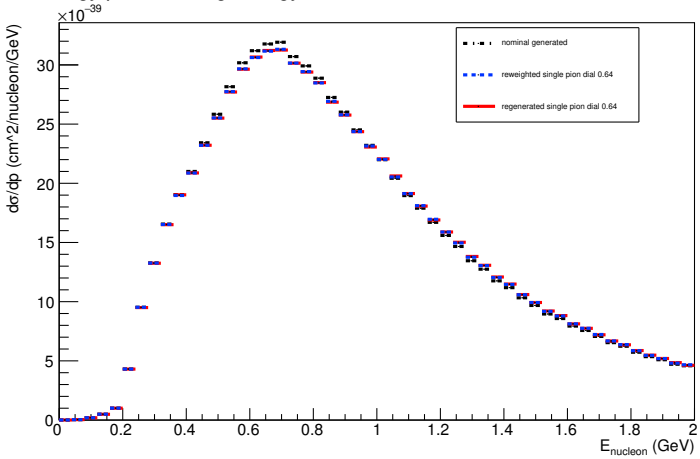

Energy plot: Every FSI Nucleon: Neut Mode =AllModesCombined

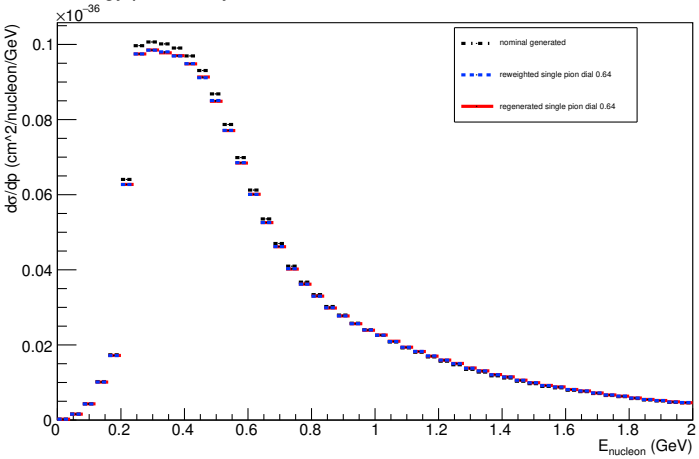

Energy plot: Leading Energy Nucleon: Neut Mode =AllModesCombined

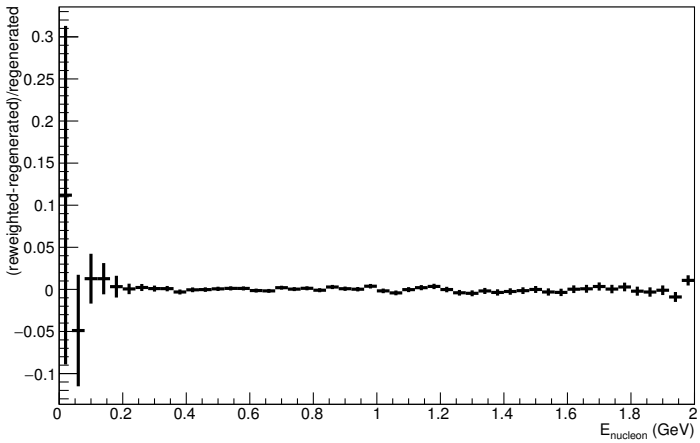

Energy plot: Every FSI Nucleon: Neut Mode =AllModesCombined

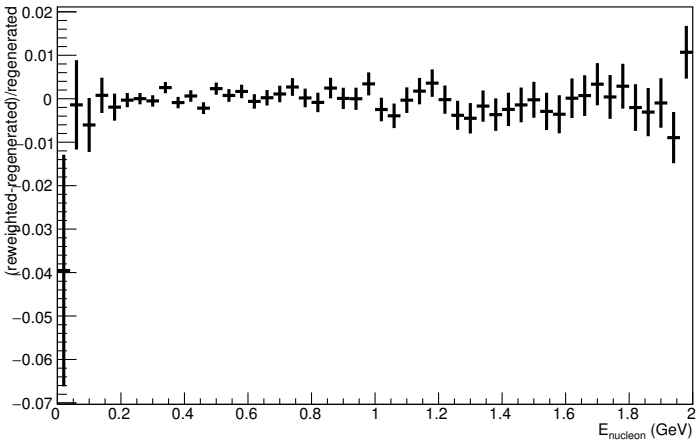

Angle plot: Leading Energy Nucleon: Neut Mode =AllModesCombined

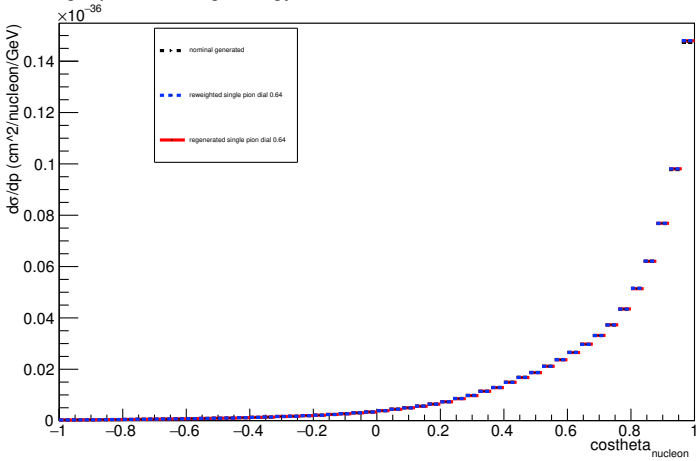

Angle plot: Every FSI Nucleon: Neut Mode =AllModesCombined

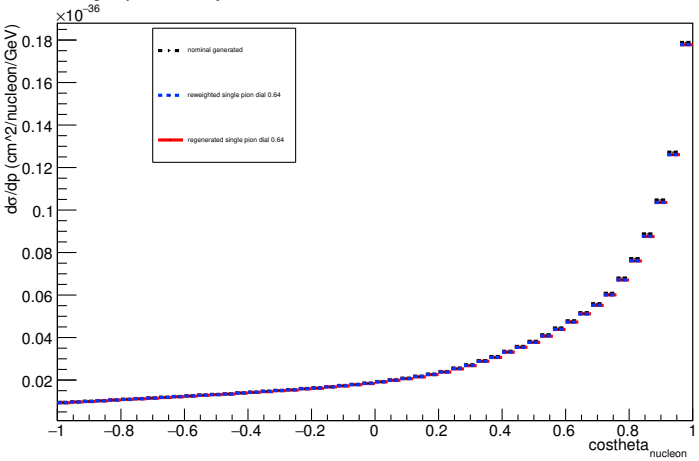

Angle plot: Leading Energy Nucleon: Neut Mode =AllModesCombined

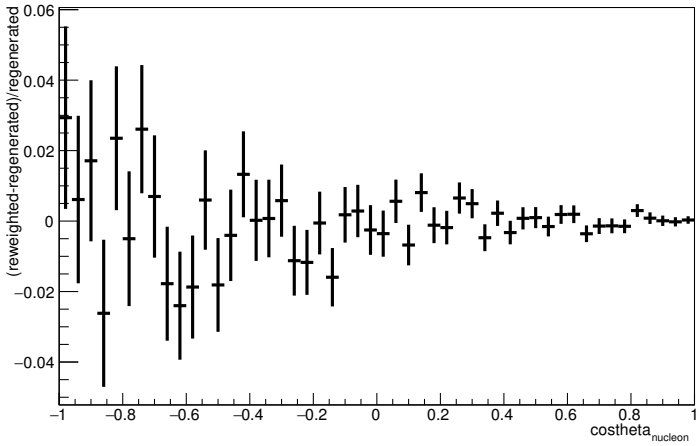

Angle plot: Every FSI Nucleon: Neut Mode =AllModesCombined

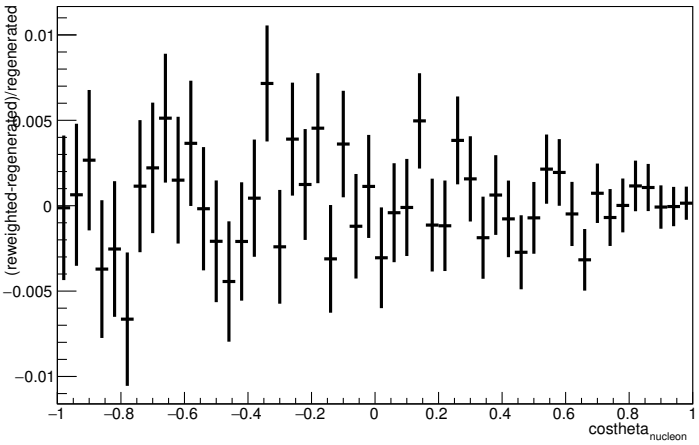

Energy plot: Leading Energy Proton: Neut Mode =AllModesCombined

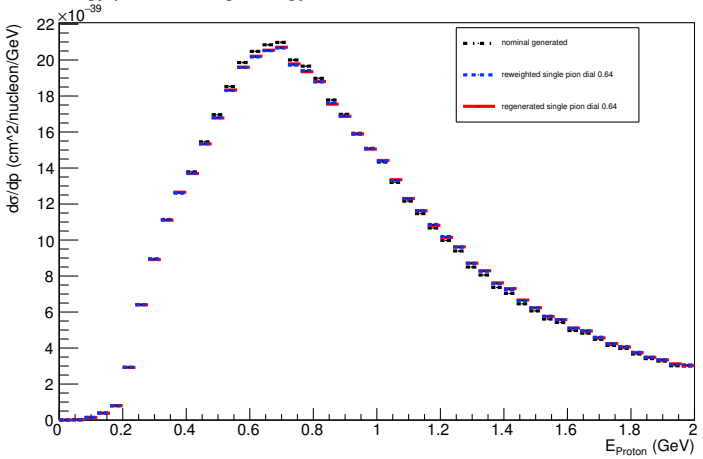

Energy plot: Every FSI Proton: Neut Mode =AllModesCombined

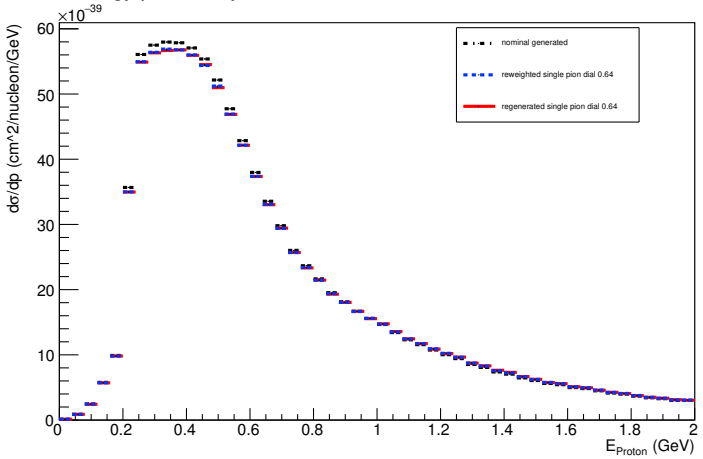

Energy plot: Leading Energy Proton: Neut Mode =AllModesCombined

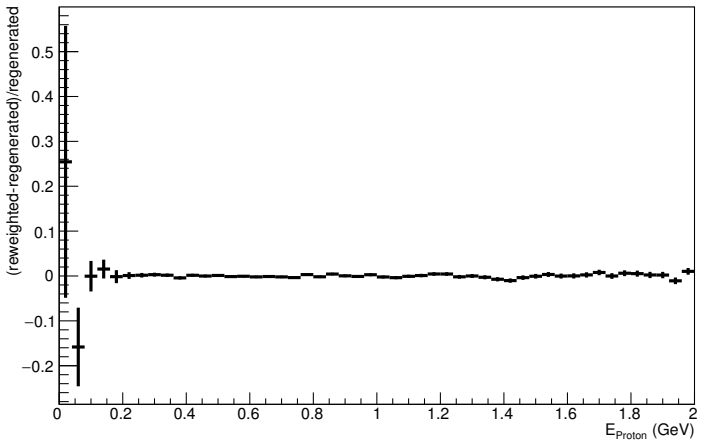

Energy plot: Every FSI Proton: Neut Mode =AllModesCombined

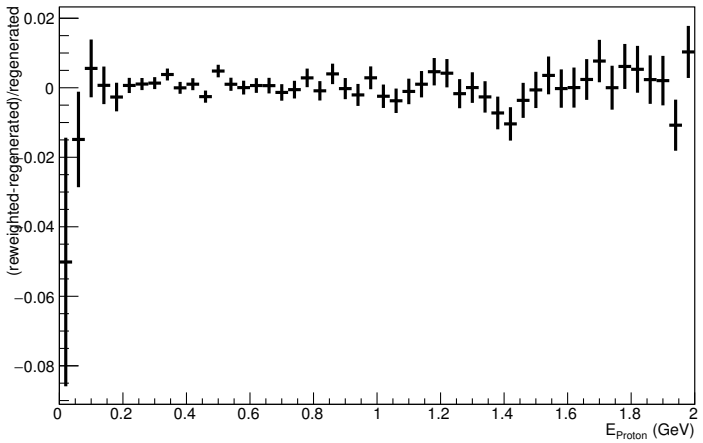

Angle plot: Leading Energy Proton: Neut Mode =AllModesCombined

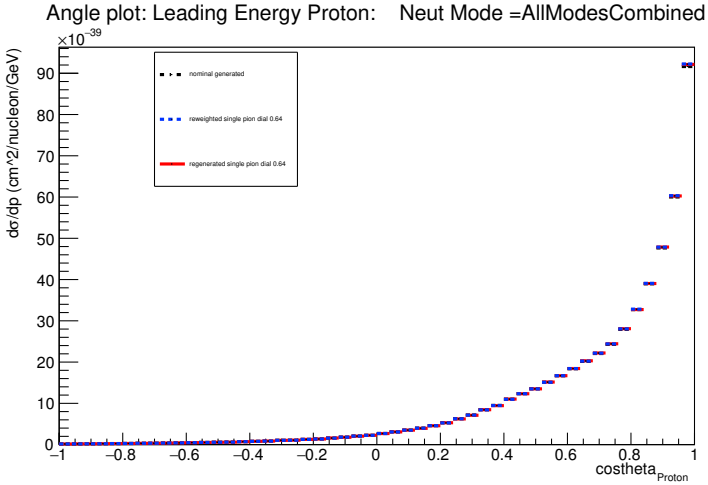

Angle plot: Every FSI Proton: Neut Mode =AllModesCombined

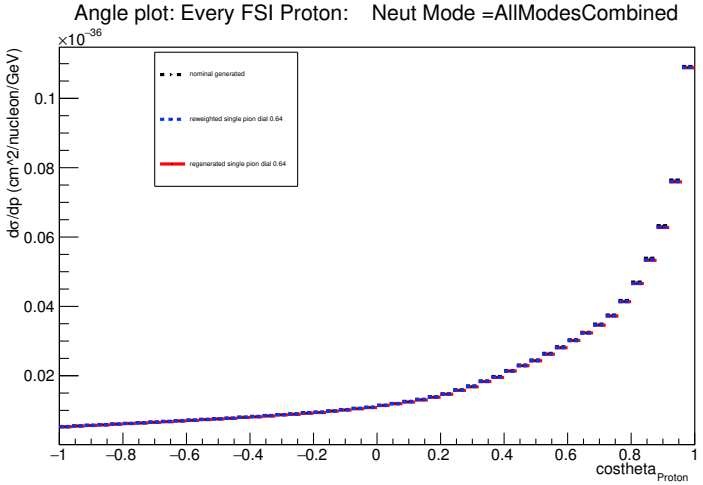

Angle plot: Leading Energy Proton: Neut Mode =AllModesCombined

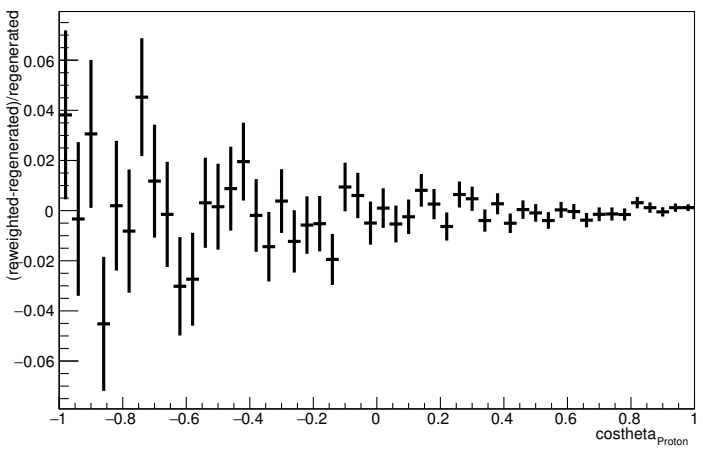

Angle plot: Every FSI Proton: Neut Mode =AllModesCombined

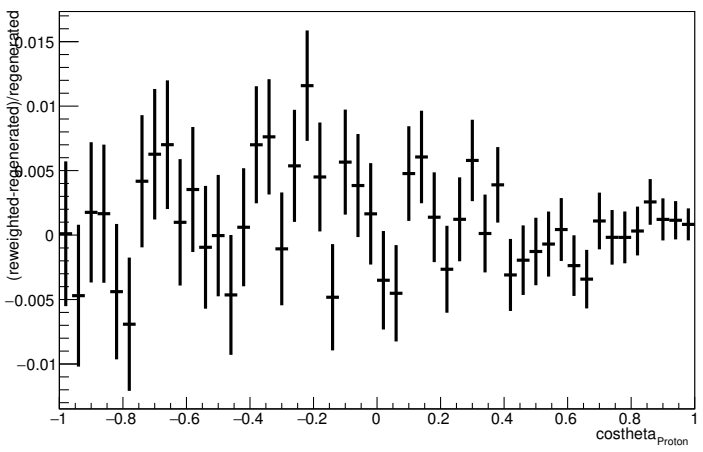

Energy plot: Leading Energy Neutron: Neut Mode =AllModesCombined

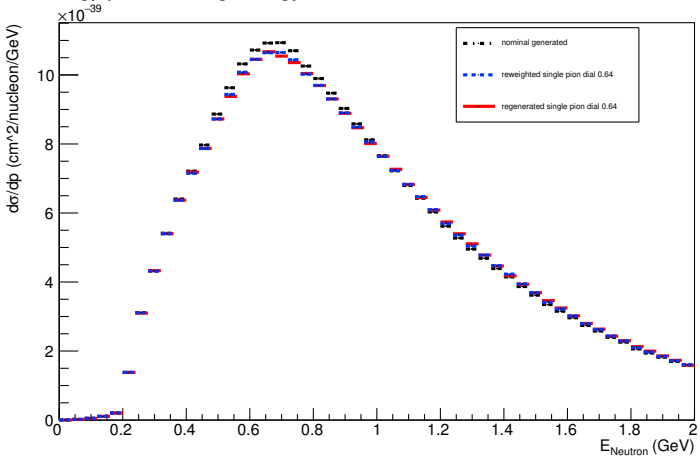

Energy plot: Every FSI Neutron: Neut Mode =AllModesCombined

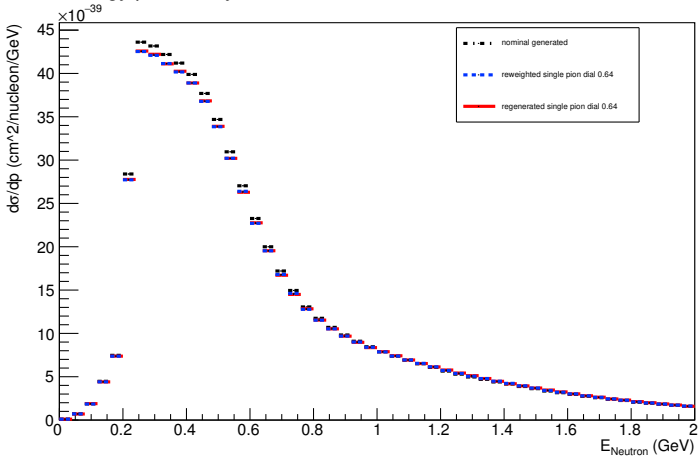

Energy plot: Leading Energy Neutron: Neut Mode =AllModesCombined

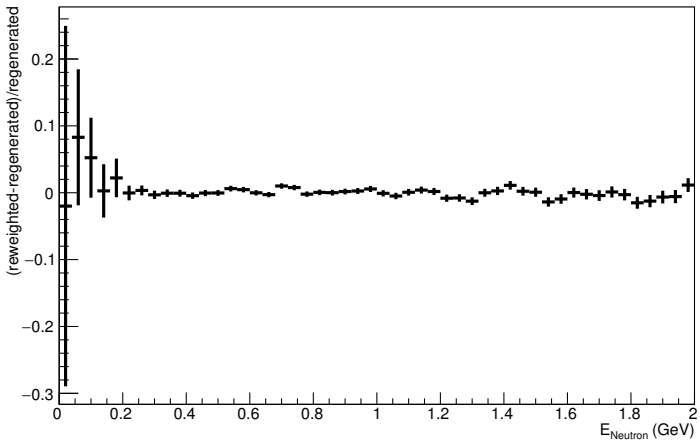

Energy plot: Every FSI Neutron: Neut Mode =AllModesCombined

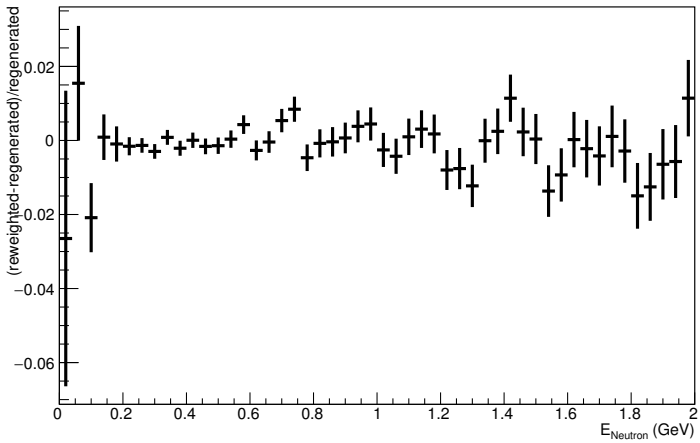

Angle plot: Leading Energy Neutron: Neut Mode =AllModesCombined

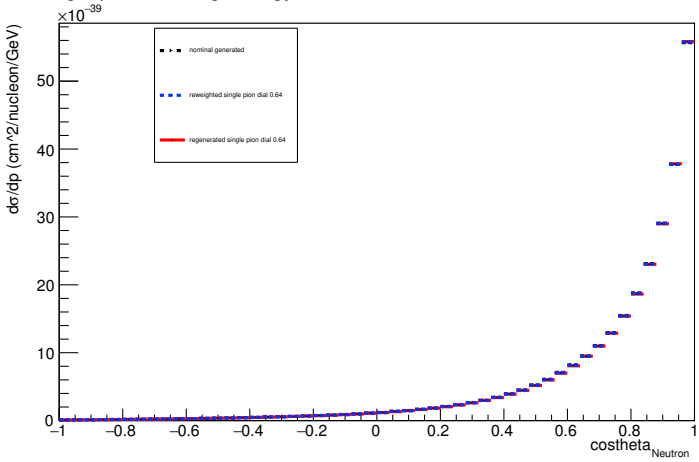

Angle plot: Every FSI Neutron: Neut Mode =AllModesCombined

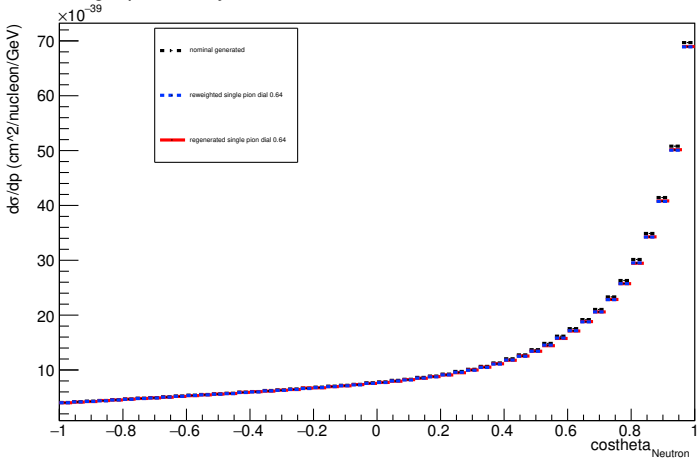

Angle plot: Leading Energy Neutron: Neut Mode =AllModesCombined

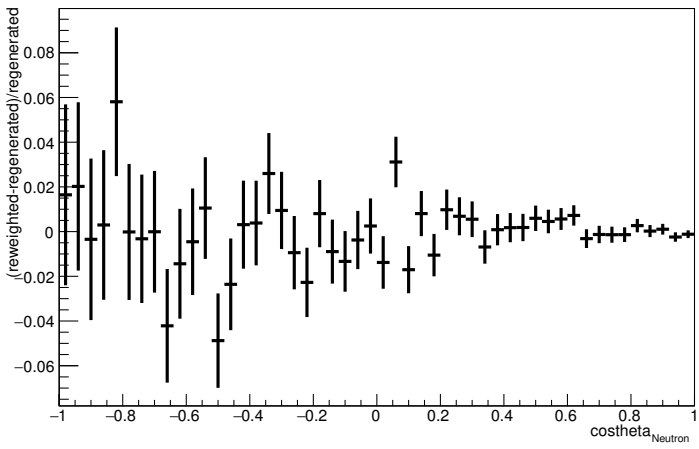

Angle plot: Every FSI Neutron: Neut Mode =AllModesCombined

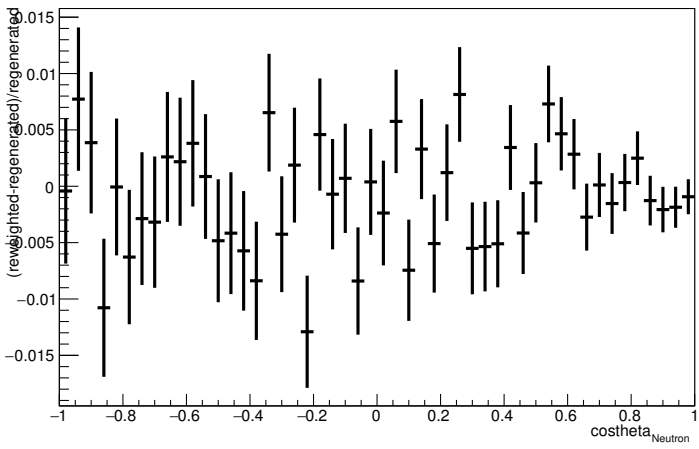

Energy plot: Leading Energy Lepton: Neut Mode =AllModesCombined

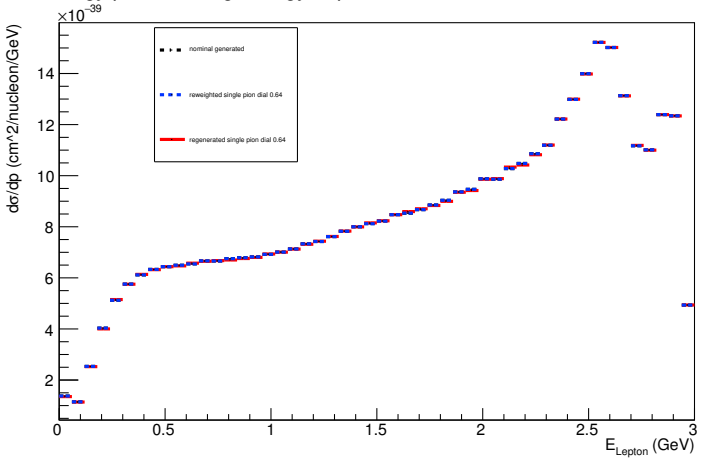

Angle plot: Leading Energy Lepton: Neut Mode =AllModesCombined

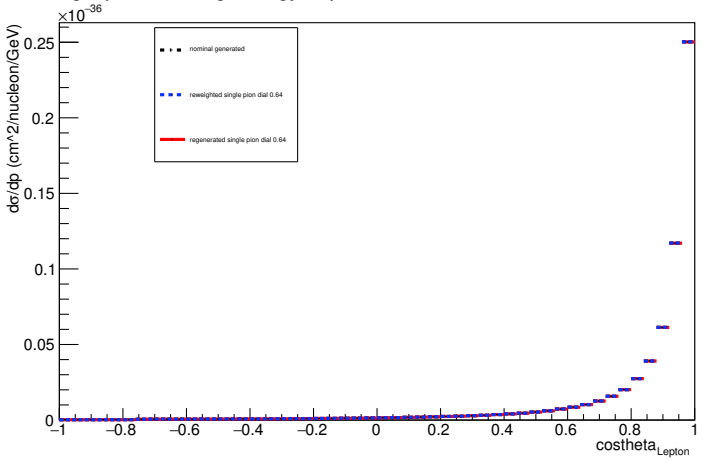

Energy plot: Leading Energy Lepton: Neut Mode =AllModesCombined

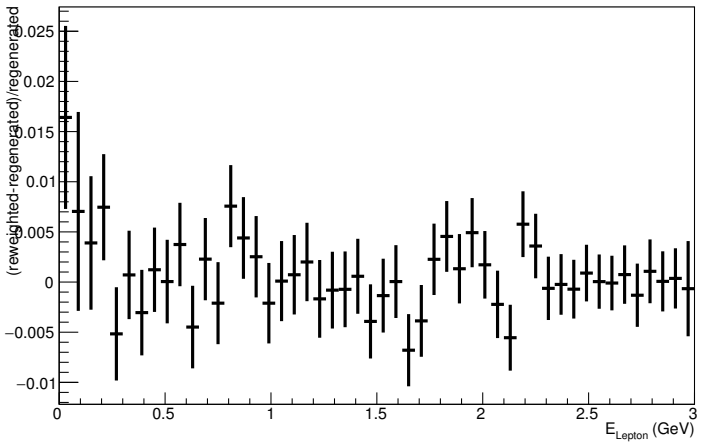

Angle plot: Leading Energy Lepton: Neut Mode =AllModesCombined

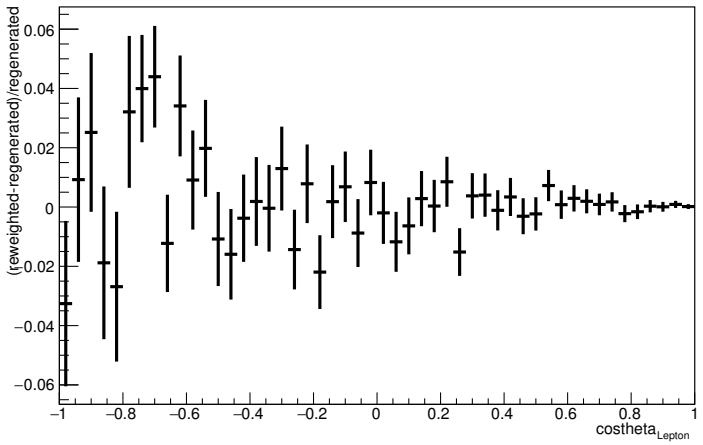

Energy plot: Leading Energy Pion: Neut Mode =AllModesCombined

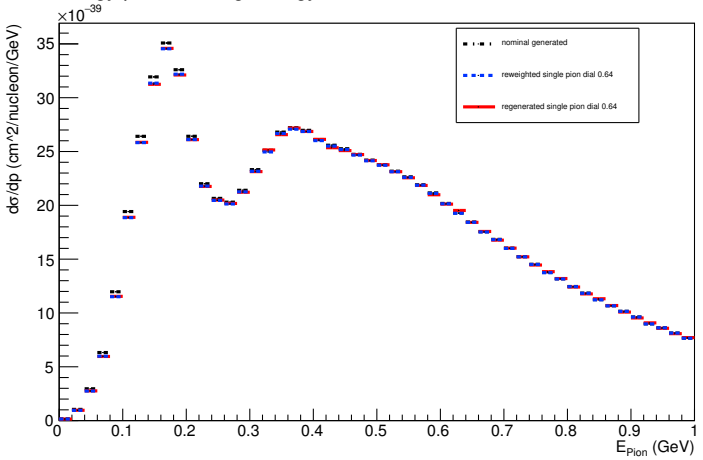

Energy plot: Every FSI Pion: Neut Mode =AllModesCombined

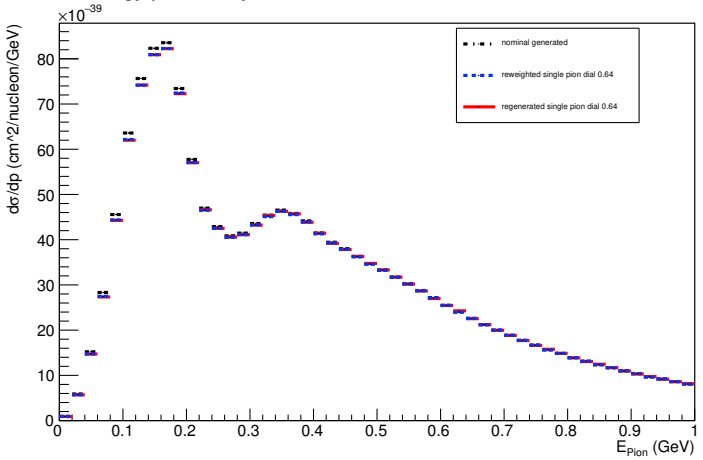

Energy plot: Leading Energy Pion: Neut Mode =AllModesCombined

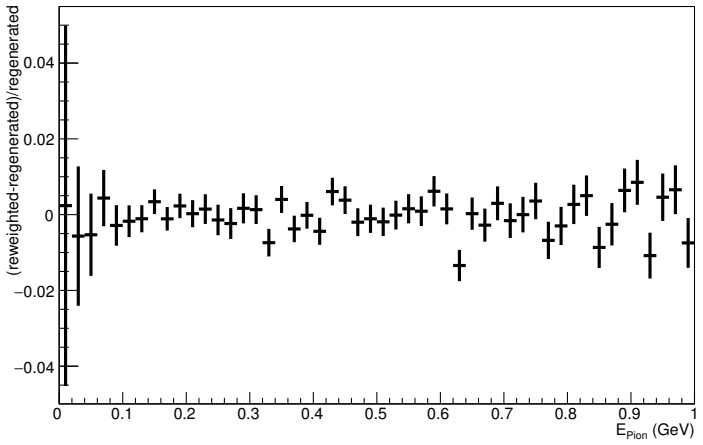

Energy plot: Every FSI Pion: Neut Mode =AllModesCombined

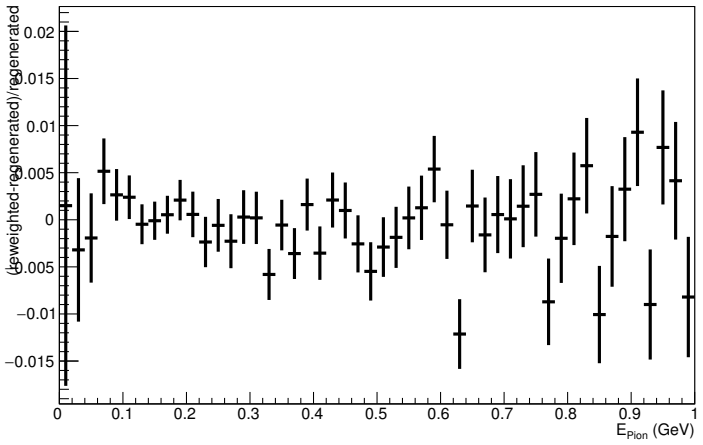

Angle plot: Leading Energy Pion: Neut Mode =AllModesCombined

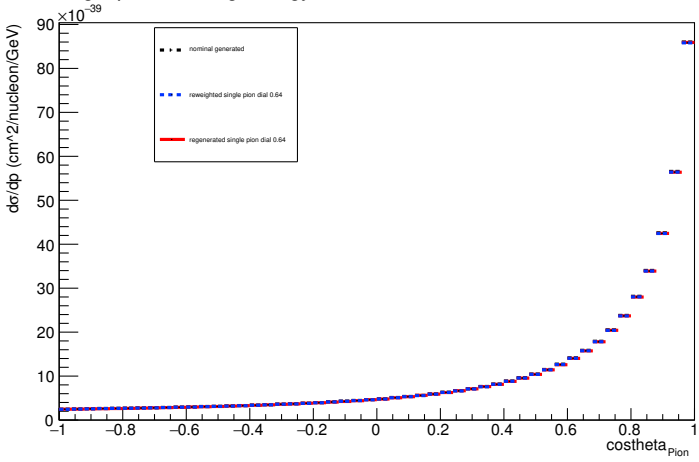

Angle plot: Every FSI Pion: Neut Mode =AllModesCombined

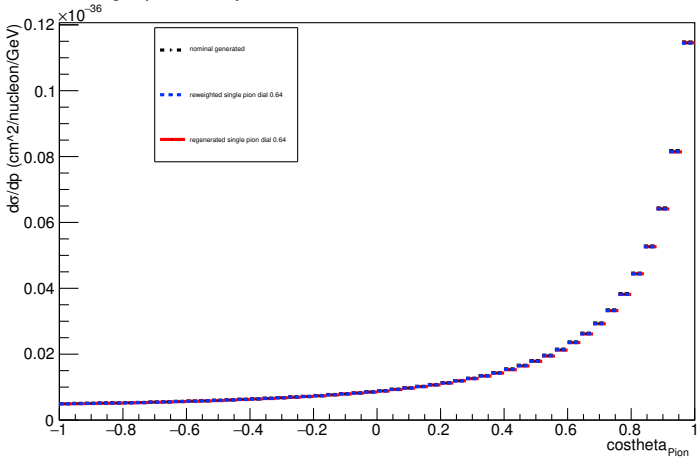

Angle plot: Leading Energy Pion: Neut Mode =AllModesCombined

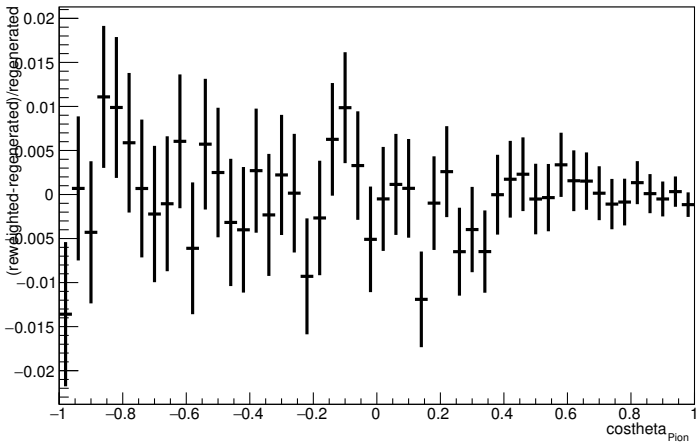

Angle plot: Every FSI Pion: Neut Mode =AllModesCombined

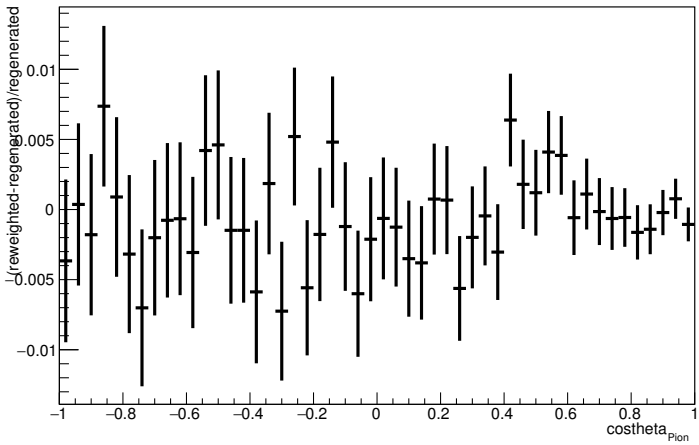

Energy plot: Leading Energy Nucleon: Neut Mode =1

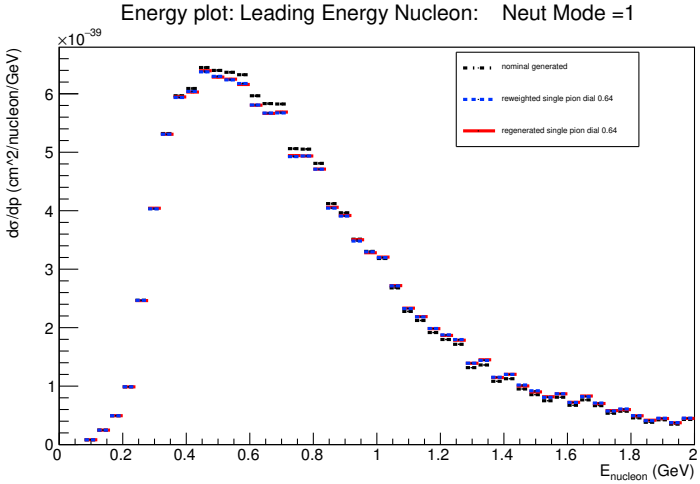

Energy plot: Every FSI Nucleon: Neut Mode =1

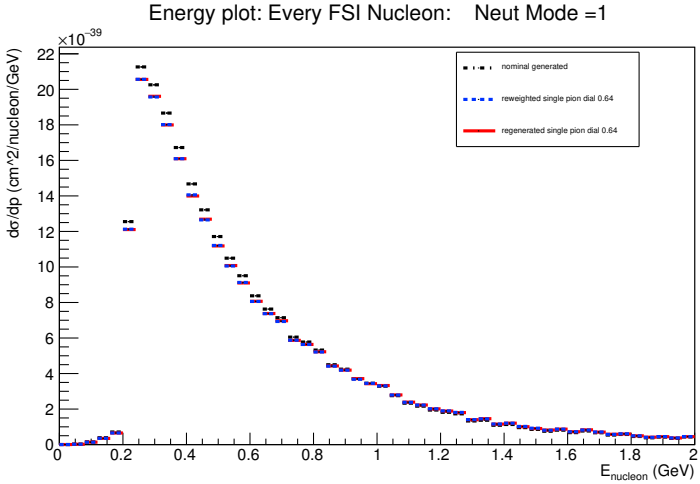

Energy plot: Leading Energy Nucleon: Neut Mode =1

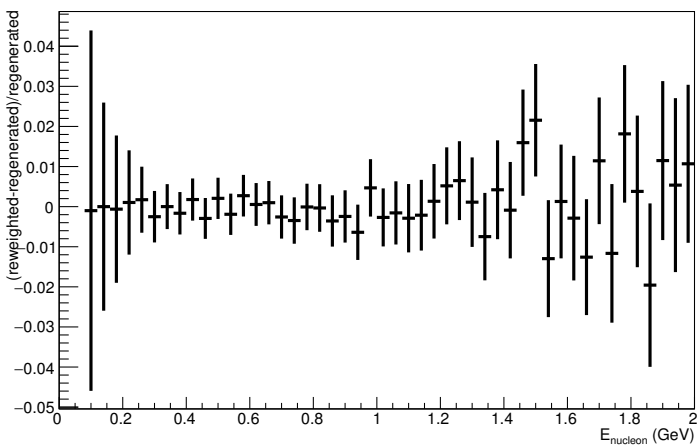

Energy plot: Every FSI Nucleon: Neut Mode =1

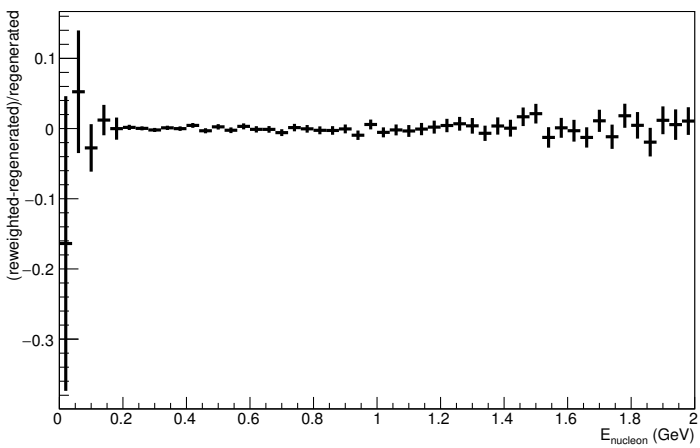

Angle plot: Leading Energy Nucleon: Neut Mode =1

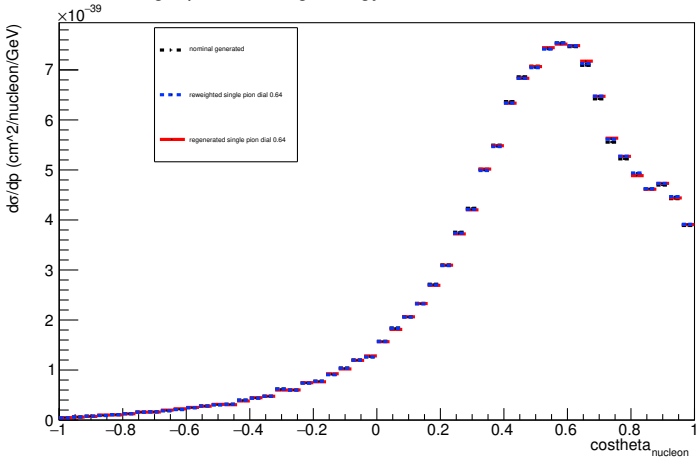

Angle plot: Every FSI Nucleon: Neut Mode =1

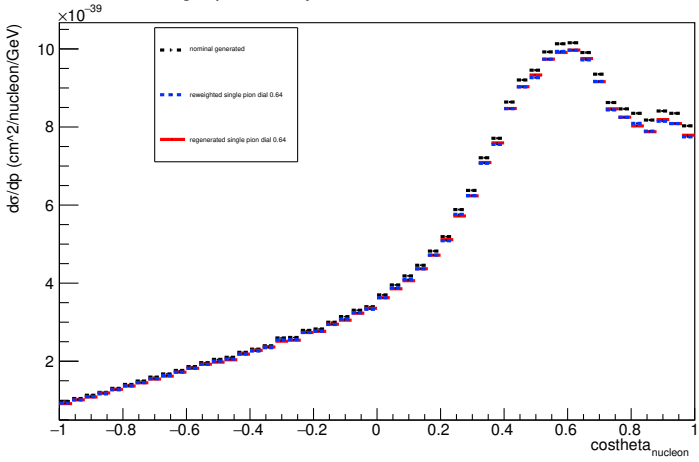

Angle plot: Leading Energy Nucleon: Neut Mode =1

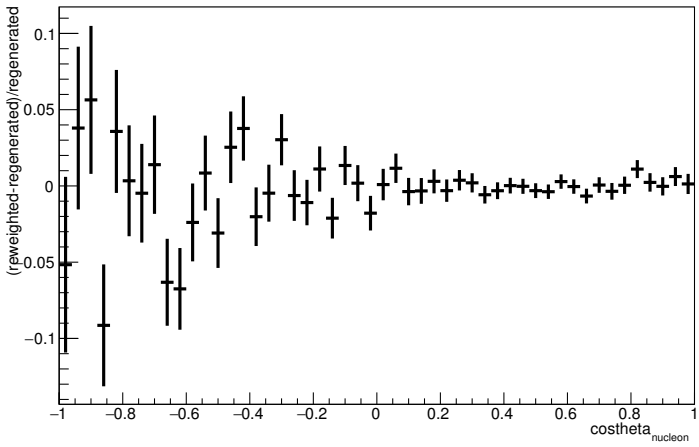

Angle plot: Every FSI Nucleon: Neut Mode =1

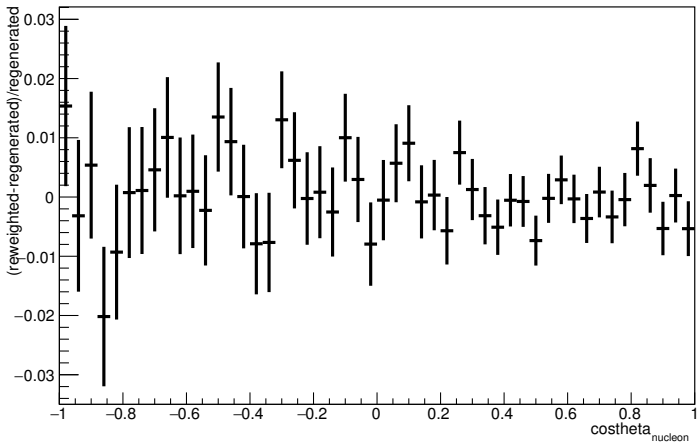

Energy plot: Leading Energy Proton: Neut Mode =1

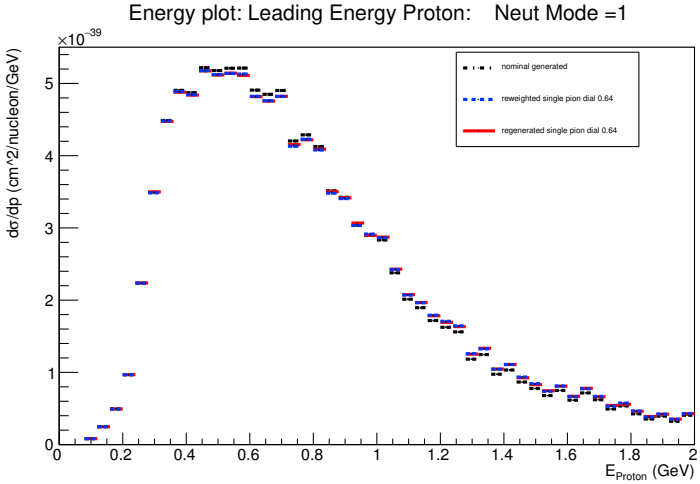

Energy plot: Every FSI Proton: Neut Mode =1

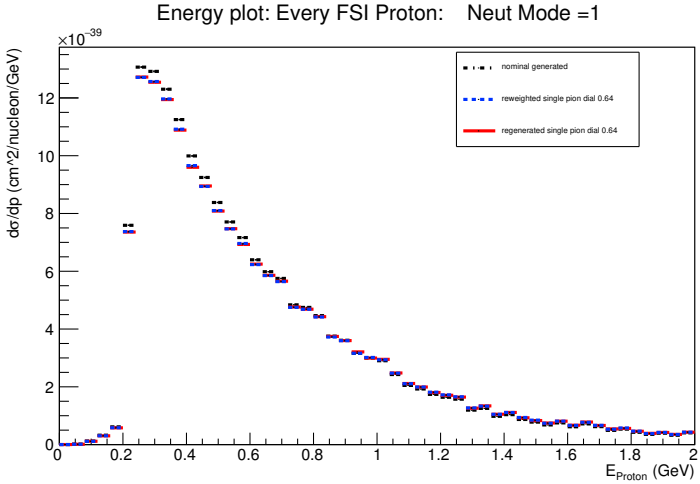

Energy plot: Leading Energy Proton: Neut Mode =1

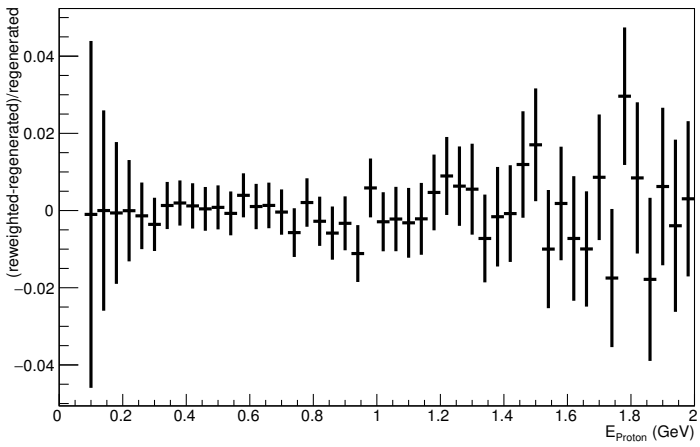

Energy plot: Every FSI Proton: Neut Mode =1

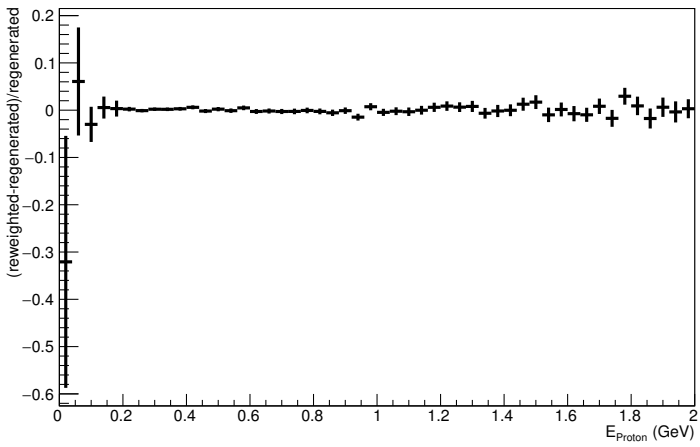

Angle plot: Leading Energy Proton: Neut Mode =1

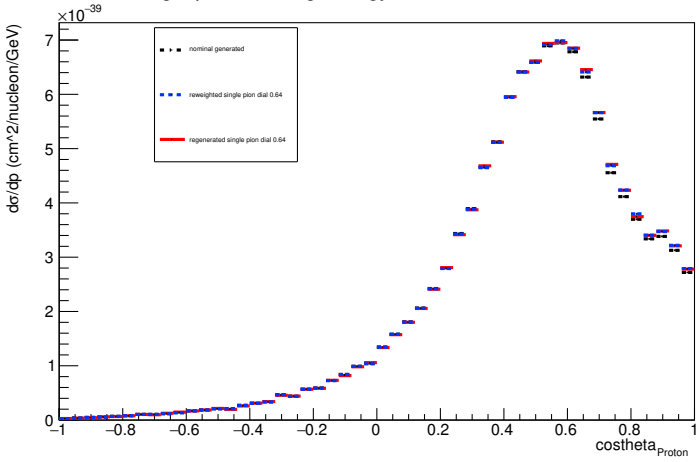

Angle plot: Every FSI Proton: Neut Mode =1

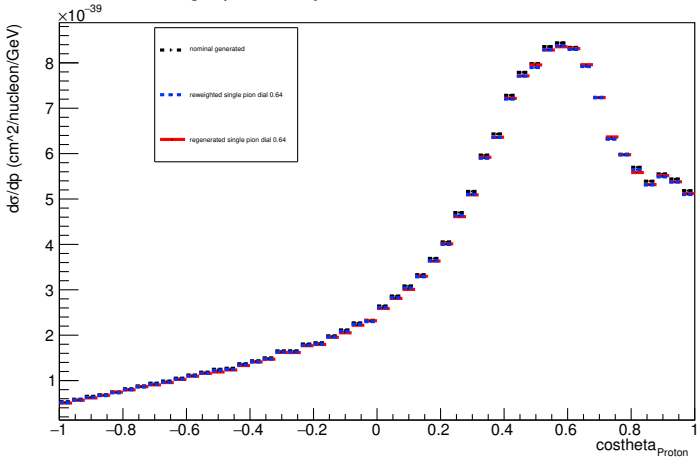

Angle plot: Leading Energy Proton: Neut Mode =1

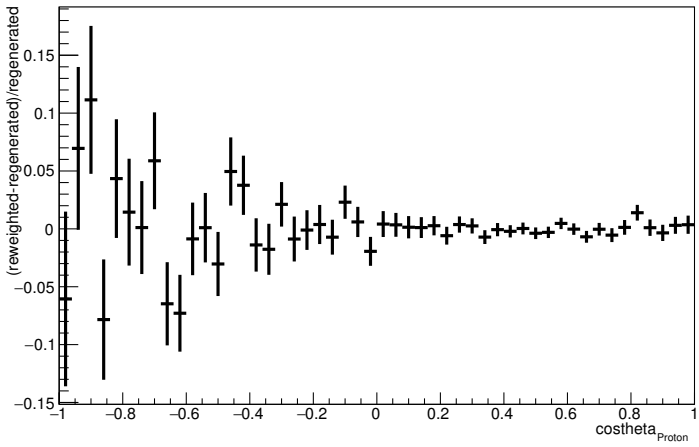

Angle plot: Every FSI Proton: Neut Mode =1

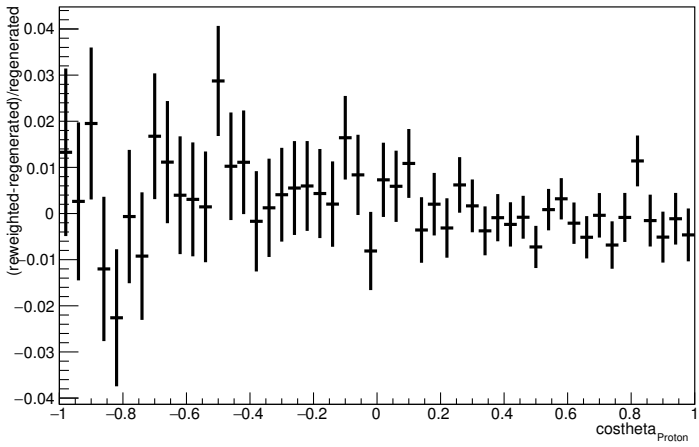

Energy plot: Leading Energy Neutron: Neut Mode =1

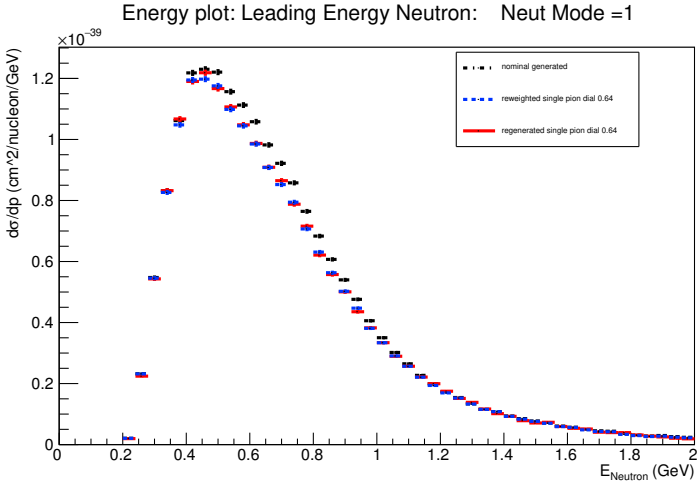

Energy plot: Every FSI Neutron: Neut Mode =1

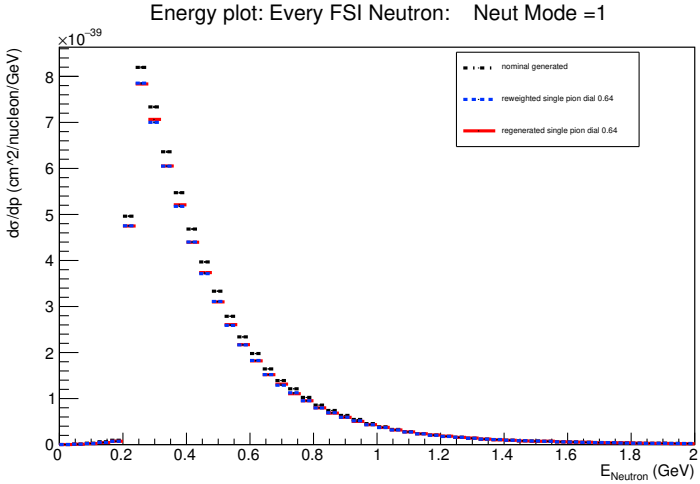

Energy plot: Leading Energy Neutron: Neut Mode =1

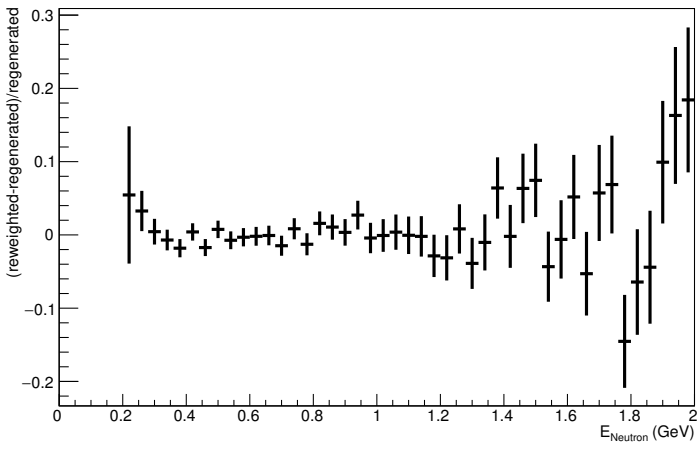

Energy plot: Every FSI Neutron: Neut Mode =1

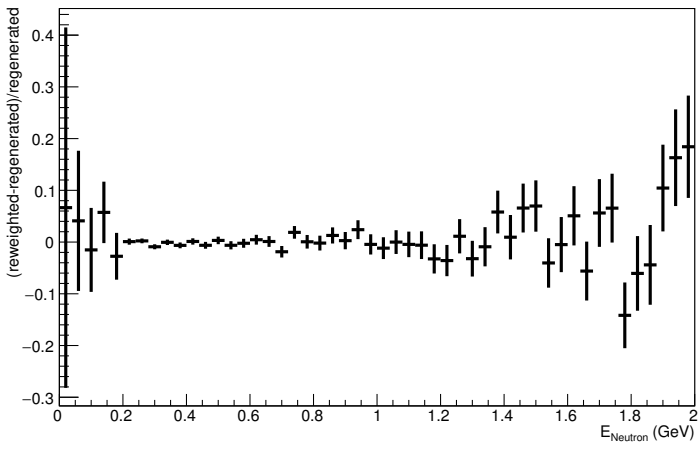

Angle plot: Leading Energy Neutron: Neut Mode =1

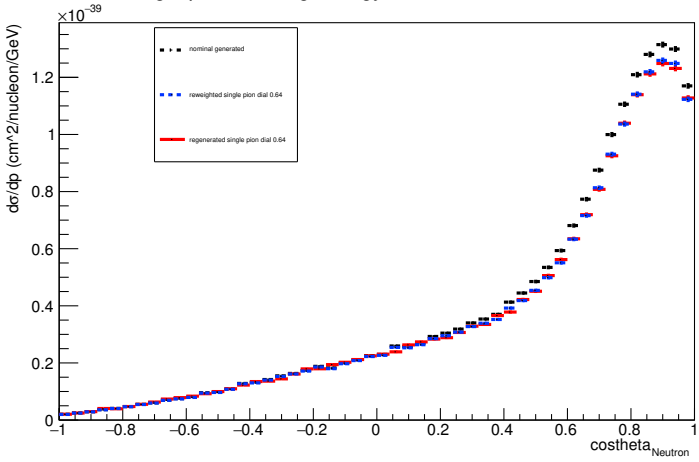

Angle plot: Every FSI Neutron: Neut Mode =1

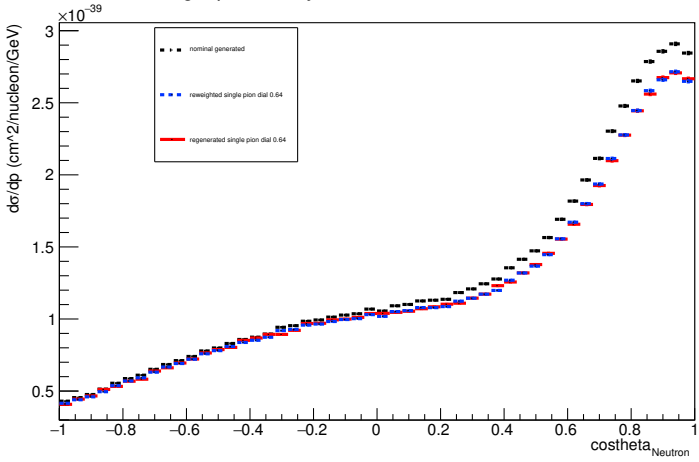

Angle plot: Leading Energy Neutron: Neut Mode =1

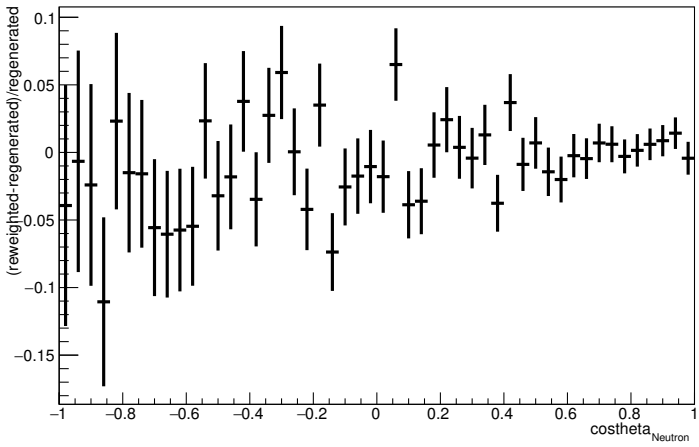

Angle plot: Every FSI Neutron: Neut Mode =1

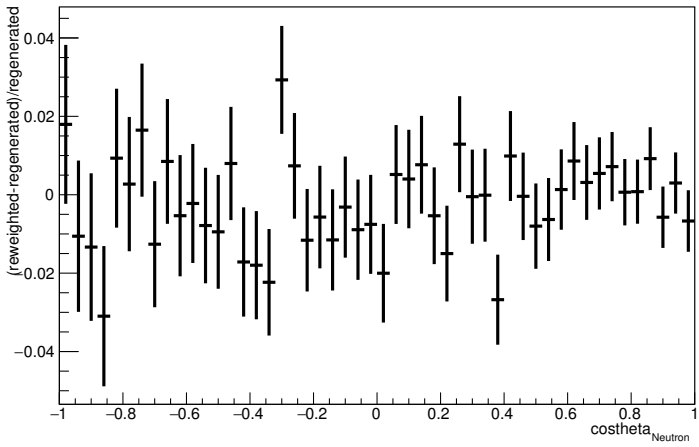

Energy plot: Leading Energy Lepton: Neut Mode =1

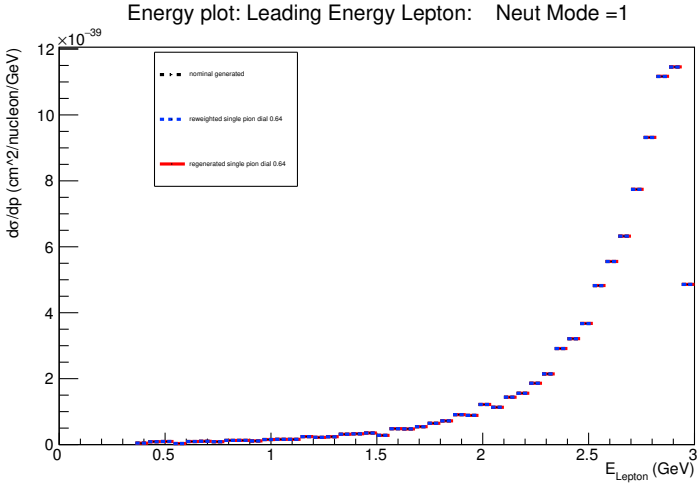

Angle plot: Leading Energy Lepton: Neut Mode =1

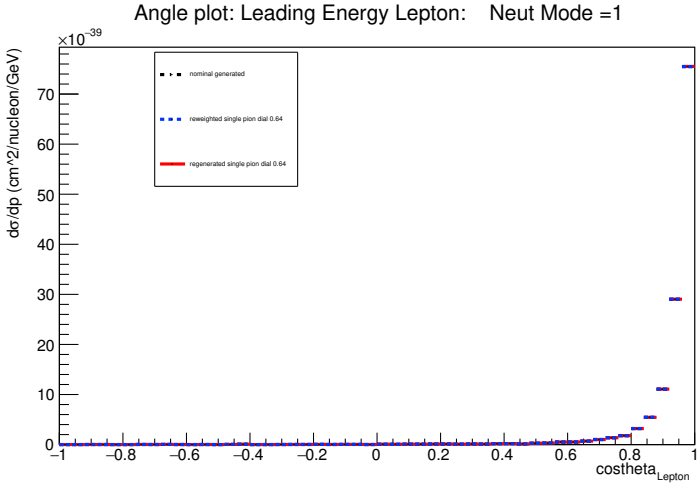

Energy plot: Leading Energy Lepton: Neut Mode =1

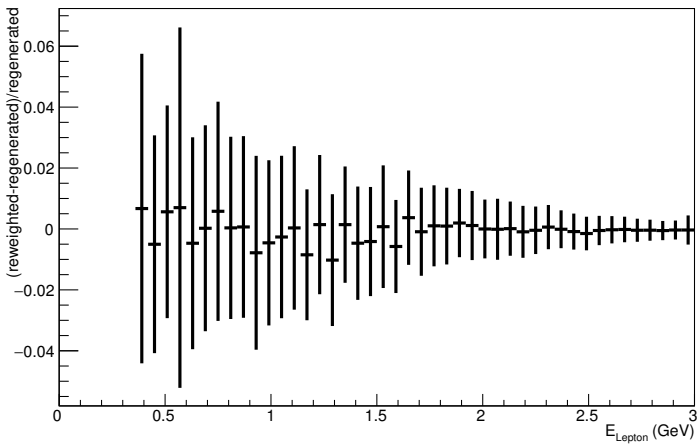

Angle plot: Leading Energy Lepton: Neut Mode =1

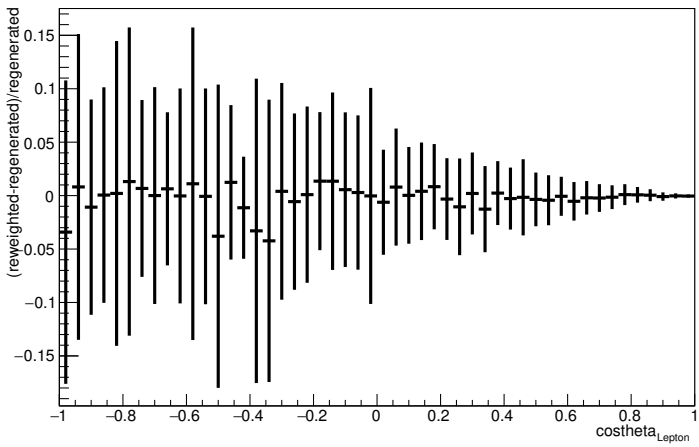

Energy plot: Leading Energy Pion: Neut Mode =1

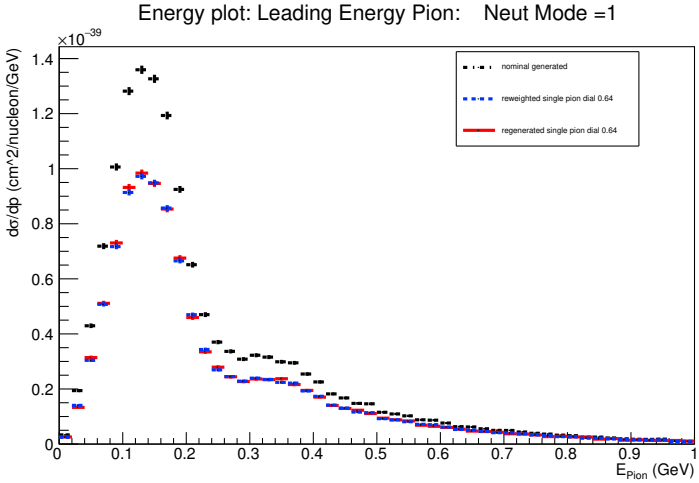

Energy plot: Every FSI Pion: Neut Mode =1

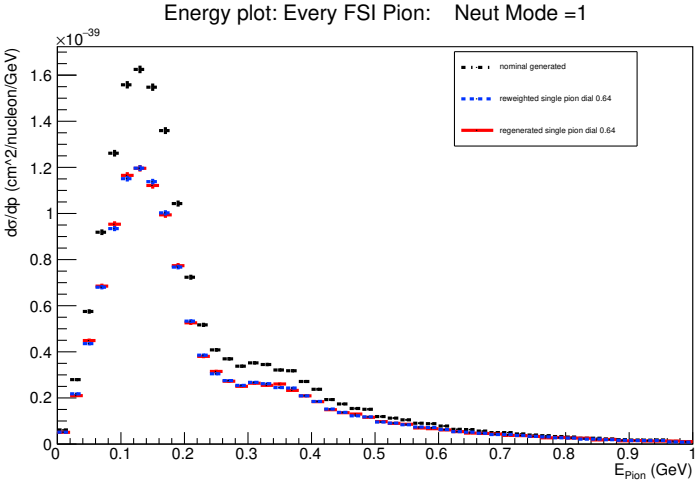

Energy plot: Leading Energy Pion: Neut Mode =1

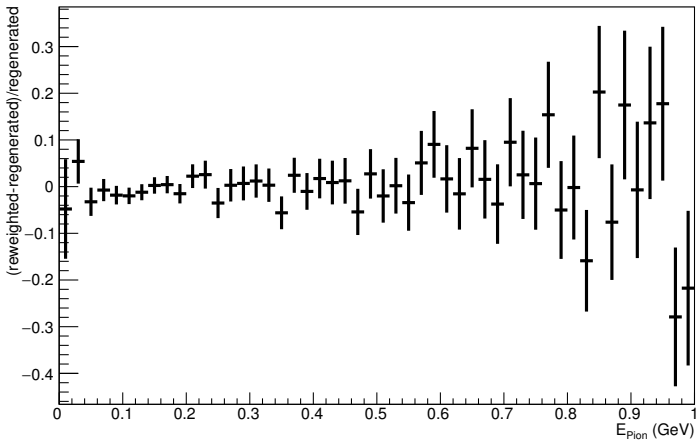

Energy plot: Every FSI Pion: Neut Mode =1

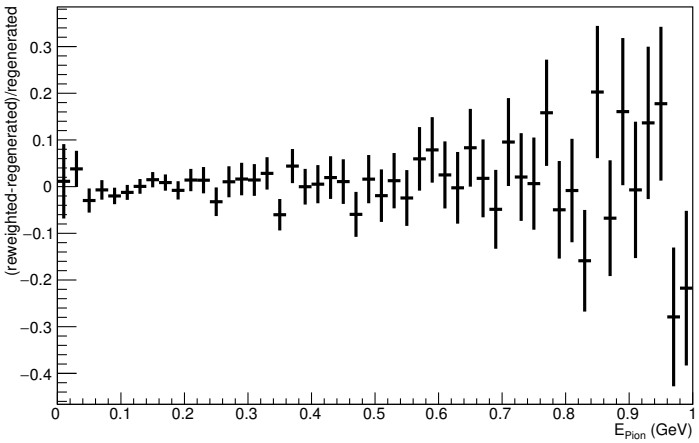

Angle plot: Leading Energy Pion: Neut Mode =1

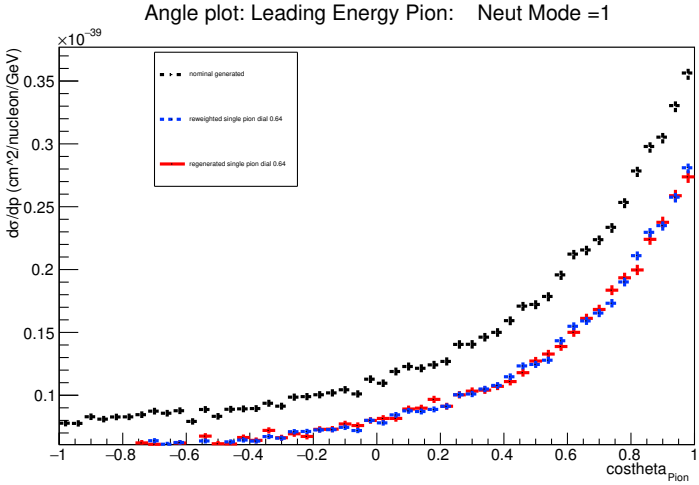

Angle plot: Every FSI Pion: Neut Mode =1

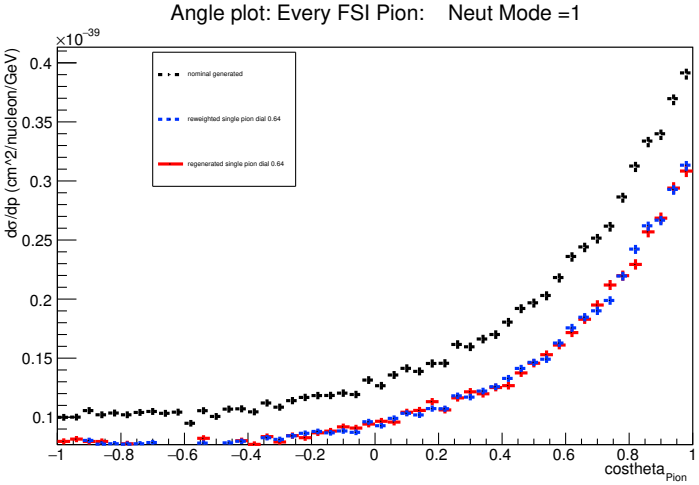

Angle plot: Leading Energy Pion: Neut Mode =1

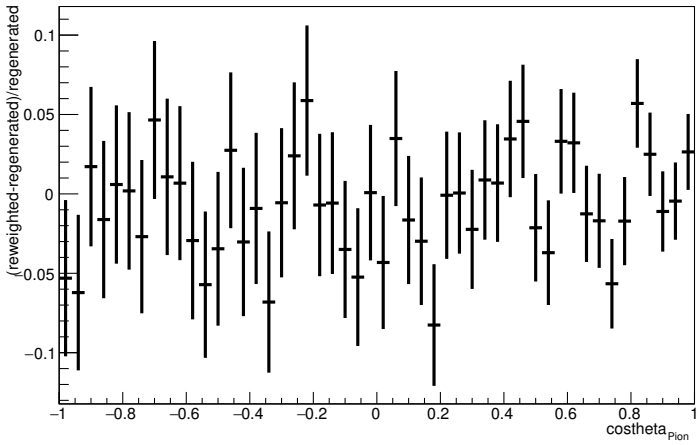

Angle plot: Every FSI Pion: Neut Mode =1

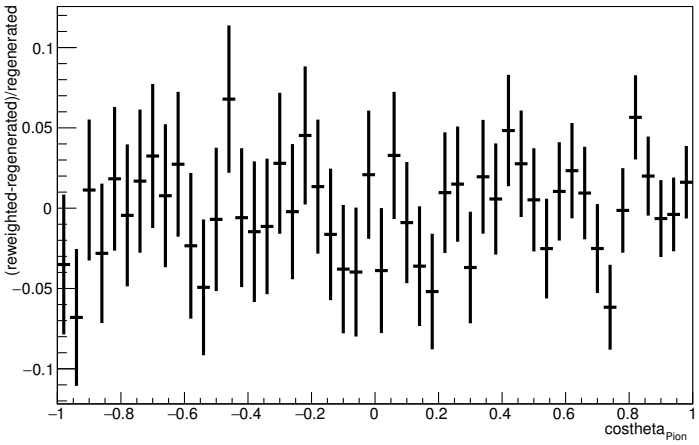

Energy plot: Leading Energy Nucleon: Neut Mode =2

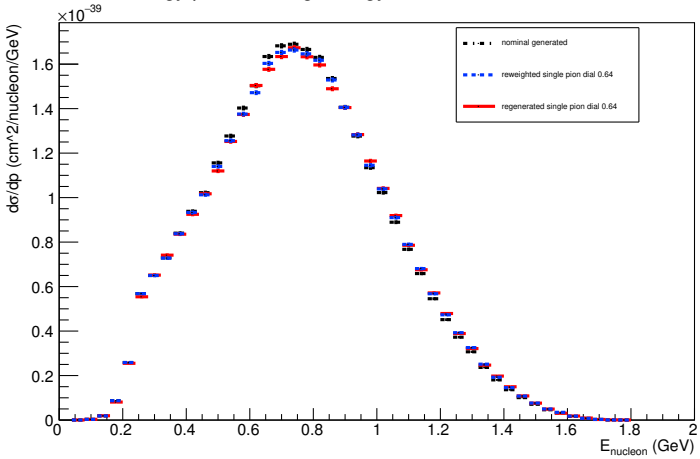

Energy plot: Every FSI Nucleon: Neut Mode =2

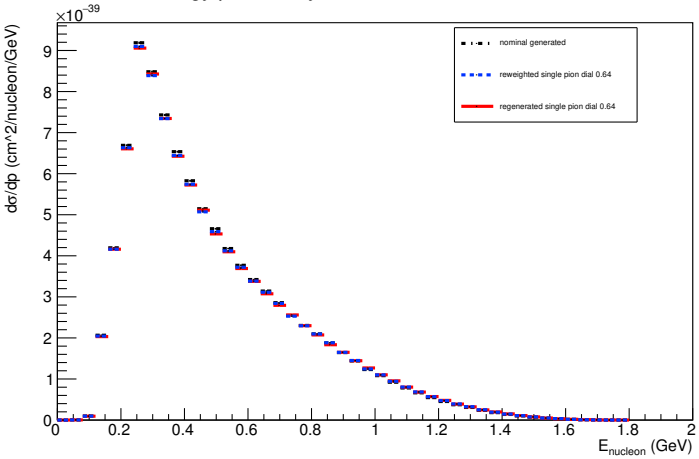

Energy plot: Leading Energy Nucleon: Neut Mode =2

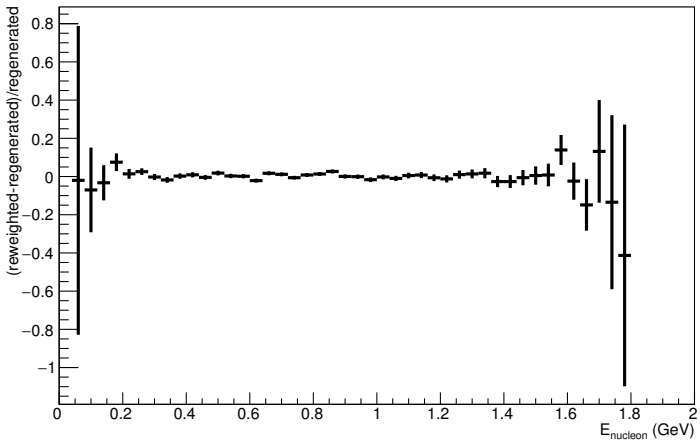

Energy plot: Every FSI Nucleon: Neut Mode =2

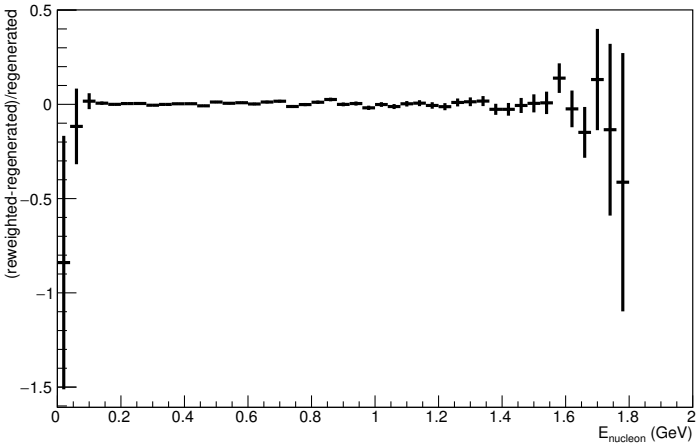

Angle plot: Leading Energy Nucleon: Neut Mode =2

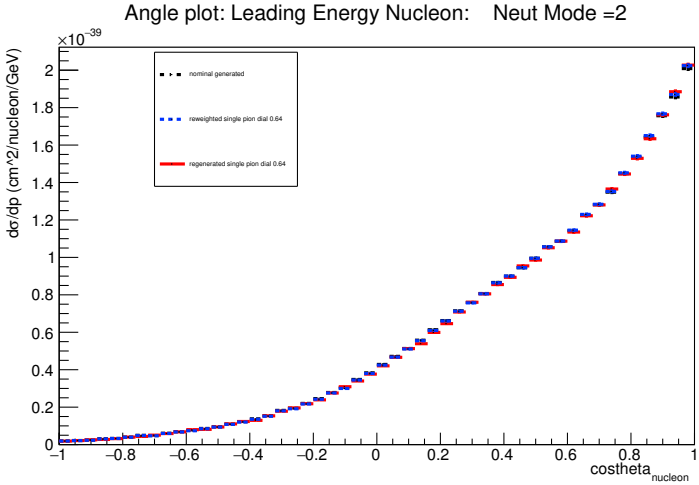

Angle plot: Every FSI Nucleon: Neut Mode =2

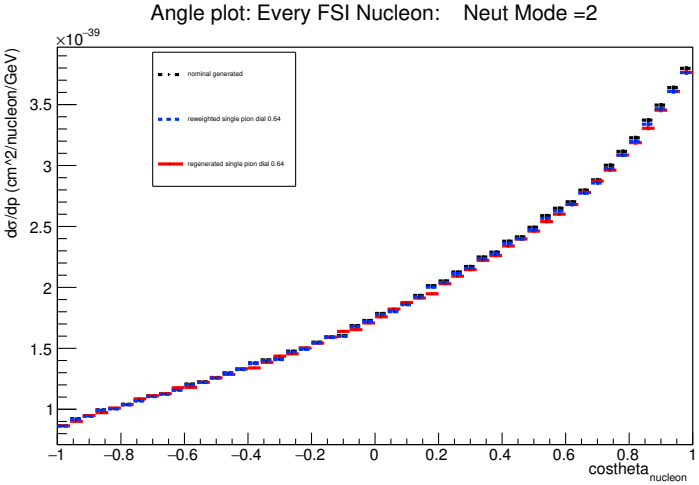

Angle plot: Leading Energy Nucleon: Neut Mode =2

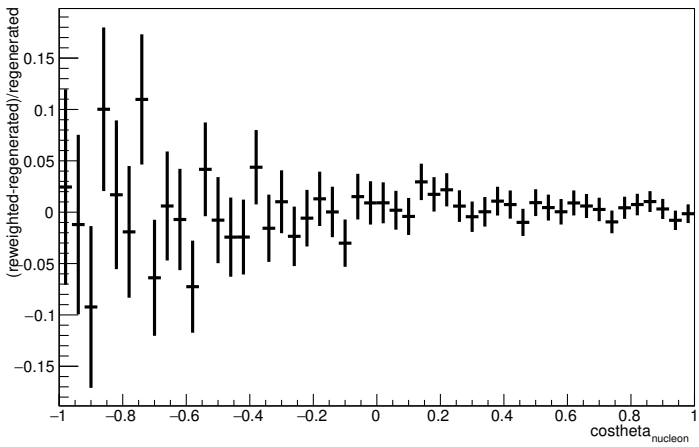

Angle plot: Every FSI Nucleon: Neut Mode =2

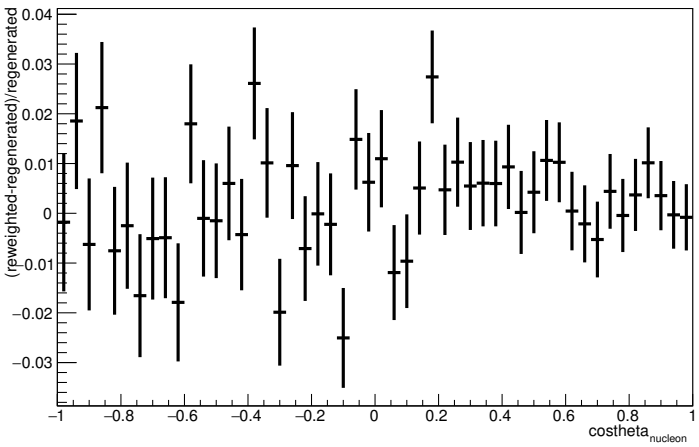

Energy plot: Leading Energy Proton: Neut Mode =2

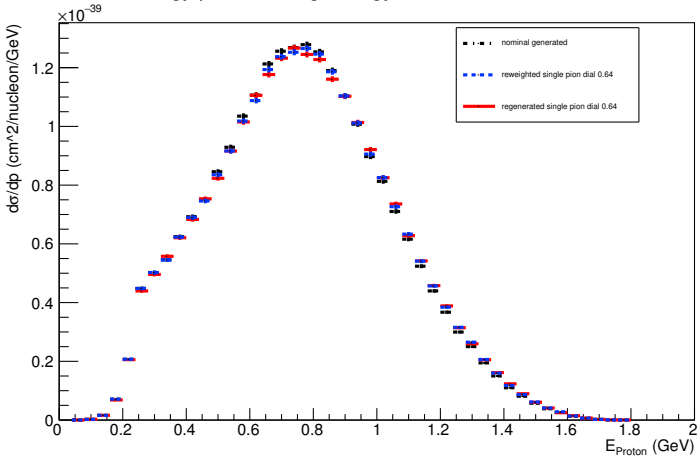

Energy plot: Every FSI Proton: Neut Mode =2

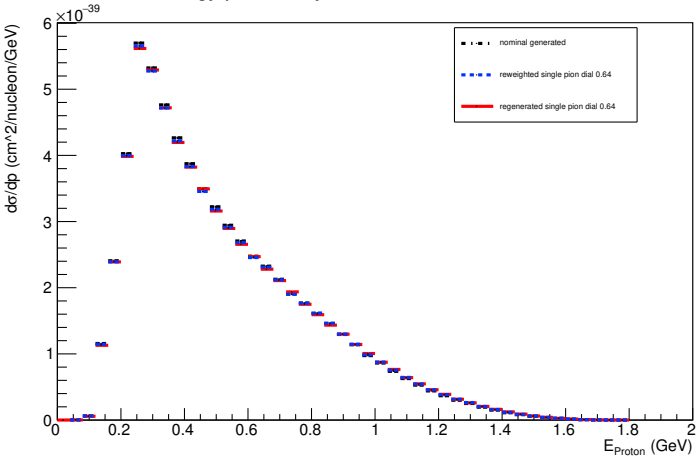

Energy plot: Leading Energy Proton: Neut Mode =2

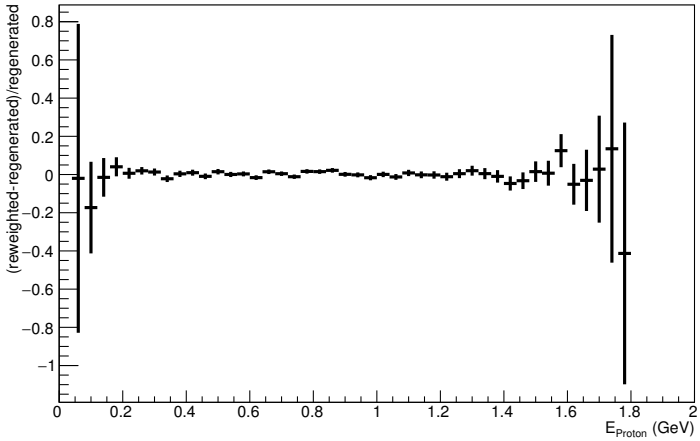

Energy plot: Every FSI Proton: Neut Mode =2

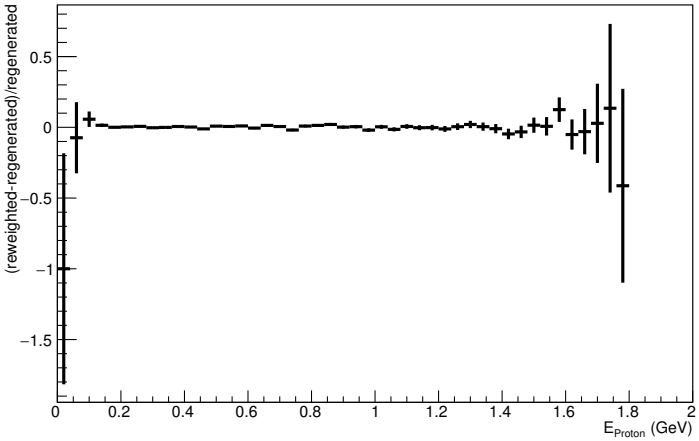

Angle plot: Leading Energy Proton: Neut Mode =2

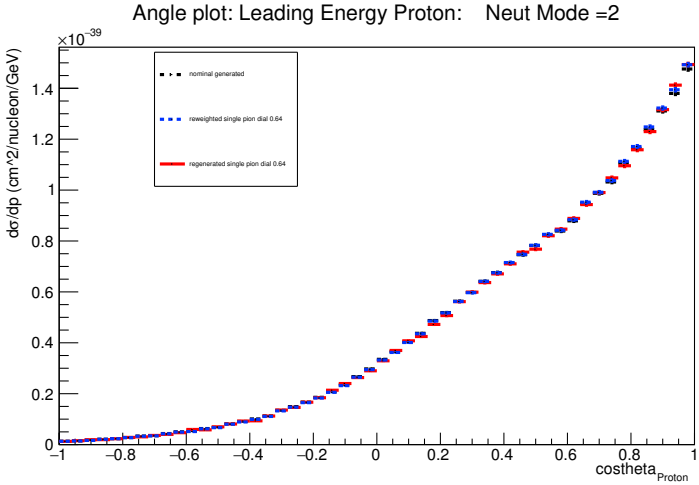

Angle plot: Every FSI Proton: Neut Mode =2

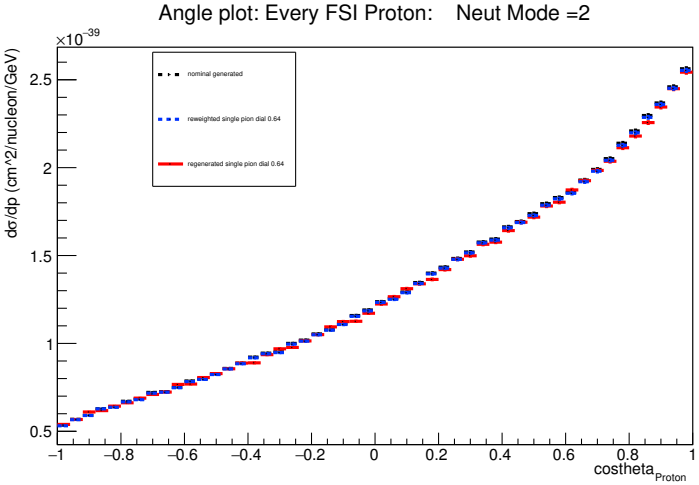

Angle plot: Leading Energy Proton: Neut Mode =2

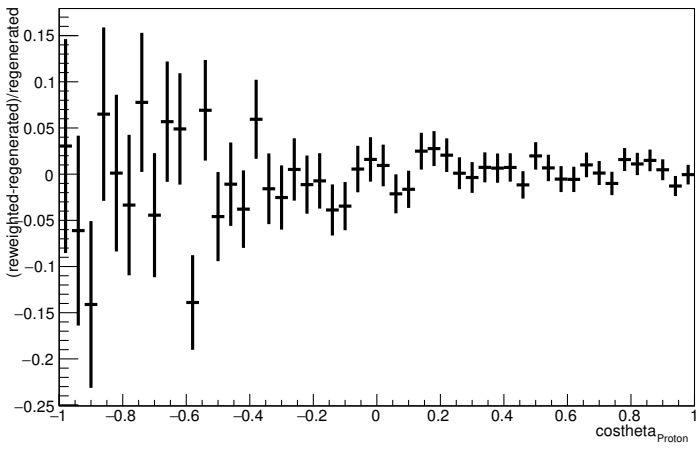

Angle plot: Every FSI Proton: Neut Mode =2

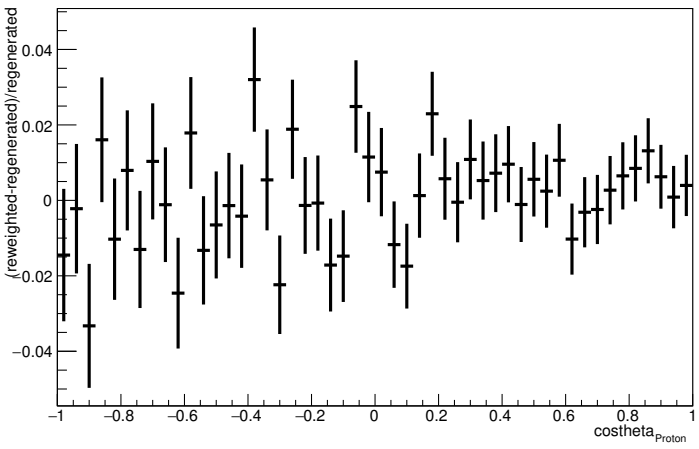

Energy plot: Leading Energy Neutron: Neut Mode =2

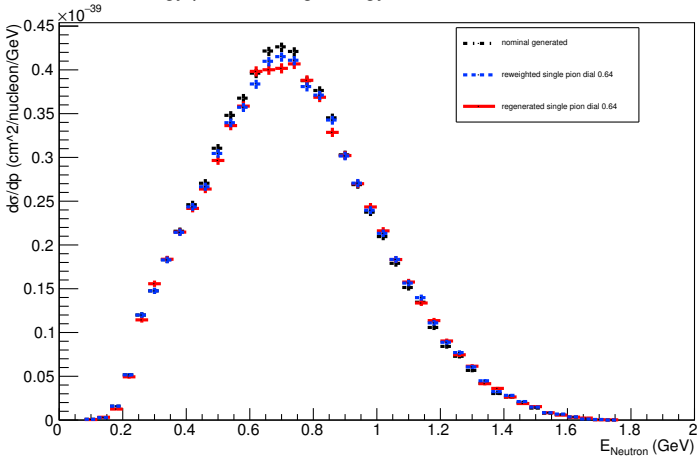

Energy plot: Every FSI Neutron: Neut Mode =2

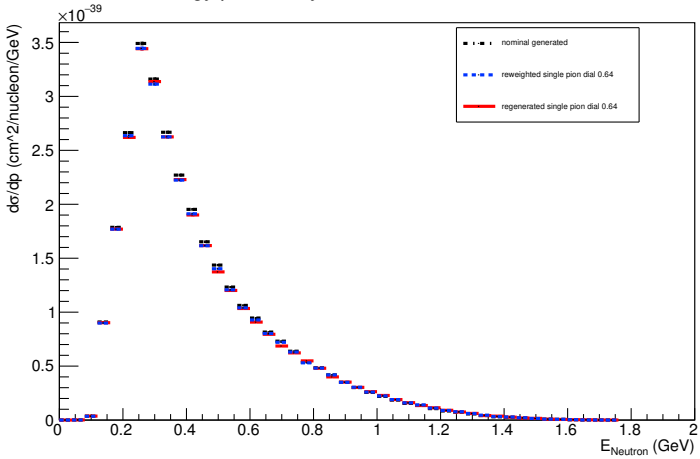

Energy plot: Leading Energy Neutron: Neut Mode =2

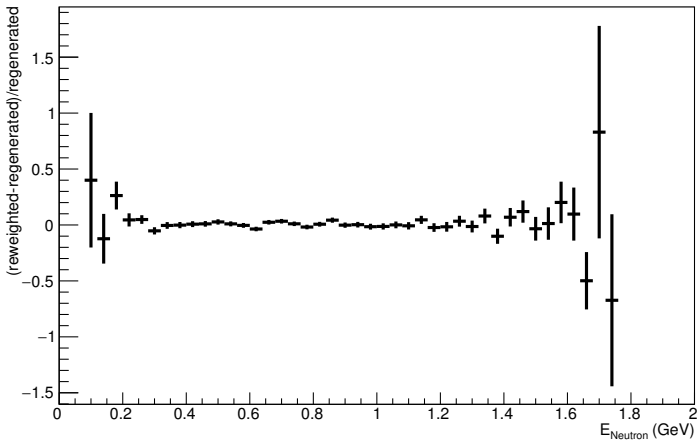

Energy plot: Every FSI Neutron: Neut Mode =2

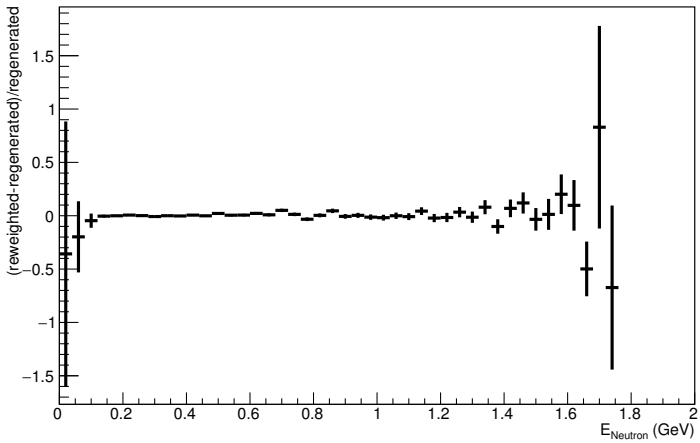

Angle plot: Leading Energy Neutron: Neut Mode =2

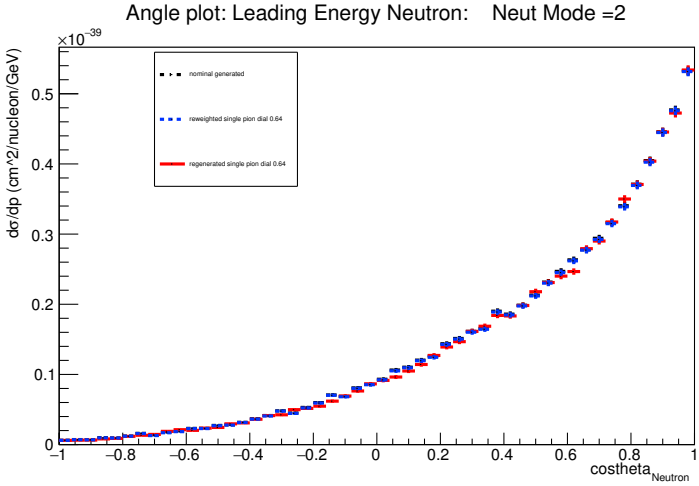

Angle plot: Every FSI Neutron: Neut Mode =2

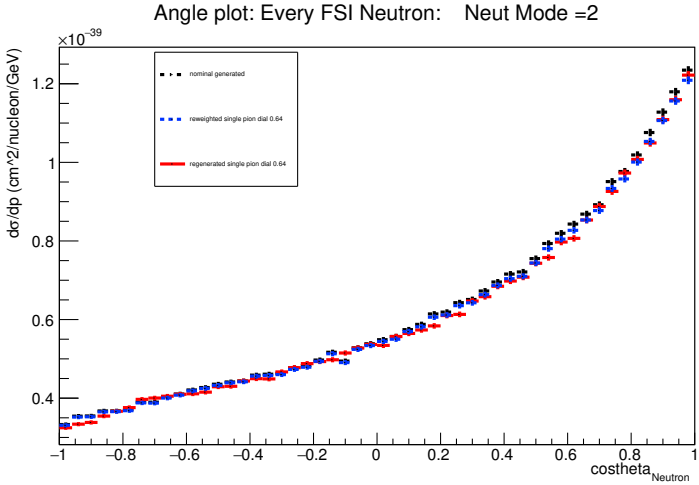

Angle plot: Leading Energy Neutron: Neut Mode =2

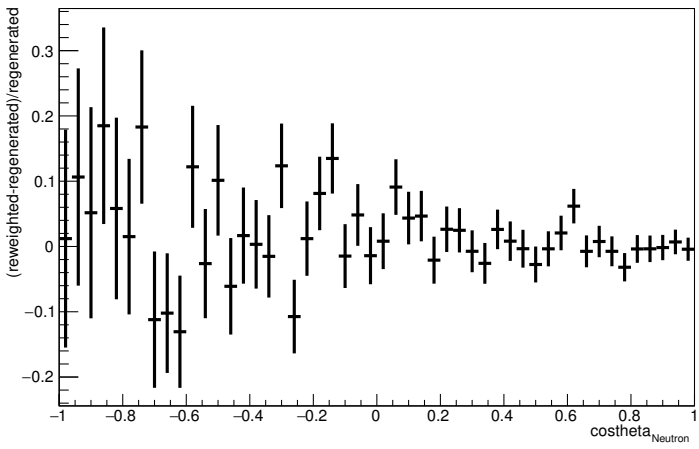

Angle plot: Every FSI Neutron: Neut Mode =2

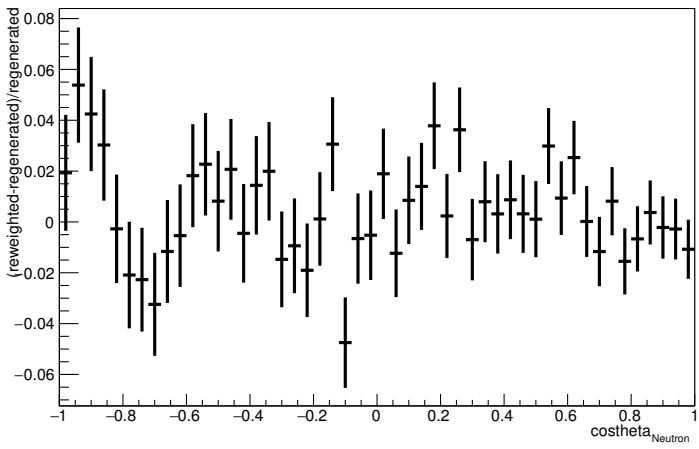

Energy plot: Leading Energy Lepton: Neut Mode =2

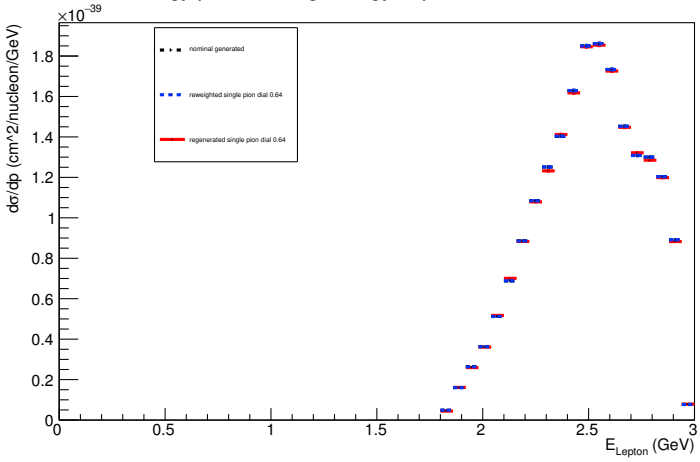

Angle plot: Leading Energy Lepton: Neut Mode =2

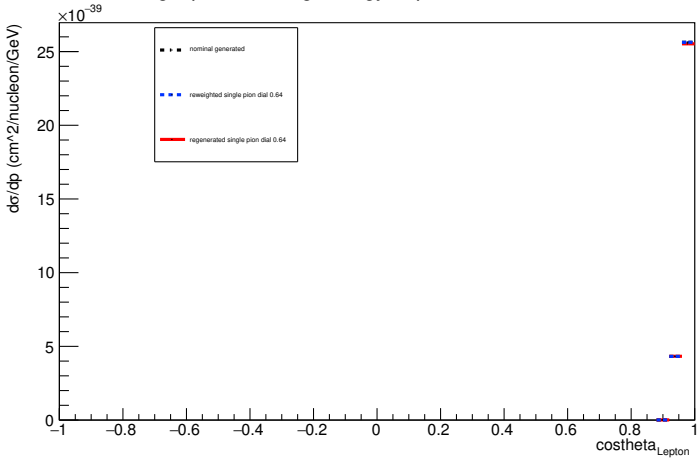

Energy plot: Leading Energy Lepton: Neut Mode =2

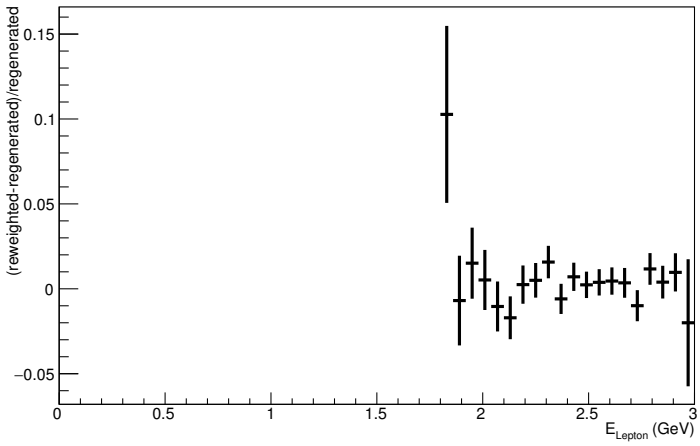

Angle plot: Leading Energy Lepton: Neut Mode =2

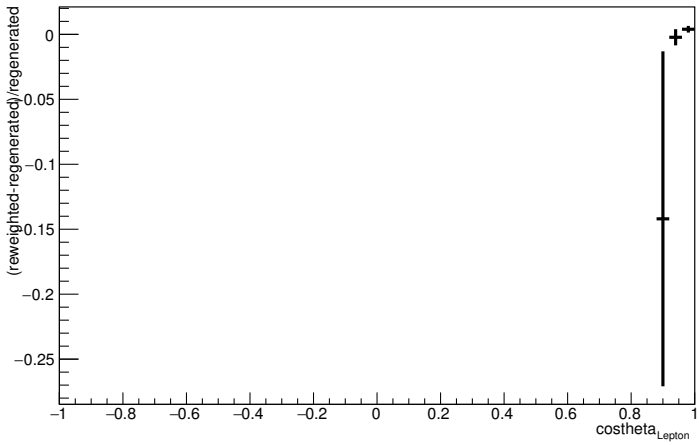

Energy plot: Leading Energy Pion: Neut Mode =2

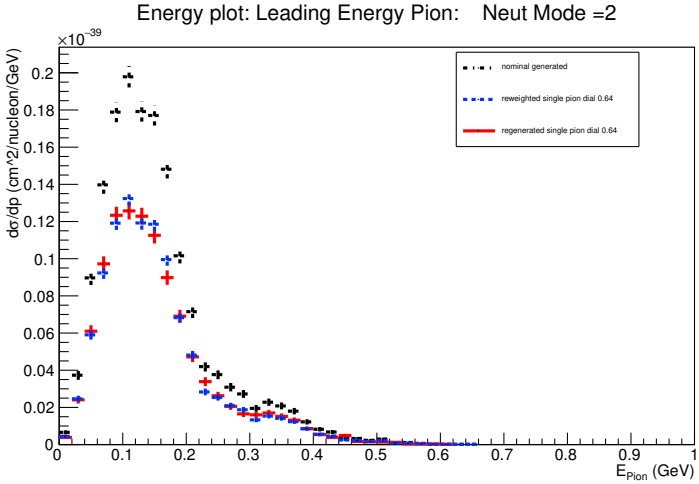

Energy plot: Every FSI Pion: Neut Mode =2

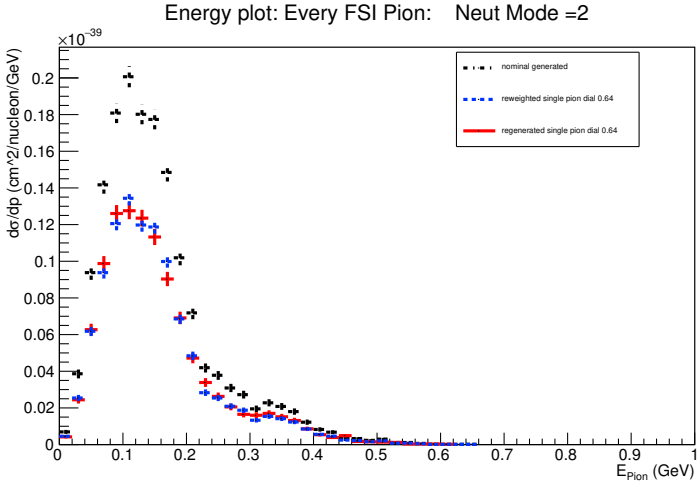

Energy plot: Leading Energy Pion: Neut Mode =2

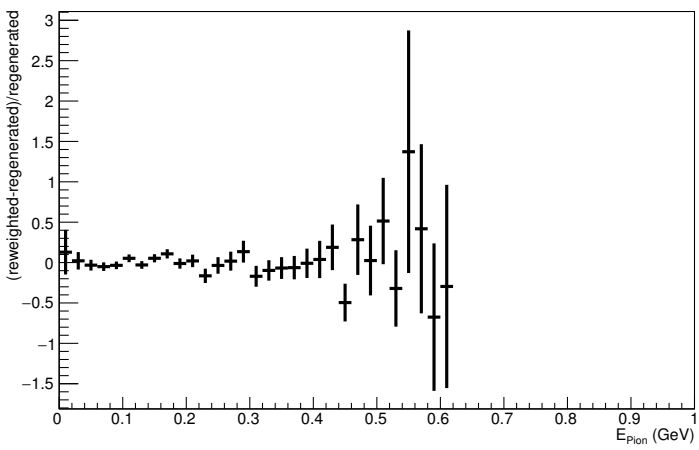

Energy plot: Every FSI Pion: Neut Mode =2

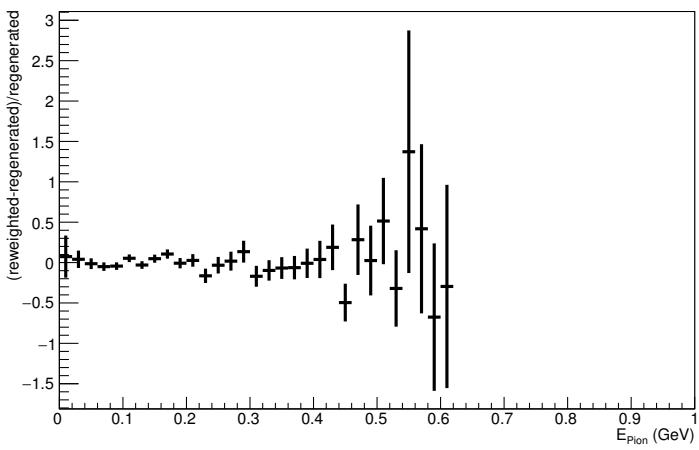

Angle plot: Leading Energy Pion: Neut Mode =2

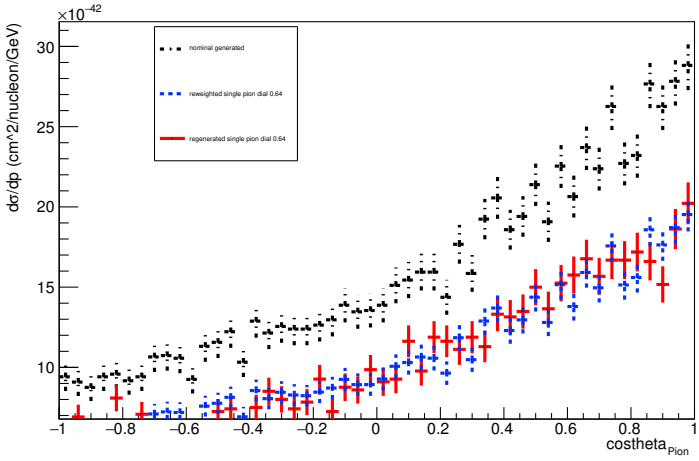

Angle plot: Every FSI Pion: Neut Mode =2

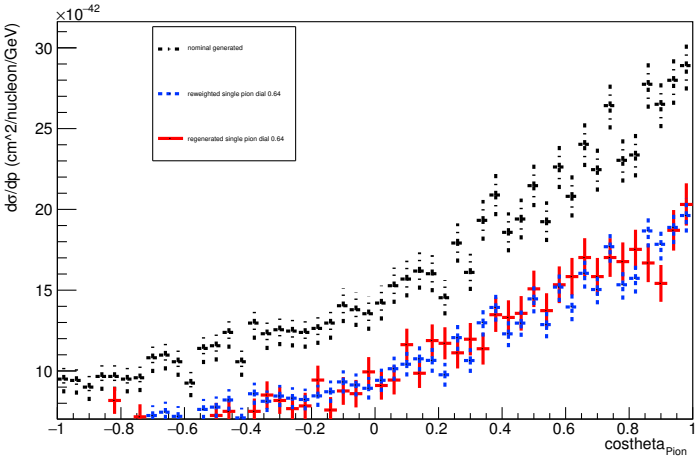

Angle plot: Leading Energy Pion: Neut Mode =2

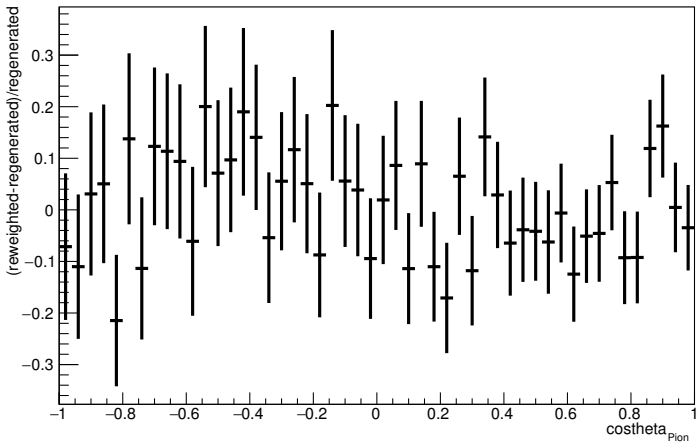

Angle plot: Every FSI Pion: Neut Mode =2

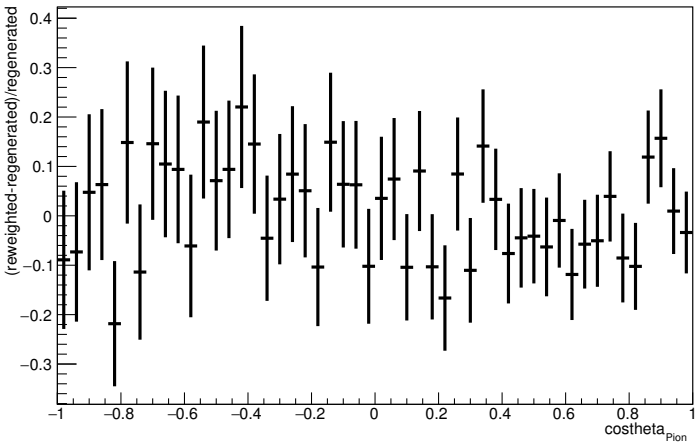

Energy plot: Leading Energy Nucleon: Neut Mode =11

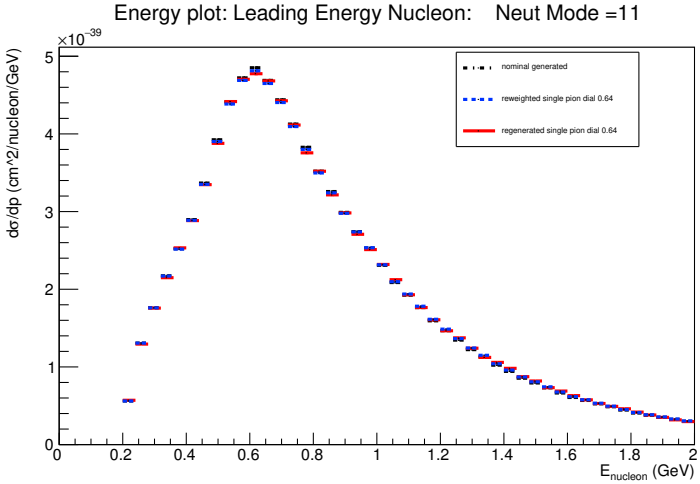

Energy plot: Every FSI Nucleon: Neut Mode =11

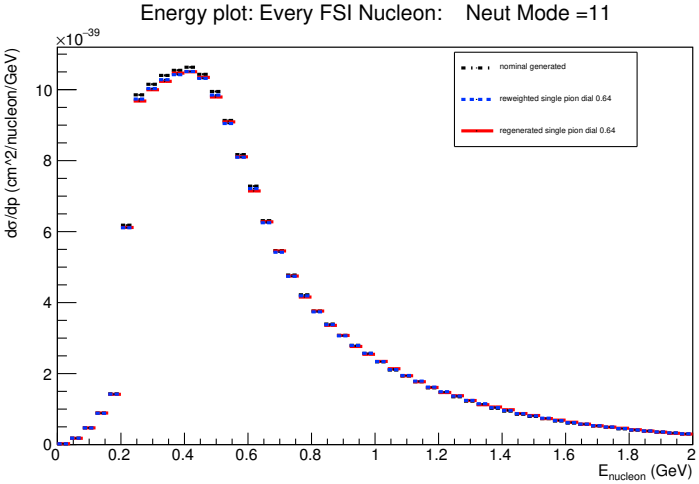

Energy plot: Leading Energy Nucleon: Neut Mode =11

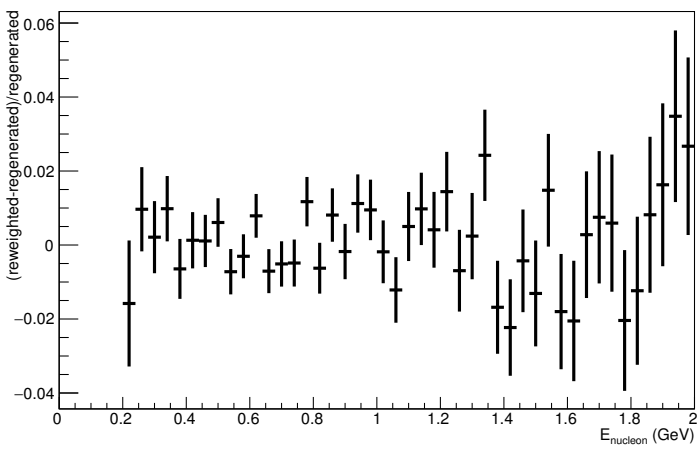

Energy plot: Every FSI Nucleon: Neut Mode =11

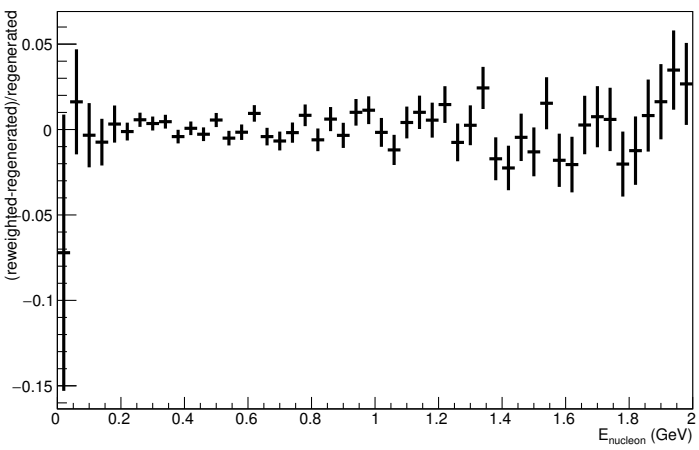

Angle plot: Leading Energy Nucleon: Neut Mode =11

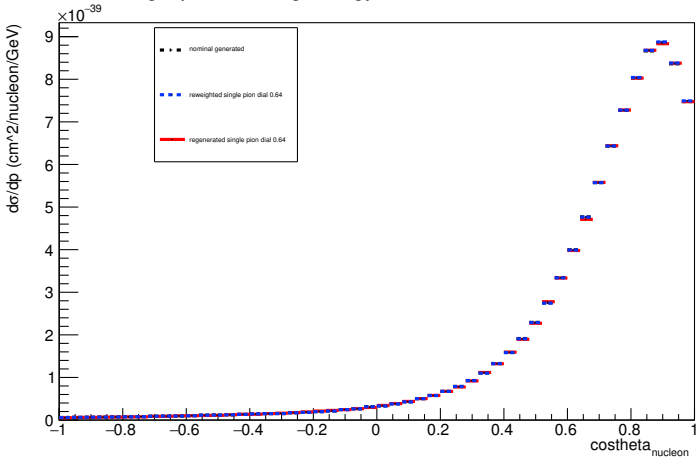

Angle plot: Every FSI Nucleon: Neut Mode =11

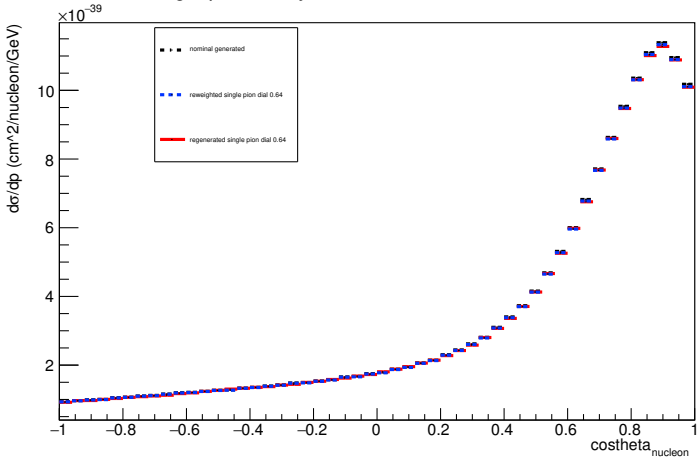

Angle plot: Leading Energy Nucleon: Neut Mode =11

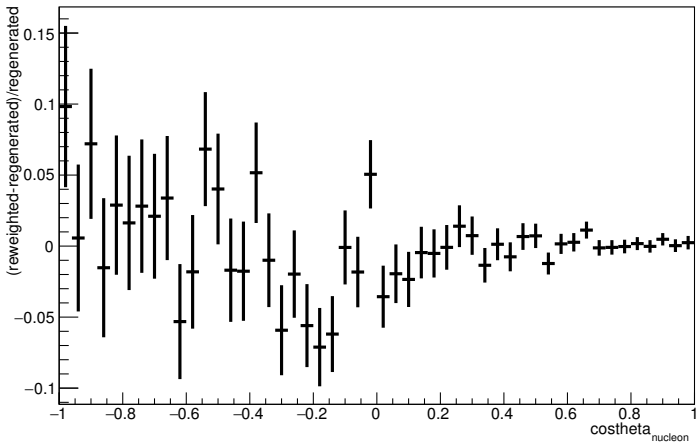

Angle plot: Every FSI Nucleon: Neut Mode =11

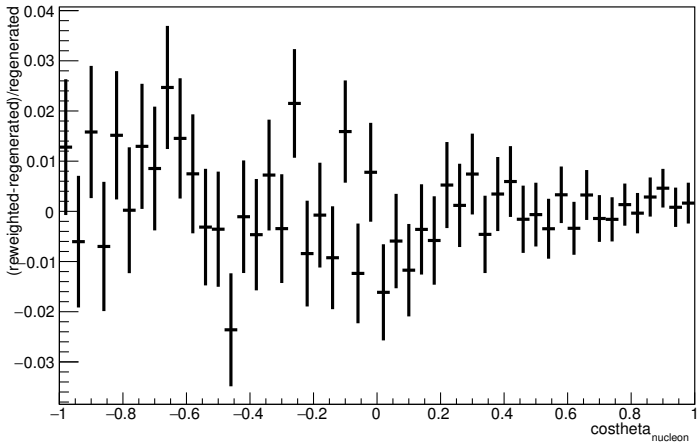

Energy plot: Leading Energy Proton: Neut Mode =11

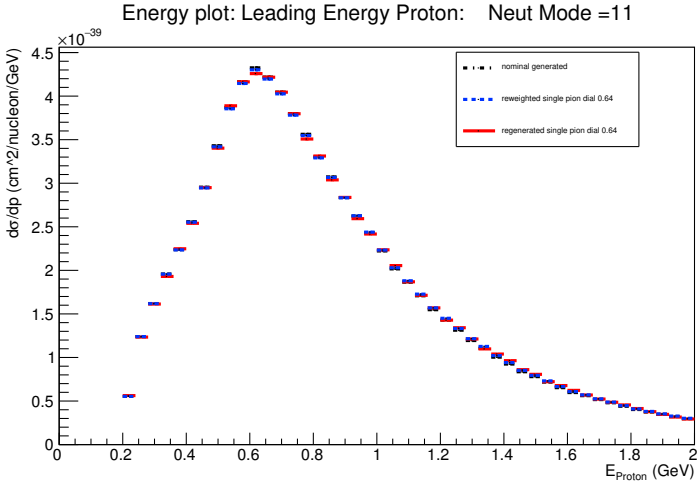

Energy plot: Every FSI Proton: Neut Mode =11

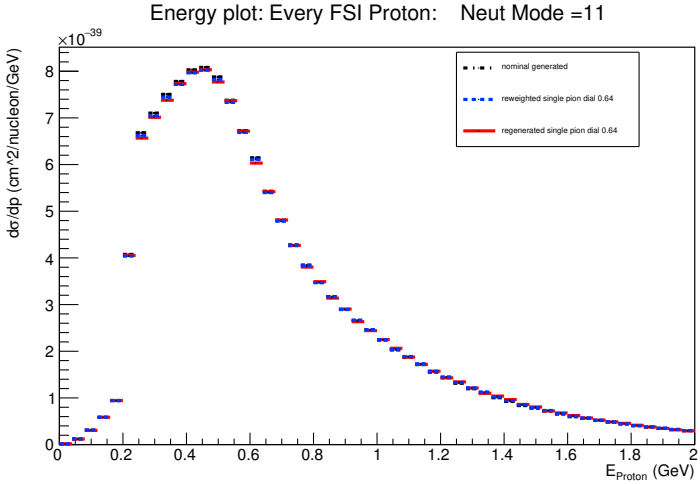

Energy plot: Leading Energy Proton: Neut Mode =11

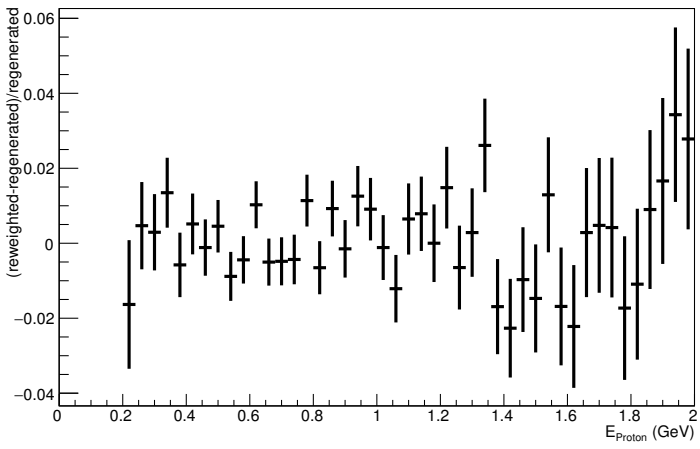

Energy plot: Every FSI Proton: Neut Mode =11

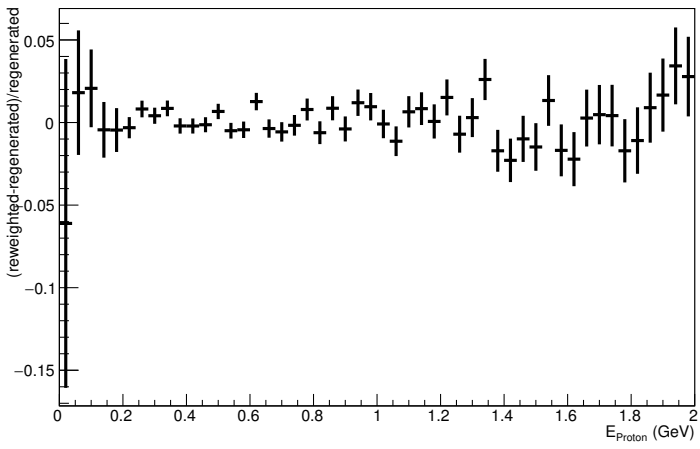

Angle plot: Leading Energy Proton: Neut Mode =11

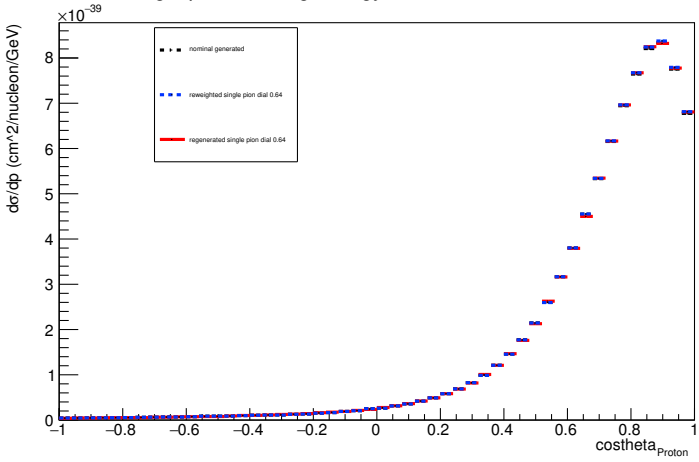

Angle plot: Every FSI Proton: Neut Mode =11

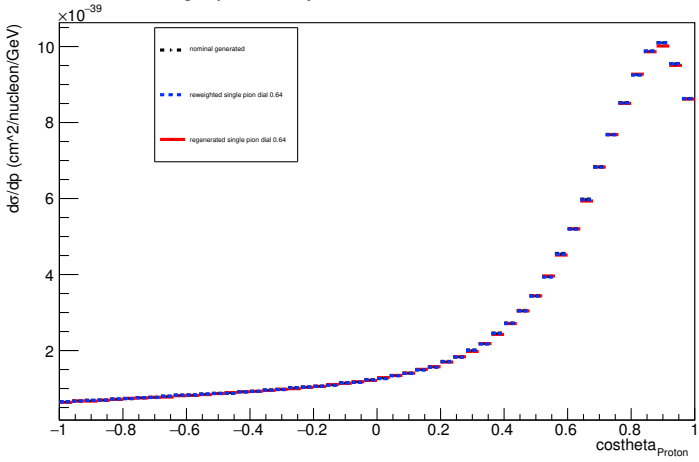

Angle plot: Leading Energy Proton: Neut Mode =11

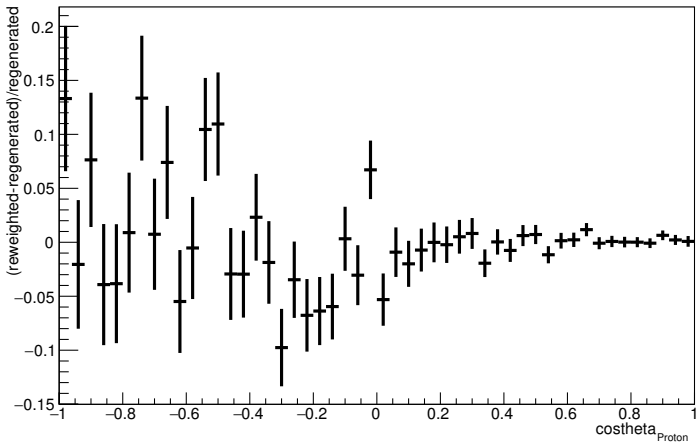

Angle plot: Every FSI Proton: Neut Mode =11

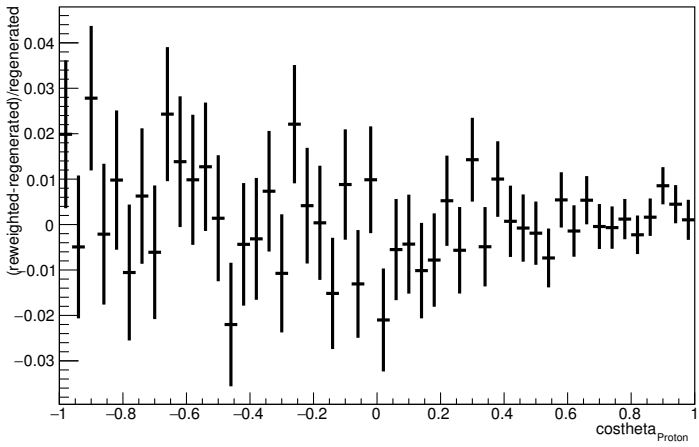

Energy plot: Leading Energy Neutron: Neut Mode =11

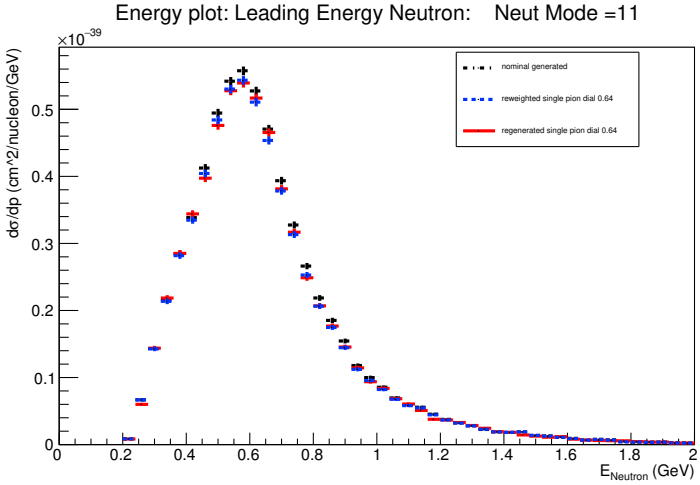

Energy plot: Every FSI Neutron: Neut Mode =11

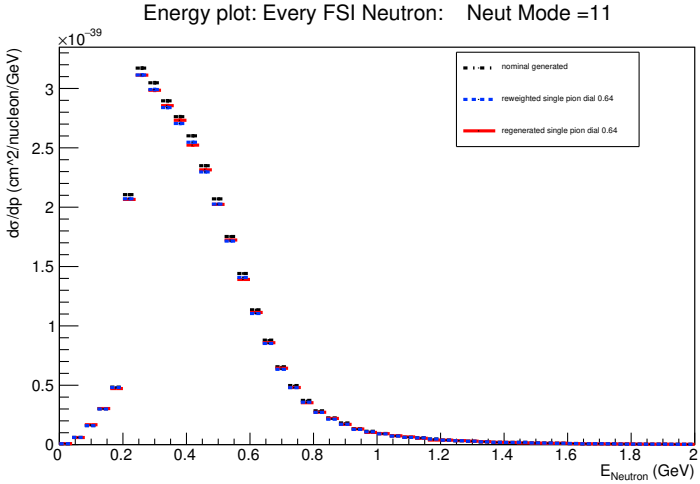

Energy plot: Leading Energy Neutron: Neut Mode =11

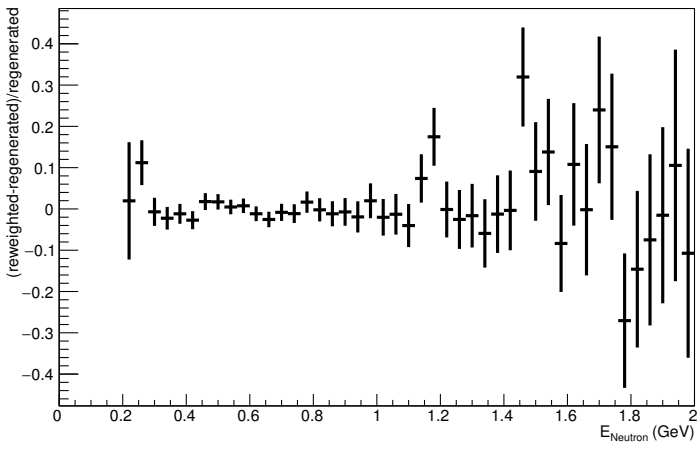

Energy plot: Every FSI Neutron: Neut Mode =11

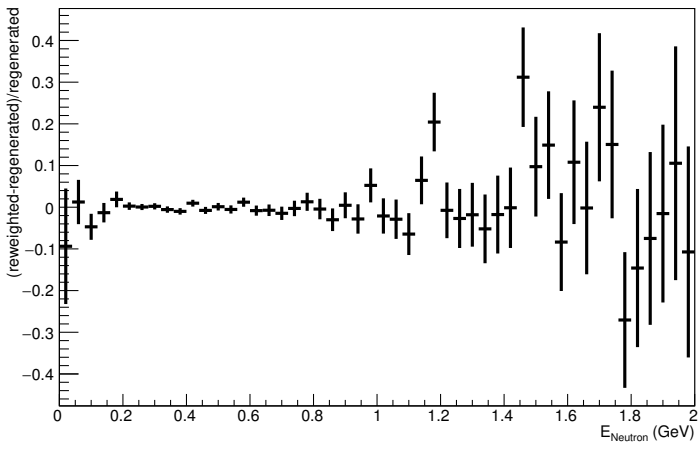

Angle plot: Leading Energy Neutron: Neut Mode =11

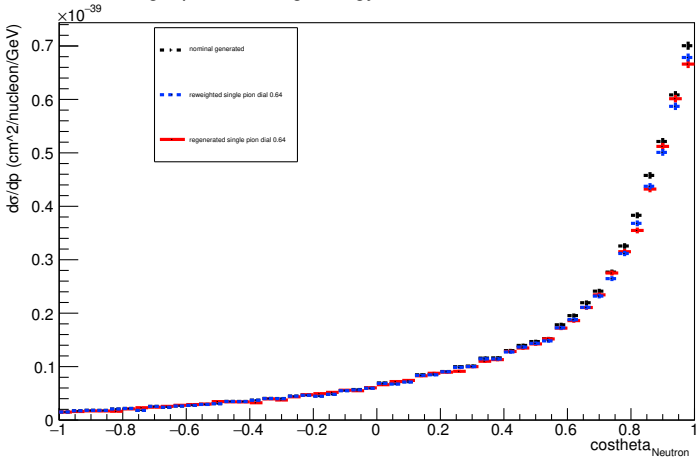

Angle plot: Every FSI Neutron: Neut Mode =11

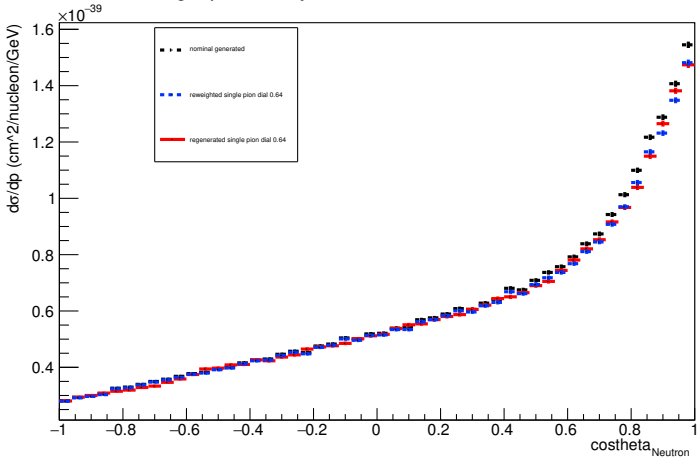

Angle plot: Leading Energy Neutron: Neut Mode =11

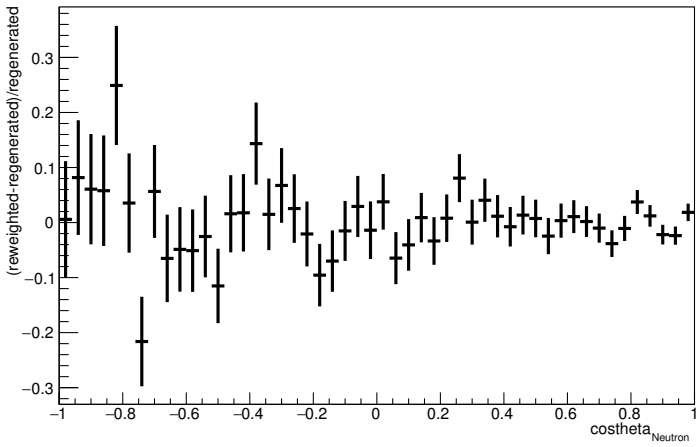

Angle plot: Every FSI Neutron: Neut Mode =11

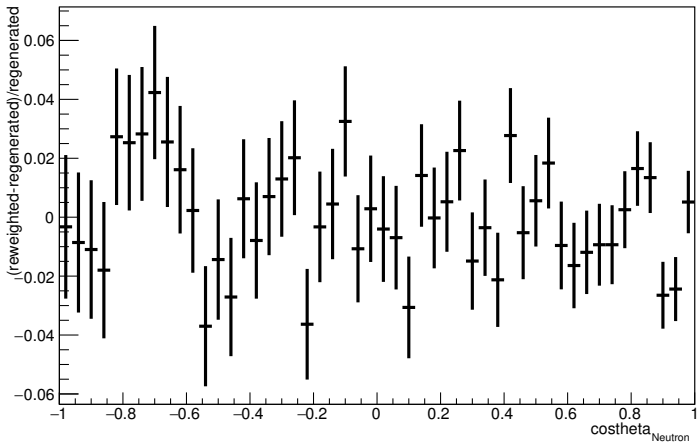

Energy plot: Leading Energy Lepton: Neut Mode =11

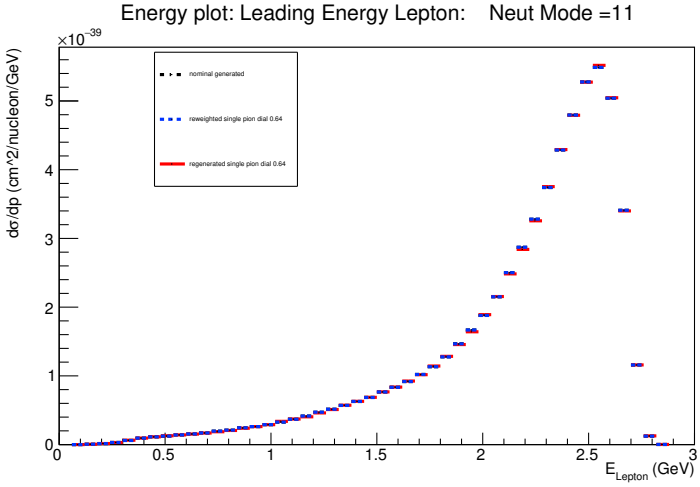

Angle plot: Leading Energy Lepton: Neut Mode =11

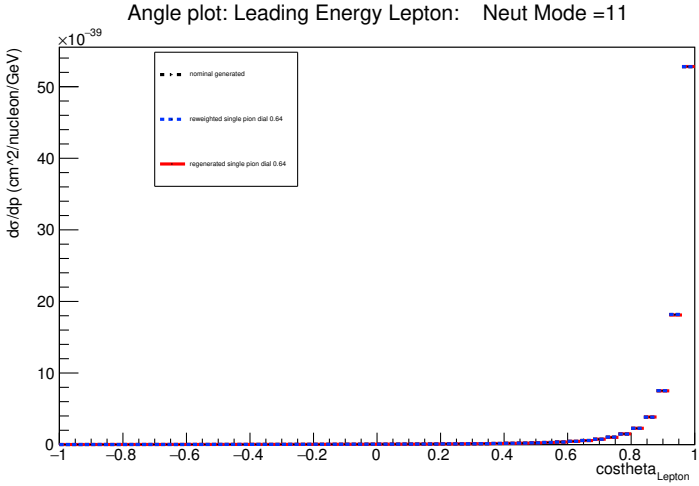

Energy plot: Leading Energy Lepton: Neut Mode =11

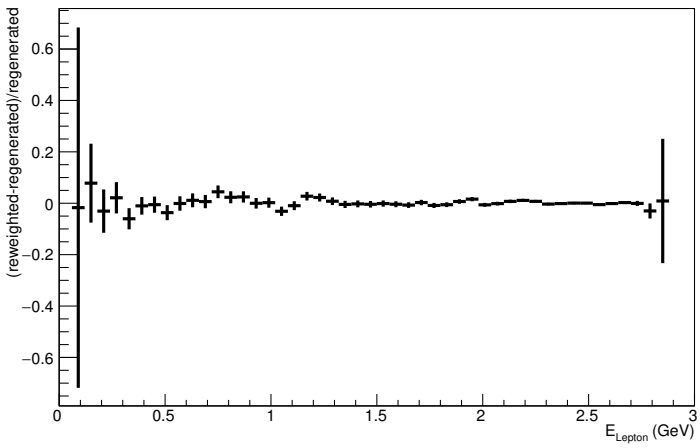

Angle plot: Leading Energy Lepton: Neut Mode =11

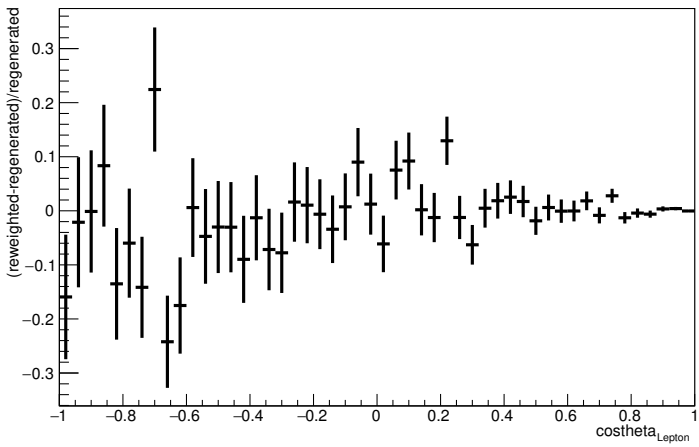

Energy plot: Leading Energy Pion: Neut Mode =11

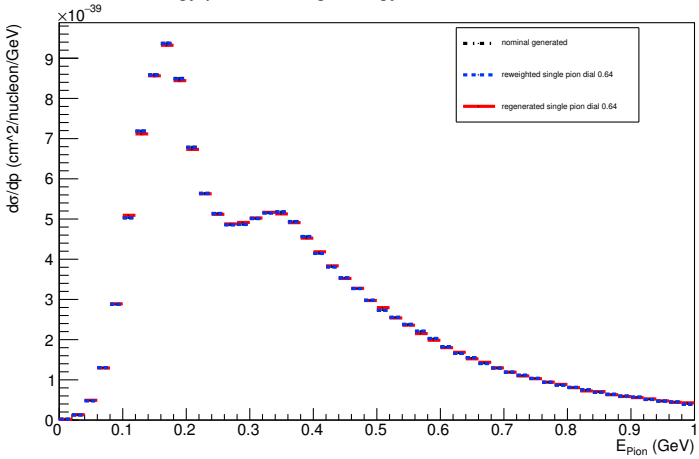

Energy plot: Every FSI Pion: Neut Mode =11

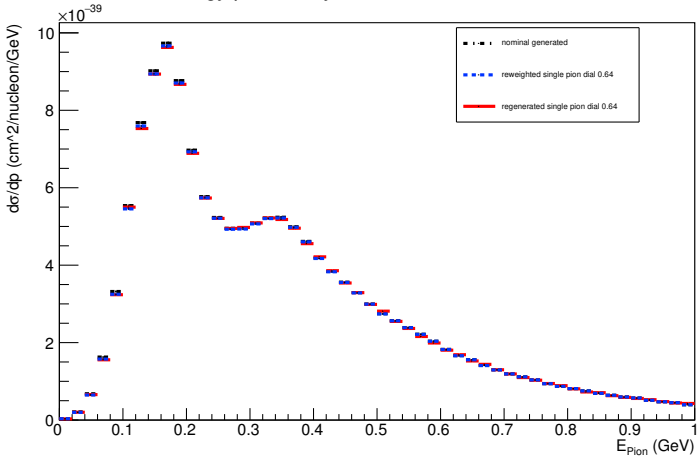

Energy plot: Leading Energy Pion: Neut Mode =11

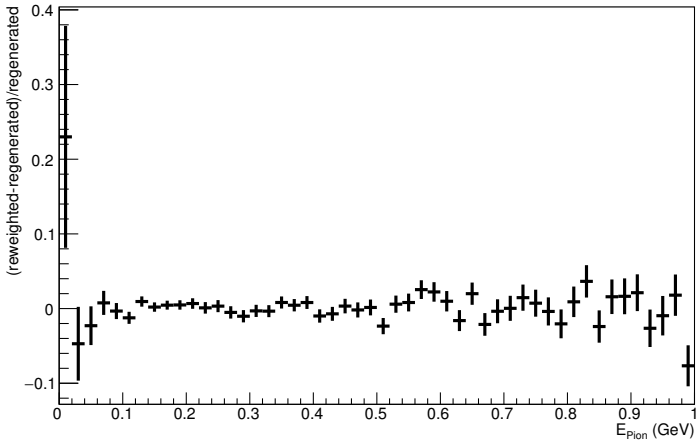

Energy plot: Every FSI Pion: Neut Mode =11

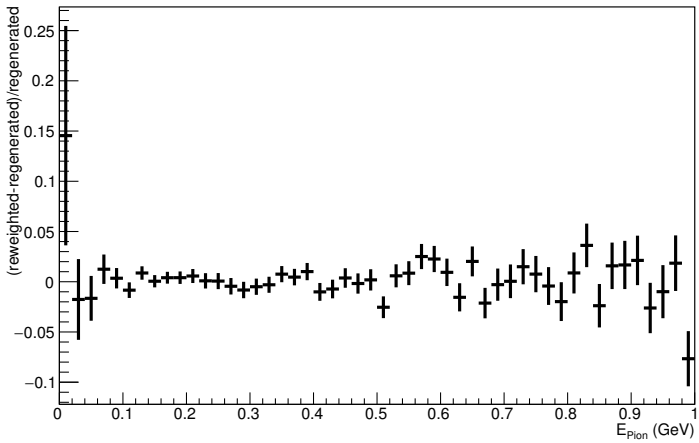

Angle plot: Leading Energy Pion: Neut Mode =11

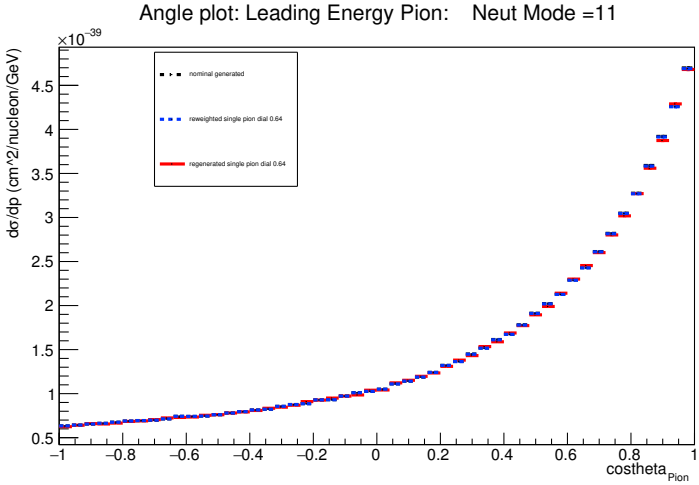

Angle plot: Every FSI Pion: Neut Mode =11

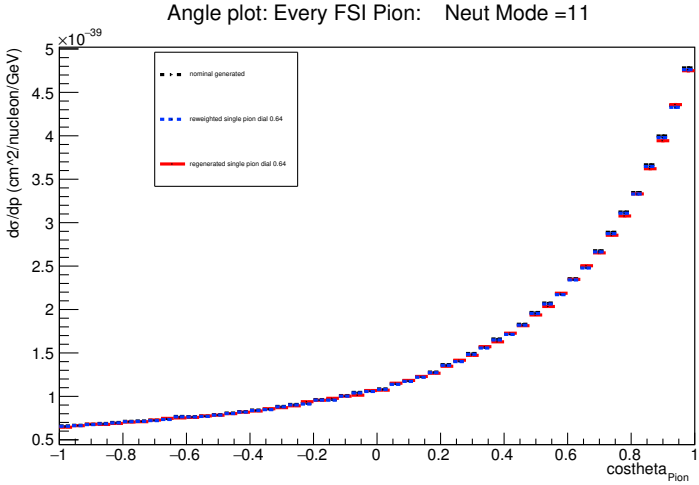

Angle plot: Leading Energy Pion: Neut Mode =11

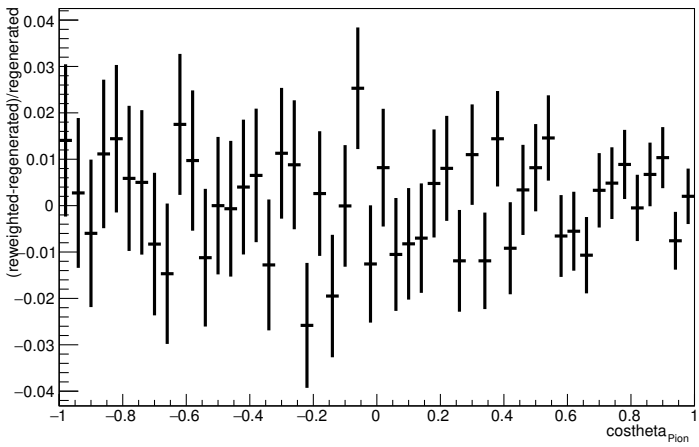

Angle plot: Every FSI Pion: Neut Mode =11

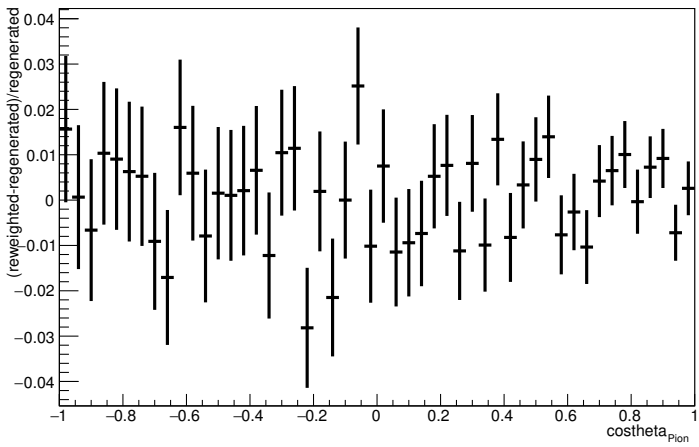

A.7. Double Pion Dial: varied up to 1.44

Energy plot: Leading Energy Nucleon: Neut Mode =AllModesCombined

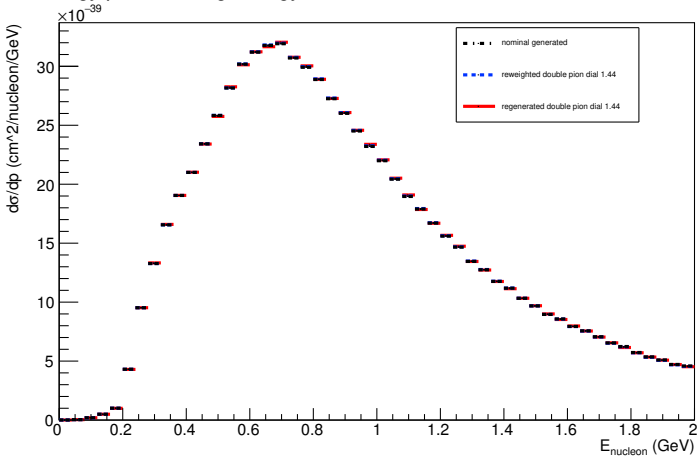

Energy plot: Every FSI Nucleon: Neut Mode =AllModesCombined

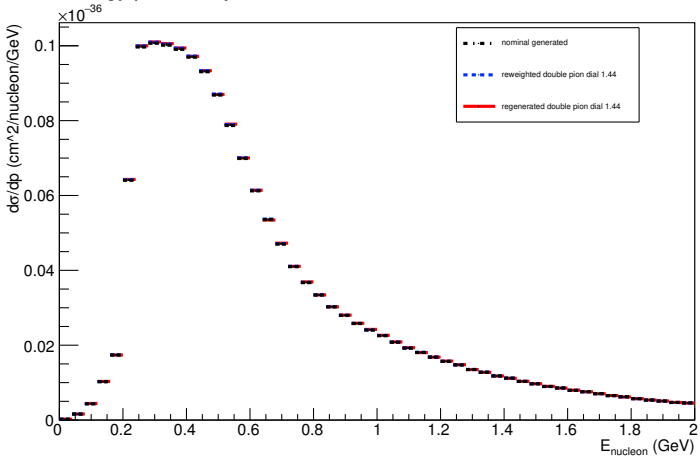

Energy plot: Leading Energy Nucleon: Neut Mode =AllModesCombined

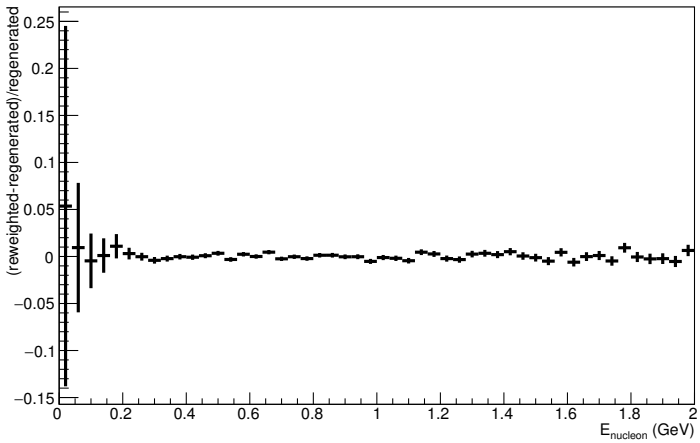

Energy plot: Every FSI Nucleon: Neut Mode =AllModesCombined

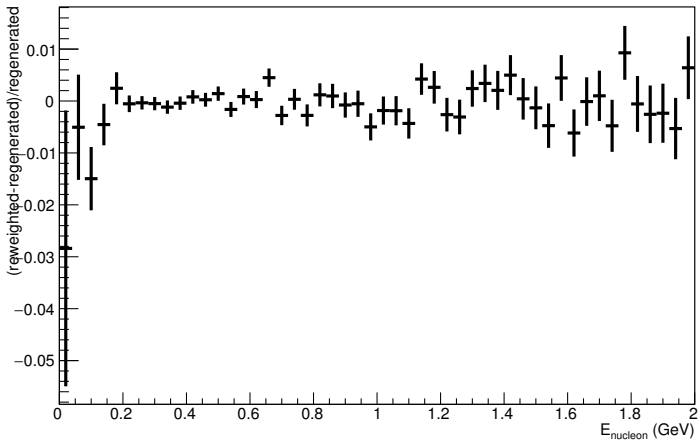

Angle plot: Leading Energy Nucleon: Neut Mode =AllModesCombined

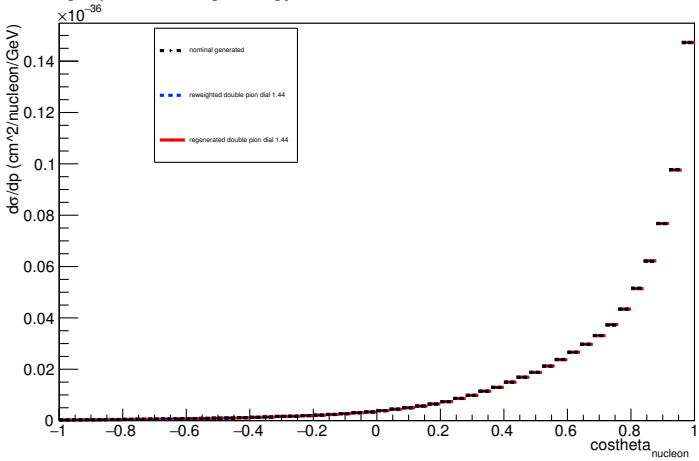

Angle plot: Every FSI Nucleon: Neut Mode =AllModesCombined

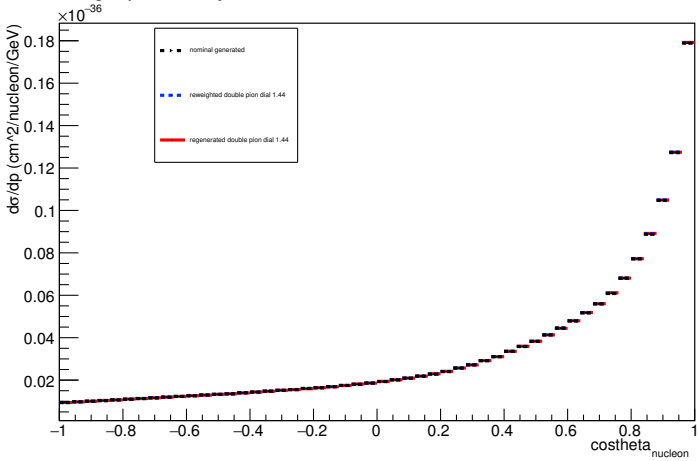

Angle plot: Leading Energy Nucleon: Neut Mode =AllModesCombined

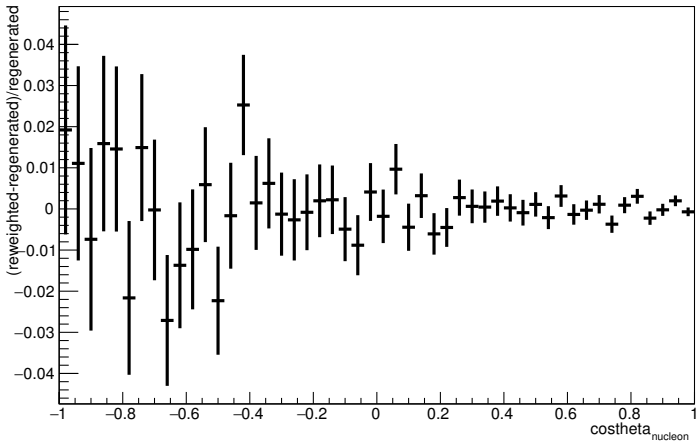

Angle plot: Every FSI Nucleon: Neut Mode =AllModesCombined

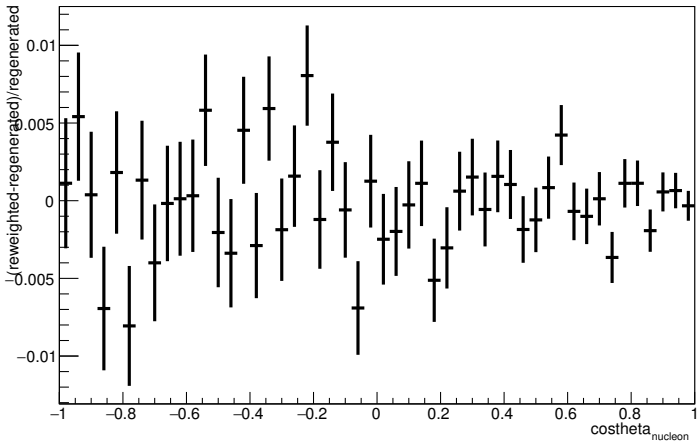

Energy plot: Leading Energy Proton: Neut Mode =AllModesCombined

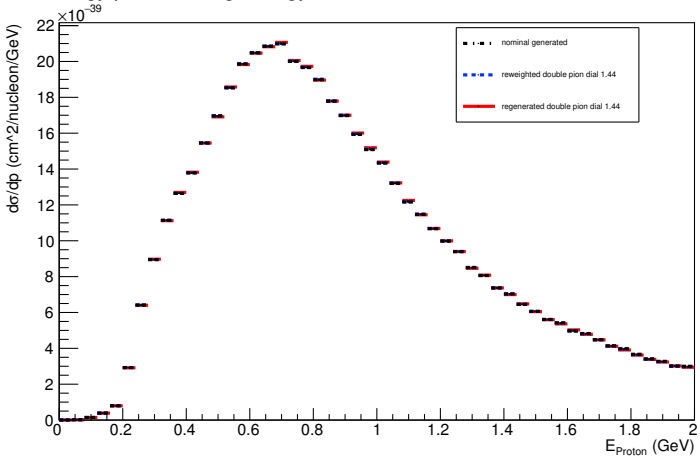

Energy plot: Every FSI Proton: Neut Mode =AllModesCombined

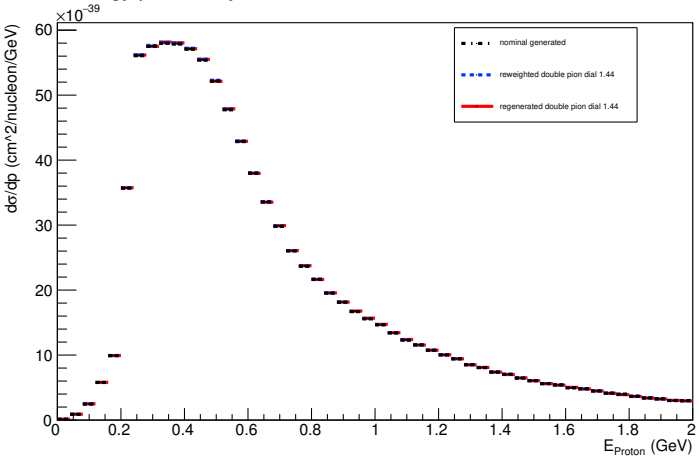

Energy plot: Leading Energy Proton: Neut Mode =AllModesCombined

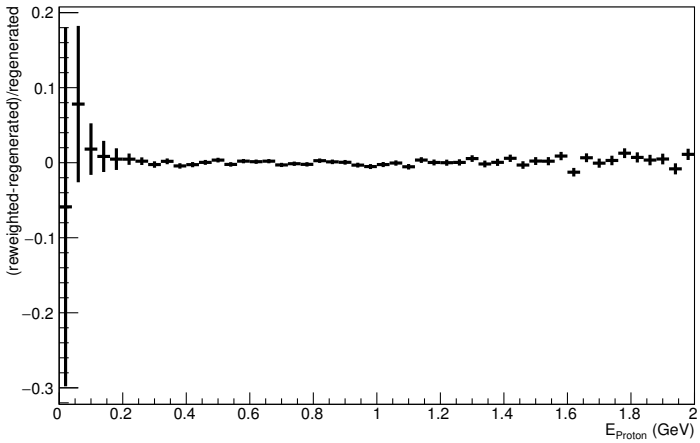

Energy plot: Every FSI Proton: Neut Mode =AllModesCombined

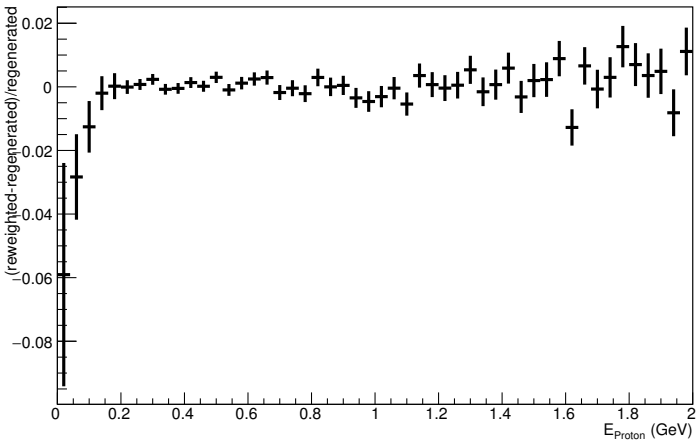

Angle plot: Leading Energy Proton: Neut Mode =AllModesCombined

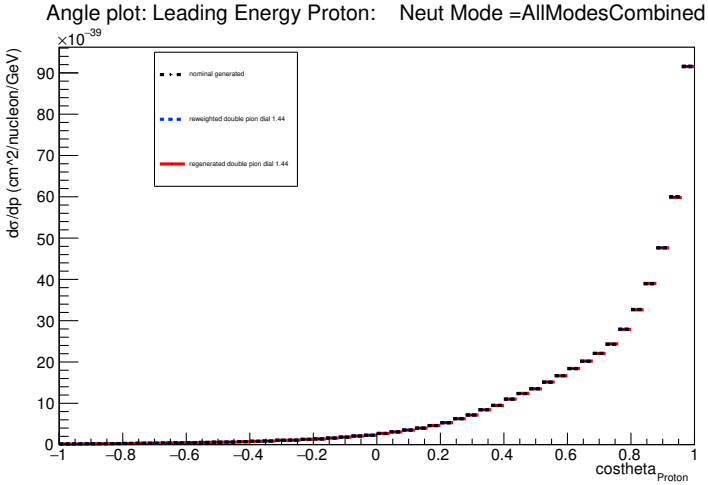

Angle plot: Every FSI Proton: Neut Mode =AllModesCombined

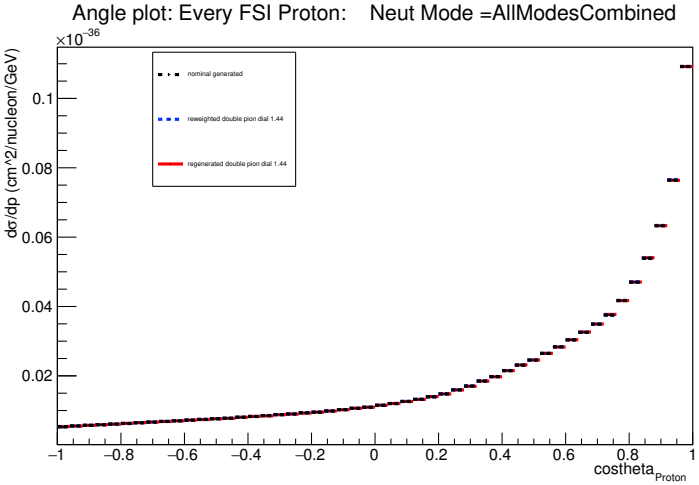

Angle plot: Leading Energy Proton: Neut Mode =AllModesCombined

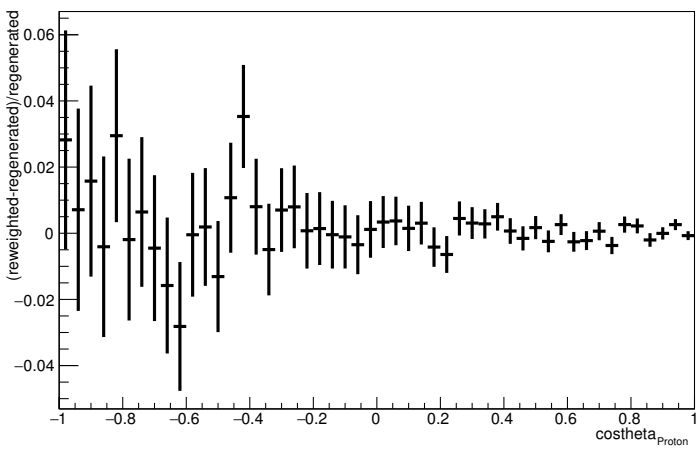

Angle plot: Every FSI Proton: Neut Mode =AllModesCombined

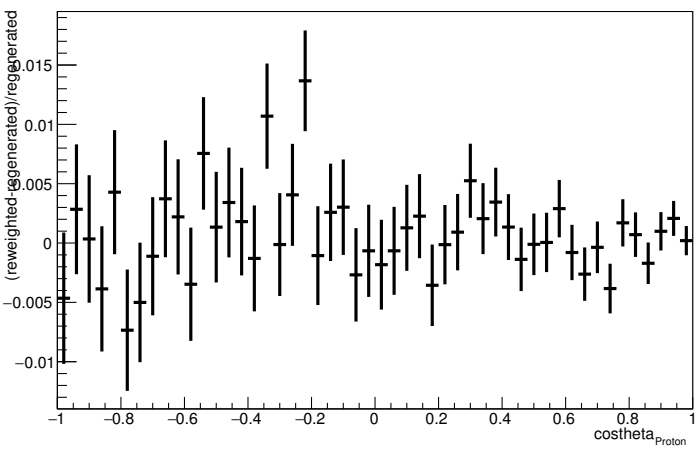

Energy plot: Leading Energy Neutron: Neut Mode =AllModesCombined

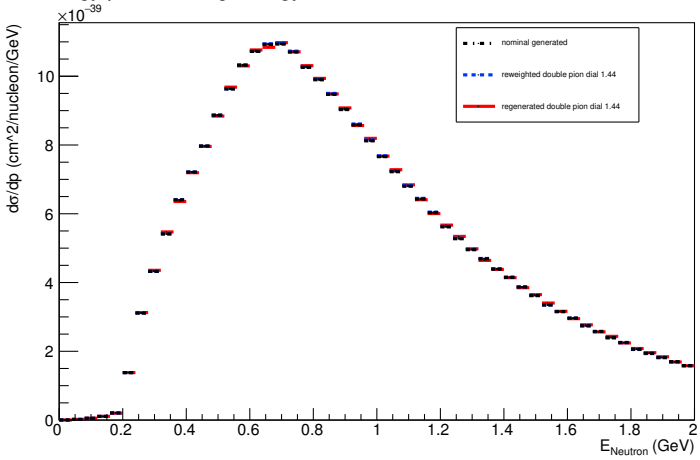

Energy plot: Every FSI Neutron: Neut Mode =AllModesCombined

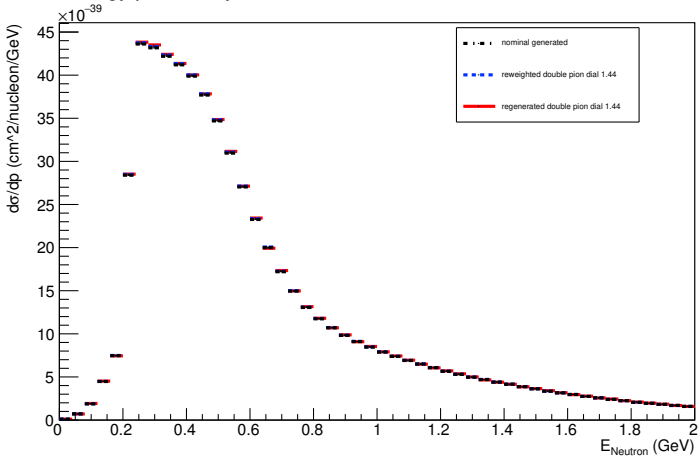

Energy plot: Leading Energy Neutron: Neut Mode =AllModesCombined

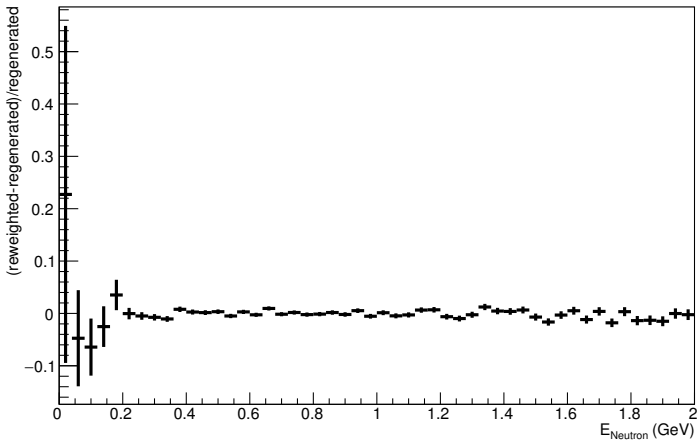

Energy plot: Every FSI Neutron: Neut Mode =AllModesCombined

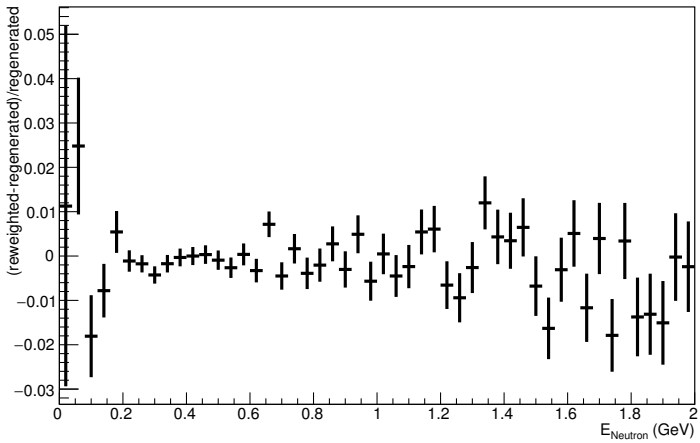

Angle plot: Leading Energy Neutron: Neut Mode =AllModesCombined

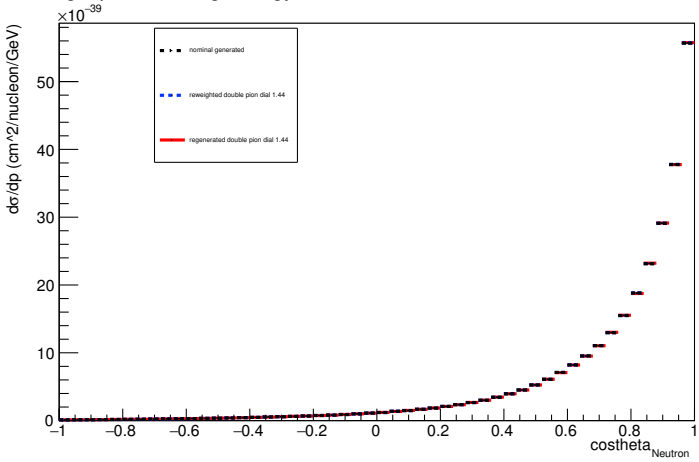

Angle plot: Every FSI Neutron: Neut Mode =AllModesCombined

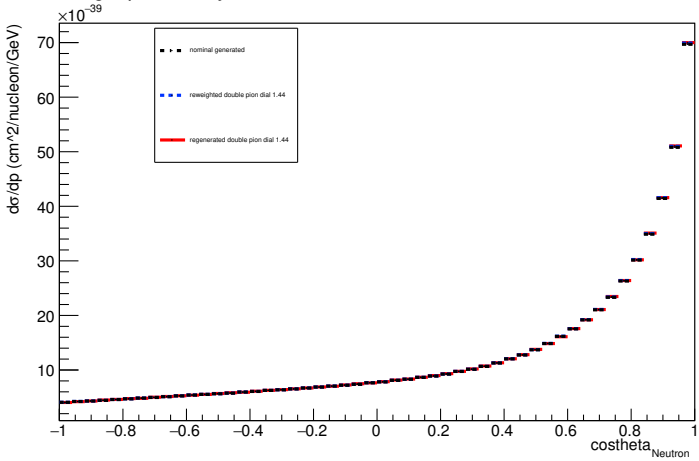

Angle plot: Leading Energy Neutron: Neut Mode =AllModesCombined

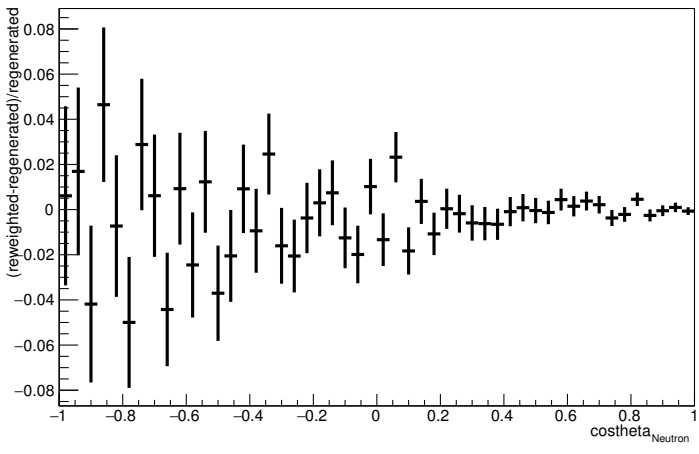

Angle plot: Every FSI Neutron: Neut Mode =AllModesCombined

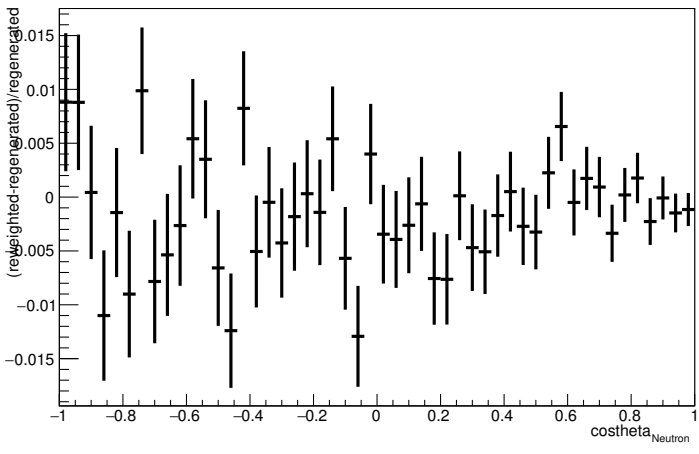

Energy plot: Leading Energy Lepton: Neut Mode =AllModesCombined

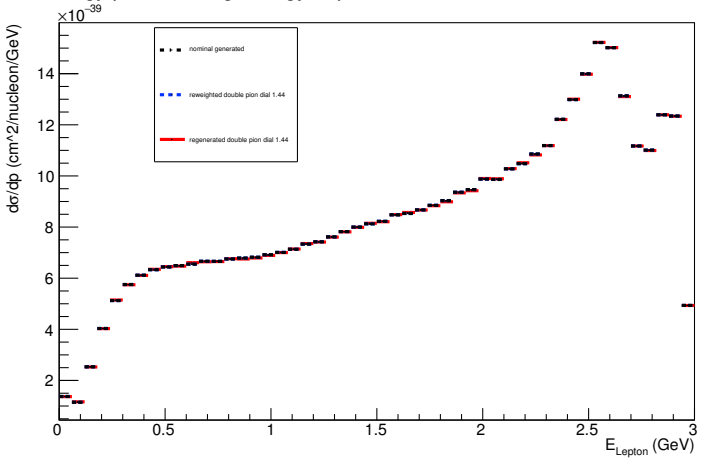

Angle plot: Leading Energy Lepton: Neut Mode =AllModesCombined

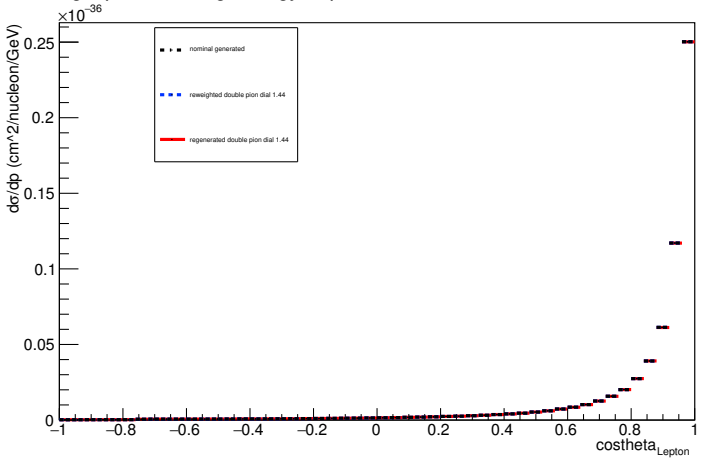

Energy plot: Leading Energy Lepton: Neut Mode =AllModesCombined

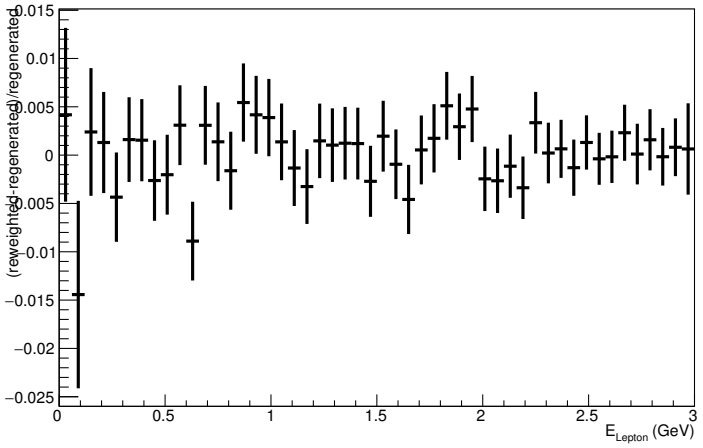

Angle plot: Leading Energy Lepton: Neut Mode =AllModesCombined

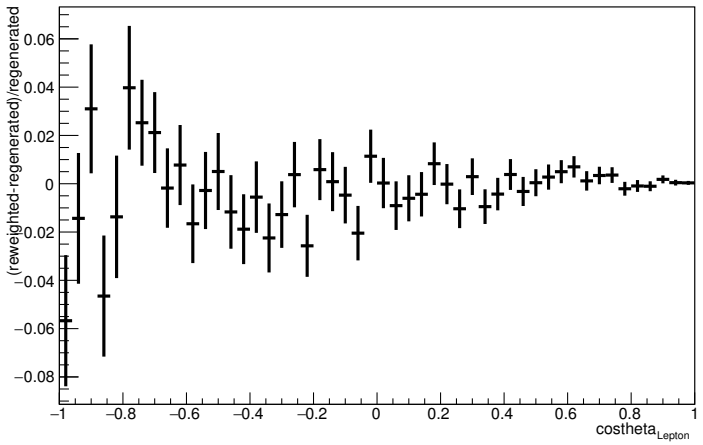

Energy plot: Leading Energy Pion: Neut Mode =AllModesCombined

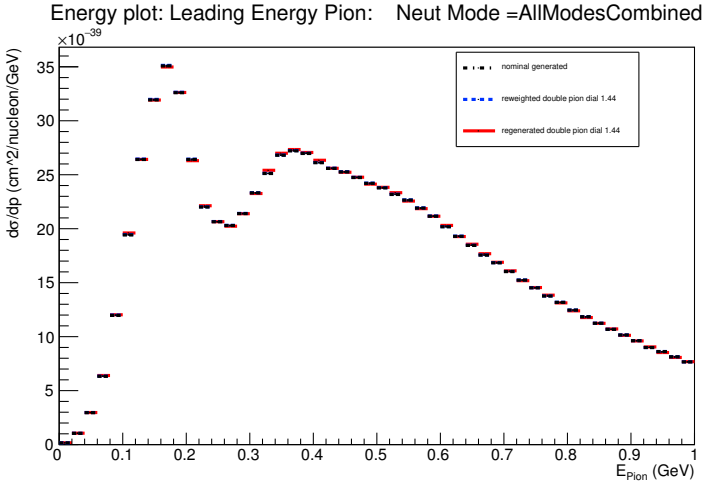

Energy plot: Every FSI Pion: Neut Mode =AllModesCombined

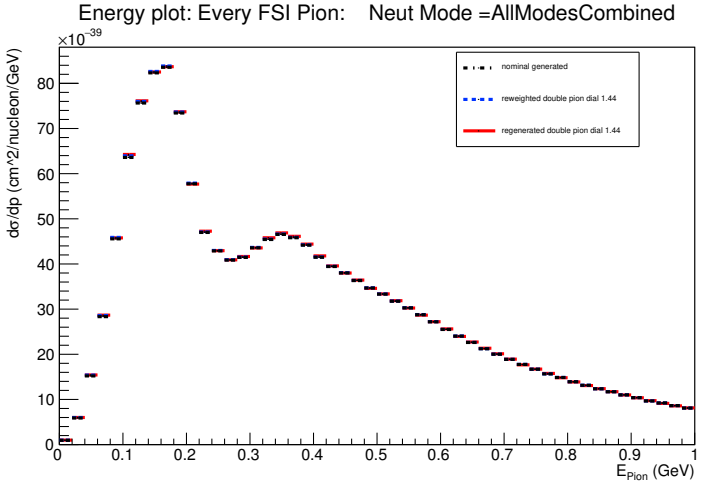

Energy plot: Leading Energy Pion: Neut Mode =AllModesCombined

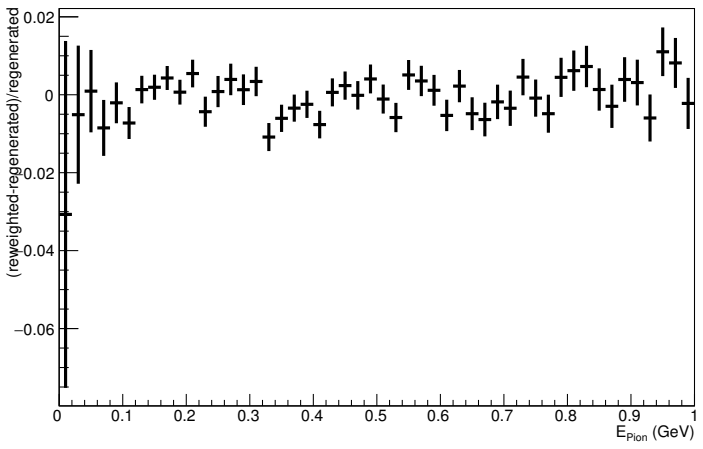

Energy plot: Every FSI Pion: Neut Mode =AllModesCombined

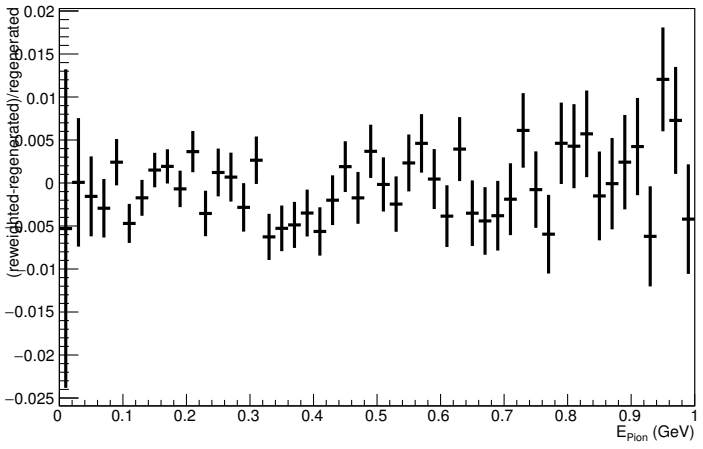

Angle plot: Leading Energy Pion: Neut Mode =AllModesCombined

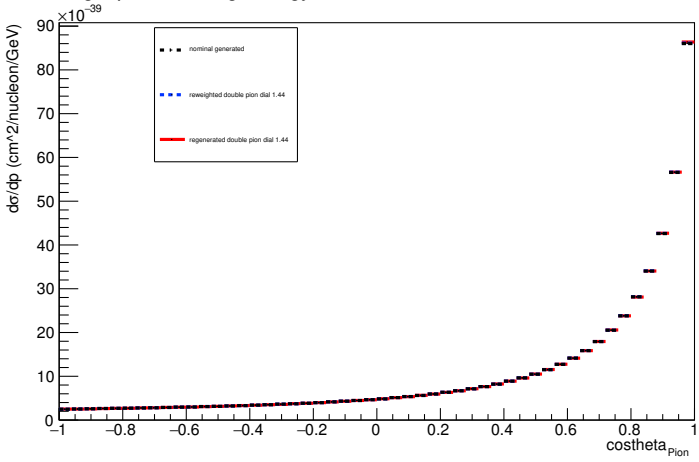

Angle plot: Every FSI Pion: Neut Mode =AllModesCombined

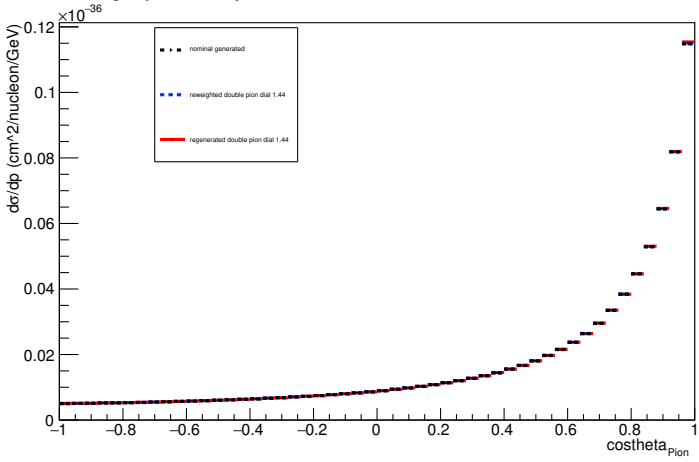

Angle plot: Leading Energy Pion: Neut Mode =AllModesCombined

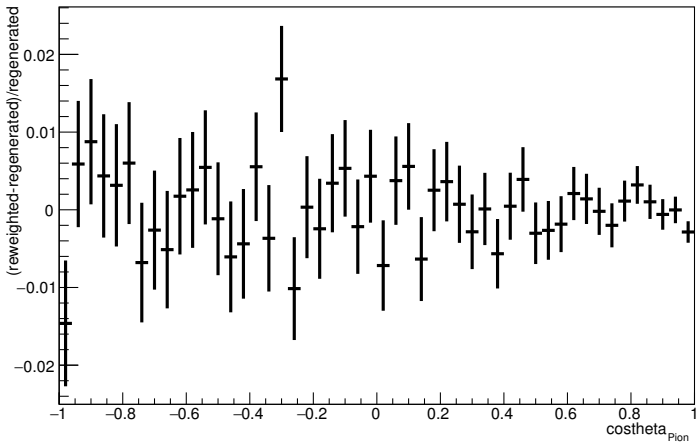

Angle plot: Every FSI Pion: Neut Mode =AllModesCombined

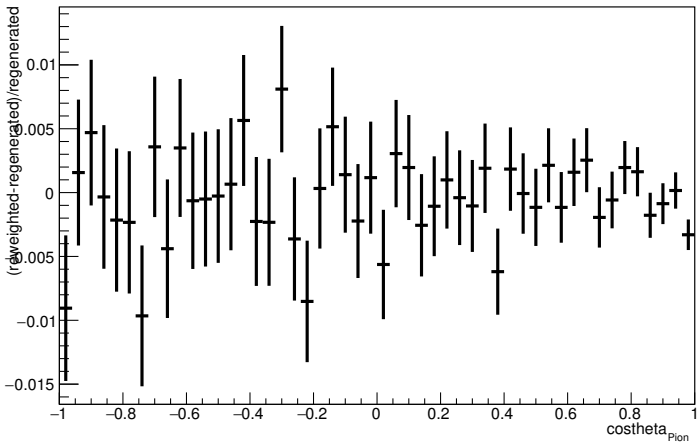

Energy plot: Leading Energy Nucleon: Neut Mode =1

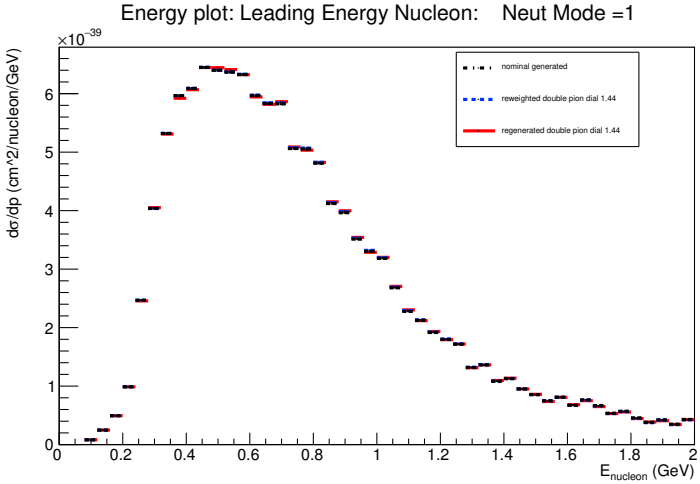

Energy plot: Every FSI Nucleon: Neut Mode =1

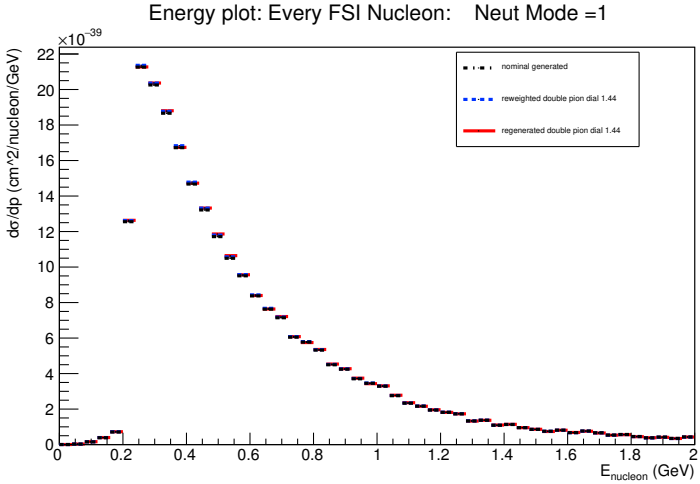

Energy plot: Leading Energy Nucleon: Neut Mode =1

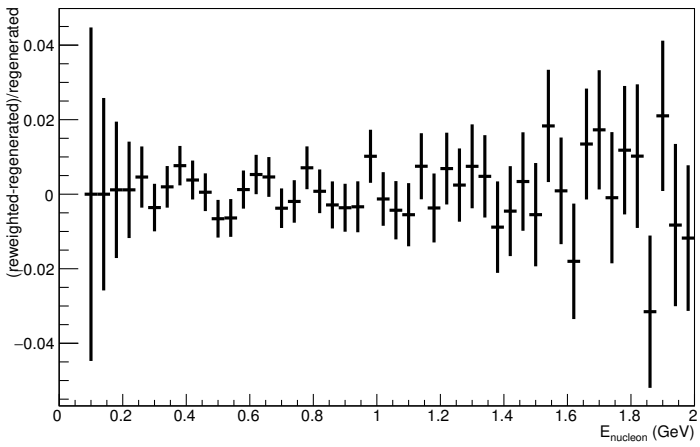

Energy plot: Every FSI Nucleon: Neut Mode =1

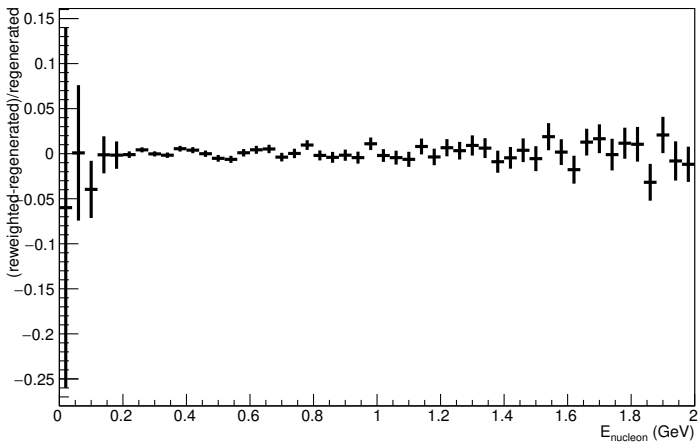

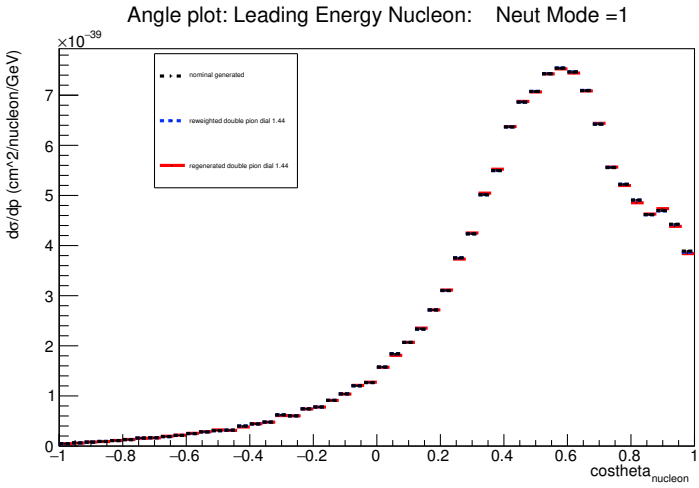
Angle plot: Leading Energy Nucleon: Neut Mode =1
nominal generated
reweighted double pion dial 1.44
regenerated double pion dial 1.44
dσ/dp (cm^2/nucleon/GeV)
costheta_nucleon

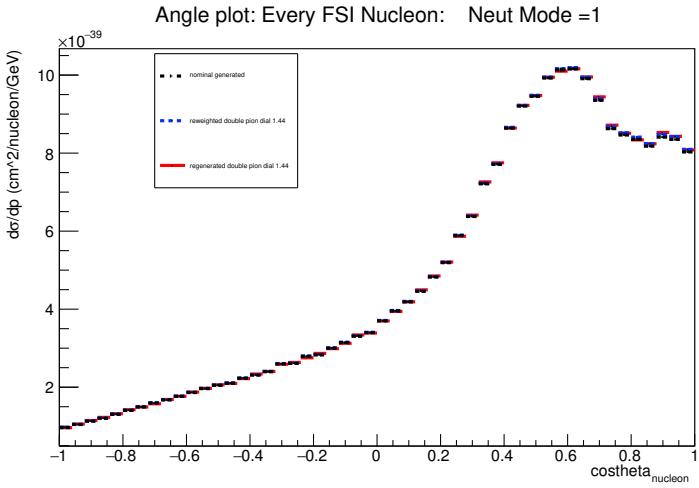
Angle plot: Every FSI Nucleon: Neut Mode =1
nominal generated
reweighted double pion dial 1.44
regenerated double pion dial 1.44
dσ/dp (cm^2/nucleon/GeV)
costheta_nucleon

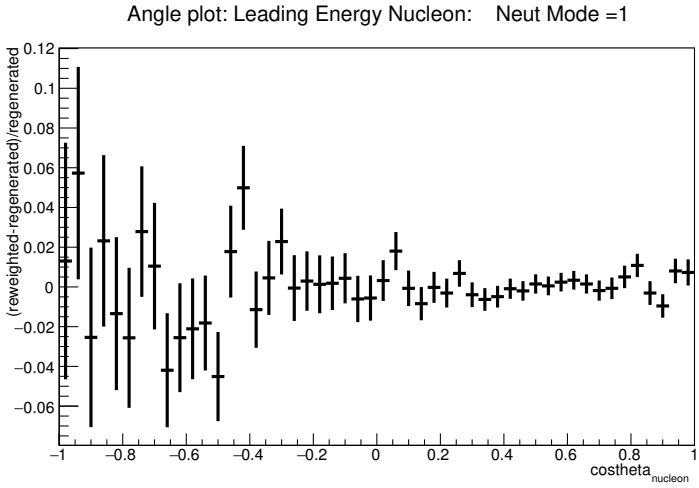
Angle plot: Leading Energy Nucleon: Neut Mode =1
(reweighted-regenerated)/regenerated
costheta_nucleon

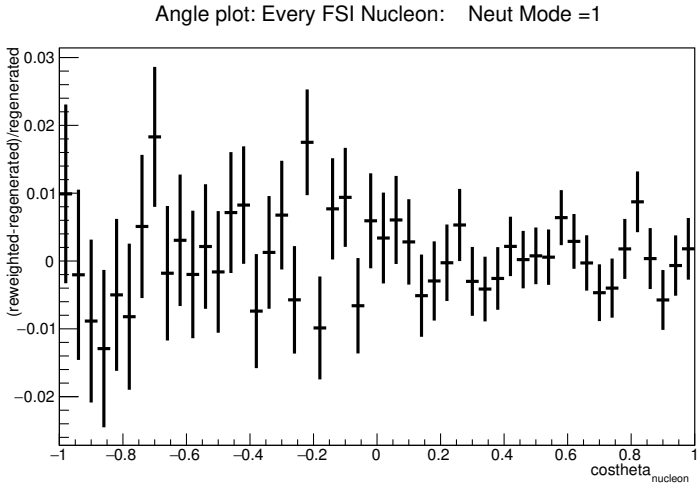
Angle plot: Every FSI Nucleon: Neut Mode =1
(reweighted-regenerated)/regenerated
costheta_nucleon

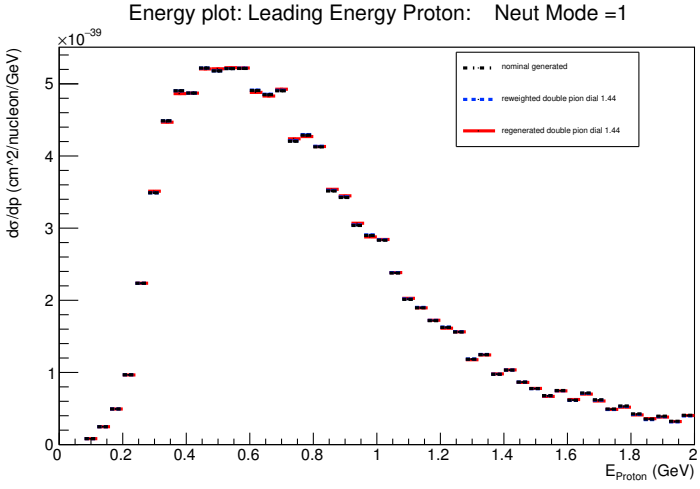
Energy plot: Leading Energy Proton: Neut Mode =1
nominal generated
reweighted double pion dial 1.44
regenerated double pion dial 1.44
dσ/dp (cm^2/nucleon/GeV)
E_Proton (GeV)

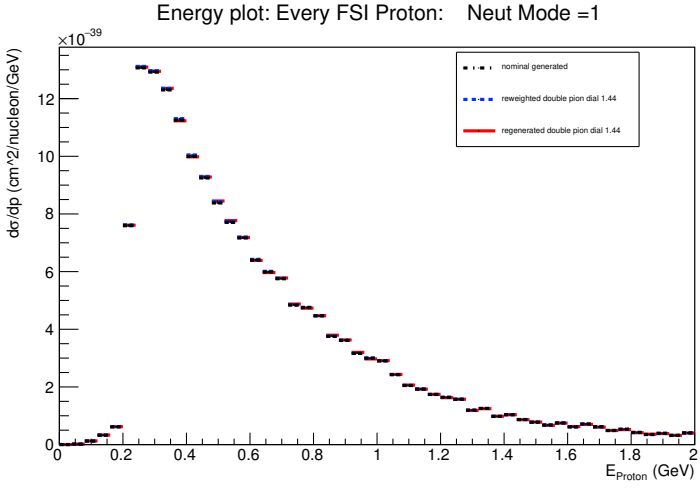
Energy plot: Every FSI Proton: Neut Mode =1
nominal generated
reweighted double pion dial 1.44
regenerated double pion dial 1.44
dσ/dp (cm^2/nucleon/GeV)
E_Proton (GeV)

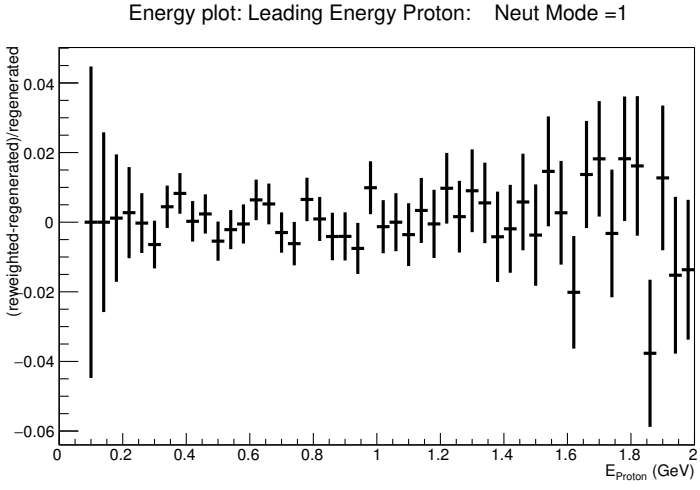
Energy plot: Leading Energy Proton: Neut Mode =1
(reweighted-regenerated)/regenerated
E_Proton (GeV)

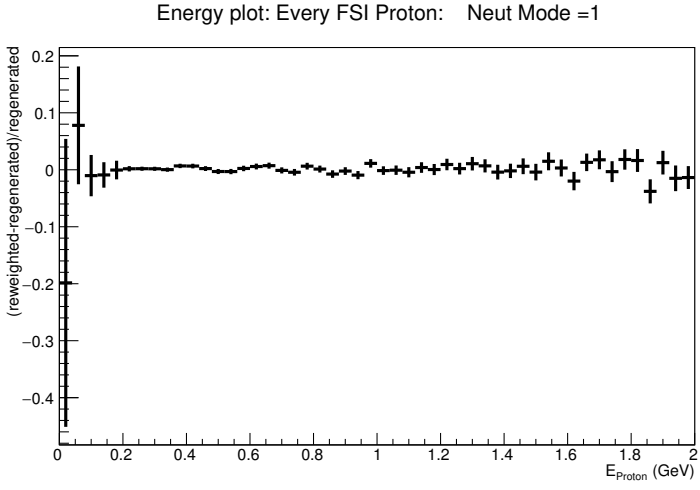
Energy plot: Every FSI Proton: Neut Mode =1
(reweighted-regenerated)/regenerated
E_Proton (GeV)

Angle plot: Leading Energy Proton: Neut Mode =1

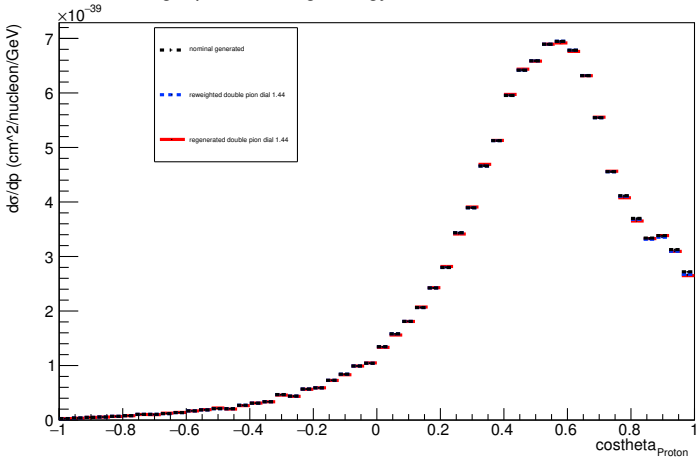

Angle plot: Every FSI Proton: Neut Mode =1

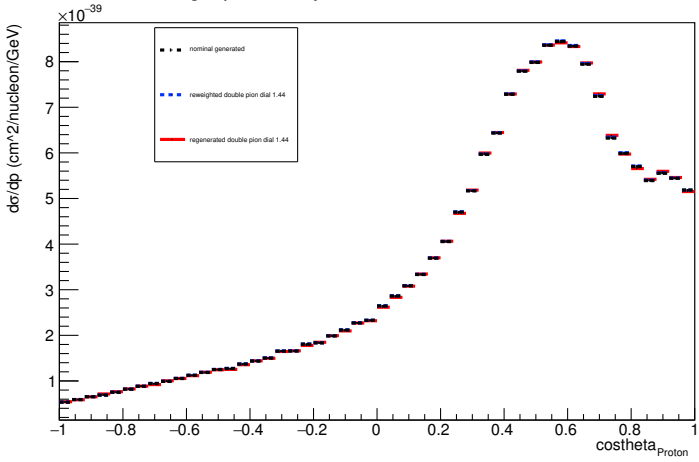

Angle plot: Leading Energy Proton: Neut Mode =1

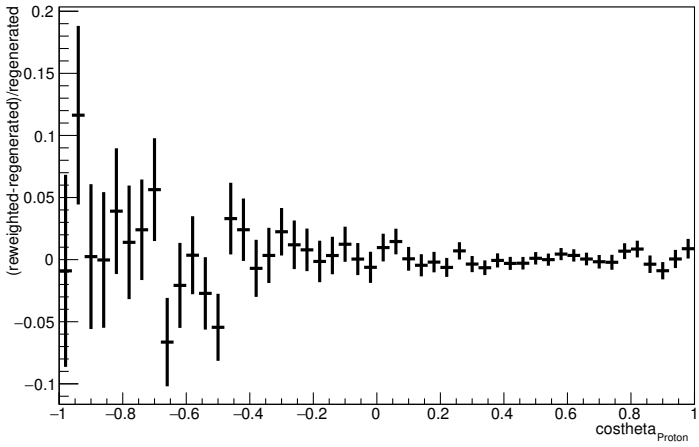

Angle plot: Every FSI Proton: Neut Mode =1

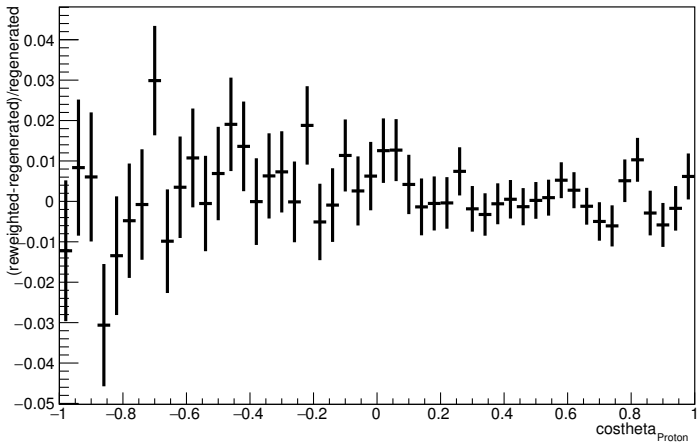

Energy plot: Leading Energy Neutron: Neut Mode =1

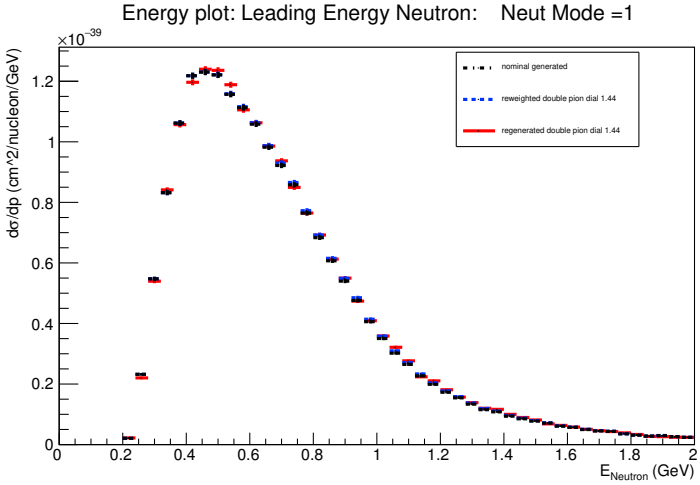

Energy plot: Every FSI Neutron: Neut Mode =1

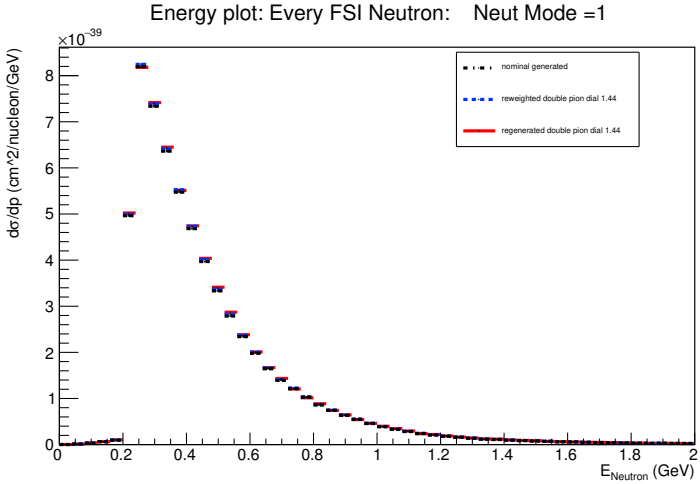

Energy plot: Leading Energy Neutron: Neut Mode =1

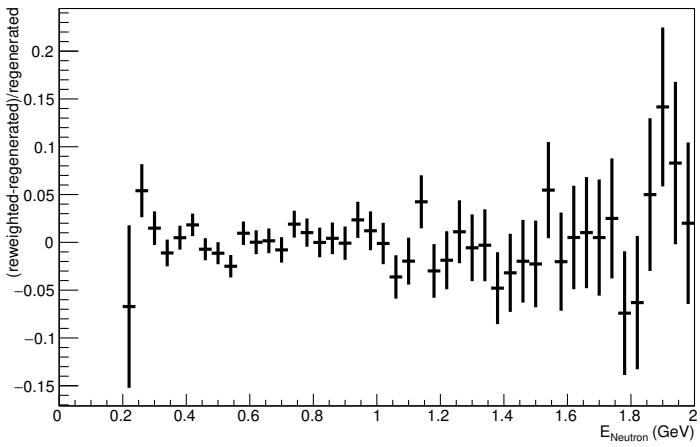

Energy plot: Every FSI Neutron: Neut Mode =1

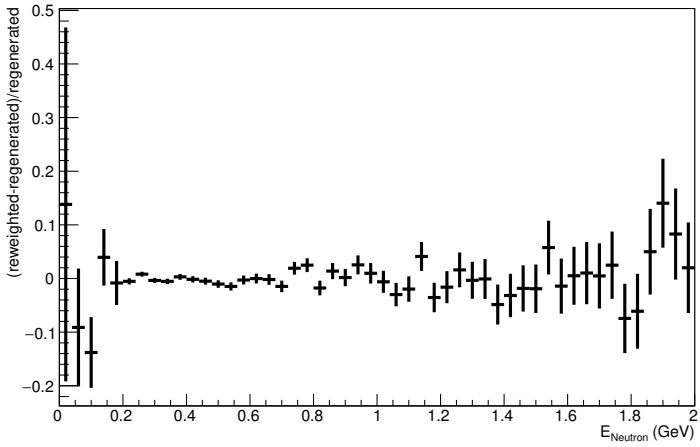

Angle plot: Leading Energy Neutron: Neut Mode =1

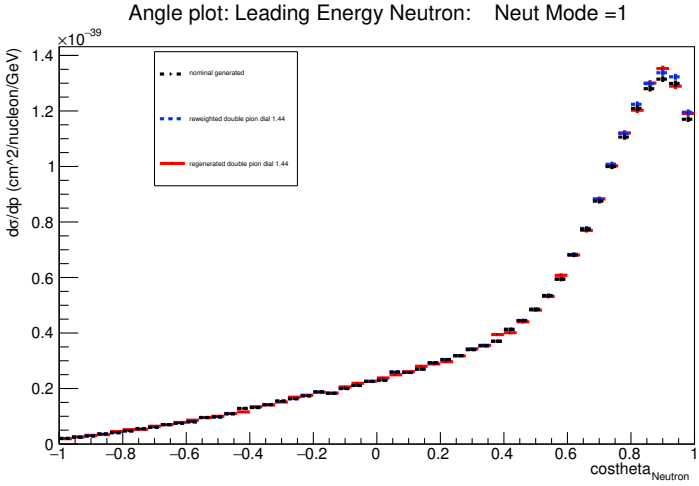

Angle plot: Every FSI Neutron: Neut Mode =1

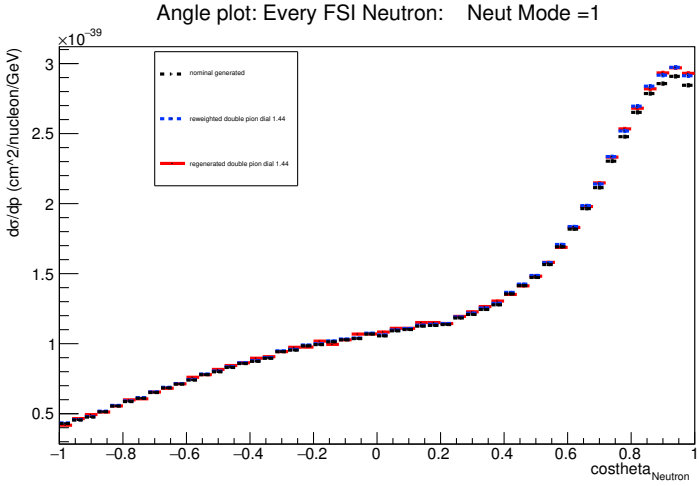

Angle plot: Leading Energy Neutron: Neut Mode =1

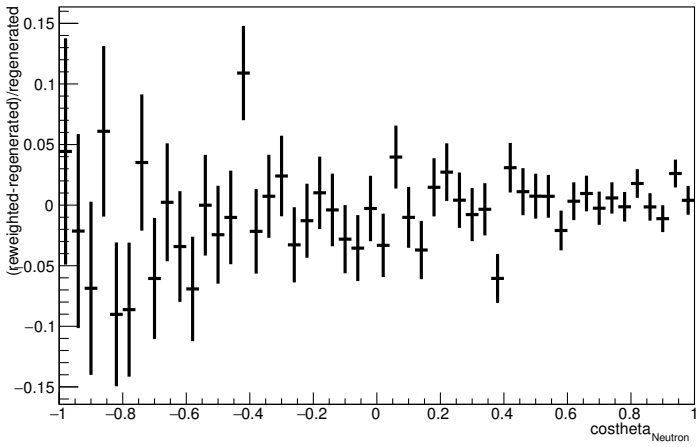

Angle plot: Every FSI Neutron: Neut Mode =1

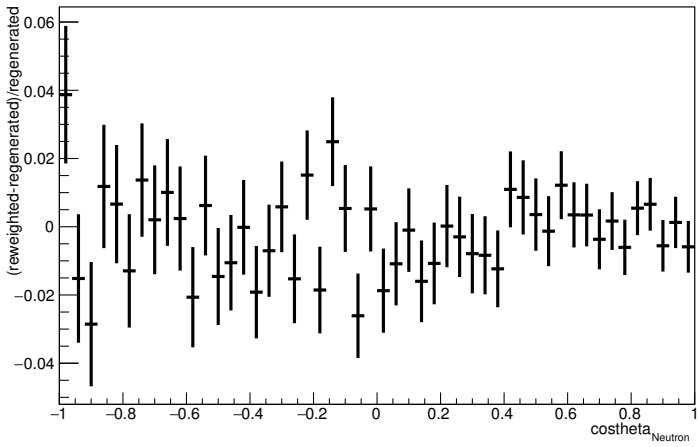

Energy plot: Leading Energy Lepton: Neut Mode =1

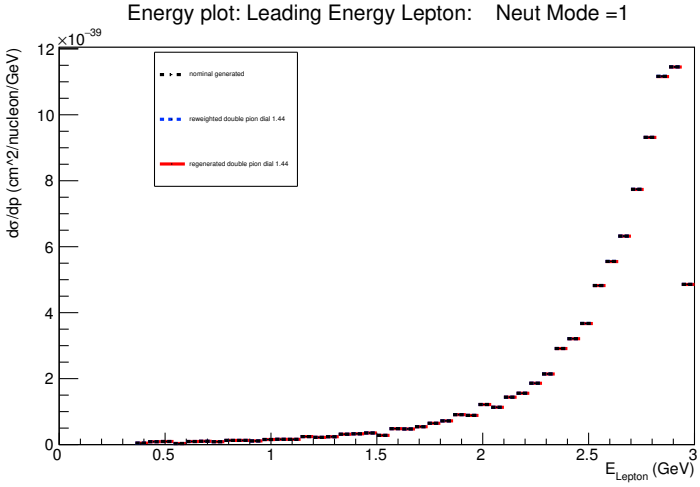

Angle plot: Leading Energy Lepton: Neut Mode =1

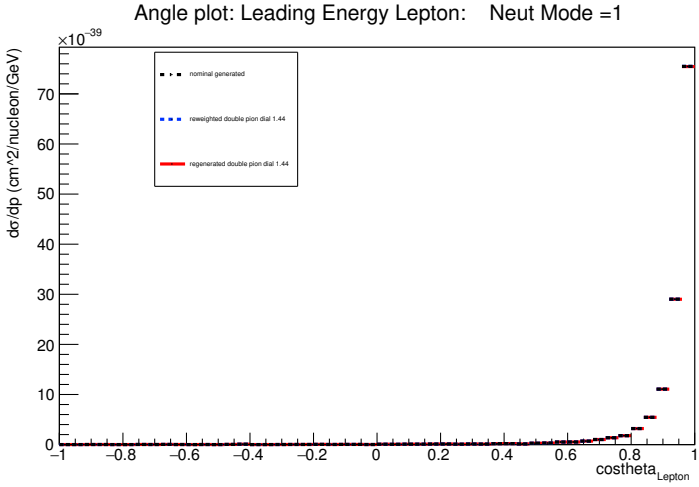

Energy plot: Leading Energy Lepton: Neut Mode =1

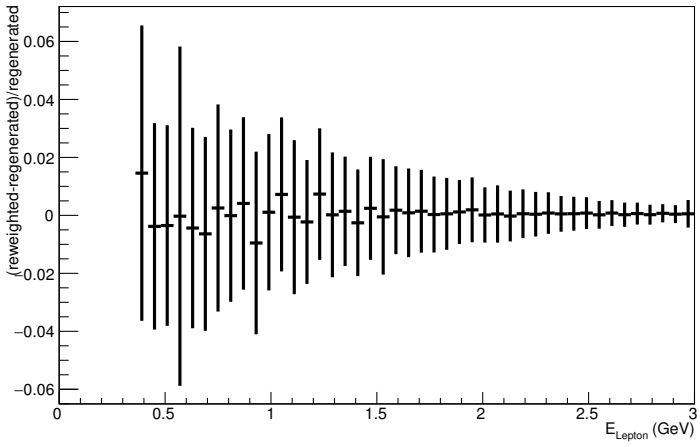

Angle plot: Leading Energy Lepton: Neut Mode =1

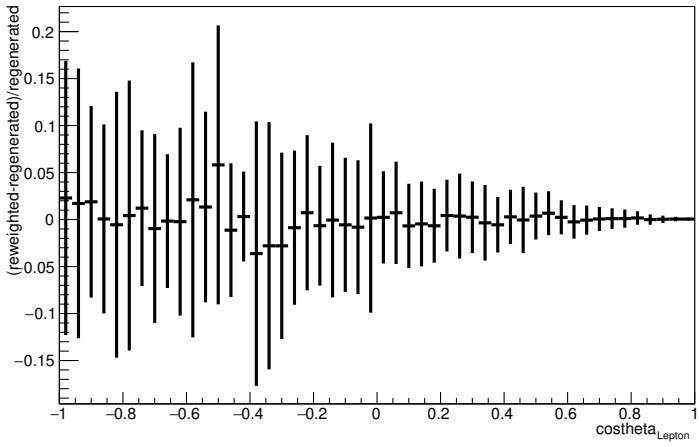

Energy plot: Leading Energy Pion: Neut Mode =1

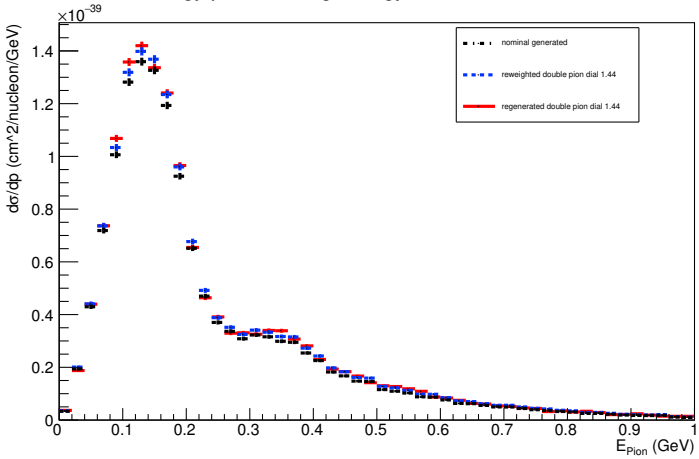

Energy plot: Every FSI Pion: Neut Mode =1

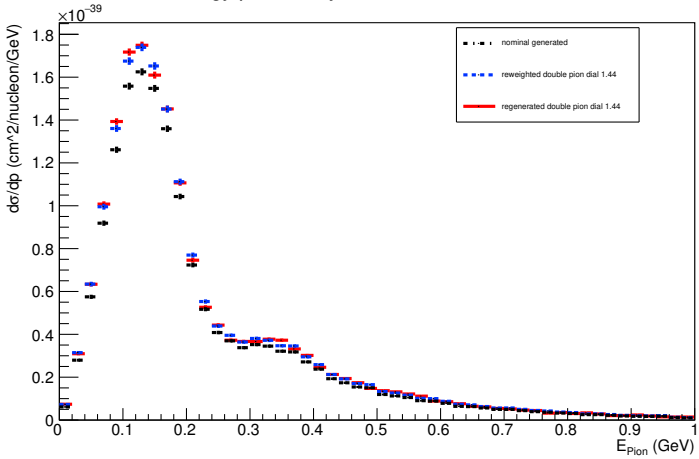

Energy plot: Leading Energy Pion: Neut Mode =1

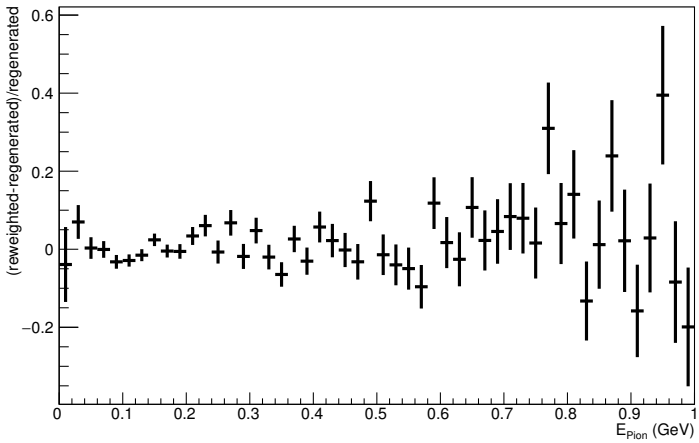

Energy plot: Every FSI Pion: Neut Mode =1

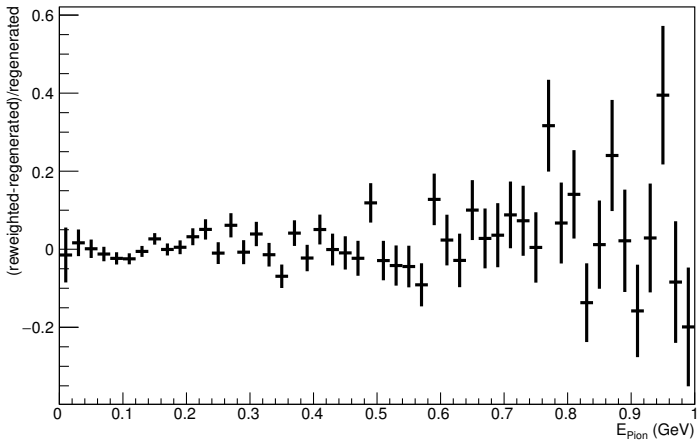

Angle plot: Leading Energy Pion: Neut Mode =1

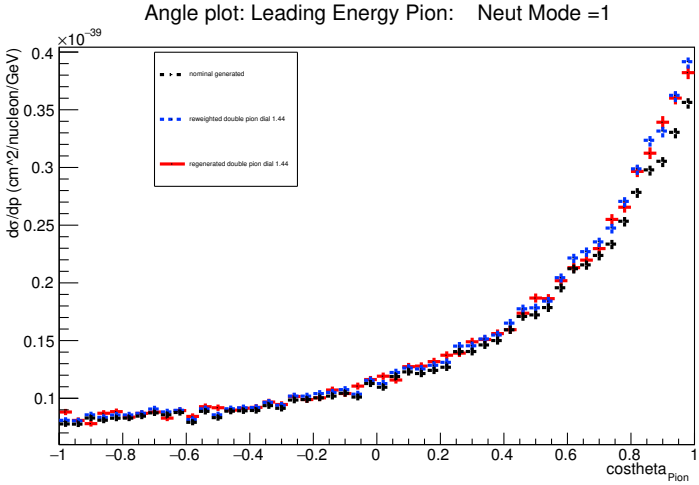

Angle plot: Every FSI Pion: Neut Mode =1

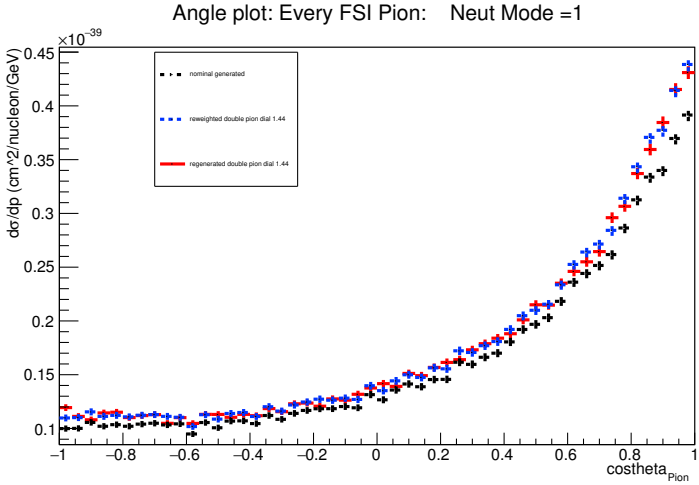

Angle plot: Leading Energy Pion: Neut Mode =1

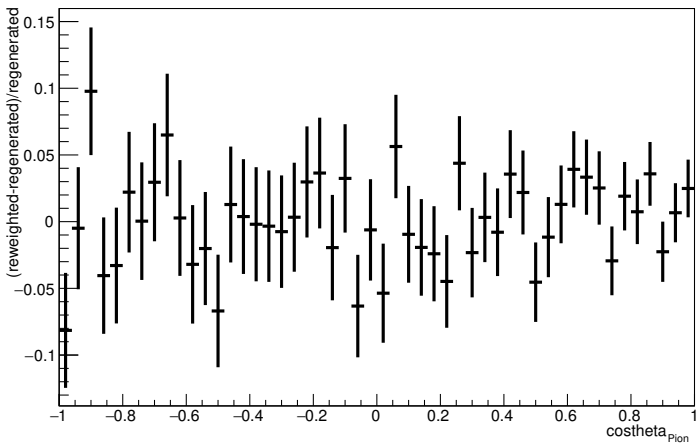

Angle plot: Every FSI Pion: Neut Mode =1

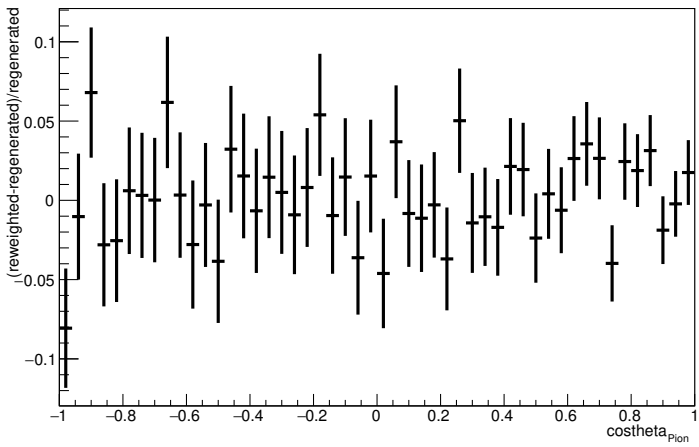

Energy plot: Leading Energy Nucleon: Neut Mode =2

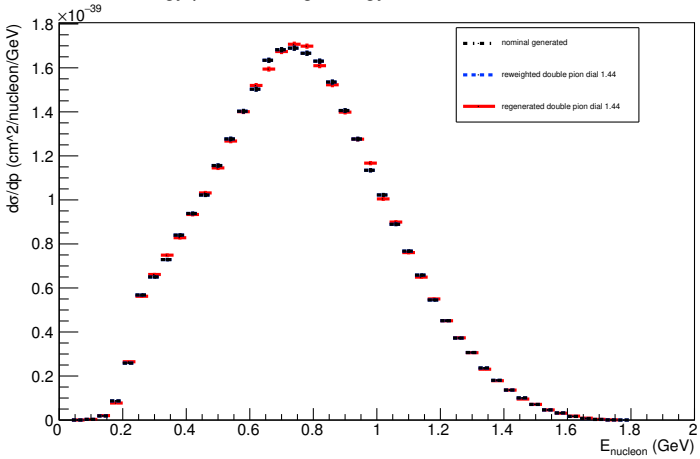

Energy plot: Every FSI Nucleon: Neut Mode =2

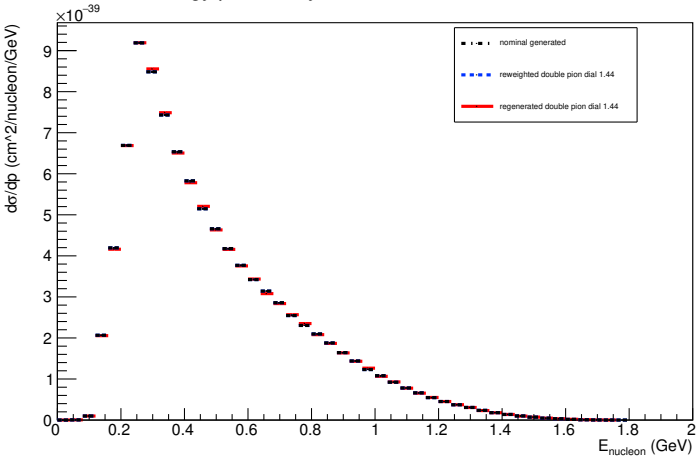

Energy plot: Leading Energy Nucleon: Neut Mode =2

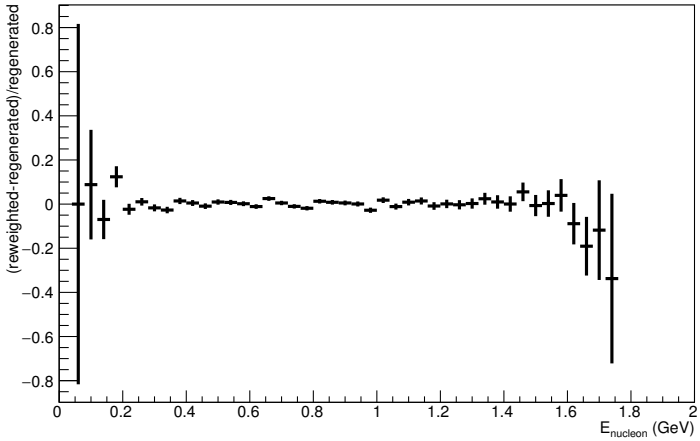

Energy plot: Every FSI Nucleon: Neut Mode =2

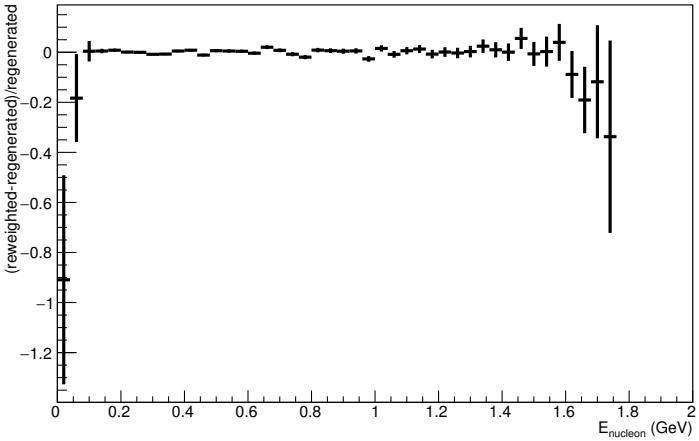

Angle plot: Leading Energy Nucleon: Neut Mode =2

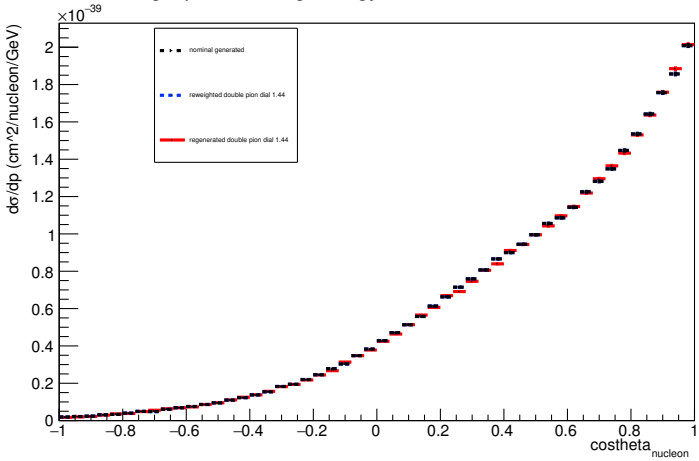

Angle plot: Every FSI Nucleon: Neut Mode =2

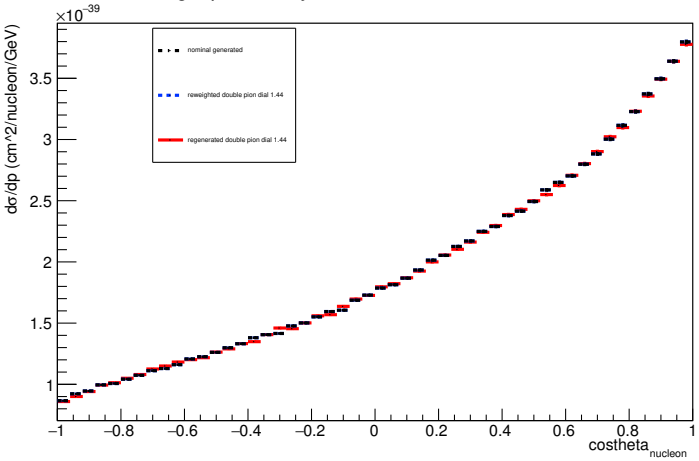

Angle plot: Leading Energy Nucleon: Neut Mode =2

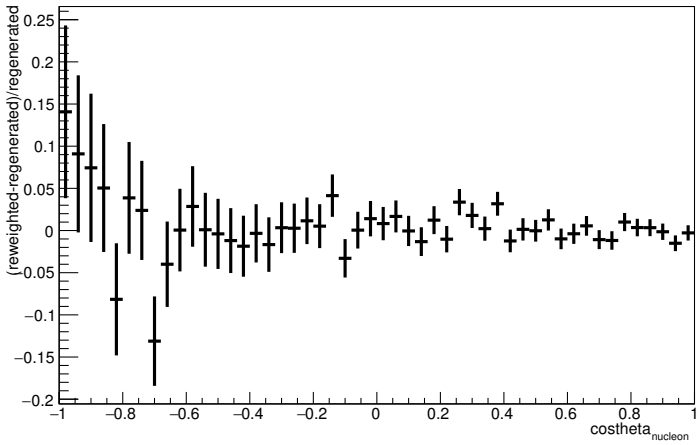

Angle plot: Every FSI Nucleon: Neut Mode =2

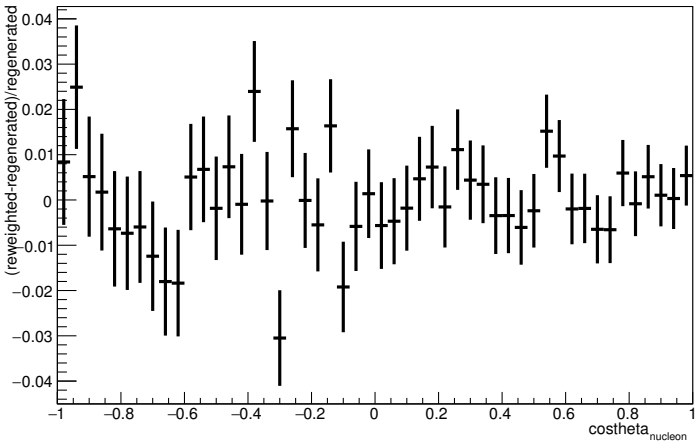

Energy plot: Leading Energy Proton: Neut Mode =2

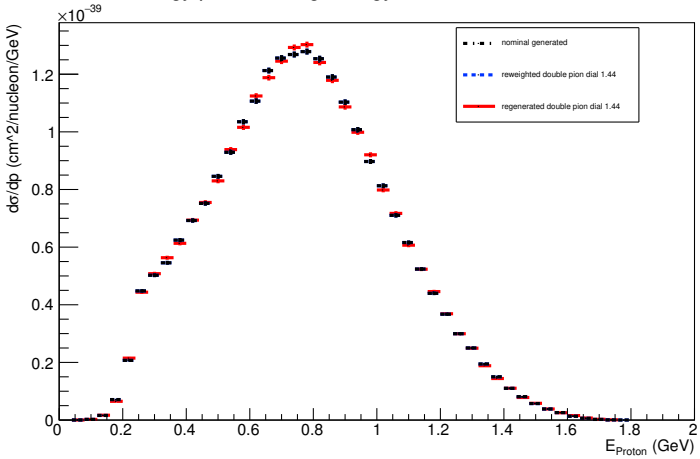

Energy plot: Every FSI Proton: Neut Mode =2

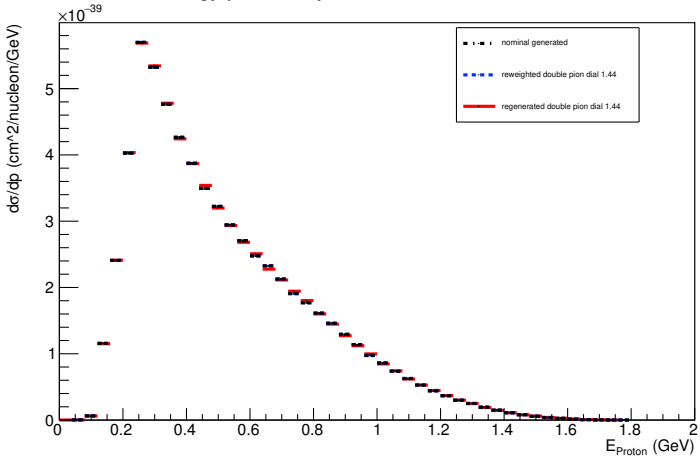

Energy plot: Leading Energy Proton: Neut Mode =2

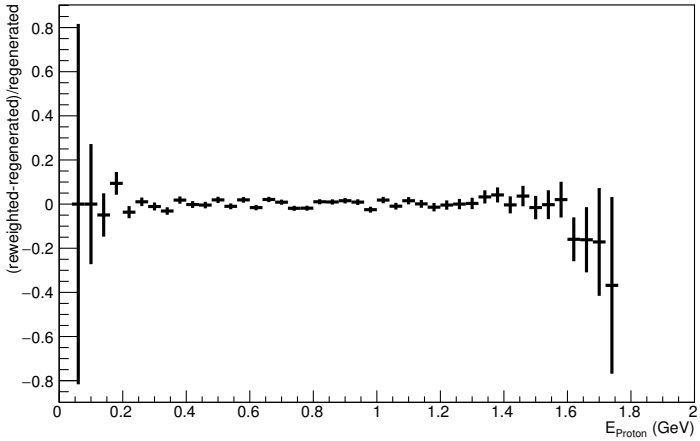

Energy plot: Every FSI Proton: Neut Mode =2

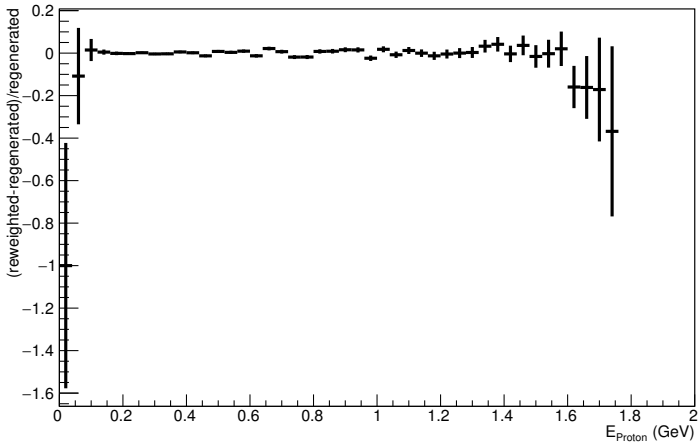

Angle plot: Leading Energy Proton: Neut Mode =2

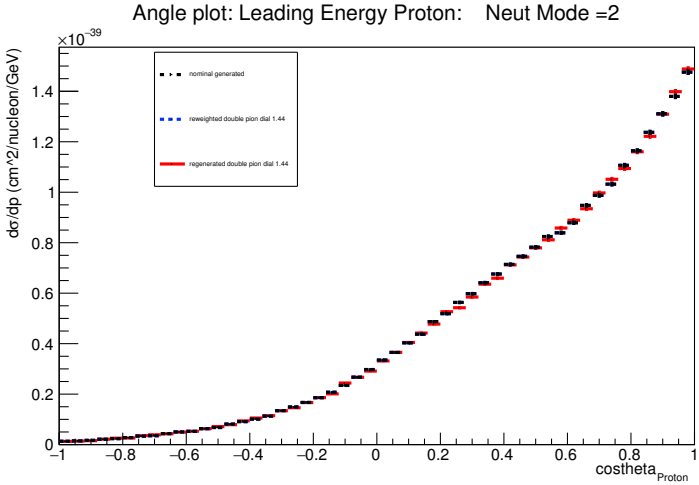

Angle plot: Every FSI Proton: Neut Mode =2

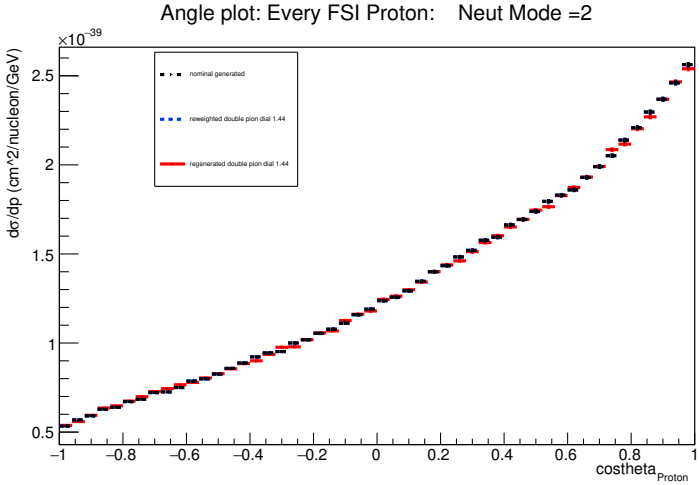

Angle plot: Leading Energy Proton: Neut Mode =2

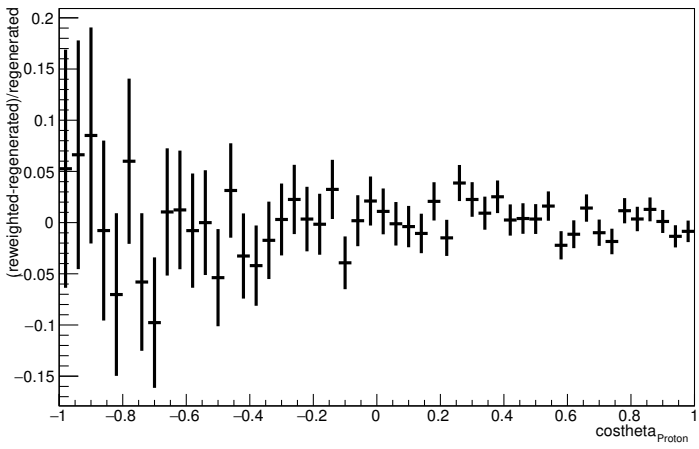

Angle plot: Every FSI Proton: Neut Mode =2

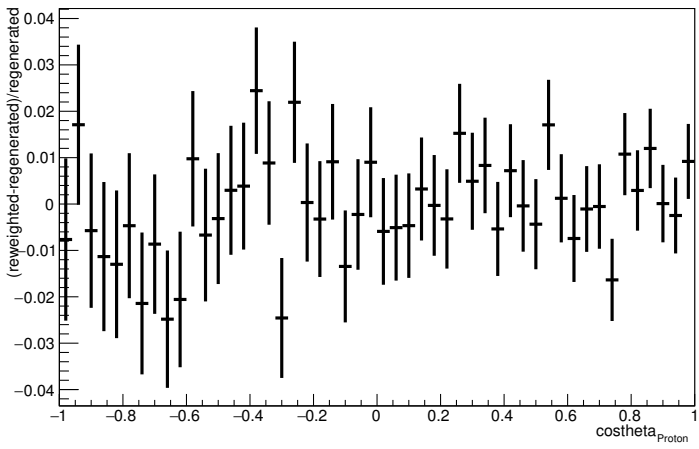

Energy plot: Leading Energy Neutron: Neut Mode =2

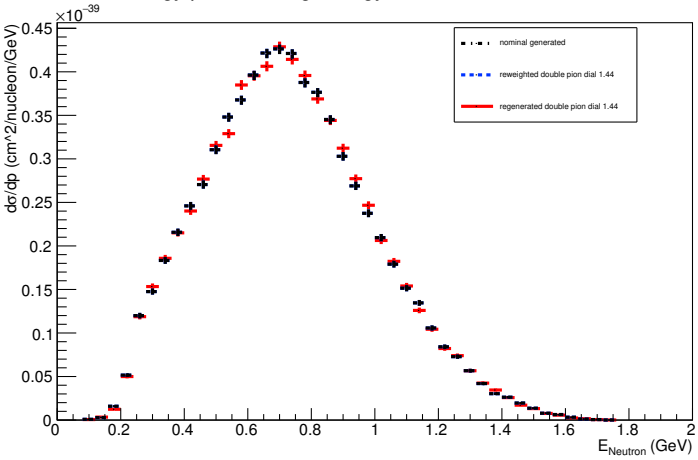

Energy plot: Every FSI Neutron: Neut Mode =2

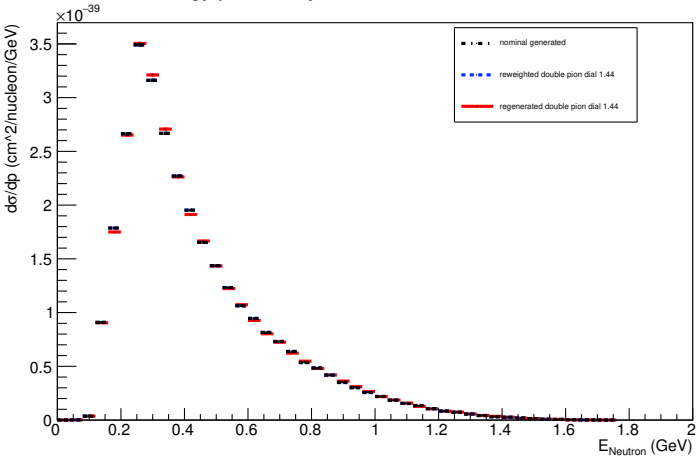

Energy plot: Leading Energy Neutron: Neut Mode =2

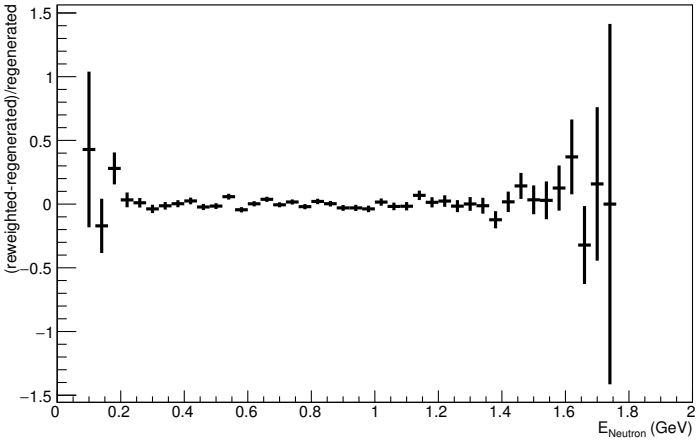

Energy plot: Every FSI Neutron: Neut Mode =2

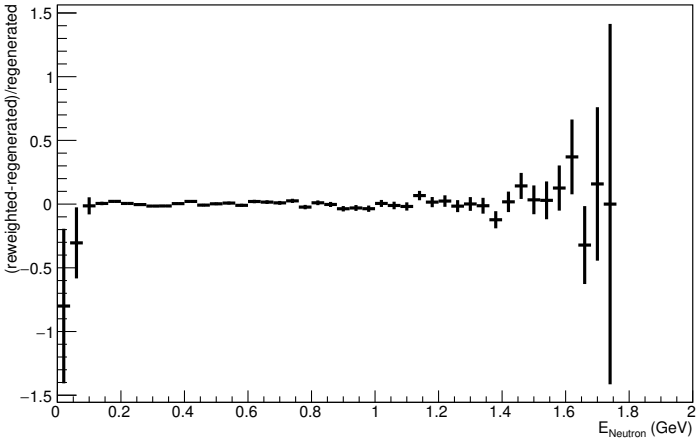

Angle plot: Leading Energy Neutron: Neut Mode =2

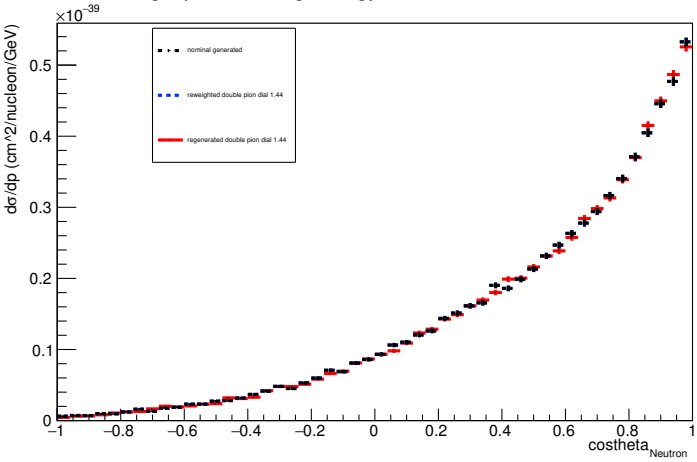

Angle plot: Every FSI Neutron: Neut Mode =2

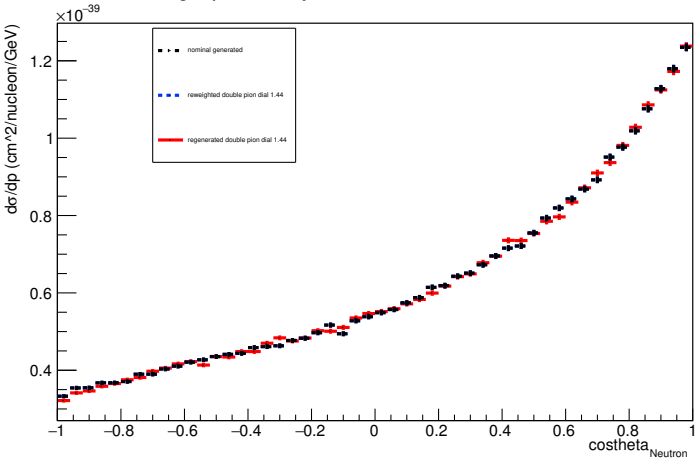

Angle plot: Leading Energy Neutron: Neut Mode =2

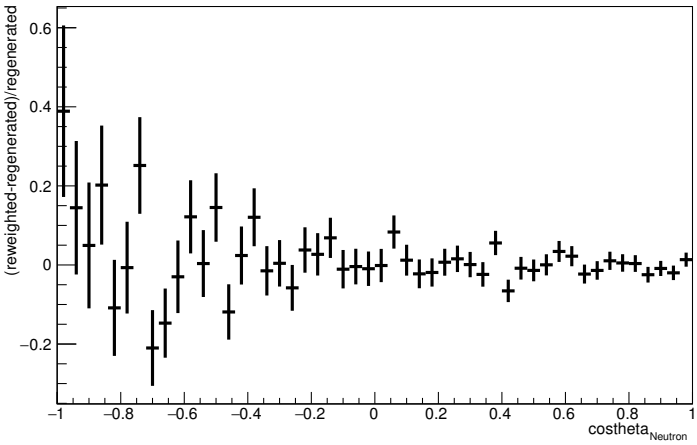

Angle plot: Every FSI Neutron: Neut Mode =2

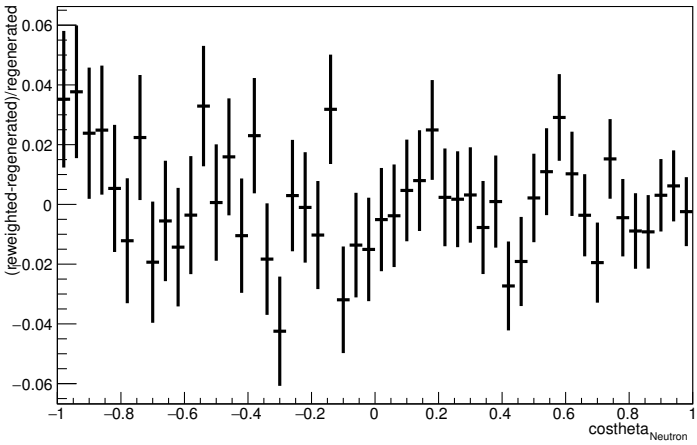

Energy plot: Leading Energy Lepton: Neut Mode =2

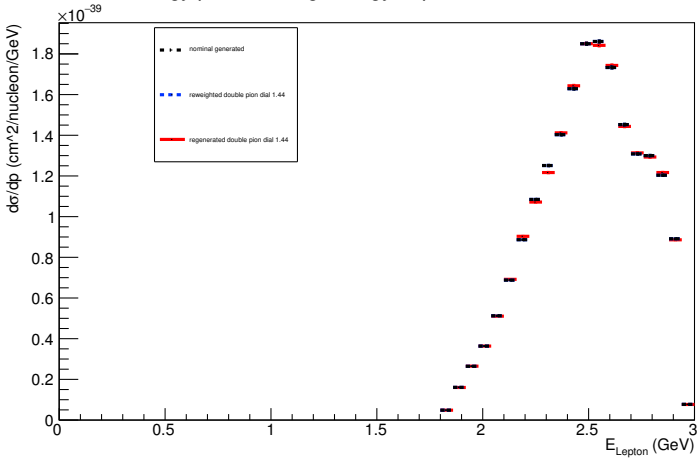

Angle plot: Leading Energy Lepton: Neut Mode =2

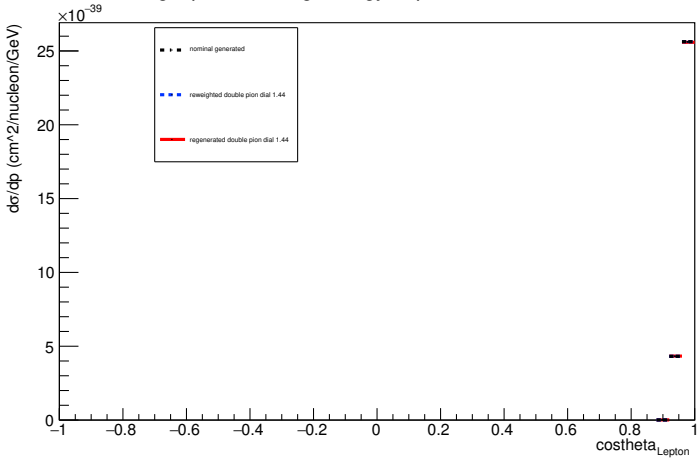

Energy plot: Leading Energy Lepton: Neut Mode =2

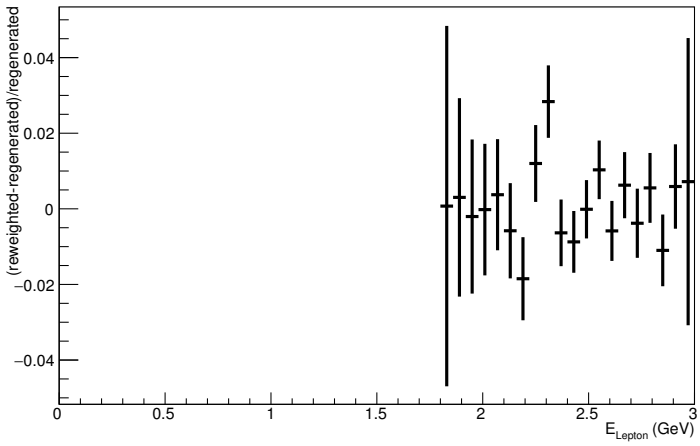

Angle plot: Leading Energy Lepton: Neut Mode =2

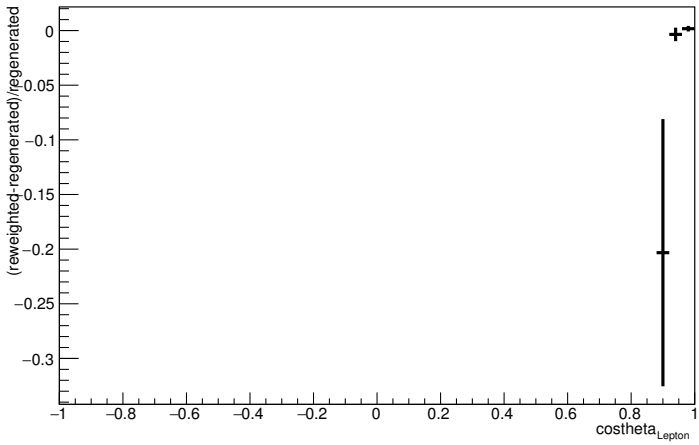

Energy plot: Leading Energy Pion: Neut Mode =2

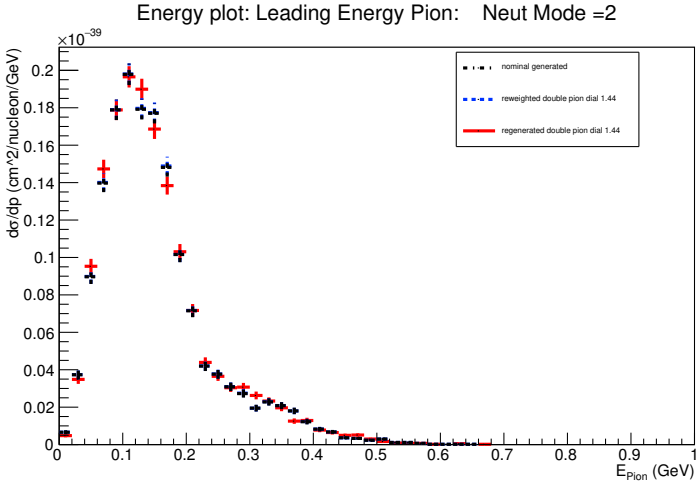

Energy plot: Every FSI Pion: Neut Mode =2

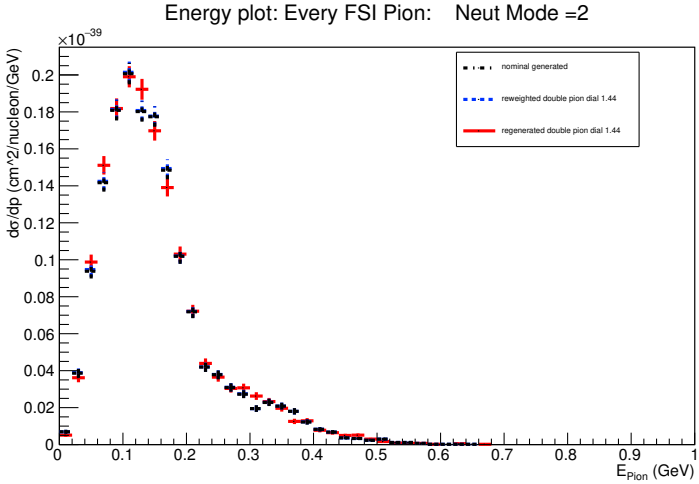

Energy plot: Leading Energy Pion: Neut Mode =2

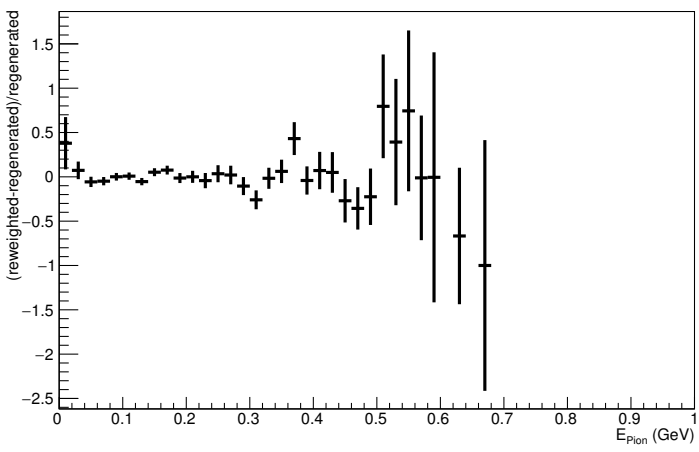

Energy plot: Every FSI Pion: Neut Mode =2

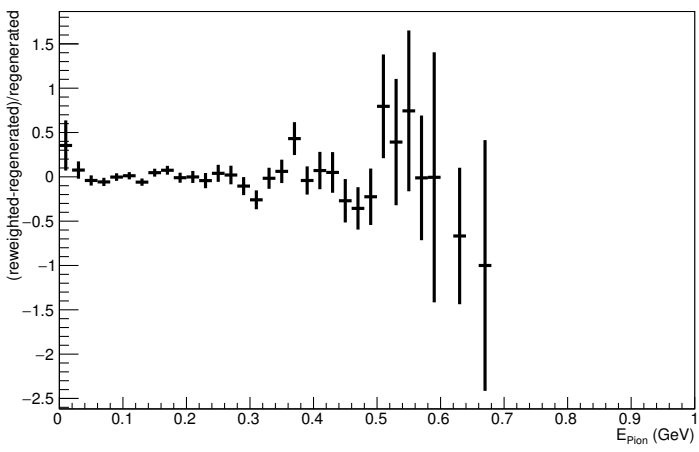

Angle plot: Leading Energy Pion: Neut Mode =2

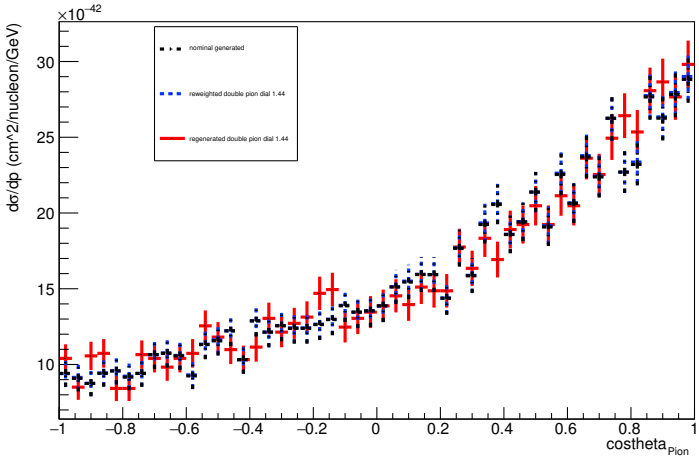

Angle plot: Every FSI Pion: Neut Mode =2

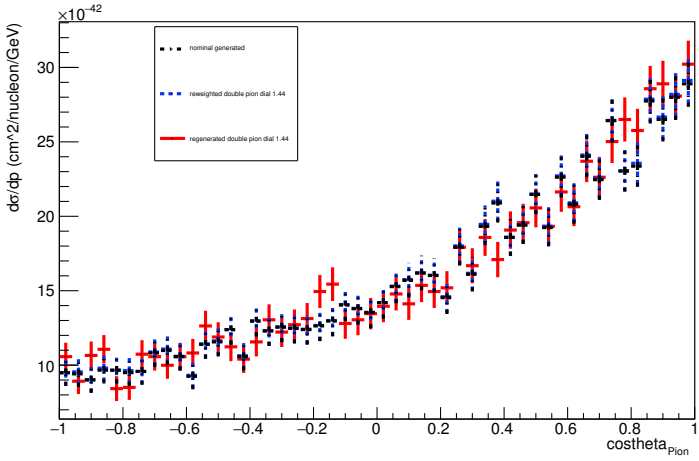

Angle plot: Leading Energy Pion: Neut Mode =2

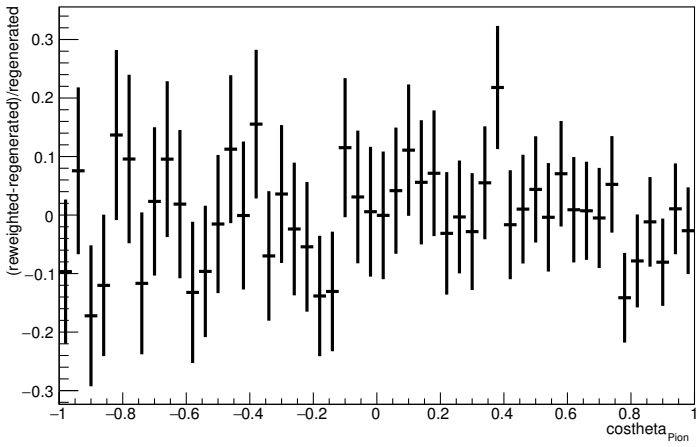

Angle plot: Every FSI Pion: Neut Mode =2

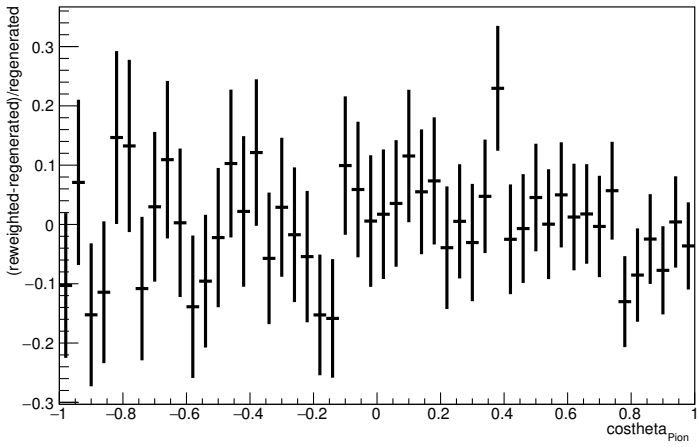

Energy plot: Leading Energy Nucleon: Neut Mode =11

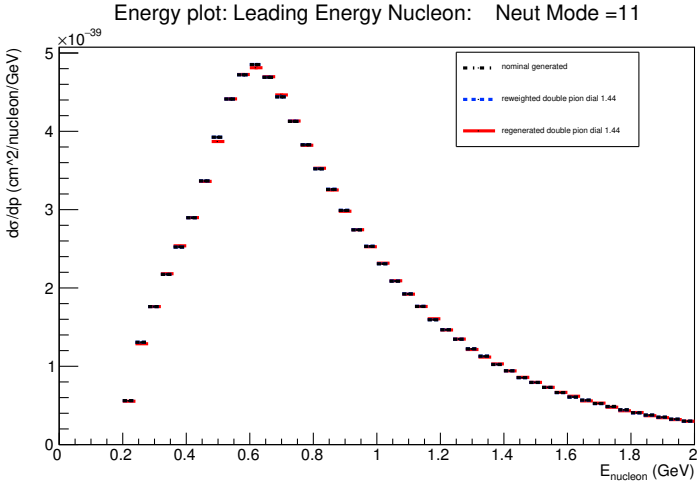

Energy plot: Every FSI Nucleon: Neut Mode =11

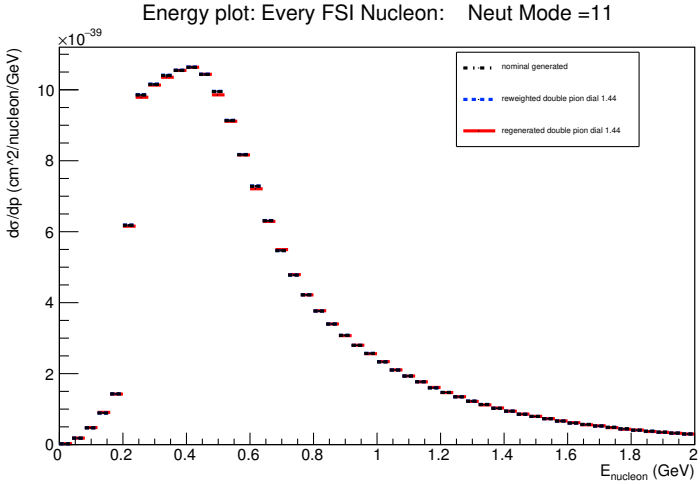

Energy plot: Leading Energy Nucleon: Neut Mode =11

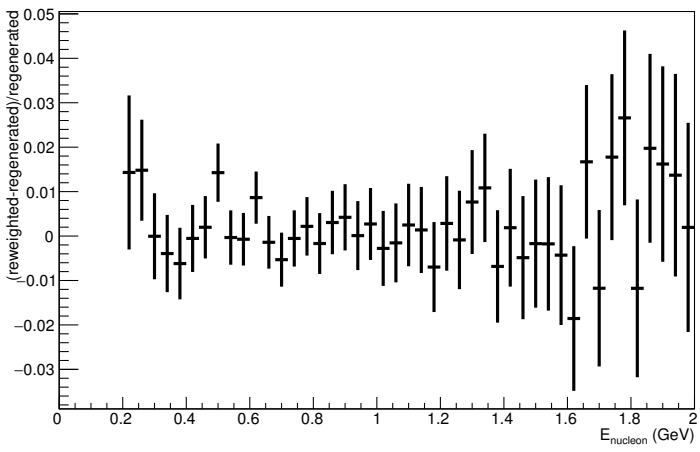

Energy plot: Every FSI Nucleon: Neut Mode =11

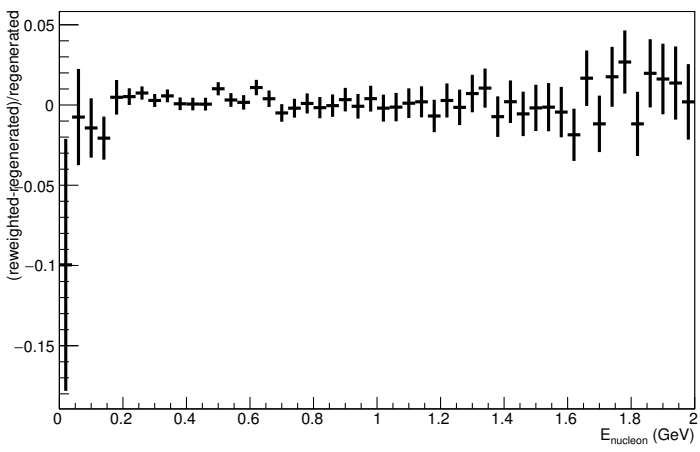

Angle plot: Leading Energy Nucleon: Neut Mode =11

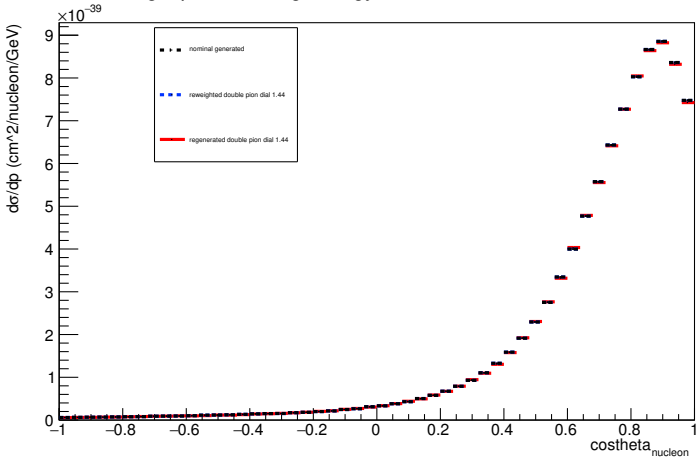

Angle plot: Every FSI Nucleon: Neut Mode =11

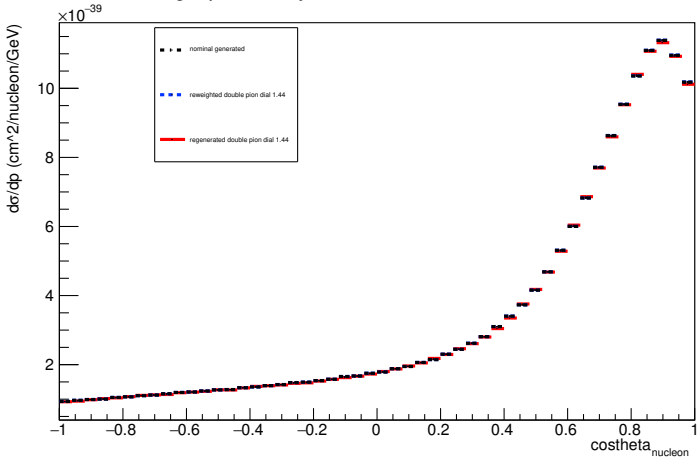

Angle plot: Leading Energy Nucleon: Neut Mode =11

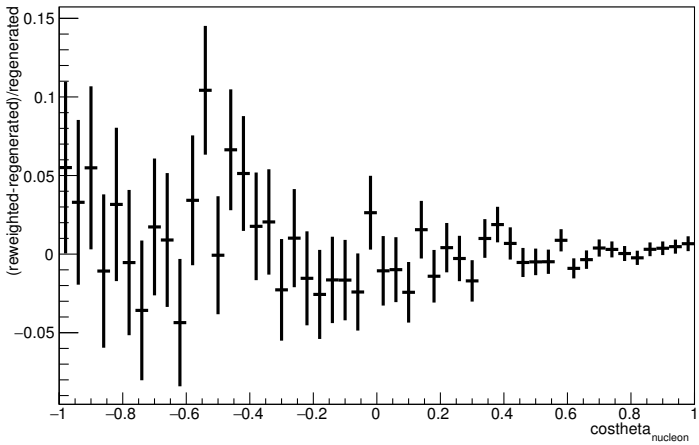

Angle plot: Every FSI Nucleon: Neut Mode =11

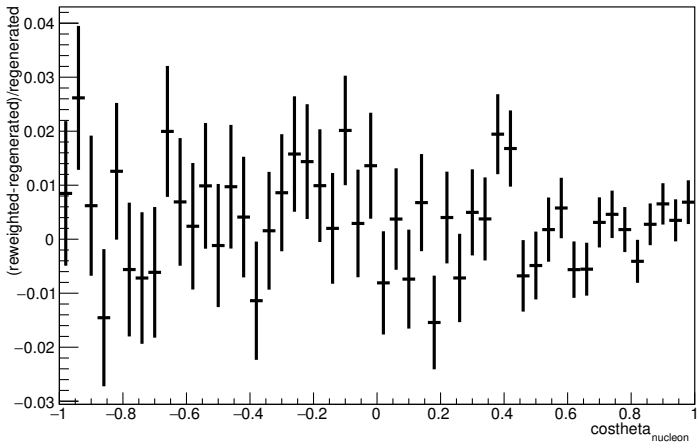

Energy plot: Leading Energy Proton: Neut Mode =11

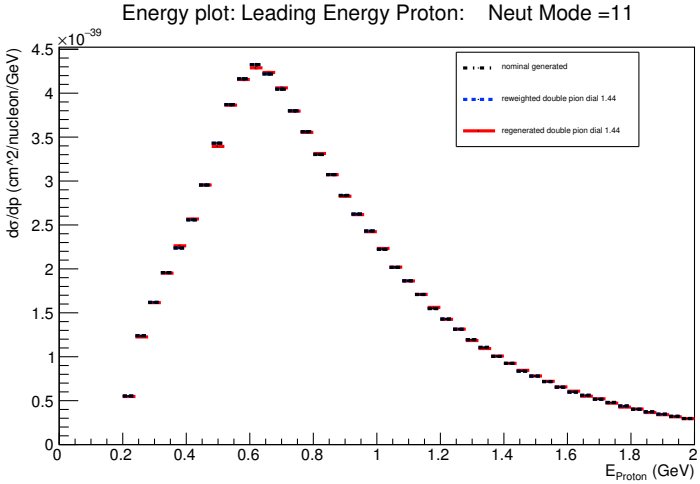

Energy plot: Every FSI Proton: Neut Mode =11

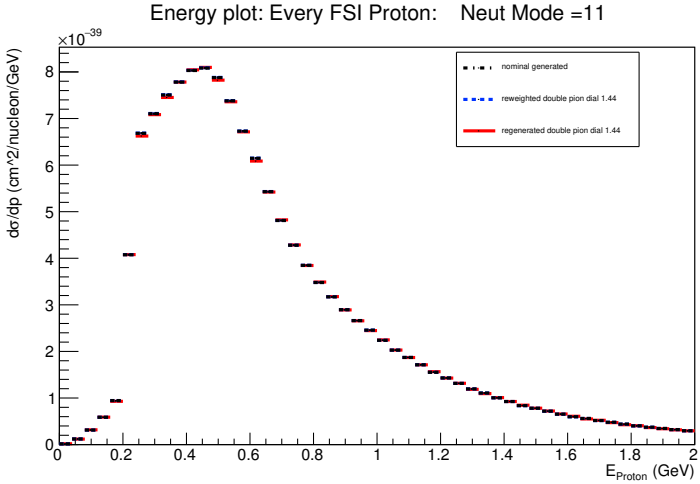

Energy plot: Leading Energy Proton: Neut Mode =11

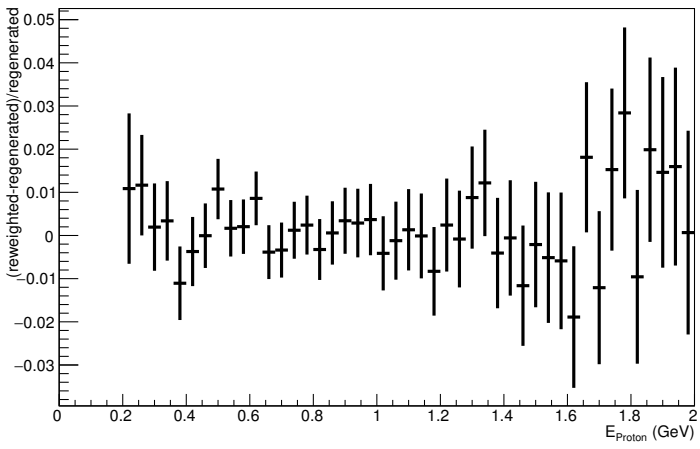

Energy plot: Every FSI Proton: Neut Mode =11

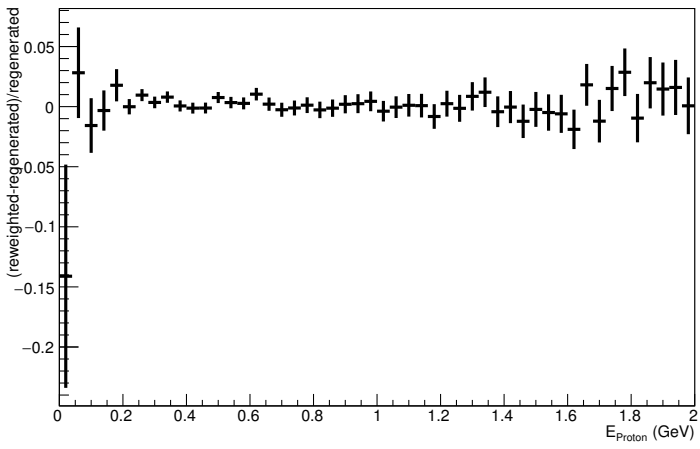

Angle plot: Leading Energy Proton: Neut Mode =11

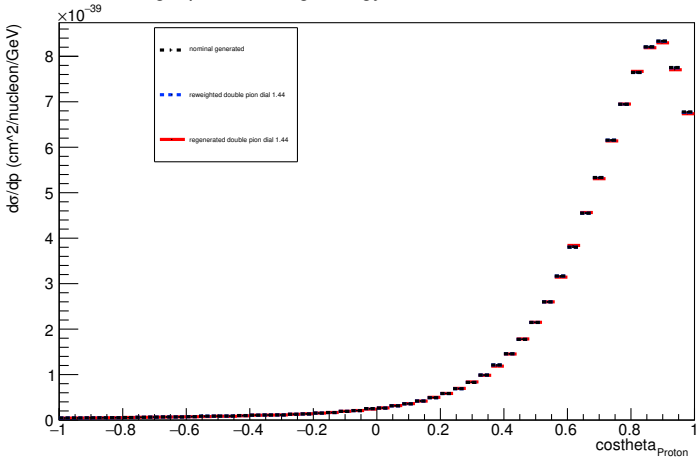

Angle plot: Every FSI Proton: Neut Mode =11

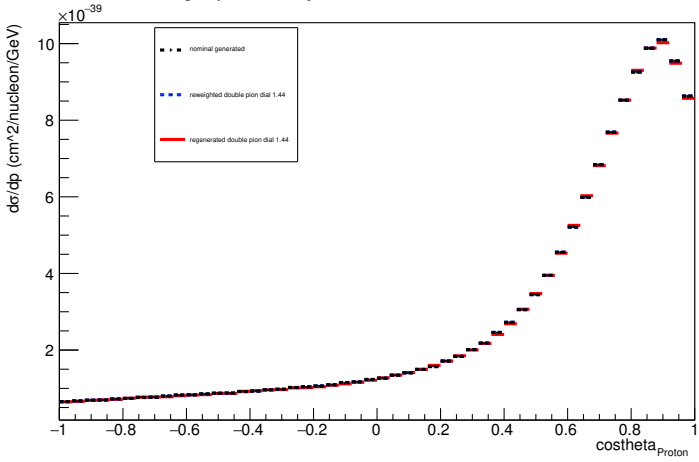

Angle plot: Leading Energy Proton: Neut Mode =11

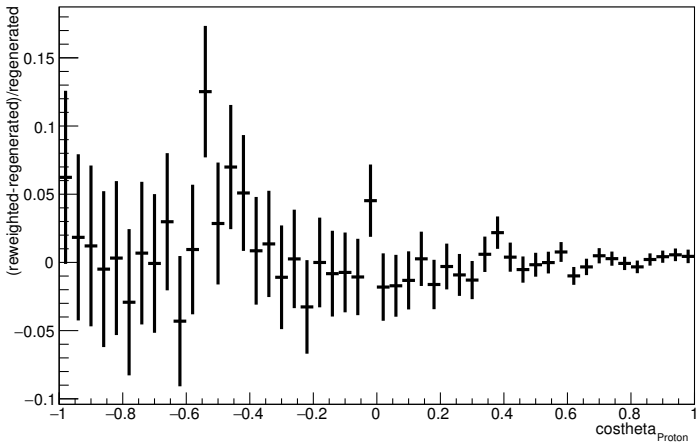

Angle plot: Every FSI Proton: Neut Mode =11

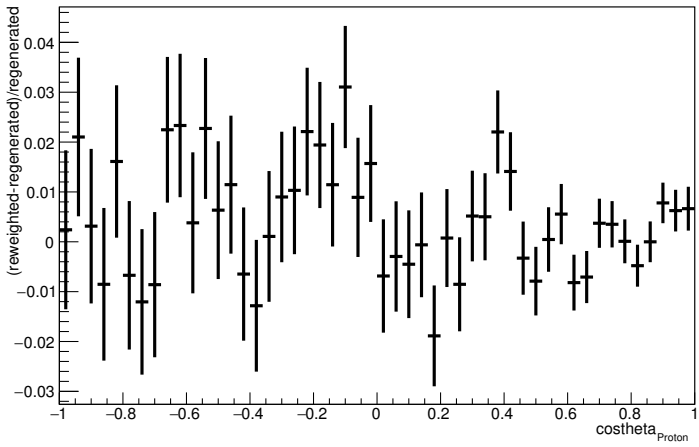

Energy plot: Leading Energy Neutron: Neut Mode =11

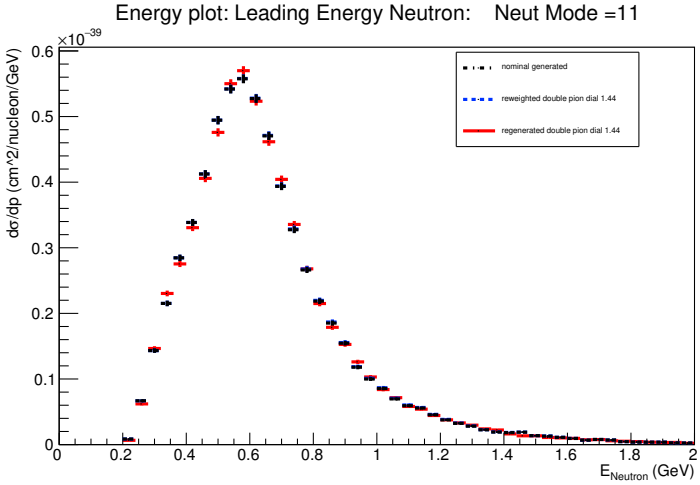

Energy plot: Every FSI Neutron: Neut Mode =11

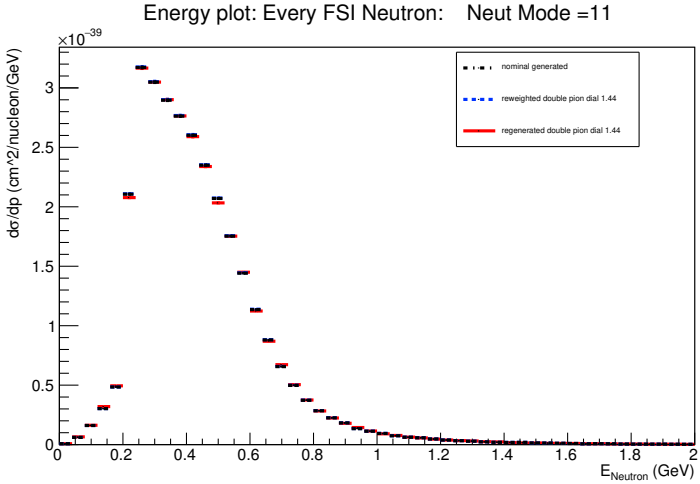

Energy plot: Leading Energy Neutron: Neut Mode =11

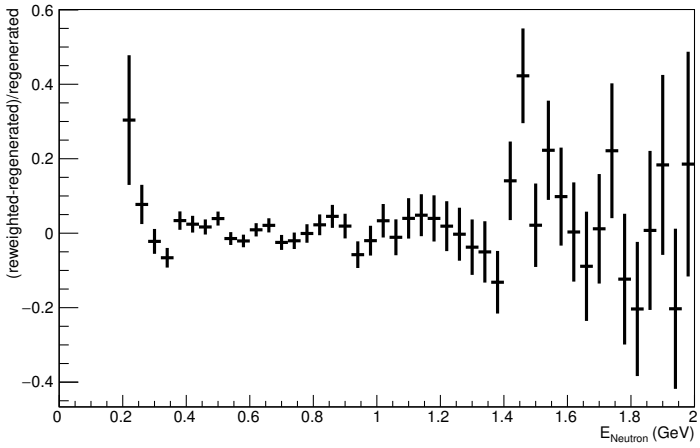

Energy plot: Every FSI Neutron: Neut Mode =11

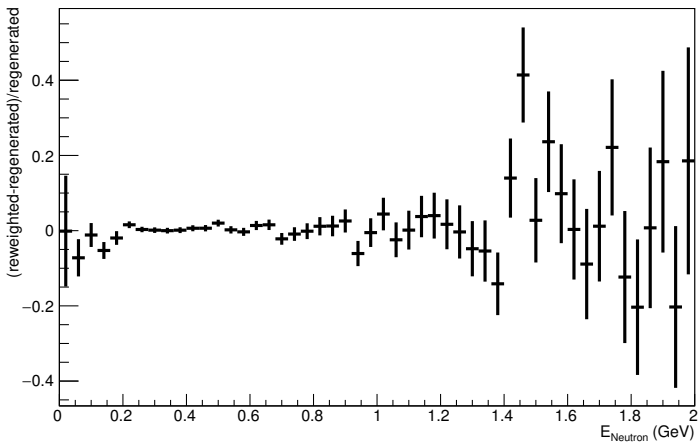

Angle plot: Leading Energy Neutron: Neut Mode =11

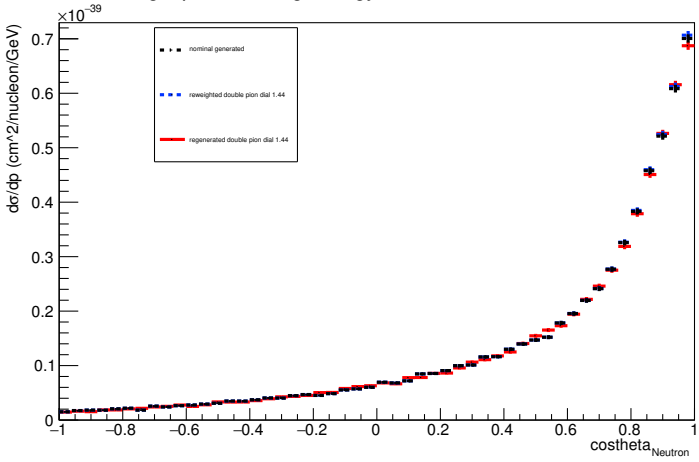

Angle plot: Every FSI Neutron: Neut Mode =11

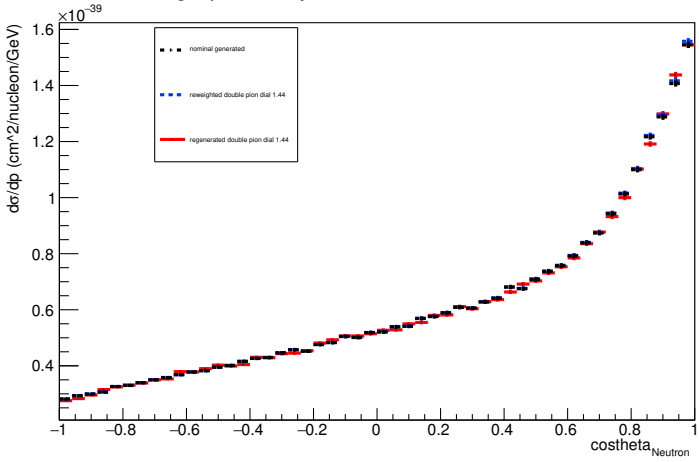

Angle plot: Leading Energy Neutron: Neut Mode =11

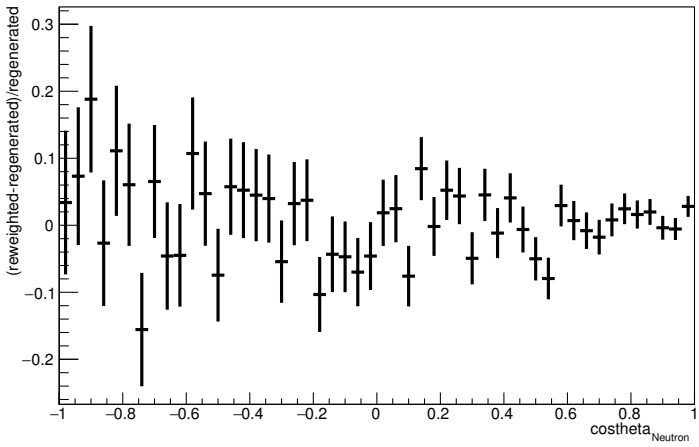

Angle plot: Every FSI Neutron: Neut Mode =11

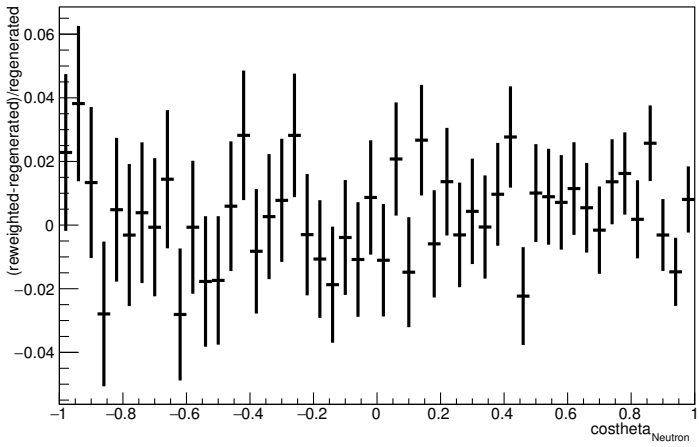

Energy plot: Leading Energy Lepton: Neut Mode =11

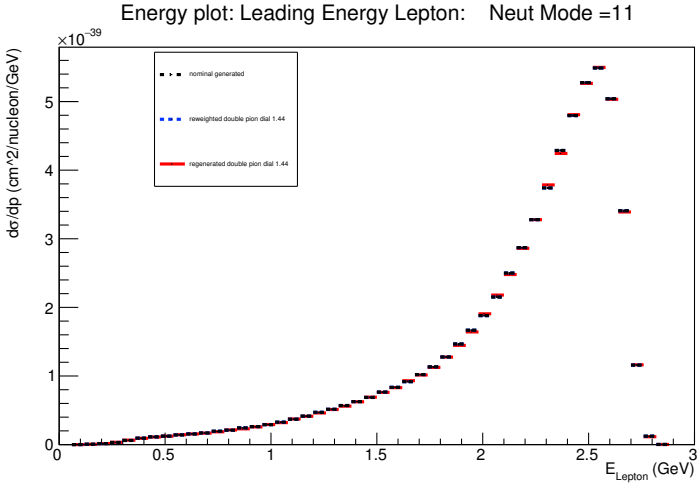

Angle plot: Leading Energy Lepton: Neut Mode =11

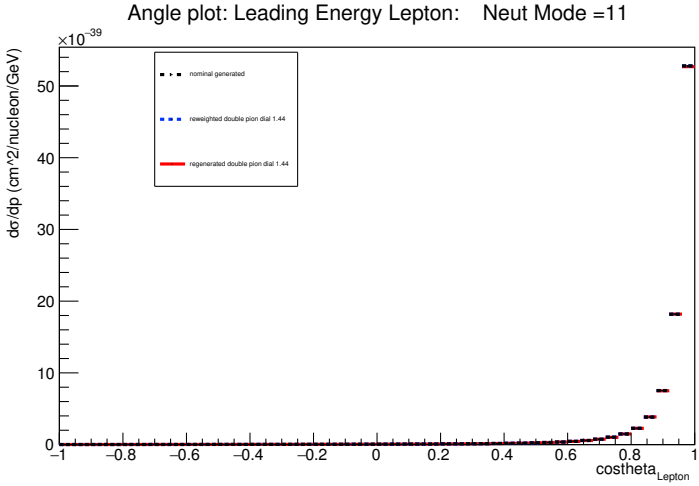

Energy plot: Leading Energy Lepton: Neut Mode =11

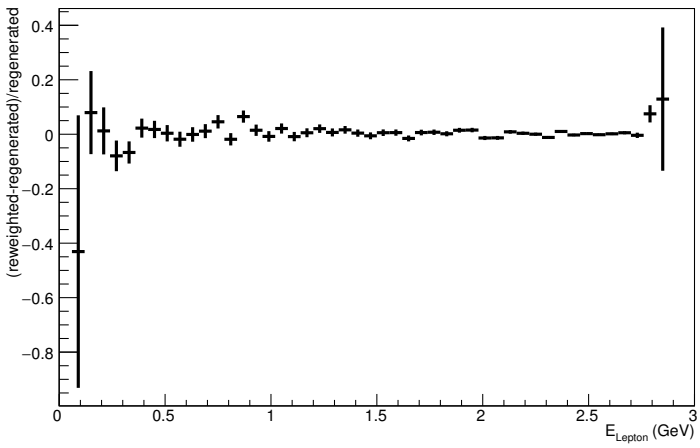

Angle plot: Leading Energy Lepton: Neut Mode =11

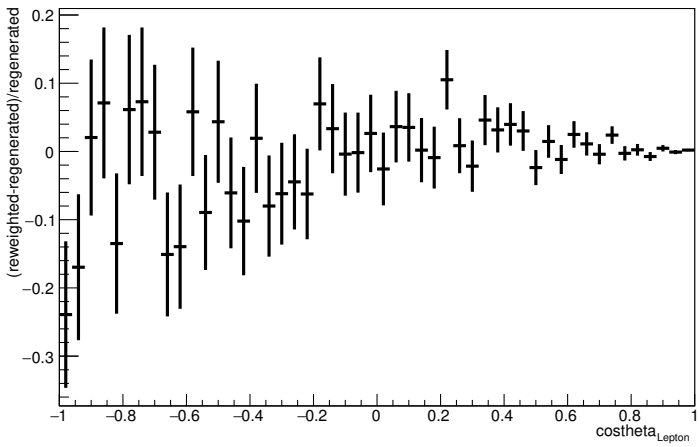

Energy plot: Leading Energy Pion: Neut Mode =11

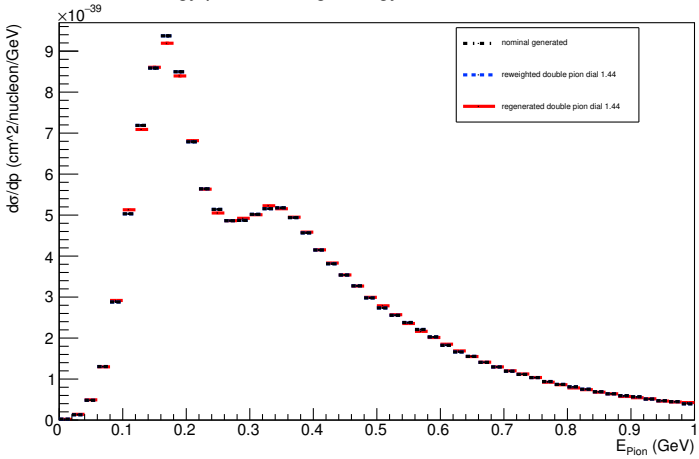

Energy plot: Every FSI Pion: Neut Mode =11

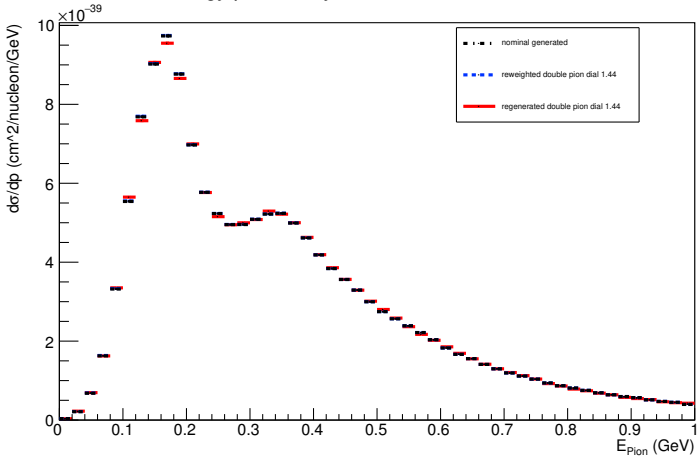

Energy plot: Leading Energy Pion: Neut Mode =11

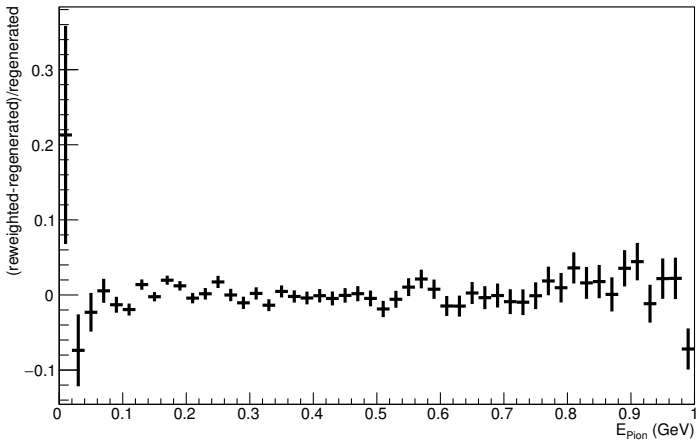

Energy plot: Every FSI Pion: Neut Mode =11

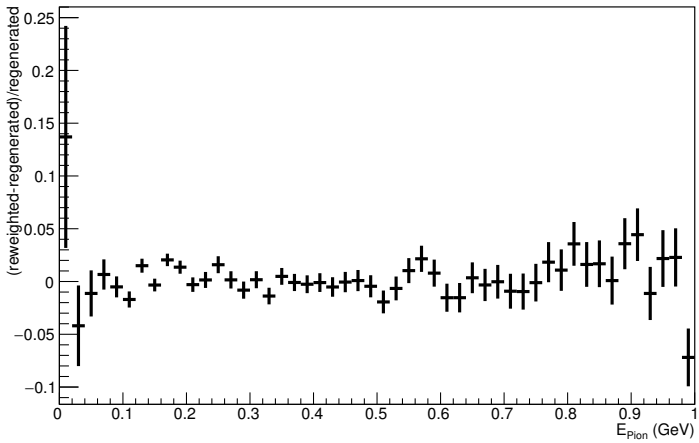

Angle plot: Leading Energy Pion: Neut Mode =11

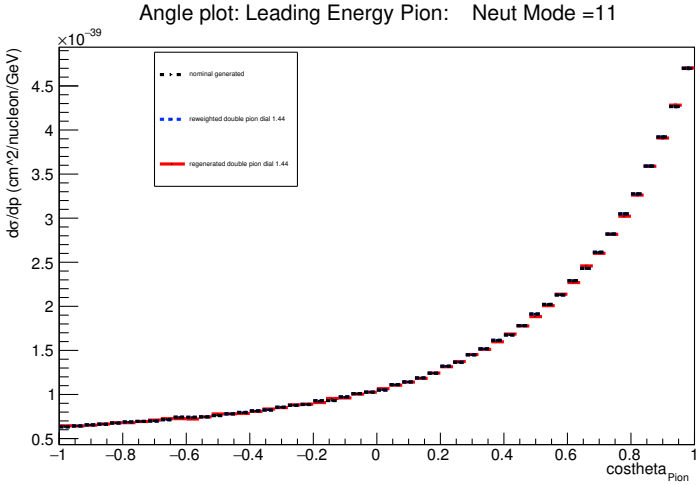

Angle plot: Every FSI Pion: Neut Mode =11

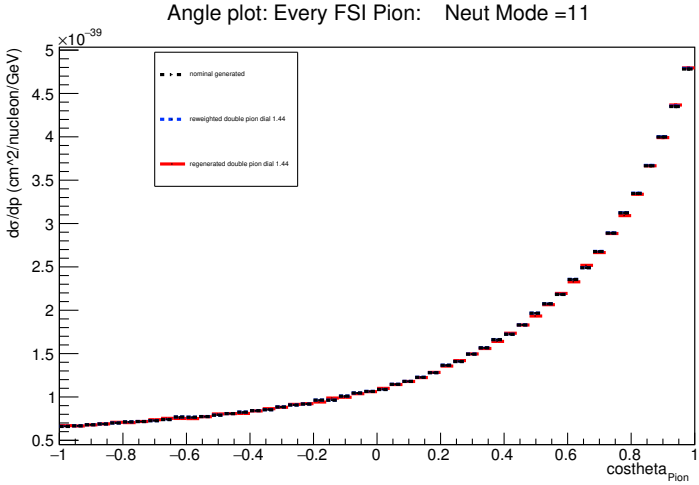

Angle plot: Leading Energy Pion: Neut Mode =11

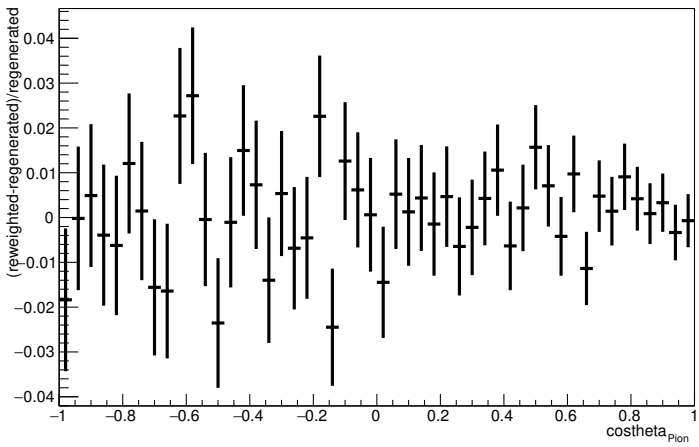

Angle plot: Every FSI Pion: Neut Mode =11

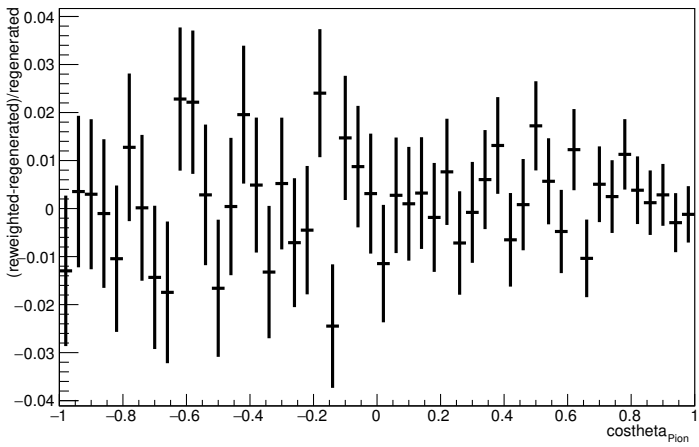

A.8. Double Pion Dial: varied down to 0.64

Energy plot: Leading Energy Nucleon: Neut Mode =AllModesCombined

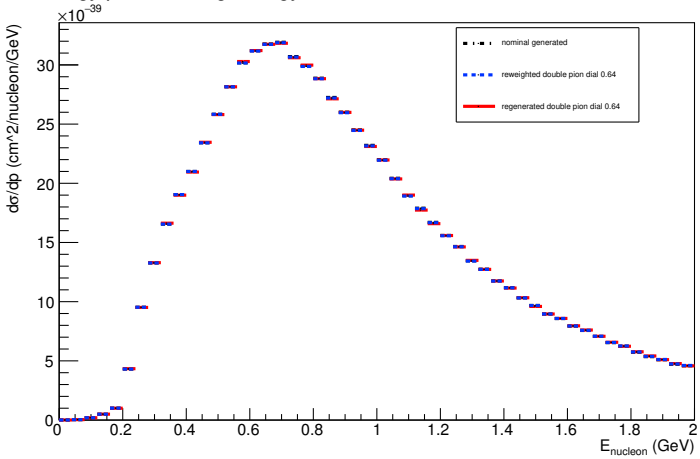

Energy plot: Every FSI Nucleon: Neut Mode =AllModesCombined

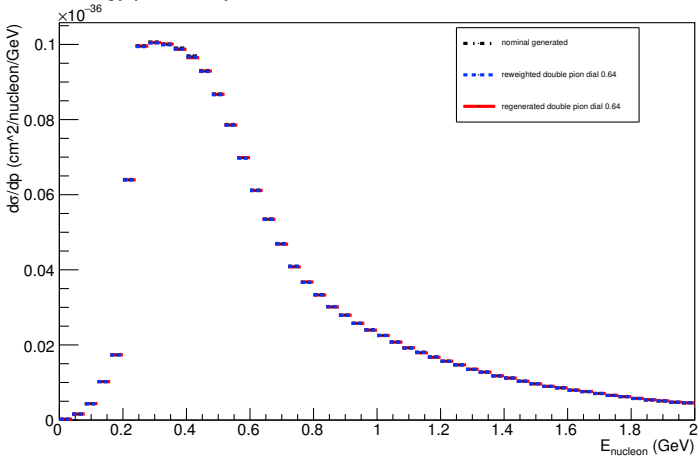

Energy plot: Leading Energy Nucleon: Neut Mode =AllModesCombined

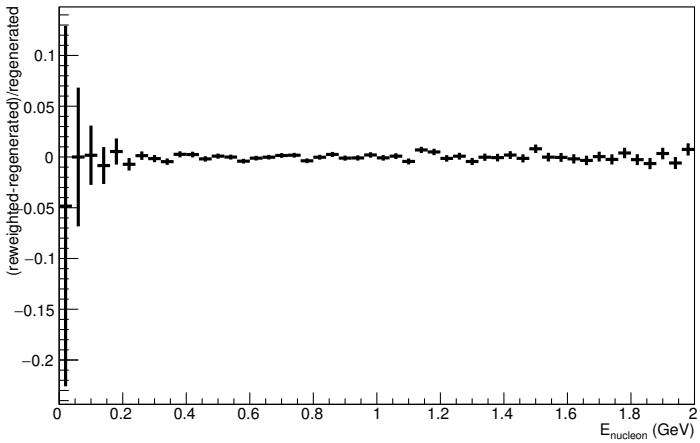

Energy plot: Every FSI Nucleon: Neut Mode =AllModesCombined

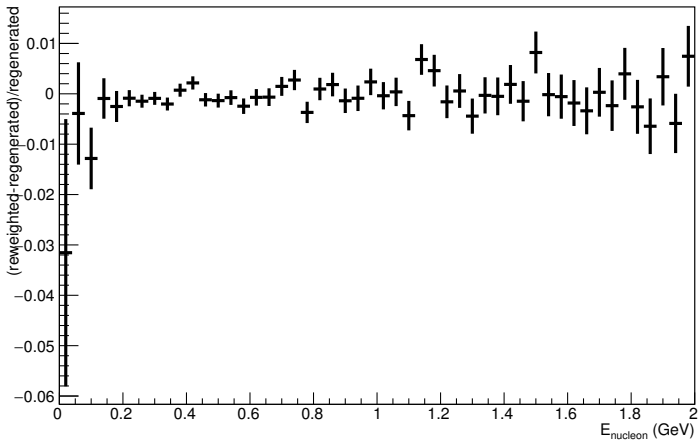

Angle plot: Leading Energy Nucleon: Neut Mode =AllModesCombined

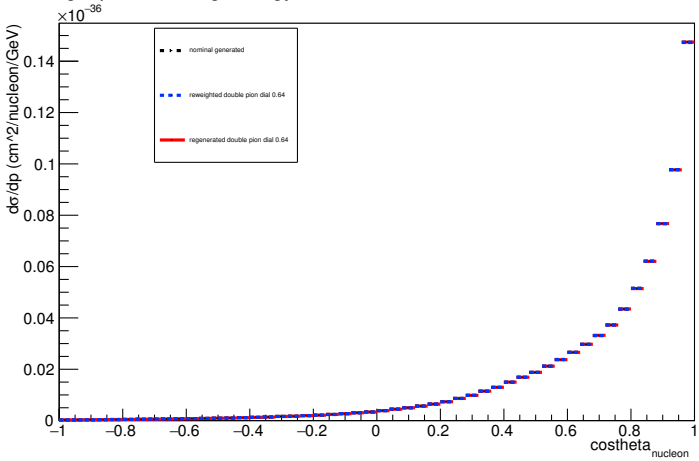

Angle plot: Every FSI Nucleon: Neut Mode =AllModesCombined

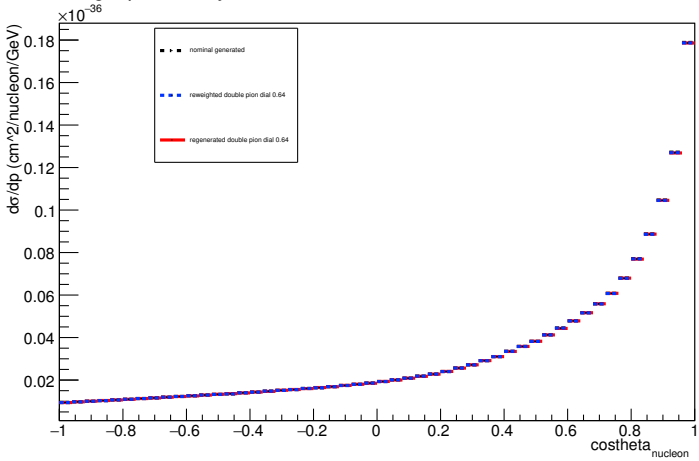

Angle plot: Leading Energy Nucleon: Neut Mode =AllModesCombined

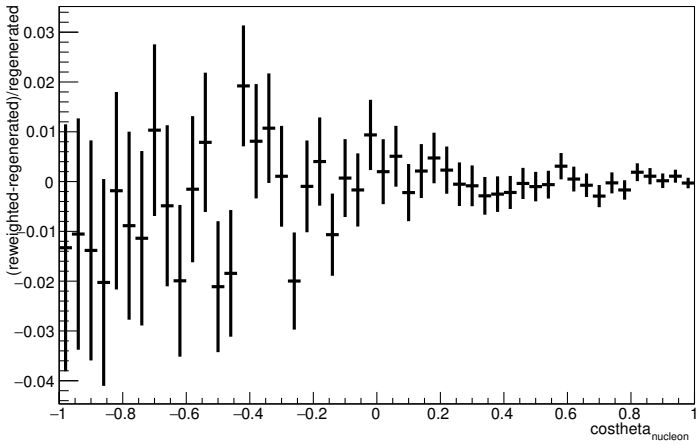

Angle plot: Every FSI Nucleon: Neut Mode =AllModesCombined

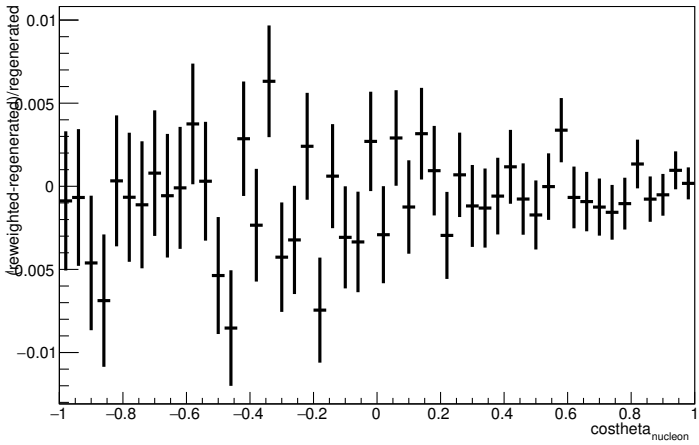

Energy plot: Leading Energy Proton: Neut Mode =AllModesCombined

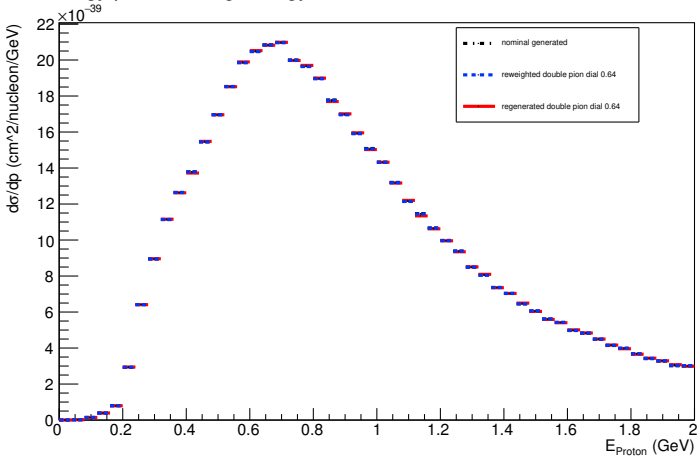

Energy plot: Every FSI Proton: Neut Mode =AllModesCombined

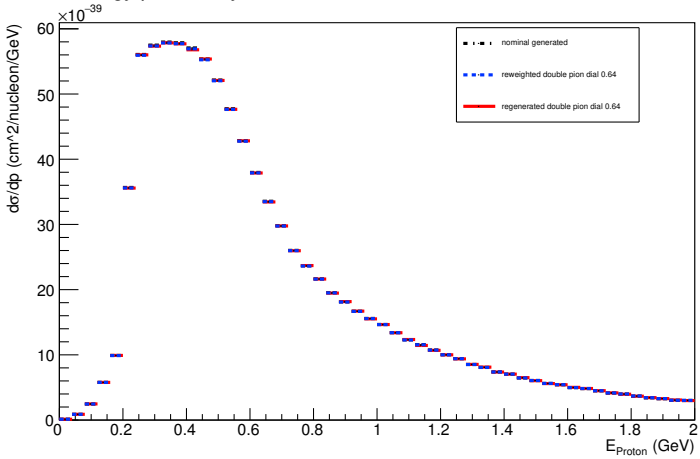

Energy plot: Leading Energy Proton: Neut Mode =AllModesCombined

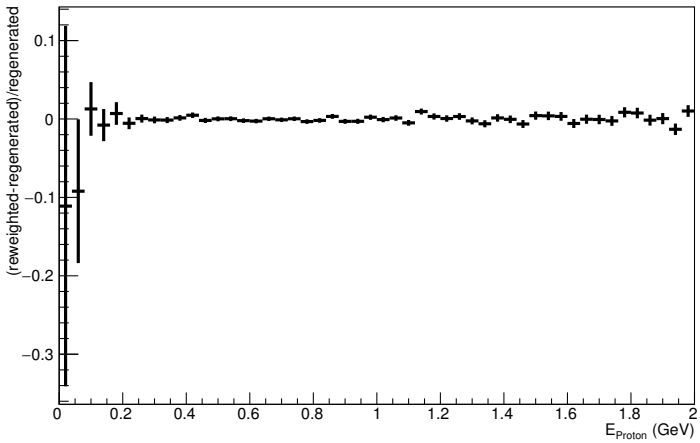

Energy plot: Every FSI Proton: Neut Mode =AllModesCombined

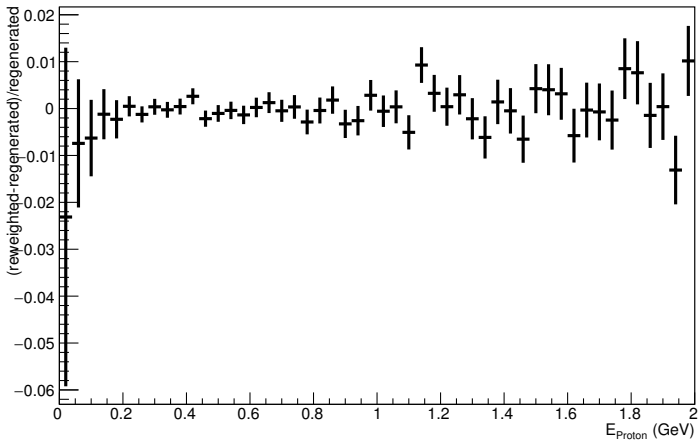

Angle plot: Leading Energy Proton: Neut Mode =AllModesCombined

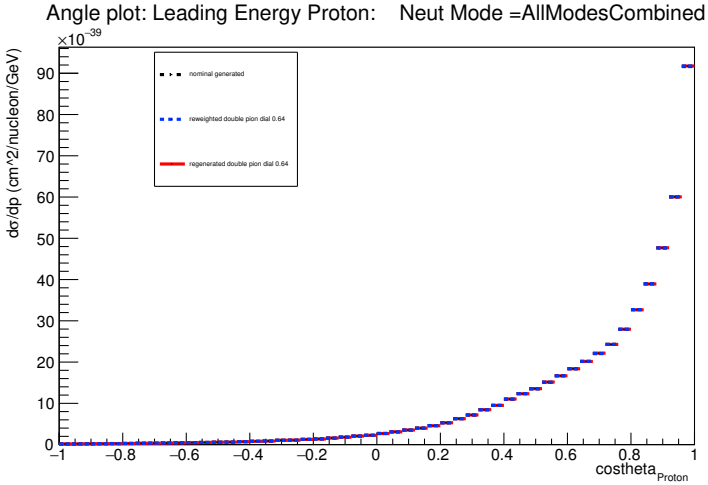

Angle plot: Every FSI Proton: Neut Mode =AllModesCombined

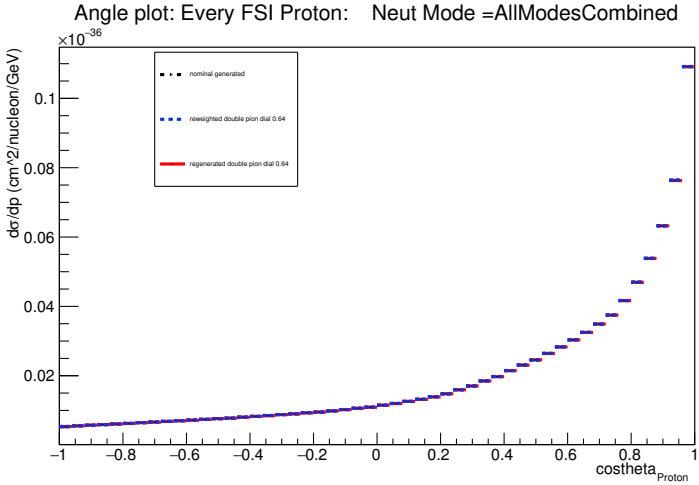

Angle plot: Leading Energy Proton: Neut Mode =AllModesCombined

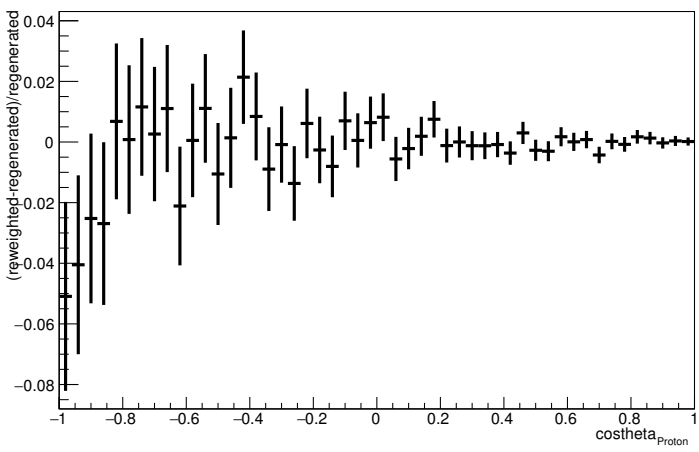

Angle plot: Every FSI Proton: Neut Mode =AllModesCombined

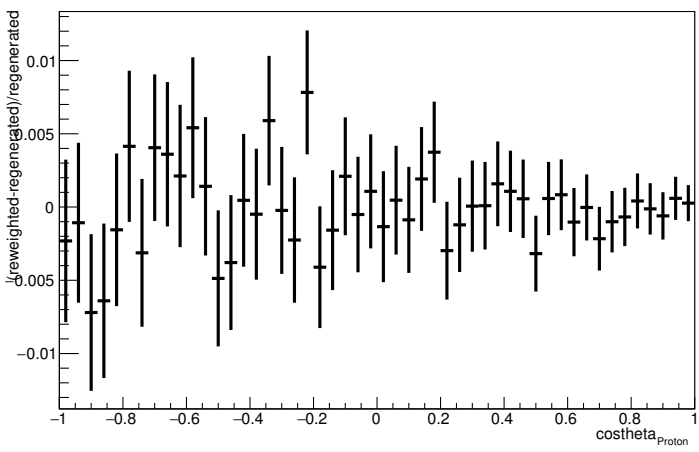

Energy plot: Leading Energy Neutron: Neut Mode =AllModesCombined

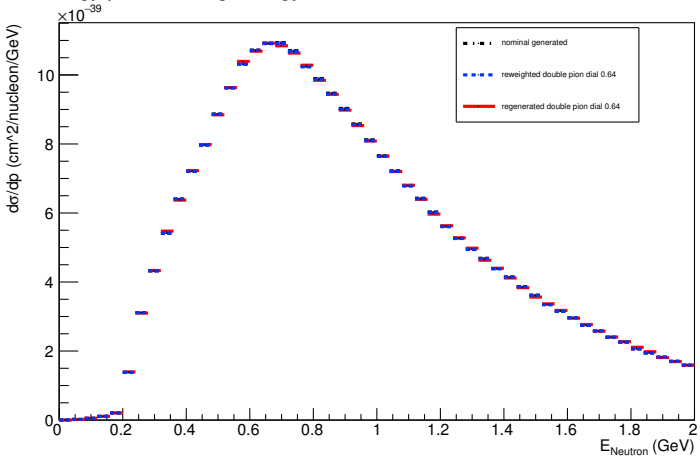

Energy plot: Every FSI Neutron: Neut Mode =AllModesCombined

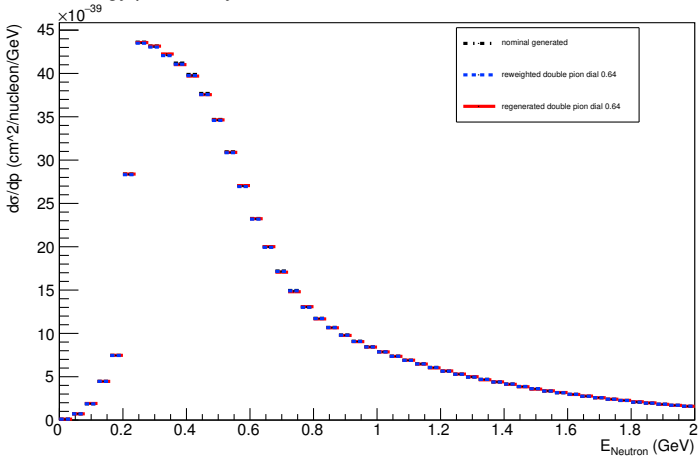

Energy plot: Leading Energy Neutron: Neut Mode =AllModesCombined

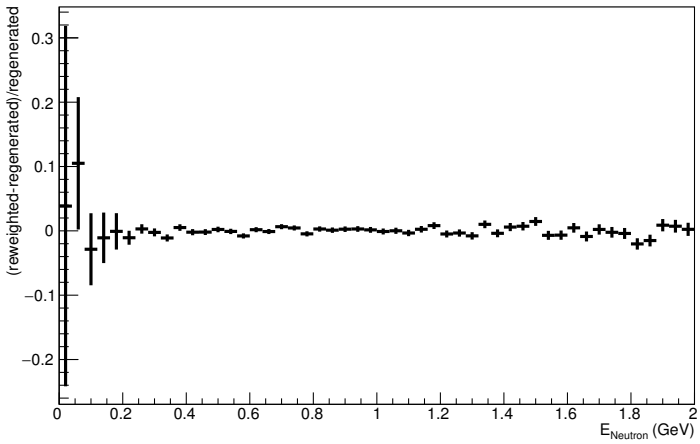

Energy plot: Every FSI Neutron: Neut Mode =AllModesCombined

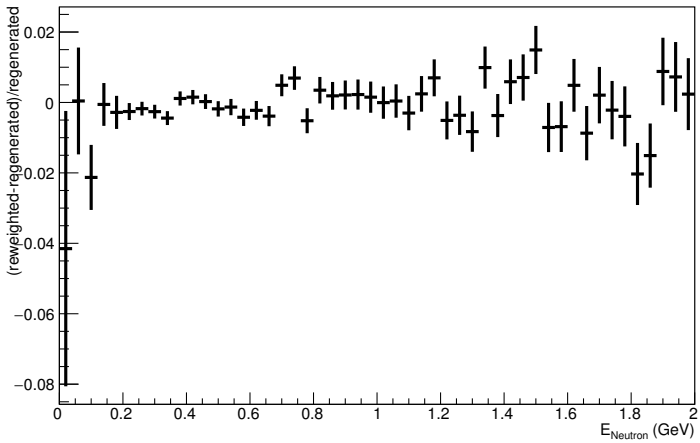

Angle plot: Leading Energy Neutron: Neut Mode =AllModesCombined

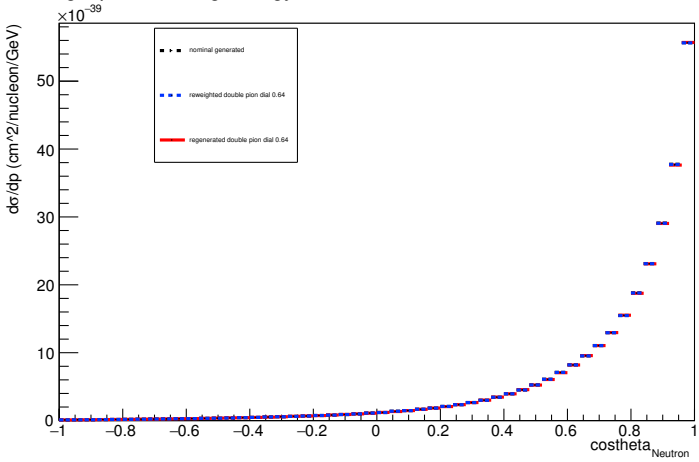

Angle plot: Every FSI Neutron: Neut Mode =AllModesCombined

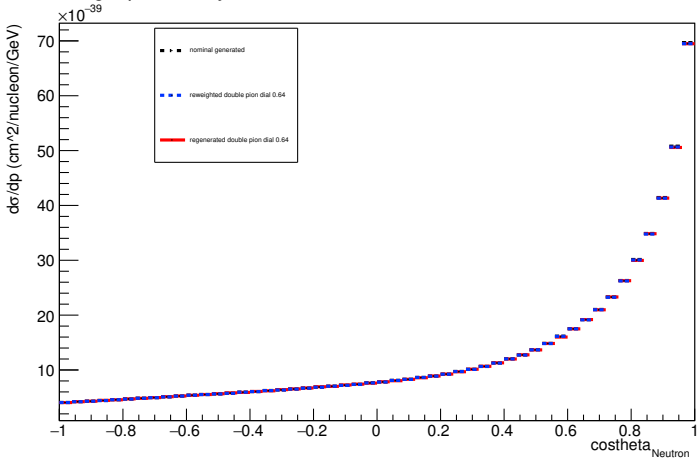

Angle plot: Leading Energy Neutron: Neut Mode =AllModesCombined

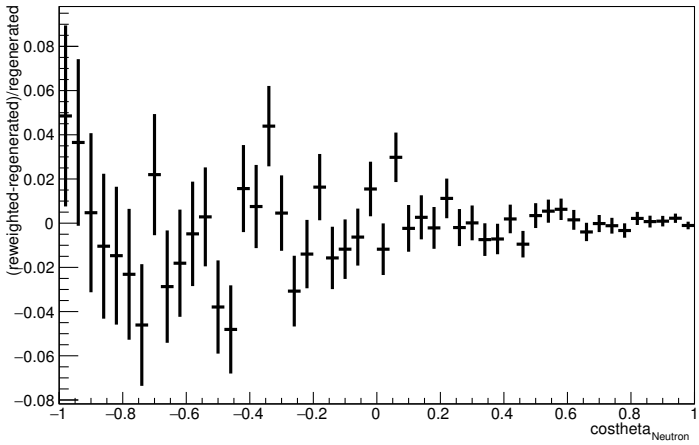

Angle plot: Every FSI Neutron: Neut Mode =AllModesCombined

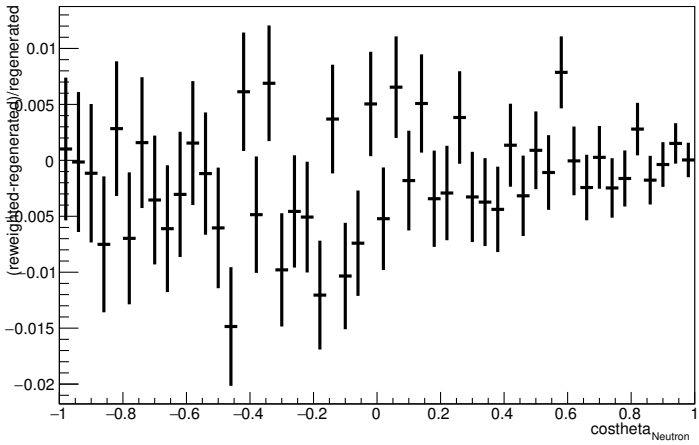

Energy plot: Leading Energy Lepton: Neut Mode =AllModesCombined

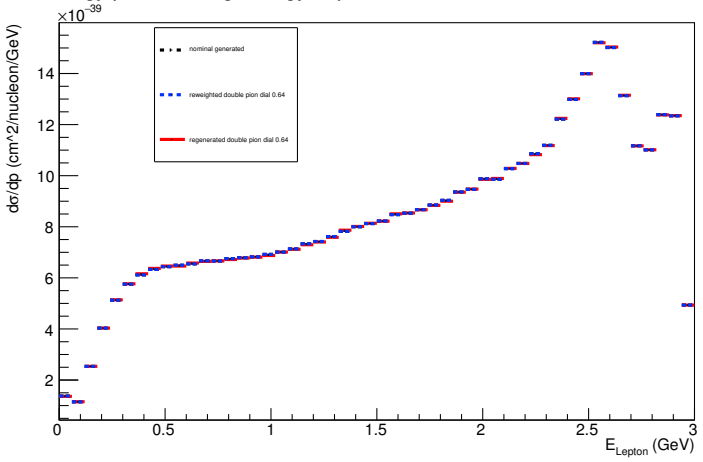

Angle plot: Leading Energy Lepton: Neut Mode =AllModesCombined

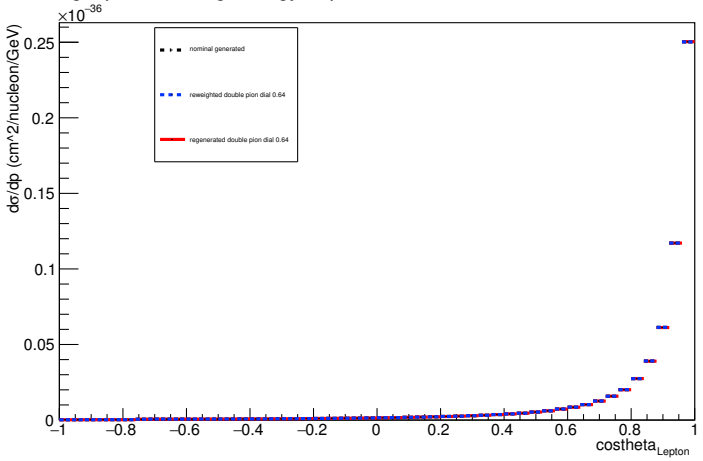

Energy plot: Leading Energy Lepton: Neut Mode =AllModesCombined

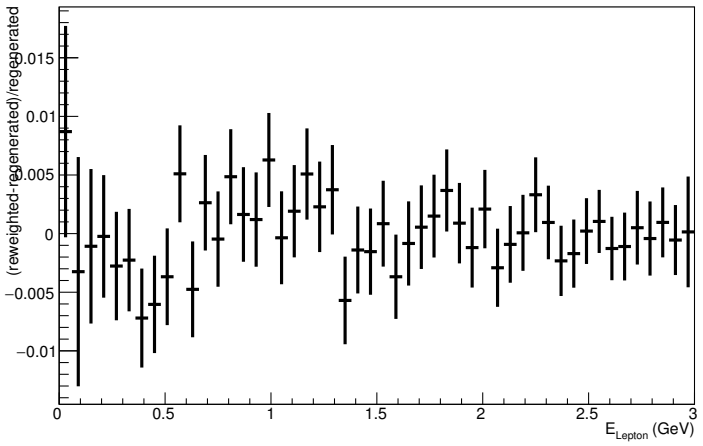

Angle plot: Leading Energy Lepton: Neut Mode =AllModesCombined

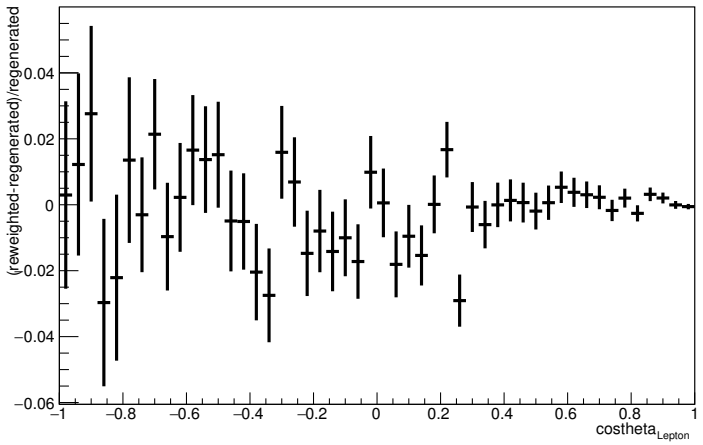

Energy plot: Leading Energy Pion: Neut Mode =AllModesCombined

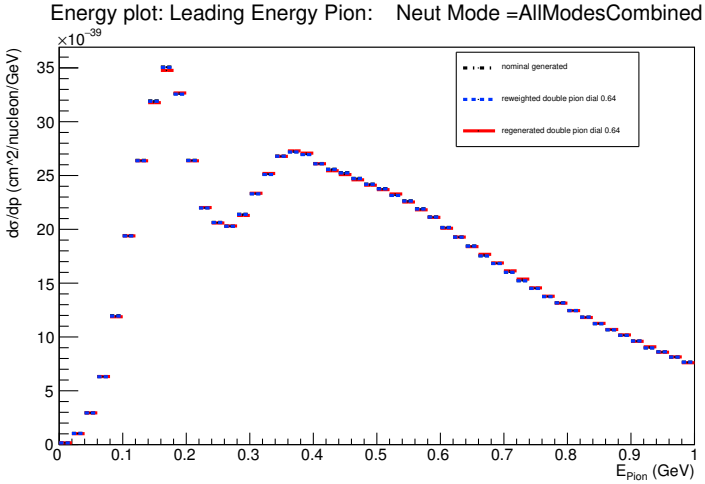

Energy plot: Every FSI Pion: Neut Mode =AllModesCombined

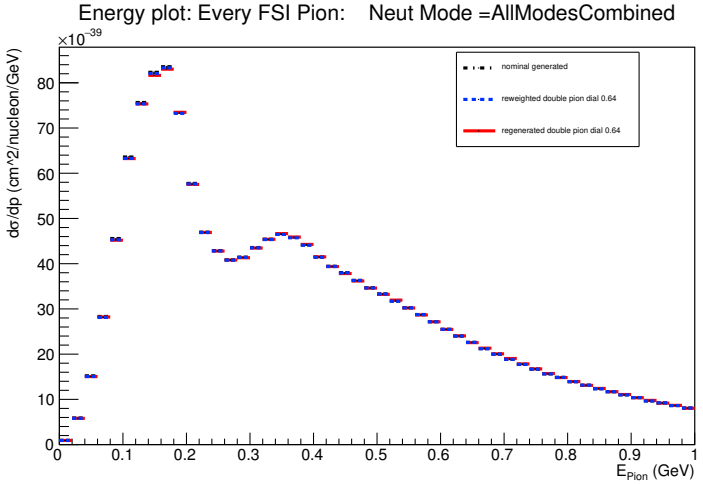

Energy plot: Leading Energy Pion: Neut Mode =AllModesCombined

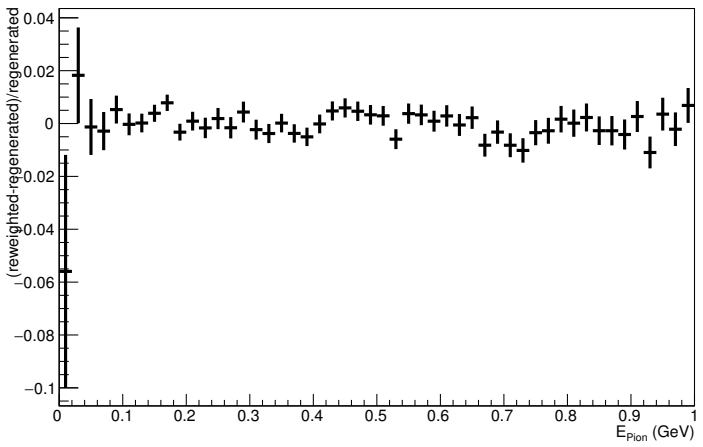

Energy plot: Every FSI Pion: Neut Mode =AllModesCombined

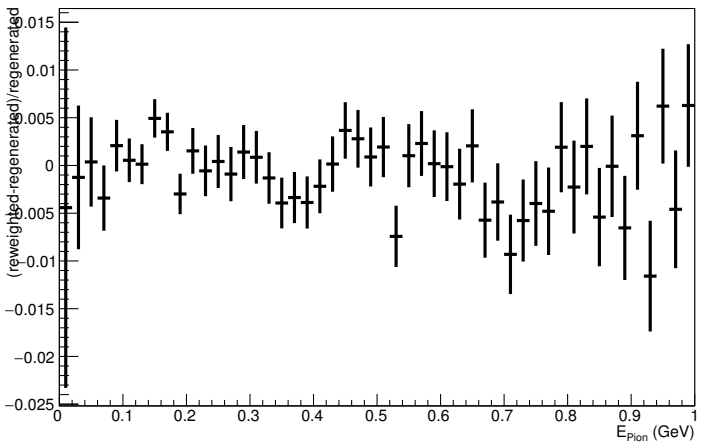

Angle plot: Leading Energy Pion: Neut Mode =AllModesCombined

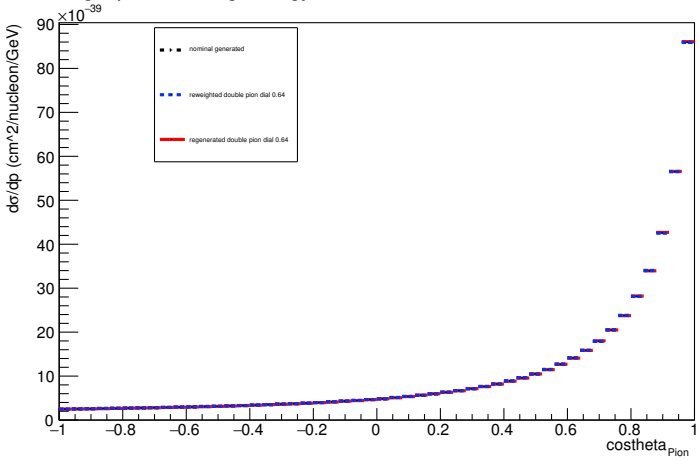

Angle plot: Every FSI Pion: Neut Mode =AllModesCombined

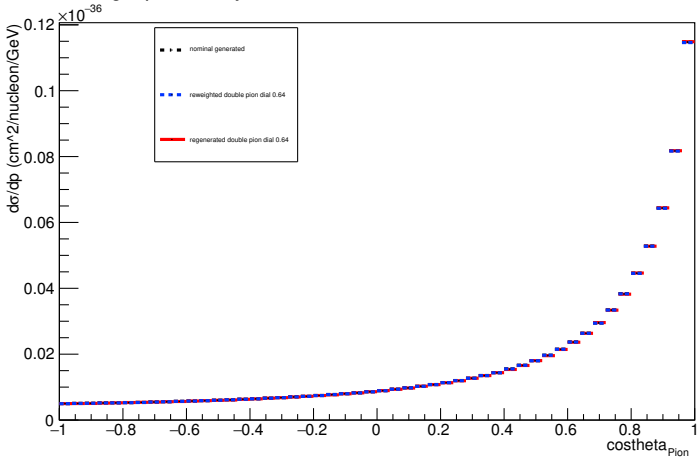

Angle plot: Leading Energy Pion: Neut Mode =AllModesCombined

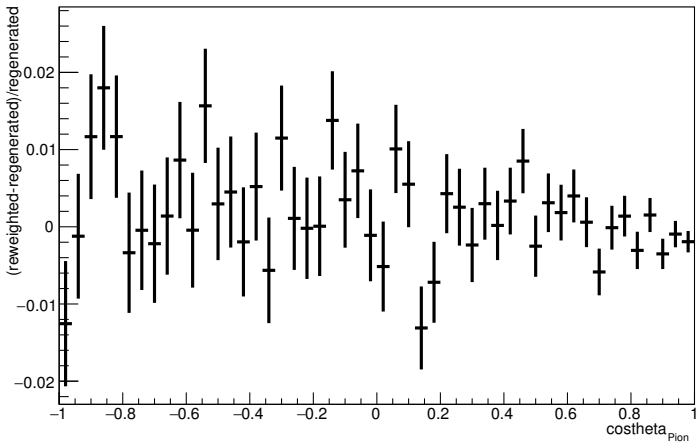

Angle plot: Every FSI Pion: Neut Mode =AllModesCombined

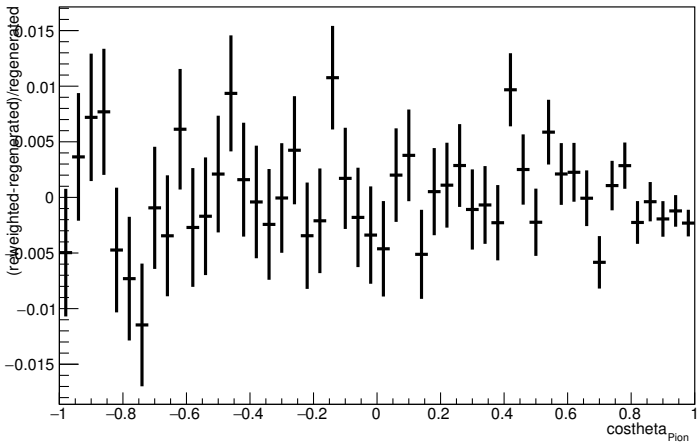

Energy plot: Leading Energy Nucleon: Neut Mode =1

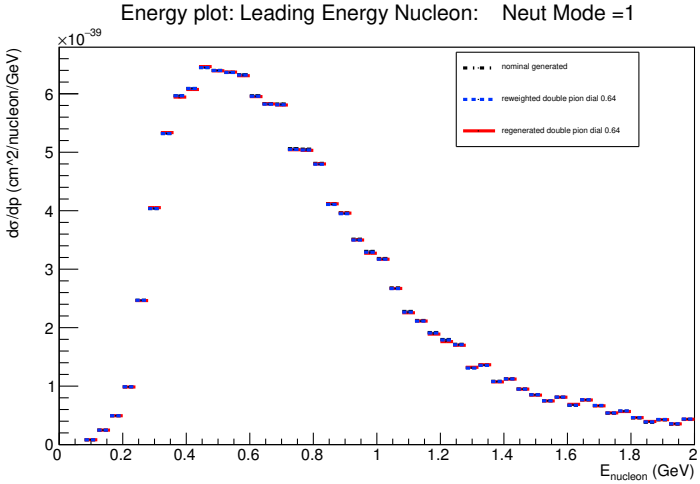

Energy plot: Every FSI Nucleon: Neut Mode =1

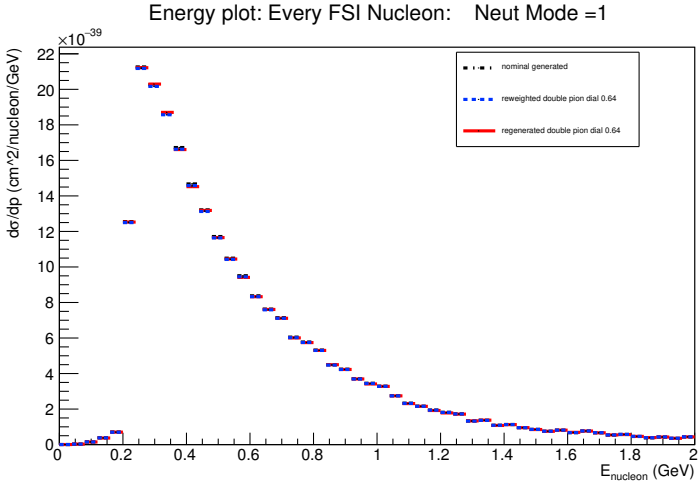

Energy plot: Leading Energy Nucleon: Neut Mode =1

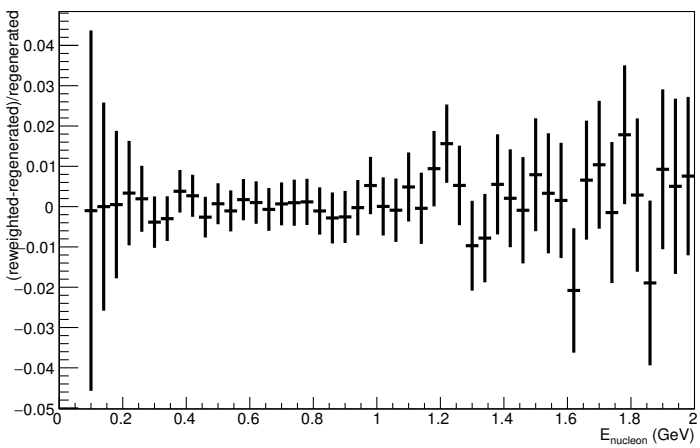

Energy plot: Every FSI Nucleon: Neut Mode =1

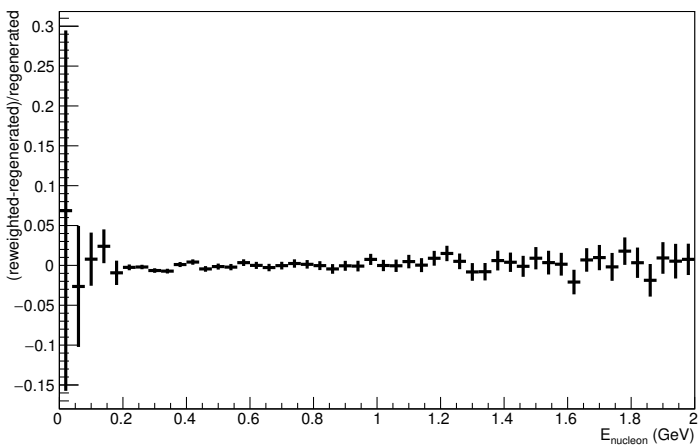

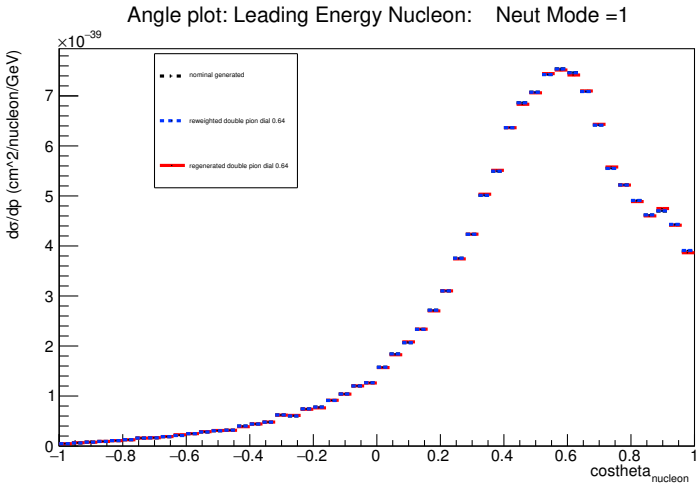
Angle plot: Leading Energy Nucleon: Neut Mode =1
nominal generated
reweighted double pion dial 0.64
regenerated double pion dial 0.64
dσ/dp (cm^2/nucleon/GeV)
costheta_nucleon

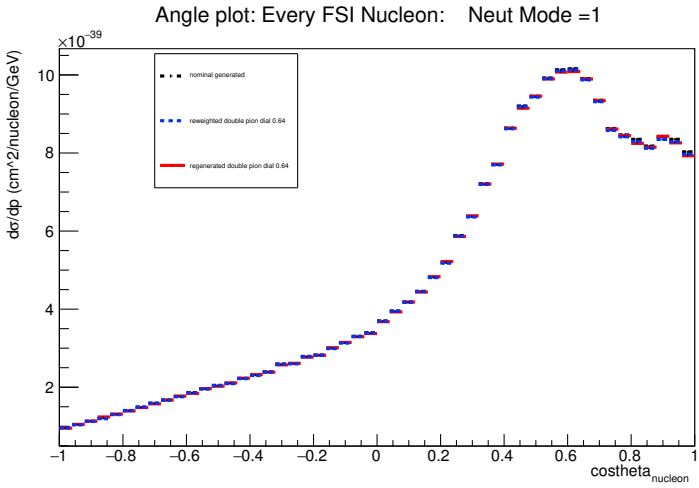
Angle plot: Every FSI Nucleon: Neut Mode =1
nominal generated
reweighted double pion dial 0.64
regenerated double pion dial 0.64
dσ/dp (cm^2/nucleon/GeV)
costheta_nucleon

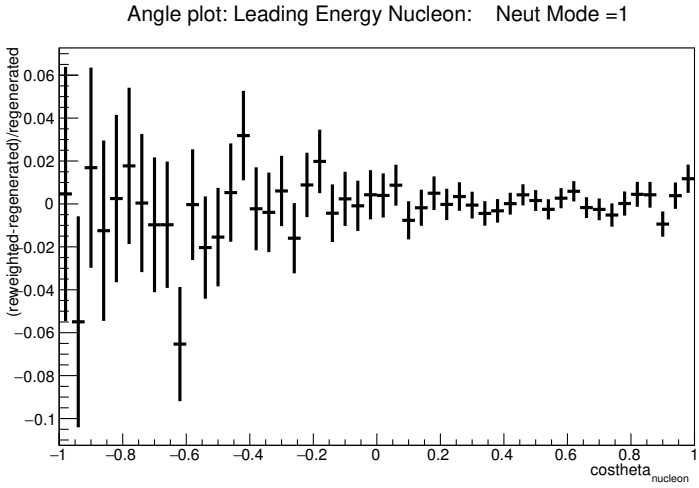
Angle plot: Leading Energy Nucleon: Neut Mode =1
(reweighted-regenerated)/regenerated
costheta_nucleon

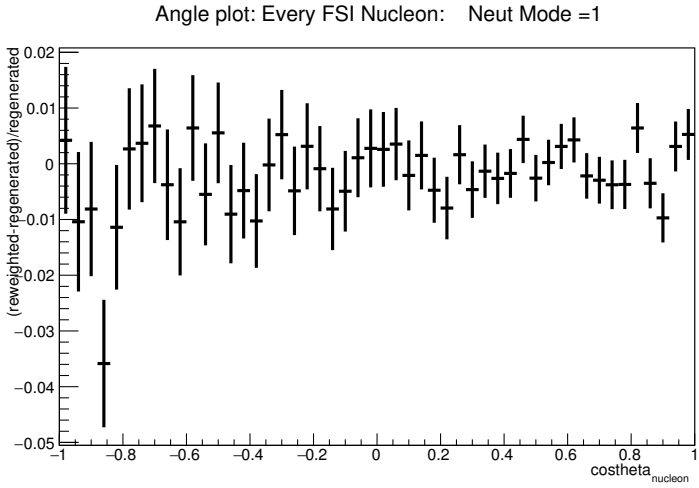
Angle plot: Every FSI Nucleon: Neut Mode =1
(reweighted-regenerated)/regenerated
costheta_nucleon

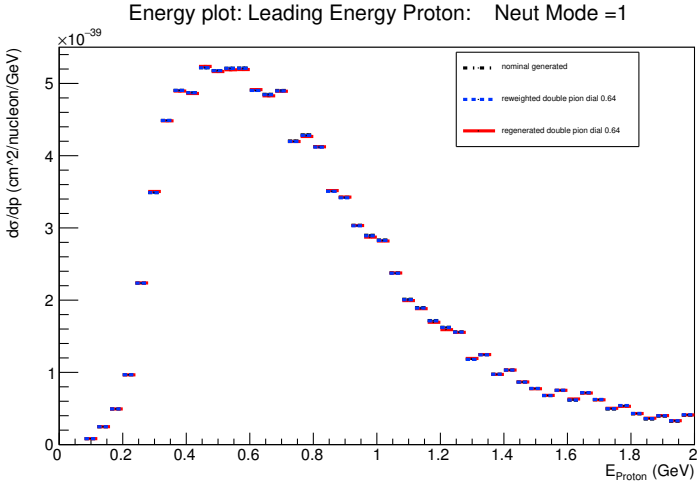
Energy plot: Leading Energy Proton: Neut Mode =1
nominal generated
reweighted double pion dial 0.64
regenerated double pion dial 0.64
dσ/dp (cm^2/nucleon/GeV)
E_Proton (GeV)

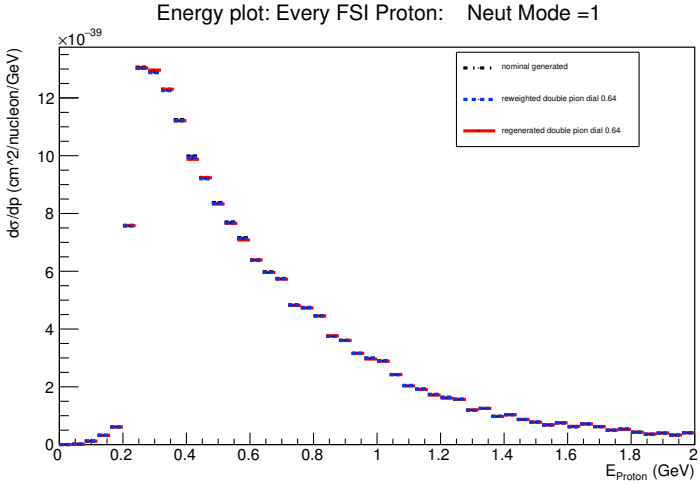
Energy plot: Every FSI Proton: Neut Mode =1
nominal generated
reweighted double pion dial 0.64
regenerated double pion dial 0.64
dσ/dp (cm^2/nucleon/GeV)
E_Proton (GeV)

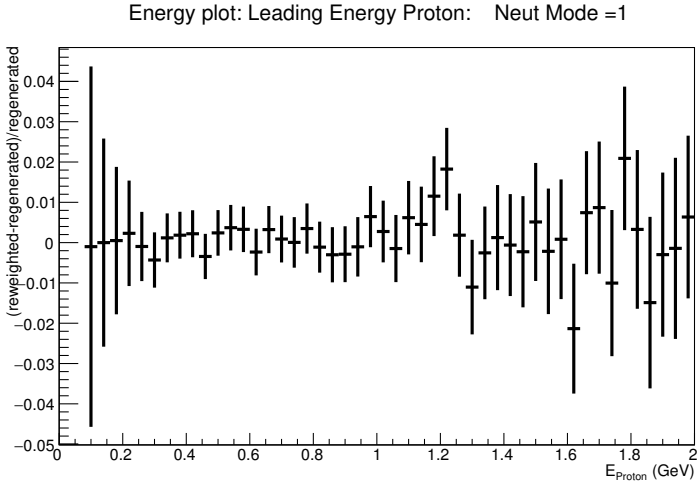
Energy plot: Leading Energy Proton: Neut Mode =1
(reweighted-regenerated)/regenerated
E_Proton (GeV)

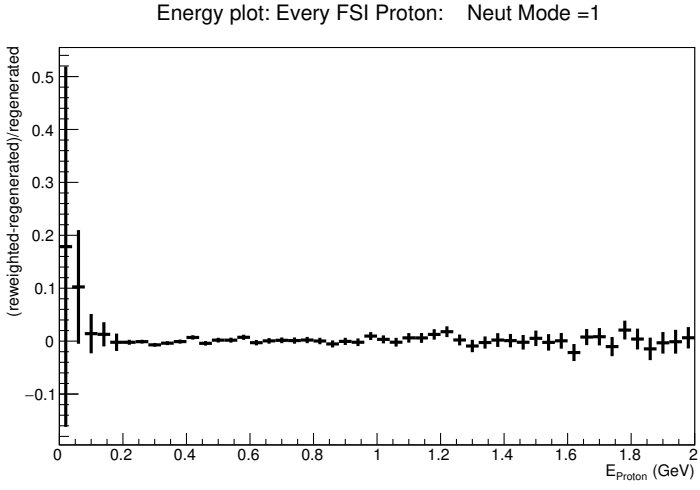
Energy plot: Every FSI Proton: Neut Mode =1
(reweighted-regenerated)/regenerated
E_Proton (GeV)

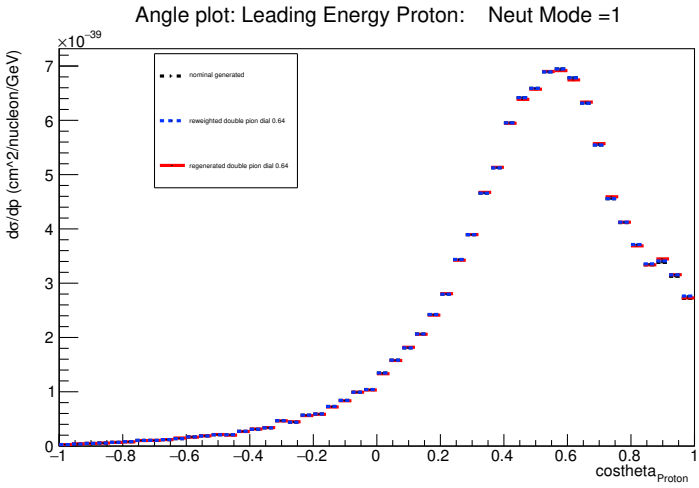
Angle plot: Leading Energy Proton: Neut Mode =1
nominal generated
reweighted double pion dial 0.64
regenerated double pion dial 0.64
dσ/dp (cm^2/nucleon/GeV)
costheta_Proton

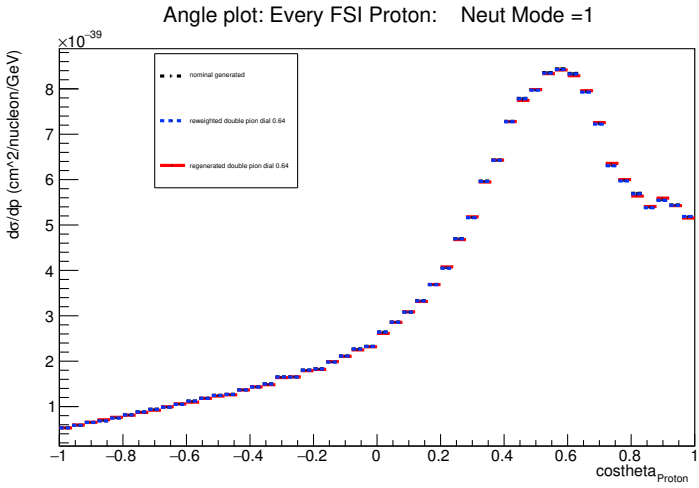
Angle plot: Every FSI Proton: Neut Mode =1
nominal generated
reweighted double pion dial 0.64
regenerated double pion dial 0.64
dσ/dp (cm^2/nucleon/GeV)
costheta_Proton

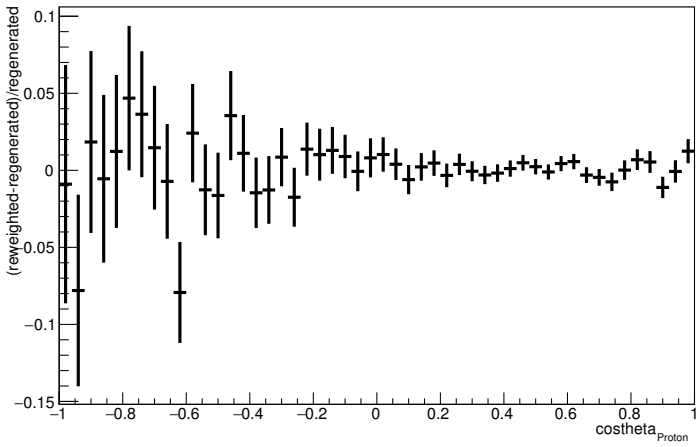
Angle plot: Leading Energy Proton: Neut Mode =1
(reweighted-regenerated)/regenerated
costheta_Proton

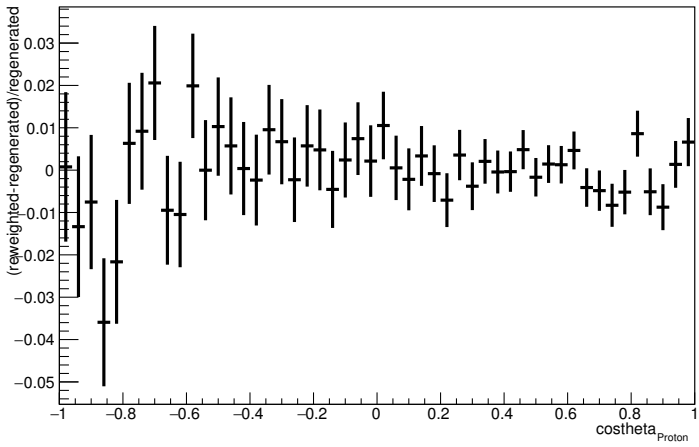
Angle plot: Every FSI Proton: Neut Mode =1
(reweighted-regenerated)/regenerated
costheta_Proton

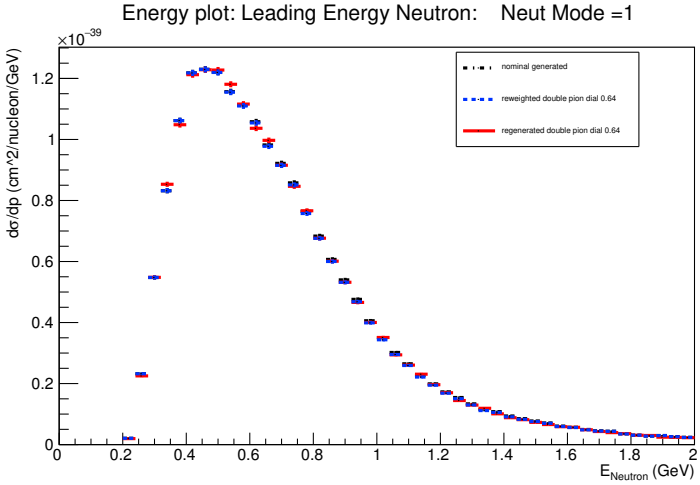
Energy plot: Leading Energy Neutron: Neut Mode =1
nominal generated
reweighted double pion dial 0.64
regenerated double pion dial 0.64
dσ/dp (cm^2/nucleon/GeV)
E_Neutron (GeV)

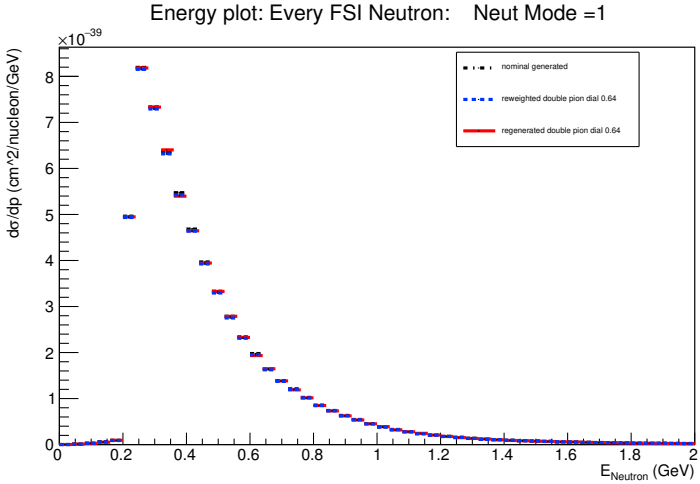
Energy plot: Every FSI Neutron: Neut Mode =1
nominal generated
reweighted double pion dial 0.64
regenerated double pion dial 0.64
dσ/dp (cm^2/nucleon/GeV)
E_Neutron (GeV)

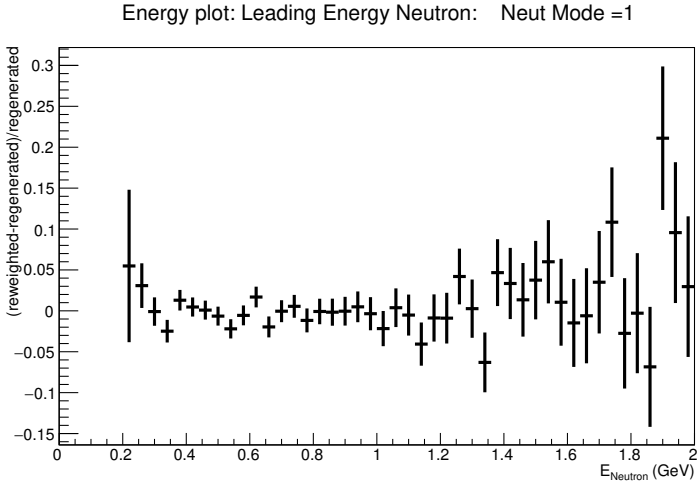
Energy plot: Leading Energy Neutron: Neut Mode =1
(reweighted-regenerated)/regenerated
E_Neutron (GeV)

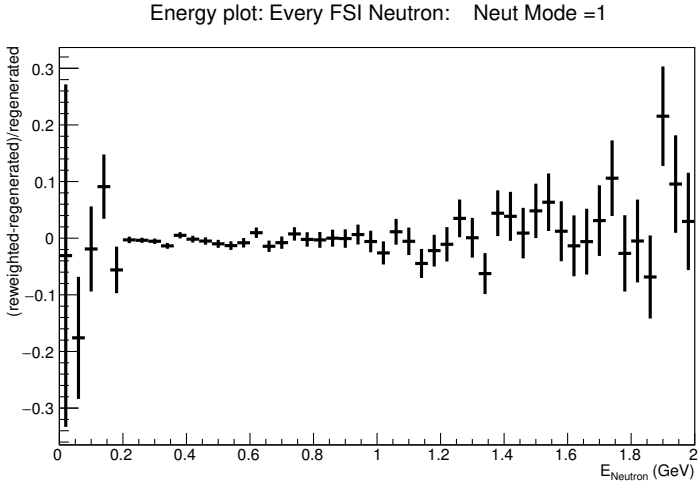
Energy plot: Every FSI Neutron: Neut Mode =1
(reweighted-regenerated)/regenerated
E_Neutron (GeV)

Angle plot: Leading Energy Neutron: Neut Mode =1

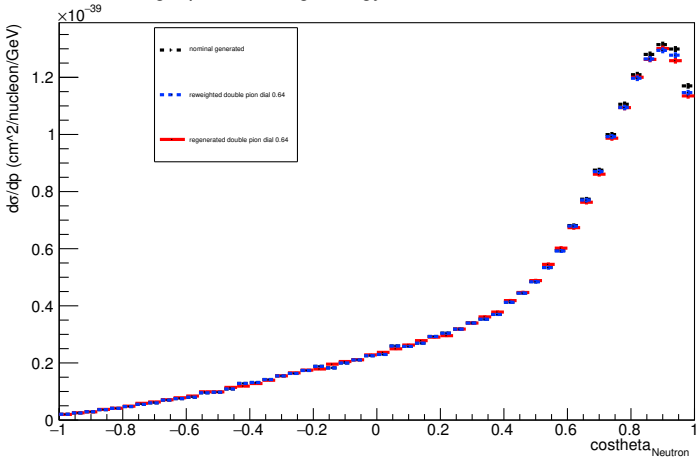

Angle plot: Every FSI Neutron: Neut Mode =1

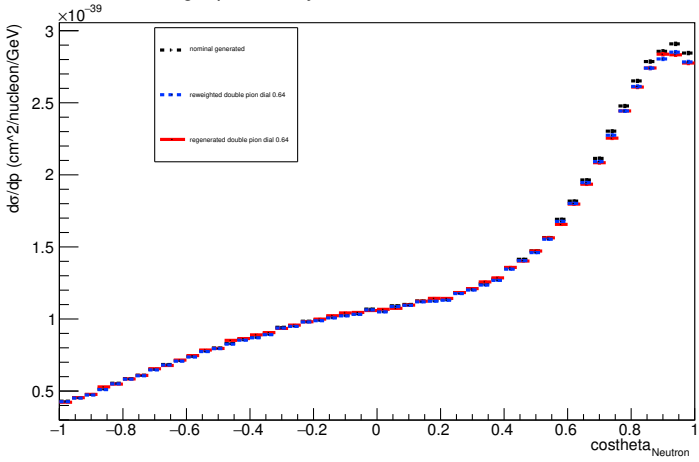

Angle plot: Leading Energy Neutron: Neut Mode =1

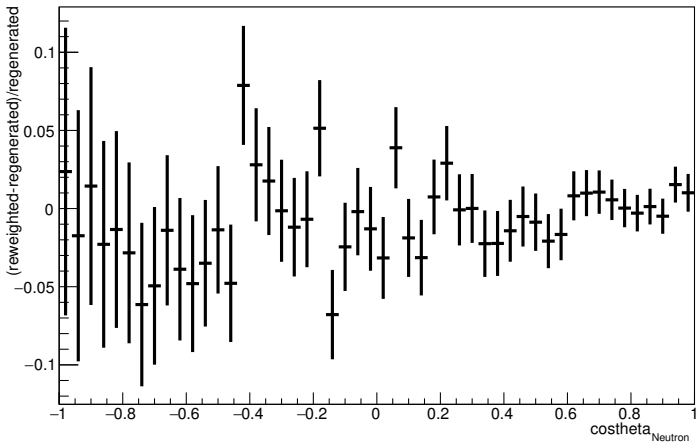

Angle plot: Every FSI Neutron: Neut Mode =1

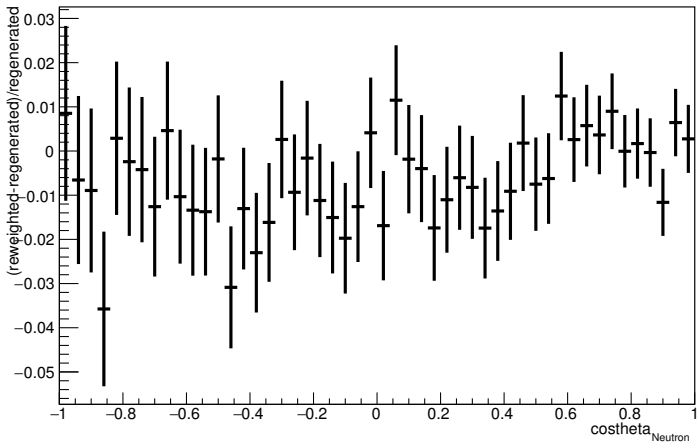

Energy plot: Leading Energy Lepton: Neut Mode =1

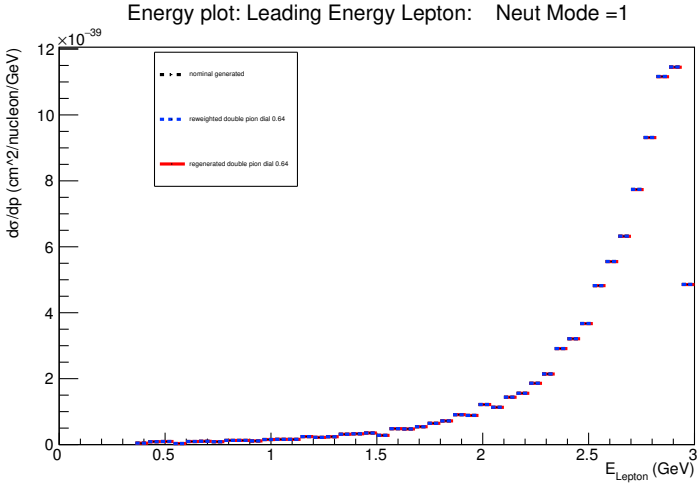

Angle plot: Leading Energy Lepton: Neut Mode =1

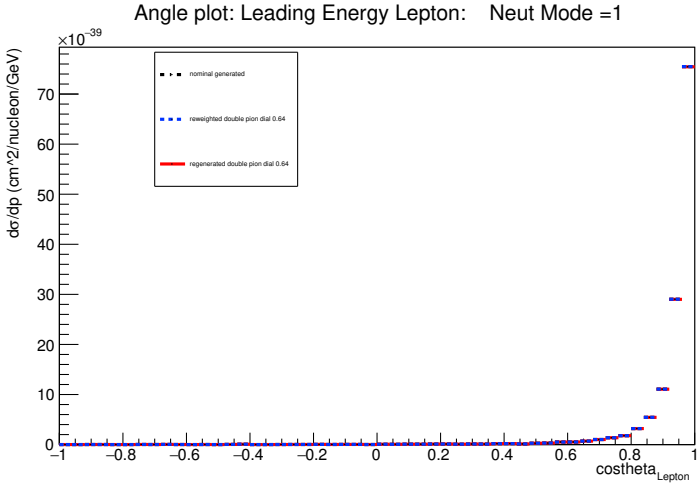

Energy plot: Leading Energy Lepton: Neut Mode =1

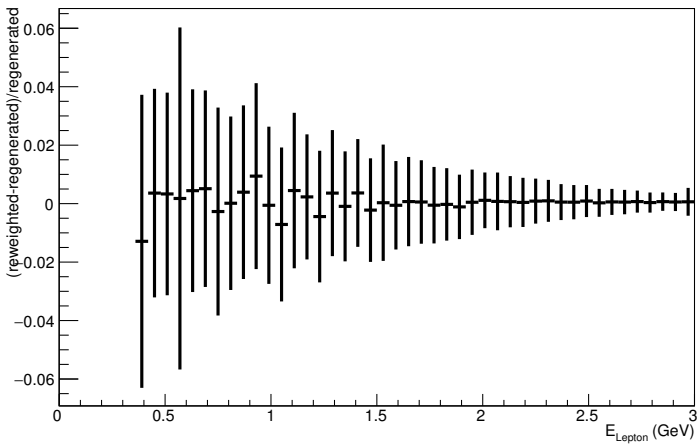

Angle plot: Leading Energy Lepton: Neut Mode =1

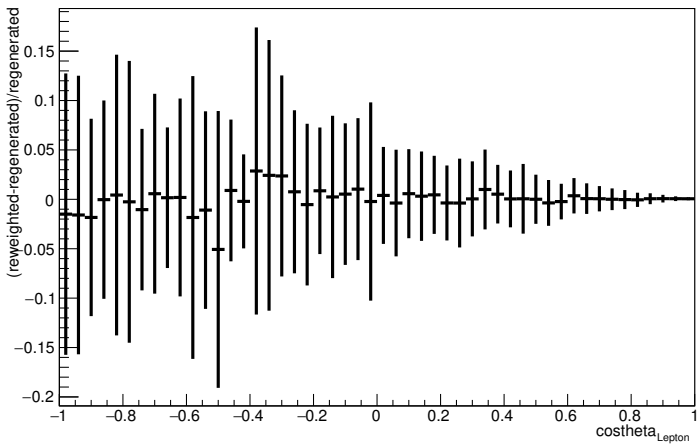

Energy plot: Leading Energy Pion: Neut Mode =1

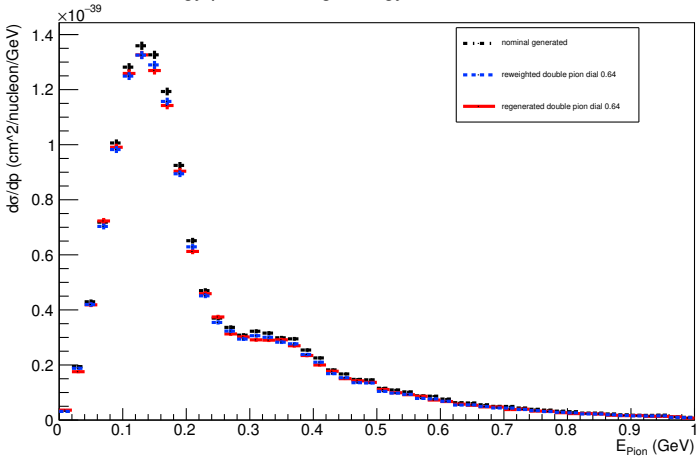

Energy plot: Every FSI Pion: Neut Mode =1

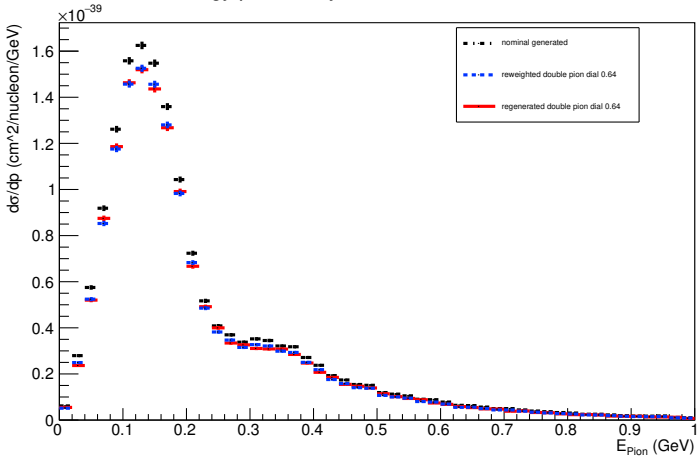

Energy plot: Leading Energy Pion: Neut Mode =1

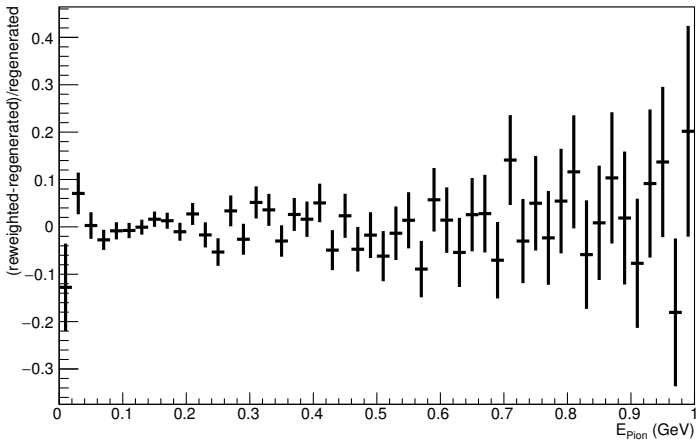

Energy plot: Every FSI Pion: Neut Mode =1

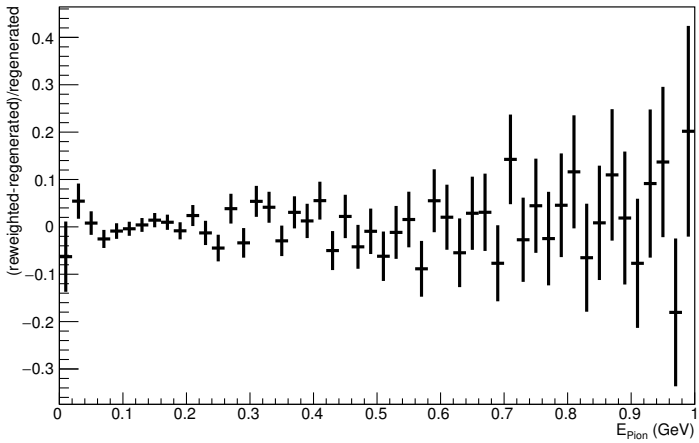

Angle plot: Leading Energy Pion: Neut Mode =1

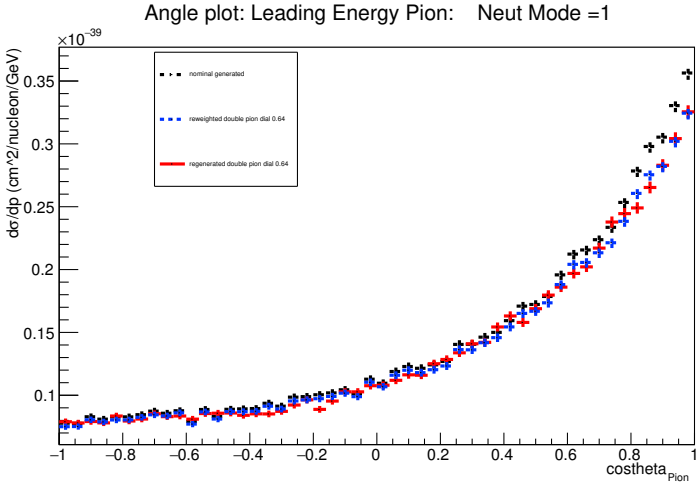

Angle plot: Every FSI Pion: Neut Mode =1

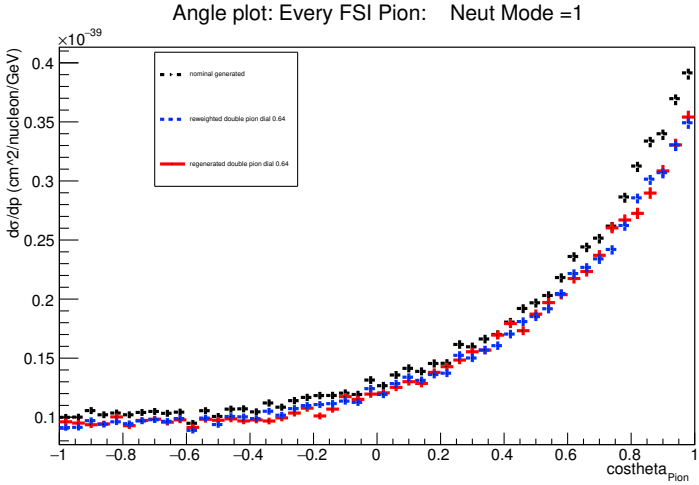

Angle plot: Leading Energy Pion: Neut Mode =1

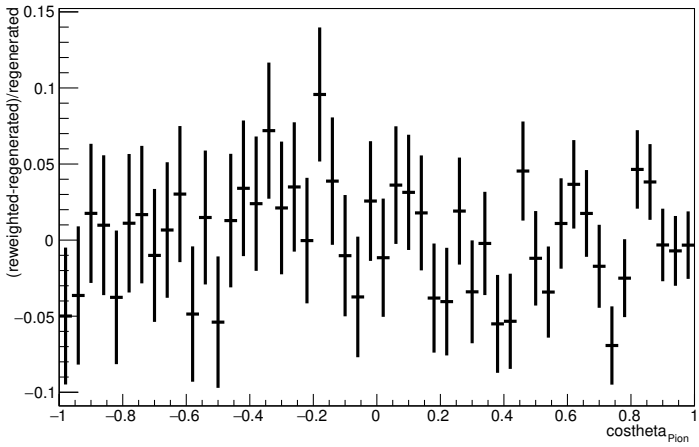

Angle plot: Every FSI Pion: Neut Mode =1

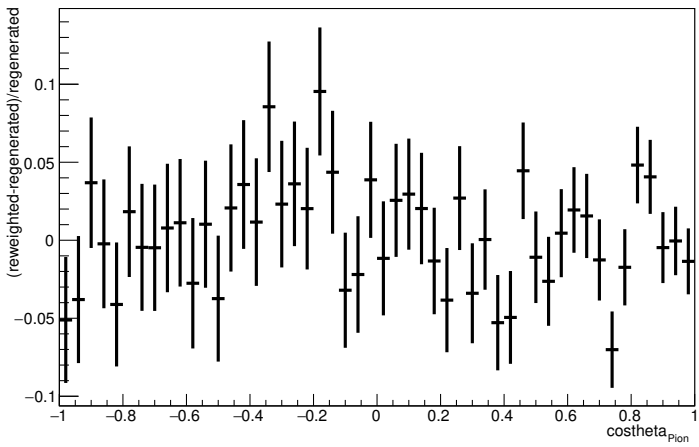

Energy plot: Leading Energy Nucleon: Neut Mode =2

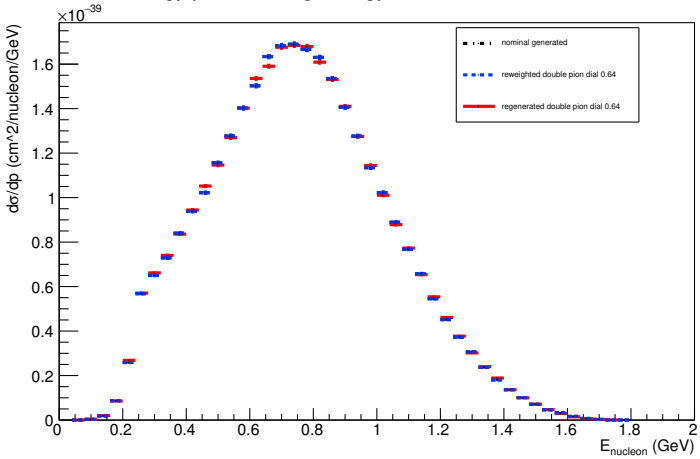

Energy plot: Every FSI Nucleon: Neut Mode =2

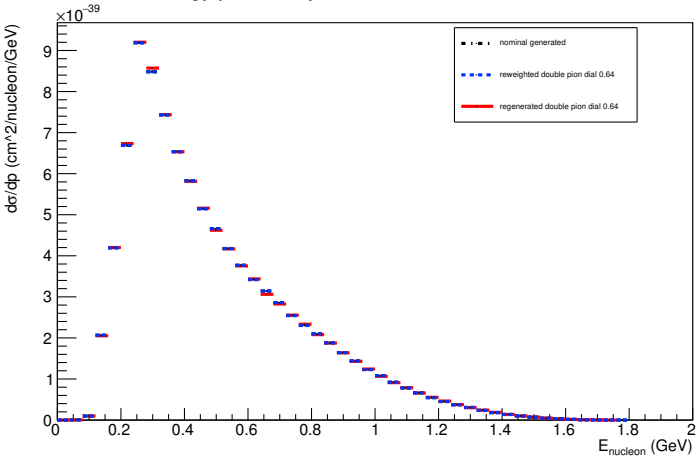

Energy plot: Leading Energy Nucleon: Neut Mode =2

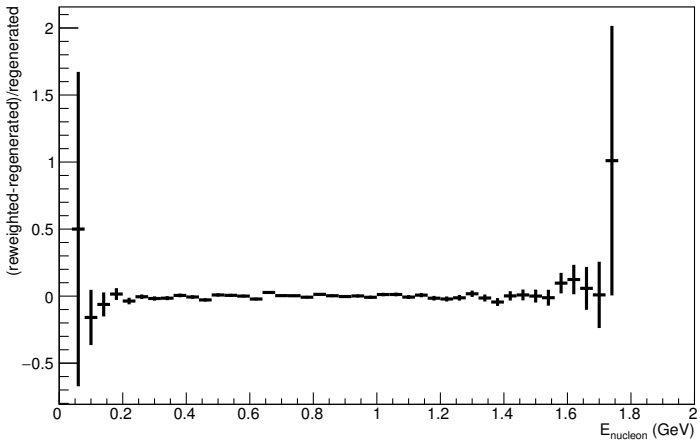

Energy plot: Every FSI Nucleon: Neut Mode =2

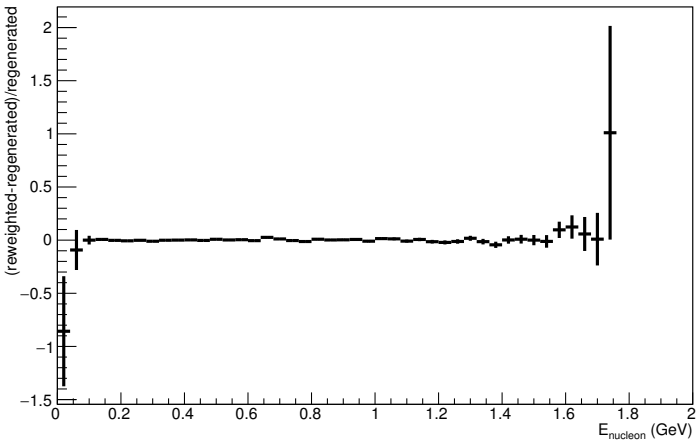

Angle plot: Leading Energy Nucleon: Neut Mode =2

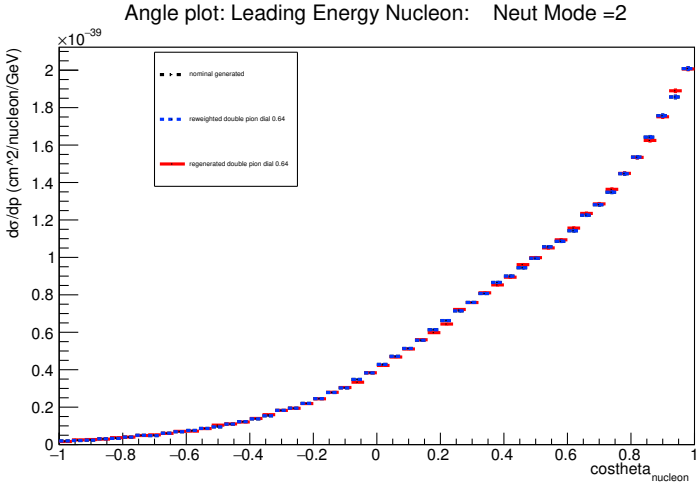

Angle plot: Every FSI Nucleon: Neut Mode =2

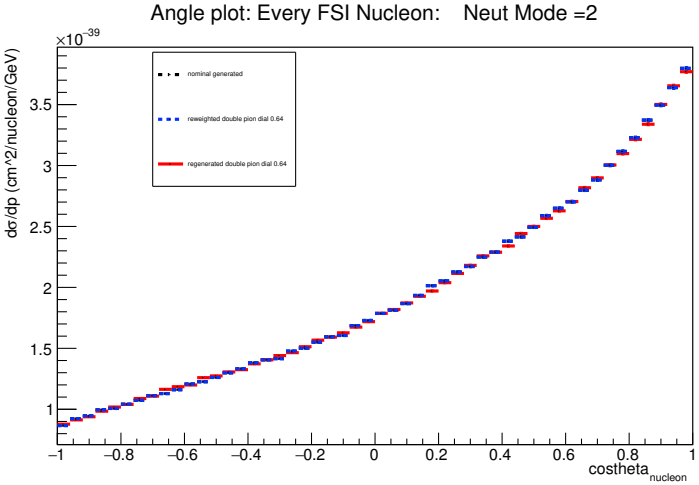

Angle plot: Leading Energy Nucleon: Neut Mode =2

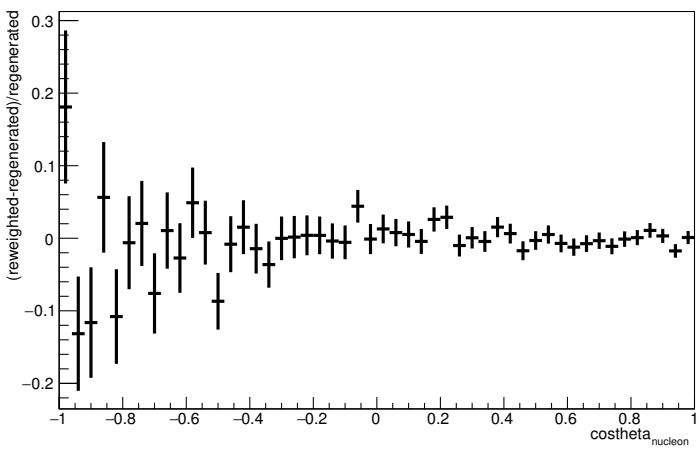

Angle plot: Every FSI Nucleon: Neut Mode =2

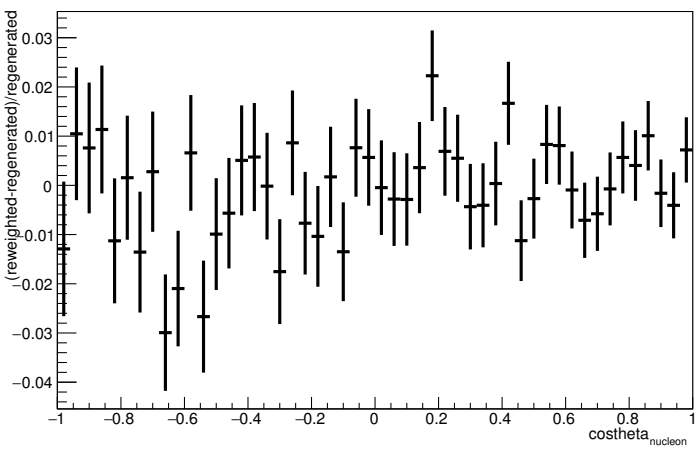

Energy plot: Leading Energy Proton: Neut Mode =2

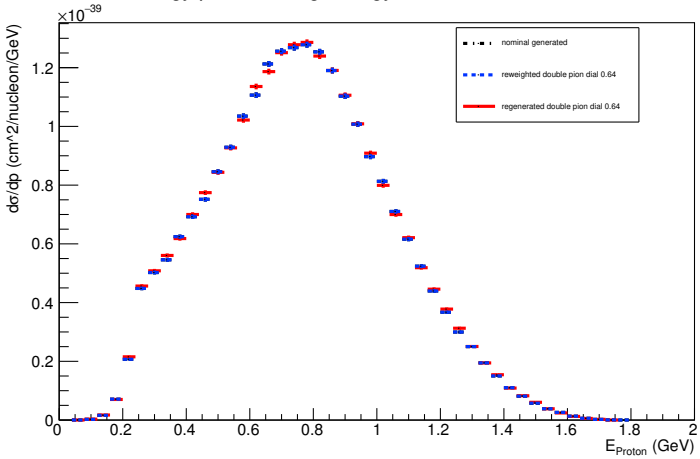

Energy plot: Every FSI Proton: Neut Mode =2

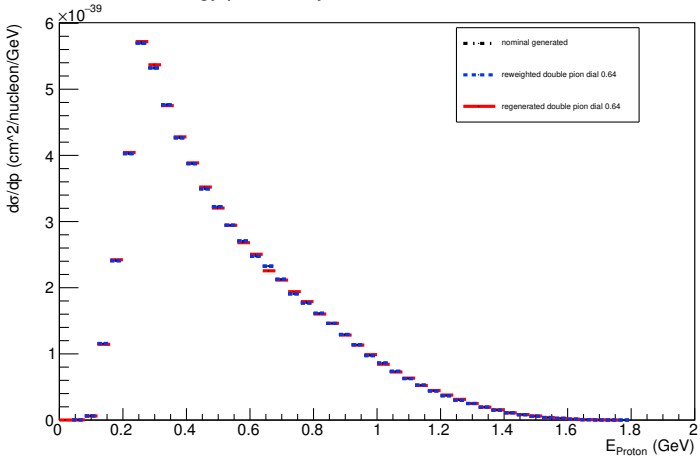

Energy plot: Leading Energy Proton: Neut Mode =2

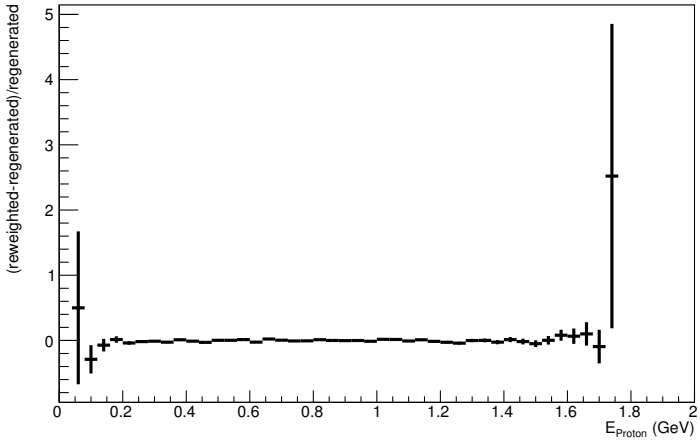

Energy plot: Every FSI Proton: Neut Mode =2

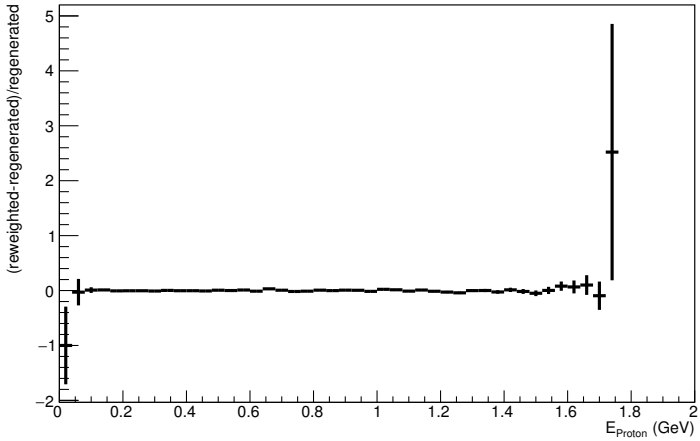

Angle plot: Leading Energy Proton: Neut Mode =2

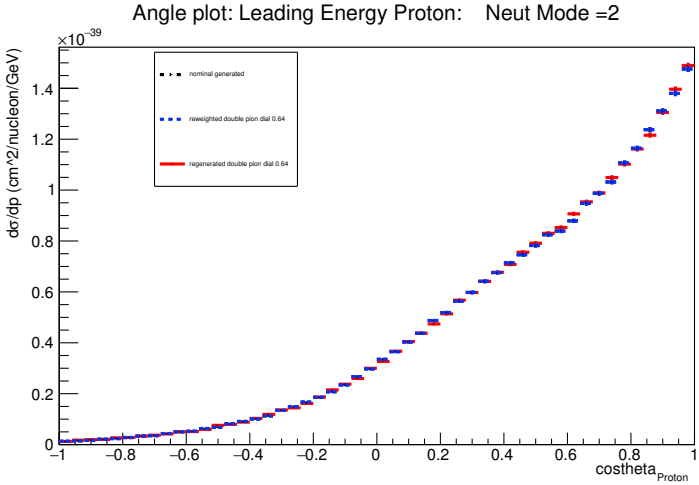

Angle plot: Every FSI Proton: Neut Mode =2

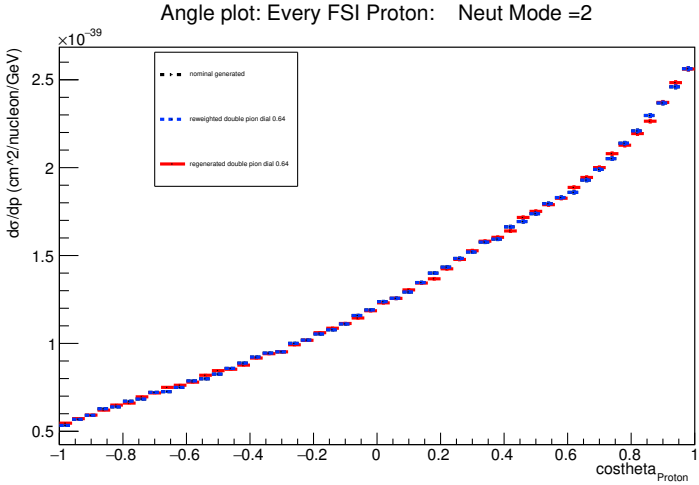

Angle plot: Leading Energy Proton: Neut Mode =2

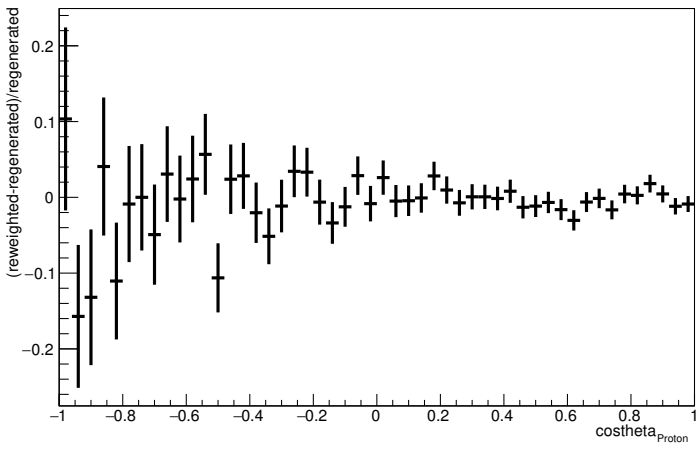

Angle plot: Every FSI Proton: Neut Mode =2

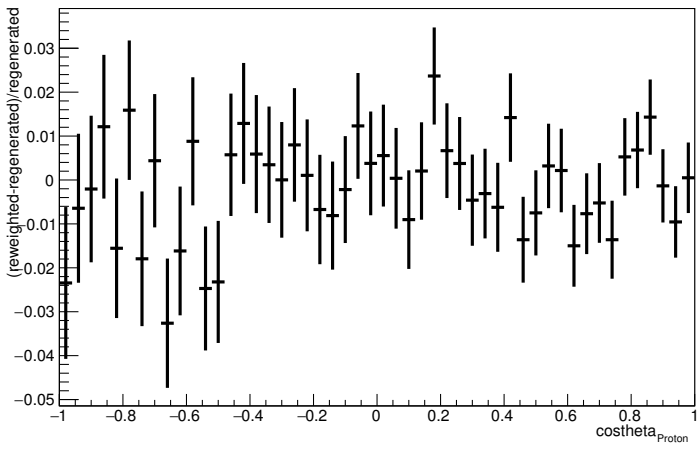

Energy plot: Leading Energy Neutron: Neut Mode =2

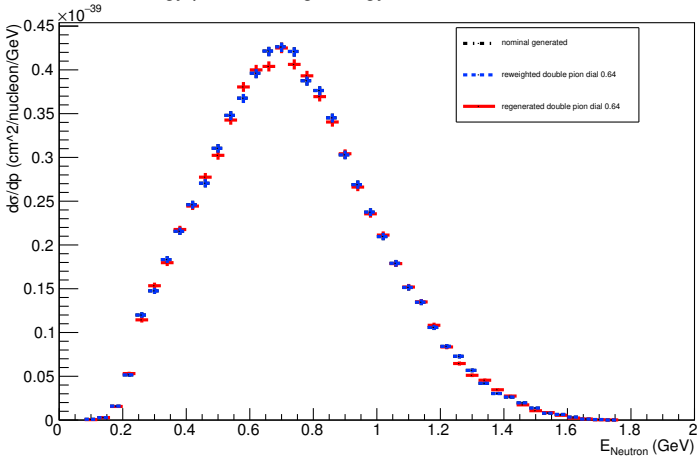

Energy plot: Every FSI Neutron: Neut Mode =2

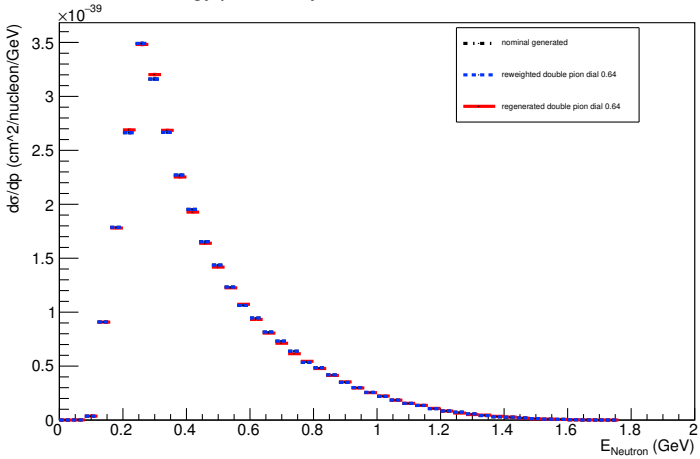

Energy plot: Leading Energy Neutron: Neut Mode =2

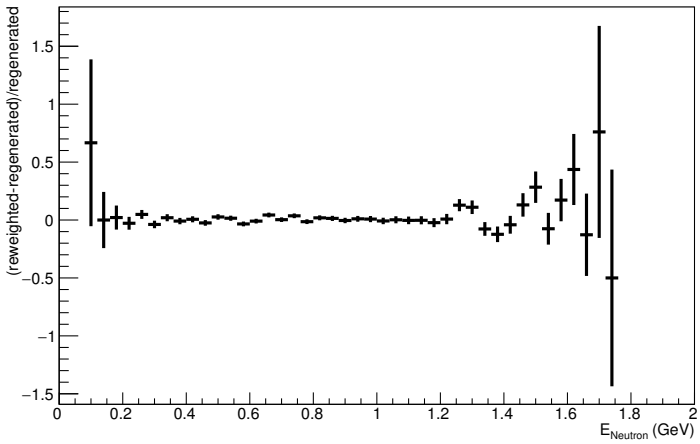

Energy plot: Every FSI Neutron: Neut Mode =2

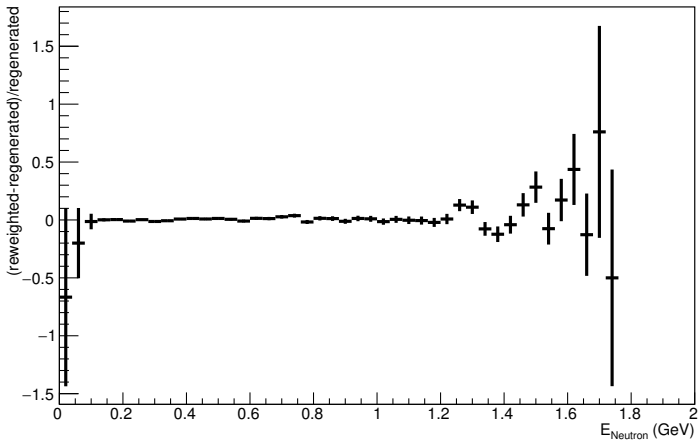

Angle plot: Leading Energy Neutron: Neut Mode =2

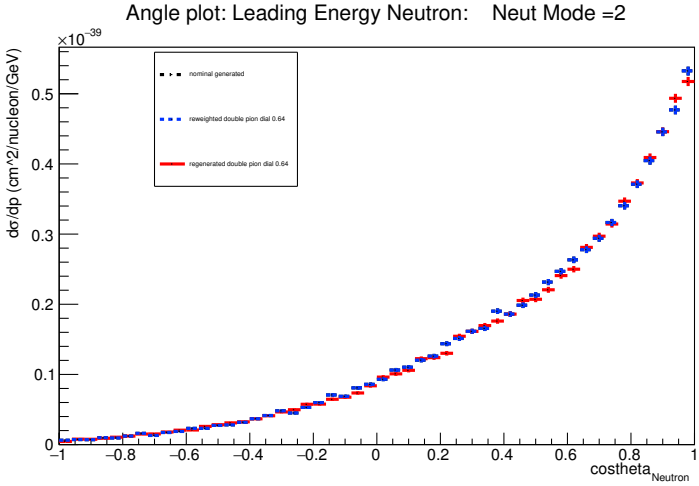

Angle plot: Every FSI Neutron: Neut Mode =2

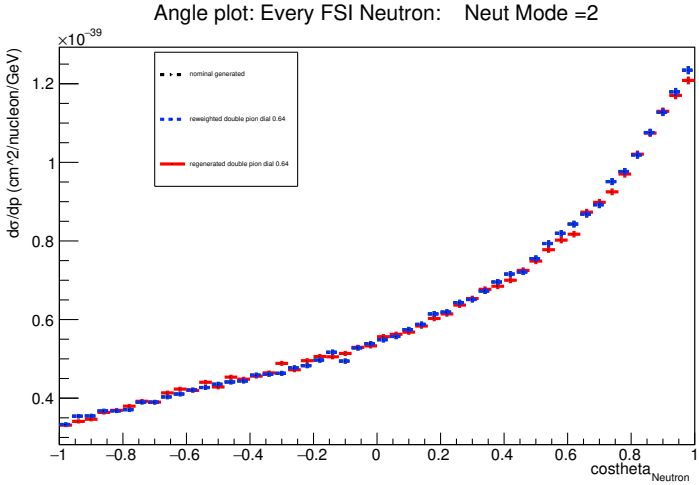

Angle plot: Leading Energy Neutron: Neut Mode =2

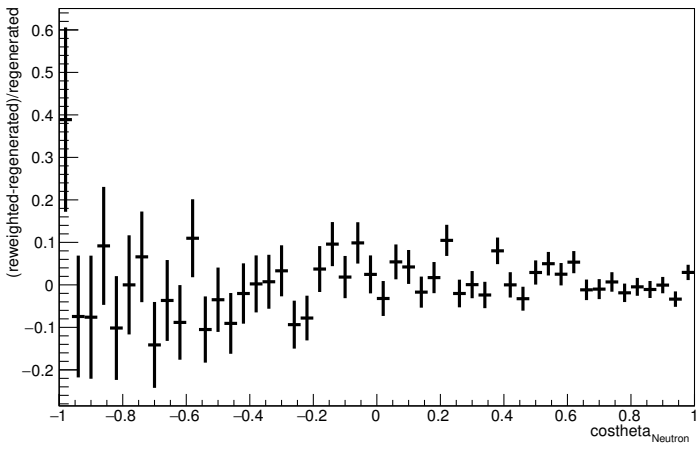

Angle plot: Every FSI Neutron: Neut Mode =2

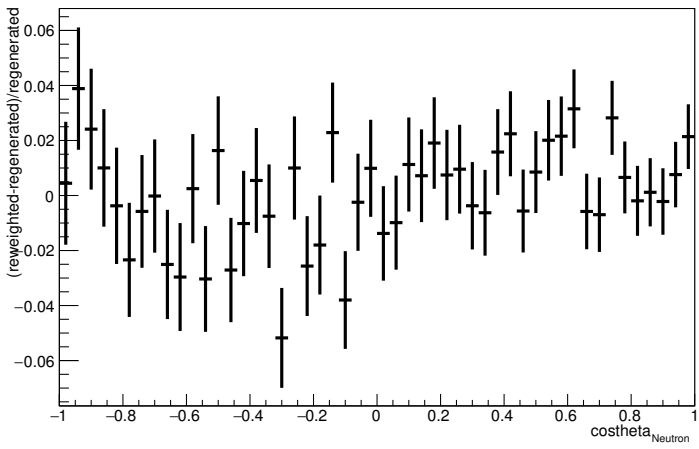

Energy plot: Leading Energy Lepton: Neut Mode =2

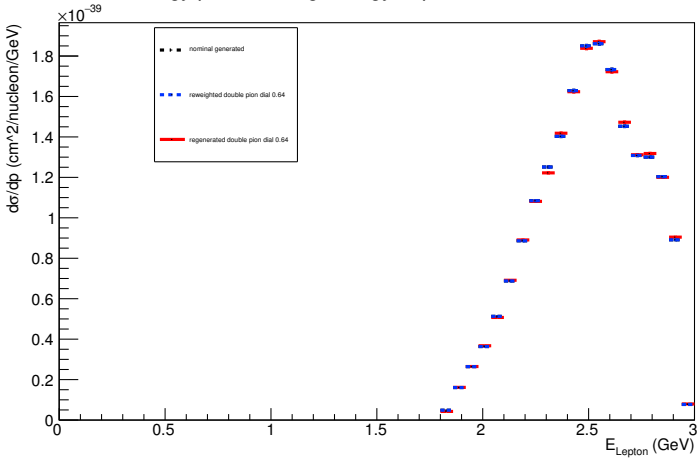

Angle plot: Leading Energy Lepton: Neut Mode =2

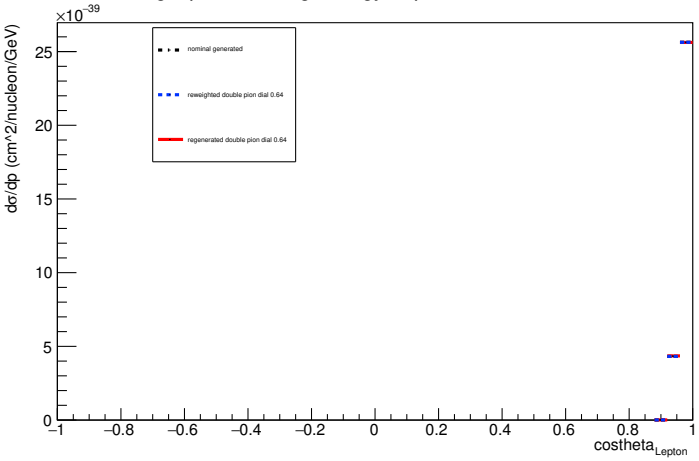

Energy plot: Leading Energy Lepton: Neut Mode =2

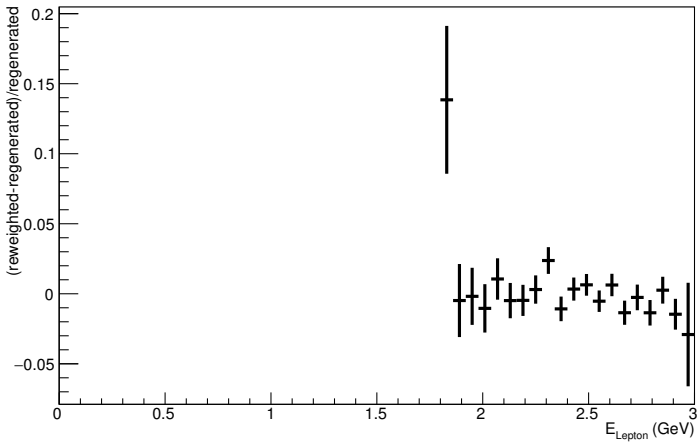

Angle plot: Leading Energy Lepton: Neut Mode =2

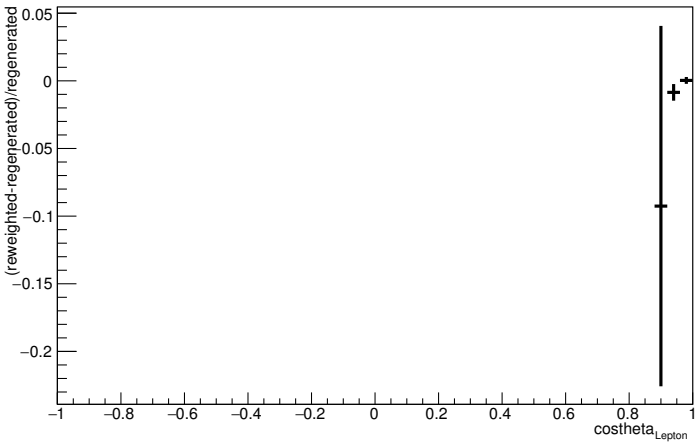

Energy plot: Leading Energy Pion: Neut Mode =2

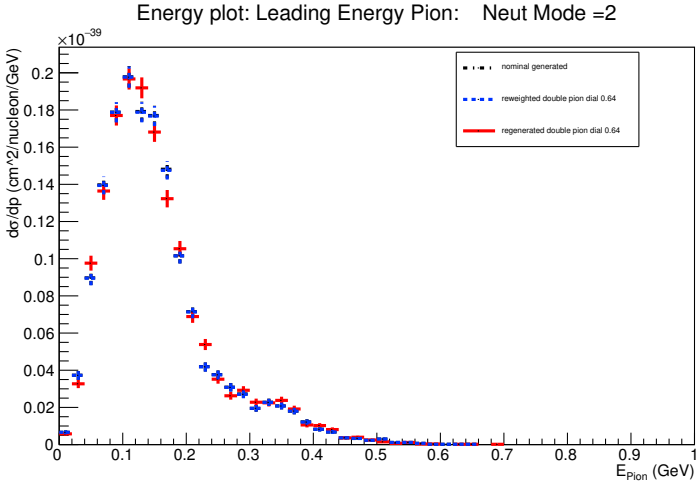

Energy plot: Every FSI Pion: Neut Mode =2

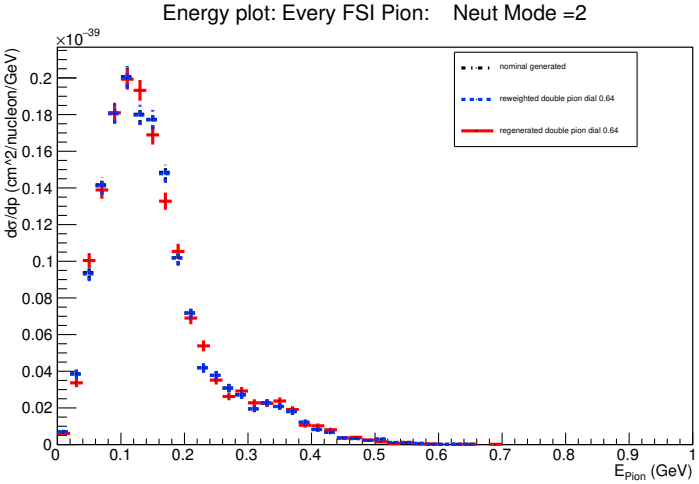

Energy plot: Leading Energy Pion: Neut Mode =2

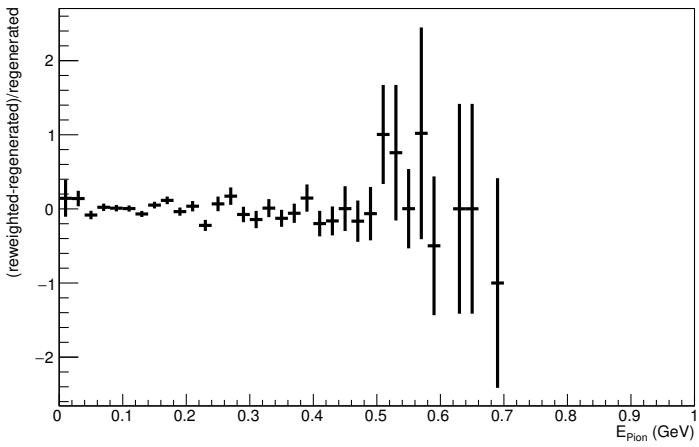

Energy plot: Every FSI Pion: Neut Mode =2

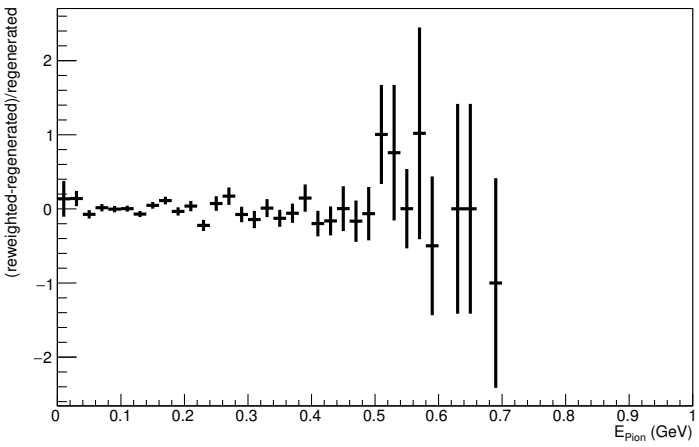

Angle plot: Leading Energy Pion: Neut Mode =2

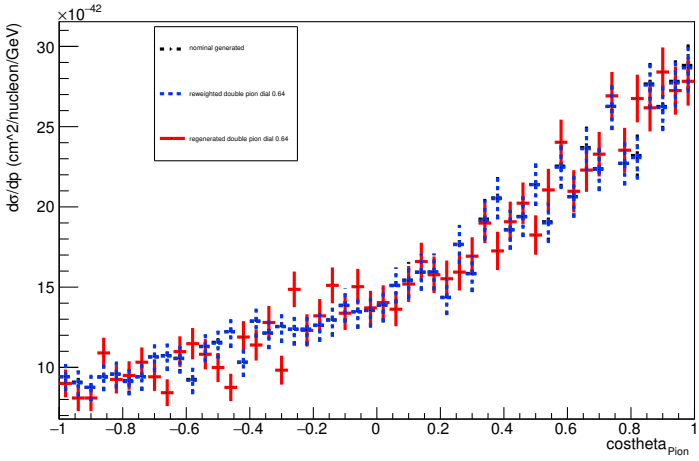

Angle plot: Every FSI Pion: Neut Mode =2

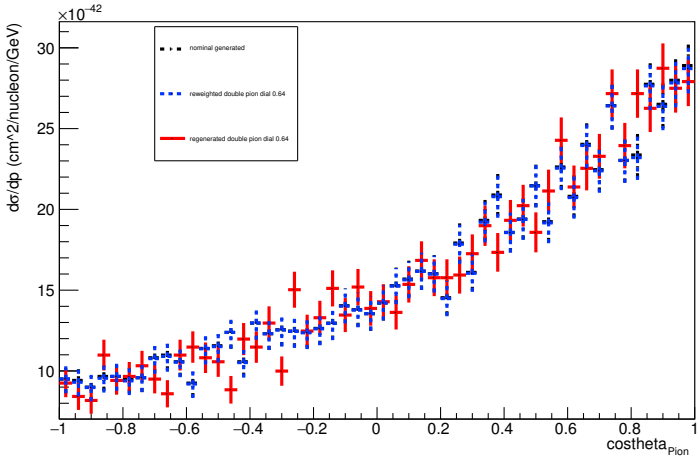

Angle plot: Leading Energy Pion: Neut Mode =2

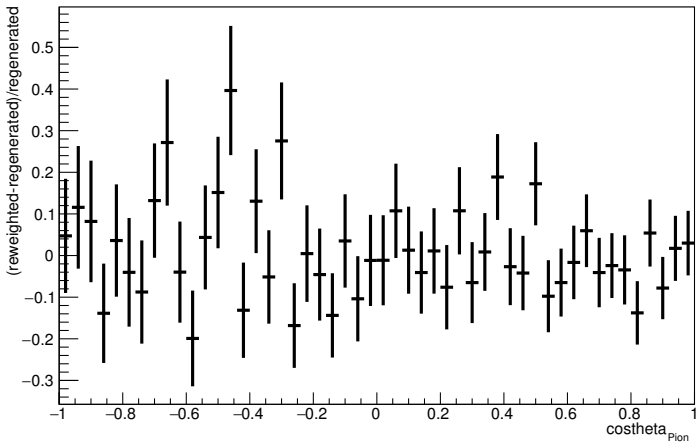

Angle plot: Every FSI Pion: Neut Mode =2

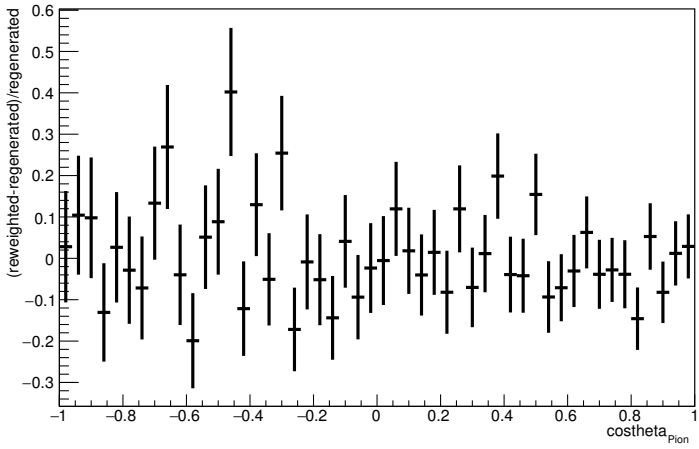

Energy plot: Leading Energy Nucleon: Neut Mode =11

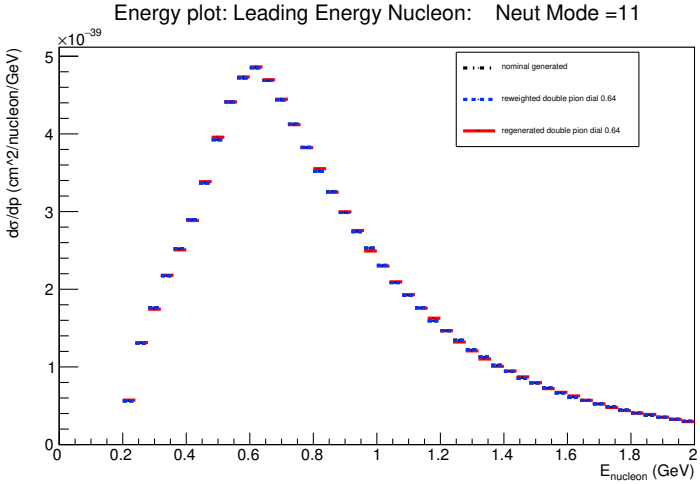

Energy plot: Every FSI Nucleon: Neut Mode =11

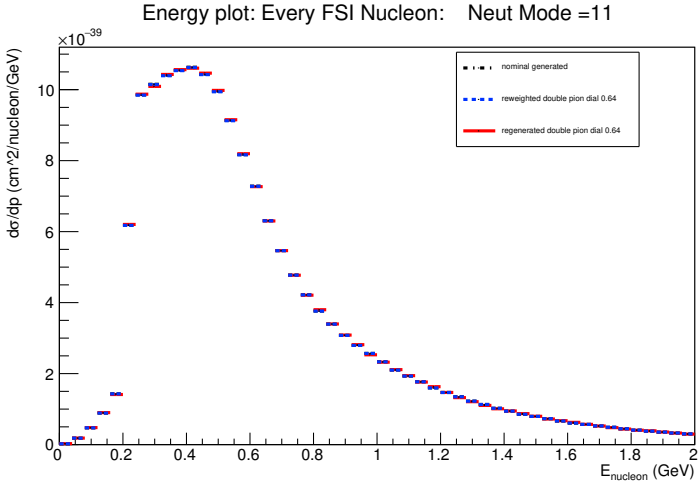

Energy plot: Leading Energy Nucleon: Neut Mode =11

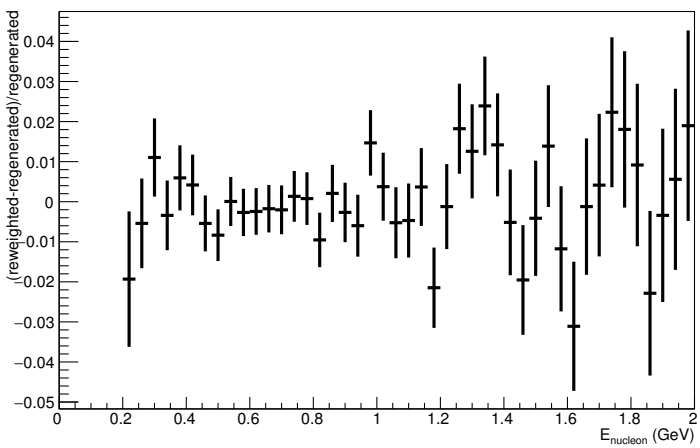

Energy plot: Every FSI Nucleon: Neut Mode =11

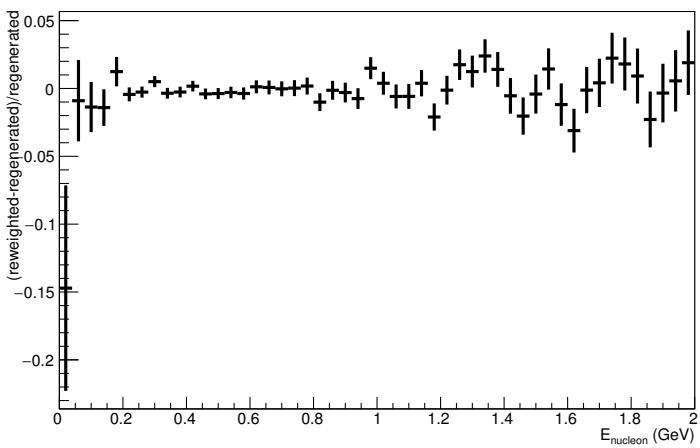

Angle plot: Leading Energy Nucleon: Neut Mode =11

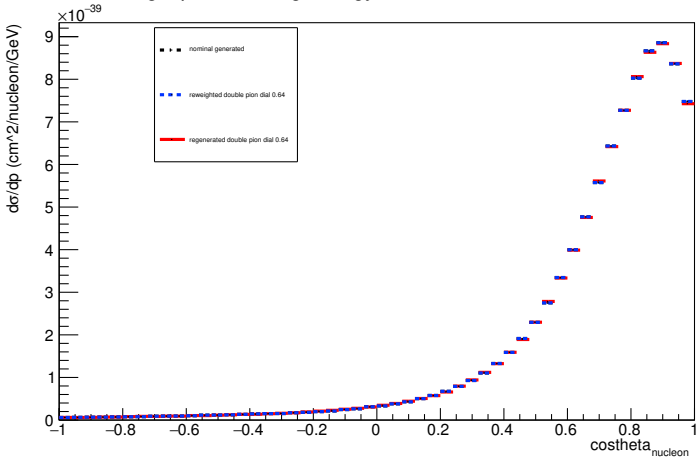

Angle plot: Every FSI Nucleon: Neut Mode =11

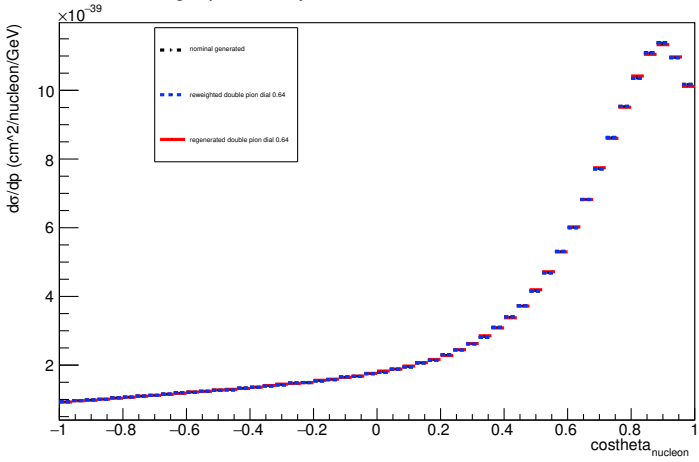

Angle plot: Leading Energy Nucleon: Neut Mode =11

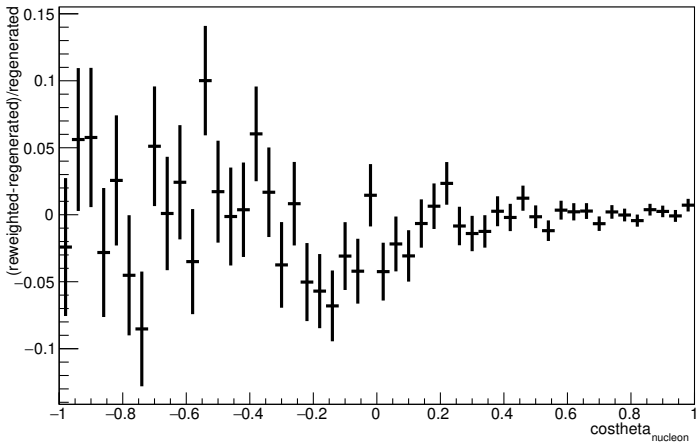

Angle plot: Every FSI Nucleon: Neut Mode =11

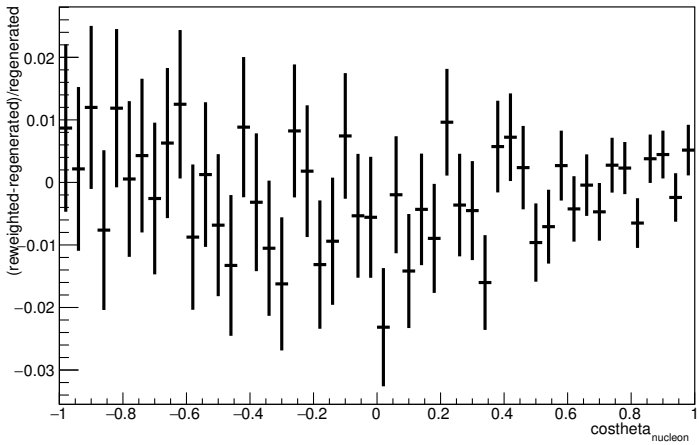

Energy plot: Leading Energy Proton: Neut Mode =11

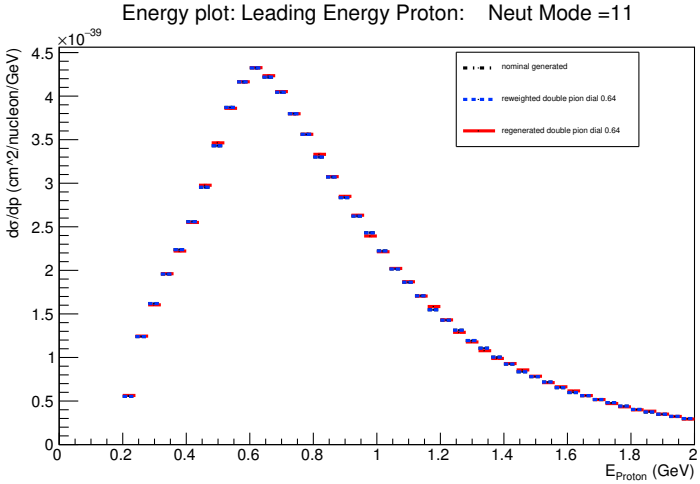

Energy plot: Every FSI Proton: Neut Mode =11

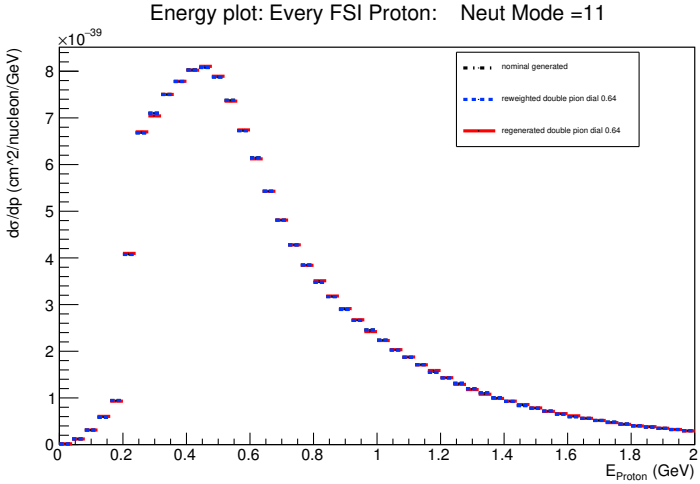

Energy plot: Leading Energy Proton: Neut Mode =11

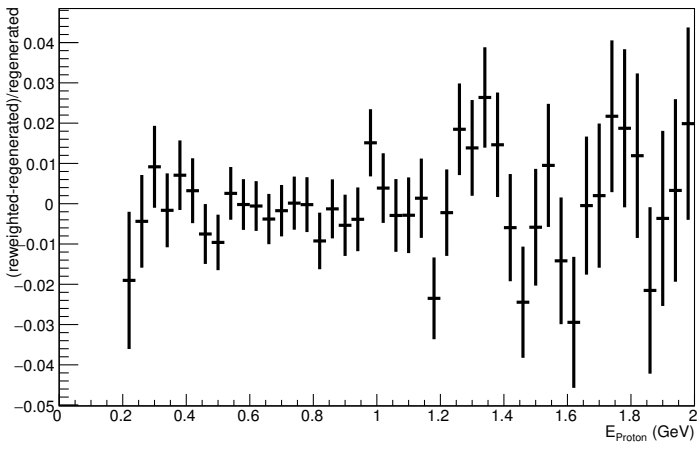

Energy plot: Every FSI Proton: Neut Mode =11

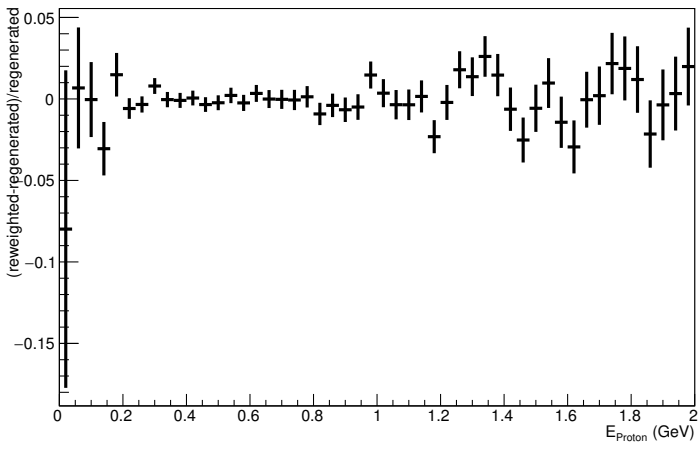

Angle plot: Leading Energy Proton: Neut Mode =11

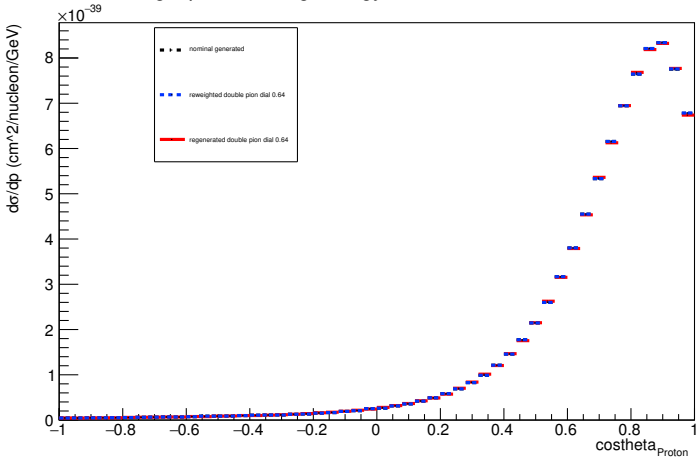

Angle plot: Every FSI Proton: Neut Mode =11

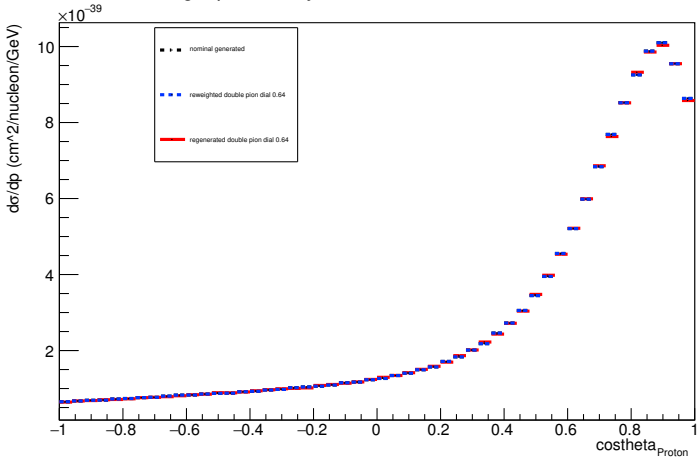

Angle plot: Leading Energy Proton: Neut Mode =11

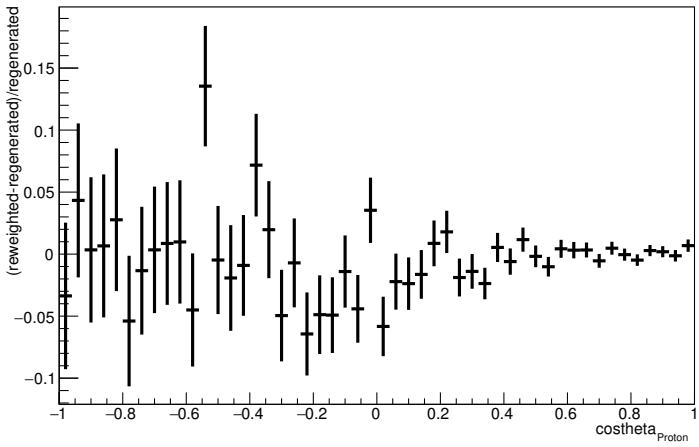

Angle plot: Every FSI Proton: Neut Mode =11

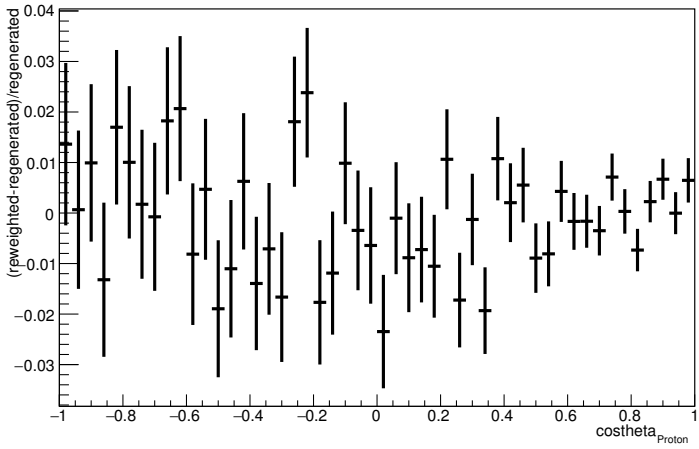

Energy plot: Leading Energy Neutron: Neut Mode =11

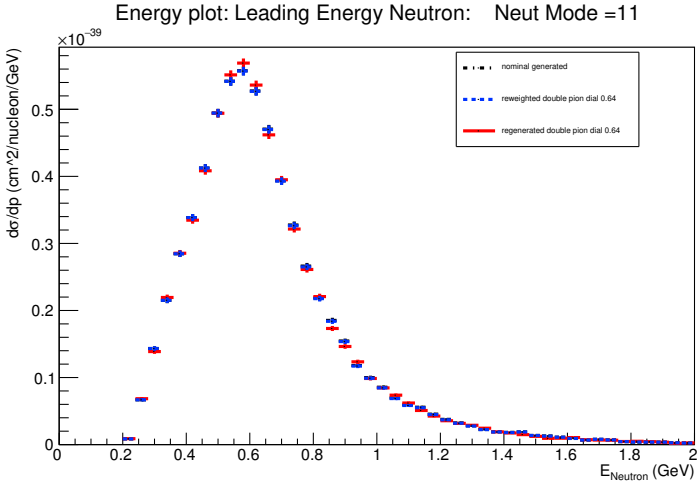

Energy plot: Every FSI Neutron: Neut Mode =11

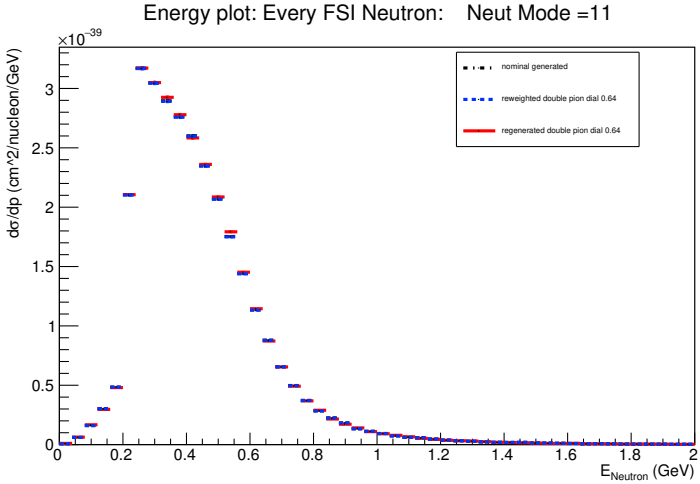

Energy plot: Leading Energy Neutron: Neut Mode =11

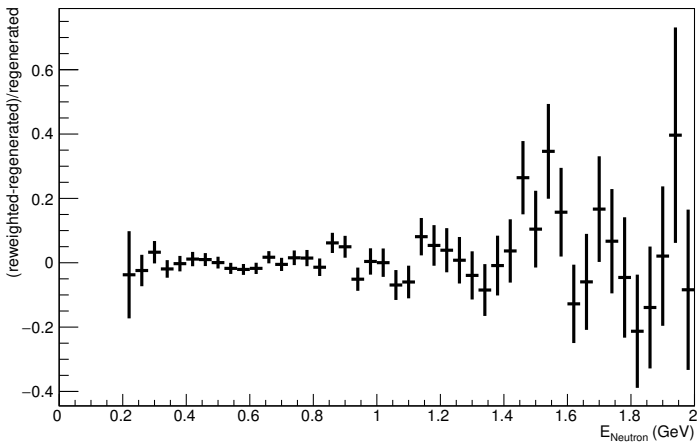

Energy plot: Every FSI Neutron: Neut Mode =11

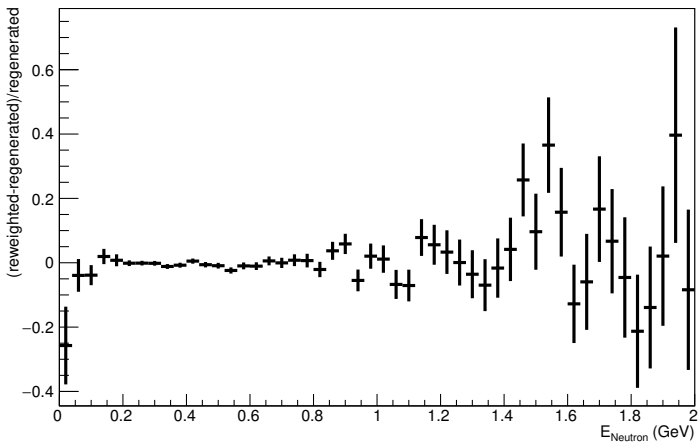

Angle plot: Leading Energy Neutron: Neut Mode =11

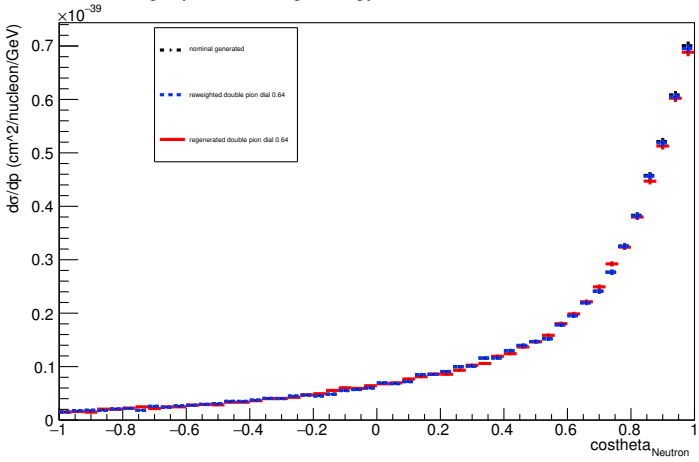

Angle plot: Every FSI Neutron: Neut Mode =11

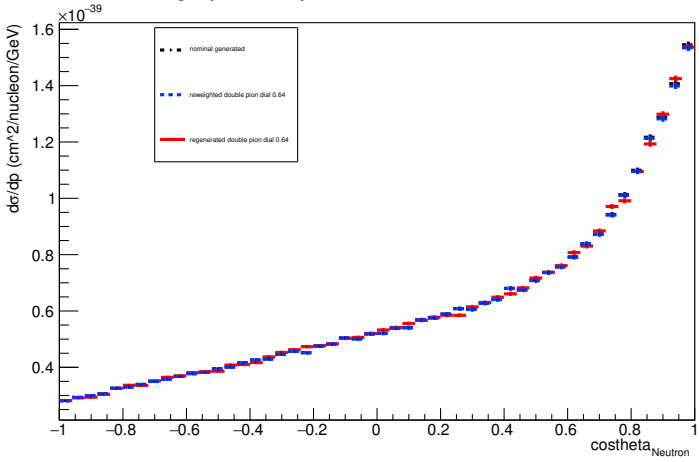

Angle plot: Leading Energy Neutron: Neut Mode =11

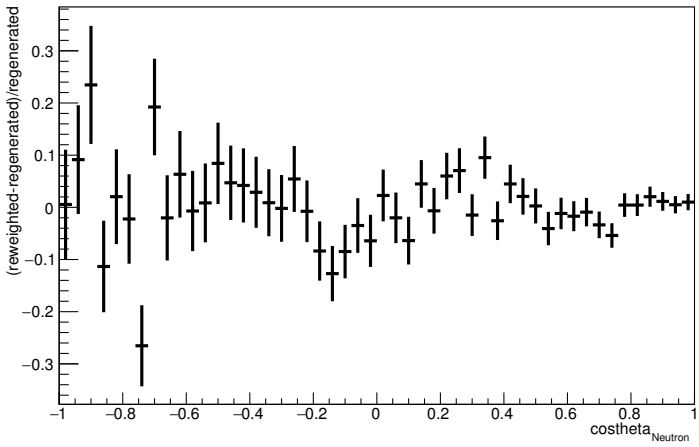

Angle plot: Every FSI Neutron: Neut Mode =11

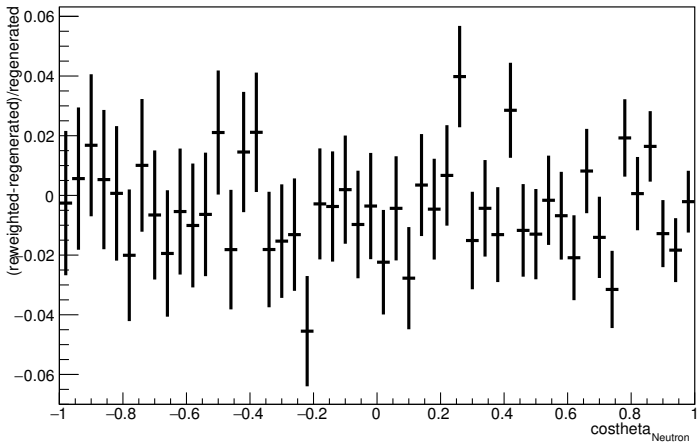

Energy plot: Leading Energy Lepton: Neut Mode =11

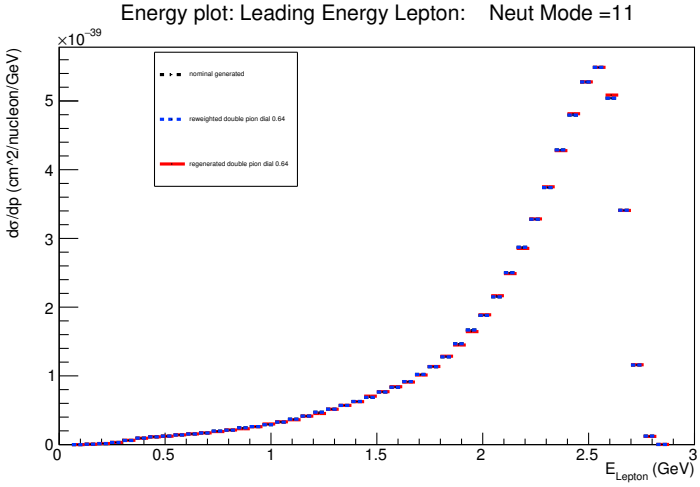

Angle plot: Leading Energy Lepton: Neut Mode =11

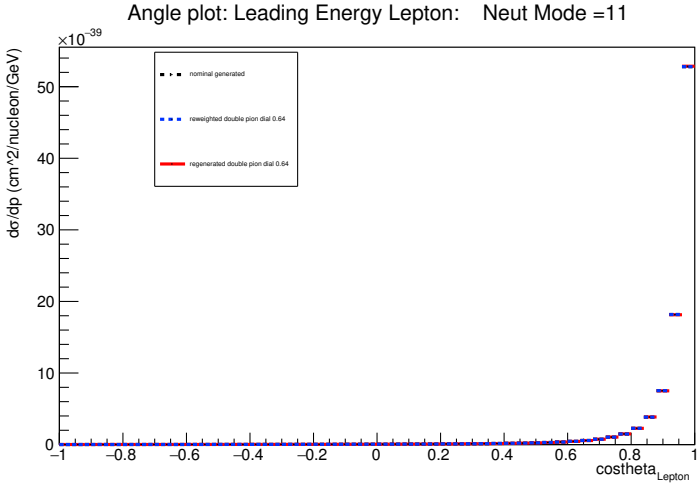

Energy plot: Leading Energy Lepton: Neut Mode =11

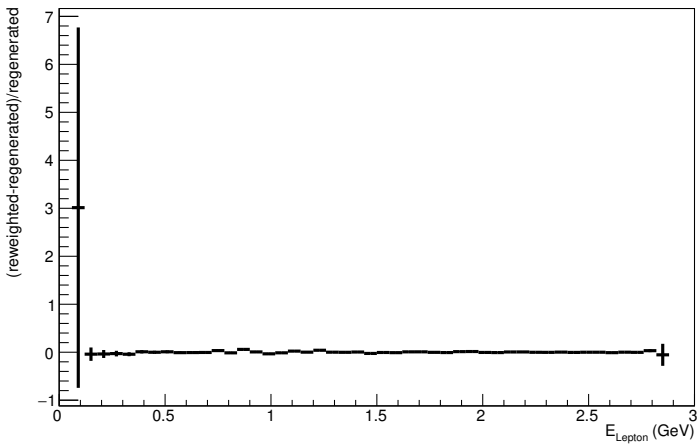

Angle plot: Leading Energy Lepton: Neut Mode =11

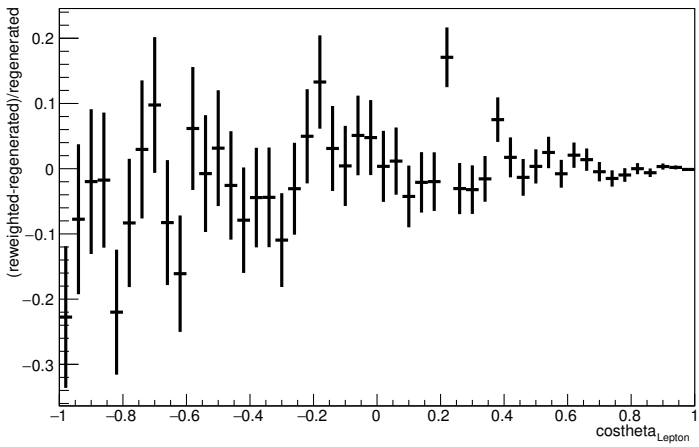

Energy plot: Leading Energy Pion: Neut Mode =11

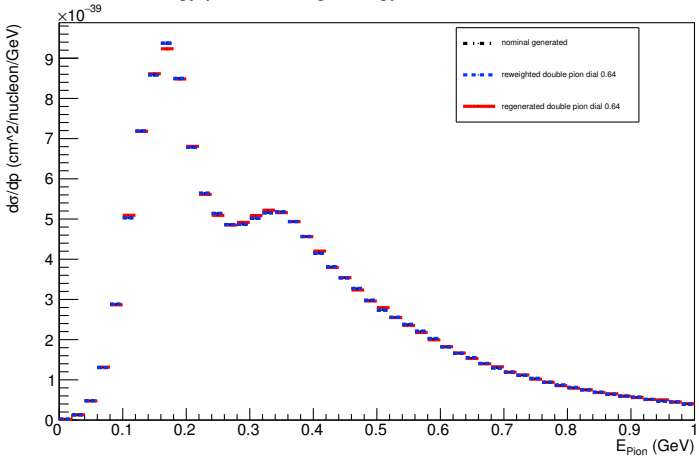

Energy plot: Every FSI Pion: Neut Mode =11

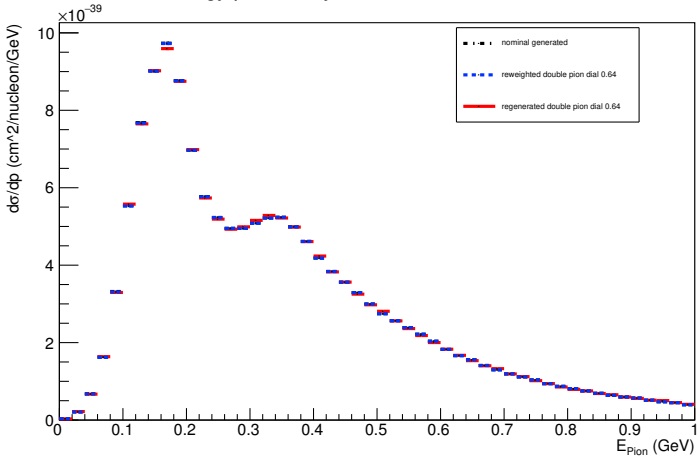

Energy plot: Leading Energy Pion: Neut Mode =11

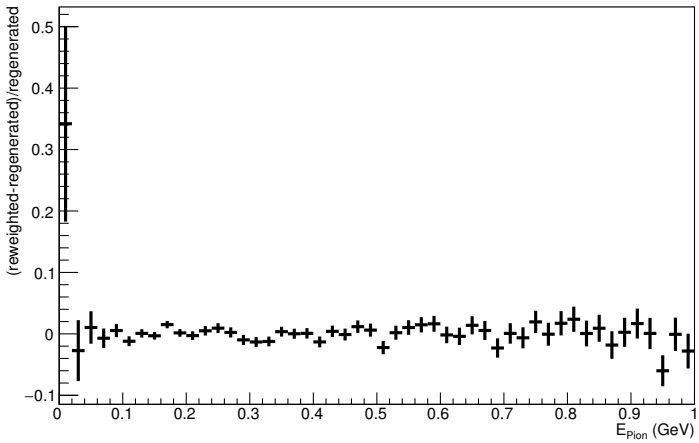

Energy plot: Every FSI Pion: Neut Mode =11

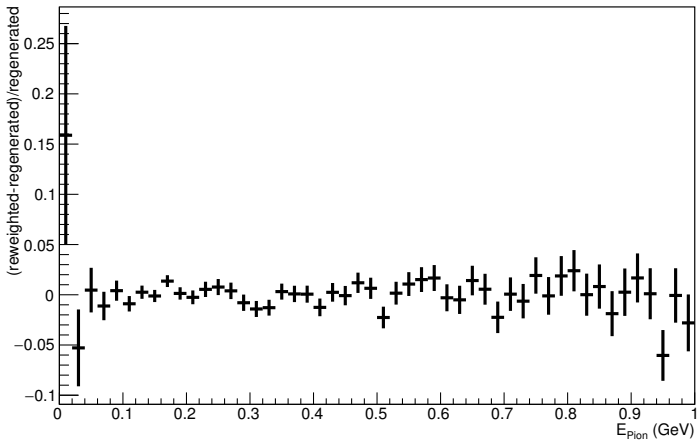

Angle plot: Leading Energy Pion: Neut Mode =11

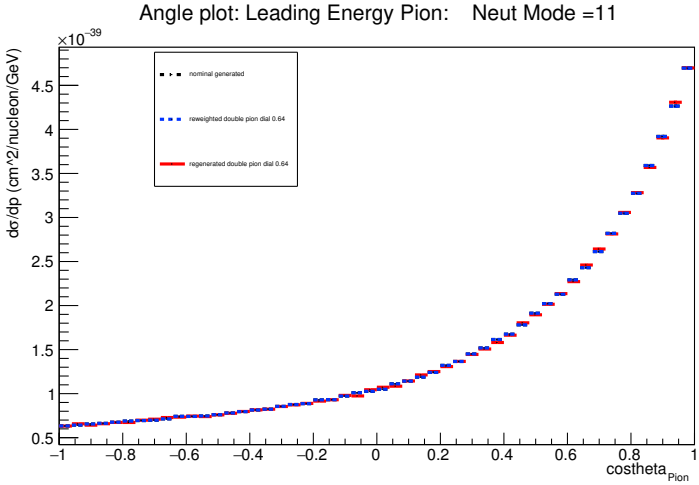

Angle plot: Every FSI Pion: Neut Mode =11

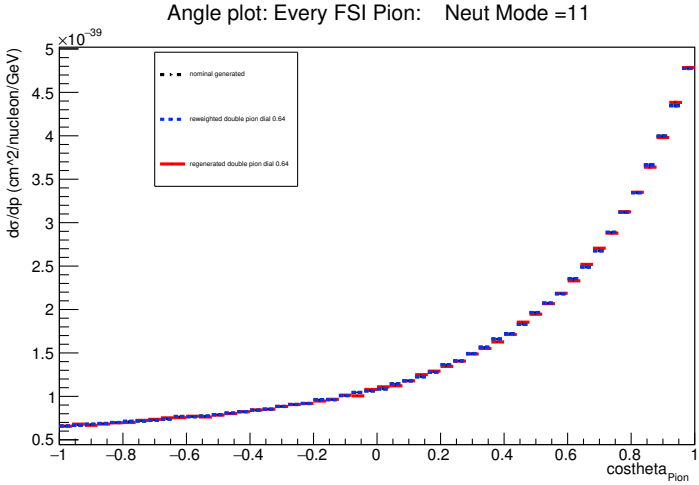

Angle plot: Leading Energy Pion: Neut Mode =11

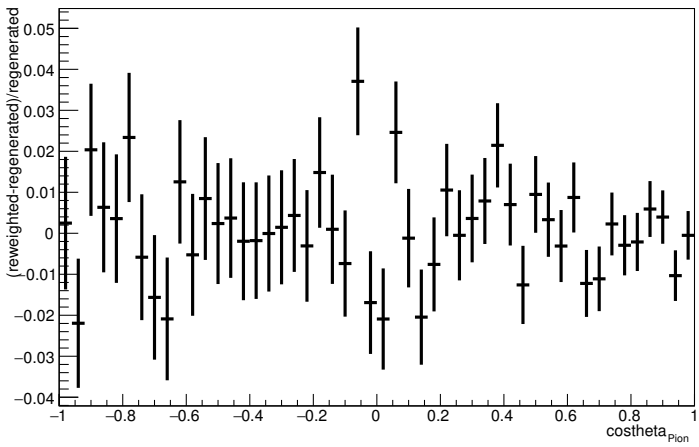

Angle plot: Every FSI Pion: Neut Mode =11

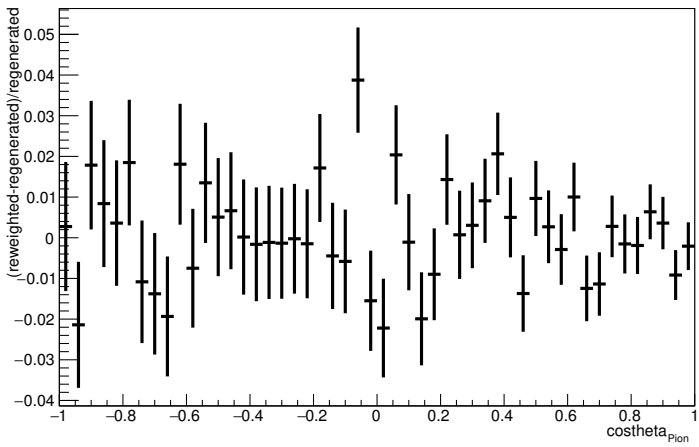

Bibliography

[1] S. Jones, T. Nonnenmacher, E. Atkin et al., "Off-Axis Characterisation of the CERN T10 Beam for low Momentum Proton Measurements with a High Pressure Gas Time Projection Chamber", *Instruments* **4** (Jul, 2020) 21, doi:10.3390/instruments4030021.

[2] F. Reines and C. Cowan Jr, "Detection of the free neutrino", *Physical Review* **92** (1953), no. 3, 830.

[3] W. Pauli, "Rapports du septieme conseil de physique solvay", *Brussels (Gauthier Villars, Paris, 1934)* (1933).

[4] E. Fermi and E. Segrè, "Zur theorie der hyperfeinstruktur", *Zeitschrift für Physik* **82** (1933), no. 11-12, 729–749.

[5] R. Davis Jr, "Solar neutrinos. ii. experimental", *Physical Review Letters* **12** (1964), no. 11, 303.

[6] G. Danby, J. M. Gaillard, K. Goulianos et al., "Observation of high-energy neutrino reactions and the existence of two kinds of neutrinos", *Physical Review Letters* **9** (1962), no. 1, 36.

[7] M. M. Block, "Neutrino interactions in the CERN heavy liquid bubble chamber", *Physical Review Letters* **12** (1964), no. 1, 281.

[8] M. L. Perl, G. Abrams, A. Boyarski et al., "Evidence for anomalous lepton production in e+- e- annihilation", *Physical Review Letters* **35** (1975), no. 22, 1489.

[9] K. Kodama, N. Ushida, C. Andreopoulos et al., "Observation of tau neutrino interactions", *Physics Letters B* **504** (2001), no. 3, 218–224.

[10] T. S. Electroweak, H. F. Groups, A. Collaboration et al., "Precision electroweak measurements on the Z resonance", *Physics Reports* **427** (2006), no. 5-6, 257–454.

[11] Y. Fukuda, T. Hayakawa, E. Ichihara et al., "Evidence for oscillation of atmospheric neutrinos", *Physical Review Letters* **81** (1998), no. 8, 1562.

[12] Q. R. Ahmad, R. Allen, T. Andersen et al., "Direct evidence for neutrino flavor transformation from neutral-current interactions in the Sudbury Neutrino Observatory", *Physical review letters* **89** (2002), no. 1, 011301.

[13] K. Eguchi, S. Enomoto, K. Furuno et al., "First results from KamLAND: evidence for reactor antineutrino disappearance", *Physical review letters* **90** (2003), no. 2, 021802.

[14] F. An, J. Bai, A. Balantekin et al., "Observation of electron-antineutrino disappearance at Daya Bay", *Physical Review Letters* **108** (2012), no. 17, 171803.

[15] B. Kayser, "B-meson and neutrino oscillation: a unified treatment", *arXiv preprint arXiv:1110.3047* (2011).

[16] R. Mohapatra, S. Antusch, K. Babu et al., "Theory of neutrinos: a white paper", *Reports on Progress in Physics* **70** (2007), no. 11, 1757.

[17] L. Wolfenstein, "Neutrino oscillations in matter", *Physical Review D* **17** (1978), no. 9, 2369.

[18] S. Mikheev and A. Y. Smirnov, "Resonance enhancement of oscillations in matter and solar neutrino spectroscopy", *Soviet Journal of Nuclear Physics* **42** (1985), no. 6, 913–917.

[19] A. Y. Smirnov, "The MSW effect and matter effects in neutrino oscillations", *Physica Scripta* **2005** (2005), no. T121, 57.

[20] T. DeYoung, "Latest results from IceCube and ANTARES", in *XXVIII International Conference on Neutrino Physics and Astrophysics*. 2018.

[21] R. Davis Jr, "Attempt to Detect the Antineutrinos from a Nuclear Reactor by the Cl 37 (ν, e-) A 37 Reaction", *Physical Review* **97** (1955), no. 3, 766.

[22] K. S. Hirata, T. Kajita, T. Kifune et al., "Observation of Boron-8 solar neutrinos in the kamiokande-ii detector", *Physical Review Letters* **63** (1989), no. 1, 16.

[23] B. T. Cleveland, T. Daily, R. Davis Jr et al., "Measurement of the solar electron neutrino flux with the Homestake chlorine detector", *The Astrophysical Journal* **496** (1998), no. 1, 505.

[24] J. Abdurashitov, T. Bowles, M. Cherry et al., "Measurement of the solar neutrino capture rate by SAGE and implications for neutrino oscillations in vacuum", *Physical Review Letters* **83** (1999), no. 23, 4686.

[25] W. Hampel, J. Handt, G. Heusser et al., "GALLEX solar neutrino observations: Results for GALLEX IV", *Physics Letters B* **447** (1999), no. 1-2, 127–133.

[26] A. Bellerive, J. Klein, A. McDonald et al., "The sudbury neutrino observatory", *Nuclear Physics B* **908** (2016) 30–51.

[27] K. A. Olive, "Review of particle physics", *Chinese physics C* **38** (2014), no. 9, 090001–090001.

[28] S. Moriyama, S.-K. Collaboration, et al., "New atmospheric and solar results from Super-Kamiokande", *Journal of Physics: Conference Series* **888** (2017), no. 1, 012005.

[29] F. Reines, M. Crouch, T. Jenkins et al., "Evidence for high-energy cosmic-ray neutrino interactions", *Physical Review Letters* **15** (1965), no. 9, 429.

[30] C. Achar, M. Menon, V. Narasimham et al., "Detection of muons produced by cosmic ray neutrinos deep underground", *Physics letters* **18** (1965) 196–199.

[31] K. Hirata, A. Mann, M. Takita et al., "Experimental study of the atmospheric neutrino flux", *Phys. Lett.* **205** (1988), no. UPR-0149E, 416.

[32] S.-K. Collaboration et al., "Y. Fukuda et al., Evidence for oscillation of atmospheric neutrinos", *Phys. Rev. Lett* **81** (1998), no. 8, 1562–1567.

[33] T. Kajita, "Atmospheric neutrinos", *New Journal of Physics* **6** (2004), no. 1, 194.

[34] B. Aharmim, B. Cleveland, X. Dai et al., "High sensitivity measurement of 224Ra and 226Ra in water with an improved hydrous titanium oxide technique at the Sudbury Neutrino Observatory", *Nuclear Instruments and Methods in Physics Research Section A: Accelerators, Spectrometers, Detectors and Associated Equipment* **604** (2009), no. 3, 531–535.

[35] K. Abe, C. Bronner, Y. Haga et al., "Atmospheric neutrino oscillation analysis with external constraints in Super-Kamiokande I-IV", *Physical Review D* **97** (2018), no. 7, 072001.

[36] A. Albert, M. André, M. Anghinolfi et al., "Search for high-energy neutrinos from binary neutron star merger GW170817 with ANTARES, IceCube, and the Pierre Auger Observatory", *arXiv preprint arXiv:1710.05839* (2017).

[37] M. Aartsen, M. Ackermann, J. Adams et al., "Measurement of atmospheric neutrino oscillations at 6–56 GeV with IceCube DeepCore", *Physical review letters* **120** (2018), no. 7, 071801.

[38] M. H. Ahn, E. Aliu, S. Andringa et al., "Measurement of neutrino oscillation by the K2K experiment", *Physical Review D* **74** (Oct, 2006) doi:10.1103/physrevd.74.072003.

[39] D. Michael, P. Adamson, T. Alexopoulos et al., "Observation of muon neutrino disappearance with the MINOS detectors in the NuMI neutrino beam", *Physical Review Letters* **97** (2006), no. 19, 191801.

[40] K. Abe, N. Abgrall, H. Aihara et al., "The T2K experiment", *Nuclear Instruments and Methods in Physics Research Section A: Accelerators, Spectrometers, Detectors and Associated Equipment* **659** (2011), no. 1, 106–135.

[41] J. Bian, "The NOvA experiment: overview and status", *arXiv preprint arXiv:1309.7898* (2013).

[42] K. Abe, J. Amey, C. Andreopoulos et al., "Combined analysis of neutrino and antineutrino oscillations at T2K", *Physical review letters* **118** (2017), no. 15, 151801.

[43] "KEK proposal for the T2K Collaboration 2001". http://neutrino.kek.jp/jhfnu/loi/loi.v2.030528.pdf.

[44] "KEK proposal for the T2K Collaboration 2006". http://j-parc.jp/researcher/Hadron/en/pac_0606/pdf/p11-Nishikawa.pdf.

[45] G. Battistoni, S. Muraro, P. Sala et al., "FLUKA: a multi-particle transport code", in *Proceedings of the hadronic shower simulation workshop*, volume 896, pp. 31–49, AIP. 2006.

[46] R. Brun, L. Urban, F. Carminati et al., "GEANT: detector description and simulation tool", technical report, CERN, (1993).

[47] C. Zeitnitz and T. Gabriel, "The GEANT-CALOR interface and benchmark calculations of ZEUS test calorimeters", *Nuclear Instruments and Methods in Physics Research Section A: Accelerators, Spectrometers, Detectors and Associated Equipment* **349** (1994), no. 1, 106–111.

[48] A. Laszlo, N. Collaboration, et al., "Na61/Shine at the CERN SPS", *arXiv preprint arXiv:0709.1867* (2007).

[49] K. Abe, J. Amey, C. Andreopoulos et al., "Characterization of nuclear effects in muon-neutrino scattering on hydrocarbon with a measurement of final-state kinematics and correlations in charged-current pionless interactions at T2K", *Physical Review D* **98** (2018), no. 3, 032003.

[50] T. N. F. Collaboration et al., "The T2K fine-grained detectors", *arXiv preprint arXiv:1204.3666* (2012).

[51] K. Abe, C. Andreopoulos, M. Antonova et al., "Measurement of the muon neutrino inclusive charged-current cross section in the energy range of 1–3 GeV with the T2K INGRID detector", *Physical Review D* **93** (2016), no. 7, 072002.

[52] K. Abe, N. Abgrall, Y. Ajima et al., "Measurements of the T2K neutrino beam properties using the INGRID on-axis near detector", *Nuclear Instruments and Methods in Physics Research Section A: Accelerators, Spectrometers, Detectors and Associated Equipment* **694** (2012) 211–223.

[53] "Super Kamiokande official website". `http://www-sk.icrr.u-tokyo.ac.jp/sk/index-e.html`.

[54] H. Sekiya, "The Super Kamionade Gadolinium Project", *Journal of Physics: Conference Series* **1342** (2020), no. 1, 012044.

[55] C. Simpson, K. Abe, C. Bronner et al., "Sensitivity of Super-Kamiokande with Gadolinium to Low Energy Antineutrinos from Pre-supernova Emission", *The Astrophysical Journal* **885** (2019), no. 2, 133.

[56] C. Xu, S.-K. Collaboration, et al., "Current status of SK-Gd project and EGADS", in *Journal of Physics Conference Series*, volume 718, p. 062070. 2016.

[57] Y. Hayato, "A neutrino interaction simulation program library NEUT", *Acta Phys. Polon.* **40** (2009) 2477–2489.

[58] D. R. Nygren, "The time projection chamber",.

[59] B. Abi, R. Acciarri, M. A. Acero et al., "Deep Underground Neutrino Experiment (DUNE), Far Detector Technical Design Report, Volume II DUNE Physics", *arXiv preprint arXiv:2002.03005* (2020).

[60] K. Abe, R. Akutsu, A. Ali et al., "Constraint on the matter-antimatter symmetry-violating phase in neutrino oscillations", *arXiv preprint arXiv:1910.03887* (2019).

[61] L. Alvarez-Ruso, M. Sajjad Athar, M. Barbaro et al., "NuSTEC White Paper: Status and challenges of neutrino nucleus scattering", *Progress in Particle and Nuclear Physics* **100** (May, 2018) 1–68, doi:10.1016/j.ppnp.2018.01.006.

[62] J. Raaf et al., "DUNE HPgTPC White Paper",. forthcoming.

[63] D. H. working group et al., "High-Pressure Argon gas TPC Option for the DUNE Near Detector", *DUNE doc* **6652** (2018).

[64] A. Rafique, "Measurement of Reconstructed Charged Particle Multiplicities of Neutrino Interactions in MicroBooNE", *arXiv preprint arXiv:1709.00146* (2017).

[65] HPTPC Collaboration, "Proposal to Measure Hadron Scattering with a Gaseous High Pressure TPC for Neutrino Oscillation Measurements", Technical Report CERN-SPSC-2017-030. SPSC-P-355, CERN, Geneva, (Sep, 2017).

[66] A. Deisting et al., "Commissioning and beam test of a high pressure time projection chamber", *Nuclear Instruments and Methods in Physics Research Section A: Accelerators, Spectrometers, Detectors and Associated Equipment* **958** (2020) 162153.

[67] A. Deisting et al., "A High Pressure Time Projection Chamber with Optical Readout", (2020). In Preparation.

[68] H. Ritchie-Yates, "Commissioning a New Particle Detector Technology: The High Pressure Time Projection Chamber". PhD thesis, Royal Holloway University of London at Egham (UK), Egham (UK), March, 2018. Masters Thesis.

[69] A. Korzenev et al., "Plastic scintillator detector with the readout based on an array of large-area SiPMs for the ND280/T2K upgrade and SHiP experiments", in *International Workshop on New Photon Detectors (PD18) Tokyo, Japan, November 27-29, 2018*. 2019. arXiv:1901.07785.

[70] "Eljen Technology - EJ-200, EJ-204, EJ-208, EJ-212", (accessed August, 2019). http://https://eljentechnology.com/products/plastic-scintillators/ej-200-ej-204-ej-208-ej-212.

[71] "Hamamatsu Photonics K.K.", (accessed March, 2019). http://www.hamamatsu.com.

[72] C. Betancourt et al., "Application of large area SiPMs for the readout of a plastic scintillator based timing detector", *JINST* **12** (2017), no. 11, P11023, doi:10.1088/1748-0221/12/11/P11023, arXiv:1709.08972.

[73] E. Delagnes et al., "The SAMPIC Waveform and Time to Digital Converter", in *2014 IEEE Nuclear Science Symposium (2014 NSS/MIC)*. Seattle, US, Nov, 2014. Sce Electronique.

[74] C. Betancourt, A. Dätwyler, N. Serra et al., "A timing detector for the SHiP experiment", *Nuclear Instruments and Methods in Physics Research Section A: Accelerators, Spectrometers, Detectors and Associated Equipment* **924** (2019) 369–372.

[75] "NuviaTech Instruments", (accessed July, 2019). http://www.nuviatech-instruments.com.

[76] C. H. Llewellyn Smith, "Neutrino reactions at accelerator energies", *Phys. Rept.* **3** (1971), no. SLAC-PUB-0958, 261–379.

[77] D. Rein and L. M. Sehgal, "Neutrino-excitation of baryon resonances and single pion production", *Annals of Physics* **133** (1981), no. 1, 79–153.

[78] O. Lalakulich, T. Leitner, O. Buss et al., "One pion production in neutrino reactions: Including nonresonant background", *Physical Review D* **82** (2010), no. 9, 093001.

[79] E. Hernandez, J. Nieves, and M. Valverde, "Weak pion production off the nucleon", *Physical Review D* **76** (2007), no. 3, 033005.

[80] U. Mosel and K. Gallmeister, "Muon-neutrino-induced charged-current pion production on nuclei", *Physical Review C* **96** (2017), no. 1, 015503.

[81] V. Lyubushkin, B. Popov, J. Kim et al., "A study of quasi-elastic muon neutrino and antineutrino scattering in the NOMAD experiment", *The European Physical Journal C* **63** (2009), no. 3, 355–381.

[82] A. Aguilar-Arevalo, C. Anderson, A. Bazarko et al., "Measurement of neutrino-induced charged-current charged pion production cross sections on mineral oil at E ν 1 GeV", *Physical Review D* **83** (2011), no. 5, 052007.

[83] M. Guthrie, R. Alsmiller Jr, and H. Bertini, "Calculation of the capture of negative pions in light elements and comparison with experiments pertaining to cancer radiotherapy", *Nuclear Instruments and Methods* **66** (1968), no. 1, 29–36.

[84] H. W. Bertini, "Intranuclear-cascade calculation of the secondary nucleon spectra from nucleon-nucleus interactions in the energy range 340 to 2900 MeV and comparisons with experiment", *Physical Review* **188** (1969), no. 4, 1711.

[85] H. W. Bertini and M. P. Guthrie, "News item results from medium-energy intranuclear-cascade calculation", *Nuclear Physics A* **169** (1971), no. 3, 670–672.

[86] L. Salcedo, E. Oset, M. Vicente-Vacas et al., "Computer simulation of inclusive pion nuclear reactions", *Nuclear Physics A* **484** (1988), no. 3-4, 557–592.

[87] P. D. Group et al., "K. Nakamura et al", *J. Phys. G* **37** (2010) 260.

[88] HPTPC Collaboration, "Proposal to Measure Hadron Scattering with a Gaseous High Pressure TPC for Neutrino Oscillation Measurements",.

[89] H. Wellisch and D. Axen, "Total reaction cross section calculations in proton-nucleus scattering", *Physical Review C* **54** (1996), no. 3, 1329.

[90] R. F. Carlson, "Proton-Nucleus Total Reaction Cross Sections and Total Cross Sections Up to 1 GeV", *Atom. Data Nucl. Data Tabl.* **63** (1996) 93–116, doi:10.1006/adnd.1996.0010.

[91] D. J. Simon, L. Durieu, K. Bätzner et al., "Secondary beams for tests in the PS East experimental area", Technical Report PS-PA-EP-Note-88-26, CERN, Geneva, (Aug, 1988).

List of figures

2.1. Interacton diagrams for different neutrino flavours with electrons in matter. The difference in diagrams corresponding to different matter effects for electron type neutrinos and antineutrinos is highlighted. . . 7
2.2. Overview of neutrino experiments, distinguished by characteristic baseline and neutrino energy. Plot taken from [20]. 8
2.3. Flux from different solar fusion processes. The thresholds of different experiments are shown. Figure taken from [26]. 9
2.4. Historic flavour ratios of atmospheric neutrino experiments. Figure taken from [33]. 11
2.5. The state of measurements of $|\Delta m^2_{23}|$ and $sin^2(2\theta_{23})$ by five neutrino experiments in 2017. Plot taken from [42]. 13

3.1. Schematic view of the T2K experiment. 15
3.2. Schematic view of T2K beamline. Top: top-view of the primary and secondary beamlines. Bottom: side view of the secondary beamline. . 17
3.3. Protons on target and beam power for T2K runs 1-10. 18
3.4. Diagram of the subdetectors that comprise ND280. 19
3.5. Deposited energy against range for particles stopping in the first FGD. The curves show the simulated expectations for different particle types - above an energy momentum threshold, protons may be distinguished from pions and muons. Figure taken from [50]. 21
3.6. Reconstruction efficiencies, following selection steps, as a function of true proton kinematics, as predicted by NEUT 5.3.2 and GENIE 2.8.0. Left: momentum distribution. Right: angular distribution. The square points show the efficiency prediction before any phase-space constraints whilst the circular points have had additional proton and muon kinematic constraints applied. The grey areas shows the shape of the pionless charged current cross section predicted by NEUT 5.3.2.2. Figure taken from [49]. 22

3.7. The INGRID detector used for neutrino beam monitoring. Left: the downstream beam view of the full detector. Right: an individual INGRID module. 22

3.8. The SK detector. Left: schematic of the detector within the Mozumi mine. Right: schematic of a neutrino event within SK. The neutrino enters the inner detector, interacts with the water, and the resulting ring of photons is detected by the surrounding PMTs. Diagram taken from [53]. 24

3.9. Reconstructed images from SK. Left: a muon-like ring. Right: an electron-like ring. The muon-like ring is more sharply focussed. The overall shape of the plot is the cylindrical shape of the detector, represented in two dimensions. Figure taken from [40]. 25

3.10. Predicted proton energy spectra from GENIE, NEUT, and NuWro [62]. Left: the full energy spectrum up to 1 GeV. Right: the specific low momentum region of interest. The figure uses the Long Baseline Neutrino Facility (LBNF) simulation for DUNE's beam energy and flux. The dashed vertical line indicates the expected proton automated-reconstruction/ID threshold in liquid argon, and the solid vertical line shows the same for gaseous argon at 10 atm. These plots are taken from [63]. 27

3.11. Schematic diagram of the HPTPC. Left: the plane of the HPTPC parallel to the drift field E. Right: the plane perpendicular to E. A particle scattering on a gas atom at time t_0 ejects a charged particle from the nucleus, in turn ionising other gas atoms (shown as circles, left) along its trajectory. These ionisation electrons are moved by E toward the anode meshes at t_1, and are amplified at t_2. Photons produced during the amplification (shown as thick lines, left) are then imaged by cameras, providing a 2D projection of the interaction as seen, right. Additionally, the voltage changes on the meshes during this avalanche are observed. Figure taken from [66]. 29

3.12. CAD model of the HPTPC pressure vessel. Left: the feed-through side. Middle: the main body. Right: the door side which houses the cameras. Figure taken from [67]. 30

3.13. Left: the field cage before insertion into the pressure vessel. Right: the field cage after insertion. The right hand picture is photographed through the high-transparency cathode mesh in the direction of the amplification region, showing the full TPC. Figure taken from [67]. . . 31
3.14. Circuit diagram of the high voltage system. Meshes are provided ($V_{\text{anode}i}$) while the signal is decoupled from the meshes ($S_{\text{anode}i}$). Bias boxes are used with $B_{\text{anode}i}$, which feature a protection and filtering circuit consisting of a bias resistor ($R_{\text{bias}} = 200\ \text{M}\Omega$), filter capacitor ($C_{\text{filter}} = 10$ nF) and input resistor at the detector input (R_{in}). Figure taken from [67]. 35
3.15. Left: drawing of the optical flange with the camera mount.The thickness of the quartz is required to ensure that the assembly can withstand the pressure difference between vessel and ambient pressure. Right: the full assembly including a flange is shown. Figure taken from [67]. . . . 36
3.16. The S1 and S2 beam counters. Events were determined by coincidence of signals in the beam counters and recorded by the DAQ systems. Figure taken from [67]. 38
3.17. Timing spread of *S1* hits. The time is calculated from the mean of the hit times in each of the four PMTs. 39
3.18. Photo illustrating the *S1* and *S2* counters and the stand with four acrylic moderator blocks between them. 40
3.19. Sketch of the *S3* wall [69]. Left: front view. Right: rotated view. 40
3.20. Reconstructed spatial distribution of hits observed in *S3*. In this case a timing cut and an amplitude cut have been applied to select only those hits thought to come from protons. Left: data taken without moderator blocks in the beamline. Right: data taken with 4 moderator blocks in the beamline. 42
3.21. Difference in signal arrival time PMTs at each end of a bar as measured using a ^{90}Sr source placed 64 cm from one end of the bar. 43
3.22. Schematic of the *S4* wall. Left: front facing view. Right: rotated view. The staggering of the scintillator bars and PMTs is seen clearly in the rotated view. 43

4.1. Feynman diagrams for three charged-current scattering channels. Left: quasi elastic scattering. Middle: resonant pion production. Right: deep inelastic scattering. 46

4.2. Schematic diagram of a two particle two hole interaction. The neutrino scatters not just off one bound nucleon, but off two in combination. . . 47

5.1. Figure showing general state of measurements in the low momentum proton region. A number of data points have been collected for Carbon, but measurements in the region are sparse for other elements. The applied curves show the semi-empirical Wellisch and Axen model [89] applied to the data points [90]. 54
5.2. Figure showing ToF spectrum measured at the T10 beamline, at an energy of 0.9 GeV. A Gaussian is fitted to each peak in red. Figure taken from [65]. 56
5.3. Particle rates at the T10 beamline measured in 2016. The proton and pion rates are shown at multiple different beam energies. For clarity, the pion rate has been scaled by a factor of 0.1. Figure taken from [65]. 57
5.4. Composition of simulated particles arriving at the active region of the TPC as a function of off-axis angle. Left: Number of particles of each type per spill. Right: Ratio of pions to protons. 58
5.5. Energy of simulated protons reaching the active TPC region as a function of off axis angle, on a log scale. 59
5.6. Momentum profile of different simulated particle species reaching the TPC active region in a spill. Left: Directly on the beam axis. Right: 4° off the beam axis. 59
5.7. Plan view diagram of the HPTPC beam test configuration at the CERN T10 area. 60
5.8. The full HPTPC beam test set up. Left: the downstream section of the set up including the *S3*, *S4* detectors and HPTPC. Right: the *S1* and *S2* counters and the stand with four acrylic moderator blocks further upstream. 61
5.9. Angular position of the detectors the T10 beamline. The origin in this view is at the centre of *S1*; the true centre of the steered beam is at $+1^\circ$ in θ and 0° in ϕ. 63

6.1. Calculated time of flight between *S1* and *S3* for different particle species as a function of particle momentum. 66
6.2. Calculated time of flight between *S2* and *S4* for different particle species as a function of particle momentum. 66
6.3. *S3* time of flight spectra for different moderator block configurations. . 67

6.4. Measurements of the unmoderated and unbent T10 beam over a baseline of 10.8 m for a selected beam momentum of 0.8 GeV/c. Measurements are made in the *S3* detector. The peak between 50 ns and 60 ns is produced by protons. Left: Time of flight spectrum. Right: Measured kinetic energy of protons. 68

6.5. Reconstructed mass spectrum of the beam contents with 0 moderator blocks calculated from the upstream time of flight wall. The time difference between *S3* and *S1* was used to calculate mass. Red arrows show the predicted mass squared of particles given a momentum of 0.8 GeV/c. The inset figure shows the area around 0 mass in greater detail. 70

6.6. Examples of SiPM signal amplitude against the time of flight from *S1* to *S3* for different numbers of moderator blocks from 0 to 3. The voltage recorded in the SiPM is labelled as A1. The red dashed line shows the amplitude cut used for that SiPM. The population corresponding to the enclosed areas in red dashed rectangles is that of protons. The population corresponding to the enclosed areas in green dashed rectangles is that of MIPs. 71

6.7. *S4* time of flight spectra for different numbers of moderator blocks. In the case of each configuration, a flat background has been fit to and subtracted from the data. Furthermore, a correction has been made for the differing efficiencies of the various bars and for the variation in efficiency as a function of position along the bar. As in the case of *S3*, a proton peak and a MIP peak are observed. 71

6.8. Reconstructed mass spectrum for the data taken without moderator blocks calculated from the downstream time of flight wall. The spectrum was determined using the time difference between *S4* and *S2*. Vertical arrows show the calculated predicted position of particles. . . 72

6.9. Relative detection efficiency of *S4* as a function of bar number and position along each bar calculated from cosmic ray data. The efficiency of bar 10 is very low, so it was excluded from the data analysis. 73

6.10. Time of flight spectrum observed in *S4*: a combined signal and background function (red) has been fit to the data. 74

6.11. Proton momentum spectrum as measured in *S3*. Left: all protons. Right: the subset of protons passing through the HPTPC drift volume. 75

6.12. Proton kinetic energy spectrum as measured in *S3* for only those protons passing through the HPTPC drift volume. 76

6.13. Distribution of hits in *S3*. The hits are measured from *S1* and shown as a function of the horizontal off-axis angle, and for varying numbers of moderator blocks. No coincident hit in *S2* is required. Left: minimum ionizing particles. Right: protons. 77

6.14. Proton-MIP ratio in *S3* as measured from *S1*, as a function of off-axis angle and for varying numbers of moderator blocks. Left: horizontal angle. Right: vertical angle. The TPC spans horizontal angles 0.4–2.6° and vertical angles -2.6–+2.6° off the nominal beam axis. 78

6.15. Distribution of hits in *S4* as a function of the horizontal off-axis angle and the number of moderator blocks. Left: minimum ionizing particles. Right: protons. 79

6.16. Proton-MIP ratio in *S4* as a function of off-axis angle and for varying numbers of moderator blocks. Left: horizontal off-axis angle. Right: vertical off-axis angle. 79

6.17. Initial momentum profile of the simulation of protons at the *S3* wall in the direction of the TPC. 80

6.18. Energy profile of simulated protons that reach *S4* with a kinetic energy greater than the detection threshold of 10 MeV. 81

6.19. Kinematic profiles of simulated protons reaching the active region of the TPC. Left: momentum profile. Right: energy profile. 83

6.20. Cross-sectional view of the TPC prototype. The locations of the ^{241}Am sources are marked by circles. Figure taken from [67]. 84

6.21. Light yield from the five calibration sources imaged by the CCD cameras. The intensity of the image in the top left frame differs from the other three frames, because the corresponding camera has a different conversion gain. The ^{241}Am sources are visible against the background noise in the top left, top right, and bottom left cameras. In the bottom right image, where bias subtraction was not performed, the sources are not visible. Figure taken from [67]. 86

6.22. Effect of the clustering algorithm on light from a single ^{241}Am source. Left: the image prior to application of the clustering algorithm. Right: the result of the algorithm's application. Figure taken from [67]. 87

7.1. Schematic of the nucleon cascade. The movement of the nucleon through the nucleus is divided into small steps, at which survival or other interactions may occur. In the schematic, s represents a survival, qe represents a quasi-elastic interaction, and 1pi represents a single pion production. The individual interaction probabilities are governed by the multiplicative nucleon FSI factors. 90

7.2. Simulated interaction cross-sections as a function of true initial nucleon momentum from neutrino interactions on carbon. The reactive cross-section is defined as the total minus the quasi-elastic cross-section. . . 91

7.3. Simulated interaction cross-sections as a function of true outgoing nucleon momentum from neutrino interactions on carbon for a total interaction dial value of 1.5. 92

7.4. Simulated interaction cross-sections as a function of true outgoing nucleon momentum from neutrino interactions on carbon. For a total interaction dial value of 0.5. 93

7.5. Effect of different variations of the dial governing elastic interactions on the cross-sections of the total (blue), quasi-elastic (red), reactive (orange), single pion (cyan), and double pion (green) channels. 94

7.6. Effect of different variations of the dial governing single pion production on the cross-sections of the total (blue), quasi-elastic (red), reactive (orange), single pion (cyan), and double pion (green) channels. 95

7.7. Effect of different variations of the dial governing double pion production on the cross-sections of the total (blue), quasi-elastic (red), reactive (orange), single pion (cyan), and double pion (green) channels. 96

7.8. Schematic of the reweighted nucleon cascade. In this example, the value of the dial governing quasi-elastic interactions has been increased, while the others have been held constant. The total probability of the cascade is recalculated. 98

7.9. Energy distribution for reweighting the total interaction dial to values of 1.44, top left, and 0.64 top right. Only the leading order final state nucleon is shown. The distribution generated with nominal dial values is shown in black, the distribution reweighted to changed dial values in blue, and the regenerated distribution with those dial values in red. Statistical errors are shown as a vertical error band, but in the case of some bins are too small to be visible due to the large number of events contributing to the data points. Bottom left and right: residual plots for these dial variations are shown. 100

7.10. Angular distribution for reweighting the total interaction dial to values of 1.44, top left, and 0.64, top right. Only the leading order final state nucleon is shown. The distribution generated with nominal dial values is shown in black, the distribution reweighted to changed dial values in blue, and the regenerated distribution with those dial values in red. Statistical errors are shown as a vertical error band, but in the case of some bins are too small to be visible due to the large number of events contributing to the data points. Bottom left and right: residual plots for these dial variations are shown. 101

7.11. Energy distribution for reweighting the total interaction dial to values of 1.44, top left, and 0.64, top right. All final state nucleons are included. The distribution generated with nominal dial values is shown in black, the distribution reweighted to changed dial values in blue, and the regenerated distribution with those dial values in red. Statistical errors are shown as a vertical error band, but in the case of some bins are too small to be visible due to the large number of events contributing to the data points. Bottom left and right: residual plots for these dial variations are shown. 102

7.12. Angular distribution for reweighting the total interaction dial to values of 1.44, top left, and 0.64, top right. All final state nucleons are included. The distribution generated with nominal dial values is shown in black, the distribution reweighted to changed dial values in blue, and the regenerated distribution with those dial values in red. Statistical errors are shown as a vertical error band, but in the case of some bins are too small to be visible due to the large number of events contributing to the data points. Bottom left and right: residual plots for these dial variations are shown. 103

7.13. Lepton energy distribution for reweighting the total interaction dial to values of 1.44, top left, and 0.64, top right. All final state leptons are included. The distribution generated with nominal dial values is shown in black, the distribution reweighted to changed dial values in blue, and the regenerated distribution with those dial values in red. Statistical errors are shown as a vertical error band, but in the case of some bins are too small to be visible due to the large number of events contributing to the data points. Bottom left and right: residual plots for these dial variations are shown. 105
7.14. Energy distribution for reweighting the total interaction dial to an extreme value of 4.00. Only the leading order final state nucleon is shown. The distribution generated with nominal dial values is shown in black, the distribution reweighted to changed dial values in blue, and the regenerated distribution with those dial values in red. Statistical errors are shown as a vertical error band, but in the case of some bins are too small to be visible due to the large number of events contributing to the data points. 107
7.15. Distribution of weights for dial variations. Left: small total dial variation of 1.44. Right: Large total dial variation of 4.00. 108

List of tables

5.1. Total number of spills recorded for each moderator block configuration included in this paper. 55
5.2. Angular positions of detector elements within the T10 beamline as measured with respect to *S1*. 62
5.3. Relative distances between centres of detectors in the T10 beamline. US and DS refer to upstream and downstream, respectively. 63

6.1. Background rates for the time of flight spectra measured in *S4*. To convert these to the number of expected background events in a spill, the rate is multiplied by the size of the timing window for either MIPs or protons. 74
6.2. Ratio of protons reaching *S4* to protons reaching *S3* for changing moderator block number in simulation and data. The combined statistical and systematic errors are shown. 81
6.3. Breakdown of systematic errors for data and simulation. The values shown are the percentage error on the *S4* proton count with the exception of the uncertainty on the efficiency of *S3*, which is the percentage error in the *S3* proton count. All uncertainties are treated as uncorrelated. $n_{S4,\ MC}$ refers to the number of protons reaching *S4* in simulations 83

7.1. Names and brief descriptions of each of the four nucleon FSI scaling factors 90
7.2. Time taken for reweighting nucleon dials vs regeneration. 100,000 events were generated and reweighted. Time for the full generation, the subset of time spent just in the nucleon cascade, and for reweighting are shown. 109

List of Acronyms

2p2h "two particle, two hole"

ANTARES a Neutrino Telescope and Abyss environmental RESearch project

CCD Charge-Coupled Device

CCQE Charged current quasi-elastic

CERN the European Organization for Nuclear Research

CP Charge Parity

DAQ Data Acquisition

DUNE Deep Underground Neutrino Experiment

DsECal sampling electromagnetic calorimeter

ECal electromagnetic calorimeter

FGD fine grained detector

FLUKA FLUktuierende KAskade

FSI Final State Interactions

GALLEX Gallium Experiment

GEANT3 GEometry ANd Tracking - 3

HPTPC High Pressure gaseous Time Projection Chamber

HV high voltage

ID Inner Detector

IMB Irvine-Michigan-Brookhaven

INGRID Interactive Neutrino GRID

J-PARC Japan Proton Accelerator Research Complex

K2K KEK to Kamioka

KamLAND Kamioka Liquid Scintillator Antineutrino Detector

LEP Large Electron-Positron collider

LINAC linear accelerator

MC Monte Carlo

MINOS Main Injector Neutrino Oscillation Search

MIP minimum ionizing particle

MSW Mikheyev-Smirnov-Wolfenstein

NA61/SHINE NA61/SPS Heavy Ion and Neutrino Experiment

NOvA NuMI Off-Axis ν_e Appearance

OD Outer Detector

OTR optical transition radiation

PMNS Pontecorvo-Maki-Nakagawa-Sakata

PMT photomultiplier tube

POT protons on target

PS Power Supply

QE Quantum Efficiency

RCS rapid-cycling synchrotron

SAGE Soviet-American Gallium Experiment

SHiP Search for Hidden Particles

SK Super Kamiokande

SLAC Stanford Linear Accelerator

SMRD side muon range detector

SNO Sudbury Neutrino Observatory

SciBooNE SciBar Booster Neutrino Experiment

T2K Tokai to Kamioka

TPC time projection chamber